Recurrence Plot Techniques for the Investigation of Recurring Phenomena in the System Earth

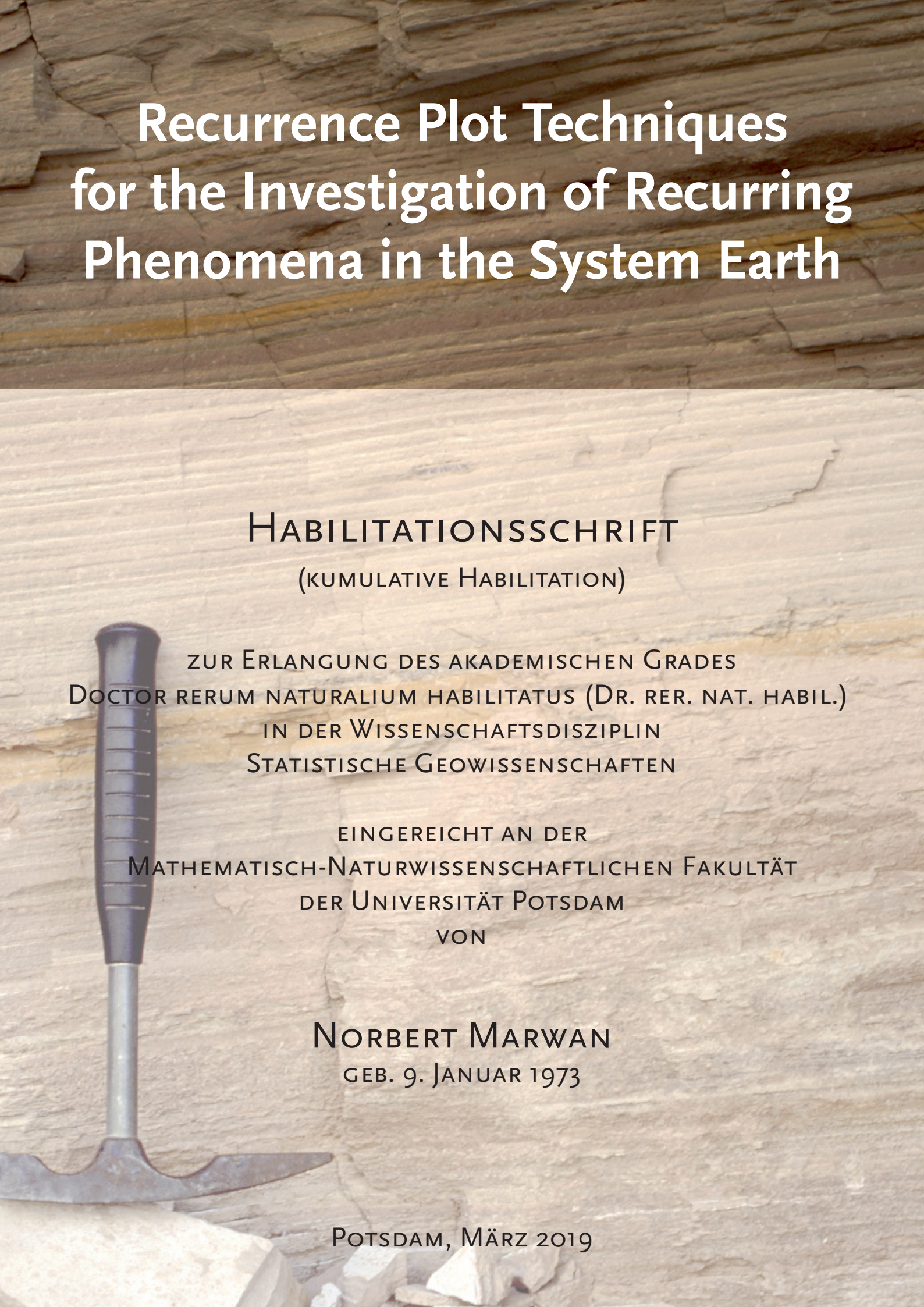

Habilitationsschrift

(kumulative Habilitation)

zur Erlangung des akademischen Grades
Doctor rerum naturalium habilitatus (Dr. rer. nat. habil.)
in der Wissenschaftsdisziplin
Statistische Geowissenschaften

eingereicht an der
Mathematisch-Naturwissenschaftlichen Fakultät
der Universität Potsdam
von

Norbert Marwan
geb. 9. Januar 1973

Potsdam, März 2019

Published online at the
Institutional Repository of the University of Potsdam:
https://doi.org/10.25932/publishup-44197
https://nbn-resolving.org/urn:nbn:de:kobv:517-opus4-441973

Recurrence Plot Techniques for the Investigation of Recurring Phenomena in the System Earth

Norbert Marwan

Potsdam, March 2019
ISBN 978-3-00-064508-2

Abstract

The habilitation deals with the numerical analysis of the recurrence properties of geological and climatic processes. The recurrence of states of dynamical processes can be analysed with recurrence plots and various recurrence quantification options. In the present work, the meaning of the structures and information contained in recurrence plots are examined and described. New developments have led to extensions that can be used to describe the recurring patterns in both space and time. Other important developments include recurrence plot-based approaches to identify abrupt changes in the system's dynamics, to detect and investigate external influences on the dynamics of a system, the couplings between different systems, as well as a combination of recurrence plots with the methodology of complex networks. Typical problems in geoscientific data analysis, such as irregular sampling and uncertainties, are tackled by specific modifications and additions. The development of a significance test allows the statistical evaluation of quantitative recurrence analysis, especially for the identification of dynamical transitions. Finally, an overview of typical pitfalls that can occur when applying recurrence-based methods is given and guidelines on how to avoid such pitfalls are discussed. In addition to the methodological aspects, the application potential especially for geoscientific research questions is discussed, such as the identification and analysis of transitions in past climates, the study of the influence of external factors to ecological or climatic systems, or the analysis of landuse dynamics based on remote sensing data.

Zusammenfassung

Die Habilitation beschäftigt sich mit der Analyse der Wiederkehreigenschaften geologischer und klimatischer Prozesse. Die Wiederkehr von Zuständen dynamischer Prozesses kann mit *recurrence plots* und deren verschiedenen Quantifizierungsmöglichkeiten untersucht werden. In der Arbeit wird die Bedeutung der Strukturen und Informationen, die in *recurrence plots* enthalten sind, untersucht und beschrieben. Neue Entwicklungen führen zu Erweiterungen, die zur Beschreibung räumlich und raumzeitlich wiederkehrender Muster genutzt werden können. Weitere wichtige Entwicklungen umfassen Erweiterungen zur Identifizierung von abrupten Änderungen in der Dynamik, zum Aufspüren und Untersuchen äußerer Einflüsse auf die Dynamik eines Systems als auch von Kopplungen zwischen verschiedenen Systemen, sowie eine Kombination mit der Methodik der komplexen Netzwerke. Typische Probleme geowissenschaftlicher Datenanalyse, wie unregelmäßiges Datensampling und Unsicherheiten in den Daten, werden durch spezielle Modifikationen und Ergänzungen behandelt. Die Entwicklung eines Signifikanztests erlaubt die statistische Bewertung der quantitativen Analyse vor allem für die Betrachtung dynamischer Übergänge. Den Abschluß bildet ein Überblick typischer Fehler, die im Zusammenhang mit dieser Methode auftreten können und wie man diese vermeidet. Neben den methodischen Aspekten werden Anwendungsmöglichkeiten vor allem für geowissenschaftliche Fragestellungen vorgestellt, wie die Analyse von Klimaänderungen, von externen Einflußfaktoren auf ökologische oder klimatische Systeme, oder der Landnutzungsdynamik anhand von Fernerkundungsdaten.

Contents

Dust Pattern at a Cave Wall ("Vermiculations")
Photo: N. Marwan

List of Abbreviations and Notations

Abbreviations

AUC	area under the curve
BP	before present (taken conventionally to be before 1950)
CCS	California Current System
CHL	chlorophyll concentration
CT	computer tomography
CRP	cross recurrence plot
DJF	December, January and February
EAIASM	East Asian-Indonesian-Australian summer monsoon
EASM	East Asian summer monsoon
EEG	electroencephalography
ENSO	El Niño/Southern Oscillation
ERP	event-related potential
EVI	extended vegetation index
FAN	fixed amount of nearest neighbours (neighbourhood criterion)
FT	Fourier transform
GMT	global mean temperature
IASM	Indonesian-Australian summer monsoon
ITCZ	Intertropical Convergence Zone
JJA	June, July and August
ka	thousand years
kyr	thousand years
IS	interstadial
JRP	joint recurrence plot
LOI	line of identity (the main diagonal line in an RP)
LOS	line of synchronization (the distorted main diagonal line in a CRP)
pQCT	peripheral quantitative computer tomography
Ma	million years
MCR	mean conditional probability of recurrence
RMD	recurrence-based measure of dependence
RN	recurrence network

RP	recurrence plot
ROC	receiver operating characteristic
RQA	recurrence quantification analysis
SMI	Summer monsoon index
SOI	Southern Oscillation index
SST	sea surface temperature
SSTA	sea surface temperature anomaly
TACTS	transformation cost time series

Notations

$\langle \cdot \rangle$	average
$\lvert \cdot \rvert$	absolut value
$\lVert \cdot \rVert$	norm
$\{\cdot\}$	set
$\delta(\cdot)$	delta function ($\delta(x) = \{1 \lvert\, x = 0;\ 0 \lvert\, x \neq 0\}$)
$\delta_{i,j}$	Kronecker delta ($\delta_{i,j} = \{1 \lvert\, i = j;\ 0 \lvert\, i \neq j\}$)
ε	small distance in the phase space in general; threshold value (neighbourhood radius) for the construction of a recurrence plot
λ_2	second eigenvalue of the Laplace matrix
ρ	complex network measure: averaged degree centrality
σ	standard deviation
$\Theta(\cdot)$	Heaviside function ($\Theta(x) = \{1 \lvert\, x > 0;\ 0 \lvert\, x \leq 0\}$)
τ	time delay (index-based units)
ξ	random number
$\mathbf{A}$	adjacency matrix of a network
BC	complex network measure: betweenness centrality
$\mathbf{C}$	covariance matrix
$\mathscr{C}$	complex network measure: clustering coefficient
$\mathbf{CR}$	cross recurrence matrix between two phase space trajectories
$\mathbf{D}$	distance matrix
$D_{\mathscr{T}}$	complex network measure: transitivity dimension
DET	measure for recurrence quantification: determinism
DIV	measure for recurrence quantification: divergence
$ENTR$	measure for recurrence quantification: entropy
$H(\cdot)$	histogram or frequency distribution
$\mathbf{JR}$	joint recurrence matrix
k_i	complex network measure: degree centrality
ℓ	length of diagonal line in the RP
$\mathbf{L}$	Laplace matrix
L	measure for recurrence quantification: average line length of diagonal lines
$L_{\max}$	measure for recurrence quantification: length of the longest diagonal line
$\mathscr{L}$	complex network measure: average shortest path length
LAM	measure for recurrence quantification: laminarity
m	embedding dimension
N	length of a data series
$p(\cdot)$	probability distribution

p_τ	probability of recurrence after time τ
$P(\cdot)$	histogram or frequency distribution (same as $H(\cdot)$)
$\mathbf{R}$	recurrence matrix
RMD	recurrence-based measure of dependence
RR	measure for recurrence quantification: recurrence rate
RT	measure for recurrence quantification: recurrence time
RTE	measure for recurrence quantification: recurrence time entropy
$S(\tau)$	joint recurrence based measure of synchronization
$\mathscr{T}$	complex network measure: transitivity
$TREND$	measure for recurrence quantification: trend
TT	measure for recurrence quantification: trapping time
$V_{\max}$	measure for recurrence quantification: length of the longest vertical line

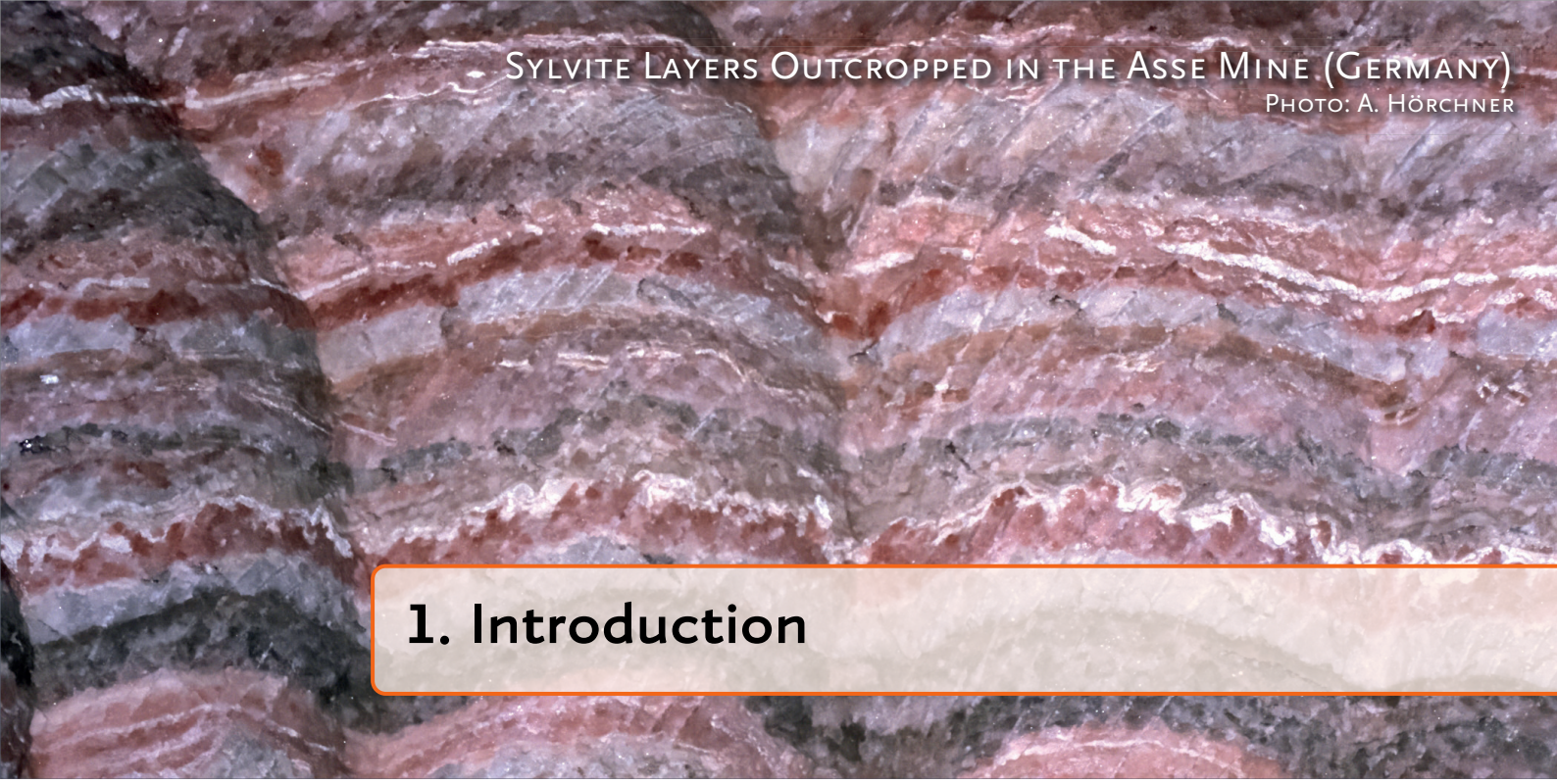

Sylvite Layers Outcropped in the Asse Mine (Germany)
Photo: A. Hörchner

1. Introduction

1.1 Recurrence – A fundamental concept in the system Earth and geoscience

A key principle in geoscience is the *Doctrine of Uniformity*, which states that physical laws do not change throughout time: A (geological) process producing a specific geological phenomenon today which can be directly observed, measured, and investigated now, would most likely be the same (physical, chemical) process that formed a similar geological phenomenon in the past. Inherent in this axiom is another fundamental principle, which is often not so explicitly noticed: recurrence. Without recurrence in the system Earth, we would not be able to apply and use the Doctrine of Uniformity. Although recurrence is a ubiquitous and fundamental feature in the system Earth at many scales in time and space, such as the rock cycle, activity of an active geyser, celestial mechanics, repeating patterns in a landscape, or alternating sediment layers, this property is used for geoscientific investigations in only a few specific contexts, such as cycles of glaciation or epochs of geomagnetic polarity – and even then the term "recurrence" is usually not applied.

Recurring features appear, for example, in lake sediments, where the seasonally changing environmental conditions can cause differences in the grain size or the colours of the deposited material. The Swedish geologist De Geer was one of the first who linked the alternating appearance of the lake sediments with the annual cycle and even the width of these layers to changing environmental/climatological conditions (Fig. 1.1). In the beginning of the 20th century, he was able to associate the layers in clay sediments in Sweden with a seasonal cycle because of the obvious similarity to tree rings [115], which are also well separated by annual pattern and whose width reflect seasonal weather conditions. For the annually layered clay deposits he finally introduced the term "varves", using the Swedish word *varv* for "periodically recurring layers" (see footnote 1 at p. 458 of the original paper [115]), which is now the standard term for such laminated sediments. Before De Geer, a method to assign an exact chronology to geological samples was more or less non-existent, the only common approach being that of a *relative dating*, based, e.g., on index fossils. With varve based counting, De Geer introduced the discipline of geochronology allowing to

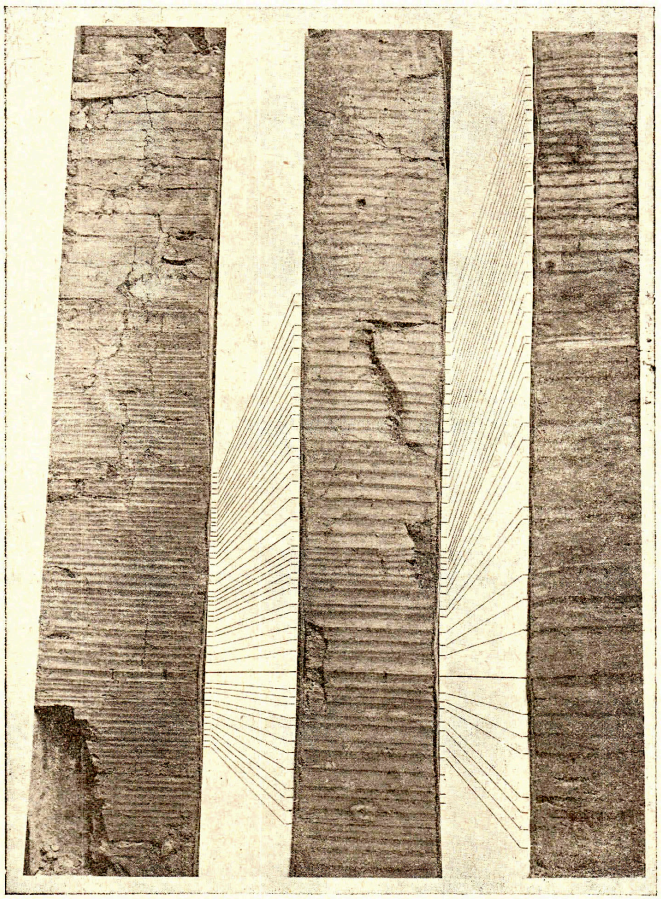

Figure 1.1: Annually layered clay deposits representing coinciding recurring patterns from three different sites in Finland (Heinäjoki, Leppäkoski, Vanaja) used 1918 in a study by Sauramo [337].

assign *absolute ages*[1] to a geological sample. With a real time information along geological profiles, it is possible to study temporal changes, rate of changes, and return periods of geological processes [337]. Moreover, De Geer compared different Holocene varve series from different sites (e.g., Sweden, Denmark, USA, Canada) and found that they showed similar, recurring patterns [114]. He inferred that this can happen only with a common external factor, which he supposed to be the sun. The results of De Geer's investigations offer two important implications: (1) Recurring features in temporally well-resolved geological profiles can be used for the comparison or assignment of features in records from different sites, and (2) recurring features open opportunities for interpretations (such as the climate as a common influencing factor). With his interpretation that the observed changes in the varves' thickness are caused by solar variation (via climate), De Geer was also one of the first to relate geological data with palaeoclimate variation and to produce a time series representing past solar variability. Past variation of the solar influence (solar insolation, to be more precise) was also discovered in sediments of different origin: for instance, in sapropels of the Mediterranean Sea.

[1]From a physicist's point of view the term "absolute age" or "absolute time" is misleading, because the measured age of a geological sample (measured using layer counting or any radiometric dating) is only an estimate and can significantly deviate from the true (physical) time when the sample was formed. Actually, only the true (physical) time is the "absolute time".

Sapropels are dark coloured sediments rich of organic material, formed in the anoxic zone of the deep sea. In the Mediterranean Sea, the sapropels form recurring layers of several centimeters up to a meter (Fig. 1.2). Already before their first recovery in 1947 [58], it was hypothesized that climate variation would have an effect on the organic content of the deep part of the Mediterranean sea sediments [33]. Enhanced fresh water input as a result of deglaciation in warming phases of the northern hemispheric climate would cause and increase the anoxic zone, supporting the sapropel formation. First investigations claim to have found such a link between warming climate and the occurrence of sapropels [e.g., 359], supported by the fact that the recurring sapropel layers coincide well with variations in the solar insolation, in particular with the recurring cycles of precession and eccentricity of the Earth orbit [123, 141, 326]. Further studies have revealed that the reason for the formation of sapropels is actually more complex [58]. Sapropel formation is modulated by several other factors besides solar insolation, e.g., a repositioning of the Intertropical Convergence Zone or an increased African monsoon. Comparison with other regions of recurring sapropel formation, e.g., the Japan Sea, could help to better understand the mechanisms leading to enhanced anoxic deep sea. Because of the found link to precession and eccentricity cycles, an “astronomical fingerprinting” within the sapropel recurrences might be a way to resolve the open questions [58].

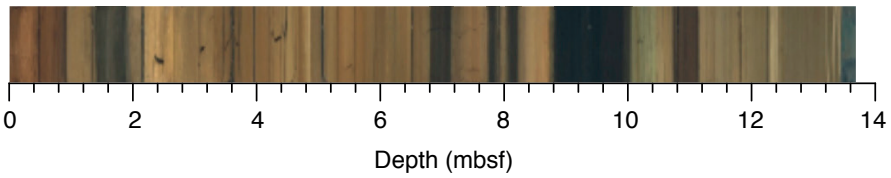

Figure 1.2: Sapropel layers in a mediterranean sediment (core LC21, figure modified after [123]).

Variations in proxy records are not the only evidence for solar variations. For example, lake sediments reveal recurring patterns at time scales from a few years to several decades: cycles of 2 to 8 years or 13 to 16 years have been found in lake sediments in South America and are related to an impact of the El Niño/ Southern Oscillation [264] or the tropical Atlantic [394]. Recurring variations in proxies can also be found at other places, such as in the Indian monsoon realm, and can be related to further climatological phenomena, such as the Asian summer monsoon [66], droughts [171], glacial cycles [61], permafrost thawing periods [400], or spatio-temporal seesaw-like patterns [94, 194]. Besides information about the climate of the past, proxy records can also provide information about past variability of the environment or the geological conditions, such as vegetation dynamics [140] or the change of the Earth’s magnetic field (wandering of the magnetic poles) [32, 200]. Furthermore, mass movements, such as landslides, are of high interest, because of their potential triggering by enhanced or extreme rainfall, variations in groundwater levels, or deglaciation, as to be expected due to global warming [154, 393, 430]. Their recurrence properties can be statistically linked with regional and global climate variation, such as El Niño/ Southern Oscillation [393]. Typical recurrence patterns occur also in other geoecological processes, such as river discharge with extreme floods. The recurrence property is then often used to quantify risks, e.g., in terms of flood frequency (i.e., flood recurring only after 100 or 1000 years) [7].

Turning back to the palaeoclimate, internal and external drivers cause high-frequent, slow, gradual, or abrupt changes in palaeoclimatic conditions. These variations represent intrinsic recurrences at different scales. For example, recurring patterns in palaeoclimate

data are often linked to changes in the solar insolation. Solar insolation varies at different time-scales [21]:

- seasonal rotation of the Earth around the sun: annual time scale,
- solar activity: decadal time scale, e.g., 11 yrs cycle,
- and orbital variation: time scales of ten to hundred thousands of years, i.e., the slow rotation of the Earth' axis itself (precession), a change of the tilt of the Earth axis (obliquity), and a deformation of the Earth orbit between more circular and more elliptic shape (eccentricity).

The orbital variations are known as Milankovich cycles and are the main drivers for recurring dramatic climate changes such as between glaciations and warm periods [22, 267]. Whereas the palaeoclimate variation as derived from the geoscientific archives are only estimates and contain a degree of uncertainty, the Milankovich cycles can be determined with high accuracy, because the equation of motion for the dynamics of the Earth orbit in space can be solved in good approximation using Hamiltonian mechanics. The planetary motion along elliptical orbits goes back to Kepler in the early 17th and Newton in the late 17th century. Classical (Newtonian) mechanics can be used to solve the equations of motion of an object in a gravitational field of another object, resulting in the three Kepler's laws of planetary motion, which is a two-body problem. However, the celestial motion of objects in the solar system is, in general, a many-body system, where the planets' gravitational fields mutually influence their orbits around the sun. Solving such a many-body problem (and even of a three-body system) is not as simple as for a two-body problem and it was, therefore, at the forefronts of science for a long time [267]. In this spirit and in honor of the 60th birthday of the King of Sweden, Oscar II, in 1887, a prize was announced to solve the many-body problem. The French mathematician Poincaré finally won this prize with his seminal work on the three-body system and discovering the chaotic nature of the orbits [292]. In this work, he proved an important theorem which not only affects the recurring orbits of objects in a celestial system, but which is also a fundamental property of many complex dynamical systems. The now well-known recurrence theorem states that a (conservative) system recurs infinitely many times as close as one wishes to its initial state [292]. This theoretical finding is compellingly confirmed by the real world, where recurrences can be observed in our daily life and across all scientific disciplines. The investigation of recurrences has, therefore, attracted attention and several approaches have been developed for this purpose.

Recurrences are not only limited to states of a low-dimensional process. Many processes happen on multiple scales, levels, locations, and dimensions. The weather system is a good example, representing dynamics at different scales and with multistable regimes, such as local convection circulation, more regional advective moisture transport, and global dynamics represented by jetstreams/ Rossby waves, Inter-Tropical Convergence Zone (ITCZ), and Walker cells. The interplay, feedbacks, and multiple temporal and spatial scales form a high-dimensional complex system, difficult to predict on time scales longer than a few days. Conceptual modelling, e.g., with the famous models by Lorenz [204, 205], has demonstrated the chaotic nature of the dynamics of such complex systems, but has also confirmed that recurrence is a fundamental property, even in such high-dimensional systems [205]. High-dimensional processes can also represent extended spatial variability, probably leading to spatial recurring patterns (created by dynamical processes). Characterizing spatial or even spatio-temporal pattern (pattern which changes over time) is not a trivial task. Ideas from complex systems science have led to new approaches, such as climate networks (complex networks for analysing spatio-temporal climate data [70]), but also the use of recurring structures [232].

Recurring dynamics, in temporal, spatial, or spatio-temporal domain, are often not easily visible. Changes can occur in more subtle aspects of the dynamics than what is observed in first and second statistical moments. It is also often not obvious whether cyclical variations are really periodical; they could also be chaotic or stochastic. Another problem seriously affects geoscientific data analysis when using sediments as proxy records. During deposition the sedimentation rate is usually not constant. However, after collecting, they are usually sampled along a regular length scale (e.g., from top to bottom). This results in a non-equidistant temporal sampling of the time series and even in larger gaps. Most methods are not able to analyse such irregularly sampled time series and require interpolation as a data preprocessing step.

1.2 Recurrence analysis

For the study of recurring processes, several approaches are of interest. The power spectrum analysis is probably one of the best known and widely used technique for the analysis of periodicities in time series [344]. It allows us to find the main periods within the measured signal (Fig. 1.3B). Wavelet analysis reveals similar information, but it additionally allows us to identify the change of the detected periods over time (Fig. 1.3C). Both approaches are useful, although they have some limitations, especially in the presence of windowing effect, harmonics, nonstationarity, trends and noise, non-periodic signals, or generalisations for analysing spatial or spatio-temporal data.

Another fundamental approach that can be used to investigate recurring features in time series (and even in spatial data) is the *recurrence plot*. This approach is not restricted to periodic variations and has its roots in the theory of dynamical systems (Fig. 1.3D):

Definition 1.2.1 — Recurrence plot. A recurrence plot (RP) is a binary, square matrix $\mathbf{R}$ in which the matrix elements $R_{i,j}$ correspond to those times j at which a state $\vec{x}_i$ of a dynamical system X recurs (in a Poincaré sense):

$$R_{i,j} = \Theta(\varepsilon - \|\vec{x}_i - \vec{x}_j\|) \tag{1.1}$$

with Θ the Heaviside function, $\|\cdot\|$ a norm, and ε a preselected recurrence threshold.

In the last years, RP has become a powerful tool of nonlinear time series analysis. RPs were first introduced in 1987 by Eckmann, Oliffson Kamphorst, and Ruelle [86] as tools that "are rather easily obtained aids for the diagnosis of dynamical systems". In the following years, RPs were firstly heuristically extended by several quantification approaches in order to distinguish the differently appearing RPs derived from different dynamics [224, 444]. In the last two decades, a lot of research has been performed to further develop this approach and provide a theoretical foundation, leading to a well developed, theoretically founded, and "active field, with many ramifications we [Eckmann et al.] had not anticipated" [240]. A historical overview on the developments within the RP field up to the year 2008 will be presented in chapter 2.

RPs of different dynamics represent different, but characteristic appearances (Fig. 1.3D). Such differences are quantified with the *recurrence quantification analysis (RQA)* (Fig. 1.3E). The first RQA measures introduced were mainly based on the distribution of diagonal lines (and their lengths) in the RP, expressed by the length distribution $H(\ell)$ that counts the number of diagonal lines in the RP that have exact length ℓ. One interesting, frequently used RQA measure that uses $H(\ell)$ is the *determinism*:

Definition 1.2.2 — Determinism. The determinism is the fraction of recurrence points forming diagonal lines of at least length ℓ in the RP:

$$DET = \frac{\sum_{\ell \geq \ell_{\min}} \ell H(\ell)}{\sum_{i,j} R_{i,j}}. \tag{1.2}$$

It measures the likelihood that the dynamics of the system sustains to follow a dynamics that had been already occurred at a previous time; it is, therefore, related to the predictability of the dynamics.

A change of such a measure over time is an indication for a changing dynamics [225, 239, 397]. Studying the variation of a recurrence measure with time is one of the basic and fundamental applications of RPs in order to detect transitions between different dynamical regimes and has been applied in many scientific disciplines, in Earth science, e.g., to detect changes in the dynamics of the palaeoclimate represented by proxy records (e.g., in chapters 11 to 13).

Changes in recurrence measures are often discussed with respect to external drivers, such as the solar variability or Milankovich cycles. For this purpose it would be interesting and helpful to compare the recurrence properties of the external forcings with those of the proxy records. We have suggested several approaches for multivariate recurrence analysis

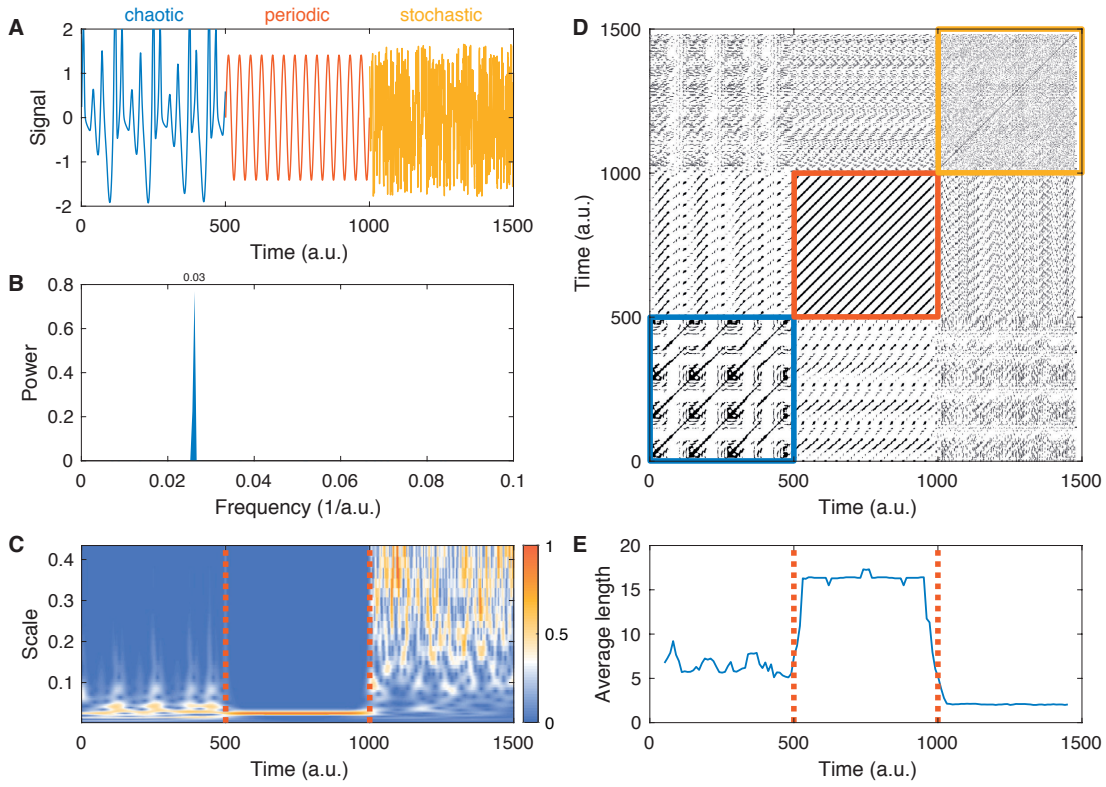

Figure 1.3: Exemplary recurrence plot (D) showing the recurrence structure of a sequence of chaotic, periodic, and stochastic dynamics (A). The power spectrum (B) only reveals the dominating frequency of the periodic epoch, although the signal consists of further frequencies; the wavelet diagram (C) represents the different scales within the three segments of different dynamics. Quantifying the recurrence plot (E) allows further insights into the dynamics, such as predictable time as derived from the average line length in the recurrence plot.

that can be used to study temporal differences [230, 236], different types of synchronisation [239, 322], and even causal relationships [103, 305].

A first approach, the *cross recurrence plot (CRP)*, checks for the simultaneous occurrence of a similar state in systems X and Y [228, 236].

Definition 1.2.3 — Cross recurrence plot. A cross recurrence plot is a binary, not necessarily square, matrix **CR** in which the matrix elements $CR_{i,j}$ correspond to those times j at which a state $\vec{x}_i$ of one dynamical system X is similar to the state $\vec{y}_j$ of a second dynamical system Y:

$$CR_{i,j} = \Theta(\varepsilon - \|\vec{x}_i - \vec{y}_j\|). \tag{1.3}$$

The state vectors $\vec{x}$ and $\vec{y}$ must have the same dimensionality, but they can have different length (thus causing non-square **CR**).

Besides testing for an interrelationship, this CRP can be used to align the time axis between two observations as shown in chapter 5.

In contrast to the test for similar states in two dynamical systems, RPs offer additionally a test for simultaneous occurrence of a recurrence in two different systems by the *joint recurrence plot (JRP)* [322]:

Definition 1.2.4 — Joint recurrence plot. A joint recurrence plot is a binary, square matrix **JR** in which the matrix elements $JR_{i,j}$ correspond to those times j at which the state $\vec{x}_i$ of one dynamical system X recurs and at which the state $\vec{y}_i$ of a second dynamical system Y recurs as well:

$$JR_{i,j} = \Theta(\varepsilon_x - \|\vec{x}_i - \vec{x}_j\|) \cdot \Theta(\varepsilon_y - \|\vec{y}_i - \vec{y}_j\|). \tag{1.4}$$

The state vectors $\vec{x}$ and $\vec{y}$ can have different dimensionality, but they have to have the same length (thus causing square **JR**); moreover, the recurrence threshold can be selected differently for the both systems.

Joint recurrences are important when looking at generalized synchronizations [239, 322] or coupling directions [324, 456]. For example, using the fraction of recurrence points in the RP and the JRP, we can use ideas from information theory and define conditional measures of dependence (see chapter 10).

The recurrence matrix **R** is a binary matrix and, when based on a metric, it is symmetric. There is a striking similarity of this matrix with another mathematical object used in complexity science: complex networks can be described using an adjacency matrix whose entries represent links between pairs of nodes. For unweighted and undirected complex networks, such adjacency matrix **A** is a symmetric and binary square matrix! Therefore, we have simply identified the RP with the adjacency matrix of a complex network (Fig. 1.4) [78, 241, 368, 431]. The seminal work introducing this concept is presented in chapter 11. The resulting *recurrence network (RN)* consists of nodes representing the time points of the phase space trajectory and links that represent the similarity (recurrence) between a pair of time points.

Definition 1.2.5 — Recurrence network. A recurrence network **A** is the network representation of the recurrence structure of a dynamical system X, represented by its states $\vec{x}_i$ in the m-dimensional phase space:

$$A_{i,j} = R_{i,j} - \delta_{i,j} \tag{1.5}$$

with **R** the recurrence matrix, Eq. (1.1), and $\delta_{i,j}$ the Kronecker delta (to avoid self-loops). Network nodes represent the time points of the phase space trajectory and network links represent their recurrences.

Similar states of a system are highly linked with each other in the RN, whereas diverging states are far away in the network (Fig. 1.4B). A RN can be analyzed by the known network measures. We have shown the relationship between specific network properties with the geometrical properties of the phase space attractor [79, 457]. The network measures can, thus, be used as additional diagnostic tools for time series analysis that complement the other measures obtained from RPs [77, 78, 241]. The recurrence network based measures can also be calculated within sliding windows, analogously to the approach for the RQA measures. As with the RPs, here too, this procedure allows us to study subtle changes of the processes encoded by the measured time series [73, 241].

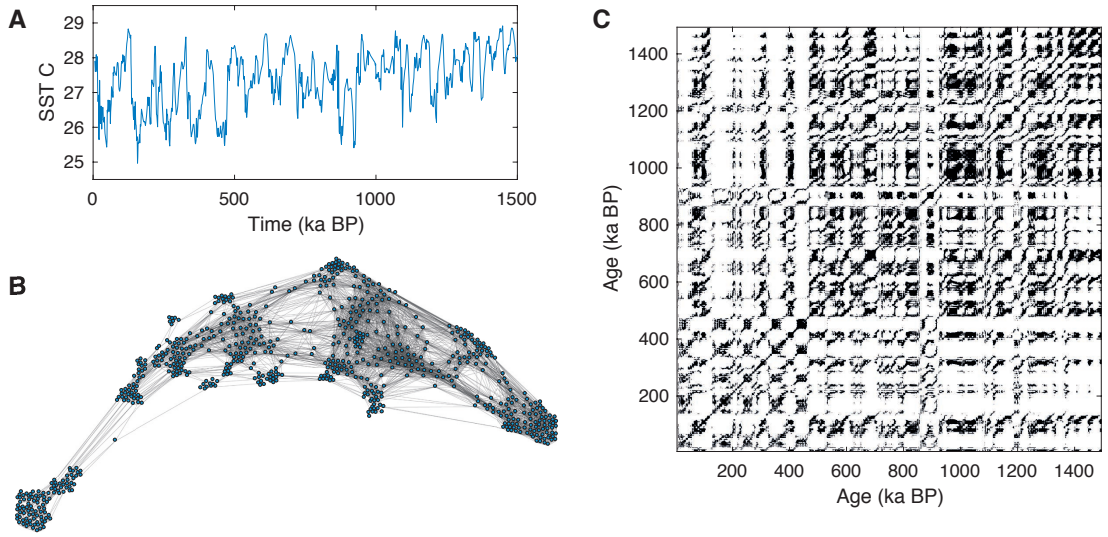

Figure 1.4: Exemplary complex network representation (B) of a recurrence plot (C) of reconstructed sea surface temperature variability (A) in the South China Sea for the past 1.5 Ma BP [198]. The network consists of distinguished communities of nodes, representing the alternating behavior of the SST values.

1.3 Objectives of this thesis

The first applications of the RP approach have already demonstrated the potential of the method [237, 397, 418, 442], but they have also shown the need for a better understanding of the RP features and the meanings of the heuristically developed recurrence quantification measures, and the necessity to link them with theory. By 2007, we summarized the knowledge with respect to the RPs available at this time by a review report [239]. However, a lot of methodological questions, which are of particular interest for geoscientific research, remained open:

1. How can we reliably select the parameters for the RP analysis?
2. What does the shape of the line structures in an RP mean?
3. How are RPs related to power spectra?
4. Are there any further measures of complexity that can describe the recurrence properties?
5. Does recurrence analysis also work for high-dimensional dynamics?

6. Can we analyse recurrences in spatio-temporal data?
7. Can we identify external forcing from data?
8. How can we apply the RP to irregularly sampled time series?
9. How can we apply the RP to time series with uncertainties?
10. What is the potential of RPs in comparing the recurring features in different systems? Can we identify coupling directions?
11. How significant are transitions identified with the RP approach?
12. Which method-related pitfalls occur in RP analysis?

Furthermore, when working within the geosciences, several research questions attracted my attention, such as

1. How to integrate several proxy records with different sampling times but similar geoscientific information?
2. How did climate change in the past, for example during the Plio-Pleistocence lake level high-stands in East Africa or during Holocene enhanced/weaken periods of the Asian summer monsoon?
3. Can we differentiate between abrupt and gradual changes in the palaeoclimate and how significant are such changes?
4. Can we unravel interdependencies or even causality when comparing different climate/ palaeoclimate records and potential external forcings?
5. Are there spatial differences in landscape dynamics?
6. Are spatial differences, e.g., in phytoplankton bloom, caused by external drivers?

In this thesis, I summarize selected methodological research performed by me and my students after the review report in 2007 [239] and focusing on these questions. This research is published in peer-reviewed and ISI-listed journals.

I start with a historical overview of RP analysis in chapter 2. The selection of the threshold parameter for creating the RP is a crucial step. For the purpose of signal detection, the effect of different threshold values is studied and basic rules for such selection will be suggested in chapter 3. Complex network theory offers another interesting approach for selecting the threshold. Based on the connectedness of a network, an alternative threshold selection procedure is explained in chapter 4. In chapters 5 and 6, I try to give the method a more theoretical justification with respect to the shape of lines that appear in RPs and to the information on periodicities by applying the Wiener Khinchin theorem. The question, whether RP analysis also works for high-dimensional and spatially extended dynamics is investigated in chapter 7. Alternative definitions of recurrences are introduced in chapters 8 and 9. In chapter 8, I extend the RP approach for spatial data, and in chapter 9, the approach is further modified to even infer external driving forces from spatio-temporal variability. The combination of RP and complex network analysis has lead to a new set of measures for analysing recurrence properties and to identify dynamical regime changes, presented here in the chapters 11 and 12. In the latter, I also briefly present the idea of using complex networks for spatio-temporal data analysis, however since the focus of this thesis is recurrence, I do not extend the discussion about this particular approach here. The challenge of irregularly sampled time series is addressed in chapter 13, introducing the idea of transforming a time series to a regularly sampled one using a cost function. Another challenge typical for geoscientific data is addressed in chapter 14 by introducing the novel concept of probability time series and replacing the standard binary RP with a probability matrix of recurrences. The potential for analysing coupling directions using RPs is evaluated in chapter 10 and the important topic of the significance of the recurrence quantification measures is presented in chapter 15. Here I suggest a novel approach to prepare confidence intervals for RP analysis. Finally, I discuss possible pitfalls related to RP analysis in chapter 16 and present a suggestion

how to reduce embedding-related artifacts in chapter 17. It will be demonstrated how a wrong choice of the embedding parameters can mislead to wrong results, in particular for stochastic processes. Therefore, a procedure that determines a "safe" parameter space is suggested in this chapter.

Most of these methodological developments are directly applied to geoscientific research questions, except two examples involving physiological research questions in chapters 3 and 8. Nevertheless, these approaches can be also applied to geoscientific problems. In chapter 5, I use recurrence features to temporally align different proxy records from the same lake but different boreholes, allowing for a potential integration of these different records, e.g., to prepare a stacked record. Differences in spatiotemporal landscape (vegetation) dynamics are investigated on the base of satellite images in chapter 7. Phytoplankton bloom is studied in chapter 9 and the likely forcing of such algae bloom is reconstructed in this study. The interaction between different drivers of global temperature are investigated in chapter 10. In chapters 11 to 15, I identify subtle changes in the palaeoclimate and relate them to Milankovich cycles and solar variability. One of the first applications of recurrence analysis for river runoff data is exemplified in chapter 17.

2. Historical Review of Recurrence Plots

Paper 1 N. Marwan: A Historical Review of Recurrence Plots, European Physical Journal – Special Topics, 164(1), 3–12 (2008). DOI:10.1140/epjst/e2008-00829-1

R Since the publication of this paper in 2008 the method of RPs has been further extended by new knowledge, novel measures of complexity, and new concepts. This historical overview is, thus, not complete. The most important developments since 2008 are the combination of RPs with ideas from complex network theory in 2008/2009 [241, 368, 431] (see also Chapter 11), the introduction of multi-scale RP analysis in 2012 [50] significance tests for RP quantification 2009 and 2013 [235, 341] (see also Chapter 15), and of schemes for the analysis of directed, indirect, and hidden couplings 2010 to 2012 [103, 144, 456] (see also Chapter 10).

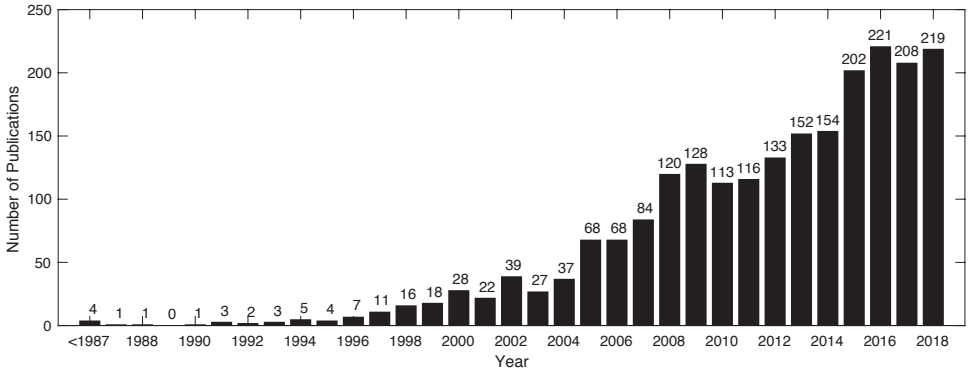

Figure 2.1: Publications about RPs and RQA for the last three decades (updated Fig. 2.3 of this paper, January 2019).

Abstract

In the last two decades recurrence plots (RPs) were introduced in many different scientific disciplines. It turned out how powerful this method is. After introducing approaches of quantification of RPs and by the study of relationships between RPs and fundamental

properties of dynamical systems, this method attracted even more attention. After 20 years of RPs it is time to summarise this development in a historical context.

2.1 Introduction

The technique known as recurrence plot is 20 years old. However, recurrences were studied and employed long before. The Maya calender is one example where we can find the principle of recurrences as the basic idea. We encounter recurrences in different aspects in nature and social life.

With the birth of the modern mathematics in the 19th century recurrence was discovered to be a fundamental property of conservative dynamical systems. Poincaré formulated his thesis in the work about the restricted three-body system, which won him a prize sponsored by Oscar II of Sweden and Norway. Poincaré found that "In this case, neglecting some exceptional trajectories, the occurrence of which is infinitely improbable, it can be shown, that the system recurs infinitely many times as close as one wishes to its initial state." (translated from [292]). In the following years, several important mathematical works were performed (e.g. [161]).

However, more than a half century had to pass for recurrences to be comprehensively studied on numerical simulations and real measurements. Not until the introduction of powerful computers such numerically costly studies were possible. As an example, we may take the Lorenz system, which was one of the first numerical models exhibiting recurrences and chaotic behaviour [204]. Recurrences were analysed by *first return maps* [297], *space time separation plots* [300], *return time* and *recurrence time statistics* [10, 143]

The persistent growth of computer power allowed even more computer intense investigations, as a pair-wise comparison of all possible combinations of pairs of a data series. This can be done by the similarity matrix, a graphical representation of the similarity of all pair-wise combinations in the considered data series. Although strictly speaking, the idea of a distance metric can be traced back to the Pythagorean Theorem, the modern concept of this tool dates back to the 1920s in both applicative [387] as well as methodological fields [207]. The work of Kruskal in the 1960s [182] was one of the most quoted works in statistics and deeply affected many fields of investigation from ecology to psychology and economics. All these fields appeared as separate by physical science so that the appreciation of these works remained limited in physics. However, these authors deeply investigated and exploited this approach for an analysis of distance spaces allowing for an unbiased representation of virtually all kind of data without any constraint about their characteristics. In this manner, they paved the way for the nowadays recognized ability of recurrence based methods to deal with non-stationary, non-linear and relatively short data series.

With the intense usage of computers, the similarity matrix was re-invented by several scientific disciplines around the change from the 1970s to 1980s, and therefore different terms for the same technique, like *dot plot* [55], *contact map* [67, 148], *similarity matrix* [181, 183] or *distance matrix* [332] emerged. In the field of chaos theory it found its way a few years later as the *recurrence plot* [86] (Fig. 2.2A). Now the aim was to compare all possible states represented by a higher-dimensional phase space trajectory. In case the trajectory runs through a region in the phase space it passed before, then we consider it as a recurrence. A recurrence means that the recurrent state is somehow similar to a former state. This definition of similarity offers leeway to adopt the method to the needs of the investigation, as we will see later. Thus, the recurrence plot technique was not really new. The intention of Eckmann et al. was to have another representation of the dynamics of the systems. However, they immediately noted that further important information, like determinism, divergence

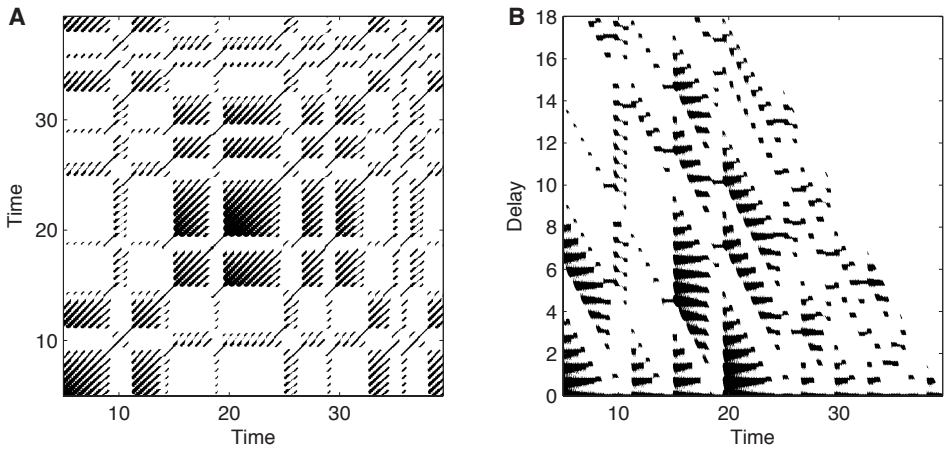

Figure 2.2: (A) Recurrence plot and (B) "close returns plot" of the x-component of the Lorenz system [204]. Used RP parameters: $m = 5$, $\tau = 5$, $\varepsilon = 7.6$, L_∞-norm.

and drifting behaviour can be found in such plots. They also stated that the lengths of the diagonal line structures in the RP are related to the positive Lyapunov exponent.

2.2 The birth of the recurrence plot

By utilisation of the similarity matrix as a tool to visualise recurrences of higher-dimensional phase space trajectories, Eckmann et al. did not expect to establish a new direction in nonlinear data analysis. Nevertheless, 1987 is considered to be the birth of *recurrence plots* and their quantification as a modern tool of nonlinear data analysis.

Short time later (no later than 1992), different authors independently introduced another kind of representation of recurrences [258, 446]. They did not compare all possible time points, but only a given time into the past and future (Fig. 2.2B). Here a further name appeared: the *close returns plot*. Such a representation can be more intuitive, in particular for beginners, because the line structures of the recurrence plot will be parallel to the x-axis.

2.3 Recurrence quantification analysis

These first years were characterised by a rather rare application of this method (Fig. 2.3). The appearance of recurrence plots in publications was somehow exotic. Moreover, up to this time, recurrence plots were just a visualisation tool, what yielded to the disadvantage that the user had to detect and interpret the patterns and structures revealed by the recurrence plot. Low screen and printer resolutions further worsened this issue. To overcome this subjective part of the method, starting in the late eighties, Zbilut and Webber tried to quantify the structures of the RP. At first they just determined the density of recurrence points in the RP and studied the histogram of the lengths of diagonal lines [418, 442, 444]. In the following five years, they introduced the known measures of complexity based on diagonal line structures of recurrence plots and therewith established the *recurrence quantification analysis (RQA)*:

- percentage recurrences or recurrence rate
- percentage determinism
- maximal line length and divergence
- Shannon entropy of the distribution of the line lengths
- trend.

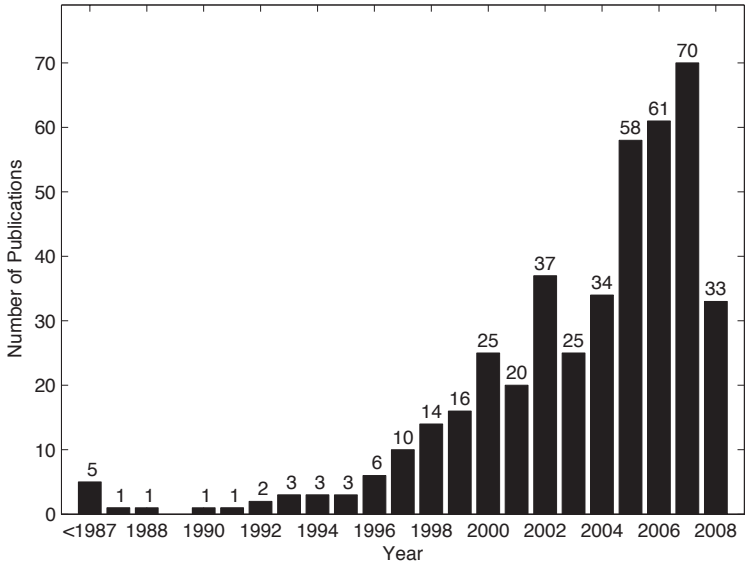

Figure 2.3: Publications about RPs and RQA for the last 20 years (May 2008).

For a definition of these measures we refer to [239]. The usefulness of these measures was shown by an increasing number of applications to real data. However, until 1995, only few applications of RPs and RQA appeared in publications.

Since the early nineties, Webber provides a freely available software (*RQA Software*) which can be used to compute RPs and the RQA measures. In 1996, Kononov started the *Visual Recurrence Analysis (VRA)* software. It has a user-friendly graphical interface and computational enhancements. Therefore, this software is rather popular. The TISEAN package, provided by Hegger, Kantz and Schreiber, was also one of the first software packages able to compute RPs (but without quantification, just RPs). For locations of these software in the WWW we refer to the web site `http://www.recurrence-plot.tk`.

As a next milestone we find the introduction of the time-dependent RQA. The RQA measures are calculated from windows moved along the main diagonal of the RP. This allows for the study of the evolution of the RQA measures over time [397]. It was shown that with this approach it would be possible to detect transitions in dynamical systems. At this moment, only transitions between regular and non-regular dynamics (like period-chaos transitions) could be detected. In the same year, a publication with the promising title "Recurrence plots revisited" by [45] appeared. It suggested to use RPs to reconstruct the driving force of dynamical systems and introduced the idea of *meta recurrence plots*, based on windowing and correlation sum.

The major methodological work on the RP and RQA during the 1990s was performed by the group around Zbilut and Webber in Chicago. Since the mid-1990s, the scientific community became more and more aware of RPs, as the continuously increasing number of publications between 1996 and 2004 demonstrates (Fig. 2.3).

Towards the end of the 1990s, first theoretical studies on the RP regarding their relationship with dynamical invariants and the preservation of the topology appeared. McGuire et al. analytically demonstrated that the distance matrix as the base of the RP preserves all information to reconstruct the underlying data series [250]. Faure and Korn have shown that the cumulative distribution of the lengths of the diagonal lines is directly related to the K_2 entropy [101]. The link between the columns of the RP and the *information dimension* was discussed by Gao and Cai [110].

In 1998, Iwanski et al. already discussed the issue whether it is really necessary to embed in order to derive quantities for the description of the dynamics. The authors based their discussion on more heuristic numerical work and by using the RQA measure *maximal line length*. This issue was further discussed by Gao and Cai [110], who also used the RP in order to estimate recurrence times. They defined two types of recurrence times based on the vertical distance between recurrence points in the RP.

In 1999, the *perpendicular RP* was suggested as a refinement in order to estimate the divergence of the states [53]. Here a recurrence is defined using the additional condition that the recurrence points have to lie on a plane which is perpendicular to the phase space trajectory of the reference point. The *iso-directional RP*, introduced in 2002, goes in a similar direction [151]. Its additional recurrence condition requires that the recurrent phase space trajectories have to evolve in parallel, i.e. in the same direction. Unfortunately, these variants of an RP are not popular, probably because of their higher computational efforts.

2.4 Extensions for the recurrence plot and quantification analysis

Also around the change to the new millennium, the RP technique was extended to the bivariate *cross recurrence plot (CRP)* [222, 439]. This bivariate extension tests for simultaneous occurrences of similar states in two different systems. Consequently, cross recurrence quantification analysis followed. This technique can be used to detect deterministic signals [439] and to study complex interrelations between different systems [228, 238]. Here delay based variants of the RQA measures were introduced [228]. Furthermore, CRPs appeared rather illustrative to study differences or transformations of time scales of similar observations [236]. This feature was later used to understand changing shapes of line structures in RPs [230]. The detection of deterministic signals by using RQA was further demonstrated by Zbilut et al. [440].

With the introduction of CRPs, the freely available *CRP Toolbox* for MATLAB, written by Marwan, appeared. This toolbox is platform independent and contains almost all RP related tools and measures. It is noteworthy that also commercial software started to include at least the computation of RPs, like *Dataplore* (ixellence GmbH, Germany). For locations of these software in the WWW we again refer to the web site `http://www.recurrence-plot.tk`

With the new millennium, further measures of complexity were added to the RQA. Marwan et al. introduced measures based on vertical line structures in the RP and are called *laminarity* and *trapping time* [237]. Using these measures it was possible to detect chaos-chaos transitions.

At the same time, in bio-informatics RPs and RQA were employed to investigate the spatial structure of biopolymers [118]. This was a deep change in perspective, because here these methods do not analyse time series but spatial series or even spatial structures (starting directly from distance matrices without the need of a pre-existing series, [420]) and makes the technique to come back to its 'purely statistical' lineage (as opposite to the dynamical lineage).

2.5 Theoretical basis and dynamical invariants

Between 2002 and 2006, Romano and Thiel published several pioneering articles related to different aspects of RPs. They theoretically justified the choice of the recurrence threshold for data with observational noise and were able to analytically describe an RP for noise [380, 383]. They explained the link between the line lengths of the diagonal lines and the dynamical invariants [384]. This work led to further studies about the influence of embedding [216, 381, 382]

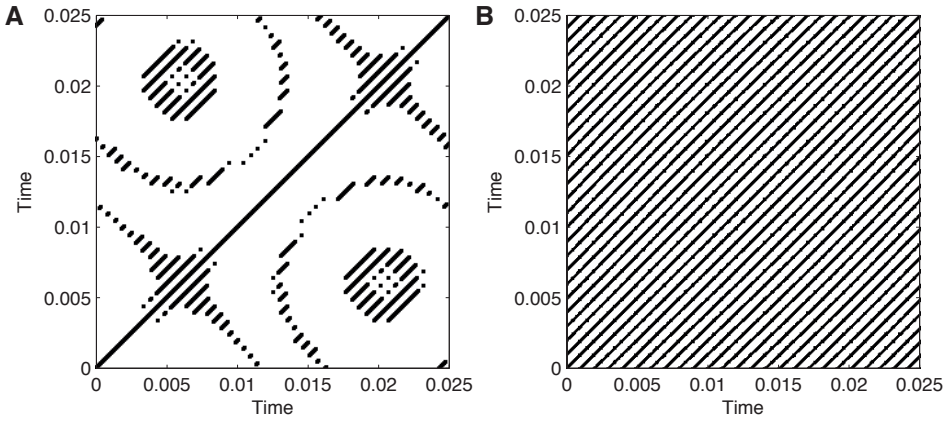

Figure 2.4: (A) Pattern of gaps (all white areas) in a recurrence plot of a modulated harmonic oscillation $\cos(2\pi 1000t + 0.5\sin(2\pi 38t))$ sampled with 1 kHz. These gaps represent missing recurrences due to the sampling frequency close to the frequency of the harmonic signal. (B) Corresponding RP as shown in (A), but for a higher sampling rate of 10 kHz. As expected, the entire RP now consists of the periodic line structures due to the oscillation. Used RP parameters: $m = 3$, $\tau = 1$, $\varepsilon = 0.05\sigma$, L_∞-norm.

In 2004, a real multivariate extension of RPs, the *joint recurrence plot (JRP)* was introduced [322]. JRPs test for simultaneous occurrences of recurrences in different systems and are proper means for the detection of general synchronisation [321]. Romano et al. have further demonstrated how to use a delay based RQA measure for the detection of phase synchronisation, even for non-phase coherent oscillators [323]. This technique can be used to detect the direction of the coupling between systems [324]. During this time, the idea of twin surrogates appeared, which are dynamics preserving surrogates based on recurrences [239, 386]. Such surrogates can be used to derive a statistical inference for a synchronisation analysis. Moreover, a spatial extension of RPs was introduced, resulting in RPs of higher dimension (like 4D or 6D) [232].

As we can see, a main part of theoretical and methodical work was now done by the group of Marwan, Romano and Thiel in Potsdam. Consequently, a first international workshop exclusively dedicated to recurrence plots was organised in 2005 in Potsdam, Germany (33 participants).

Instead of using spatial information of the phase space trajectory for the definition of recurrence, Groth has suggested to use the local rank order [128]. The local rank order defines specific order patterns whose recurrences are represented by the *order patterns RP*. This definition of an RP can help to overcome problems with changing amplitudes (e.g. drift).

The work of the Potsdam group was continued by Zou, Ngamga, and Schinkel who worked on a theoretical approach for recurrences of quasiperiodic systems [453, 454], on different kinds of transitions, as to strange non-chaotic attractors [274], and on order patterns RPs [339].

The sampling rate of oscillating signals can be of importance for the detection of recurrences [96, 97]. Under certain conditions, large gaps can appear in an RP where actually recurrence points should be (Fig. 2.4). This feigned disadvantage can be indeed rather helpful for the detection of slight frequency changes in oscillating signals which are not visible by standard spectral analysis.

A second international workshop on RPs was organised in 2007, this time in Siena, Italy (44 participants).

In 2008, Rohde et al. linked statistical properties of the distance matrix to the variance and covariance (at least for stochastic processes) [320]. Krishnan et al. considered RPs from a completely different point [179, 180]. They stressed the fact that an RP can be considered as the adjacency matrix of a complex network, allowing topological analysis of networks or graphs by means of RQA. This approach is especially interesting in many interdisciplinary scientific research.

2.6 The spreading application fields

In the last years, RPs again received more attention. Since 2005, more than 50 publications appear per year (Fig. 2.3). Whereas in the beginning of the applications of RPs, the method was mainly applied in life sciences (e.g. cardiology, neuro-psychology), the method became popular in other scientific fields during the years. Starting in 1994, a first application in earth sciences [185], in 1996 in finance [117], and in 1999 in engineering [90], chemistry [331] and applied physics [408] appeared. Since 2000 we find numerous applications in many disciplines, from physiology, to biology, earth sciences, acoustics, engineering and material sciences, finance and economics, to fundamental research in chemistry and physics (for examples we refer to [239]).

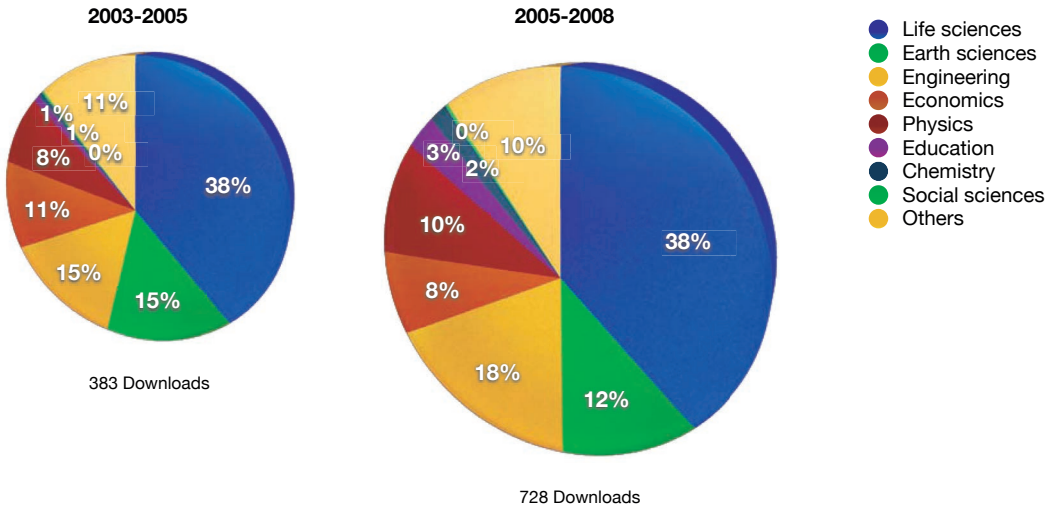

Figure 2.5: Usage of the CRP Toolbox for Matlab since 2003.

For the usage of the CRP Toolbox (cf. `http://www.recurrence-plot.tk`) we have a statistic of the main purposes of application, which allows us to estimate the distribution of applications of recurrence plot based techniques in different scientific disciplines since 2003 (Tab. 2.1, Fig. 2.5). Although we found few repetitions of downloads, the main distribution of application fields is not affected by such repetitions. A further problem in analysing these data is, that we sometimes got multiple choices of scientific fields, even rather unlike combinations, like earth science and neuro science. The selection of the scientific fields and sub-fields may occur rather arbitrary. We do not claim that it is a complete and best selection. However, it is mainly based on the submitted scientific fields or research interests of the users. Some noteworthy and interesting fields are hidden within the more general subjects, like artificial intelligence (in engineering), image processing or telecommunications (in computer and IT networks) or volcanology (in geophysics). Several users have not provided information about the intended purpose. We should also mention that we ensure a high data policy and use the provided data only for a statistical analysis like this.

Table 2.1: Scientific fields of usage of the CRP Toolbox since 2003 (May 2003 – October 2005, November 2005 – May 2008; descending order of usage in period 2005–2008).

Field	Subject	2003–2005		2005–2008	
Life sciences	Psychology/ cognitive and neuro sciences	54	147	152	275
	Medicinal research/ bio-electronics	59		75	
	Cardiology	24		36	
	Genomics/ DNA sequencing	2		6	
	Proteins/ systems biology	8		6	
Engineering	Engineering	39	56	63	131
	Computer and IT networks	7		30	
	Speech signals/ audio analysis	8		18	
	Traffic and transportation	2		14	
	Metal processing and analysis	0		6	
Earth sciences	Atmosphere and weather/ climatology	10	59	29	89
	Solar and astrophysics	9		14	
	Hydrology	4		12	
	Ecology	19		11	
	Geology	5		9	
	Geophysics	4		5	
	Seismology	6		4	
	Geography	2		5	
Physics	Applied physics	20	31	38	72
	Theoretical physics	11		34	
Economics	Finance and markets	35	41	41	55
	Economics	6		14	
Education			3		21
Chemistry			2		12
Social sciences			1		2
Others			43		71

For a usage statistics we consider two separate periods: a first period between May 2003 and October 2005 with 383 downloads and a second between November 2005 and May 2008 with 728 downloads, revealing the increasing popularity of RPs and the needs of a corresponding Matlab toolbox. The distribution of the application fields has only slightly changed between these two periods; only the increase of applications in engineering (from 15% to 18%) and the slight decrease in earth sciences (from 15% to 12%) is remarkable (Fig. 2.5). Therefore, in the following we discuss only the second period. The main application fields are life sciences (275 downloads), where psychology, neuro and cognitive sciences (EEG measurements) take the largest part (152 downloads) and cardiology only the third largest part (36 downloads) behind different medical problems (75 downloads). The next application fields are engineering (131), earth sciences (89), physics (72), economics (55), education (21), chemistry (12) and even social sciences (2). For 71 downloads we have not received sufficient information about the purpose of the usage.

2.7 Outlook

A rather curious sign that RPs are at the final step to really become widely known and accepted, we conclude with the 2008 April hoax of the Australian office of the internet company Google. In a press release on April 1st, 2008, Google announced the launch of a new search technology called *gDay*, which would be able to accurately predict future internet content [119]:

> "...Using Google's index of historic, cached web content and a mashup of numerous factors including recurrence plots and fuzzy measure analysis, gDay creates a sophisticated model of what the internet will look like 24 hours from now – including share price movements, sports results and news events. ..."

As we know, many things Google introduced turned out to be quite popular later.

Acknowledgement

The author thanks A. Giuliani, C. Webber Jr. and J. P. Zbilut for helpful comments and suggestions. This work has been supported by the project MAP AO-99-030 of the Microgravity Application Program/ Biotechnology from the Human Spaceflight Program of the European Space Agency (ESA).

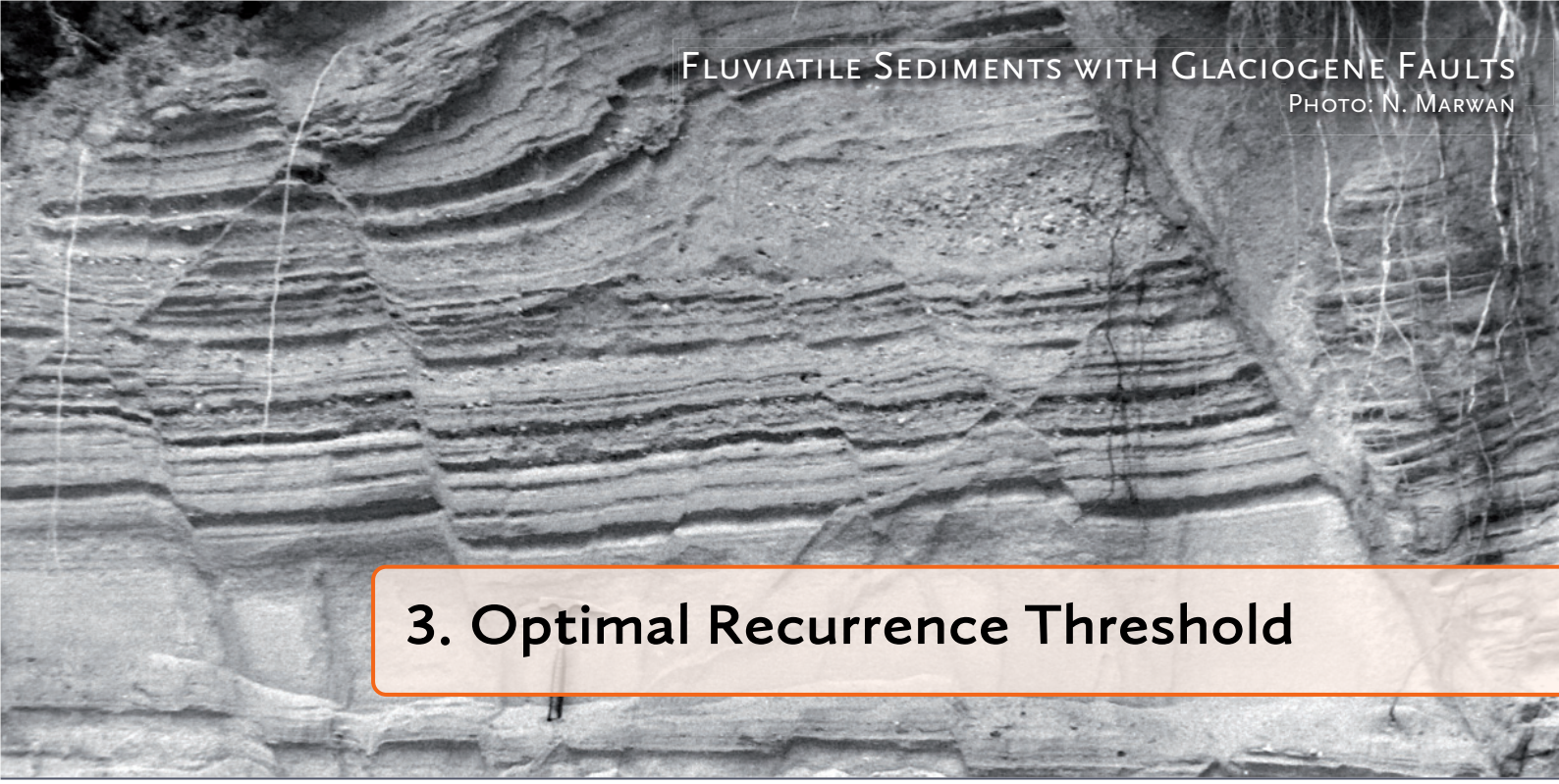

Fluviatile Sediments with Glaciogene Faults
Photo: N. Marwan

3. Optimal Recurrence Threshold

Paper 2 S. Schinkel, O. Dimigen, N. Marwan: Selection of recurrence threshold for signal detection, European Physical Journal – Special Topics, 164(1), 45–53 (2008). DOI:10.1140/epjst/e2008-00833-5

R The presented work in this chapter is a student's paper, where the idea, design, and implementation of the study was mainly performed by myself.

Abstract

Over the last years *recurrence plots* (RPs) and *recurrence quantification analysis* (RQA) have become quite popular in various branches of science. One key problem in applying RPs and RQA is the selection of suitable parameters for the data under investigation. Whereas various well-established methods for the selection of embedding parameters exists, the question of choosing an appropriate threshold has not yet been answered satisfactorily. The recommendations found in the literature are rather rules of thumb than actual guidelines. In this paper we address the issue of threshold selection in RP/RQA. The core criterion for choosing a threshold is the power in signal detection that threshold yields. We will validate our approach by applying it to model as well as real-life data.

3.1 Introduction

As *recurrence plots* (RPs) and their quantification (*recurrence quantification analysis*, RQA) [239] are becoming ever more popular in many disciplines, beginners are often faced with the problem of finding suitable parameters for embedding and recurrence threshold. For finding suitable embedding parameters, different approaches were suggested, like auto-correlation, mutual information, false nearest neighbours etc., and were already discussed in the literature [42, 109, 165, 398]. Yet the choice of the neighbourhood size is still under discussion and often causes uncertainties in applying RPs and RQA.

Several rules of thumb for the choice of the threshold have been suggested – a few per cent of the maximum phase space diameter [258], a value which should not exceed 10%

of the mean or the maximum phase space diameter [172, 442], or a value that ensures a recurrence point density of approximately 1% [445]. Further suggestions are to choose ε according to the recurrence point density of the RP by seeking a scaling region in the recurrence point density [445] or to take into account that a measurement of a process is a composition of the real signal and some observational noise with standard deviation σ [383]. In order to get similar results as in noise-free situations, ε has to be about five times larger than the standard deviation of the observational noise, i. e. $\varepsilon > 5\,\sigma$. But this approach fails for signals of very low signal-to-noise ratio (SNR) or if the amount of noise is unknown. In any case, the choice of the threshold depends on the aim of the analysis. For example, in a recurrence based synchronisation analysis or for joint recurrence plots (JRPs) [323], the threshold should be chosen in a fashion, that the recurrence point density is the same in the individual RPs.

In the following we will study the impact of recurrence threshold on signal detection [6, 439, 440]. As a prototypical and analytically well understood example we consider deterministic signals in a noisy environment (additive noise) and use several recurrence based measures in order to separate a signal from noise. We evaluate the applicability of this procedure in signal detection by *receiver operating characteristics* (ROC) [102, 320, 459]. To assess our findings in the model system we apply it to electroencephalographic (EEG) data obtained in a classical setup – the oddball paradigm [372].

3.2 Recurrence based detectors

Deterministic signals have a different recurrence structure than purely stochastic ones. Therefore, it was suggested to apply RQA to distinguish stochastic and deterministic processes [6, 320, 439, 440]. The base of the RQA is the recurrence plot, which visualises recurrences in the phase space of a state vector $\vec{x}_i$ $(i = 1, \ldots, N)$,

$$R_{i,j} = \Theta(\varepsilon - ||\vec{x}_i - \vec{x}_j||), \tag{3.1}$$

where Θ is the Heaviside function, $||\cdot||$ is a norm and ε is the recurrence threshold. For an overview about RPs and related aspects see [239]. RQA provides several measures of complexity. The *recurrence rate RR*

$$RR = \frac{1}{N^2} \sum_{i,j} R_{i,j}, \tag{3.2}$$

is the density of recurrence points in an RP and can be interpreted as the probability that any state will recur. A phase space trajectory of a deterministic system is characterised by epochs where different segments of this trajectory run parallel for some time. This behaviour is mirrored in the formation of diagonal line structures in the RP.

Denoting the number of lines of exact length l with $P(l)$, the RQA measure *determinism* DET is defined by

$$DET = \frac{\sum_{l \geq l_{\min}} l\, P(l)}{\sum_l l\, P(l)}, \tag{3.3}$$

where $l_{\min}$ is the minimal length of a diagonal line necessary to be considered as a line; in the present work we use $l_{\min} = 2$. DET can be interpreted as the probability that two closely evolving segments of the phase space trajectory will remain close for the next time step. Note that *determinism* does not relate to the mathematical notion of the term as such but

rather stresses the fact that RPs of stochastic processes usually reveal fewer diagonal lines, whereas RPs of deterministic processes contain more and longer diagonal line structures.

Instead of considering diagonal lines, we can measure vertical recurrence lines and estimate histograms $P(v)$ of vertical line lengths v. The measure

$$LAM = \frac{\sum_{v \geq v_{\min}} l\, P(v)}{\sum_{v} v\, P(v)} \tag{3.4}$$

is called *laminarity* (in the present work we use $v_{\min} = 2$) and measures the probability that a state will not change (within the ε error) for the next time step. Such behaviour is typical for intermittency and laminar states [237].

The last measure considered here is the mean *recurrence time* RT,

$$RT = \frac{\sum_{w=1}^{N} w\, P(w)}{\sum_{w=1}^{N} P(w)}. \tag{3.5}$$

As an estimator of recurrence time, we measure the vertical distance w between recurrence structures in an RP (corresponding to the length of white vertical lines if $R_{i,j} = 1$ is black and $R_{i,j} = 0$ is white). The number of vertical distances of exact length w is denoted by $P(w)$. Note that this estimator is a lower limit estimator. A definition of an upper limit estimator can be found in [110].

3.3 Receiver operating characteristic

Signal detection can be considered as a binary classification procedure by using a measure λ, where for $\lambda \geq \eta$ the signal is detected otherwise not. The *receiver operating characteristic* (ROC) is a plot of the probability to detect the signal correctly with λ (true positives, p_t) vs. the probability to classify the measurement as a signal although it is not (false positives, p_f) [102, 459]. In the theory of statistical testing p_t is also referred to as the *power* of a test. As the values of p_t and p_f correspond to the *sensitivity* and $(1 - specificity)$ respectively, for an optimal detection, a high value of p_t and a low value of p_f is desired.

The ROC curve serves as a performance measure of the chosen detector λ. A diagonal line means that classification of the signal or the noise as signal is equiprobable. Therefore, a reliable signal detection is only achieved, if the ROC curve evolves above the diagonal (Fig. 3.3C).

As a summary of the ROC the area under the curve (AUC) is frequently used. The higher the AUC the better the detector performs. The AUC corresponds to the probability that a signal will have a higher λ than the "no-signal". A value of AUC=1 corresponds to a 100% correct classification, whereas for AUC=0.5 we are not able to distinguish signal from noise.

To calculate the ROC we use 10,000 realisations of Gaussian white noise ξ, where we consider a signal s to be modified by additive noise resulting in the measurement $x = s + \xi$. For each realisation we compute the measures RR, DET and RT of the measurement x as well as for the noise ξ, providing the frequency distributions $h_x(\lambda)$ and $h_\xi(\lambda)$ of the values of the detector for the measurement x and the noise ξ (Fig. 3.3A, B). From the probability distributions $\tilde{h}_x = h_x / \sum h_x$ and $\tilde{h}_\xi = h_\xi / \sum h_\xi$ we calculate the probabilities of true and false positives by

$$p_t = \int_{\eta}^{\infty} h_x(\lambda) d\lambda \qquad \text{and} \qquad \mathrm{p_f} = \int_{\eta}^{\infty} \mathrm{h}_\xi(\lambda) \mathrm{d}\lambda. \tag{3.6}$$

In order to get the ROC curve, p_t and p_f are calculated for $\eta \in [\min(\lambda)\ \max(\lambda)]$.

3.4 Optimal recurrence threshold for a prototypical example

The main purpose of this work is to find a suitable criterion for the selection of an optimal recurrence threshold ε capable of detecting a deterministic signal in a noisy environment. Therefore the threshold with the highest AUC would be optimal for our purpose.

In order to study the AUC for different ε, we use a prototypical example providing a deterministic chaotic signal. We employ the first component of the quasiperiodically forced logistic map [403] as the deterministic signal s

$$s_{i+1} = f\cos(2\pi\theta_i) - as_i + s_i^3 \tag{3.7}$$
$$\theta_{i+1} = \theta_i + \omega \bmod 1. \tag{3.8}$$

For parameters $a = 1.3$ and $f = 0.7$, the system is in a chaotic regime (Fig. 3.1). For the analysis we used only 600 values (transients at the beginning were removed). The measurement x is formed by the composition of the normalised signal s ($\mu = 0,\ \sigma = 0$) and Gaussian white noise ξ ($\mu = 0,\ \sigma = 0$), i.e. $x = s + a\xi$, where a is the noise level, μ the mean and σ the standard deviation. In this example we use a noise level of $a = 0.75$.

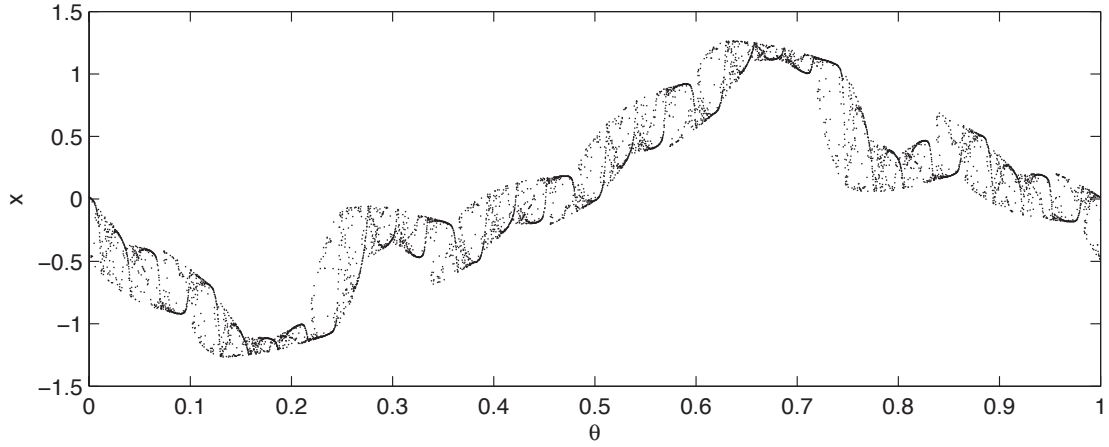

Figure 3.1: Quasiperiodically forced logistic map.

As the map is 2-dimensional the RP is calculated using an embedding dimension of $m = 2$ and a delay of $\tau = 1$. The RP of this signal s clearly reveals diagonal line structures indicating deterministic behaviour (Fig. 3.2A). These structures persist if the signal is slightly corrupted by noise (Fig. 3.2C).

For a given recurrence threshold ($\varepsilon = 0.5$), the histograms for the *RR* measure are presented in Fig. 3.3A and B. The overlap of the histograms of *RR* for the noise corrupted signal and the Gaussian white noise is small, providing a good discrimination of the signal. The corresponding ROC confirms the good performance of this measure (Fig. 3.3C). It should be noted that the distributions of the measures do not follow a normal distribution (gray line in Fig. 3.3A, B). This is important for the calculation of the ROC, because it can yield different results [231].

We calculate the AUC for the measures *RR*, *DET*, *LAM* and *RT* with varying $\varepsilon \in [0\,1.5]$. If ε is too small, recurrences mainly appear due to the fluctuations caused by the noise. A discrimination of the signal is therefore difficult and the AUC is low (Fig. 3.4). For increasing ε the RP obtains the recurrence structure contained in the signal. The detection of the signal becomes better and the AUC is high. If ε becomes too large almost every point is in the neighbourhood of every other point, thus hiding the characteristic recurrence structure. The signal is again not well detectable and the AUC is decreasing. Such a behaviour can be

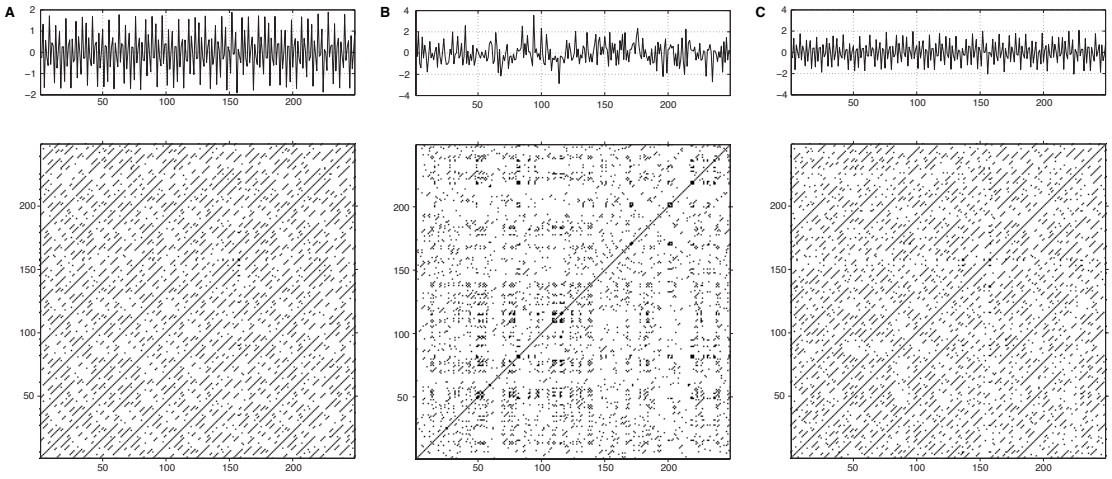

Figure 3.2: Detail of the recurrence plot of (A) the quasiperiodically forced logistic map, (B) Gaussian white noise and (C) a noise corrupted signal of the quasiperiodically forced logistic map (noise level 0.1). Embedding parameters $m = 2$, $\tau = 1$, recurrence threshold $\varepsilon = 0.5$.

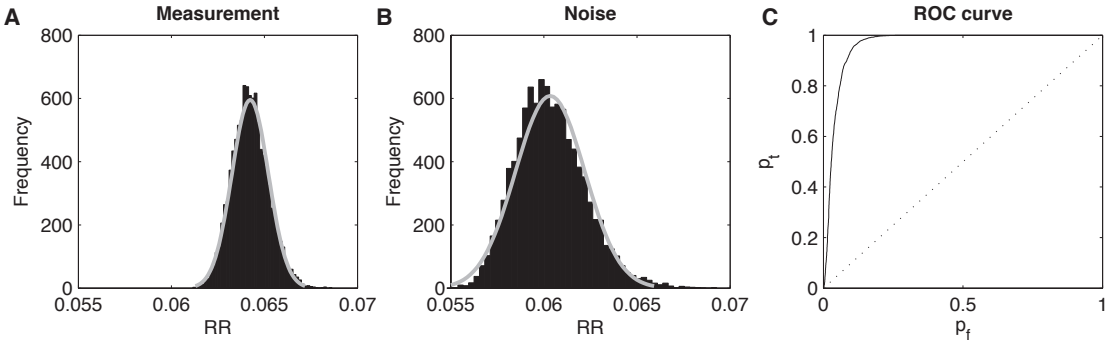

Figure 3.3: Histogram of the *RR* detector for 10,000 realisations of a measurement containing (A) a signal from the quasiperiodically forced logistic map and (B) Gaussian white noise. A fit of a normal distribution is presented as a gray line. Applying a threshold on the detector *RR* we will be able to detect the signal in most cases. This is characterised by (C) the ROC curve, which is based on the probabilities to detect true positives (p_t) and false positives (p_f). If the ROC curve would follow the diagonal line (dotted line), we would not be able to distinguish the signal from noise.

observed in *RR*, *DET* and *RT* (Fig. 3.4). The measures *RR* and *DET* perform best with a maximum AUC of about .8 (*RR*) or even .9 (*DET*) for $\varepsilon = 0.4$. In contrast, the AUC for *RT* is significantly smaller and has its maximum of 0.6 for an $\varepsilon = 0.15$. This suggests that *RT* is not an optimal detector for chaotic maps. The measure *LAM* shows a completely different behaviour. Its values are below 0.5, indicating that *LAM* falsely classifies noise as the signal. That is due to the fact the RP of noise contains more vertical structures than the RP of the signal (Fig. 3.2) which does not contain any laminar phases. Therefore, the measure *LAM* is not appropriate for detecting a deterministic signal as considered here. However, as we will see later, this measure is a useful detector for signals like EEGs which do contain laminar phases.

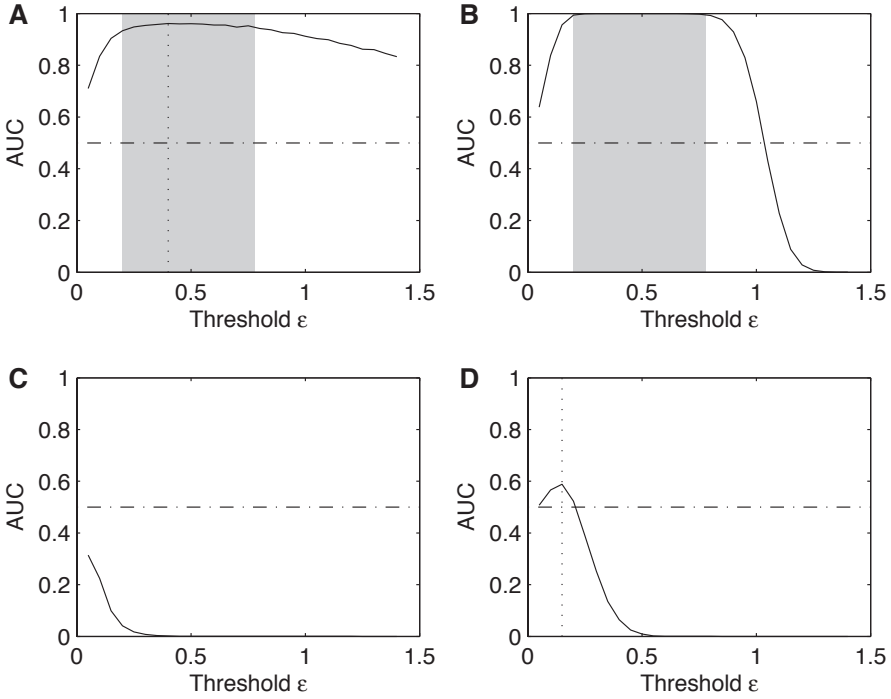

Figure 3.4: AUCs vs. ε for the measures (A) *RR*, (B) *DET*, (C) *LAM* and (D) *RT* for the quasiperiodically forced logistic map. The AUC for *RR* and *DET* (A, B) is rather high in a range of $\varepsilon \in [0.2\,0.78]$, with the maximum at $\varepsilon = 0.4$ (dotted line). The AUC of *RT* (D) is significantly lower, with a maximum at $\varepsilon = 0.15$ (dotted line). The AUC of *LAM* is lower than 0.5, indicating that this measure falsely classifies noise as signal. An AUC level of 0.5 (dash-dotted line) means that the detector is not able to find the signal.

3.5 Application on EEG measurements

We apply the suggested procedure to EEG measurements of a study on event-related potentials (ERPs). The paradigm used was a visual *oddball* featuring a prominent P300, which is a centro-parietal positivity peaking at about 300 ms after the presentation of a stimulus. The P300 has been shown to be senstive to stimulus category (target vs. non-target) of the eliciting stimulus [372].

The simuli were red and green disks presented in randomized, equiprobable order. Stimulation duration was 100 ms, the interval between successive stimuli 900 ms. The task was to count the items of one colour (green or red) thereby constituting the target (A) (items

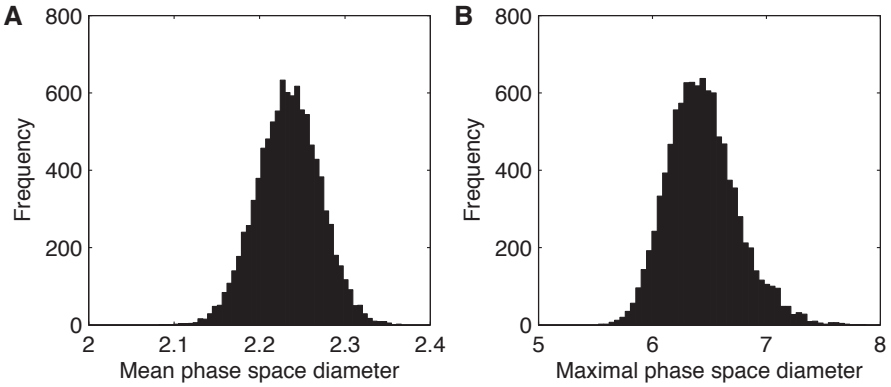

Figure 3.5: Distribution of (A) mean and (B) maximal phase space diameter of 10,000 realisations of the noise corrupted quasiperiodically forced logistic map in an embedding space of $m = 2$ and $\tau = 1$.

to be counted) and non-target condition (B). This setup is known to elicit a prominent and reproducible P300 in the target condition (compared to the non-target condition).

The EEG was recorded from 40 Ag/AgCl electrodes (impedances ≤ 5 kΩ) at a sampling rate of 250 Hz using a BrainAmp DC amplifier (Brain Products GmbH, Munich, Germany). All electrodes were initially referenced to an electrode on the left mastoid bone (A1) and converted to average reference off-line. After standard artifact rejection about 250 trials remained in each condition. For our purpose we selected 200 trials of one subject recorded at electrode PZ. The data was baseline corrected to 100 ms pre-stimulus. Details of artifact rejection and pre-processing can be found in [401].

We consider a pre-stimulus interval of 250 ms duration, immediately before the stimulus (−200–50 ms) and a 250 ms interval during the P300 (200–450 ms). During the pre-stimulus, the two measurements of condition A and B should not be distinct, resulting in a AUC of around 0.5. In contrast, if the detectors are able to distinguish the two conditions, their AUC values should be higher than 0.5. For the computation of the ROC the 200 trials are used as realisations. The AUCs are calculated for recurrence thresholds ε between 0.1 and 1.0 with steps of 0.01, and using an embedding of $m = 3$ and $\tau = 2$. The embedding parameters were estimated using the commonly accepted methods of false nearest neighbours and mutual information [165].

As expected, the AUCs for all detectors in the pre-stimulus interval are around 0.5, indicating that there is no difference between the measurements before the onset of the stimulus (Fig. 3.6). Only *LAM* and *RT* reveal slightly smaller or higher values for ε between 0.1 and 0.2.

During the occurrence of the P300, the AUCs for the detectors *RR*, *DET*, and *LAM* are higher than 0.5, indicating that these measures are able to discriminate between condition A and B. However, the highest AUC value is 0.61 for *RR* and *LAM*, and 0.63 for *DET*, what is not really high. The *RT* is not a good detector as it again fails in discriminating the two conditions. As we found in previous works, other RQA measures (like *trapping time*) [233] or the application of *order pattern recurrence plots* [227, 339] reveal better results. Nevertheless, we find the optimal recurrence threshold as $\varepsilon = 0.25$, for *RR* and *LAM*, or as $\varepsilon = 0.22$, for *DET*. The mean and maximal phase space diameter for the pre-stimulus and the P300 epochs of the ERP data of both conditions are 2.40 and 5.55, respectively. Thus, the optimal $\varepsilon = 0.25$ found corresponds to 10% of the mean and 5% of the maximal phase space diameter. Regarding the standard deviation $\sigma(x) = 1$ of the ERP signal itself, ε is 25%

of the standard deviation.

In contrast to the prototypical example of the quasiperiodically forced logistic map discussed above, the ERP signal contains laminar states at the P300. Therefore, *LAM* now is a suitable detector for the P300.

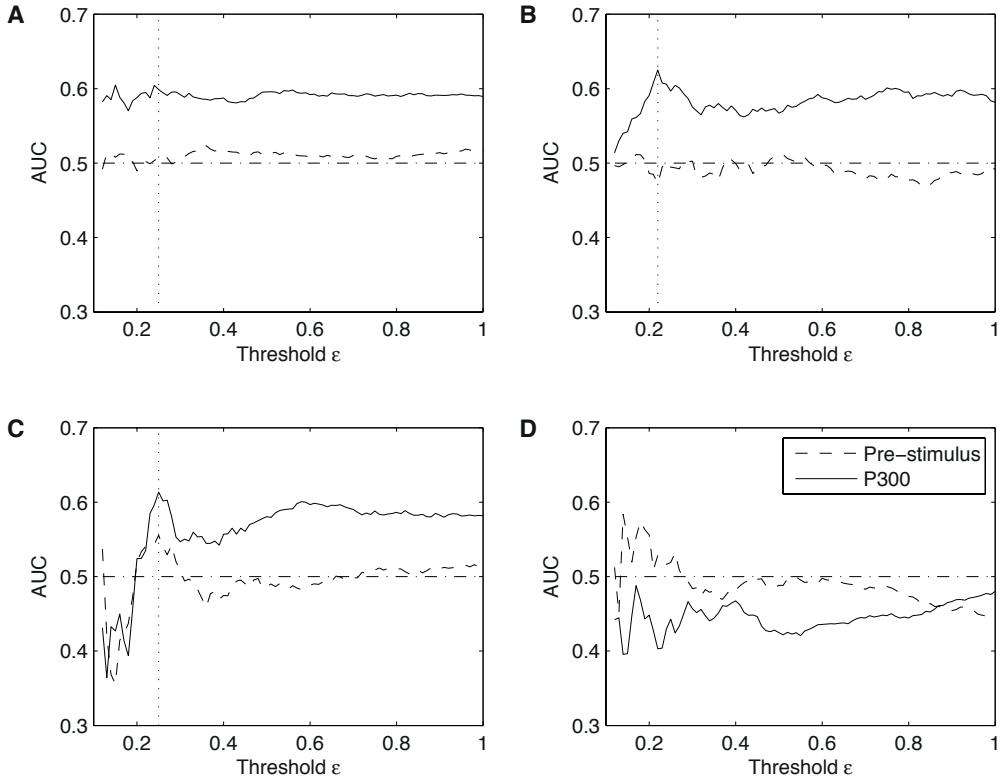

Figure 3.6: AUCs vs. ε for the measures (A) *RR*, (B) DET, (C) *LAM* and (D) *RT* for ERP data on a pre-stimulus period (dashed line) and during the P300 event (line). AUC maxima for *RR* and *LAM* at $\varepsilon = 0.25$, and for DET at $\varepsilon = 0.22$ (dotted line). An AUC level of 0.5 (dash-dotted line) means that the detector is not able to find the signal. Embedding parameters are $m = 3$ and $\tau = 2$.

3.6 Discussion

The search for a recurrence threshold for an optimal discrimination of signals has revealed different optimal thresholds ε depending on the application and considered type of signal (Tab. 3.1). Using the recurrence probability alone for the detection may require another threshold than using diagonal line structures or vertical line structures. However, the differences in the optimal ε are not big, and of course the optimal threshold also depends on the amount of noise present in the measurement.

For the quasiperiodically forced logistic map the threshold $\varepsilon = 0.4$ at the maximum of AUC corresponds to a calculated *RR* of the system of 4%. This suggests that the threshold should be chosen in such a way that the *RR* would be around 5%. Several authors suggested values of ε relative to the mean and maximal phase space diameter [172, 442]. The mean phase space diameter of the noise corrupted quasiperiodically forced logistic map (normalised to standard deviation one) is 2.23 and its maximal diameter is 6.43 (Fig. 3.5). Therefore $\varepsilon = 0.4$ corresponds to 18% of the mean and 6% of the maximal phase space diameter

Table 3.1: Optimal recurrence thresholds ε and corresponding percentages of mean and maximal phase space diameter (mean PSD and max. PSD) as well as signal standard deviation σ.

	ε	mean PSD	max. PSD	σ
quasiperiodically forced logistic map	0.4	18%	6%	40%
ERP data	0.25	10%	5%	25%

respectively. As our aim here is an appropriate classification of signal and noise and not the detection of the original recurrence structure, choosing $\varepsilon > 5\,\sigma$, as suggested for the case of observational noise [383], is not beneficial here. Considering the noise level of $a = 0.7$, $5\,\sigma(\xi)$ would result in a value of 2.5 for ε. Indeed, this value is too high to correctly classify signal and noise. Compared to the standard deviation of the entire, normalised signal $\sigma(x) = 1$, ε equals 40% of $\sigma(\xi)$.

For the experimental data, we found that the optimal threshold is 10% of the mean phase space diameter or 25% of the standard deviation. For the prototypical example, where the influence of noise is far smaller than in the experimental data, we found a threshold almost twice as large, given as 18% of the mean phase space diameter and 40% of the standard deviation. The most consistent choice would be regarding the maximal phase space diameter, where we found values of around 5–6% of the maximal phase space diameter in both experiments.

Although only demonstrated using two examples and knowing well that the matter needs to be investigated more comprehensively, our study confirms the suggested rule of thumb that the threshold should be around 5% of the maximal phase space diameter. This suggestion remained valid for two very different kinds of signal of different complexity, a priori knowledge and noise influence. Hence it seems to be rather robust, at least for the purpose of signal detection.

3.7 Conclusions

We have proposed a new approach for the choice of an optimal recurrence threshold ε for the classification of signals. Our method uses the notion of *receiver operating characteristics* (ROC), a statistical tool to validate a classification process and investigate its discriminative power in dependence of a given detector, in the present case the complexity measures as derived from an RP using the RQA. We could demonstrate the discrimination of (i) signals from pure noise and (ii) of different experimental conditions given as extremely noisy and instationary time series typical for EEG measurements. Our results support the proposed rule of thumb, that the recurrence threshold ε for optimal signal classification/discrimination should be about 5% of the maximal phase space diameter.

Acknowledgement

This work was supported by grants of the European Union through the Network of Excellence BioSim, contract LSHB-CT-2004-005137 & No. 65533, the German Science Foundation (DFG) in the SFB 555 *Komplexe nichtlineare Systeme* and the Research Group FOR 868: *Computational Modeling of Behavioral, Cognitive and Neural Dynamics*, and the COST Action BM0601 *NeuroMath: Advanced Methods For The Estimation Of Human Brain Activity And Connectivity*. The software (CRP Toolbox) used for this work is partly available for download at `http://tocsy.agnld.uni-potsdam.de`.

Karren Field in the Swiss Alps
Photo: N. Marwan

4. Automatic Threshold Selection

Paper 3 D. Eroglu, N. Marwan, S. Prasad, J. Kurths: Finding recurrence networks' threshold adaptively for a specific time series, Nonlinear Processes in Geophysics, 21, 1085–1092 (2014). DOI:10.5194/npg-21-1085-2014

R The presented work in this chapter is a student's paper, where my contribution was the idea to use the second minimum eigenvalue of the Laplace matrix for the recurrence threshold, which is the main innovation of this paper.

Abstract

Recurrence plot based recurrence networks are an approach to analyze time series using complex networks theory. In both approaches, recurrence plots and recurrence networks, a threshold to identify recurrent states is required. The selection of the threshold is important in order to avoid bias of the recurrence network results. In this paper we propose a novel method to choose a recurrence threshold adaptively. We show a comparison between constant threshold and adaptive threshold cases to study period-chaos and even period-period transitions in the dynamics of a prototypical model system. This novel method is then used to identify climate transitions from a lake sediment record.

4.1 Introduction

Recurrence based approaches have taken an important place in dynamical systems analysis. Related approaches have been used for several decades. The basis of this analysis is finding recurrent points on a trajectory in the phase space of a dynamical system. The first recurrence based analysis method was introduced by Poincaré as the method of the first recurrence times [292]. A Poincaré recurrence is the sequence of time intervals between two visits of a trajectory to the same interval (or volume, depending on the dimension of the trajectories).

Among the different approaches to investigate dynamical properties by recurrence, the recurrence plot (RP) is a multifaceted and powerful approach to study different aspects of dynamical systems. RPs were first introduced as a visualization of recurrent states of

phase space trajectories [86], but then enriched by different quantification techniques for characterizing dynamical properties, regime transitions, synchronization, etc. [239]. In the study of complex systems, one of the most important issues is finding dynamical transitions or regime changes. Transitions in the dynamics can be detected by different RP based measures, which in general are powerful to study complex, real-world systems [73, 237, 397]. Examples of their successful application in real-world systems can be found in life science [44, 237, 270, 316], Earth science [73, 238, 246], astrophysics [9, 452], and others [224].

The measures defined by the RP framework, called *recurrence quantification analysis* (RQA), are based on point density and on the length of diagonal and vertical line structures visible in the RP, being regarded as alternative measures to quantify the complexity of physical systems. In order to uncover their time-dependent behaviour, RQA measures are often computed by applying a sliding window on the time series, which then can be used to identify dynamical transitions, such as period-chaos transitions [397] or chaos-chaos transitions [237].

Another popular method to analyse complex systems is the complex network approach [27, 416]. Complex network measurements are useful to investigate and understand the complex behaviour of real world systems such as social, computer [273], or brain networks [352]. The adjacency matrix of a complex network explains the structure of the system, thus, determines the links between the nodes of a network. For unweighted and undirected networks, the adjacency matrix is binary and symmetric, hence very similar to an RP. In our previous work, we have shown that time series can be analysed by complex networks by identifying the RP by the adjacency matrix of a network [78, 241], forming so-called recurrence networks (RNs). Complex network measures applied to RNs have been used to investigate real-world systems such as the climate system [73] or the cardio-respiratory system [303]. RNs have been shown to be more sensitive for the detection of periodic-chaos or chaos-periodic regime transitions than some of the standard RQA measures [225, 455].

Although recurrence based methods are powerful tools to study complex systems, they come with an important, non-trivial issue [225]. To identify recurrences, usually a spatial distance (or volume, depending on the dimension of the system) in the phase space is used and a sufficient closeness between the trajectories is determined by applying a so-called recurrence threshold ε to the distances [76, 239]. Several approaches for selecting a meaningful threshold value has been suggested [74, 239, 338]. Of particular interest are such methods that help to overcome the problem of sliding window based analyses of systems with varying amplitude fluctuations (as coming from different dynamical regimes or non-stationarities), e.g., based on normalizing time series or fixing recurrence density. However, in real-world applications, time series are usually not smooth all the time. When considering the time series by a RN representation, extreme points (very high jumps or falls in the fluctuation of time series) in the time series could break the connected components in the network since the distance between an extreme point and other points would be larger than the threshold value. The normalization method would then result in non-optimal recurrence thresholds biasing the recurrence analysis.

In this work we will suggest a novel method of an adaptive threshold selection basing on the network's spectral properties [27]. We will present a comparison between the constant and the adaptive threshold approach for detecting certain regime transitions (chaos to periodic or periodic to chaos). Finally we will demonstrate the novel approach for analyzing lake sediment based palaeoclimate variation.

4.2 Recurrence plots, recurrence networks and the adaptive threshold

In the m-dimensional phase space reconstruction of a time series, a state is considered to be recurrent if its state vector falls into the ε-neighbourhood of another state vector. Formally, for a given trajectory $\vec{x}_i$ ($i = 1, \ldots, N, \vec{x}_i \in \mathbb{R}^m$), the recurrence plot $\mathbf{R}$ is defined as

$$R_{i,j}(\varepsilon) = \Theta(\varepsilon - \|\vec{x}_i - \vec{x}_j\|),\ i, j = 1, \ldots, N, \tag{4.1}$$

where N is the trajectory length, $\Theta(\cdot)$ is the Heaviside function, and $\|\cdot\|$ is the norm of the adopted phase space [239]. Thus, $R_{i,j} = 1$ if states at times i and j are recurrent, and $R_{i,j} = 0$ otherwise. The trajectory in the phase space can be reconstructed via time delay embedding from a time series $\{u_i\}_{i=1}^N$ [286]

$$\mathbf{x}_i = (u_i, u_{i+\tau}, ..., u_{i+\tau(m-1)}), \tag{4.2}$$

where m is the embedding dimension and τ is the embedding delay. The embedding dimension m can be found by false nearest neighbours and the delay τ by mutual information or auto-correlation [165].

The main diagonal of the RP, $R_{i,i} = 1$, represents the line of identity (LOI). As we have mentioned the RP is a symmetric, binary matrix. The structures formed by line segments, which are parallel to the LOI in an RP, characterize typical dynamical properties. We observe homogeneously distributed recurrence points if the dynamics is white noise. If the system is deterministic, diagonal line segments which are parallel to the LOI will dominate. The dynamics is related to the length of the diagonal line segments: chaotic dynamics causes mainly short line segments, but contrary, regular (periodic) dynamics causes long line segments. The RQA quantifies this relation and can be used to detect transitions in the system's dynamics [239, 397].

Recurrence networks are based on the recurrence matrix, Eq. (4.1) which is a $N \times N$ matrix where N is the length of the phase space trajectory (the number of time steps). We now consider these time steps as nodes of a network; if the nodes are sufficiently close to each other, in other words, if the space vectors are neighbours, there is a link between them. In network theory, connections between network nodes can be described with the adjacency matrix $\mathbf{A}$, with $A_{i,j} = 1$ if there is a link between nodes i and j, otherwise $A_{i,j} = 0$. To obtain the adjacency matrix from the recurrence matrix, we discard self-loops in the recurrence matrix, i.e.,

$$A_{i,j} = R_{i,j} - \delta_{i,j}, \tag{4.3}$$

where $\delta_{i,j}$ is the Kronecker delta ($\delta_{i,j} = 1$ if $i = j$, otherwise $\delta_{i,j} = 0$).

The number of links at the ith node (the degree) is given by $k_i = \sum_j A_{ij}$. In this paper we use the eigenvalue spectrum of the Laplacian matrix $\mathbf{L}$ to find an adaptive threshold ε_c, where $L_{i,j} = \delta_{i,j} k_i - A_{i,j}$.

The crucial point in the paper is choosing the adaptive threshold for calculating the RN. A threshold for recurrence based methods should be *sufficiently* small [74, 76, 239]. Too small ε cause very sparsely connected RN with many isolated components; too large ε results in an almost completely connected network. For data sets which are not smooth, choosing an actually reasonable small threshold could nevertheless result in unconnected recurrence network components. These unconnected components would cause problems for some complex network measures, since some of them need a connected network to be computed for the entire network. For example, even if we have just one node that is not connected to the network, the average path length will be always infinite for the entire network. An even more important motivation for avoiding isolated components in the RN is that the

RN provides a large amount of information about the dynamics of the underlying system although it contains only binary information. This has been demonstrated by reconstructing time series from RPs [146, 381]. The condition for reconstructing a time series from an RP is that all points are connected by their neighborhoods, i.e., there are no isolated components. By applying recurrence measures we would like to quantify the dynamics encoded by the RN. This can be ensured by the above mentioned condition.

To find a *sufficiently* small threshold ε that fulfills the desired condition of connected neighborhoods, we will use the connectivity properties of the network. In particular, we choose the value for ε that is the smallest one for the RN to be connected. In order to find such an adaptive threshold, we start from very small values of the threshold and vary the ε parameter until we get a connected network. In order to apply this approach efficiently, we use iterative bisection method in the simulations. The connectivity of a network can be measured by the second smallest eigenvalue λ_2 of the Laplacian matrix. If the network is connected, $\lambda_2 > 0$ [27]. We choose the adaptive threshold value as the minimum value of the sequence of thresholds $\mathbf{T} = T_i, T_{i+1}, \ldots$ when the second minimum eigenvalue λ_2 is positive,

$$\varepsilon_c = \min(\mathbf{T}) \text{ with } \mathbf{T} = \{T_i \,|\, \forall i : \lambda_2(T_i) > 0\}. \tag{4.4}$$

Values ε below the critical value ε_c are indicating the existence of unconnected components in the RN (Fig. 4.1). After that critical threshold, λ_2 becomes positive and if we still increase the threshold the connectivity of the RN is increasing. By choosing the critical point ε_c as the recurrence threshold, we ensure that the RN will be connected by the smallest threshold possible.

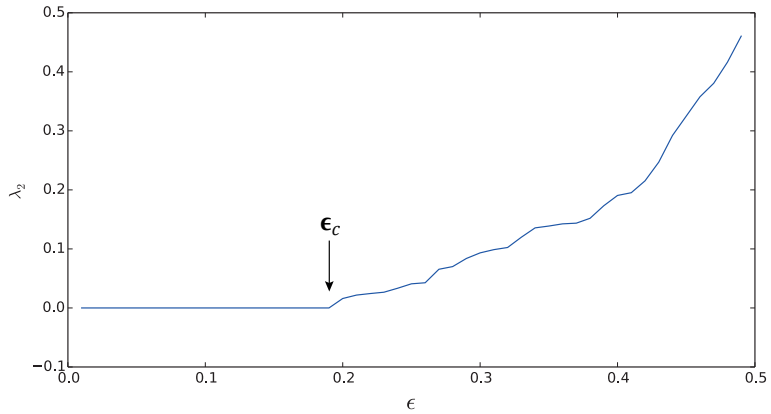

Figure 4.1: Variation of the second smallest eigenvalue of the Laplacian λ_2 due to changing threshold value, using the logistic map as an illustrative example (control parameter $a = 4.0$). $\lambda_2 = 0$ for thresholds below a critical value ε_c, indicating the existence of unconnected components in the RN. For $\varepsilon > \varepsilon_c$, there are no unconnected components in the RN anymore. The adaptive threshold value for this time series is $\varepsilon_c \approx 0.19$.

4.3 Applications

4.3.1 Logistic map

As a first application we compare some RN measures for using first the adaptive and then constant threshold approach by analysing the logistic map,

$$x_{i+1} = a x_i (1 - x_i). \tag{4.5}$$

It is one of the most popular iterated maps which has different regimes for different control parameter a. The detection of the transitions of the logistic map between these different regimes was studied with RP and RN previously[241, 397]. The logistic map shows interesting dynamics in the range of the control parameter $a \in [3.5, 4.0]$, which is studied here with a step size of $\Delta a = 0.0005$, there occur e.g., periodic and chaotic regimes, bifurcations, inner and outer crises. We compute a time series of length $N = 5000$ for each value of a. In order to discard transients, we delete the first 2000 values, resulting in time series consisting of 3000 values that have been used for all analysis of the logistic map in this paper.

As the constant threshold selection method, we use the recurrence rate method to choose a threshold value: a threshold is selected in such a way that the recurrence rate RR is constant even for different time series with different dynamics (e.g., different values of a) [239]. In this paper, we use $RR = 5\%$ arbitrarily for further analysis.

Now we compute the RNs by using the given threshold selection techniques ε and ε_c for each control parameter a. We then calculate transitivity T and betweenness centrality BC as the complex networks measures in order to detect the transitions from periodic to chaotic, chaotic to periodic states, bifurcations and inner(outer)-crisis. The network transitivity is given by,

$$T = \frac{\sum_{i,j,k} A_{i,j} A_{j,k} A_{k,i}}{\sum_{i,j,k} A_{k,i} A_{k,j}}. \tag{4.6}$$

The average betweenness centrality of network,

$$BC = \frac{1}{N} \sum_{v} \sum_{s \neq v \neq t} \frac{\sigma_{st}(v)}{\sigma_{st}}, \tag{4.7}$$

where σ_{st} is the total number of shortest paths from node s to node t and $\sigma_{st}(v)$ is number of those paths that pass through v. As mentioned in the previous chapter, not all complex network measures can be applied to a disconnected network. However, it would cause problems for computing the measures on RNs calculated by using the constant threshold technique, since the network could be disconnected. For instance, to compute the average shortest path length or assortativity for an entire network, the network must be connected. Disconnected nodes of the network could be discarded from the calculation, but in this case, we would lose information. In the adaptive threshold case, we could calculate all these measurements on the entire network since the selection of the adaptive threshold ensures that the recurrence network is connected.

Both threshold selection methods could detect transitions between dynamical regimes (periodic-chaos or chaos-periodic). Transitivity gives large values for the chaotic regime and small values for periodic. In the betweenness centrality case, it is contrary to transitivity, large values for periodic and small values for the chaotic regimes. Although the constant threshold selection detects the periodic windows (chaos-period transitions) more sharply than the adaptive threshold case, the transitivity and betweenness centrality for the constant threshold selection case in the constant threshold case, as general, the threshold arbitrarily chosen by $RR = 5\%$), T_{constant} and BC_{constant}, cannot distinguish between different periodic dynamics, i.e., cannot detect certain bifurcation points such as for period doublings, e.g., at $a \approx 3.544, 3.564, 3.84$. Contrary, in the adaptively chosen threshold case, T_{adaptive} and BC_{adaptive} are sensitive to these bifurcations (Figs. 4.2, 4.3). Thus, using the adaptive threshold allows also the detection of period-period transitions (i.e., the study of bifurcation points where the maximal Lyapunov exponent keeps non-positive).

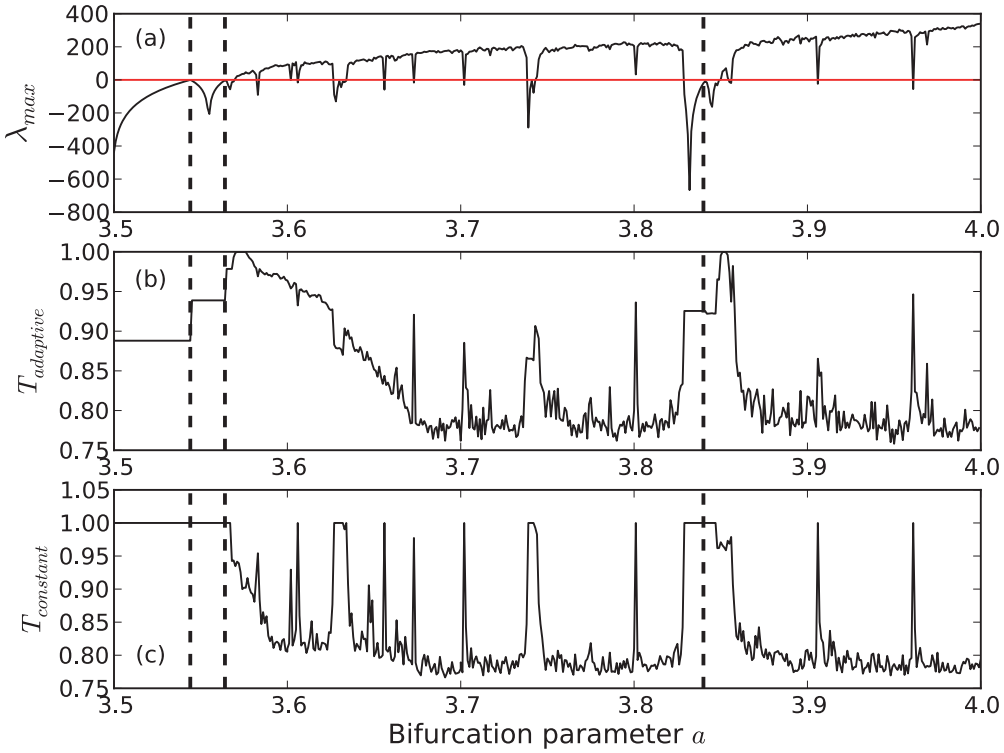

Figure 4.2: (a) Lyapunov exponent and transitivity using (b) adaptive threshold and (c) constant threshold for the logistic map. Dashed lines show certain bifurcation points before the chaotic regime.

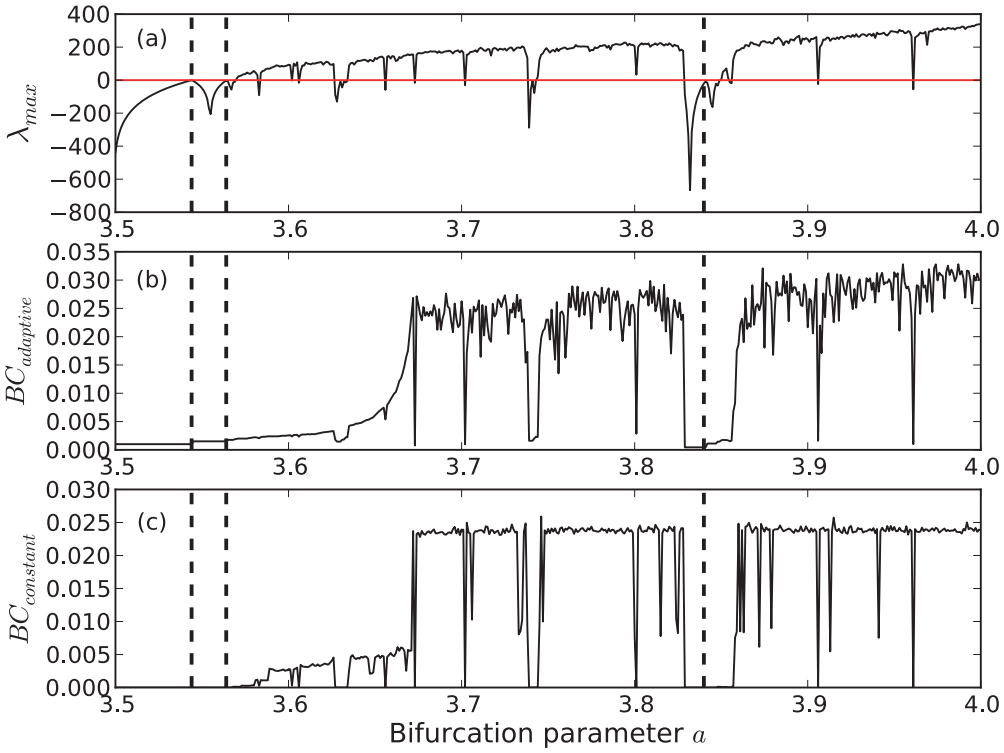

Figure 4.3: (a) Lyapunov exponent and betweenness centrality using (b) adaptive threshold and (c) constant threshold for the logistic map. Dashed lines show certain bifurcation points before the chaotic regime.

4.3.2 Application to palaeoclimate record

The study of palaeoclimate variation helps in understanding and evaluating possible future climate change. Lake sediments provide valuable archives of past climate variations.

In the following we will focus on a well dated high resolution climate archive from palaeolake Lisan located beneath the archaeological site of Massada in the Near East [295, 296]. The sediments from the Upper Member were deposited ($26-18$ cal ka BP) when the lake reached its highest stands [14, 390]. The sedimentary sequence contains varves comprising seasonally deposited primary (evaporitic) aragonite and silty detritus [296]. The pure aragonite sublaminae were precipitated from the upper layer of the lake during summer evaporation. Their formation requires inflow of HCO_3^- ions into the lake from the catchment area during winter floods [360] that also bring in silty detrital material. One detrital and overlying aragonite sublaminae constitute a varve. Previous studies [296, 390] indicate that small ice-rafting events (denoted as a, b, c, and d), as well as prominent Heinrich events in the North Atlantic, are associated with the Eastern Mediterranean arid intervals. The study of seasonal sublaminae yields evidence of decadal to century scale arid events that correlate with cooler temperatures at higher latitudes. Analyses in the frequency domain indicate the presence of periodicities centered at 1500 yr, 500 yr, 192 yr, 139 yr, 90 yr, and $50-60$ yr, suggesting a solar forcing on climate [296].

We use the yearly sampled pure aragonite proxy ($CaCO_3$) from the palaeolake Lisan for our RN analysis (Fig. 4.4a). We use a time delay embedding with dimension $m = 3$ and delay $\tau = 2$ (these parameters have been computed by standard procedure using false nearest neighbours and mutual information [165, 286]) for reconstructing the phase space. To detect dynamical transitions in the palaeoclimate data, we adopt a sliding window of W data points with a step size of ΔW. RNs are computed for each window of the time series one by one. We have chosen a sampling window size of $\Delta T = 100$ yr with 90% overlap corresponding to a time window size of $W \approx 100$ data points (since there are some gaps in the data, it is not exactly 100). The time series' length is $N = 7665$ and the total number of the windows analysed is

$$\frac{N-W}{\Delta W} \approx 755.$$

Transitivity and betweenness centrality is then calculated within these windows (Fig. 4.4b and c). As we have shown for the logistic map, transitivity and betweenness centrality are both sensitive to detect transitions. Larger values of transitivity T refer to regular behaviour, whereas smaller values to more irregular dynamics in the considered window of the time series.

The grey shaded horizontal band in Fig. 4.4b, c is the confidence interval of the network measures. We apply a rather simple test in order to see whether the characteristics of the dynamics at a certain time statistically differs from the general characteristics of the dynamics. In order to apply this test, we use the following approach. We create surrogate data segments of length W by drawing data points randomly from the entire time series and we compute the RN and the network measures from such a surrogate segment. We repeat this 10,000 times and have an empirical test distribution of transitivity T and betweenness centrality BC. A confidence interval is then estimated from these distributions by their 0.05 and 0.95 quantiles.

Previous studies [296] had identified multiple climate fluctuations in the varved Lisan record and correlated them with the Greenland oxygen isotope data (indicative of temperature changes, [369]) and ice rafting events in the north Atlantic [30]. The blue and orange vertical bars in Fig. 4.4 delineate periods of cooling and warming respectively in the higher latitudes that resulted in drier and wetter episodes in the eastern Mediterranean.

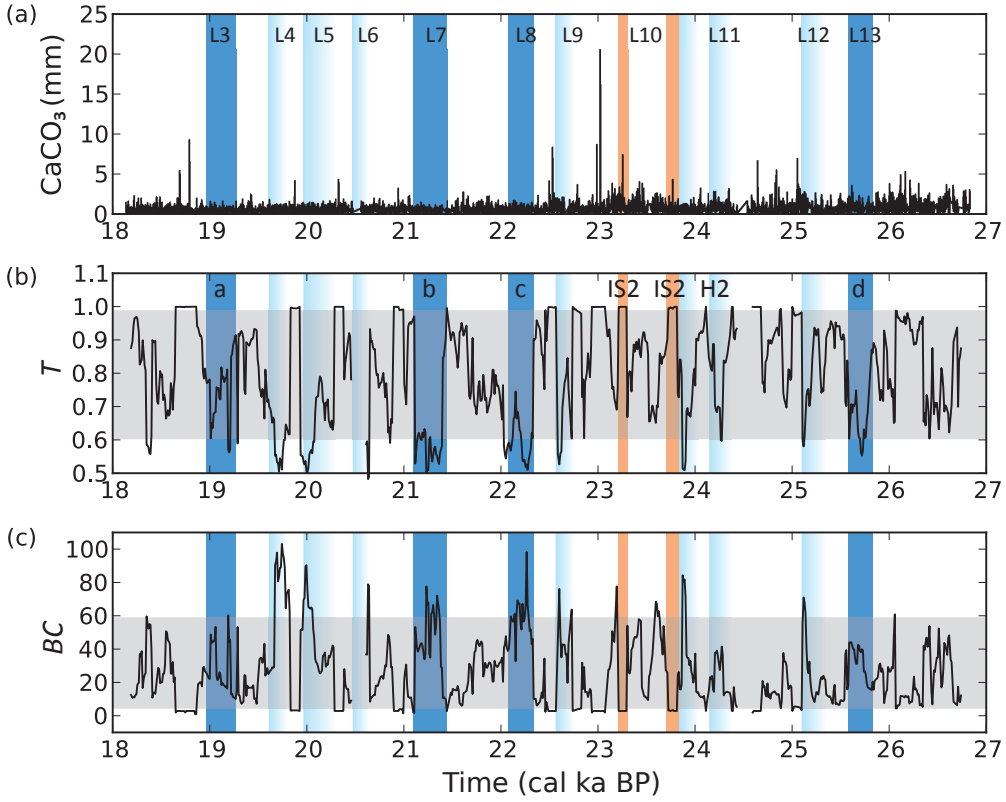

Figure 4.4: (a) Aragonite ($CaCO_3$) record from palaeolake Lisan, (b) transitivity, and (c) betweenness centrality results of RN using the adaptive threshold. Abrupt changes in T and BC indicate transitions between different climate regimes. Dry events in Lake Lisan (cooling of the higher latitudes) are marked by blue bars and two interstadial peaks (warming) by orange bars. The gray shaded band is the 90% confidence interval for the networks measures.

The network measures T and BC both indicate well abrupt transitions (Fig. 4.4b, c). In particular for T, the values jump between high and low values. T reveals epochs of significantly low values at around 25.8–25.6, 25.2–25.1, 24.3–24.2, 24.0–23.9, 22.8–22.6, 22.3–22.1, 21.5–21.1, 21.7, 20.6–20.5, 20.1–19.9, 19.8–19.6, and 19.3–18.9 cal ka BP. The periods 25.8–25.6, 22.3–22.1, 21.5–21.1, and 19.3–18.9 cal ka BP correspond to the known Bond events d, c, b, and a, and the epoch between 24.3 and 23.9 cal ka BP coincides with the Heinrich H2 event. During the interstadial peaks IS2 at 23.8–23.7 and 23.3–23.2 cal ka BP, T shows significant high values, almost reaching the value one. BC exhibits a rather similar behavior of abrupt transitions like T, but with opposite sign. A general observation is that low values in T can be found during dry but high values during wet regimes, and that such regimes change abruptly.

A high transitivity value indicates a more regular deposition of aragonite, and, thus, a more regular, or even periodic climate variability. This could be an indication for a dominant role of the (more or less periodic) solar forcing via its influence on the temperature in the higher latitudes. During phases of a colder North Atlantic, the solar forcing become less important but regional climate effects more important and dominating, causing a more complex, irregular climate variability, finally indicated by low values of T.

Combining the maxima of T and minima of BC, we can identify the above mentioned periods of non-regular climate dynamics. Most of these periods correspond to cold events, e.g., the Bond events and Heinrich event, and the found Lisan lake events L3 till L13 [296].

Several regular periods can be identified, some of them coinciding with the warm period during the interstadial IS2. Few remaining periods of high or low regularity have not yet been identified in the literature so far and call for further investigation.

The abrupt changes in T are available due to the adaptive threshold. By using a constant threshold, T varies only slowly and more gradual. Defining the time points of the climate regime shifts becomes more difficult in this case.

4.4 Conclusions

We have represented a novel method to chose a recurrence threshold adaptively and compared with the constant threshold selection technique. The selection of recurrence thresholds for recurrence plots and recurrence networks is a crucial step for these techniques. So far, the threshold had to be chosen arbitrarily, taking into account different criteria and application cases as well as requiring some expertise. Here we have proposed a novel technique to determine such a threshold value automatically depending on the time series. Such adaptive threshold is directly derived from the topology of the recurrence network. It is selected in such a way that the recurrence network does not have unconnected components. We have discussed transitivity and betweenness centrality measures of the complex network approach. Both measures are related to the regularity of the dynamics.

Moreover, the proposed threshold selection can also be useful for the recurrence quantification analysis. A systematic investigation of the different threshold selections remains future work.

We have compared the novel adaptive threshold selection with the arbitrarily selected threshold by applying them to the logistic map. Although both methods distinguish the dynamical regimes clearly, the adaptively chosen threshold approach detects much more bifurcations, in particular such as period doubling. Such bifurcations are important characteristics of the dynamical systems, since these bifurcations route to chaos from periodicity.

Moreover, we have used our approach to investigate a palaeoclimate proxy record from the palaeolake Lisan representing the climate variability in the near East between 27 and 18 cal ka BP. Both transitivity and betweenness centrality measures clearly identified transitions between wet and dry (and vice versa) periods by an abrupt decrease of dynamical regularity, perhaps due to a reduced solar influence. Our method identified some transitions which have not been know so far from the literature and require further investigation, e.g., by analyzing other proxy records from this region. By choosing the adaptive threshold, we have been able to identify the transitions more clearly than by using the arbitrary selected threshold approach.

Acknowledgements

We thank Reik V. Donner for fruitful discussions. Part of the work was supported by the project “Gradual environmental change versus single catastrophe – Identifying drivers of mammalian evolution” (SAW-2013-IZW-2) funded by the Leibniz Association (WGL).

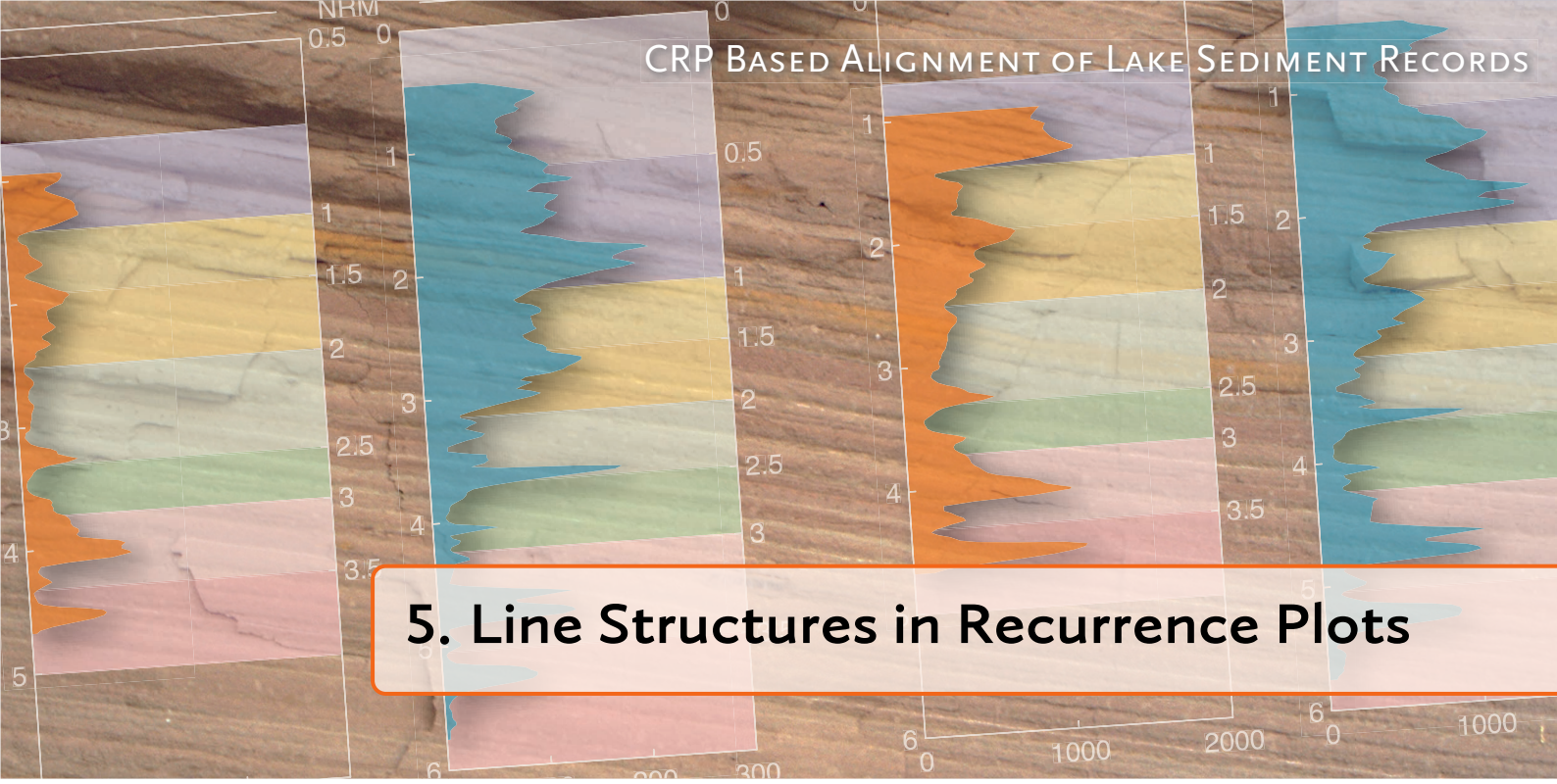

5. Line Structures in Recurrence Plots

Paper 4 N. Marwan, J. Kurths: Line structures in recurrence plots, Physics Letters A, 336(4–5), 349–357 (2005). DOI:10.1016/j.physleta.2004.12.056

Abstract

Recurrence plots exhibit line structures which represent typical behaviour of the investigated system. The local slope of these line structures is connected with a specific transformation of the time scales of different segments of the phase-space trajectory. This provides us a better understanding of the structures occuring in recurrence plots. The relationship between the time-scales and line structures are of practical importance in cross recurrence plots. Using this relationship within cross recurrence plots, the time-scales of differently sampled or time-transformed measurements can be adjusted. An application to geophysical measurements illustrates the capability of this method for the adjustment of time-scales in different measurements.

5.1 Introduction

In the last decade of data analysis an impressive increase of the application of methods based on recurrence plots (RP) can be observed. Introduced by Eckmann et al. [86], RPs were firstly only a tool for the visualization of the behaviour of phase-space trajectories. The following development of a quantification of RPs by Zbilut and Webber [418, 442] and later by Marwan et al. [237], has consolidated the method as a tool in nonlinear data analysis. With this quantification the RPs have become more and more popular within a growing group of scientists who use RPs and their quantification techniques for data analysis. Last developments have extended the RP to a bivariate and multivariate tool, as the cross recurrence plot (CRP) or the multivariate joint recurrence plot (JRP) [228, 229, 322]. The main advantage of methods based on RPs is that they can also be applied to rather short and even nonstationary data.

The initial purpose of RPs was the visual inspection of higher dimensional phase space trajectories. The view on RPs gives hints about the time evolution of these trajectories. The RPs exhibit characteristic large scale and small scale patterns. Large scale patterns can

be characterized as homogeneous, periodic, drift and disrupted. They obtain the global behaviour of the system (noisy, periodic, auto-correlated etc.). The quantification of RPs and CRPs uses the small-scale structures which are contained in these plots. The most important ones are the diagonal and vertical/horizontal straight lines because they reveal typical dynamical features of the investigated system, such as range of predictability or properties of laminarity. However, under a closer view a large amount of bowed, continuous lines can also be found. The progression of such a line represents a specific relationship within the data. In this paper we present a theoretical background of this relationship and discuss a technique to infer the adjustment of time-scales of two different data series. Finally, an example from earth siences is given.

5.2 Recurrence Plots

A recurrence plot (RP) is a two-dimensional squared matrix with black and white dots and two time-axes, where each black dot at the coordinates (t_1, t_2) represents a recurrence of the system's state $\vec{x}(t_1)$ at time t_2:

$$\mathbf{R}(t_1, t_2) = \Theta\left(\varepsilon - \|\vec{x}(t_1) - \vec{x}(t_2)\|\right), \quad \vec{x}(t) \in \mathbb{R}^m, \tag{5.1}$$

where m is the dimension of the system (degrees of freedom), ε is a small threshold distance, $\|\cdot\|$ a norm and $\Theta(\cdot)$ the Heaviside function. This definition of an RP is only one of several possibilities (an overview of recent variations of RPs can be found in [223]).

Since $\mathbf{R}(t_1, t_1) = 1$ by definition, the RP has a black main diagonal line, the *line of identity (LOI)*, with an angle of $\pi/4$. It has to be noted that a single recurrence point at (t_1, t_2) in an RP does not contain any information about the actual states at the times t_1 and t_2 in phase space. However, it is possible to reconstruct dynamical properties of the data from the totality of all recurrence points [381].

5.3 Line Structures in Recurrence Plots

The visual inspection of RPs reveals (among other things) the following typical small scale structures: *single dots*, *diagonal lines* as well as *vertical* and *horizontal lines* (the combination of vertical and horizontal lines plainly forms rectangular clusters of recurrence points).

Single, isolated recurrence points can occur if states are rare, if they do not persist for any time, or if they fluctuate heavily. However, they are not a clear-cut indication of chance or noise (for example in maps).

A *diagonal line* $\mathbf{R}(t_1 + \tau, t_2 + \tau) = 1$ (for $\tau = 1 \ldots l$, where l is the length of the diagonal line in time units) occurs when a segment of the trajectory runs parallel to another segment, i. e. the trajectory visits the same region of the phase space at different times. The length of this diagonal line is determined by the duration of such a similar local evolution of the trajectory segments. The direction of these diagonal structures can differ. Diagonal lines parallel to the LOI (angle $\pi/4$) represent the parallel running of trajectories for the same time evolution. The diagonal structures perpendicular to the LOI represent the parallel running with contrary times (mirrored segments; this is often a hint of an inappropriate embedding if an embedding algorithm is used for the reconstruction of the phase-space). Since the definition of the Lyapunov exponent uses the time of the parallel running of trajectories, the relationship between the diagonal lines and the Lyapunov exponent is obvious (but this relationship is more complex than usually mentioned in literature, cf. [384]).

A *vertical (horizontal) line* $\mathbf{R}(t_1, t_2 + \tau) = 1$ (for $\tau = 1 \ldots v$, with v the length of the vertical line in time units) marks a time length in which a state does not change or changes

very slowly. It seems, that the state is trapped for some time. This is a typical behaviour of laminar states [237].

5.4 Slope of the Line Structures

In a more general sense the line structures in recurrence plots exhibit locally the time relationship between the current trajectory segments. A line structure in an RP of length l corresponds to the closeness of the segment $\vec{x}(T_1(t))$ to another segment $\vec{x}(T_2(t))$, where $T_1(t)$ and $T_2(t)$ are two local time-scales (or transformations of an imaginary absolute time-scale t) which preserve that $\vec{x}(T_1(t)) \approx \vec{x}(T_2(t))$ for some time $t = 1 \ldots l$. Under some assumptions (e. g. piecewise existence of an inverse of the transformation $T(t)$, the two segments visit the same area in the phase space), a line in the RP can be simply expressed by the time-transfer function

$$\vartheta(t) = T_2^{-1}(T_1(t)). \tag{5.2}$$

Especially, we find that the local slope $b(t)$ of a line in an RP represents the local time derivative ∂_t of the inverse second time-scale $T_2^{-1}(t)$ applied to the first time-scale $T_1(t)$

$$b(t) = \partial_t T_2^{-1}(T_1(t)) = \partial_t \vartheta(t). \tag{5.3}$$

This is the fundamental relation between the local slope $b(t)$ of line structures in an RP and the time scaling of the corresponding trajectory segments. From the slope $b(t)$ of a line in an RP we can infere the relation $\vartheta(t)$ between two segments of $\vec{x}(t)$ ($\vartheta(t) = \int b(t)dt$). Note that the slope $b(t)$ depends only on the transformation of the time-scale and is independent from the considered trajectory $\vec{x}(t)$.

This feature is, e. g., used in the application of CRPs as a tool for the adjustment of time-scales of two data series [229, 236] and will be discussed later. Next, we present the deforming of line structures in RPs due to different transformations of the time-scale.

5.5 Illustration Line Structures

For illustration we consider some examples of time transformations for different one-dimensional trajectories $f(t)$ (i. e. functions; no embedding). We study the recurrence behaviour between two segments f_1 and f_2 of these trajectories, where we apply different time transformations to these segments (Tab. 5.1). In order to illustrate that the found relation (5.3) is independent from the underlying trajectory, we will use at first the function $f(t) = t^2$ (Figs. 5.1A1, B1, C1 etc.) and then $f(t) = \sin(\pi t)$ (Figs. 5.1A2, B2, C2 etc.) as a trajectory. The local representation of RPs between these segments corresponds finally to cross recurrence plots (CRP) between two different trajectories/functions as will be mentioned later.

Assuming that the second segment of a trajectory f_2 is twice as fast as the first segment f_1 (Figs. 5.1A), i. e., the time transformations are $T_1(t) = t$ and $T_2(t) = 2t$, we get a constant slope $b = 0.5$ by using Eq. (5.3). A line in an RP which corresponds to these both segements follows $\vartheta(t) = 0.5\,t$ (Figs. 5.1A1, A2). This result corresponds with the solution we had already discussed in [236] using another approach. In [236] we considered a simple case of two harmonic functions $f_1(t) = \sin(T_1(t))$ and $f_2(t) = \sin(T_2(t))$ with different time transformation functions $T_1 = \varphi \cdot t + \alpha$ and $T_2 = \psi \cdot t + \beta$. Using the inverse $T_2^{-1} = \frac{t-\beta}{\psi}$ and Eq. (5.3), we get the local slope of lines in the RP (or CRP) $b = \partial_t T_2^{-1}(T_2(t)) = \varphi/\psi$, which equals the ratio between the frequencies of the considered harmonic functions.

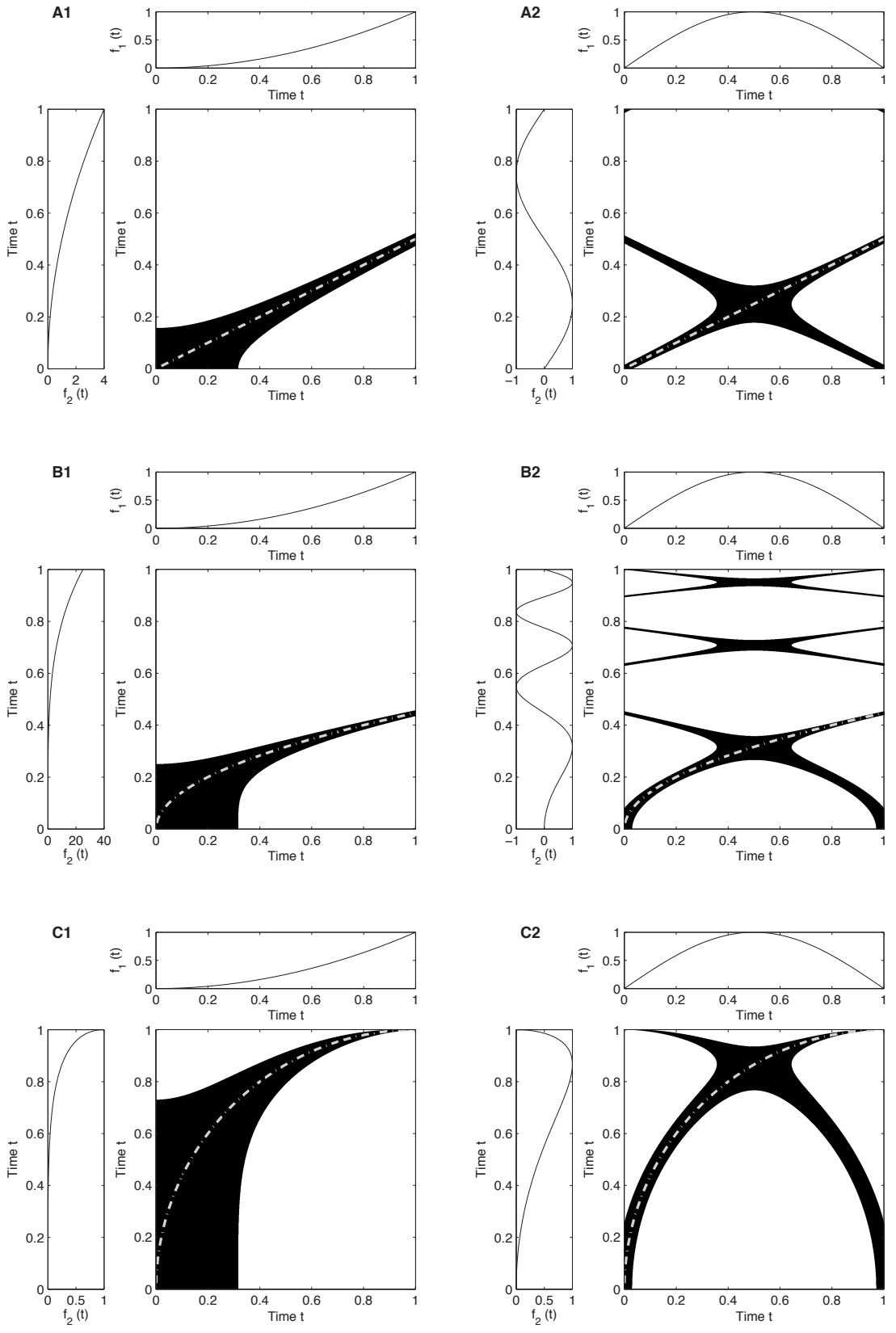
A1
A2
B1
B2
C1
C2
f1 (t)
f2 (t)
Time t
Time t

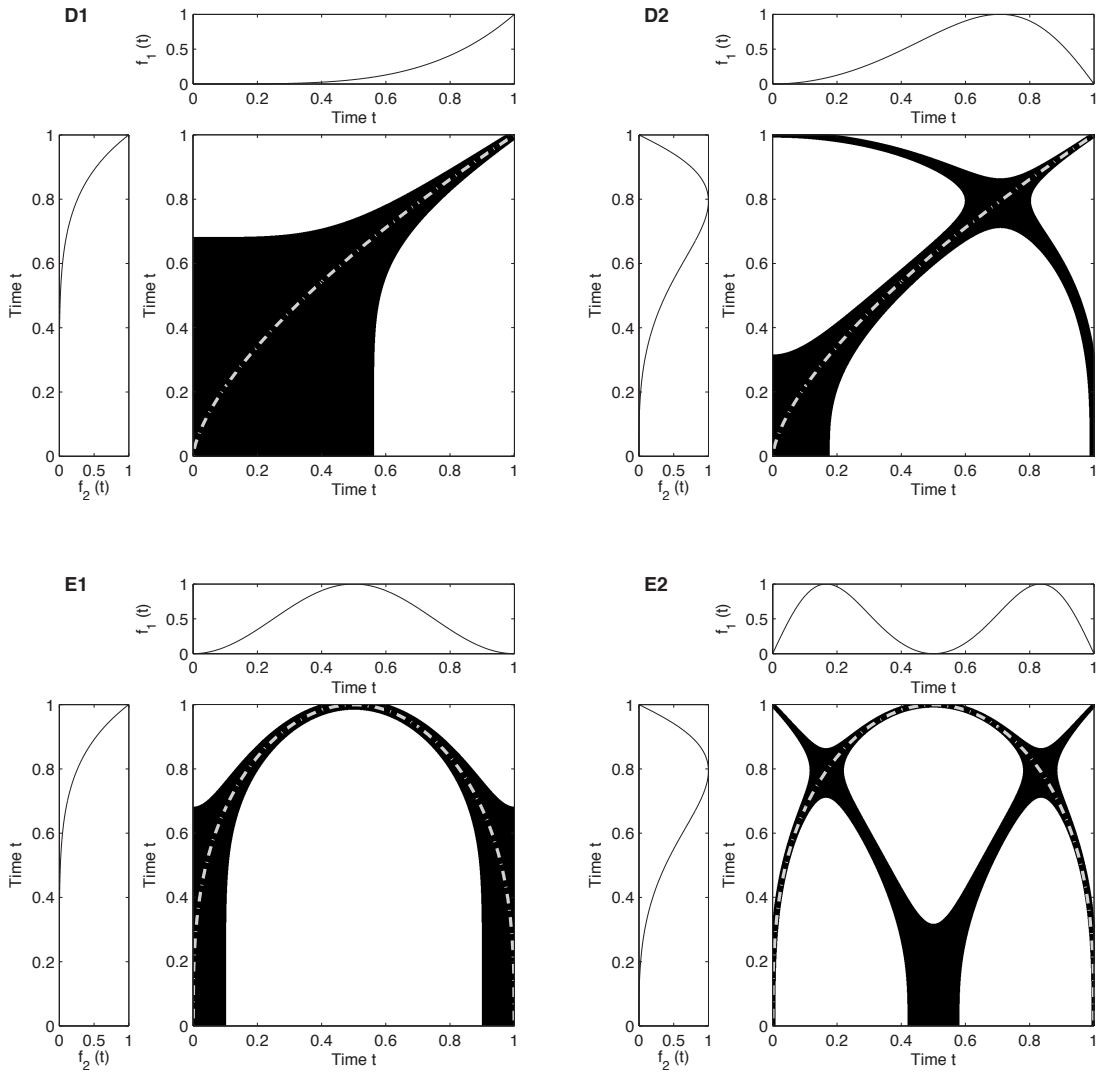

Figure 5.1: Details of recurrence plots for trajectories $f(t)$ whose sub-sections $f_1(t)$ and $f_2(t)$ undergo different transformations in time-scale (Tab. 5.1). Black areas correspond to times where $f_1(t) \approx f_2(t)$. The dash-dotted lines represent the time-transfer functions $\vartheta(t)$. Note that these are not the entire RPs, only a small detail of them (an entire RP cannot contain only these structures – there are more features, like the line of identity (diagonal line from lower left to upper right) and a more or less symmetric plot around this line). RPs were constructed by using the Euclidean norm, $\varepsilon = 0.1$ and without embedding (for embedding dimensions $m > 1$, line segments running from upper left to lower right will disappear, but line segments from lower left to upper right will remain, even if they are bowed).

Table 5.1: Examplary time transformation functions $T_1(t)$ and $T_2(t)$, the inverse $T_2^{-1}(t')$, their corresponding slopes $b(t)$ and time-transfer functions $\vartheta(t)$ for lines in RPs shown in Fig. 5.1.

Fig.	$T_1(t)$	$T_2(t)$	$T_2^{-1}(t')$	$b(t)$	$\vartheta(t)$
A	t	$2t$	$0.5\,t'$	0.5	$0.5\,t$
B	t	$5t^2$	$\sqrt{0.2\,t'}$	$\sqrt{\frac{0.2}{t}}$	$\sqrt{0.2\,t}$
C	t	$1-\sqrt{1-t^2}$	$\sqrt{1-(1-t')^2}$	$\frac{1-t}{\sqrt{1-(1-t)^2}}$	$\sqrt{1-(1-t)^2}$
D	t^2	t^3	$\sqrt[3]{t'}$	$\frac{1}{3\sqrt[3]{t^2}}$	$\sqrt[3]{t^2}$
E	$\sin(\pi\,t)$	t^3	$\sqrt[3]{t'}$	$\frac{\pi\cos(\pi\,t)}{3\sqrt[3]{\sin^2(\pi\,t)}}$	$\sqrt[3]{sin(\pi\,t)}$

In the second example we will transform the time-scale of the second segment with the square function $T_2(t) = 5t^2$. Using Eq. (5.3) we get $b(t) = \sqrt{0.2/t}$ and $\vartheta(t) = \sqrt{0.2\,t}$, which corresponds with a bowed line in the RP (Figs. 5.1B1, B2). Since $\sin(\pi\,t)$ has some periods in the considered intervall, we get some more lines in the RP (Figs. 5.1B2). These lines underly the same relationship, but we have to take higher periodicities into account: $\vartheta(t) = \sqrt{0.2\,k\,\pi\,t}$ $(k \in \mathbb{Z})$.

The third example refers to a hyperbolic time transformation $T_2(t) = 1-\sqrt{1-t^2}$. The resulting line in the RP has the slope $b(t) = (1-t)/\sqrt{1-(1-t)^2}$ and follows $\vartheta(t) = \sqrt{1-(1-t)^2}$, which corresponds with a segment of a circle (Figs. 5.1C1, C2). We can use this information in order to create a full circle in an RP. Let us consider a one-dimensional system, where the trajectory is simply the function $f(T) = T(t)$, and with a section of a monotonical, linear increase $T_{lin} = t$ and another (hyperbolic) section which follows $T_{hyp} = -\sqrt{r^2-t^2}$. After these both sections we append the same but mirrored sections (Fig. 5.2A). Since the inverse of the hyperbolic section is $T_{hyp}^{-1} = \pm\sqrt{r^2-t^2}$, the line in the corresponding RP follows $\vartheta(t) = T_{hyp}^{-1}(T_{lin}(t)) = \pm\sqrt{r^2-t^2}$, which corresponds with a circle of radius r (Fig. 5.2B).

An examplary data series from earth science reveals that such structures are not only restricted to artificial models. Let us consider the January solar insolation for the last 100 kyr on the latitude 44°N (Fig. 5.3A). The corresponding RP shows a circle (Fig. 5.3B), similar as in Fig. 5.2B. From this geometric structure we can infer that the insolation data contains a more-or-less symmetric sequence and that subsequent sequences are equal after a suitable time transformation which follows the relation $T_2^{-1}(T_1) = \sqrt{r^2-t^2}$. For instance, the subsequent sequences could be a linear increasing and a hyperbolic decreasing followed by a reverse of this sequence, a hyperbolic increasing and a linear decreasing part. Such bowed line structures are expected in RPs applied to data from biology, ecology and economics as well (e.g. [219, 316, 367, 392]). These deformations can obtain hints about the change of frequencies during the evolution of a process and may be of major interest especially in the analysis of sound data (an example of an RP of speech data containing pronounced bowed lines can be found in [137]).

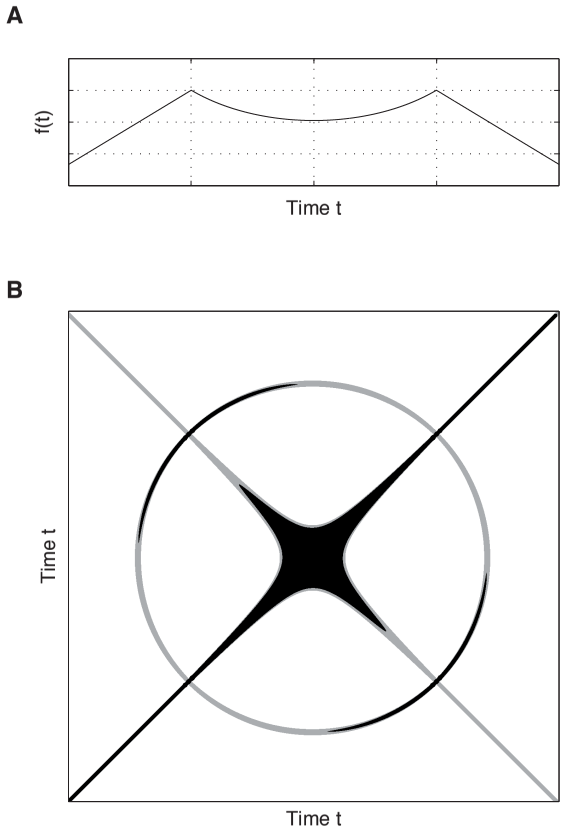

Figure 5.2: Illustrative example of the relationship between the slope of lines in an RP and the local derivatives of the involved trajectory segments. Since the local derivative of the transformation of the time-scales of the linear and the hyperbolic sections (A) corresponds to the derivative of a circle line, a circle occurs in the RP (B). The gray coloured recurrence plot is derived from the one-dimensional phase-space (no embedding used). For higher embedding dimensions segments of the line structures which are more or less perpendicular to the line of identity disappear (black recurrence plot, embedding dimension $m = 3$ and delay $\tau = 0.2N$, where N is the data length). Nevertheless, the remaining line segments have the slope of the circle.

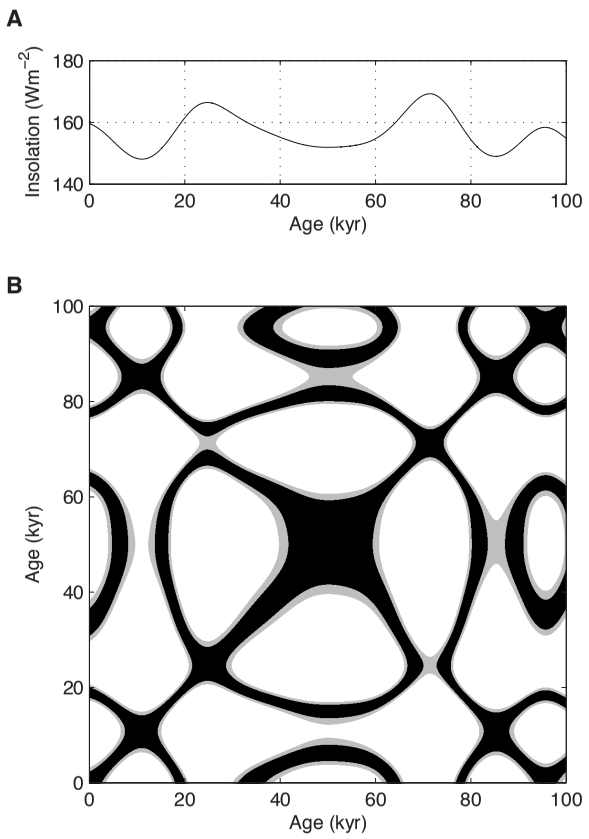

Figure 5.3: A corresponding structure found in experimental data: (A) the solar insolation on the latitude 44°N for the last 100 kyr (data from [20]) and its corresponding recurrence plot (B). The recurrence plot parameters were $m = 1$ and $\varepsilon = 2$ (black) and $\varepsilon = 3.5$ (gray).

Whereas in the examples above only the second section of the trajectory undergoes a time transformation, in the last two examples (Figs. 5.1D and E) the time-scale of the first section is also transformed. Nevertheless, the time-transfer function can be again determined with Eq. (5.2) as well.

From these examples we can conclude that the line in a recurrence plot follows Eq. (5.2) and depends only on the transformations of the time-scale.

Although we considered only examples in a one-dimensional phase-space, these findings hold also for higher-dimensional phase-space and for discrete systems (see the example in the section about cross recurrence plots). The line structures in recurrence plots, which are more or less perpendicular to the LOI, will disappear for higher-dimensional phase-space (Fig. 5.2B). Nevertheless, the remaining lines reveal the relation between the corresponding time-scales.

5.6 Cross Recurrence Plots

The relationship between the local slope of line structures in RPs and the corresponding different segments of the *same* phase-space trajectory holds also for the structures in CRPs,

$$\mathbf{CR}(t_1, t_2) = \Theta\big(\varepsilon - \|\vec{x}(t_1) - \vec{y}(t_2)\|\big). \tag{5.4}$$

which are based on *two different* phase-space trajectories $\vec{x}(t_1)$ and $\vec{y}(t_2)$. This relationship is more important for the *line of identity (LOI)* which then becomes a *line of synchronization (LOS)* in a CRP [229, 236].

We start with two identical trajectories, i. e. the CRP is the same as the RP of one trajectory and contains an LOI. If we now slightly modify the amplitudes of the second trajectory, the LOI will become somewhat disrupted. This offers a new approach to use CRPs as a tool to assess the similarity of two systems [228]. However, if we do not modify the amplitudes but stretch or compress the second trajectory slightly, the LOI will remain continuous but not as a straight line with an angle of $\pi/4$. The line of identity (LOI) now becomes the *line of synchronization (LOS)* and may eventually not have the angle $\pi/4$. This line can be rather bowed. Finally, a time shift between the trajectories causes a dislocation of the LOS, hence, the LOS may lie rather far from the main diagonal of the CRP.

Now we deal with a situation which is typical in earth sciences and assume that two trajectories represent the same process but contain some transformations in their time-scales. The LOS in the CRP between the two trajectories can be described with the found relation (5.2). The function $\vartheta(t)$ is the transfer or rescaling function which allows to readjust the time-scale of the second trajectory to that of the first one in a non-parametrical way. This method is useful for all tasks where two time-series have to be adjusted to the same scale, as in dendrochronology or sedimentology [229].

Next, we apply this technique in order to re-adjust two geological profiles (sediment cores) from the Italian lake *Lago di Mezzano* [34]. The profiles cover approximately the same geological processes but have different time-scales due to variations in the sedimentation rates. The first profile (LMZC) has a length of about 5 m and the second one (LMZG) of about 3.5 m (Fig. 5.4). From both profiles a huge number of geophysical and chemical parameters were measured. Here we focus on the rock-magnetic measurements of the normalized remanent magnetization intensity (NRM) and the susceptibility κ.

We use the time-series NRM and κ as components for the phase-space vector, resulting in a two-dimensional system. However, we apply an additional embedding using the time-delay method [379] (we do not ask about the physical meaning here). A rather small embedding decreases the amount of line structures representing the progress with negative time [223].

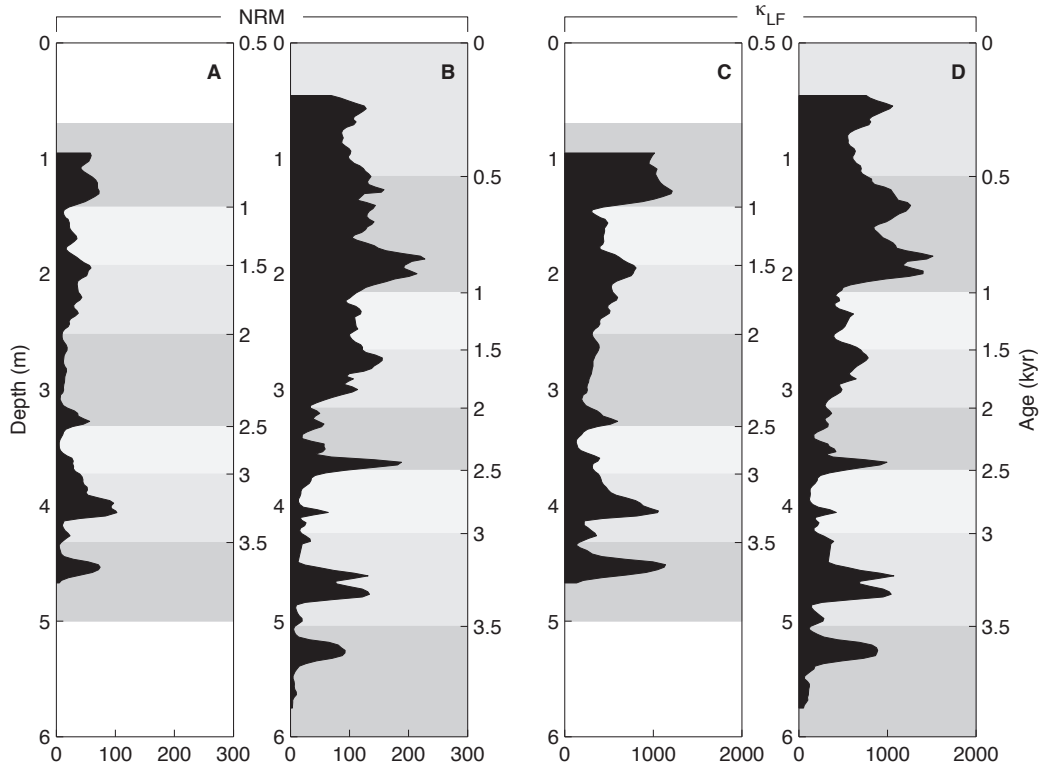

Figure 5.4: Rock-magnetic measurements of lake sediments with different time-scales. Corresponding sections are marked with different gray values.

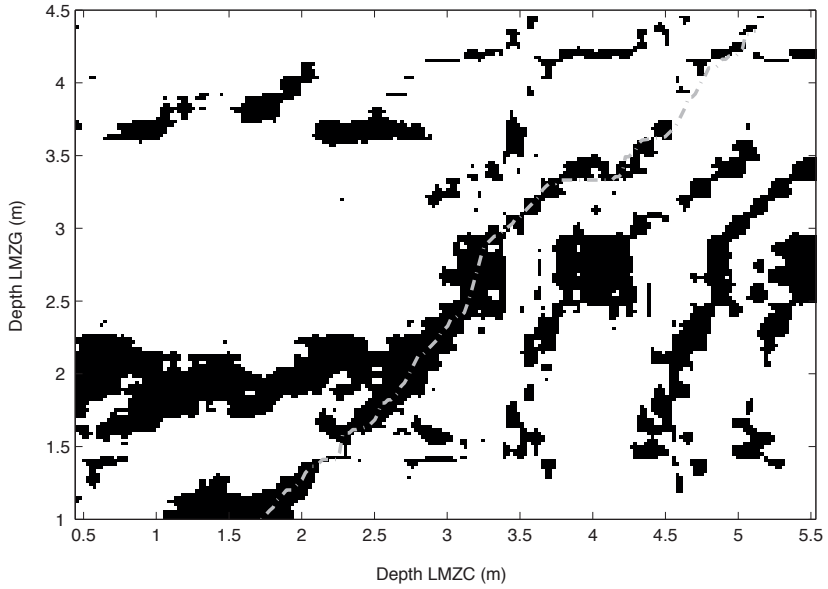

Figure 5.5: Cross recurrence plot between rock-magnetic data shown in Fig. 5.4. The dash-dotted line is the resolved LOS which can be used for re-adjustment of the time-scales of both data sets.

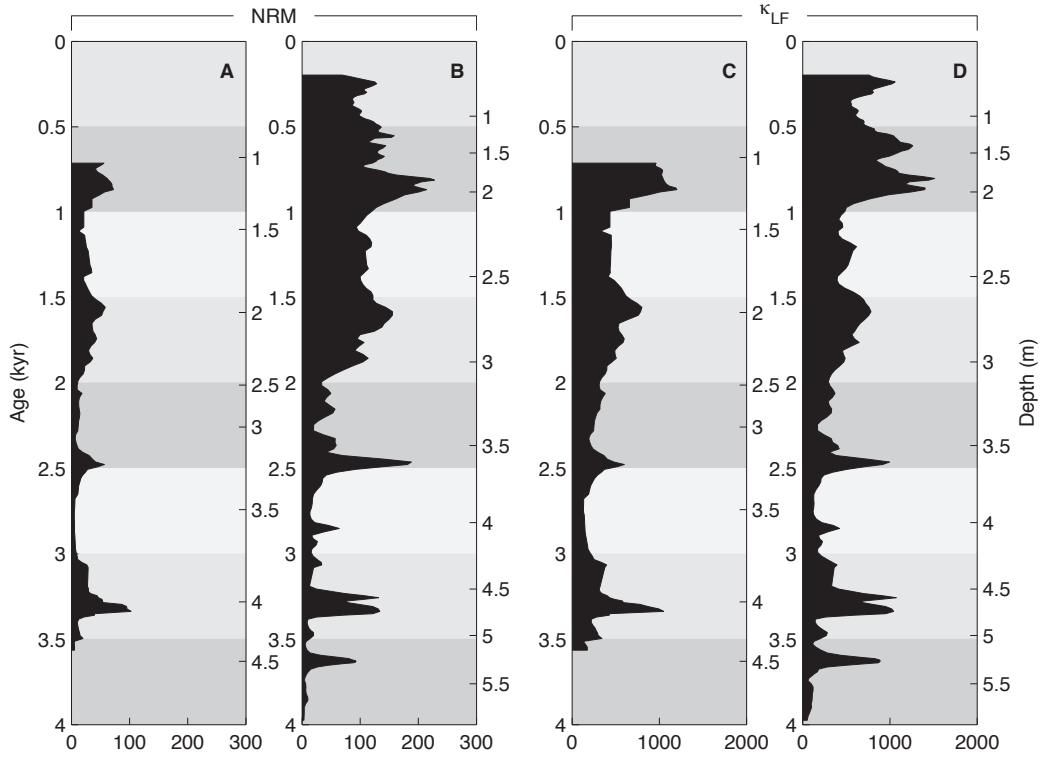

Figure 5.6: Geological profiles after re-adjustment using the LOS which was found with the CRP shown in Fig. 5.5. Corresponding sections are marked with different gray values.

Using embedding parameters dimension $m = 3$ and delay $\tau = 5$ (empirically found for these time-series), the final dimension of the reconstructed system is six. The corresponding CRP reveals a partly disrupted, swollen and bowed LOS (Fig. 5.5). This LOS can be automatically resolved, e. g. by using the LOS-tracking algorithm as described in [236]. The application of this LOS as the time-transfer function to the profile LMZG re-adjusts its time-series to the same time-scale as LMZC (Fig. 5.6). This method offers a helpful tool for an automatic adjustment of different geological profiles, which offers advantages compared to the rather subjective method of "wiggle matching" (adjustment by harmonizing maxima and minima by eye) used so far.

5.7 Conclusion

Line structures in recurrence plots (RPs) and cross recurrence plots (CRPs) contain information about epochs of a similar evolution of segments of phase-space trajectories. Moreover the local slope of such line structures is directly related with the difference in the velocity the system changes at different times. We have demonstrated that the knowlege about this relationship allows a better understandig of even bowed structures occuring in RPs. This relationship can be used to analyse changes in the time domain of data series (e. g. frequencies), as it is of major interest, e. g., in the analysing of speech data. We have used this feature in a CRP based method for the adjustment of time-scales between different time-series. The potential of this technique is finally shown for experimental data from geology.

Although it is obvious that the discussed line structures become more interrupted due to an increasing amount of noise, the influence of noise still needs a more systematic work.

Acknowledgements

This work was partly funded or supported by the Special Research Programmes SPP1097 and SPP1114 of the German Science Foundation (DFG) as well as by the Microgravity Application Programme AO-99-030 of the European Space Agency (ESA). We gratefully acknowledge N. Nowaczyk and U. Frank (GeoForschungsZentrum Potsdam) for the helpful discussions and for providing the geophysical data. The recurrence plots and cross recurrence plots were created by using the CRP toolbox for Matlab (http://tocsy.agnld.uni-potsdam.de).

6. The Wiener-Khinchin Theorem

Paper 5 J. P. Zbilut, N. Marwan: The Wiener-Khinchin theorem and recurrence quantification, Physics Letters A, 372(44), 6622–6626 (2008). DOI:10.1016/j.physleta.2008.09.027

R This paper is a joint research with Joe Zbilut, one of the reviewers of my PhD thesis, and who, unfortunately, passed away shortly after this study. My contribution was the idea and implementation of the power spectral estimate based on the recurrence rate.

Abstract

The Wiener-Khinchin Theorem states that the power spectrum is the Fourier transform of the autocovariance function. One form of the autocovariance function can be obtained through recurrence quantification. We show that the advantage of defining the autocorrelation function with recurrences can demonstrate higher dimensional dynamics.

6.1 Introduction

Recurrence plots (RP) and techniques related to RPs have become popular in the last two decades for its unique abilities to discern subtle processes, especially in the case where the requirements for classical techniques such as the Fourier transform are not met; i.e., stationarity, linearity, and/or where the dynamics reside in higher dimensional spaces [239, 419, 443, 444]. What has not been appreciated is that the two techniques can be used together due to the well-known Wiener-Khinchin theorem. The theorem states that the power spectral density of a wide-sense-stationary random process is the Fourier transform of the corresponding autocovariance function [49].

6.2 Power spectral estimate by recurrences

The power spectrum of a deterministic, finite length, discrete-time signal, $x(i)$, is the magnitude squared of the signal's Fourier transform

$$S_x(\omega) = \frac{1}{N}\left|\sum_{i=0}^{N-1} x(i)e^{-j\omega i}\right|^2 . \tag{6.1}$$

Using the Wiener-Khinchin theorem, the power spectrum of a signal equals the Fourier transform of the autocovariance function C_x of the signal:

$$S_x(\omega) = \sum_{\tau=-\infty}^{\infty} C_x(\tau) e^{-j\omega\tau}, \tag{6.2}$$

where the autocovariance function of a stochastic time series $x(n)$ is defined as

$$C_x(\tau) = \frac{1}{N} \sum_{i=0}^{N-1-\tau} x(i)\, x^*(i+\tau). \tag{6.3}$$

The calculation of an RP from phase space vectors $\vec{x}(i) \in \mathbb{R}^m$ ($i = 1 \ldots N$ and m the dimension of the system) is based on the distance matrix $\mathbf{D}$ of the pair-wise distances between all data points (state space vectors):

$$D(i,j) = \|\vec{x}(i) - \vec{x}(j)\| \quad \text{with} \quad \vec{x} \in \mathbb{R}^m \tag{6.4}$$

For single dimensional observations x, we may consider embeddings of the time series with embedding dimension m [286]. [For the following equations until Eq.(6.8), $m = 1$.]

The average of the distance values $d(\tau)$ for a given lag τ defined as

$$d(\tau) = \frac{1}{N} \sum_i D(i, i+\tau), \tag{6.5}$$

can be considered as a generalisation of the auto-covariance. In fact, the distance matrix can be directly related to the auto-covariance $C_x(\tau)$ [320]. For this purpose we consider the squared distance matrix

$$\begin{aligned} D^2(i, i+\tau) &= \|x(i) - x(i+\tau)\|^2 \\ &= \Big(x(i) - x(i+\tau)\Big)\Big(x(i) - x(i+\tau)\Big) \\ &= x^2(i) - 2x(i)x(i+\tau) + x^2(i+\tau). \end{aligned} \tag{6.6}$$

Next we calculate $d(\tau)$ from $\mathbf{D}^2$ and get

$$\begin{aligned} \frac{1}{N} \sum_i D^2(i, i+\tau) &= \frac{1}{N}\Big(\sum_i x^2(i) - \sum_i 2x(i)x(i+\tau) + \sum_i x^2(i+\tau) \Big) \\ &= \sigma^2 - C_x(\tau) + \sigma^2 \\ &= 2\Big(\sigma^2 - C_x(\tau)\Big) \end{aligned} \tag{6.7}$$

and find as the relation between $C_x(\tau)$ and D^2

$$\frac{1}{2} d_\tau - \sigma^2 = -C_x(\tau), \tag{6.8}$$

with σ^2 as the variance of the data. Obviously, the average distance $d(\tau)$ corresponds to the auto-covariance up to a shift by the variance and the factor $1/2$. Note that we have considered the squared distance matrix. However, the sign flip also remains for the simple distance matrix, because the distance matrix consists only of positive values, and, therefore, the quadrature of $\mathbf{D}$ has no effect on the sign.

Considering embedding dimensions $m > 1$ and embedding delay 1, and using the Euclidean norm, the squared distance matrix $\mathbf{D}^2$ is calculated by

$$\begin{aligned} D^2(i,i+\tau) &= \|\vec{x}(i)-\vec{x}(i+\tau)\|^2 \\ &= \sum_{k=1}^{m}\Big(x_k(i)-x_k(i+\tau)\Big)\Big(x_k(i)-x_k(i+\tau)\Big) \\ &= \sum_{k=1}^{m}\Big(x_k^2(i)-2x_k(i)x_k(i+\tau)+x_k^2(i+\tau)\Big) \\ &= \|\vec{x}(i)\|^2-2\vec{x}^*(i)\vec{x}(i+\tau)+\|\vec{x}(j)\|^2. \end{aligned} \tag{6.9}$$

The term $\vec{x}^*(i)\vec{x}(i+\tau)$ corresponds to the auto-covariance of the segment of the time series for time $i, i+1, \ldots i+(m-1)$. Moreover, by summarising over index i (and for large N), we find that

$$\sum_i \vec{x}^*(i)\vec{x}(i+\tau) = m\sum_i x(i)x(i+\tau), \tag{6.10}$$

i.e. it corresponds to the auto-covariance up to a factor of mN.

However, here we propose to go one step further and to consider only recurrences, defined by applying a threshold to the distance matrix $\mathbf{D}$. This limits the matrix to periodic orbits:

$$\mathbf{R} = \Theta(\varepsilon - \mathbf{D}), \tag{6.11}$$

i.e., $\mathbf{R}$ is then the recurrence matrix. Then we consider the probability that the systems recurs after time τ (τ recurrence rate) [228, 239]

$$RR(\tau) = \frac{1}{N-\tau}\sum_{i=1}^{N-\tau} R(i,i+\tau), \tag{6.12}$$

and replace $C_x(\tau)$ in Eq. (6.2) by $RR(\tau)$. In other words, we replace the expectation values

$$E\{x(i)\,x^*(i+\tau)\} \longrightarrow E\{\Theta(\varepsilon - \|\vec{x}(i)-\vec{x}(i+\tau)\|)\}. \tag{6.13}$$

The putative advantages of using a recurrence-derived FT includes not only its relaxed assumptions of stationarity and nonlinearity, but also its use of the embedding theorem to capture dynamics of higher dimensional spaces. Thus, periodicities are demonstrated not seen in either the regular FT periodogram, or the (standard) autocovariance-derived Fourier transform. Additionally, there is the "smoothing" effect inherent in the FT. (Whereas we use the autocovariance, it should be noted that the autocorrelation can also be used, since it is simply the normalization of the autocovariance by the total autocovariance.)

6.3 Example

We illustrate the advantage of the proposed recurrence based Fourier spectrum with an example of high dimensional dynamics. Lathrop and Kostelich previously studied the attractor of the oscillating Belousov-Zhabotinsky (BZ) chemical reaction [190, 282]. The bromide ion concentration was recorded, and a phase-space strange attractor was constructed from the method of time-delays. Their analysis recommended an embedding of 3 and a delay of 124. Further analysis of 3-dimensional recurrences demonstrated saddle orbits of period-1, -2 and -3 (Fig. 6.1). The fundamental period was approximately 125 time steps.

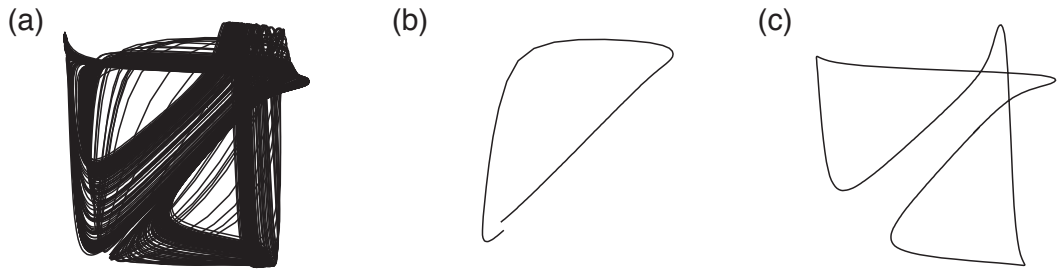

Figure 6.1: (a) The BZ reactor (50,000 points). (b) Trajectory near saddle-1. (c) Trajectory near saddle-2.

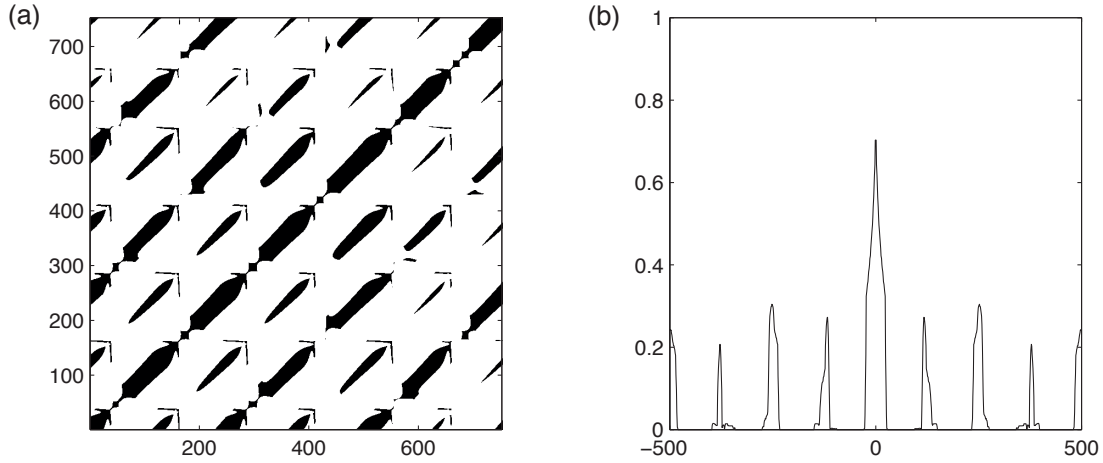

Figure 6.2: (a) Recurrence plot for 1,000 points of the BZ reactor. (b) Recurrence spectrum derived from the Plot.

To determine if the recurrence plot (RP)-based FT could capture these periods, a sample of 1000 points was selected from the original data, and submitted to the technique. We used the suggested embedding (dimension 3, and delay 124), and a recurrence threshold ε of 0.75. We also calculated a standard FT spectrum (rectangular window, no overlapping) and the autocovariance-based FT.

The RP of the BZ data reveals periodically occurring structures of different width and length (Fig. 6.2a), depending on the different periodic orbits. These periodically occurring structures are measured by the recurrence spectrum (Fig. 6.2b). Note that although the peaks are relatively sharp, they are not smooth due to the thresholding, ε.

Next we apply the FT on the recurrence spectrum (Fig. 6.3c). The RP-based FT not only demonstrates the fundamental, but also the period-2 (near 0.5), as well as a period-3 (near 0.2-0.25). These peaks have been smoothed by the application of the FT.

By contrast, the standard FT does not demonstrate any significant peaks (broad band noise is seen with log scales–not shown). The autocovariance-based FT does show the fundamental frequency, plus a period-2 (near 0.5), but is not able to find the period-3. Only the RP-based FT is able to detect all the period-1, -2 and -3 orbits in the dynamics of the BZ system.

6.4 Discussion and conclusion

We have proposed an alternative technique for the detection of periodicities in dynamical systems based on recurrences. Applying the FT on the probability that a state recurs after

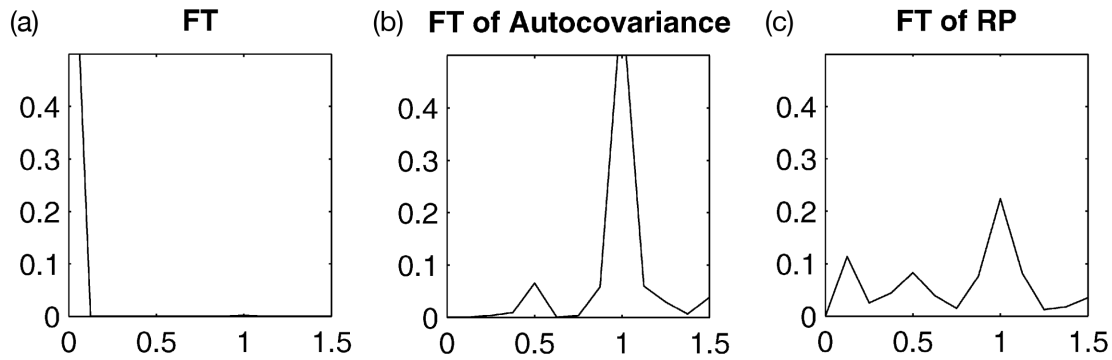

Figure 6.3: Power spectra of 1,000 points of BZ reactor with frequency normalized to saddle-1 and power normalized to total power. (a) FT spectrum with rectangular window. (b) Autocovariance based spectrum. (c) RP-based spectrum.

certain time, also known as the τ-recurrence rate [239], we link the recurrence quantification with spectral analysis. In the present study we used 1000 points to limit computational time. When other 1000 point segments were chosen, the frequencies shifted due to the sampling of different sections of the attractor (see Fig. 6.1, also Fig. 6.4). Thus it is important to estimate the extent of the attractor, in order to avoid making the conclusion that the dynamics are nonstationary as a result of inadequate sampling. (See also [323].)

Another consideration is the choice of embedding dimension. In the present example the choice was made for $m = 3$ in keeping with the analysis of Lathrop and Kostelch. A comprehensive discussion of the subject is beyond the scope of this Letter, and the interested reader is referred to [239] for a fuller discussion. However, we did perform a brief analysis with results in Fig. 6.5. For embeddings 1 to 2 the FT and autocovariance-based FT remain the same, while the RP-based FT reveals new peaks until reaching the putatively correct embedding of 3. At an embedding of 4, however, the plot begins to diminish and the peaks are smoothed out. This occurred even with adjusting the value of ε in accordance with the recognition of the "curse of dimensionality" (results not shown.) This suggests a practical method of determining an appropriate embedding once a delay via mutual information has been established: increasing the embedding beyond the optimal embedding simply brings in more points whose dynamics begin to obscure the true close in points, since the points tend to be distributed over a more narrow range of the interior of an m-dimensional hypersphere. And as $m \to \infty$, the standard deviation of the inter-point distances approaches 0 [287]. Thus one can increase the embedding until such a result is encountered. Certainly, additional research is required to confirm this observation.

One drawback of the technique is that the RP-based FT may require extended computational time with either long or highly embedded dynamics. Nonetheless, when oscillatory dynamics are suspected which move in higher dimensions, it might be useful to consider the RP-based FT.

Acknowledgments

JPZ thanks the National Science Foundation for support under grant #BCS-0728967. All computations were performed in MATLAB with the CRP Toolbox (`http://www.agnld.uni-potsdam.de/~marwan/toolbox/`).

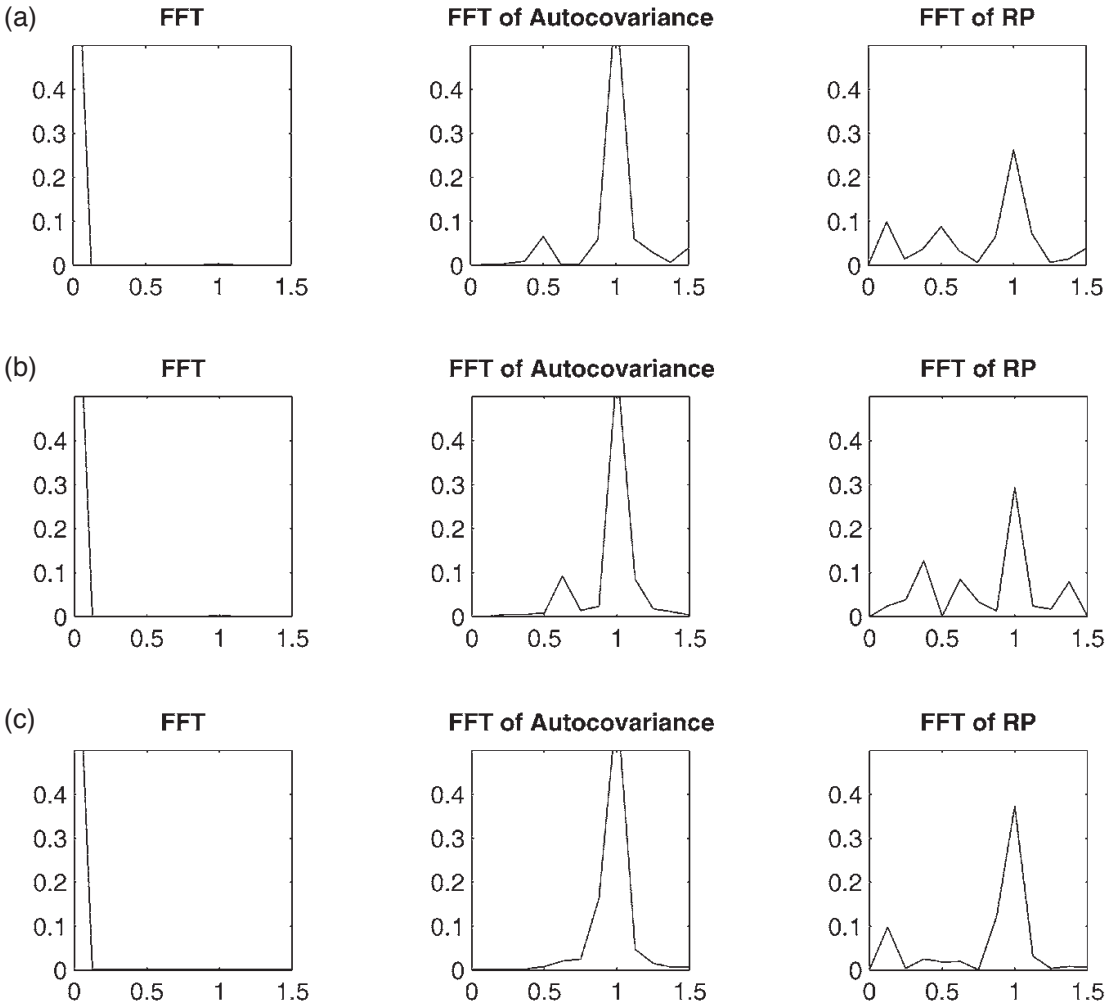

Figure 6.4: Result of analyzing three sequential series of 1,000 points (a)–(c) of the BZ attractor. This is due to inadequate sampling of the total extent of the attractor as seen in Fig. 6.1.

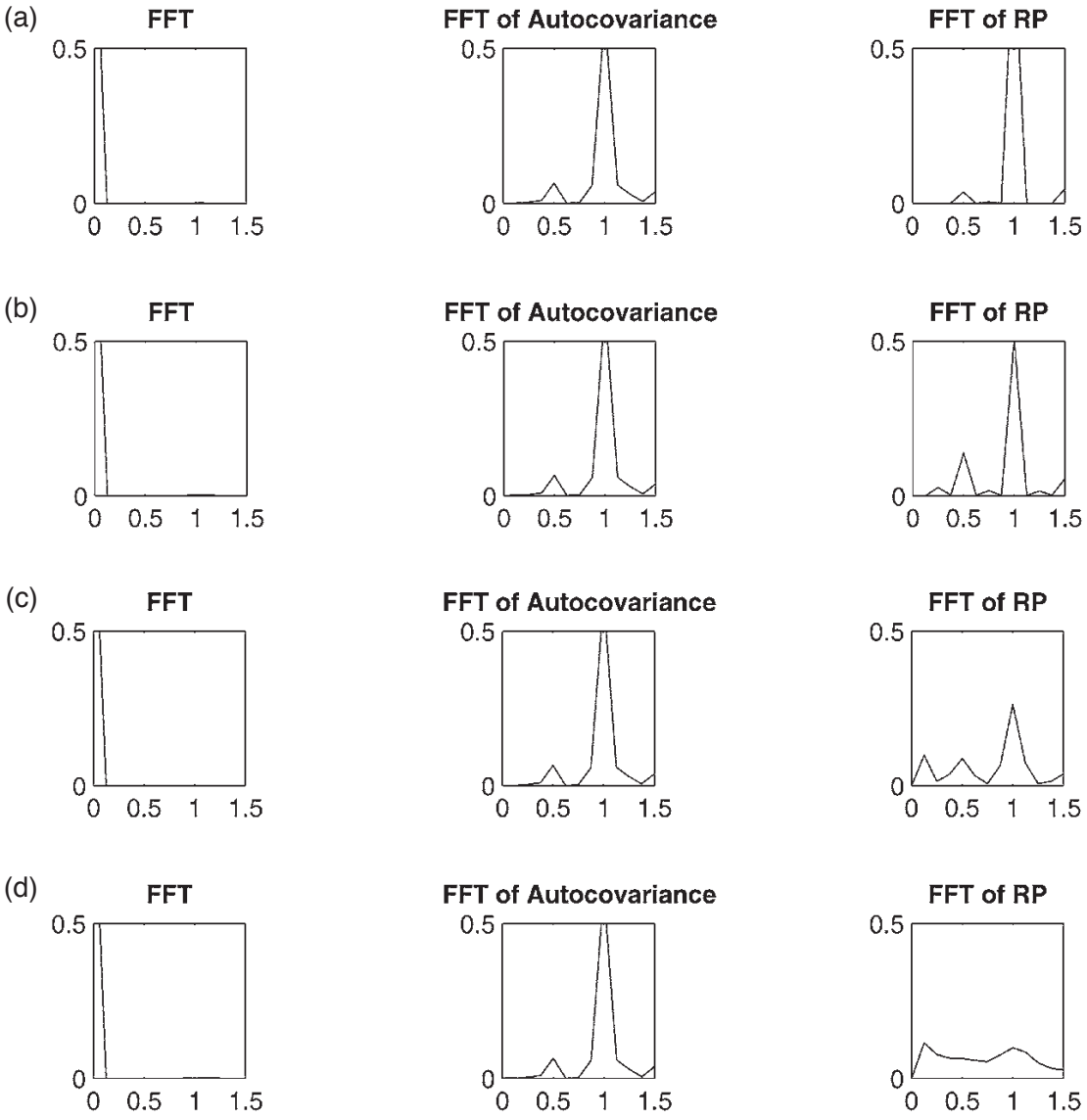

Figure 6.5: Results for progressive embedding of the time series from 1 to 4 (a)–(d). The correct periods are found for an embedding of 3, but are obscured with an embedding of 4.

7. Spatially Extended Dynamics

Paper 6 N. Marwan, S. Foerster, J. Kurths: Analysing spatially extended high-dimensional dynamics by recurrence plots, Physics Letters A, 379, 894–900 (2015). DOI:10.1016/j.physleta.2015.01.013

Abstract

Recurrence plot based measures of complexity are capable tools for characterizing complex dynamics. In this letter we show the potential of selected recurrence plot measures for the investigation of even high-dimensional dynamics. We apply this method on spatially extended chaos, such as derived from the Lorenz96 model and show that the recurrence plot based measures can qualitatively characterize typical dynamical properties such as chaotic or periodic dynamics. Moreover, we demonstrate its power by analyzing satellite image time series of vegetation cover with contrasting dynamics as a spatially extended and potentially high-dimensional example from the real world.

7.1 Introduction

The recurrence plot (RP) is a modern and versatile tool for the study of the complex behavior of dynamical systems [86, 224]. They represent time points of recurring states even of high-dimensional phase space trajectories. Quantitative extensions, such as recurrence quantification analysis and recurrence networks, enable the investigation of dynamical transitions and regime changes, the quantitative characterization of the dynamics, or the detection of phase synchronization [79, 239, 417]. As proven by several examples, the RP based quantities work quite well even with short time series (e.g.,[130, 175, 201, 241]). The practical and powerful use of RP based methods has been demonstrated by their growing and interdisciplinary application, such as for cardiovascular health diagnosis, behavioral, cognitive and neurological studies, studying fluid dynamics and plasma, analyzing optical effects, material health monitoring, palaeoclimate regime change detection, etc. [73, 91, 130, 174, 178, 303, 312, 374]. In general, such studies have so far been restricted to rather low-dimensional systems. However, when studying the complex behavior of real world systems, we often end up on extended complex systems, and the question arises whether the RP based

tools can be applied to high-dimensional systems, such as exhibiting high-dimensional chaos. So far, the ability of RP based methods for studying high-dimensional dynamics has not yet been demonstrated, although it was already used to investigate spatial recurrences [232, 294, 402] and spatio-temporal chaos in turbulence and a reaction-diffusion system [129, 259]. Moreover, the classic characterization of complex dynamics by using, e.g., entropy [87], correlation dimension [125], and Lyapunov exponents requires very long time-series [88] or the knowledge of the differential equations of the system which are in practical examples not known. The study of extended spatio-temporal dynamics is even more challenging because of the large degrees of freedom.

In this letter we demonstrate the potential of RP based measures of complexity for identifying hardly accessible extended spatio-temporal dynamics and for characterizing high-dimensional chaos. We will use the Lorenz96 model [205, 206, 288] which is a paradigmatic system for extended complex spatio-temporal chaotic dynamics and was systematically studied by Karimi et al. [168] and apply the method on an example of a satellite time series imagery.

7.2 The Lorenz96 model

The Lorenz96 model is a conceptual time-continuous linear lattice model that was developed to demonstrate fundamental aspects of weather predictability [205]:

$$\frac{dx_k}{dt} = (x_{k+1} - x_{k-2})x_{k-1} - x_k + f \tag{7.1}$$

for $k = 1, \ldots, N$, with a constant external forcing f, and with periodic boundary conditions $x_{N+1} = x_1$. Depending on the system size N and the forcing f, the dynamics on the lattice can be periodic or chaotic and can exhibit a high dimensionality [168]. Therefore, this model is very appropriate for our study.

For integrating Eq. (7.1) we use a Runge-Kutta integration of 4th order with time step $\delta t = 1/64$. In order to remove transients, we neglect the first 10,000 values from each $x_k(t)$. In the numerical experiments discussed below, we will use 20 slightly varying initial conditions for each selected setting of N and f.

In our study we consider $f = 5$ (as used by Karimi et al. [168]). Then, for example, for $N = 38$, we find periodic dynamics, but for $N = 47$, the dynamics is chaotic (Fig. 7.1).

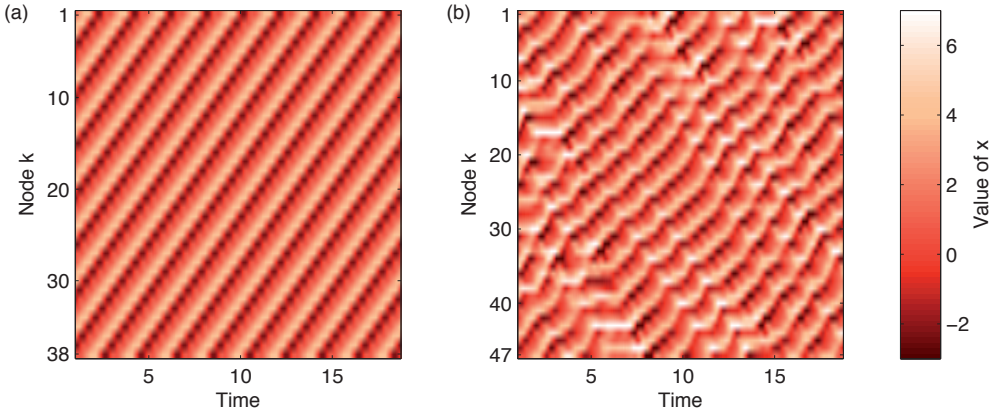

Figure 7.1: Space-time representation of $x_k(t)$ of the Lorenz96 system, Eq. (7.1), for $f = 5$ and system size of (a) $N = 38$ and (b) $N = 47$, showing periodic and chaotic dynamics.

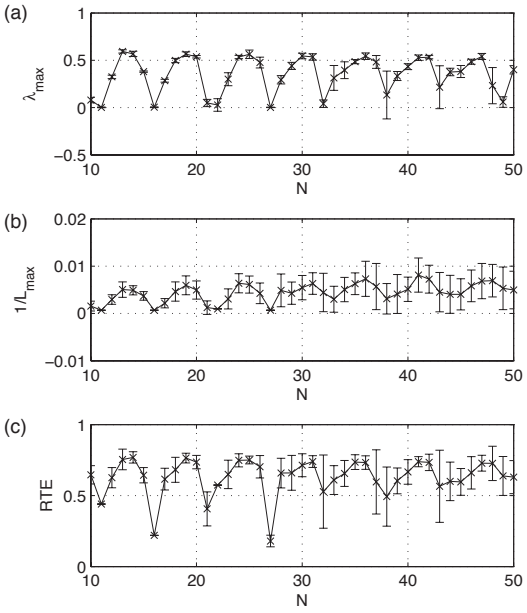

Figure 7.2: (a) Maximal Lyapunov exponent $\lambda_{\max}$ for the Lorenz96 system, Eq. (7.1), with different system size N. The RP based measures (b) $1/L_{\max}$ and (c) RTE reveal a similar variation with the N as $\lambda_{\max}$. Averaged values for 20 different initial states are presented. The standard deviation of the measures for the different initial conditions are presented by the error bars.

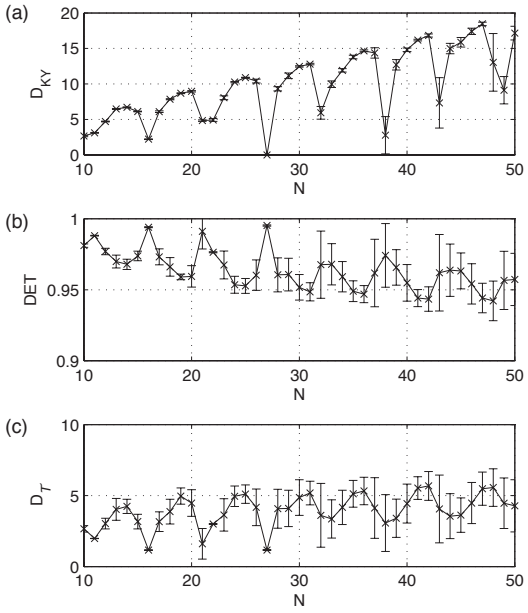

Figure 7.3: (a) Kaplan-Yorke dimension D_{KY} for the Lorenz96 system, Eq. (7.1), with different system size N. The RP based measures (b) DET and (c) $D_{\mathcal{T}}$ reveal a similar variation with the N as D_{KY}. Averaged values for 20 different initial states are presented. The standard deviation of the measures for the different initial conditions are presented by the error bars.

The change of the dynamical regimes with systems size N can be measured by the maximal Lyapunov exponent $\lambda_{\max}$ and the Kaplan-Yorke dimension D_{KY}. Here we compute the Lyapunov spectrum from the set of N differential equations by linearizing the corresponding evolution and using a Gram-Schmidt Orthonormalization scheme [54, 302]. For stable results, we integrate 200,000 iterations. The Kaplan-Yorke dimension D_{KY} can then be derived from the N (ordered) Lyapunov exponents by the Kaplan-Yorke algorithm

$$D_{\mathrm{KY}} = K + \sum_{i=1}^{K} \frac{\lambda_i}{|\lambda_{K+1}|}, \tag{7.2}$$

where K is the largest number of the first largest Lyapunov exponents with $\sum_{i=1}^{K} \lambda_i \geq 0$ [87]. Increasing the system size from $N = 10$ to $N = 50$ reveals a periodic alternation between periodic and chaotic dynamics by periodic variations of $\lambda_{\max}$ (Fig. 7.2a). The dimension of the system's dynamics as measured by D_{KY} is increasing by trend (Fig. 7.3a). The calculation of λ and D_{KY} is expensive for such systems with large degrees of freedom. Moreover, for accurate values we need very long time series (here, even for $N = 200,000$ we find some spread in the results of $\lambda_{\max}$ and D_{KY}).

7.3 Recurrence plot analysis

RP quantification may be suitable for a simpler estimation of the dynamical properties. an RP $R_{i,j} = \Theta(\varepsilon - \|\vec{x}_i - \vec{x}_j\|)$ is a binary matrix $\mathbf{R}$ representing the time points j when a state

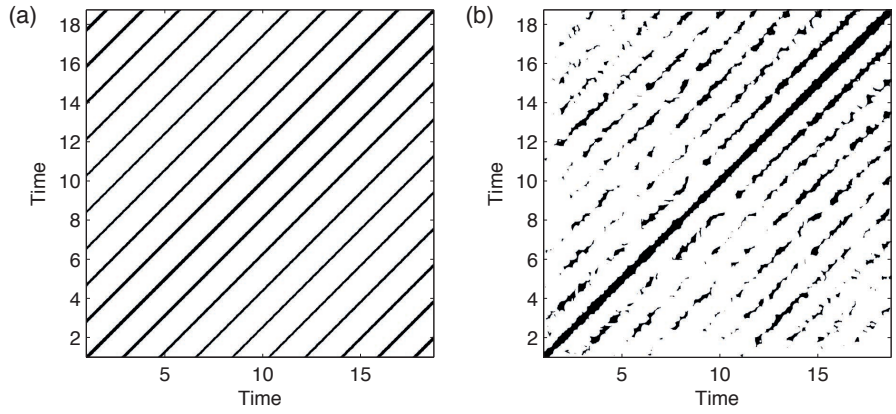

Figure 7.4: Recurrence plots of the Lorenz96 system $x_k(t)$ for $f = 5$ and system size of (a) $N = 38$ and (b) $N = 47$, showing periodic and chaotic dynamics.

$\vec{x}_i$ at time i recurs [239] (Fig. 7.4). The recurrence criterion is usually defined as a spatial distance between two states $\vec{x}_i$ and $\vec{x}_j$ is falling below a threshold ε. Besides the ability to discuss the visual aspect of an RP, several quantification approaches are based on this matrix. The diagonal line structures in an RP correspond to periods of parallel evolution of two segments of the phase space trajectory. The scaling of the length distribution of such lines is related to the K_2 entropy. A good proxy for this is measuring the inverse of the length of the longest diagonal line $1/L_{\max}$, with

$$L_{\max} = \arg\max_{l} H_D(l), \tag{7.3}$$

and l the length of the diagonal lines, and $H_{\mathrm{D}}(l)$ the length distribution of diagonal lines in $\mathbf{R}$ [239].

Based on a heuristic approach, the fraction of recurrence points that form such diagonal lines is a qualitative measure of predictability, called *determinism (DET)* [239],

$$DET = \frac{\sum_{l=2}^{N} l\, H_{\mathrm{D}}(l)}{\sum_{i,j=1}^{N} R_{i,j}}. \tag{7.4}$$

Systems possessing deterministic dynamics are characterized by diagonal lines indicating repeating recurrences within a state (and, hence, higher DET values).

The vertical empty space between two recurrence points in the RP correspond to Poincaré recurrence times, i.e., the distance v between recurrence points in a column of $\mathbf{R}$ [276]. From the distribution $H_{\mathrm{V}}(v)$ we can derive the *recurrence time entropy (RTE)*, also called *recurrence period density entropy* [202]

$$RTE = -\frac{1}{\ln V_{\max}} \sum_{v=1}^{V_{\max}} H_{\mathrm{V}}(v) \ln H_{\mathrm{V}}(v). \tag{7.5}$$

This measure quantifies the extent of recurrences and is related to the Pesin dimension [5].

In the last years, the similarity of the binary, squared matrix $\mathbf{R}$ with the adjacency matrix of an unweighted, undirected complex network was used to apply complex network measures on recurrence plots in order to quantify the geometrical properties of the system's attractor encoded in the RP [241]. For example, the *transitivity coefficient* ($\mathscr{T}$)

$$\mathscr{T} = \frac{\sum_{i,j,k=1}^{N} R_{j,k} R_{i,j} R_{i,k}}{\sum_{i,j,k=1}^{N} R_{i,j} R_{i,k} (1 - \delta_{j,k})}. \tag{7.6}$$

allows the differentiation of periodic and chaotic dynamics [455]. Moreover, $\mathscr{T}$ can be used to define a novel dimensionality measure, the *transitivity dimension* ($D_{\mathscr{T}}$)

$$D_{\mathscr{T}} = \frac{\log(\mathscr{T})}{log(3/4)}, \tag{7.7}$$

allowing the calculation of the dimension without explicit consideration of scaling behaviors. Using the RP, the correlation dimension D_2 can also be derived [124]. However, the advantage of $D_{\mathscr{T}}$ is that it results directly from the RP without analyzing any scaling behavior depending on the recurrence threshold ε.

Although still rather novel, such recurrence quantification is meanwhile widely accepted and applied in different disciplines to study diverse problems. For more details on this methodology we refer to [225, 239, 243, 417].

7.4 Recurrence analysis of spatially extended chaos

For the application of the RP approach to spatially extended high-dimensional data such as from the Lorenz96 model, we consider each variable as one component of the phase space representation: $\vec{x}(t) = (x_1(t), x_2(t), \ldots, x_N(t))$. We remove transients by deleting the first 10,000 data points and then downsample the time series by considering only every 2nd value. Then, for only 1,500 time points of the vector $\vec{x}(t)$ we calculate the RP and the above mentioned measures DET, $1/L_{\max}$, RTE, and $D_{\mathscr{T}}$. We calculate this set of measures for different system size $N \in \{10, \ldots, 50\}$ and repeat the calculation for 20 different initial conditions. For the line based RP measures DET and $1/L_{\max}$ we choose a minimal line length of two. We apply a Theiler window of length 20 (in units of iteration steps) and a recurrence threshold such that the fraction of recurrences in the RP is 10% (and using the Euclidean norm). We estimated the size of the Theiler window by the auto-correlation time, which is in average 20. The choice of the fixed recurrence rate for the threshold selection is justified by the increase of the state space dimension with growing N that would require a rescaling of the recurrence threshold. By fixing the recurrence rate we can avoid this rescaling.

The inverse of the longest diagonal line $1/L_{\max}$ as well as the RTE reveal a similar alternating variation with N as $\lambda_{\max}$ (Fig. 7.2b,c). The Pearson correlation between these two RP based measures and $\lambda_{\max}$ is 0.745 (for $1/L_{\max}$) and 0.750 (for RTE). The strong correlation even for the used rather short data segment suggests that these RP based measures are good estimators for studying the divergence behavior of high-dimensional systems.

The DET measure varies between values of 0.94 and 1, indicating the deterministic nature of the model (Fig. 7.3b). During the periodic regimes, the DET shows maxima, whereas during the chaotic regime, DET falls to lower values. The transitivity dimension $D_{\mathscr{T}}$ varies rather similar compared to the Kaplan-Yorke dimension D_{KY}. It also shows the upward trend with increasing N (Fig. 7.3c), but D_{KY} is in average 2.5 times higher than $D_{\mathscr{T}}$. The correlation of D_{KY} with DET and $D_{\mathscr{T}}$ is -0.715 and 0.723, respectively.

The recurrence based measures are able to reveal the dynamics using very short time series of length 1,500, obtained from 3,000 iterations, in comparison to the classic measures where 200,000 iterations and the differential equations had been necessary. One explanation is that an RP compares the states at all time points with those at all other time points (i.e., a N^2 pair-wise test), and that the measures are of statistical nature. The method will also work up to a certain level of noise. In the following we investigate the influence of noise by adding normally distributed random numbers to the time series. The standard deviation of the noise is chosen relativ to the mean amplitude m_A of the time series and is varied between 0 (no noise) and $0.5 \times m_A$. We find that even for a large portion of noise with

standard deviation half of the mean amplitude, the RQA measures distinguish clearly between the different dynamics (Fig. 7.5). In particular, $D_{\mathcal{T}}$ shows almost identical results for the considered noise levels (Fig. 7.5(d)). With increasing noise, DET and RTE decrease, and $1/L_{\max}$ increases. However, there are differences in their variations with respect to the noise level. As the variation of DET and $1/L_{\max}$ increases for growing noise (Fig. 7.5(b,d)), the variation for RTE decreases (Fig. 7.5(c)). It is remarkable that $D_{\mathcal{T}}$ is the measure with the lowest sensitivity on noise, whereas $1/L_{\max}$ is less sensitive for low noise levels but becomes abruptly high sensitive for high noise levels (Fig. 7.5(a)). Nevertheless, these results suggest that the approach is quite robust even for higher level of observational noise (at least for differentiating chaotic and periodic dynamics).

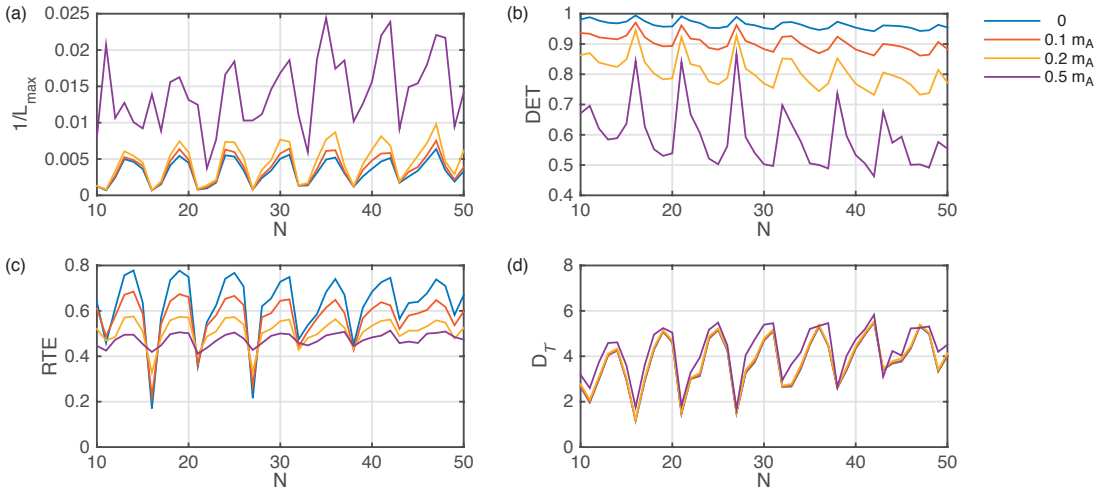

Figure 7.5: Influence of noise on the RQA results. Observational, normally distributed noise is added to the time series of the Lorenz96 system. The standard deviation of the noise is relative to the averaged mean amplitude m_A of the time series.

7.5 Application on satellite time series imagery

In order to illustrate the applicability of the proposed RP quantitative measures on spatially extended and potentially high-dimensional real world data, we use MODIS satellite time series imagery of the extended vegetation index (EVI) of two test sites in NE Spain, centre coordinate 42.37°N, 0.51°E, and NE Brazil, 5.00°S, 39.50°W (Fig. 7.6). The test sites are characterized by differently complex vegetation dynamics both in the temporal (inter-annual and intra-annual) and spatial domain (Fig. 7.7) as a result of diverse natural processes and human interactions [12, 142]. Thus, these sites are seen as ideal to study the usefulness of the proposed RP measures in order to objectively quantify and evaluate this complex behavior and decipher changes in vegetation cover dynamics related to land extensification/ intensification or climate change and drought. The subhumid Spanish test site shows a pronounced seasonal variation in precipitation and temperature with cold and dry winters and hot and stormy summers, whereas the Brazilian test site located in the so-called drought polygon is characterized by a semiarid climate with distinct dry and wet seasons and rainfall of high temporal and spatial irregularity. The Spanish test site has undergone severe land use changes during the last 50 years with the abandoning of former agricultural areas and subsequent reforestation as well as setting aside of lands from agriculture promoted by the European Agricultural Policy [189]. The Brazilian test site has been more intensively

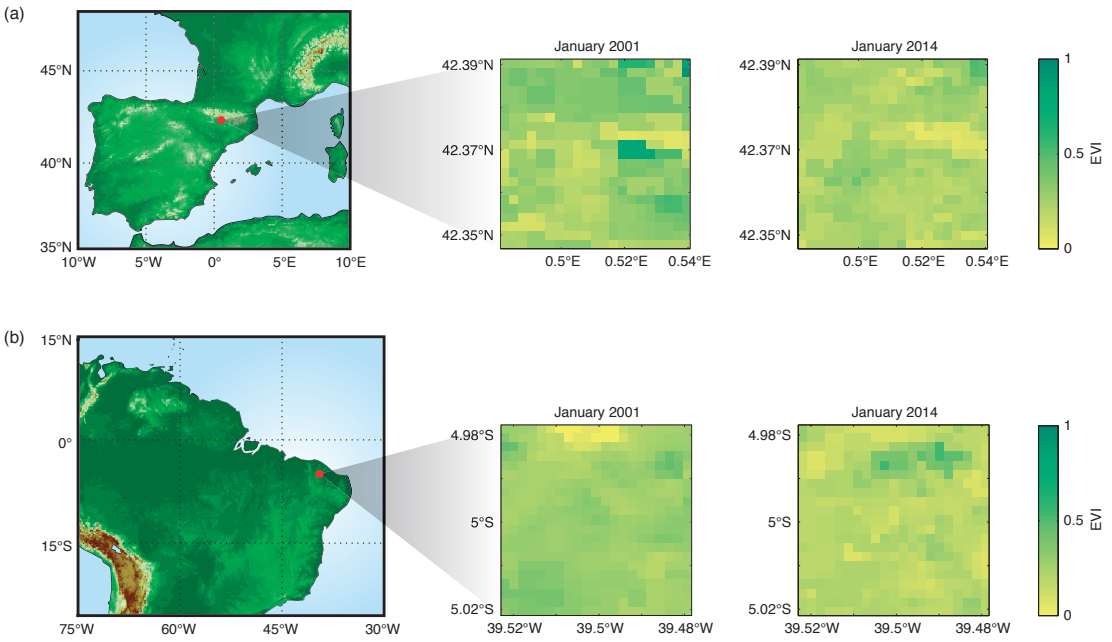

Figure 7.6: Geographical location and MODIS extended vegetation index (EVI) within the 5×5 km^2 subarea used for the analysis for the regions (a) NE Spain and (b) NE Brazil.

occupied since 1985, when the Federal Government accomplished a land reform leading to the intensification of agricultural and livestock practices. A dense water surface reservoir network has been built in the last decades to mitigate water scarcity problems [389].

The MODIS-Terra MOD13Q1 product used for this real world application is a 16-day composite image of the enhanced vegetation index (EVI) in a sinusoidal projection with a spatial resolution of 250 m. Global MODIS vegetation indices are designed to provide consistent spatial and temporal datasets used for global monitoring of vegetation conditions. The EVI is chosen since it minimizes canopy background variations and maintains sensitivity over dense vegetation. We obtained 316 MOD13Q1 images for the period February 2000 to November 2013 for both the MODIS tiles h18v04 (Spain) and h14v09 (Brazil) from the Land Processes Distributed Active Archive Center (LP DAAC), located at the US Geological Survey (USGS) Earth Resources Observation and Science (EROS) Center (`lpdaac.usgs.gov`).

In both regions we consider subareas of 5×5 km^2 ($N = 441$ grid points) varying around the centre point by 0.25° and within a range of $[-0.5°\ 0.5°]$ (resulting in 25 subareas for both regions). That way, the subareas contain a mixture of land covers representative for the test sites. For calculating the RP, we create the phase space vector $\vec{x}$ from the pixels of the satellite image subarea, i.e., $\vec{x}$ has 441 dimensions (not to be confused with the dimension of the dynamics).

For both regions we visually find periodic patterns in the corresponding RPs, revealing mainly the seasonal variability (Fig. 7.8). The appearance of the periodic patterns differ for Spain (more line-like patterns) and Brazil (more block-like patterns), indicating substantial differences in the spatial dynamics. The RP quantification by the measures DET, $1/L_{\max}$, and $D_{\mathcal{T}}$ clearly reveals quantitative differences: in Brazil we find a more erratic or chaotic spatio-temporal pattern than in Spain, indicated by lower DET and higher $1/L_{\max}$ as well as $D_{\mathcal{T}}$ for Brazil (Fig. 7.9, Tab. 7.1). Although the considered subareas consist of information that is a mixed signal of several land cover classes, the difference between Spain and Brazil is consistent for subareas of varying location. These results can be interpreted in such sense

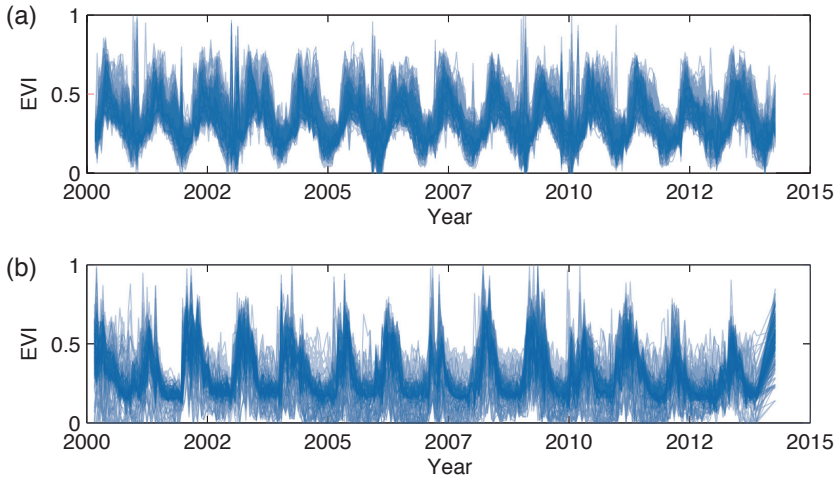

Figure 7.7: EVI time series of all pixels in the subareas as shown in Fig. 7.6 for (a) NE Spain and (b) NE Brazil. The vegetation dynamics in NE Brazil appears clearly to be more erratic in the temporal and spatial domain than in NE Spain.

that the vegetation (or land use) dynamics in Brazil is probably less regulated and less predictable than in Spain.

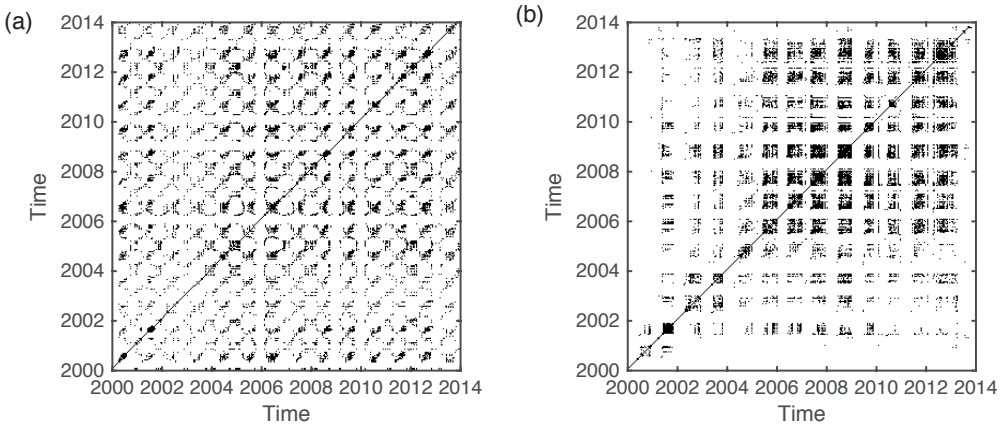

Figure 7.8: Recurrence plot of a 5×5 km^2 subarea of the EVI of test sites in (a) NE Spain and (b) NE Brazil. The selected subarea is situated at the centre point of the study region (see text).

7.6 Conclusion

By using the Lorenz96 model as a prototypical example of spatially extended dynamics with large degrees of freedom, we have shown that recurrence plot based analysis can be used to investigate high-dimensional dynamics from rather short time series and provides insights in the fundamental features of the dynamics, comparable with the Kaplan-Yorke dimension or the Lyapunov exponent. This study, thus, answers the hitherto open question, whether recurrence plots and their quantification are suitable to study high-dimensional chaos. The more systematic study on the limits of the used methods and the necessary length of time series in dependence on the degrees of freedom of the system is a subject of future work.

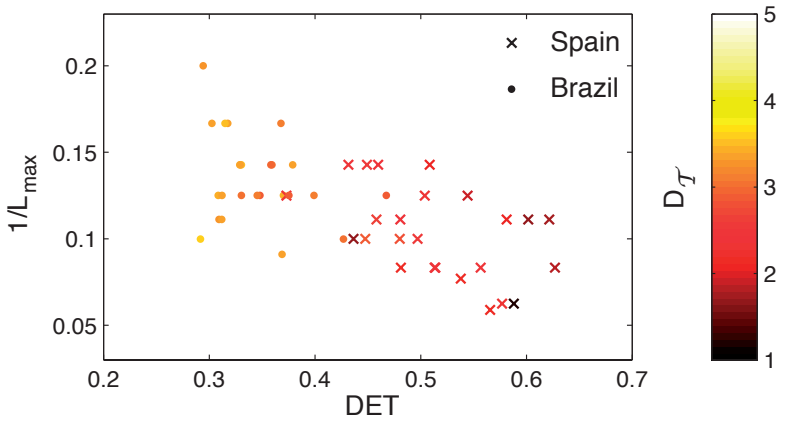

Figure 7.9: Recurrence quantification measures for the MODIS EVI data for different subareas around the study regions' centre point.

Table 7.1: Median of recurrence quantification measures for the MODIS EVI data (standard deviation in brackets).

	Spain	Brazil
DET	0.51 (0.07)	0.33 (0.04)
$1/L_{\max}$	0.10 (0.03)	0.13 (0.03)
$D_{\mathcal{T}}$	2.35 (0.45)	3.85 (0.41)

Moreover, by applying the method to MODIS satellite time series data we have demonstrated its suitability for the investigation of extended spatio-temporal dynamics of real world processes. The recurrence analysis has indicated a clear difference in the spatio-temporal vegetation dynamics in a subhumid (Spain) and in a semiarid (Brazil) climate, where the first shows a more regular pattern, whereas the latter is characterized by a more irregular and less predictable behavior.

Acknowledgement

We acknowledge support from the DFG and FAPESP (project MA 4759/4-1 and IRTG 1740/TRP 2011/50151-0) and from the Government of the Russian Federation (Agreement No. 14.Z50.31.0033).

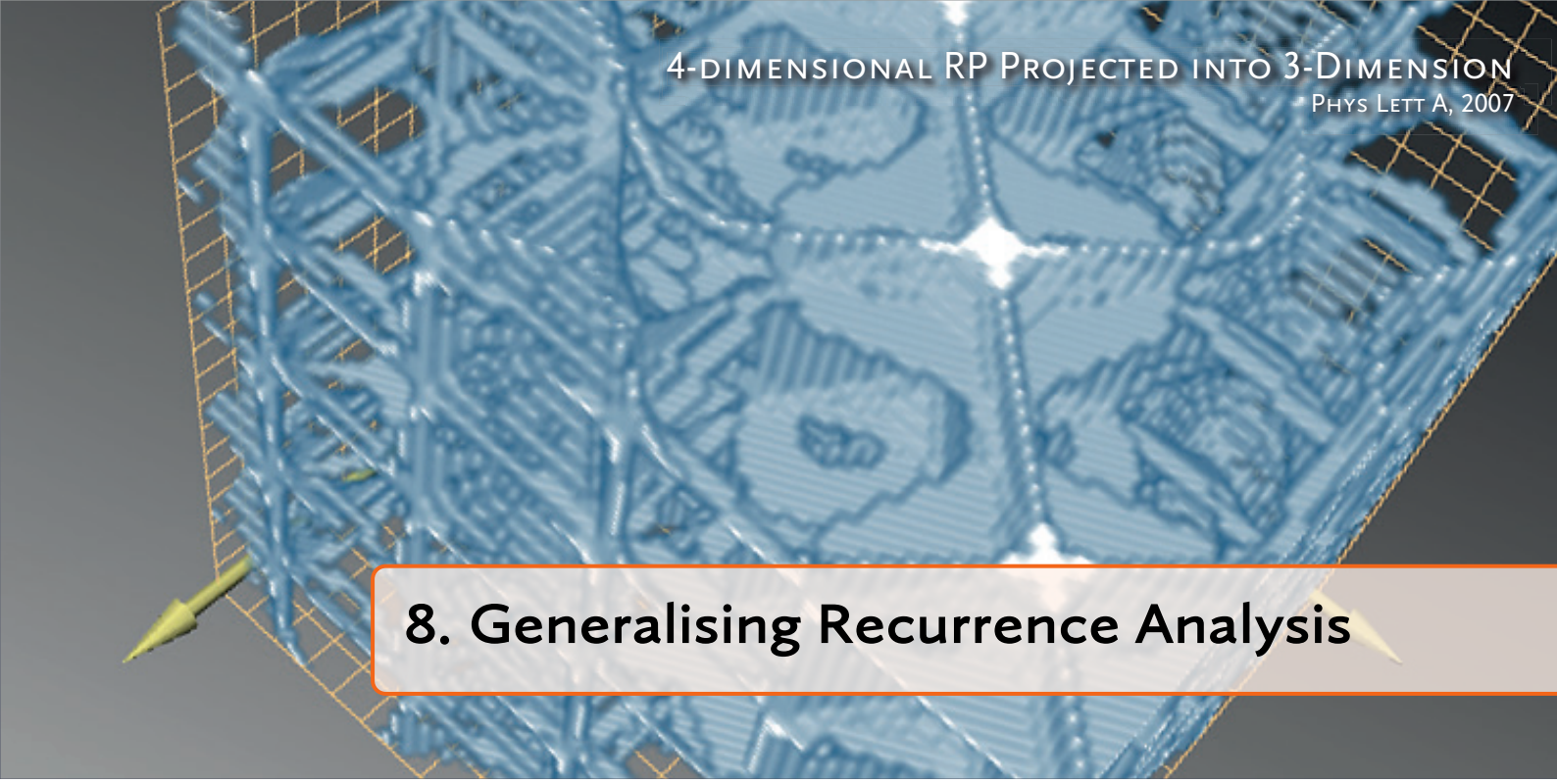

8. Generalising Recurrence Analysis

Paper 7 N. Marwan, J. Kurths, P. Saparin: Generalised Recurrence Plot Analysis for Spatial Data, Physics Letters A, 360(4–5), 545–551 (2007). DOI:10.1016/j.physleta.2006.08.058

Abstract

Recurrence plot based methods are highly efficient and widely accepted tools for the investigation of time series or one-dimensional data. We present an extension of the recurrence plots and their quantifications in order to study recurrent structures in higher-dimensional spatial data. The capability of this extension is illustrated on prototypical 2D models. Next, the tested and proved approach is applied to assess the bone structure from CT images of human proximal tibia. We find that the spatial structures in trabecular bone become more recurrent during the bone loss in osteoporosis.

8.1 Introduction

Recurrence is a fundamental property of many dynamical systems and, hence, of various processes in nature. A system may strongly diverge, but after some time it recurs "infinitely many times as close as one wishes to its initial state" [292]. The investigation of recurrence reveals typical properties of the system and may help to predict its future behaviour. With the study of nonlinear chaotic systems several methods for the investigation of recurrences have been developed. The method of recurrence plots (RPs) was introduced by Eckmann et al. [86]. Together with different RP quantification approaches [237, 418], this method has attracted growing interest for both theory and applications [223].

Recurrence plot based methods have been succesfully applied to a wide class of data from physiology, geology, physics, finances and others. They are especially suitable for the investigation of rather short and nonstationary data. This approach works with time series or phase-space reconstructions (trajectories), i. e. with data which are at least one-dimensional.

Recurrences are not restricted to one-dimensional time series or phase-space trajectories. Spatio-temporal processes can also exhibit typical recurrent structures. However, RPs as introduced in [86] cannot be directly applied to spatial (higher-dimensional) data. One possible way to study the recurrences of spatial data is to separate the higher-dimensional

objects into a large number of one-dimensional data series, and to analyse them separately [402]. A more promising approach is to extend the one-dimensional approach of the recurrence plots to a higher-dimensional one.

In the presented work, we focus on the analysis of snapshots of spatio-temporal processes, e. g., on static images. An extension of recurrence plots and their quantification to higher-dimensional data is suggested. This extension allows us to apply this method directly to spatial higher-dimensional data, and, in particular, to use it for 2D image analysis. We apply this method to 2D human bone images, derived by peripheral quantitative computer tomography (pQCT), in order to investigate differences in trabecular bone structures at different stages of osteoporosis.

8.2 Recurrence Plots

The initial purpose of recurrence plots was the visualisation of recurrences of system's states $\vec{x}_i$ in a phase-space (with dimension m) within a small deviation ε [86]. The RP efficiently visualises recurrences even for high dimensional systems. A recurrence of a state at time i at a different time j is marked within a two-dimensional squared matrix with ones and zeros dots (black and white points in the plot), where both axes represent time. The RP can be formally expressed by the matrix

$$\mathbf{R}_{i,j} = \Theta\left(\varepsilon - \|\vec{x}_i - \vec{x}_j\|\right), \quad \vec{x}_i \in \mathbb{R}^m, \quad i,j = 1 \ldots N, \tag{8.1}$$

where N is the number of considered states $\vec{x}_i$, ε is a threshold distance (an arbitrary deviation range within a recurrence is defined), $\|\cdot\|$ denotes a norm and $\Theta(\cdot)$ is the Heaviside function.

It should be emphasised that this method is a pairwise comparison of system's states at different times along a phase space trajectory, which is – although lying in an m-dimensional space – a one-dimensional curve. The axes of the RP correspond to the time which is given by pursueing a state on the trajectory. Diagonal lines in an RP represent epochs of similar dynamical evolution of the analysed system. For $i = j$ we get the *line of identity* (LOI), $\mathbf{R}_{i,i} \equiv 1\,|_{i=1}^{N}$, which is the main diagonal line in the RP (Fig. 8.1).

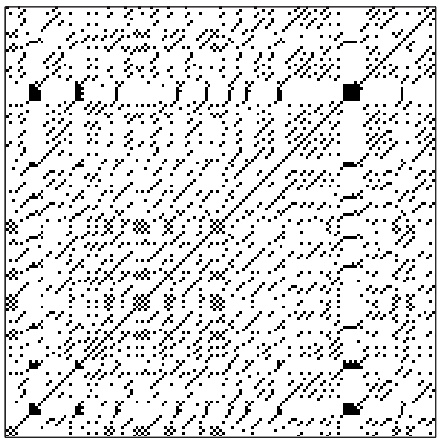

Figure 8.1: Example of a recurrence plot for the logistic map ($x_{i+1} = a x_i(1-x)$ with control parameter $a = 3.9767$). The RP consists of single dots and line structures.

Instead of using the system's states $\vec{x}_i$ which are often unknown, RPs can be created by only using a single time series or a reconstruction of the phase-space vectors (e. g. by using time-delay embedding, [375]). Such applications to experimental data have expanded the

utilisation of RPs from a tool for the investigation of *deterministic phase-space dynamics* to a tool for the investigation of *similarity and transitions in data series*, without the rather strong requirement that the data must be from a deterministic dynamical process. The idea of such a similarity plot is not new and can be found in publications earlier than [86], e. g. in [208]. This alternative understanding was (unconsciously) the base of the ever increasing amount of application of RPs in data analysis. However, in its present state the RP technique could not be applied to higher-dimensional spatial data.

The initial purpose of RPs was the visual inspection of the behaviour of phase-space trajectories. The appearance of RPs gives hints about the characteristic time evolution of these trajectories [223]. A closer inspection of RPs reveals small-scale structures which are *single dots*, *diagonal lines* as well as *vertical* and *horizontal lines* (Fig. 8.1).

A *diagonal line* $\mathbf{R}_{i+k,j+k} \equiv 1\,|_{k=0}^{l-1}$ (where l is the length of the diagonal line) occurs when one segment of the trajectory runs parallel to another one, i. e. the trajectory re-visits the same region of the phase-space at different time intervals. The length of this diagonal line is determined by the duration of intervals with similar local behaviour of the trajectory segments. We define a line in the RP as a diagonal line of length l, if it fulfils the condition

$$\big(1-\mathbf{R}_{i-1,j-1}\big)\big(1-\mathbf{R}_{i+l,j+l}\big)\prod_{k=0}^{l-1}\mathbf{R}_{i+k,j+k} \equiv 1. \tag{8.2}$$

In Eq. (8.2), the condition $1-\mathbf{R}_{i,j} \equiv 1$ holds only, if $\mathbf{R}_{i,j}$ is a non-recurrence point. Therefore, the first two factors in Eq. (8.2) mark the start and the end of the diagonal line, conditioned by non-recurrence points.

A *vertical (horizontal) line* $\mathbf{R}_{i,j+k} \equiv 1\,|_{k=0}^{v-1}$ (where v is the length of the vertical line) marks a time interval in which a system's state does not change in time or changes very slowly. It looks like the state is trapped for some time, which is a typical behaviour of laminar states [237]. Because RPs are symmetric about the LOI by definition (8.1), each vertical line has a corresponding horizontal line. Therefore, only the vertical lines are henceforth considered. Combinations of vertical and horizontal lines form rectangular clusters in an RP. We define a line as a vertical line of length v, if it fulfils the condition

$$\big(1-\mathbf{R}_{i,j-1}\big)\big(1-\mathbf{R}_{i,j+v}\big)\prod_{k=0}^{v+1}\mathbf{R}_{i,j+k} \equiv 1. \tag{8.3}$$

These small-scale structures are used for the quantitative analysis of RPs (known as recurrence quantification analysis, RQA). Using the distributions of the lengths of diagonal lines $P(l)$ or vertical lines $P(v)$, different measures of complexity have been introduced (cf. [223] for a comprehensive review of definitions and descriptions of these measures). Here we generalise the measures recurrence rate *RR*, determinism DET, averaged diagonal line length L, laminarity LAM and trapping time TT in order to quantify higher-dimensional data. (cf. Tab. 8.1).

Several measures need a predefined minimal length $l_{\min}$ or $v_{\min}$, respectively, for the definition of a diagonal or vertical line. These minimal lengths should be as minimal as possible in order to cover as much variation of the lengths of these lines. On the other hand, $l_{\min}$ and $v_{\min}$ should be large enough to exclude line-like structures which represent only single, non-recurrent states, which may occur if the threshold ε is chosen too large or if the data have been smoothed too stronlgy before computing the RP.

RQA was successfully applied for example for the detection of transitions in event related EEG potentials [233], the study of interrelations between El Niño and climate in the past [238], the investigation of economic data series [117], of nonlinear processes in electronic

devices [90] or the study of transitions in chemical reactions [331]. For a number of further applications see, e. g., [223] or www.recurrence-plot.tk.

8.3 Extension to higher dimensions

Now, we propose an extension of RPs to analyse higher dimensional data. With this step we leave the RPs as a method for investigating deterministic dynamics and focus on its potential in determining similar (recurrent) features in spatial data.

For a d-dimensional (Cartesian) system, we define an n-dimensional recurrence plot by

$$\mathbf{R}_{\vec{i},\vec{j}} = \Theta\left(\varepsilon - \left\|\vec{x}_{\vec{i}} - \vec{x}_{\vec{j}}\right\|\right), \quad \vec{x}_{\vec{i}} \in \mathbb{R}^m,\ \vec{i},\vec{j} \in \mathbb{N}^d, \tag{8.4}$$

where $\vec{i}$ is the d-dimensional coordinate vector and $\vec{x}_{\vec{i}}$ is the phase-space vector at the location given by the coordinate vector $\vec{i}$. This means that we decompose the spatial dimension of $\vec{x}_{\vec{i}}$ and consider each space direction separately, e. g. $\vec{x}_{i_1,i_2,\ldots i_d}$ for $i_1 = 1,\ldots,N$ but $i_2,\ldots,i_d =$ const. Such vectors are now one-dimensional curves in the m-dimensional space. Each of these vectors is pairwisely compared with all others. These individual sub-RPs are the components of the final higher-dimensional RP. The resulting RP has now the dimension $n = 2 \times d$ and cannot be visualised anymore. However, its quantification is still possible.

Similarly to the one-dimensional LOI given by $\mathbf{R}_{i,j} = 1\ \forall\ i = j$, we can find diagonally oriented, d-dimensional structures in this n-dimensional recurrence plot ($n = 2\,d$), called the *hyper-surface of identity* (HSOI):

$$\mathbf{R}_{\vec{i},\vec{j}} \equiv 1 \quad \forall\ \vec{i} = \vec{j}. \tag{8.5}$$

Table 8.1: Generalised recurrence quantification measures for spatial data of dimension d and with $\vec{i},\vec{j} \in \mathbb{N}^d$. Note that these measures assess recurrence information in terms of length while the original RQA measures quantify it in terms of time.

RQA measure	equation	meaning
recurrence rate	$RR = \frac{1}{N^{2d}} \sum_{\vec{i},\vec{j}}^{N} \mathbf{R}_{\vec{i},\vec{j}}$	percentage of recurrent states in the system; probability of the recurrence of any state
determinism	$DET_{HS} = \frac{\sum_{l=l_{\min}}^{N} l\,P(l)}{\sum_{\vec{i},\vec{j}}^{N} \mathbf{R}_{\vec{i},\vec{j}}}$	percentage of recurrence points which form diagonal hyper-surfaces; related to the predictability of the system
laminarity	$LAM_{\mathrm{HS}} = \frac{\sum_{v=v_{\min}}^{N} vP(v)}{\sum_{v=1}^{N} vP(v)}$	percentage of recurrence points which form vertical hyper-surfaces; related to the laminarity of the system
averaged diagonal hyper-surface size	$L_{\mathrm{HS}} = \frac{\sum_{l=l_{\min}}^{N} l\,P(l)}{\sum_{l=l_{\min}}^{N} P(l)}$	related to the prediction length of the system
trapping size	$TT_{\mathrm{HS}} = \frac{\sum_{v=v_{\min}}^{N} vP(v)}{\sum_{v=v_{\min}}^{N} P(v)}$	related to the size of the area in which the system does not change

In the special case of a two-dimensional image composed by scalar values, we have

$$\mathbf{R}_{i_1,i_2,j_1,j_2} \equiv \Theta\left(\varepsilon - \left\|x_{i_1,i_2} - x_{j_1,j_2}\right\|\right), \tag{8.6}$$

which is in fact a four-dimensional recurrence plot, and its HSOI ($\mathbf{R}_{i_1,i_2,i_1,i_2} \equiv 1$) is a two-dimensional plane.

8.4 Quantification of Higher-Dimensional RPs

The known RQA is based on the quantification of the line structures in the two-dimensional RPs. Thus, the definition of higher-dimensional equivalent structures is crucial for a quantification analysis of higher-dimensional RPs.

Based on the definition of diagonal lines, Eq. (8.2), we define a diagonal squared hyper-surface of size $\vec{l}$ ($\vec{l} = (l,\ldots,l), \vec{l} \in \mathbb{N}^d$) as

$$\left(1 - \mathbf{R}_{\vec{i}-\vec{1},\vec{j}-\vec{1}}\right)\left(1 - \mathbf{R}_{\vec{i}+\vec{l},\vec{j}+\vec{l}}\right) \prod_{\substack{k_1,k_2,\ldots,\\ k_d=0}}^{l-1} \mathbf{R}_{\vec{i}+\vec{k},\vec{j}+\vec{k}} \equiv 1. \tag{8.7}$$

In particular, for the two-dimensional case such a diagonal hyper-surface (HS) is thus defined as

$$\left(1 - \mathbf{R}_{i_1-1,i_2-1,j_1-1,j_2-1}\right)\left(1 - \mathbf{R}_{i_1+l,i_2+l,j_1+l,j_2+l}\right) \prod_{k_1,k_2=0}^{l-1} \mathbf{R}_{i_1+k_1,i_2+k_2,j_1+k_1,j_2+k_2} \equiv 1. \tag{8.8}$$

The next characteristic structure, the vertical squared HS of size $\vec{v}$ ($\vec{v} = (v,\ldots,v), \vec{v} \in \mathbb{N}^d$) is defined as

$$\left(1 - \mathbf{R}_{\vec{i},\vec{j}-\vec{v}}\right)\left(1 - \mathbf{R}_{\vec{i},\vec{j}+\vec{v}}\right) \prod_{\substack{k_1,k_2,\ldots,\\ k_d=0}}^{v-1} \mathbf{R}_{\vec{i},\vec{j}+\vec{k}} \equiv 1. \tag{8.9}$$

Its 2D equivalent is

$$\left(1 - \mathbf{R}_{i_1,i_2,j_1-1,j_2-1}\right)\left(1 - \mathbf{R}_{i_1,i_2,j_1+v,j_2+v}\right) \prod_{k_1,k_2=0}^{v-1} \mathbf{R}_{i_1,i_2,j_1+k_1,j_2+k_2} \equiv 1. \tag{8.10}$$

Using these definitions, we can construct the frequency distributions $P(l)$ and $P(v)$ of the sizes of diagonal and vertical HS in the higher-dimensional RP. This way we get generalised RQA measures DET_{HS}, LAM_{HS}, L_{HS} and TT_{HS} as defined in Tab. 8.1, which are now suitable for characterising spatial (e. g. two-dimensional) data.

8.5 Model Examples

In order to illustrate the ability of the proposed high-dimensional RP's extension, we consider three prototypical model examples from 2D image analysis. The first image (A) is produced by uniformly distributed white noise, the second one (B) is the result of a two-dimensional auto-correlated process of 2nd order (2D-AR2; $x_{i,j} = \sum_{k,l=1}^{2} a_{k,l}\, x_{i-k,j-l} + \xi$, where $a_{k,l}$ is the 2D matrix of model parameters and ξ is Gaussian white noise) and the third one (C) represents periodical recurrent structures (Fig. 8.2). All these example images have a size of 200×200 pixels and are normalised to a mean of zero and a standard deviation of one.

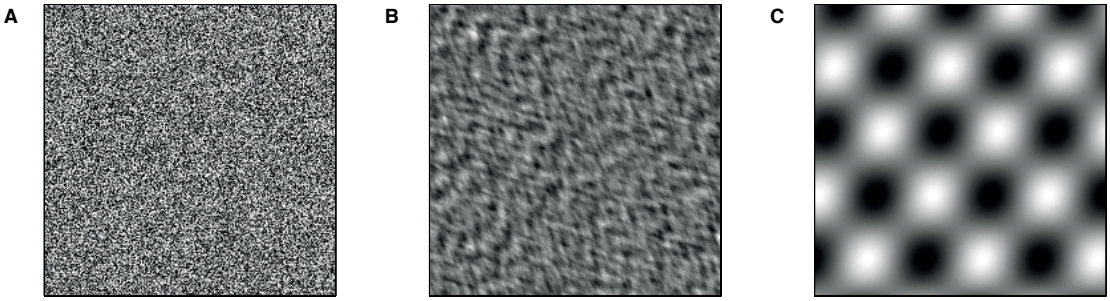

Figure 8.2: Two-dimensional prototypical examples: test images representing (A) uniformly distributed white noise, (B) a two-dimensional auto-correlated process (2D-AR2) and (C) periodical recurrent structures.

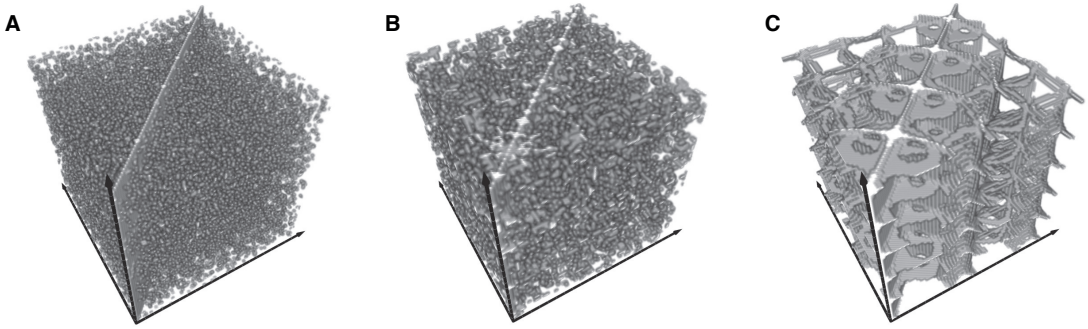

Figure 8.3: Three-dimensional subsections of four-dimensional RPs of the images shown in Fig. 8.2. As known from one-dimensional RQA, (A) random data causes homogeneous RPs consisting of single, dis-connected points, (B) correlations in data cause extended connected structures and (C) periodic data induce periodically occuring structures in the RPs.

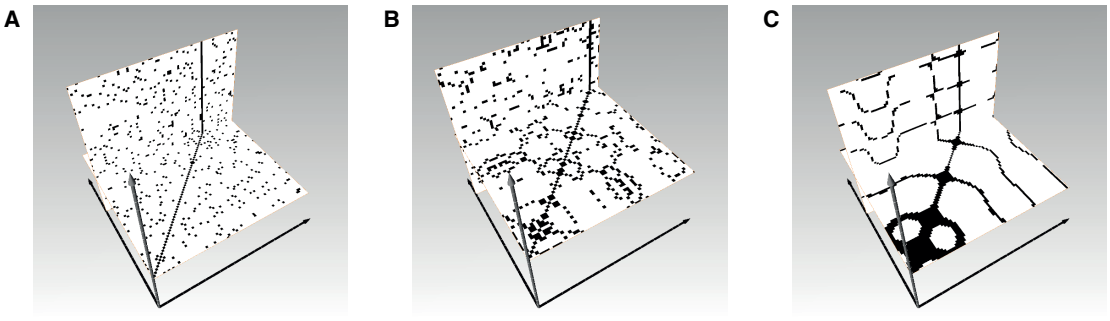

Figure 8.4: Slices of the subsections of the four-dimensional RPs shown in Fig. 8.3. The similarity to known recurrence plots is obvious: (A) noise, (B) auto-correlated data and (C) periodic data.

Table 8.2: Recurrence quantification measures for the prototypical examples shown in Fig. 8.2. The measures are explained in Tab. 8.1.

Example	RR	DET_{HS}	LAM_{HS}	L_{HS}	TT_{HS}
(A) noise	0.218	0.007	0.006	3.7	3.0
(B) 2D-AR2	0.221	0.032	0.065	3.1	3.1
(C) periodic	0.219	0.322	0.312	5.8	5.6

The resulting RPs are four-dimensional matrices of size 200×200×200×200 (cp. Eq. (8.6)), and can hardly be visualised. However, in order to visualise these RPs, we can reduce their dimension by one by considering only those part of the RPs, where $i_2 = j_2$. The resulting $200 \times 200 \times 200$ cube is a hypersurface of the four-dimensional RP along the LOI. For the threshold we use $\varepsilon = 0.2$, which gives clear representations of the RPs.

The features occuring in higher-dimensional RPs provide similar information as known from the classic one-dimensional RPs. Separated single points correspond to strongly fluctuating, uncorrelated data as it is typical for, e. g., white noise (Fig. 8.3A). Auto-correlations in data cause extended structures, which can be lines, planes or even cuboids (Fig. 8.3B). Periodical recurrent patterns in data imply periodic line and plane structures in the RP (Fig. 8.3C). Two-dimensional slices through such RPs contain similar patterns found by common RPs (Fig. 8.4).

We compute the proposed RQA measures (Tab. 8.1) for the histograms of the sizes of diagonal and vertical planes (2D HS) in the four-dimensional RPs. For all three examples we use for the minimal size of the diagonal and vertical HS $l_{\min} = 3$ pixels and $v_{\min} = 4$ pixels. Although the RQA measures depend on the value of ε, its selection is not crucial for our purpose to discriminate the three different types of structures in the test images. The chosen values for $l_{\min}$ and $v_{\min}$ are found to be optimal for discriminating the considered images. By choosing smaller values of $l_{\min}$ and $v_{\min}$ (but larger than one), the measures DET_{HS} and LAM_{HS} are closer for the 2D-AR2 and the periodic image.

Four of five RQA measures clearly discriminate between the three types of images (Tab. 8.2). Only the recurrence rate RR is roughly the same for all test objects. This is because all images were normalised to the same standard deviation. For the random image (A) the determinism DET_{HS} and laminarity LAM_{HS} tend to zero, what is expected, because the values in the image heavily fluctuate even between adjecent pixels. For the 2D-AR2 image (B), DET_{HS} and LAM_{HS} are slightly above zero, revealing the correlation between adjecent pixels. The last example (C) has, as expected, the highest values in DET_{HS} and LAM_{HS}, because same structures occur many times in this image and the image is rather smooth. Although the trend in DET_{HS} and LAM_{HS} is similar, there is a significant difference between both measures. Whereas LAM_{HS} represents the probability that a specific value will not change over spatial variation (what results in extended same-coloured areas in the image), DET_{HS} measures the probability that similar changes in the image recur. LAM_{HS} is twice of DET_{HS} for the 2D-AR2 image, obtaining that there are more areas without changes in the image than such with typical, recurrent changes.

8.6 Application to pQCT data of proximal tibia

According to the definition of the World Health Organisation, osteoporosis is a disease characterised by bone loss and changes in the structure of the bone. In the last years, the focus changed to structural assessment of the trabecular bone, because bone densitometry alone is very limited to explain all variation in bone strength. Furthermore, the rapid

progress in the development of new high-resolution computer tomography (CT) scanners facilitates investigations of the bone micro-architecture. Different approaches using methods coming from nonlinear dynamics have been recently proposed in order to evaluate structural changes [19, 82, 122, 333] or even to predict fracture risks or biomechanical properties [131, 209, 299]. These approaches use, e. g., scaling properties of bone micro-structure or symbol-encoding of the bone architecture.

Using the RP based method, we will focus here on the recurrent structures found in images of trabecular bone of proximal tibiae obtained by peripheral quantitative computer tomography (pQCT). The images were aquired from bone specimens with different stages of osteoporosis as assessed by bone mineral density (BMD). Being applied to such images, the RP provides information about recurrences of bone and soft tissue.

The spatial recurrence analysis is applied to high-resolution pQCT axial slices of human proximal tibia acquired 17 mm below the tibial plateau, with pixel size 200 μm and slice thickness 1 mm (Fig. 8.5). The images were acquired from 25 bone specimens with a pQCT scanner XCT-2000 (Stratec GmbH, Germany). The trabecular bone mineral density of these specimens ranges from 30 to 150 mg/cm^3. A standardised image pre-processing procedure was applied to exclude the cortical shell from the analysis [333, 335] (the attenuation levels were not changed). The RQA was computed by using the parameters $\varepsilon = 0.04\,\mathrm{cm}^{-1}$, $l_{\min} = v_{\min} = 400\,\mu$m. These minimal lengths correspond to two pixels and is found to be appropriate for pQCT images of such resolution (for higher values of $l_{\min}$ and $v_{\min}$, the discrimination of the RQA measures for different stages of osteoporosis get a bit worse).

In order to further evaluate the proposed RQA measures, we compare them with some recently introduced structural measures of complexity (SMCs) [333, 335]. The SMCs are based on a symbol-encoding of bone elements in the pQCT image. Here we focus on the following SMCs:

1. Entropy (S_a): quantifies the probability distribution of X-ray attenuation within the region of interest;
2. Structure Complexity Index (SCI): assesses the complexity and homogeneity of the structure as a whole;
3. Trabecular Network Index (TNI) evaluates richness, orderliness, and homogeneity of the trabecular network.

The computation of the SMCs is applied to the same trabecular area like the RQA measures.

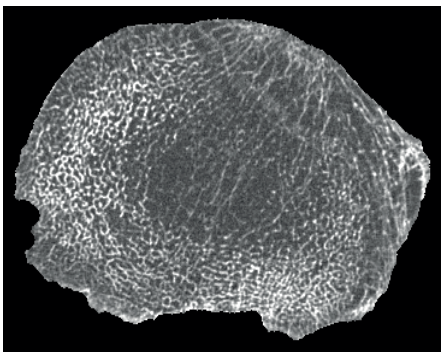

Figure 8.5: Typical axial pQCT slice of human proximal tibia acquired 17 mm below the tibial plateau. The trabecular BMD is 65.5 mg/cm^3.

The application of the recurrence plot extension to the pQCT images of proximal tibiae reveals a relationship between the recurrences in the trabecular architecture and the osteoporotic stage (Fig. 8.6 and Tab. 8.3). *RR* is largest for osteoporotic bone and shows the strongest relationship with the degree of osteoporosis: it is clearly anti-correlated with

Table 8.3: Rank correlation coefficients R for recurrence quantification measures, BMD and structural measures of complexity (only significant values are shown).

2D-RQA	BMD	S_a	SCI	TNI
RR	−0.94	−0.92	−0.91	0.84
DET	−0.65	−0.58	−0.61	0.61
LAM	−0.78	−0.73	−0.75	0.72
L	–	–	–	–
TT	−0.57	−0.51	–	0.49

BMD (Spearman's rank order correlation coefficient $R = -0.94$). DET_{HS} and LAM_{HS} are also maximal for tibiae with high degree of osteoporosis ($R = -0.66$ and -0.79; Fig. 8.7). We do not find a strong relation between L_{HS}, TT_{HS} and BMD. The comparison with the SMCs reveals good relationships between the RQA measures and S_a, SCI and TNI (Fig. 8.8 and Tab. 8.3). Thus, the RQA measures RR, DET_{HS} and LAM_{HS} contain also information about the complexity and homogeneity of the trabecular network.

Thus, the proposed RP approach reveals that during the development of osteoporosis the structures in the corresponding pQCT image become more and more recurrent. This is in a good agreement with a decreasing complexity in the micro-architecture of bone. It confirms the results of an analysis of pQCT images acquired from human proximal tibia and lumbar vertebrae based on symbolic dynamics [333, 335]. The direct comparison with the structural quantities (SMCs) shows that the RQA measures provide information about the bone architecture. The RQA measures reveal a low rate of change for bone of higher BMD, but higher rate of changes for specimens with lower BMD (Figs. 8.6 and 8.7). This reflects a higher sensitivity of these measures for osteoporotic trabecular bone and emphasises the nonlinear relationship between the bone architecture as assessed by the RQA measures and bone mass as evaluated by the BMD. As it has been recently shown that the SMCs provide a better estimation of the mechanical bone strength than BMD alone [334], the proposed RQA measures could further enhance the evaluation to assess the fracture risk of bone.

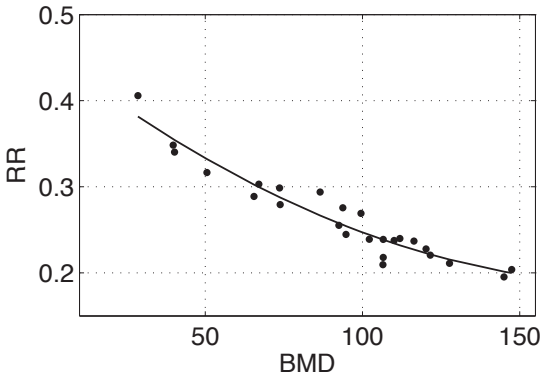

Figure 8.6: Recurrence rate RR obtained from four-dimensional RPs of pQCT images of trabecular bone in human proximal tibia of different osteoporotic stages.

8.7 Conclusions

A generalisation of the method of recurrence plots (RPs) and recurrence quantification analysis (RQA) for the application to higher-dimensional spatial data has been proposed here.

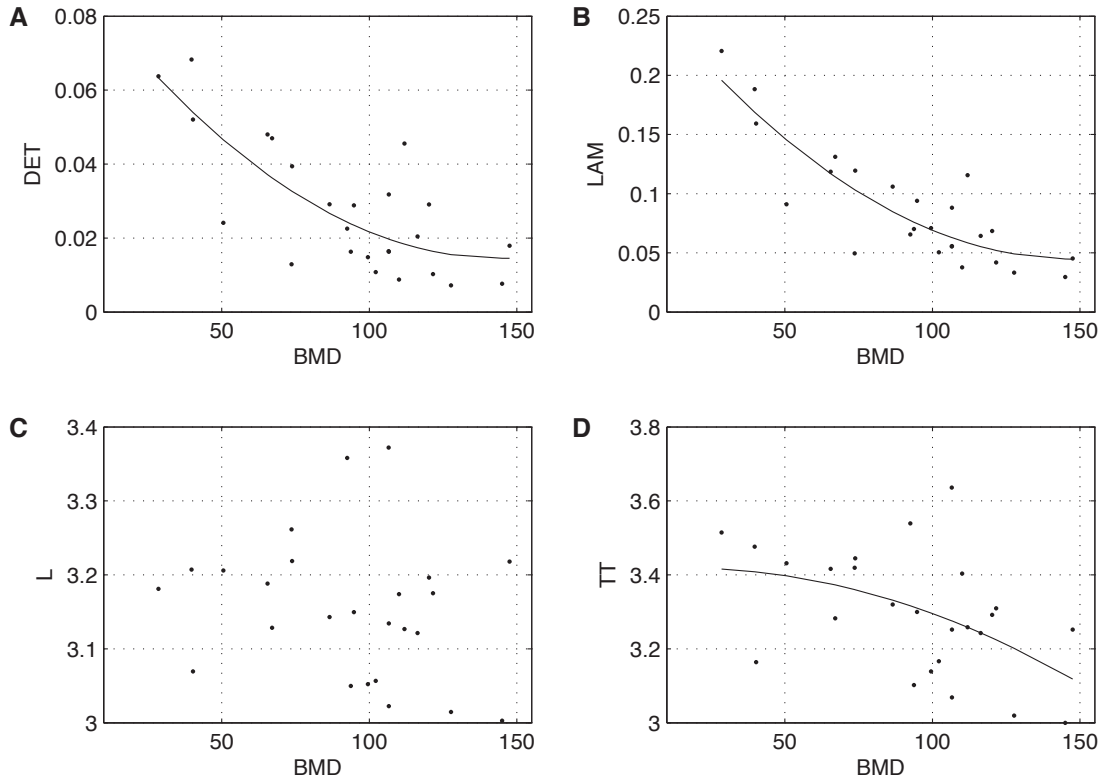

Figure 8.7: Determinism DET (A), laminarity LAM (B), mean line length L (C) and trapping time TT (D) obtained from four-dimensional RPs constructed from pQCT images of trabecular bone in human proximal tibiae with different degree of osteoporosis.

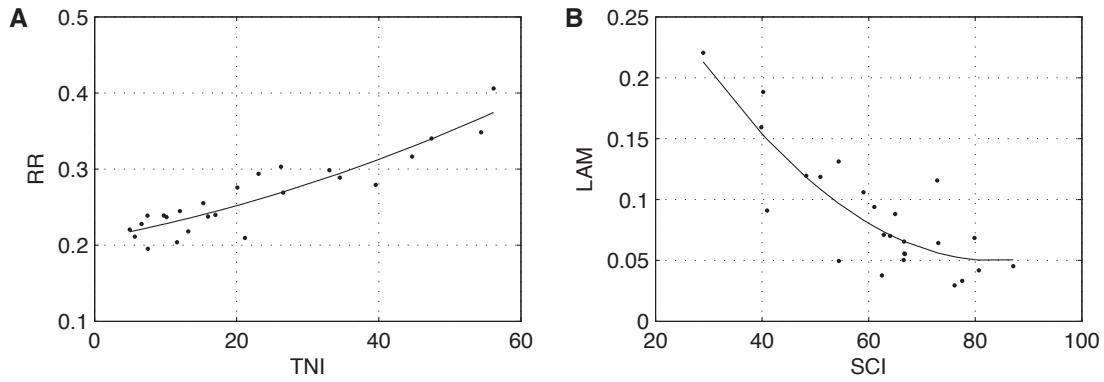

Figure 8.8: Recurrence rate RR (A) and laminarity LAM (B) compared with trabecular network index TNI and structure complexity index (SCI).

This new method can be used for 2D image analysis, in particular to reveal and quantify recurrent structures in 2D images. Applying this method on model images, we have shown that it is able to distinguish typical spatial structures by means of recurrences. As a first application, we have used this method for the comparison of CT images of human proximal tibia with different degree of osteoporosis. We have found a clear relationship between some of the proposed RQA measures and the complexity and homogeneity of the trabecular structure. Moreover, this approach can be easily extended to higher dimensions, e. g., for 3D analysis of micro-CT images of human bone. This approach will be the base for the further development of methods for the assessment of structural alteration in trabecular bone with osteoporosis in patients on Earth or in space flying personnel in microgravity conditions.

Acknowledgments

This study was supported by grants from project MAP AO-99-030 (contract #14592) of the Microgravity Application Program/Biotechnology from the Human Spaceflight Program of the European Space Agency (ESA) and by the European Union through the Network of Excellence BioSim, contract LSHB-CT-2004-005137&#65533. The authors would also like to acknowledge Scanco Medical AG, Siemens AG, and Roche Pharmaceuticals for support of the study and thank Wolfgang Gowin and Erika May for preparation and scanning of the bone specimens.

Phytoplankton Bloom (Landsat 7 image)
Courtesy: U.S. Geological Survey (USGS)

9. Driving Forces in Spatial Systems

Paper 8 M. Riedl, N. Marwan, J. Kurths: Visualizing driving forces of spatially extended systems using the recurrence plot framework, European Physical Journal – Special Topics, 226(15), 3273–3285 (2017). DOI:10.1140/epjst/e2016-60376-9

R The presented study in this chapter is a postdoc's paper, where I contributed the basic idea of adapting and applying the mapogram approach to the specific research question.

Abstract

The increasing availability of highly resolved spatio-temporal data leads to new opportunities as well as challenges in many scientific disciplines such as climatology, ecology or epidemiology. This allows more detailed insights into the investigated spatially extended systems. However, this development needs advanced techniques of data analysis which go beyond standard linear tools since the more precise consideration often reveals nonlinear phenomena, for example threshold effects. One of these tools is the recurrence plot approach which has been successfully applied to the description of complex systems. Using this technique's power of visualization, we propose the analysis of the local minima of the underlying distance matrix in order to display driving forces of spatially extended systems. The potential of this novel idea is demonstrated by the analysis of the chlorophyll concentration and the sea surface temperature in the Southern California Bight. We are able not only to confirm the influence of El Niño events on the phytoplankton growth in this region but also to confirm two discussed regime shifts in the California current system. This new finding underlines the power of the proposed approach and promises new insights into other complex systems.

9.1 Introduction

In many scientific disciplines, such as climatology, ecology, neuroscience or epidemiology, the increasing availability of highly resolved spatio-temporal data allows more detailed insights into the behavior of spatially extended systems of interest. However, this development also leads to the challenging question for advanced analytical techniques in order to describe

and to quantify the now revealing phenomena which often have a nonlinear character, e.g. threshold effects. The unabated publishing of new analytical tools for this purpose proves this methodological progression. In the last decades, the recurrence plot (RP) has emerged as one successful concept in the description of nonlinear phenomena and complex systems [86, 239] but their application to spatio-temporal problems is only in the beginning. In previous studies we have pro- posed the high dimensional RP and the mapogram-based RP (MRP), respectively, in order to bring the powerful concept to the analysis of spatially extended systems [226, 314].

The RP framework enables us not only to quantify the dynamics of these systems by means of the library of recurrence quantification analysis [239] and recurrence network analysis [78], but also to visualize the underlying high-dimensional state space. An example of this family of tools is the thresholded metan RP which was proposed by Casdagli [45] for visualizing driving forces of a system. We extend the thresholded metan RP by using a kernel estimator instead of a histogram in order to take into account even fast changes of the force and by focusing on the underlying distance matrix avoiding gaps in the RP which results from regime shifts. The potential of this novel idea is demonstrated by the application to remotely sensed data of the Southern California Bight (SCB), one of the most productive marine ecosystems of the world [411], looking for hidden determinants of the complex phytoplankton's growth in this system. In particular, the data are the chlorophyll concentration (CHL), a proxy of the phytoplankton's concentration, and the sea surface temperature (SST), a proxy of the hydrological state of the California Current System (CCS). Influences at three different time scales are discussed for this system [404]. Influences at longer time scales are annual determinants which are dominated by the coastal wind-driven upwelling which typically occurs in Spring. Other influences are short-term interannual influences, for example the El Niño-Southern Oscillation (ENSO) where El Niño events decrease the upwelling and increase the SST. A previous study only indicates a weak effect of the El Niño events on the CHL whereas La Niña periods seem ineffective except the sharp events after the strong El Niños 1982–83 and 1997–98 [404]. Finally, long-term influences enclose cycles of 10 years or longer as well as irregular regime shifts, e.g. the major regime shift 1976–77.

9.2 Method

9.2.1 Recurrence plot

The recurrence plot (RP) visualizes the recurrences of a state of a dynamical system. The temporal evolution of such dynamical system is given by its trajectory $\{\vec{x}_i\}_{i=1}^{N}$ in the system's phase space. Then, the corresponding RP is based on the recurrence matrix:

$$R_{i,j} = \Theta(\varepsilon - \|\vec{x}_i - \vec{x}_j\|), \tag{9.1}$$

i and j are the indexes of the observed states and go from 1 to N, the number of observed states. $\|\cdot\|$ denotes a norm and Θ is the Heaviside function. In the RP, the values 1 in the recurrence matrix are displayed by black dots which show that the trajectory comes close (defined by the threshold ε) to a previous state [239].

A serious problem when constructing the RP is the contamination of the data by noise (Fig. 9.1). Comparing the RP of the noisy Lorenz data with the RP of the clean Lorenz data, we find that the diagonal lines resolve into clouds of points (Fig. 9.1). Further, the patchy like structure with and without points vanishes, i.e. the points are more homogeneously distributed over the whole plot. Surprisingly, the last effect reveals the hidden structure of the underlying distance matrix which allows a qualitative description of the dynamics in the sparse regions of the undisturbed RP (Fig. 9.1A).

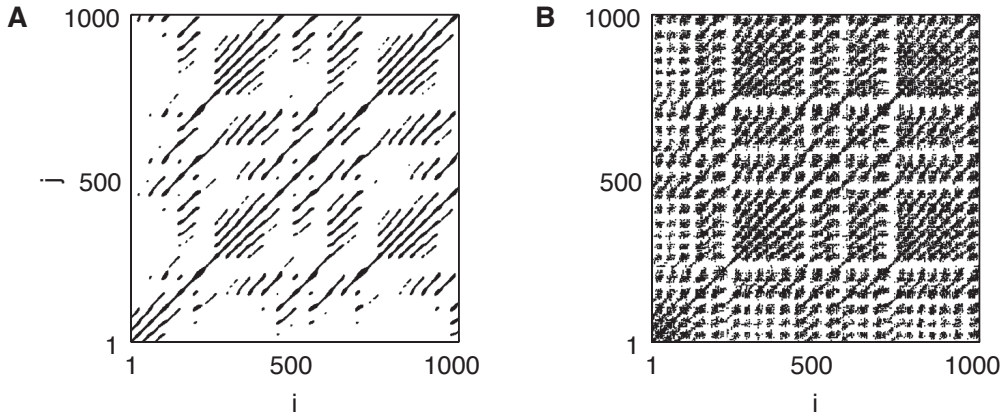

Figure 9.1: (A) Recurrence plot of the simulated Lorenz-system (cf. Appendix B); (B) recurrence plot of the same simulation with additive noise (white noise added to each component; signal-to-noise ratio: 2.5). The recurrence rate is fixed to 5% in both cases.

9.2.2 Thresholded meta recurrence plot

Casdagli [45] proposed the thresholded metan RP in order to remove the noise and to reveal footprints of the system's drivers. The thresholded metan RP results from covering of the noisy RP by means of N_b non-overlapping squares building the bins of a histogram $h_{k,l}$ with $k,l = 1,\ldots,N_b$, the indexes of the bins. $h_{k,l}$ is the relative frequency of points in the bin. On the basis of this histogram, the new distance matrix is calculated by means of

$$D^{\text{hist}}_{k,l} = (h_{k,k} + h_{l,l} - 2h_{k,l})/\varepsilon^2, \tag{9.2}$$

which is further thresholded. ε is the threshold of equation 9.1 constructing the starting RP. The thresholded metan RP of the RP in Figure 9.1B is displayed in Figure 9.2A which only reflects the global patchy like structure of the undisturbed RP (Fig. 9.1A). Here, the bin width of 8 time steps is manually selected. The recurrence rate is fixed to 5%. Although without an external driving force, the example demonstrates the effect of the thresholded metan RP to reveal long-term dynamics.

However, the application of the thresholded metan RP is limited to slowly varying dynamics. One cause of this limitation is the use of histograms which does not adapt to the distribution of the recurrence points and therefore needs larger bin sizes. So, we extend this approach by applying a kernel estimation of the point distribution instead of the histogram in order to overcome this problem. We estimate the point distribution of the noisy recurrence plot by means of a 2D Epanechnikov kernel

$$d_{i,j} = \frac{1}{N^2} \sum_{i',j'=1}^{N} K_w\left(\frac{i-i'}{w}\frac{j-j'}{w}\right) R_{i,j}. \tag{9.3}$$

This kernel K_w has a bell-like shape as the Gaussian kernel but has a bounded domain which avoids long-range effects [351]. The 2D Epanechnikov kernel is defined by

$$K_w(x,y) = \begin{cases} 3\left(1-\left((x/w)^2+(y/w)^2\right)\right)/4, & \text{if } \|(x/w)^2+(y/w)^2\| \le 1 \\ 0 & \text{otherwise,} \end{cases} \tag{9.4}$$

w is the bandwidth of the kernel and is determined by the half of the first minimum of the

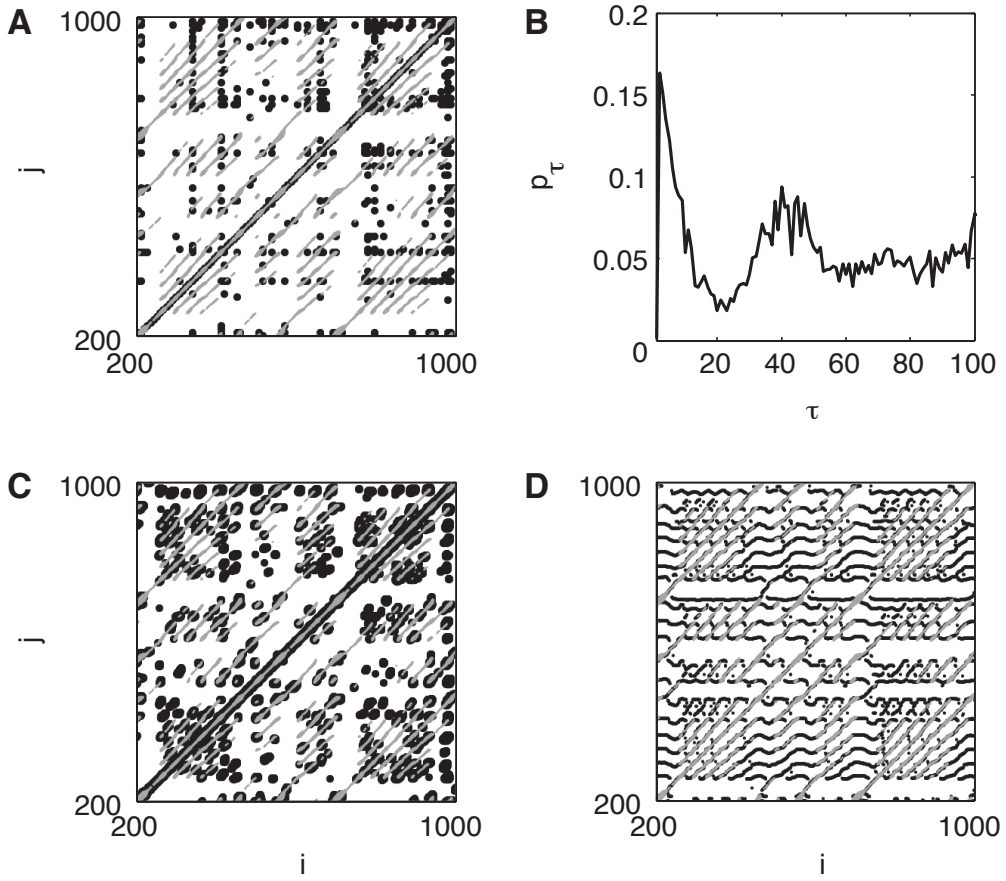

Figure 9.2: (A) Black points display the thresholded metan RP of the RP in Figure 9.1B; (B) probability of recurrence after τ time steps p_τ, Eq. (9.5), of the RP in Figure 9.1B. The remarkable local minimum at 20 determines the bandwidth of the kernel used in C and D. (C) Black points display the thresholded metan RP using a kernel estimation instead of the histogram as used in A. (D) The column-wise position of the minima in the kernel smoothed distance matrix of the RP in Figure 9.2C. For comparison, gray points in A, C, and D show the undisturbed RP from Figure 9.1A.

probability of recurrence after τ time steps which is defined by:

$$p_\tau = \frac{1}{N-\tau} \sum_{i=1}^{N-\tau} R_{i,i+\tau}, \tag{9.5}$$

N is the size of the recurrence matrix $\{R_{i,j}\}_{i,j=1,\ldots,N}$ from equation 9.1 [239]. That is, p_τ is the relative frequency of the points in the τ-th diagonal of the RP (e.g., Fig. 9.2B). The picked minimum of p_τ guarantees a high level of smoothing and the resolution of the diagonal structures in the thresholded metan RP. From the kernel estimated distribution $d_{i,j}$ in equation 9.3, we get the distance matrix

$$D_{i,j}^{\text{kernel}} = \left(d_{i,i} + d_{j,j} - 2d_{i,j}\right)/\varepsilon^2, \tag{9.6}$$

as in the case of the histogram based approach, Eq. (9.2). The extended version of the thresholded metan RP resembles the undisturbed recurrence plot much better than the original, histogram based approach. Although the same recurrence rate, the number of the

recurrence points is much higher since the down sampling by means of the histogram is not necessary anymore.

9.2.3 Local minima of the distance matrix

A second adaptation of the approach by Casdagli [45] is done in order to overcome the sparse regions of the RP which are caused by instationarities (e.g. Fig. 9.1A). For this purpose, we consider the local minima in the columns of the underlying distance matrix matrix ($D_{i-1,j} > D_{i,j} < D_{i+1,j}$). Figure 9.2D shows the column-wise minima of the distance matrix for the smoothed distance matrix of the noisy simulation of the Lorenz-system, for example. We use the same kernel smoothing as in the extended thresholded metan RP where the band width is 10 time steps, half of the first remarkable minimum of p_τ (Fig. 9.2B). Now horizontal bands are visible containing curves which remember time series of an oscillation with changing amplitude (Fig. 9.2D). At some time steps these curves are connected by diagonal lines which actually build the original RP in Figure 9.1A.

For the Lorenz-example, a selected "band" (at $j = 500$) is presented in Figure 9.3A. This horizontal structure coincides well with the z-component of the Lorenz system (Appendix B). These bands of black points represent the stay of the trajectory in one of the two wings of the attractor for one period. The curves are projections of the stay in the other wing, whereas the diagonal lines crossing the empty space display the oscillations in the corresponding wing. Further, one bound of these bands, characterized by the highest number of black dots, visualizes the closest point of the corresponding wing-internal oscillation to the oscillations in the other wing which is indicated by its location along the merging zone of the trajectory (cf. Fig. 9.3B).

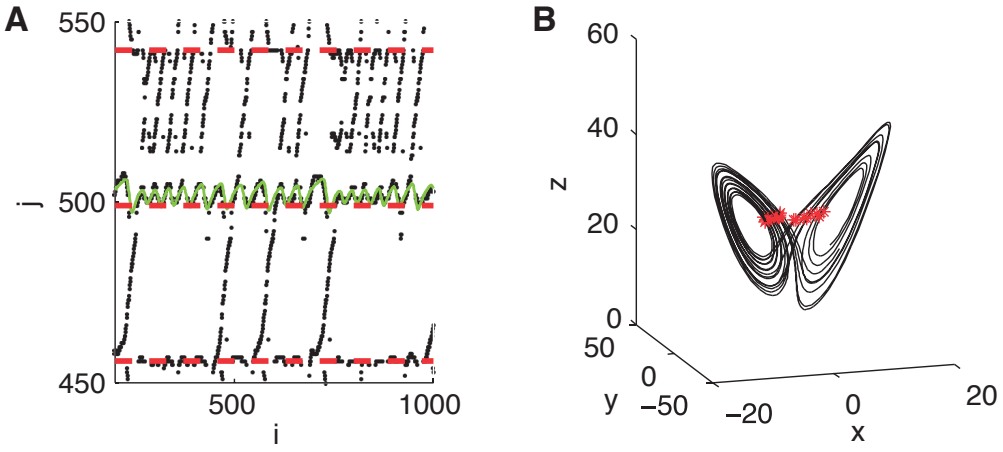

Figure 9.3: (A) Part of Figure 9.2D where the black dots mark the positions of the column-wise local minima. For comparison, the rescaled third component of the undisturbed Lorenz-system is displayed by the green solid line. The red dashed lines underline horizontal levels with an accumulation of black dots. (B) The trajectory of the undisturbed Lorenz-system in its state space (black line). The red stars represent the time stamps which correspond to red dashed lines in A.

So, we only find this horizontal band structure in systems where the trajectory stays in at least two separate regions of the state space for more than one main oscillation. This is indicated by the counterexamples, the van der Pol oscillator and the Rössler system (cf. Fig. 9.4), where the bands disappear or partly vanish, respectively. The Lorenz system

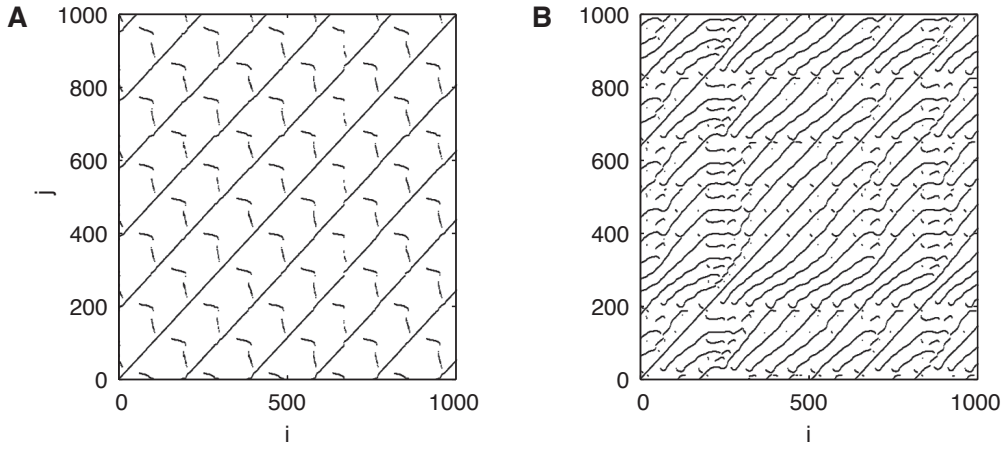

Figure 9.4: Positions of the column-wise local minima of distance matrices for simulations of: (A) the van der Pol-oscillator (Appendix B); and (B) the Rössler-system.

intrinsically fulfills the condition of separate regions in the phase space with separated oscillations, i.e. the trajectory stays in separated state space regions for more than one oscillation, but also multi-stable systems comprise this property. So, this technique of visualization does not only display a projection of the oscillation in the different parts but also indicates the switching of the trajectory from one part to another.

9.3 Application

We apply the proposed technique of the local minima of the distance matrix to spatio-temporal data of an ecological system, and demonstrate the ability of this approach to visualize driving forces of the system.

9.3.1 Data

The first data set is the estimation of the chlorophyll concentration (CHL, [min, max] = [0.0107, 62.3735] mg/m^3) in the CCS from 1998 to 2016, i.e. 1431 time steps. It results from the merging of multiple satellite sensor outputs of the ocean color and in situ measurements of CHL in this region [162, 163]. The spatial resolution of the gridded data is 4 km where the upper-left and the lower-right corners of the grid are given by (45°N, −140°E) and (30.03597°N, −115.5454°E), respectively, resulting in 61 × 87 data points. The temporal resolution is 5 days after averaging. Missing data are exchanged by a two times linear interpolation which is based on the previous and the following time stamp. The second data set is the satellite based SST ([min, max] = [10.5, 24.45]°C) in the CCS from 1981 to 2016, i.e. 2552 time steps, with the same spatial and temporal resolution as in the CHL data. In this study, we focus on the Southern Californian Bight (SCB) (upper-left corner: (34.4245°N, −120.9898°E); lower-right corner: (32.2662°N, −117.0880°E)) schematically drawn in Figure 9.5A.

9.3.2 Preprocessing

The first step of the preprocessing is the transformation of CHL by means of the decadic logarithm in order to normalize the data. Next, the logarithmic CHL as well as the SST data are centralized by subtracting the respective grid point-wise temporal median. This

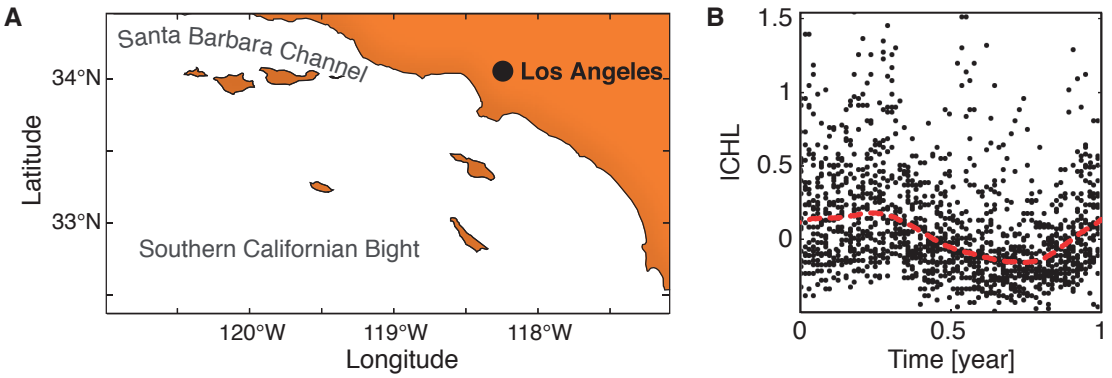

Figure 9.5: (A) Schematic draw of the considered geographic region, the Southern California Bight, with the location of Los Angeles (LA) and the Santa Barbara Channel (SBC). The black curves mark coastlines. (B) Exemplary centralized logarithmic chlorophyll concentration (lCHL), for the pixel at the location (33.2734°N, −117.7232°E). The bold line indicates the estimated annual cycle.

is done in order to reduce local differences in the mean level focusing on the dynamics of both variables. For example, the shallow water along the coast line and at submarine plateaus in the canyon structure of the continental shelf has remarkable higher values in the CHL because of an increased reflectance in the used spectral band by means of suspended sediments or land and bottom reflections. Finally, we remove the annual cycle from both data sets. This is performed for each grid point, separately: (i) wrapping the time axis; (ii) non-parametrically estimation of the annual cycle by means of a robust Loess-regression with a bandwidth which is determined by 50% of the data points, the quartile range [134]; and (iii) calculating the residuals of the fit (Fig. 9.5B). The residuals of these nonparametric annual models are called anomalies of CHL (CHLA) and anomalies of SST (SSTA).

9.3.3 Mapogram-based recurrence plot

The data of CHLA and SSTA consist of time series of images, i.e. two dimensional data fields with 61×87 pixels. In order to analyze these given spatio-temporal data by means of the RP framework, we use the mapogram-based recurrence plot (MRP) which is able to provide additional information on the observed system in comparison to a classical RP analysis of spatially averaged data [314]. The MRP is based on the similarity measure $S^{m'}_{t,t'}$ (cf. Eq. (9.12)), quantifying the spatial similarity of two images at time stamps t and t'. As the measure of similarity, we choose the weighted Bhattacharyya distance which is premised on the mapogram (cf. Appendix A). This mapogram is a representation of the image and is determined by two parameters: (i) the binning of the gray-scale values of the image which controls the level of simplification of the spatial pattern; and (ii) the blurring which determines the minimal resolved spatial scale. Hence, the tuning of the spatial scales of interest allows a multiscale investigation of the image [314]. The resulting similarity is used to construct the recurrence matrix $R_{t,t'}$ by means of

$$R_{t,t'} = \Theta(S_{t,t'} - \varepsilon), \tag{9.7}$$

Θ denotes the Heaviside function, ε is the threshold of similarity. Settings of our analysis are: (i) ε is determined by a fixed recurrence rate of 5%; (ii) there are 4 bins where the thresholds between the bins are given by the lower quartile, the median, and

the upper quartile of the data; and (iii) the blurring coefficients of the mapogram were $\{0, 2, 5, 10, 15, 20, 25, 30, 35,$
$40\}$ pixels, which relate to the minimal resolved spatial scales of about $\{1, 4, 10, 20, 30, 40, 50,$ $60, 70, 80\}$ pixels, respectively. All in all, we have 10 recurrence plots for each data set. The underlying similarity matrix will be analysed as the distance matrix by means of the proposed approach (Sect. 9.2.3) since the distance is used to encode the similarity of two states, too, by their closeness in the state space. The only difference in this application is the use of the local maxima instead of the local minima.

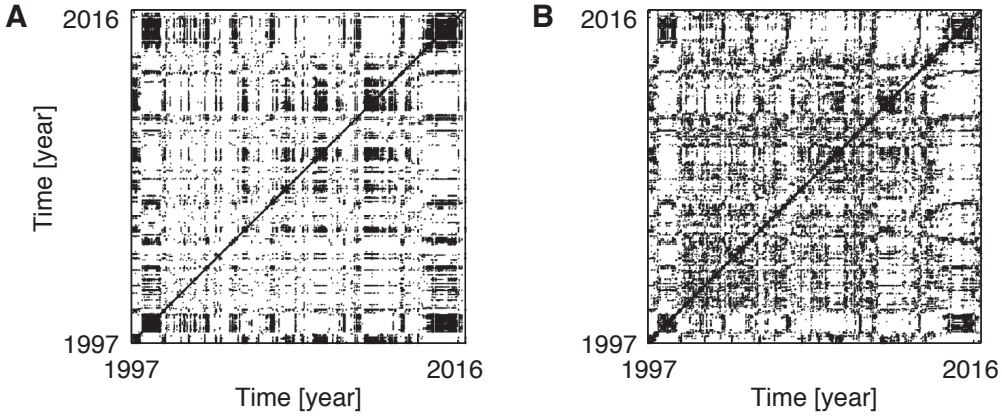

Figure 9.6: Two mapogram based recurrence plots of the anomaly data of chlorophyl concentration. They correspond to the smallest resolved spatial scales of 1 pixel (A) and 20 pixels (B).

9.3.4 Results

The recurrence structures within the MRPs of different scales differ significantly (Fig. 9.6), where the largest differences are between scale 1 (4 km) and 20 (80 km). (Figs. 9.6A and 9.6B, respectively). A further increase of the spatial scale does not lead to qualitative changes. We further focus on the latter MRP and its underlying similarity matrix taking into account spatial pattern with scales greater than 80 km.

Based on the probability of recurrence after τ time steps p_τ, Eq. (9.5), derived from the MRP in Figure 9.6B, we select a kernel's bandwidth of 18 time steps for temporal smoothing (derived from the minimum at $\tau = 36$, Fig. 9.7A). This band width corresponds to the smallest resolved temporal scale of 90 days or a quarter of a year. The underlying similarity matrix of the MRP (Fig. 9.6B) is transformed to the meta-RP by means of the introduced Epanechnikov-Kernel, Eq. (9.4). After that, the column wise local maxima are selected which are given by values greater than their upper and lower neighbors. The positions of these local maxima are shown in Figure 9.7B.

The procedure is then repeated for SSTA. For comparison, we look at the MRP with the same blurring of 20 pixel (80 km) as in the case of CHLA. Here, the bandwidth of the kernel for temporal smoothing is 15 time steps corresponding to 75 days (Fig. 9.8A). The positions of the column-wise local maxima of the smoothed similarity matrix are shown in Figure 9.8B.

In both In the case of CHLA (Fig. 9.9A), we find two global maxima in 1998 and from 2014 to 2016. In between, the baseline swings down until 2008 or 2009 and rises after. This baseline is overlaid by several peaks. In the case of SSTA (Fig. 9.9B), the baseline is rather a rectangular curve with higher values in the temporal range of the global maxima of CHLA

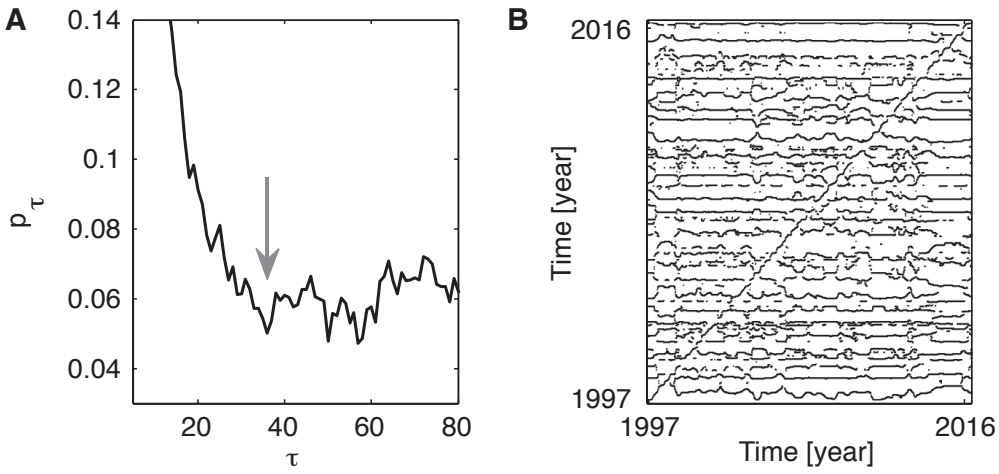

Figure 9.7: (A) Probability of recurrence after τ time steps p_τ, Eq. (9.5), based on the MRP in Figure 9.6B. The arrow marks the local minimum of p_τ at 36 which is used to determine the kernel's bandwidth of 18 time steps. (B) Positions of the column-wise local maxima of the smoothed similarity matrix which is the basis of the MRP in Figure 9.6B.

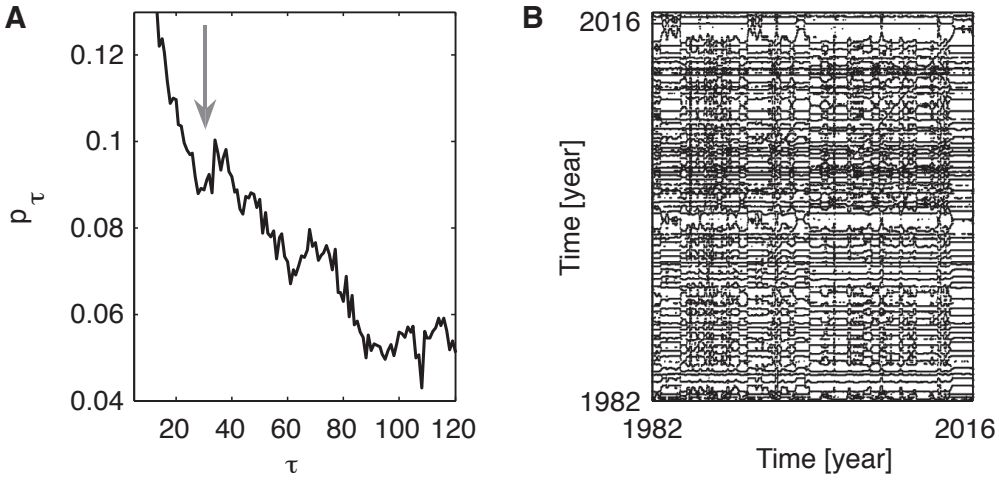

Figure 9.8: (A) Probability of recurrence after τ time steps p_τ, Eq. (9.5), based on the MRP of the sea surface temperature anomaly data (for spatial scales greater than 20 pixels). The arrow marks the local minimum of p_τ at 29 which is used to determine the kernel's bandwidth of 15 for smoothing the similarity matrix. (B) Positions of the column-wise local maxima of the smoothed similarity matrix of the sea surface temperature anomaly data SSTA.

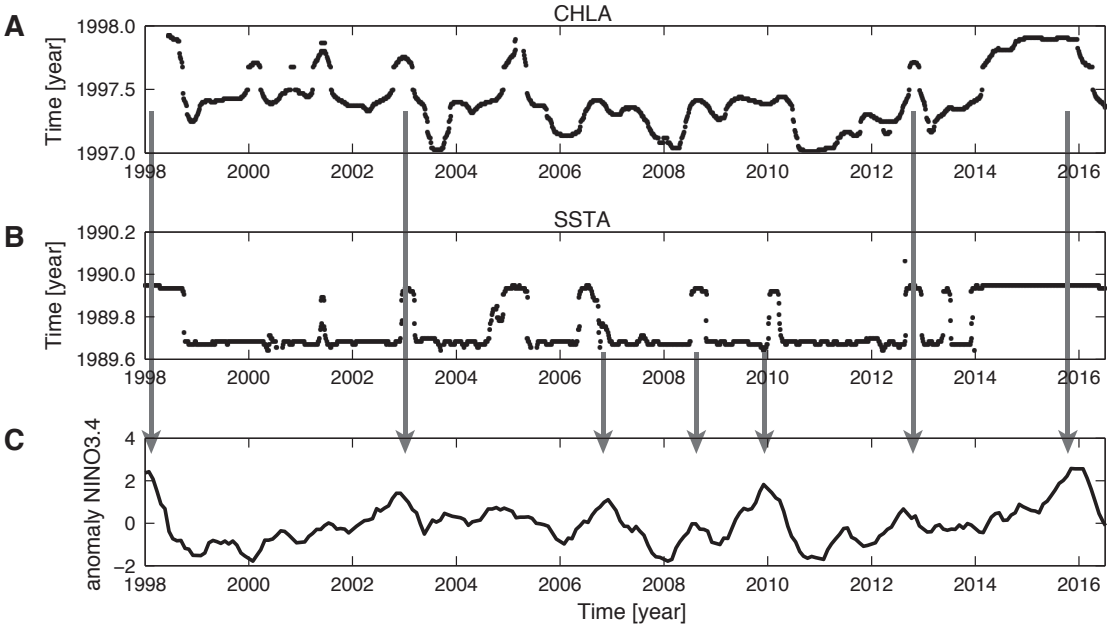

Figure 9.9: (A) Selected band from Figure 9.7B visualizes the effect of a driving force of CHLA. (B) Selected band from Figure 9.8B visualizes the effect of a driving force of SSTA. (C) The temporal evolution of the anomaly of NINO3.4, an index of the El Niño-Southern-Oscillation. The black arrows mark simultaneous local maxima in the different time series.

(Fig. 9.9A). There are also peaks in between these higher areas with values comparable to the elevated level. Almost all of these peaks coincide with peaks in CHLA (Fig. 9.9A). Next we compare these variations with the temporal evolution of the anomaly of the NINO3.4 index, representing the ENSO activity [396]. The enhanced ENSO activity in 2002–2003, 2006, 2008, 2009–2010, and 2012–2013 coincides with the identified maxima in CHLA and SSTA. Further, the two global maxima are in the range of the global maxima of CHLA (Fig. 9.9A) or the high levels of SSTA (Fig. 9.9B). Finally, the baseline in between these two global maxima behaves similar to those identified for CHLA (Fig. 9.9A) except for the period 1999 to 2002.

Finally we consider the whole sampled period of SSTA in order to further investigate the rectangular shape (Fig. 9.10). In the extended temporal range, the rectangular character of the curve continues indicating two regimes of the hydrological system: (i) an El Niño like regime occurring from 1997 to 1999, from 1983 to 1985, from 1992 to 1995, and from 2014 to 2016; (ii) an La Niña like regime occurring from 1985 to 1990, from 1995 to 1997, and from 1999 to 2014.

9.4 Discussion

In this work, we use the RP approach in an advanced way in order to get a new qualitative view on the trajectory of a spatially extended system which is described by spatio-temporal data. This new view is given by projections of the trajectories revealing systemic changes which result from driving forces. It results from the novel extension of the thresholded metan RP reconstructing the driving forces. We improve this reconstruction by using kernel estimations instead of histograms and focusing on the underlying distance matrix instead of the RP. So, we are able not only to show the influence of El Niño events on the phytoplankton's

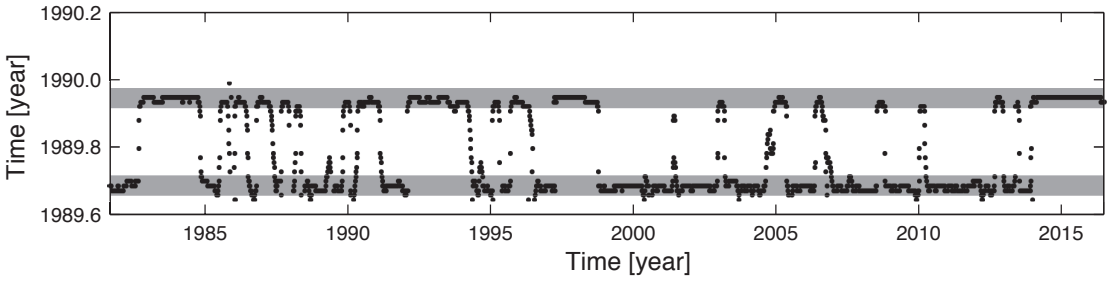

Figure 9.10: A selected band from Figure 9.9B over the whole sampled period. The gray horizontal bars mark the two different levels of the time series.

growth in the Southern Californian Bight but also the documented regime shift in 1998 and the discussed regime shift from 2014 to 2015 by means of the abrupt change between two levels of the constructed curves (Figs. 9.9 and 9.10).

In particular, the analysis of CHLA and SSTA reveals new hints about long-term effects on the phytoplankton's growth in the Southern California Bight. So, the coexisting peaks in the projections of CHLA and SSTA and in the ENSO index (Fig. 9.9) suggest that the El Niño events, documented for 2002–2003, 2009–2010 and 2014–2016, effect this growth [404]. The sea surface temperature seems to be a transmitting link. This is indicated by the peak in 2005 where no El Niño event was observed but an unusual ocean weather event in the northern California Current leads to responses of the ecosystem similar to that ones of major El Niño events [291]. Beside the extremes, the curves in Figures 9.9A and 9.9C show similar long-term behavior, except the period from 1999 to 2002, which has not been shown before. The difference in the period from 1999 to 2002 underlines previous results that strong La Niña, observed from 1998 to 2000 and shown by local minima in Figure 9.9C, do hardly effect the chlorophyll concentration (Fig. 9.9A). Only the local minimum in 2003 which breaks through the baseline indicates a La Niña like event (Fig. 9.9A). But this event results from a large anomalous intrusion of subarctic water into the CCS [405]. A new result is the indication of sharp transitions in the SSTA (Figs. 9.9A and 9.10). That is, the system seems to switch between two levels where the higher one corresponds to El Niño like conditions which is indicated by single peaks coinciding with the events (cf. Figs. 9.9B and 9.9C). We assume that the lower level represents La Niña like conditions. Three of the four largest periods of the upper level (cf. Fig. 9.10) coincide well with the strongest El Niño events, 1982–1983, 1997–1998 and 2014–2016, during the recorded time [196]. But the most impressive part is the very large period of the lower level from 1999 to 2014 which highlights the changes in 1998 and 2014. The step from the higher level to the lower one in 1998 (cf. Fig. 9.10) corresponds to a regime shift in the north Pacific ocean [283]. So we assume that the step in 2014 is a regime shifts, too.

The new findings for this example demonstrate the potential of the proposed method. The vital condition of this approach is the existence of at least two parts of the state space where the trajectory stays longer than the period of the main cycle. This condition is given for the shown example of spatio-temporal as well as a large number of other complex systems, e.g. the shown Lorenz-system. Therefore, the proposed method promises new insights into other complex systems, too.

Acknowledgments

This work was supported by the Volkswagen Foundation (Grant No. 88462), the DFG RTG 2043/1 “Natural Hazards and Risks in a Changing World”.

Appendix A: Mapogram-based similarity

The mapogram [279] is a representation of the pattern in a gray-scale image and is used to quantify the similarity of two images. Formally, an image is a two dimensional data field $F = \{f_{ij}\}_{i=1,\dots,N_i;j=1,\dots,N_j}$ where i and j are the indexes of the pixels and f_{ij} the assigned gray-scale values. $N = N_i N_j$ is the total number of pixels. The first step constructing the mapogram is a simplification of the gray-scale by means of a histogram

$$n_b = \sum_{i=1}^{N_i} \sum_{j=1}^{N_j} g_b(f_{ij}), \tag{9.8}$$

where the binary matrices g_b resulted from

$$g_b(f_{ij}) = \begin{cases} 1 & f_{ij} \in b\text{-th bin} \\ 0 & \text{otherwise,} \end{cases} \tag{9.9}$$

$b = 1, \dots, B$ is the index of the histogram's bins, B disjoint right side closed intervals which cover a contiguous part of the gray-scale. So n_b is the number of elements with values in the b-th bin. The $N_i \times N_j$ binary matrices are normalized

$$m_{b,i,j} = \frac{g_b(f_{ij})}{n_b}, \tag{9.10}$$

and convoluted with a kernel function K_γ, the blurring, which leads to the mapogram. This spatial smoothing is done for each $m_{b,i,j}$ and is controlled by the positive definite non-zero parameter γ, the band width of the kernel given in units of sample points:

$$m_{b,\gamma,i,j} = \sum_{i'=1}^{N_i} \sum_{j'=1}^{N_j} m_{b,i',j'} K_\gamma \left(\frac{\|(i',j') - (i,j)\|}{\gamma} \right), \tag{9.11}$$

K_γ is the Epanechnikov kernel, Eq. (9.4), with its bandwidth parameter γ. So, the set of $m_{b,\gamma,\cdot,\cdot}$ build the mapogram representing the pattern in one gray-scale image. The similarity between the two fields is calculated by a weighting of the Bhattacharyya coefficient, here

$$S^m_{f,f'}(\gamma, B) = \frac{\sum_{b=1}^{B} \sqrt{(n_b n'_b)}}{\sqrt{\left(\sum_b n_b\right)\left(\sum_b n'_b\right)}} \frac{\sum_{i=1}^{N_i} \sum_{j=1}^{N_j} \sqrt{m_{b,\gamma,i,j} m'_{b,\gamma,i,j}}}{\sqrt{\sum_{ij} m_{b,\gamma,i,j} \sum_{ij} m'_{b,\gamma,i,j}}} \tag{9.12}$$

where the second factor is the weight. The range of the similarity measure is from 0 to 1, respectively fully dissimilar and equal images. For $\gamma \to 0$, the $m_{b,\gamma,i,j}$ (Eq. (9.11)) tends to $m_{b,i,j}$ (Eq. (9.10)). In the limes $\gamma = 0$, the similarity measure is set to

$$S^m_{f,f'}(0, B) = \frac{\sum_{b=1}^{B} \sqrt{(n_b n'_b)}}{\sqrt{\left(\sum_b n_b\right)\left(\sum_b n'_b\right)}} \sum_{i=1}^{N_i} \sum_{j=1}^{N_j} \sqrt{m_{b,i,j} m'_{b,i,j}}, \tag{9.13}$$

which corresponds to the known κ-statistics [261].

Appendix B: Theoretical models

First, the Lorenz-system is defined by the system of differential equations:

$$\begin{aligned} \dot{x} &= s(y-x), \\ \dot{y} &= rx-y-xz, \\ \dot{z} &= -bz+xy. \end{aligned} \tag{9.14}$$

The used model parameters are $s = 10$, $r = 28$, and $b = 8/3$ related to a chaotic regime. It is integrated in the temporal range of [0, 100] with the initial condition $(x, y, z) = (1, 1, 1)$.

Second, the R/"ossler-system is given by:

$$\begin{aligned} \dot{x} &= -y-z, \\ \dot{y} &= x+ay, \\ \dot{z} &= b+z(x-c). \end{aligned} \tag{9.15}$$

The values of the parameters are: $a = 0.432$, $b = 2$, and $c = 4$. The initial condition is $(x, y, z) = (0.1, 0.1, 0.1)$ and the time span is [0, 1000].

Finally, the van der Pol-oscillator is defined by:

$$\begin{aligned} \dot{x} &= a(x-x^3)/3-y), \\ \dot{y} &= x/a. \end{aligned} \tag{9.16}$$

The model parameter is set to $a = 5$, the initial condition is $(x, y) = (0.5, 0)$, and the time span is [0, 1000].

For numerical integration of all three dynamical systems, we use the Matlab-function ode45 (DormandPrince method). In order to exclude transient behavior, we only consider values above the 2000th time step.

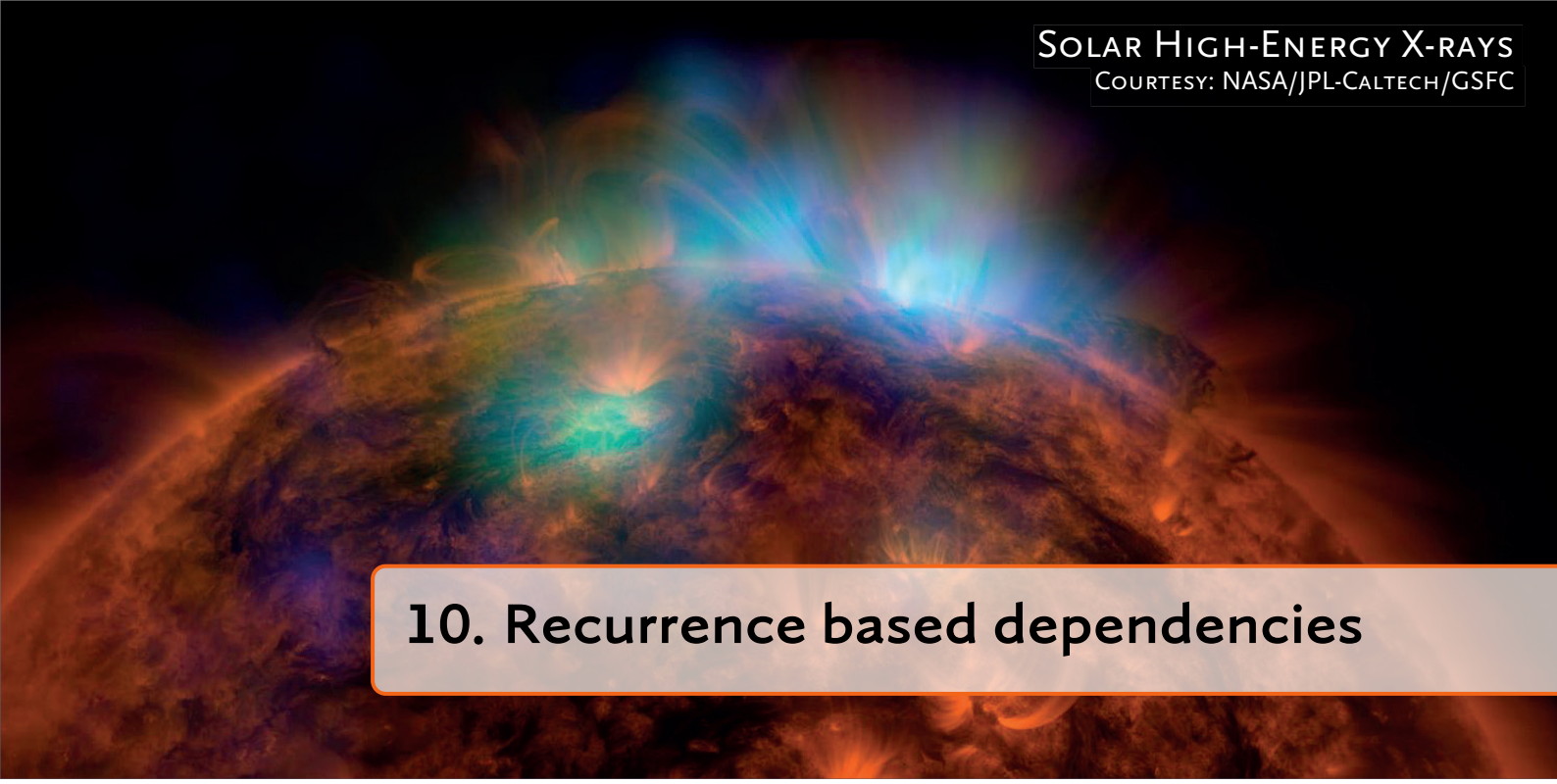

10. Recurrence based dependencies

Paper 9 B. Goswami, N. Marwan, G. Feulner, J. Kurths: How do global temperature drivers influence each other? – A network perspective using recurrences, European Physical Journal – Special Topics, 222, 861–873 (2013). DOI:10.1140/epjst/e2013-01889-8

R The paper, presented in this chapter is a student's paper. My contribution was the selection and fine-tuning of the method as well as the design of the study.

Abstract

We investigate a network of influences connected to global mean temperature. Considering various climatic factors known to influence global mean temperature, we evaluate not only the impacts of these factors on temperature but also the directed dependencies among the factors themselves. Based on an existing recurrence-based connectivity measure, we propose a new and more general measure that quantifies the level of dependence between two time series based on joint recurrences at a chosen time delay. The measures estimated in the analysis are tested for statistical significance using twin surrogates. We find, in accordance with earlier studies, the major drivers for global mean temperature to be greenhouse gases, ENSO, volcanic activity, and solar irradiance. We further uncover a feedback between temperature and ENSO. Our results demonstrate the need to involve multiple, delayed interactions within the drivers of temperature in order to develop a more thorough picture of global temperature variations.

10.1 Introduction

Global mean temperature is one of the primary quantities used to characterize Earth's climate and modern climate change. It has been, and still is, a central variable of interest in the research focussed on understanding global climate variability. In their fourth Assessment Report, the IPCC clarified to a large extent the role of anthropogenic forcings in the warming trend of the Global Mean Temperature (GMT) of the last century [136]. Although warming by

anthropogenic greenhouse gases dominates the observed rise in temperature, uncertainties continue to persist in answers to questions such as: *how much* of the temperature change is induced *by which factors*, and *how* do they change the temperature. These questions interweave two crucial strands of GMT studies: (i) efforts to understand GMT variations of the past, and (ii) efforts to foresee how the climate (and not just the temperature) is going to change in the next decades. For the twentieth century, an increasing number of observational records of temperature have enabled us to move towards more comprehensive estimates of global temperature (c.f. Section 3.2 of [395], and [133]). Despite having been able to narrow down the main suspects behind variations in global temperatures to anthropogenic influences, the El Niño Southern Oscillation (ENSO), volcanic activity, solar radiation, and internal climate variability, there still exists significant debate over the nature of the temperature response to climate change as shown by the diverse explanations put forth to explain the apparent recent 'deceleration' of global warming [18]. In this context, studies such as that of Lean & Rind [192, 193], and Foster & Rahmstorf [108] shed light on how the different factors affect global mean temperatures. Based on empirical multivariate regression models, Lean & Rind estimate the response of GMT to human activity, ENSO, volcanoes and changes in solar activity, and thereafter apply it to forecast (by various conditions) the global temperature for the next decade. The latter study of Foster & Rahmstorf presents a robust analysis to estimate the residual anthropogenic impact on the warming trend of the last three decades after removing the natural forcings to global temperature.

These studies, however, presuppose two things: (i) independence *between* the factors that impact temperature, and (ii) a linear superposition of their effects on temperature variations. Although it might be the case that both assumptions are valid to a fair (and practical) degree of approximation, it is critical to assess their validity scientifically.

The primary focus of this study is to address the first of the above assumptions and examine the manner in which, and if at all, the factors influencing global temperature interact among themselves. We use an empirical approach based on the recurrences of dynamical systems for this purpose. Recent developments in the theory of recurrences, and recurrence plots in particular, have made it an increasingly popular tool for scientific investigations (c.f. [224] for a historical overview). Recurrence-based analysis has found application in a wide range of scenarios ranging from analyses of cardiac data [441] to stock markets [15] to cover song identification [348] to speech comprehension [312]. In the context of climate analyses, cross recurrence plots (CRPs) have been used to study links between ENSO and north-western Argentinian precipitation both in modern and 'paleo' time scales [238]; and more recently, joint recurrence plots (JRPs) have been used to investigate the spatial distribution of links between vegetation and climatic variables such as temperature and precipitation [199].

We extend the idea behind the measure for lag/generalized synchronization put forth in [323]. The measure is based on JRPs and is suitable thus for the analysis of structurally different systems as in our case. We allow for delayed interactions up to delays of around 12 years among all considered datasets and test all estimated values for statistical significance — choosing only the statistically significant values for interpretations. The results presented here are an attempt to visualize a network of influences that are relevant to understanding GMT. They are intended to corroborate some of the existing ideas of links between climatic variables and GMT, as well as uncover new interactions among several of the impacting variables themselves.

The paper is organised as follows: In Sect. 10.2 we present the datasets used in this study. Section10.3 reviews the theory underlying the recurrence-based connectivity measure, and Sect. 10.4 outlines the manner of significance tests used in the analysis. In Sect. 10.5, we

detail the various steps involved in the analysis. Section 10.6 presents the results and their interpretation, and Sect. 10.7 provides a brief summary and outlook. Finally, the appendix provides the various sources of the datasets.

10.2 Data

Following Lean & Rind [192], we consider four critical contenders that have the potential to influence global mean temperature: (i) the ENSO, (ii) volcanic activity, (iii) solar irradiance, and (iv) the concentration of well-mixed greenhouse gases in the atmosphere. To characterise these phenomena, we choose: a combination of the multivariate El Niño index [426] (which extends from 1950 till present) and the index of Meyers et al. [255] (for data prior to 1950) for the ENSO; stratospheric aerosol optical thickness measurements compiled by Sato et al. [336] for volcanic activity; Wang et al.'s [413] reconstruction of total solar irradiance that

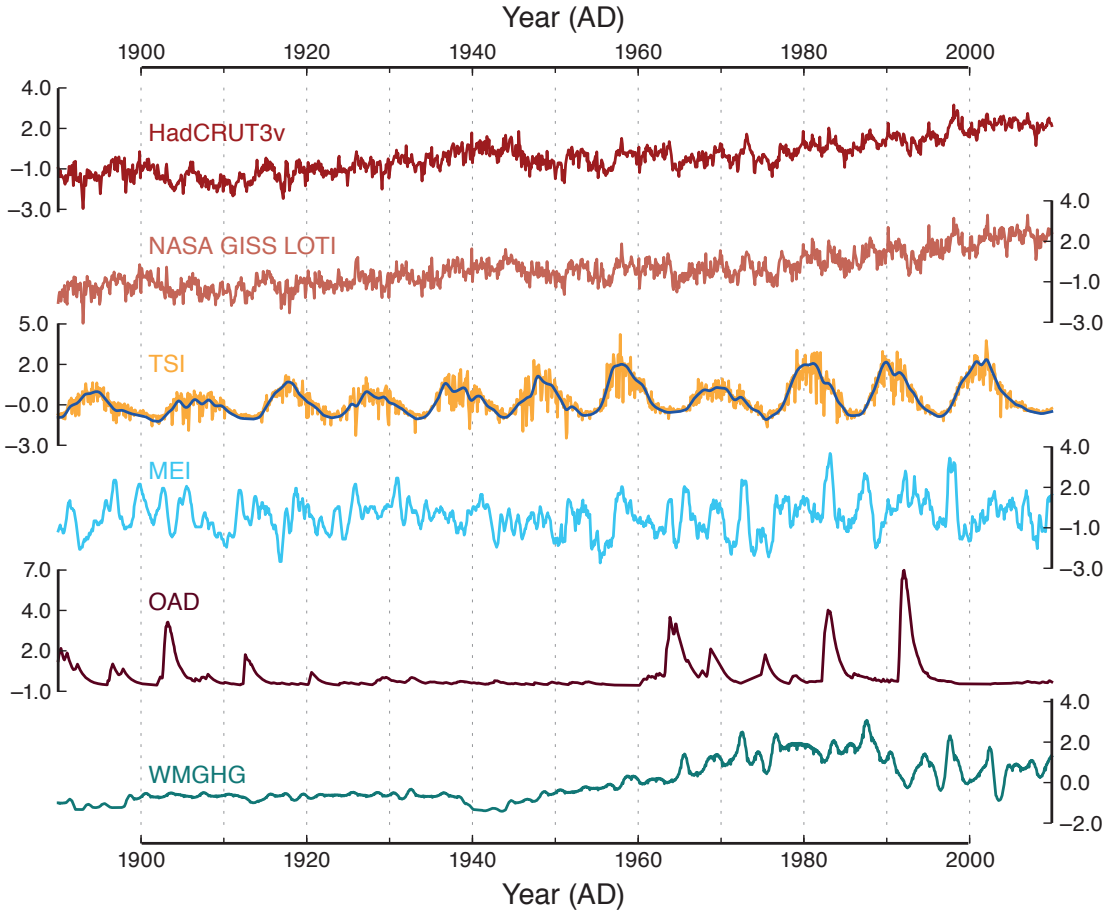

Figure 10.1: **Data used.** From top to bottom: global surface temperature from the CRU at East Anglie (HadCRUT3v, **deep red**); NASA GISS Land-Ocean Temperature Index (NASA GISS LOTI, **light red**); Wang et al.'s reconstruction of total solar irradiance (TSI, **deep yellow**) with the Gaussian-kernel (bandwidth of ≈ 11 years) filtered curve (in **blue**); the Multivariate ENSO Index (MEI, **light blue**); Sato et al's volcanic activity index based on Optical Aerosol Depth (OAD, **brown**); monthly changes in the NASA GISS's modelE global mean forcing values for Well-Mixed GreenHouse Gases (WMGHG, **teal**).

extends to around 300 years back; annual global mean forcing values used for well-mixed greenhouse gases as used in the NASA GISS modelE [132] which were then interpolated to a monthly resolution. For the global temperature itself, we use two datasets: the NASA GISS Land-Ocean Temperature Index (LOTI) [133], and the surface temperature record HadCRUT3v assimilated by the Climate Research Unit (CRU) at East Anglia University [39]. (The source of the datasets are listed in Appendix 10.7). We consider the 120 year period from January 1890 to December 2009 in which all the datasets are resolved on a monthly basis for the purpose of this study. Moreover, for the TSI dataset, we use a low pass filter using a Gaussian kernel of bandwidth $\approx$ 11 year, and we consider the first derivative of WMGHG instead of the almost monotonically increasing raw dataset (figure not shown). Note that, in contrast to Lean & Rind [192], we do not use the full anthropogenic forcing but just the well-mixed greenhouse gases. The final time series used in the analysis (normalized to mean zero and variance one) are shown in Fig. 10.1. For brevity, we henceforth refer to the datasets using the following labels: *CRUTA* for the HadCRUT3v data; *GISS* for NASA GISS LOTI; *TSI* for total solar irradiance; *VOLC* for the optical aerosol depth data; and *WMGHG* for the well-mixed greenhouse gas series.

10.3 Lagged dependencies using recurrences

Recurrence is a fundamental characteristic of dynamical systems that provide insight into their dynamical properties [86]. Defined as the return of the phase space trajectory of the system to an earlier state (up to a tiny deviation), in practice, recurrences are approximated as the return of the system to the *neighbourhood* of a previous state. If we consider a system X such that $\mathscr{X}$ is the set of all possible trajectories of X, a recurrence matrix $\mathbf{R}^X$ for a given trajectory $\vec{x} = \{\vec{x}_1, \vec{x}_2, \ldots, \vec{x}_N\} \in \mathscr{X}$ is defined as:

$$\mathbf{R}^X_{i,j}(\varepsilon) = \Theta(\varepsilon - \| \vec{x}_i - \vec{x}_j \|), \quad i,j = 1,\ldots,N. \tag{10.1}$$

Here, N is the trajectory length, ε the size of the neighbourhood, $\Theta(\cdot)$ the Heaviside function (i.e., $\Theta(\cdot) = 1$ for non-negative values and 0 otherwise) and $\| \cdot \|$ denotes an appropriate metric that quantifies 'distance'. A *recurrence plot* (RP) is a visual representation of $\mathbf{R}$ typically constructed by putting a black marker for every 1 in $\mathbf{R}$ (c.f. [239] for a more detailed treatment of recurrence plots).

If we take any arbitrary trajectory $\vec{x'} \in \mathscr{X}$, the probability $P(\vec{x'} \sim \vec{x}_i)$ that a point $\vec{x}'_i \in \vec{x'}$ visits the neighbourhood of $\vec{x}_i \in \vec{x}$ is equal to the column-sum of the recurrence matrix $\mathbf{R}^X$ (from Eq.10.1),

$$P(\vec{x}_i) = \frac{1}{N} \sum_{j=1}^{N} \mathbf{R}^X_{i,j}. \tag{10.2}$$

where $P(\vec{x}_i)$ denotes $P(\vec{x'} \sim \vec{x}_i)$. The average probability of any trajectory of the system to recur to any given state is the mean $\langle P(\vec{x}_i) \rangle = \sum_{i=1}^{N} P(\vec{x}_i)/N$, and is known as the (global) *recurrence rate* (RR^X) of X.

In this study, we compare the recurrence structures of characteristically different systems in order to infer the influences that they might have on each other. A comparison of recurrence structures of two different systems can be performed using joint recurrences, and the corresponding joint recurrence matrix, defined as:

$$\mathbf{JR}^{XY}_{i,j}(\varepsilon_x, \varepsilon_y) = \Theta(\varepsilon_x - \| \vec{x}_i - \vec{x}_j \|) \Theta(\varepsilon_y - \| \vec{y}_i - \vec{y}_j \|) \quad i,j = 1,\ldots,N, \tag{10.3}$$

where $\vec{x}$ and $\vec{y}$ are two given trajectories of systems X and Y respectively. A non-zero value $\mathbf{JR}^{XY}_{i,j}$ thus captures co-occurring recurrences of trajectories $\vec{x} \in \mathscr{X}$ and $\vec{y} \in \mathscr{Y}$ in corresponding neighbourhoods of systems X and Y respectively, i.e., $\vec{x}_i \sim \vec{x}_j$ and $\vec{y}_i \sim \vec{y}_j$ at the same time instant i (or j). Using $\mathbf{JR}^{XY}$, we now consider the joint probability that two arbitrary trajectories $\vec{x}' \in \mathscr{X}$ and $\vec{y}' \in \mathscr{Y}$ recur in the neighbourhood of $\vec{x}_i$ and $\vec{y}_i$ simultaneously,

$$P(\vec{x}_i, \vec{y}_i) = \frac{1}{N} \sum_{j=1}^{N} \mathbf{JR}^{XY}_{i,j}, \tag{10.4}$$

where $P(\vec{x}_i, \vec{y}_i)$ denotes (as previously) the probability $P(\vec{x'} \sim \vec{x}_i, \vec{y'} \sim \vec{y}_i)$.

Previously, joint recurrences have been used to detect generalized synchronization (GS) as well as lag synchronization (LS) [323]. In their approach, the authors use the results that, (i) a topological reconstruction of the phase space trajectory is possible from a given recurrence matrix, and (ii) two systems governed by a functional relationship will have similar recurrence matrices. Furthermore, if two systems X and Y are in GS, their respective global recurrence rates $\langle P(\vec{x}_i)\rangle$ and $\langle P(\vec{y}_i)\rangle$ are approximately equal to the joint recurrence rate $\langle P(\vec{x}_i, \vec{y}_i)\rangle$. They suggest to use a *fixed number of nearest neighbours* as a threshold for the computation for the recurrence matrices such that $P(\vec{x}_i) = n_0/N \; \forall \; i$ where n_0 is the predefined number of nearest neighbours (the same number is used for system Y as well). In this case, the recurrence rates of X and Y are thus set to be equal, i.e., $\langle P(\vec{x}_i)\rangle = \langle P(\vec{y}_i)\rangle = n_0/N$. The measure for synchronization is then given by,

$$JPR = \max_{\tau} \frac{S(\tau) - R_0}{1 - R_0}, \tag{10.5}$$

where $R_0 = n_0/N$ and

$$S(\tau) = \frac{\langle P(\vec{x}_i, \vec{y}_i)\rangle}{R_0}. \tag{10.6}$$

In this study, we extend this idea to allow for the more general case where the two systems X and Y may have differing overall recurrent rates as well as the case where $P(\vec{x}_i) \neq P(\vec{y}_i)$. In particular, in order to estimate how 'non-independent' X and Y are from each other, we are interested in the quantity,

$$RMD_i = \frac{P(\vec{x}_i, \vec{y}_i)}{P(\vec{x}_i)P(\vec{y}_i)}. \tag{10.7}$$

Here, RMD denotes *Recurrence-based Measure of Dependence*. (We note that such a probabilistic ratio is already a quantity of interest in medical analysis and is termed as the "*Odds-to-Expected ratio*", or the O/E ratio in short [257].) However, we wish to quantify the direction of dependency between X and Y as well. RMD_i, as defined above, is symmetric for X and Y and cannot detect the direction of influence. Other recurrence-based methods, such as that of the *Mean Conditional Probability of Recurrence* (MCR) [242, 324, 456], help to infer the direction of coupling between a pair of datasets but it is non-trivial to extend the notion of MCR for delayed couplings. We argue that, similar to $S(\tau)$ (Eq. 10.6), it is natural to incorporate lagged probabilities in RMD_i simply by introducing a relevant lag in one of the systems. We thus define the log-mean $RMD(\tau) \in \mathbb{R}$ at lag τ as:

$$RMD(\tau) = \log_2\left(\frac{1}{N'} \sum_{i=1}^{N'} RMD_i(\tau)\right), \tag{10.8}$$

where $N' = N - \tau$, and $RMD_i(\tau) = P(\vec{x}_i, \vec{y}_i(\tau))/(P(\vec{x}_i)P(\vec{y}_i(\tau)))$, if we consider Y to be shifted by τ units. For two independent systems X and $Y(\tau)$, $P(\vec{x}_i, \vec{y}_i(\tau)) = P(\vec{x}_i)P(\vec{y}_i(\tau))$, which implies that $RMD(\tau) = 0$. For $\tau > 0$, non-zero RMD implies that Y is dependent on X and the converse is true for $\tau < 0$. Note that RMD can quantify both uni- and bi-directional dependencies as well as multiple lags at which the systems might influence each other.

10.4 Testing for significance of observed values

In analyses of connectivity between pairs of experimental datasets, the measures used to quantify dynamical similarity often yield values that are intermediate, and we then cannot easily conclude whether the pair of time series are strongly or weakly connected. Even if we choose to define our measure so that it always lies within a finite interval – such as between 0 and 1 – experimental datasets can typically give ambiguous results of intermediate connectivity values such as 0.6. The connectivity measures obtained from such *passive experiments* cannot thus provide an unambiguous interpretation due to the lack of a comparative 'test case'. This is in contrast to *active experiments* (made, e.g., from laboratory experiments or numerical simulations of models) where the obtained values can be used for a consistent interpretation by its comparison to the uncoupled case. In passive experiments, the observed values of connectivity have to be statistically tested to ensure that they could not have been obtained by random chance. The statistical test is carried out using surrogate data sets generated from the observed time series in conjunction with an appropriate null hypothesis.

Surrogate time series are different from the original, observed ones, and yet preserve essential dynamical properties. There are several ways of generating surrogates and each method has its respective null hypothesis. The test statistic (which is RMD in our case) is calculated for a sufficiently high number of surrogate pairs and the observed value is tested for statistical significance using the obtained distribution and the appropriate null hypothesis.

For our analysis, we use a recurrence-based approach to generate *twin surrogates* (TS) from the observed time series [385, 386]. *Twins* are two points $\vec{x}_i$ and $\vec{x}_j$ of X such that they share the same neighbourhood upto the limit ε, i.e., for $k = 1, 2, \ldots, N$, $\mathbf{R}^X_{k,i} = \mathbf{R}^X_{k,j}$. The TS method requires that we first identify all possible twins given an observed trajectory $\vec{x}$. To generate the surrogate series $\vec{s}$, we then choose an arbitrary random point $\vec{x}_k \in \vec{x}$ and set it as $\vec{s}_1$. Now, given $\vec{s}_i = \vec{x}_l$, we append subsequent points to $\vec{s}$ iteratively according to the following rule: when $\vec{x}_l$ has no twins, $\vec{s}_{i+1} = \vec{x}_{l+1}$; on the other hand when $\vec{x}_l \in T$ such that $T = \{\vec{x}_l\} \cup \{\vec{x}_m : \vec{x}_m \text{ and } \vec{x}_l \text{ are twins}\}$ and the number of elements in T is n, then $\vec{s}_{i+1} = \vec{x}_{k+1}$ where $\vec{x}_k \in T$ with probability $1/n$.

The null hypothesis for TS is that each surrogate trajectory is an independent realization of the system corresponding to a different initial condition. To test whether the observed value of $RMD(\tau)$, between X and $Y(\tau)$, is a statistically significant measure of X driving Y we do the following: (i) generate TS of Y, (ii) obtain a test distribution of $RMD(\tau)$ using the observed time series of X and the surrogates of Y, (iii) construct a 95% confidence band from the area between the 2.5^{th} and 97.5^{th} percentiles. This interval represents the region where we fail to reject the null hypothesis.

Observed values of RMD outside the confidence band imply a statistically significant dependence between X and Y at delay τ.

10.5 Method

The analysis is divided into two parallel components corresponding to the CRUTA and GISS temperature datasets. For each of these we consider delays of up to 150 months

and estimate RMD, and test the observed values for significance. Similarly, we analyze all possible combinations for the forcing datasets as well as between the forcings and the temperature datasets. All results are grouped according to the 'driven' dataset.

We do not embed the time series while constructing the recurrence matrices. Several recurrence properties are invariant under embedding and it is not essential to embed the time series. In particular, time delay embedding was not feasible for all of the datasets considered in this study and was hence avoided. The recurrence threshold was based on fixed amount of nearest neighbours, which was kept at 5% for all datasets. The qualitative nature of our results are robust to the choice of this threshold value because small changes in the threshold do not alter the qualitative features of the recurrence plot (result not shown).

The significance tests were carried out using 500 TS of the 'driven' dataset. Significant values were then considered to construct an approximate network visualization of the dependencies involving the temperature dataset as well as the various radiative forcings.

10.6 Results and discussion

The results of the analysis for the temperature datasets are shown in Fig. 10.2, from which several points are initially evident.

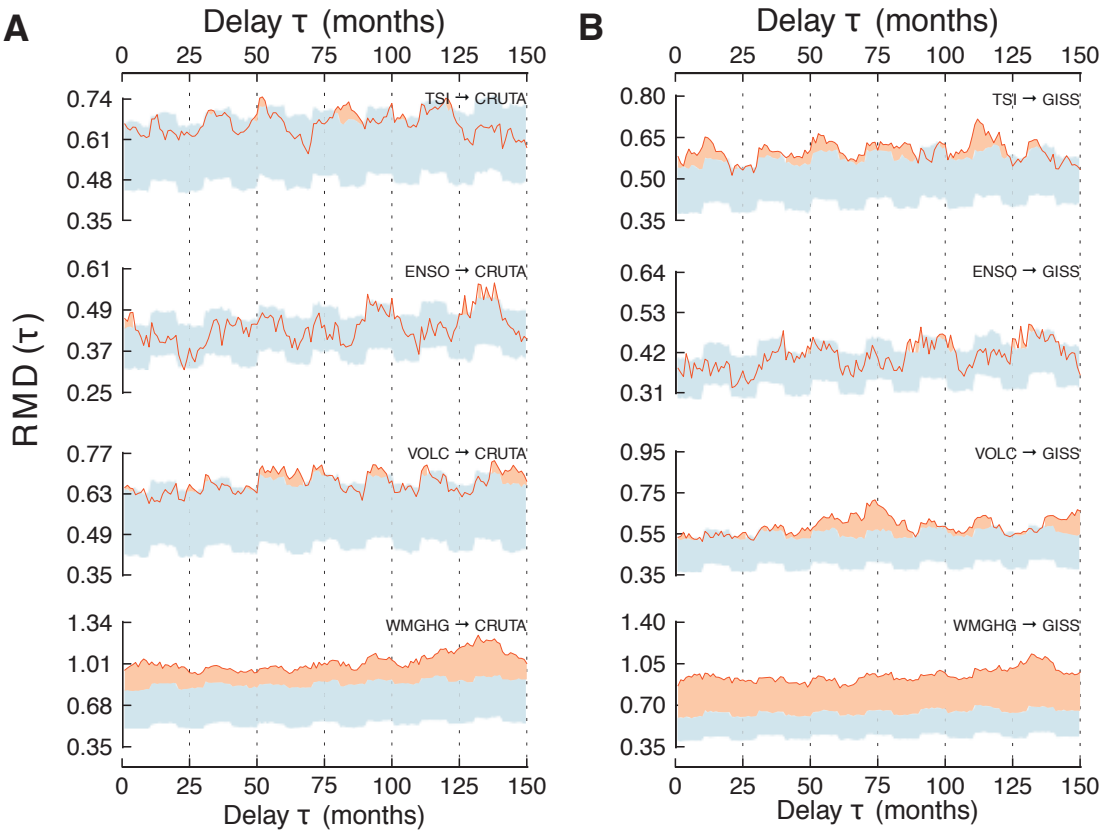

Figure 10.2: **Lagged influences on GMT. A.** The results for the HadCRUT3v dataset. **B.** The results for the NASA GISS LOTI dataset. The 95% confidence band obtained from the significance test using TS is in light blue. The observed values of $RMD(\tau)$ is in **dark orange**. Regions where the value of $RMD(\tau)$ falls outside the confidence band are shaded in apricot. The datasets are labelled as mentioned in Sec. 10.2.

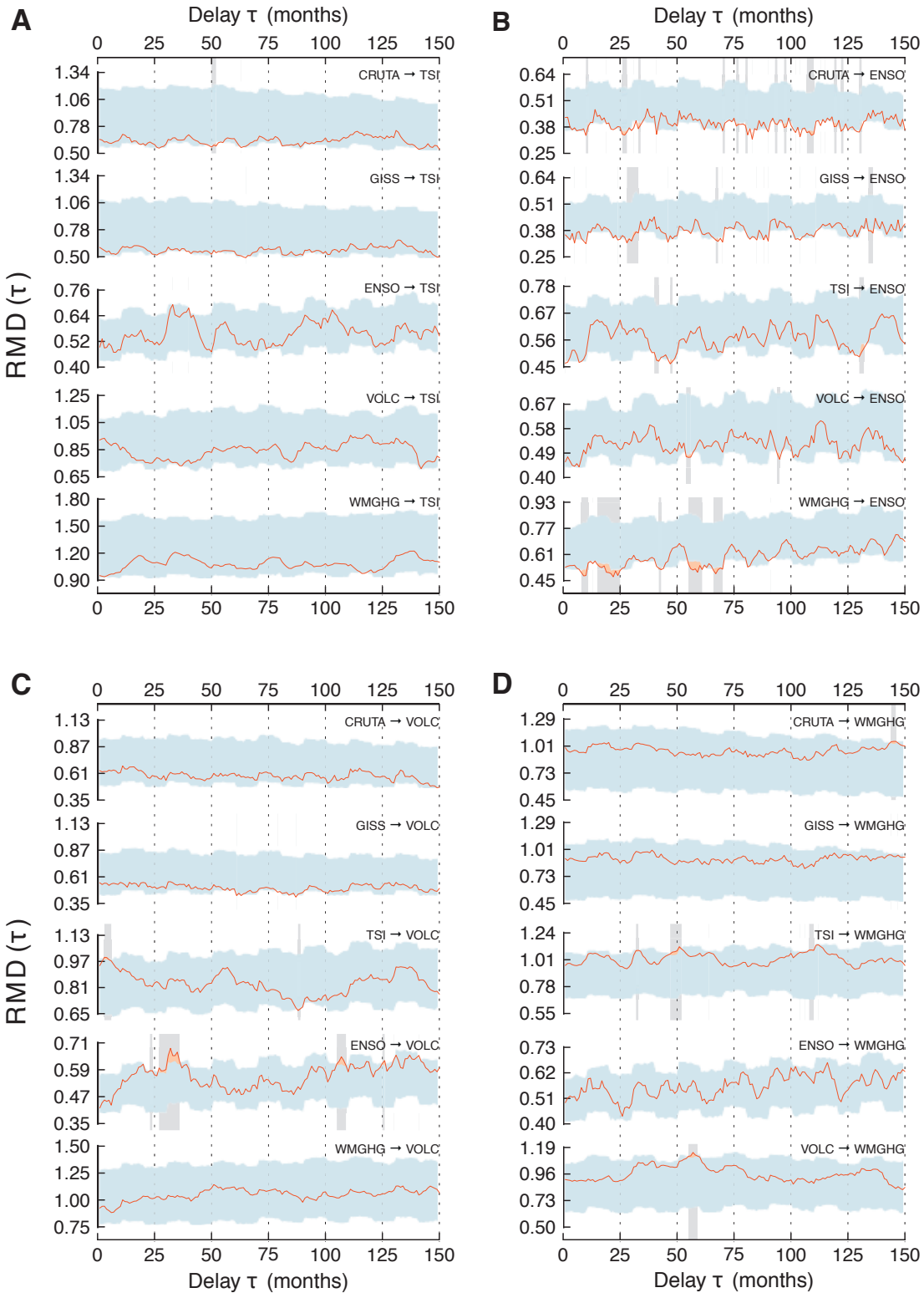

Figure 10.3: **Lagged dependencies among the forcing datasets. A.** Results for the other datasets driving TSI. **B.** Results for the other datasets driving ENSO. **C.** Results for the VOLC dataset being driven by the others. **D.** Results for the WMGHG dataset being driven by the rest. Legends and keys to the figure are same as in Fig. 10.2. The grey bars highlight the values of τ for which the observed values of RMD are statistically significant.

- TSI appears to impact the GISS dataset more than it does the CRUTA data. In fact, even on short time scales of around a few months, the impact of TSI on CRUTA is barely significant. In previous studies by Lean & Rind [192, 193] (done with the CRU data), TSI is found to influence variations in GMT on the scale of a month from their analysis based on multivariate regression.
- ENSO clearly has a sharp impact on the CRUTA series at a short delay of around 5 months (similar to Lean & Rind.). However, we also find further significant influences at delays of (approximately) 130 months for the CRU data, and at 90 months and 130 months for the GISS LOTI data. ENSO, however, does not have any impact on GISS temperatures at shorter time scales.
- Even though volcanic aerosols impact both temperature series on short time scales of around 1-10 months (Lean & Rind find 6 months), here too, there are further delayed interactions significant in the 50-75 month period and even as late as 140-150 months. This is discussed in more detail later.
- The influence of greenhouse gases on GMT is statistically significant for all values of delay considered and this influence peaks at around a delay of 130 months (approximately 11 years). This value is close to the previously considered value of 120 months in the Lean & Rind study.

The results of our analysis for the rest of the data are given in Fig. 10.3, grouped according to the 'driven' dataset. The following points are discernible from Fig. 10.3.

- None of the datasets show a significant result when being tested against the hypothesis that they drive TSI (Fig. 10.3A). This demonstrates that, provided the datasets are accurate, our approach is able to rule out physically unreasonable connections.
- Both the temperature datasets seem to drive the ENSO time series at several values of τ (Fig. 10.3B). However, a noticeable dark band around the period of 25-30 months for both CRUTA and GISS suggest a strong influence of GMT on ENSO around the quasi-biennial oscillatory period. The reverse connection from ENSO to temperature has been discussed in earlier studies (cf. [116] and [263]). However, this feedback from the temperature to ENSO around the quasi-biennial period has not been considered in much detail and thus needs more careful investigation. The greenhouse gases too seem to impact ENSO in around this period. The greenhouse gas series also impacts ENSO around 55-60 month period which might be linked to a quasi-quadrennial kind of phenomenon [159]. Similar influence of greenhouse gas emissions on the ENSO have been discussed elsewhere [363, 364].
- Only TSI and ENSO seem to have an effect on the volcanic activity dataset (Fig. 10.3C) with the former influencing VOLC at a short time scale of around 1-5 months and the latter influencing it rather strongly at around 30 months. The idea that climatic phenomena could influence volcanic activity is controversial and debatable (e.g., [306] postulates one possible mechanism based on lithospheric stress). However, [318] challenges the more popular idea that ENSO is influenced by volcanic eruptions and suggests a converse dependency, with one possible physical mechanism being the influence of oceanic angular momentum on the earth's rotation rate at subdecadal scales (c.f. Marcus et al. [217]) which in turn might influence seismic activity on the mantle. Alternatively, the transport of volcanic aerosols in the atmosphere could be influenced as well which might lead to the results observed here (also discussed below). Our results indicate that it might be worthwhile to study this more closely in order to gain a better understanding of globally relevant climatic phenomena such as volcanoes and the ENSO.
- The greenhouse data is influenced by only the TSI and the VOLC datasets (Fig. 10.3D)

at similar values of τ around 50-55 months. The impact of VOLC on the greenhouse gases most likely reflects the response of the Earth's carbon-cycle to volcanic eruptions (e.g., [160]). The observed influence of TSI on WMGHG could be an example of indirect influence of TSI on the WMGHG data via the VOLC dataset as the TSI impacts VOLC at much shorter time scales of a few months.

The above results are summarized as a network of dependencies in Fig. 10.4, where two different directed networks are visualized: one each for the two temperature datasets – CRUTA and GISS. Only statistically significant values are used to construct these networks. However, from Fig. 10.2 and Fig. 10.3, we see that, in many cases, there are multiple values of τ at which estimated values of RMD are significant for a given pair of datasets. In such cases, for the sake of visual clarity, a single value of τ is chosen as representative of (nearly) continuous intervals of τ in which RMD values are significant. In case the interval is too wide for a single value to be representative, the interval itself is mentioned. Two notable exceptions to this are the links between WMGHG and CRUTA/GISS, and TSI and GISS. In these cases, RMD values are significant for almost all values of τ considered – and hence only the presumably physically relevant values of τ are shown in Fig. 10.4 for clarity. We choose here $\tau = 135$ months as this is the peak value of $RMD(\tau)$ for these pairs and is also close to the earlier estimated value of $\tau = 120$ months in [192]. We note that the networks

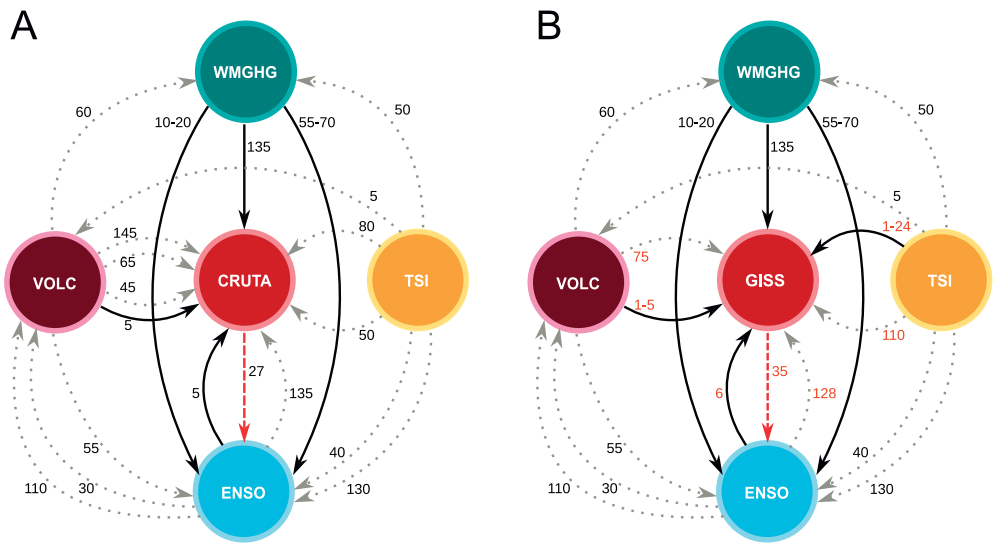

Figure 10.4: **Network of dependencies surrounding GMT. A.** For the HadCRUT3v temperature series. **B.** For the NASA GISS LOTI series. The arrows correspond to a statistically significant influence. The numbers beside the arrows denote the (interval of) delay(s) at which the statistically significant link is found. In **B**, the τ values that differ from **A** are given in red. The solid black arrows correspond to links that are known and/or are discussed to some extent in the literature. The gray dotted arrows correspond to links that are not easily explained. The red dashed arrow is the feedback from temperature to ENSO that is uncovered by our analysis. The datasets are labelled as given in Sec. 10.2: *CRUTA* for the HadCRUT3v data; *GISS* for NASA GISS LOTI; *TSI* for total solar irradiance; *VOLC* for the optical aerosol depth data; and *WMGHG* for the well-mixed greenhouse gas series. *Note*: For the links between WMGHG and temperature, and TSI and temperature, only a few of the statistically significant values are shown for visual clarity.

shown in Fig. 10.4 are not constructed on the basis of a mathematical procedure. They are, in fact, intended to reveal the *qualitative* structure of the network of interactions among global temperature drivers. We can infer the following from Fig. 10.4:

- The results for the CRUTA and GISS temperature datasets are reasonably consistent for the links with ENSO, WMGHG and VOLC, but differ in the case of their respective links with TSI.
- TSI seems to drive all the remaining four datasets. However, the delays at which TSI impacts them are much larger than what is normally assumed in studies involving TSI and GMT. Our results indicate that it might be possible that the longer time scale periodicities of solar irradiance might be an important factor influencing global climatic phenomena.
- The GMT feeds back into *only* the ENSO series near the quasibiennial period (the results are slightly different between CRUTA and GISS here). This might be a crucial point to consider in both (semi-) empirical as well as theoretical modeling of GMT in terms of natural forcings.
- Apart from having a distinctively significant impact on the GMT, greenhouse gases influence the ENSO as well at multiple delays. Two distinctive periods in which WMGHG drives the ENSO are around 1-2 years and 4-6 years.
- Volcanic aerosols seem to impact GMT not only at the evident short time scales of a few months, but also at other time scales ranging from 45 months to 145 months, which is relatively hard to justify considering that volcanic aerosols do not last in the atmosphere up to 145 months. This example demonstrates the limitations of our approach and is discussed below.

One obvious limitation of our approach is the uncertainty of the statistical test itself. Thus, even when we find a link to be significant (with respect to the previously stated null hypothesis) at a 5% level of significance, we could be wrong 5 times out of 100. A second limitation, and one that might cause, e.g., the suspicious result of VOLC impacting GMT at 145 months, is that the 'volcanic activity' is represented here by the optical depth of stratospheric aerosols. This quantity, in time periods located away from major volcanic eruptions, might be influenced by the other climatic factors. However, a third, and more critical limitation is that our approach cannot distinguish indirect/spurious links from direct ones. This means that if we have: (i) X drives A and A drives Y, or (ii) A drives both X and Y, in both cases our method would show a link between X and Y even though there is no direct connection between them. The direction of this link might then be influenced by random noise (if any) in the systems. We feel that the impact of volcanic aerosols on the GMT at delays as large as 145 months might most likely be due to spurious links that are not removed. There are other methods, e.g., multivariate transfer entropy [328], which can detect and remove spurious links. It is computationally intensive and difficult to incorporate such a principle into the current recurrence-based approach and is thus intended as a goal of future investigations.

10.7 Conclusion and outlook

We present a recurrence-based approach to investigate the network of dependencies among the various factors that are known to influence global mean temperature. To the best of our knowledge, this is a first attempt to consider various climatic factors, such as the ENSO, volcanic activity, greenhouse gas concentration, and solar irradiance, as nodes of an interacting, directed network. To construct the network, we extend the notion of an existing recurrence-based connectivity measure and propose a new, general measure that detects the level of probabilistic dependence between two datasets based on their joint

recurrences. The study also illustrates the use of twin surrogates as a suitable tool for surrogate-based hypothesis testing, crucial for the interpretation of measures estimated from passive experiments.

Our analysis uncovers an intricate, directed network with multiple edges between the nodes. We find a feedback from global temperature to ENSO around the quasi-biennial period, and also significant influences between ENSO and volcanic aerosols – both of which issues require further understanding and investigations. The results indicate the need to consider additional interactions (and at different delays) among the climatic factors considered in order to formulate a more complete picture of global mean temperature variations. This is crucial for the purpose of foreseeing future variations in the temperature. We intend the results to serve as indicators for both (semi-) empirical as well as well theoretical models of global mean temperature.

This study illustrates a new way of investigating climatic phenomena as networks, a view which can be extended, e.g., by including additional factors (such as stratospheric water levels, ozone concentrations, snow albedo, etc.) related to global mean temperature. Investigation of these connections using paleoclimatic datasets can give us further insight on the evolution of global temperature. The datasets considered here can be further considered as networks themselves – where the nodes could be geographical grid points, or sub-factors from which the data were constructed – leading to an interacting network of networks [72] involving the global mean temperature.

Acknowledgments

This study was financially supported by the DFG research group HIMPAC (FOR 1380), the German Federal Ministry of Education and Research (BMBF project PROGRESS, 03IS2191B) and the EU 7th Framework Program under a Marie Curie ITN, project LINC. The authors wish to thank Judith Lean for providing electronic data.

Appendix

Data sources

The datasets used in this analysis are available (as of December 1, 2012) for download at the web addresses listed below.

- Multivariate ENSO Index
  - From 1950 to present
    `http://www.esrl.noaa.gov/psd/enso/mei/table.html`
  - Prior to 1950
    `ftp://www.coaps.fsu.edu/pub/JMA_SST_Index/`
- Stratospheric optical aerosol depth
  `http://data.giss.nasa.gov/modelforce/strataer/tau_line.txt`
- Total Solar Irradiance
  `http://lasp.colorado.edu/sorce/tsi_data/TSI_TIM_Reconstruction.txt`
- WMGHG forcing
  `http://data.giss.nasa.gov/modelforce/RadF.txt`
- NASA GISS LOTI
  `http://data.giss.nasa.gov/gistemp/tabledata_v3/GLB.Ts+dSST.txt`
- HadCRUT3v global mean temperature
  `http://www.cru.uea.ac.uk/cru/data/temperature/hadcrut3v.zip`

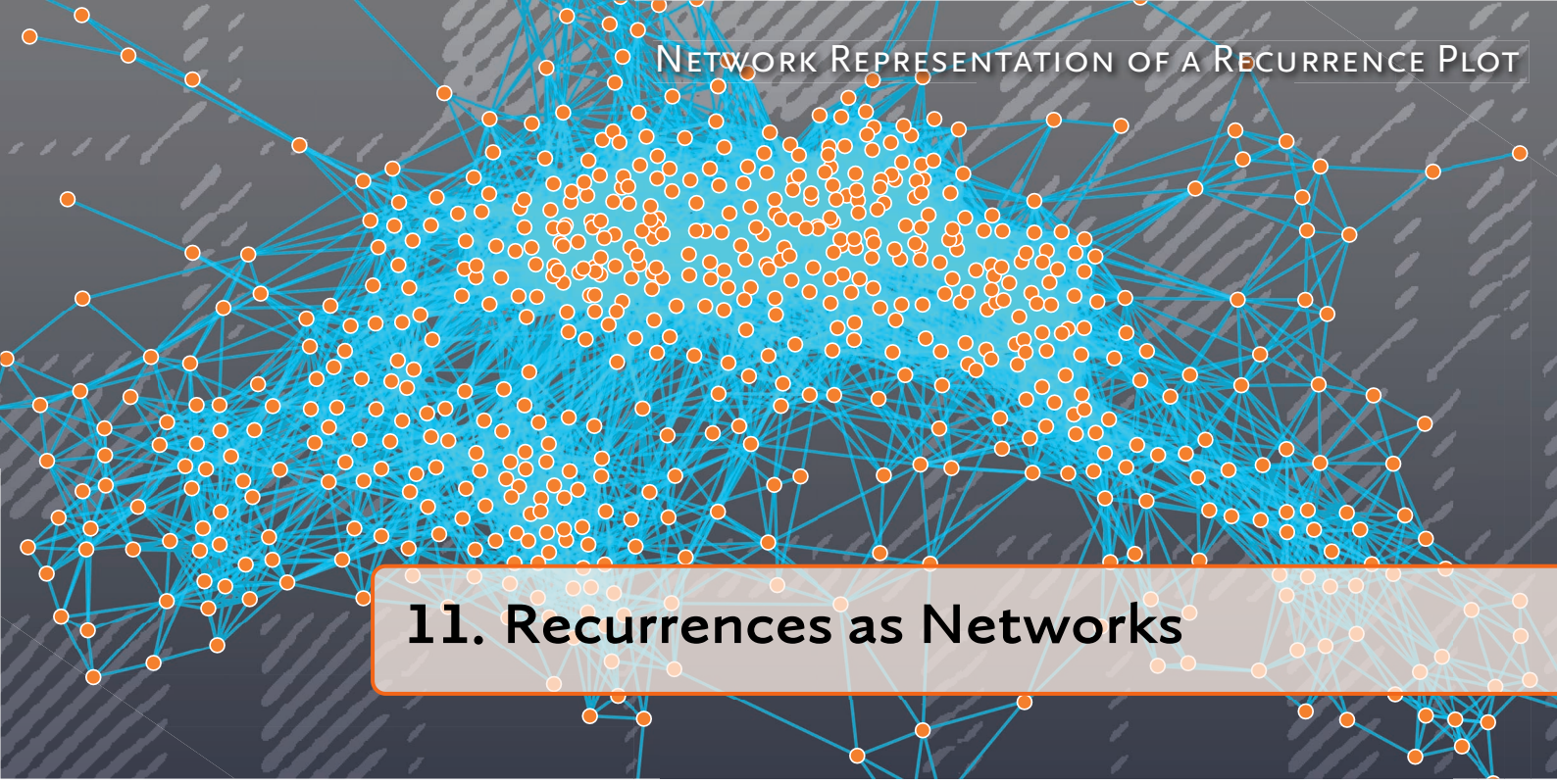

11. Recurrences as Networks

Paper 10 N. Marwan, J. F. Donges, Y. Zou, R. V. Donner, J. Kurths: Complex network approach for recurrence analysis of time series, Physics Letters A, 373(46), 4246–4254 (2009). DOI:10.1016/j.physleta.2009.09.042

Abstract

We propose a novel approach for analysing time series using complex network theory. We identify the recurrence matrix (calculated from time series) with the adjacency matrix of a complex network and apply measures for the characterisation of complex networks to this recurrence matrix. By using the logistic map, we illustrate the potential of these complex network measures for the detection of dynamical transitions. Finally, we apply the proposed approach to a marine palaeo-climate record and identify the subtle changes to the climate regime.

11.1 Introduction

In many scientific disciplines, such as engineering, astrophysics, life sciences and economics, modern data analysis techniques are becoming increasingly popular as a means of understanding the underlying complex dynamics of the system. Methods for estimating fractal or correlation dimensions, Lyapunov exponents, and mutual information have been widely used [165, 184, 213, 425]. However most of these methods require long data series and in particular their uncritical application, especially to real-world data, may often lead to pitfalls.

In the last two decades, the method of recurrence plots has been developed as another approach to describe complex dynamics [239]. A recurrence plot (RP) is the graphical representation of a binary symmetric square matrix which encodes the times when two states are in close proximity (i.e. neighbours in phase space). Based on such a recurrence matrix, a large and diverse amount of information on the dynamics of the system can be extracted and statistically quantified (using recurrence quantification analysis, dynamical invariants, etc.). Meanwhile this technique has been the subject of much interest from various disciplines [224] and it has been successfully applied to a number of areas: the

detection of dynamical transitions [274, 397] and synchronisation [323], the study of protein structures [118, 447] and in cardiac and bone health conditions [232, 237], in ecological regimes [100, 298], economical dynamics [25, 186], in chemical reactions [46] and to monitor mechanical behaviour and damages in engineering [278, 345], to name a few. It is important to emphasise that recurrence plot based techniques are even useful for the analysis of short and non-stationary data, which often presents a critical issue when studying real world data. The last few years have witnessed great progress in the development of RP-based approaches for the analysis of complex systems [230, 239, 317, 324, 381].

During the last decade, complex networks have become rather popular for the analysis of complex and, in particular, spatially extended systems [8, 27, 366, 416]. Local and global properties (statistical measures) of complex networks are helpful to understand complex interrelations and information flow between different components in extended systems, such as social, computer or neural networks [416], food webs, transportation networks, power grids [1], or even in the global climate system [69]. The basis of complex network analysis is the adjacency matrix, representing the links between the nodes of the network. Like the recurrence matrix, the adjacency matrix is also square, binary, and symmetric (in the case of an unweighted and undirected network).

In fact, the recurrence matrix and the adjacency matrix exhibit a strong analogy: a recurrence matrix represents neighbours in phase space and an adjacency matrix represents links in a network; both matrices embody a pair-wise test of all components (phase space vectors resp. nodes). Therefore, we might well proceed to explore further analogies even in the statistical analysis of both the recurrence and the adjacency matrix.

Quantitative descriptors of RPs have been first introduced in a heuristic way in order to distinguish different appearances of RPs [224]. We may also consider to apply measures of complex network theory to an RP in order to quantify the RP's structure and the corresponding topology of the underlying phase space trajectory. In this (more heuristic) sense, it is actually not necessary to consider the phase space trajectory as a network.

Recently, the very first steps in the direction of bridging complex network theory and recurrence analysis have been reported [431, 448]. In these works, the local properties of phase space trajectories have been studied using complex network measures. Zhang et al. suggested using cycles of the phase space trajectory as nodes and considering a link when two cycles are rather similar [448, 449]. The resulting adjacency matrix can be in fact interpreted as a special recurrence matrix. The recurrence criterion here is the matching of two cycles. A complementary approach was suggested by Xu et al. who studied the structural shape of the direct neighbourhood of the phase space trajectory by a motif classification [431]. The adjacency matrix of the underlying network corresponds to the recurrence matrix, using the recurrence criterion of a fixed number of neighbours (instead of the more often used fixed size of the neighbourhood [239]).

Other approaches for the study of time series by a complex network analysis suggested using linear correlations [438] or another certain condition on the time series amplitudes ("visibility") [187].

In this letter, we demonstrate that the recurrence matrix (analogously to [431]) can be considered as the adjacency matrix of an undirected, unweighted network, allowing us to study time series using a complex network approach. This ansatz on creating complex network is more natural and simple than the various suggested approaches [187, 438, 449]. Complex network statistics is helpful to characterise the local and global properties of a network. We propose using these complex network measures for a quantitative description of recurrence matrices. By applying these measures, we obtain additional information from the recurrence plots, which can be used for characterising the dynamics of the underlying

process. We give an interpretation of this approach in the context of the dynamics of a phase space trajectory. Nevertheless, many of these measures neither have an analogue in traditional RQA nor in nonlinear time series analysis in a wider sense, and hence, open up new perspectives for the quantitative analysis of dynamical systems. We illustrate our approach with a prototypical model system and a real-world example from the Earth sciences.

11.2 Recurrence plots and complex networks

A recurrence plot is a representation of recurrent states of a dynamical system in its m-dimensional phase space. It is a pair-wise test of all phase space vectors $\vec{x}_i$ ($i = 1, \ldots, N, \vec{x} \in \mathscr{R}^m$) among each other, whether or not they are close:

$$R_{i,j} = \Theta\big(\varepsilon - d(\vec{x}_i, \vec{x}_j)\big), \tag{11.1}$$

with $\Theta(\cdot)$ being the Heaviside function and ε a threshold for proximity [239]. The closeness $d(\vec{x}_i, \vec{x}_j)$ can be measured in different ways, by using, e.g., spatial distance, string metric, or local rank order [11, 239]. Mostly, a spatial distance is considered in terms of maximum or Euclidean norm $d(\vec{x}_i, \vec{x}_j) = \|\vec{x}_i - \vec{x}_j\|$. The binary recurrence matrix $\mathbf{R}$ contains the value one for all close pairs $\|\vec{x}_i - \vec{x}_j\| < \varepsilon$. A phase space trajectory can be reconstructed from a time series $\{u_i\}_{i=1}^N$ by time delay embedding [286]

$$\vec{x}_i = (u_i, u_{i+\tau}, \ldots, u_{i+\tau(m-1)}), \tag{11.2}$$

where m is the embedding dimension and τ is the delay.

The resulting matrix $\mathbf{R}$ exhibits the line of identity (the main diagonal) $R_{i,i} = 1$. Using a spatial distance as the recurrence criterion, the RP is symmetric. Small-scale features in an RP can be observed in terms of diagonal and vertical lines. The presence of such lines reflects the dynamics of the system and is related to divergence (Lyapunov exponents) or intermittency [237, 317, 397]. Following a heuristic approach, a quantitative description of RPs based on these line structures was introduced and is known as recurrence quantification analysis (RQA) [224]. We use the following two RQA measures (a comparable study using other measures can be found in [237]).

Similarly evolving epochs of the phase space trajectory cause diagonal structures parallel to the main diagonal. The length of such diagonal line structures depends on the predictability and, hence, the dynamics of the system (periodic, chaotic, stochastic). Therefore, the distribution $P(l)$ of diagonal line lengths l can be used for characterising the system's dynamics. Several RQA measures are based on $P(l)$. However, here we focus only on the maximal diagonal line length,

$$L_{\max} = \max\Big(\{l_i\}_{i=1}^{N_l}\Big), \tag{11.3}$$

where $N_l = \sum_{l \geq l_{\min}} P(l)$ is the total number of diagonal lines. For the definition of a diagonal line, we use a minimal length $l_{\min}$ [239]. The length of diagonal lines corresponds to the predictability time. In particular, the cumulative distribution of the line lengths can be used to estimate the correlation entropy K_2, i.e. the lower limit of the sum of the positive Lyapunov exponents [239]. Hence the inverse of $L_{\max}$ gives a first rough impression of the divergence (Lyapunov exponent) of the system.

Slowly changing states, as occurring during laminar phases (intermittency), result in vertical structures in the RP. Therefore, the distribution $P(v)$ of vertical line lengths v can be used to quantify laminar phases occurring in a system. A useful measure for quantifying such

laminar phases is the ratio of recurrence points forming vertical structures to all recurrence points,

$$LAM = \frac{\sum_{v=v_{\min}}^{N} v\,P(v)}{\sum_{v=1}^{N} v\,P(v)}, \tag{11.4}$$

which is called laminarity [239].

Now let us consider the phase space vectors as nodes of a network and identify recurrences with links. An undirected and unweighted network is represented by the binary adjacency matrix $\mathbf{A}$, where a connection between nodes i and j is marked as $A_{i,j} = 1$. Excluding self-loops, we obtain $\mathbf{A}$ from the RP by removing the identity matrix,

$$A_{i,j} = R_{i,j} - \delta_{i,j}, \tag{11.5}$$

where $\delta_{i,j}$ is the Kronecker delta. Removing the identity is not a problem, as this is also done in the analysis of RPs (e.g. when considering a Theiler window for RQA) [239]. Henceforth, we regard the recurrence matrix (with applied Theiler window) to be an adjacency matrix. Note that this way each state vector in phase space is represented by one distinct node; even if two time-separated state vectors are identical, they are identified with two different nodes (which are perfect neighbours and therefore linked independently of the threshold ε; such nodes are also called twins [325]).

Local and global properties of a network are statistically described by complex network measures based on the adjacency matrix $A_{i,j}$. To illustrate the potential of a recurrence analysis by means of complex network theory, we consider several global and local network measures that are well studied in literature [27].

The complex network approach allows to harness the distributions of locally defined measures for the quantification of recurrence matrices. In this work, we particularly consider the degree centrality

$$k_v = \sum_{i=1}^{N} A_{v,i}, \tag{11.6}$$

giving the number of neighbours of node v. The degree centrality is hence locally defined and depends only on local adjacency information in a topological sense. k_v is proportional to the local recurrence rate, as seen from a RQA point of view. Hence, it may be considered as a measure for the local phase space density. We refer to its frequency distribution $P(k)$ as the degree distribution.

Furthermore, a complex network may be globally described by its link density, clustering coefficient and average path length. While the normalised averaged degree centrality, called link density,

$$\rho = \frac{1}{N(N-1)} \sum_{i,j=1}^{N} A_{i,j} \tag{11.7}$$

corresponds to the global recurrence rate, the latter two measures allow quantifying novel aspects of recurrence matrices. The clustering coefficient $\mathscr{C} = \sum_v C_v/N$ gives the probability that two neighbours (i.e. recurrences) of any state are also neighbours [416]. It is obtained as the average of the local clustering coefficient

$$C_v = \frac{\sum_{i,j=1}^{N} A_{v,i}A_{i,j}A_{j,v}}{k_v(k_v-1)}. \tag{11.8}$$

The average length of shortest paths between all pairs of nodes is given by the average path length

$$\mathscr{L} = \frac{1}{N(N-1)} \sum_{i,j=1}^{N} d_{i,j}, \tag{11.9}$$

where the length of a shortest path $d_{i,j}$ is defined as the minimum number of links that have to be crossed to travel from node i to node j [27]. Disconnected pairs of nodes are not included in the average (for a detailed discussion see [271]). Note that it is particularly interesting to study clustering coefficient and average path length in unison, since both measures taken together allow to characterise “small-world" behaviour in complex networks [416]. In a separate study, we link the properties of a complex network with the topology of a phase space representation of a dynamical system in more detail [77]. In particular, a complex network based on a recurrence plot usually does not exhibit the small-world feature, since graph distances are directly related to distances in phase space (i.e. there are no “shortcuts” between distant nodes).

11.3 Application to logistic map

We illustrate the potential of the proposed approach by an analysis of the logistic map

$$x_{i+1} = a\, x_i\, (1 - x_i), \tag{11.10}$$

especially within the interesting range of the control parameter $a \in [3.5, 4]$ with a step size of $\Delta a = 0.0005$. In the analysed range of a, various dynamic regimes and transitions between them can be found, e. g., accumulation points, periodic and chaotic states, band merging points, period doublings, inner and outer crises [57, 281, 409]. This system has been used to illustrate the capabilities of RQA. It was shown that diagonal line based RQA measures are able to detect chaos-order transitions [397] and vertical line based measures even detect chaos-chaos transitions [237].

Since Eq. (11.10) is a one-dimensional map, we compute the RP without embedding. For the study of transitions, it is recommended to use a recurrence threshold ε preserving a fixed recurrence rate, say 5%. However, in the special case of the logistic map, such approach leads to problems within the periodic windows. In these windows the states are rapidly alternating between subsequent time steps, leading to a high recurrence rate (larger than 25%). Therefore, a threshold for preserving 5% recurrence rate does not exist and, hence, we cannot compute the network measures within the periodic windows. To circumvent this, we will use a fixed recurrence threshold ε for the example of the logistic map (for the real world example in Sect. 11.4, we will use the preferred criteria of constant recurrence rate). The threshold ε is selected to be 5% of the standard deviation σ of the time series [338].

For periodic dynamics, band merging, laminar states (cross points of supertrack functions, cf. [237]), and outer crisis, we investigate the network measures in more detail (Tab. 11.1). The band merging corresponds to intermittency, the inner crisis to certain chaos-chaos transition and the outer crisis to fully chaotic dynamics (all these transitions are chaos-chaos transitions).

For these four cases, we compute a time series of length $N = 10,000$. In order to exclude transient responses we remove the leading $1,000$ values from the data series in the following analysis (thus we use $9,000$ values).

The recurrence plots for the four different dynamical regimes exhibit different typical characteristics of regular, laminar and chaotic dynamics (Fig. 11.1). In the periodic regime,

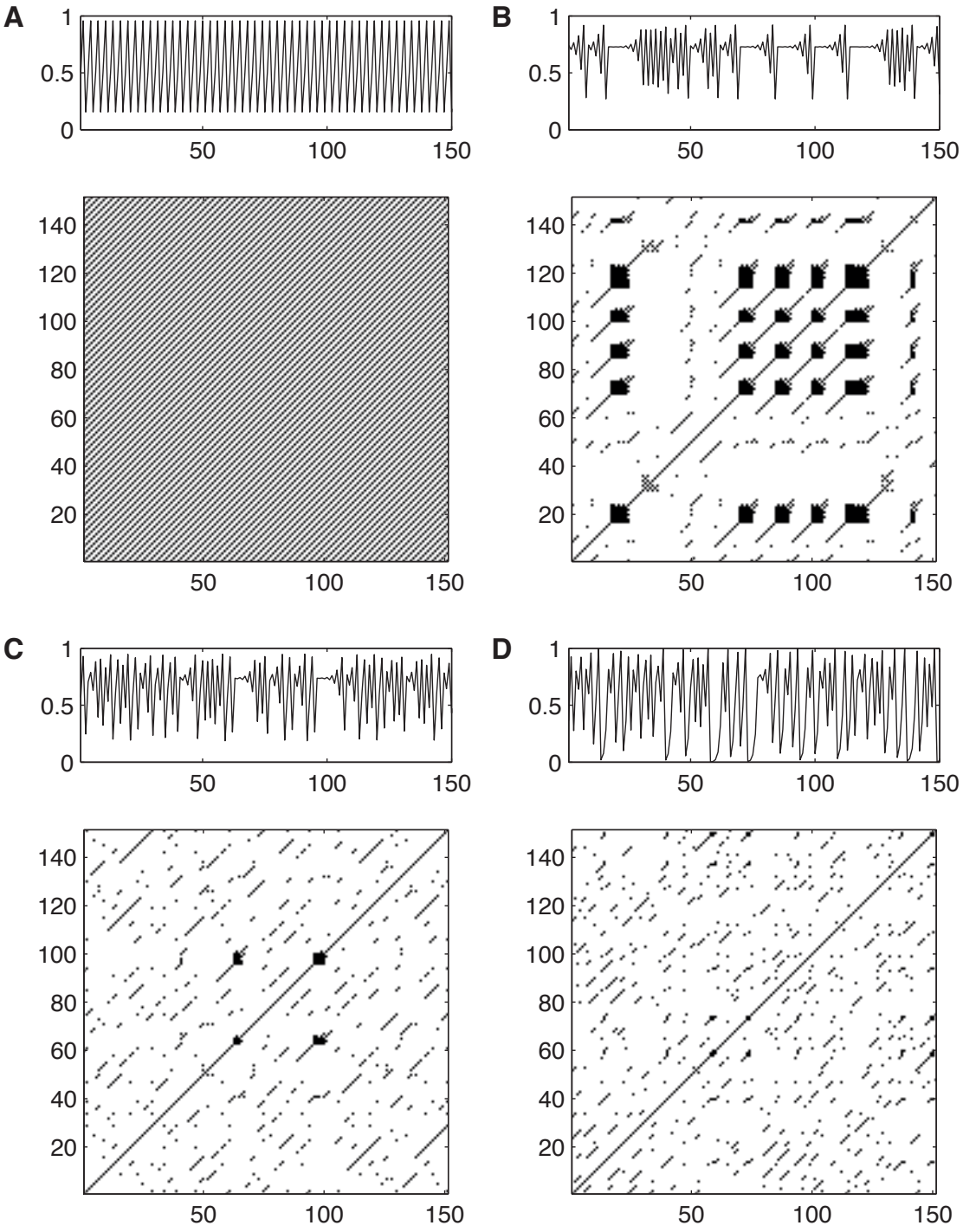

Figure 11.1: Recurrence plots for different dynamical regimes of the logistic map: (A) period-3 dynamics, $a = 3.830$; (B) band merging, $a = 3.679$; (C) laminar states, $a = 3.791$; and (D) outer crisis, $a = 4$ (RP parameters: $m = 1$, $\varepsilon = 0.05\sigma$).

Table 11.1: Control parameter, RQA and network measures for different dynamical regimes of the logistic map (RP parameter: $m = 1$, $\varepsilon = 0.05\sigma$).

Regime	a	$L_{\max}$	LAM	$\mathscr{L}$	$\mathscr{C}$	ρ
period-3	3.830	8996	0	1	1	0.333
band merging	3.679	49	0.42	22.8	0.83	0.050
laminar	3.791	39	0.12	23.3	0.79	0.040
outer crisis	4.000	23	0.20	23.6	0.82	0.046

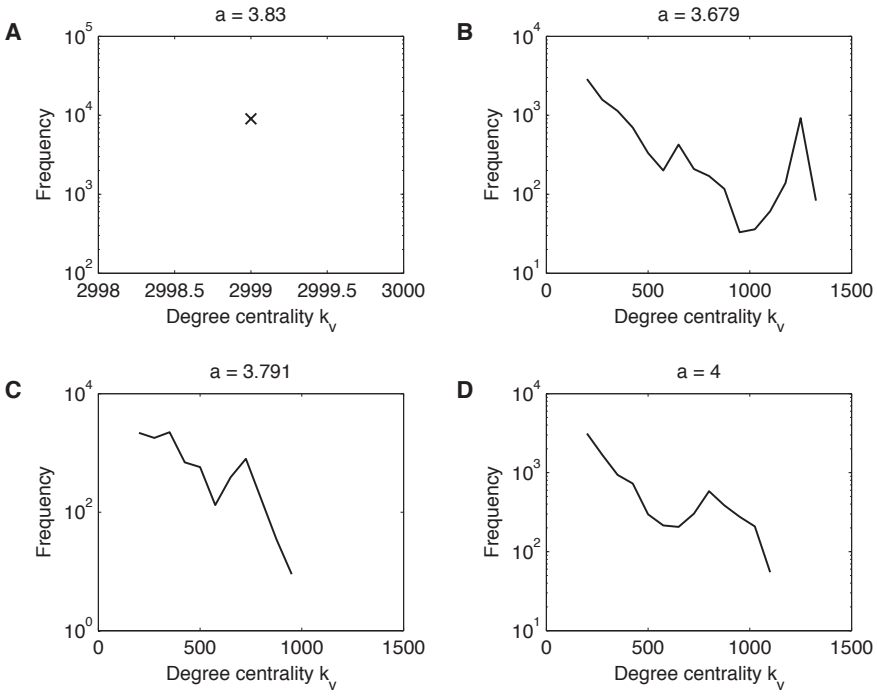

Figure 11.2: Degree centrality distributions $P(k)$ for different dynamical regimes of the logistic map: (A) period-3 dynamics, $a = 3.830$; (B) band merging, $a = 3.679$; (C) laminar states, $a = 3.791$; and (D) outer crisis, $a = 4$ (RP parameters: $m = 1$, $\varepsilon = 0.05\sigma$).

$a = 3.830$, the RP consists only of non-interrupted diagonal lines (Fig. 11.1A). Their distance is 3, corresponding to the period length of 3 for this periodic regime. At the band merging point, $a = 3.679$, the RP reveals extended clusters of recurrence points, corresponding to many laminar phases (Fig. 11.1B). Moreover, several diagonal lines appear, showing short epochs of similar evolution of the states. The RP for laminar states, $a = 3.791$, consists also of (even though less) extended clusters, but possesses more diagonal lines (Fig. 11.1C). For the outer crisis, $a = 4$, diagonal lines appear but are shorter than those appearing for smaller a (Fig. 11.1D), which is consistent with the Lyapunov exponent being largest for $a = 4$ (with respect to smaller a).

The two RQA measures $L_{\max}$ and LAM confirm these visual observations (Tab. 11.1). For the period-3 regime, we find the longest diagonal lines ($L_{\max} = 8996$, after consideration of the Theiler window [378]). The maximal length of diagonal lines decreases for increasing control parameter a. As expected, laminarity takes the highest value at the band merging point ($a = 3.679$) with $LAM = 0.42$, but is lowest for the period-3 regime, $LAM = 0$. At intersections of supertrack functions, the laminarity is slightly increased ($LAM = 0.12$), and at the outer crisis the intermittency increases apparently ($LAM = 0.20$).

The complex network measures also highlight differences in the topological structure of these dynamical regimes (Tab. 11.1).

In the period-3 regime ($a = 3.830$), the observed values jump between three distinct states. These three states are isolated in phase space and are not considered to be neighbours (in the sense of the recurrence definition). Therefore, in the sense of a complex network, we have three disconnected components where each component contains a fully connected network (because all the nodes in each component represent the same state in phase space). The average shortest path length between nodes (i.e. states) should therefore be one, and the clustering is perfect. The average path length $\mathscr{L}$ derived from the corresponding RP has indeed the smallest possible value ($\mathscr{L} = 1$), and the clustering coefficient $\mathscr{C}$ takes its largest possible value ($\mathscr{C} = 1$). The degree centrality k_v takes only one value: 2999 (Fig. 11.2A). This value corresponds approximately to a third of the size of the network, due to its partition by the period-3 cycles, which is confirmed by the link density ($\rho = 0.333$).

For the band merging ($a = 3.679$), we find $\mathscr{L} = 22.8$ and $\mathscr{C} = 0.83$. The degree distribution $P(k)$ has a multimodal shape (Fig. 11.2B), which implies that there are several states acting like super-nodes (i.e. which exhibit many links). These states lie at the merging point of the two bands (around $x = 0.73$) and at the upper and lower border of the state space, i.e. in regions with high phase-space density (Fig. 11.3A). The link density is $\rho = 0.050$.

For the laminar state at $a = 3.791$, we find $\mathscr{L} = 23.3$ and $\mathscr{C} = 0.79$. The degree centrality k_v follows a distribution with slight bimodality (Fig. 11.2C). The resulting link density approaches its lowest value within the four considered dynamical regimes ($\rho = 0.040$).

Finally, for the outer crisis ($a = 4$), we obtain $\mathscr{L} = 23.6$ and $\mathscr{C} = 0.82$. The degree centrality k_v displays similar properties as for the laminar state, but with higher average values and a resulting link density of $\rho = 0.046$ (Fig. 11.2D).

From the above results, we conclude that complex network measures applied to a recurrence matrix are indeed sensitive to changes in the dynamics. The average shortest path length can be considered as an upper bound for the phase space distance between two states (in units of the threshold value ε). Hence, its average value $\mathscr{L}$ can be interpreted as a mean distance, which depends on the total diameter and the fragmentation of the phase space. Therefore, $\mathscr{L}$ increases with growing phase space of the logistic map (with growing control parameter a). The clustering coefficient $\mathscr{C}$ is able to detect clustered phase vectors, as they appear in periodic or laminar dynamics. The degree centrality k_v quantifies the phase-space density in the direct neighbourhood of a state v, while the link density ρ measures the average phase space density. Moreover, from the k_v distribution we can infer that the considered recurrence matrices are not scale-free in the sense of the network theory.

Now we calculate $L_{\max}$, LAM, ρ, $\mathscr{L}$, $\mathscr{C}$, and k_v for different values of the control parameter a within the range $[3.5, 4]$. For each value of a, we compute a time series of length $N = 2,000$, and exclude transients by removing the first $1,000$ values.

The RQA measure $L_{\max}$ reveals periodic dynamics by maxima of its value (Fig. 11.3B). Laminar phases are clearly detected by LAM (Fig. 11.3C). ρ and $\mathscr{C}$ also show maxima during episodes of periodic dynamics (Figs. 11.3D and F). ρ corresponds to the recurrence rate and confirms previous studies [397]. Its values also depend on the periodicity during the periodic windows – the higher the periodicity, the lower ρ. Therefore, period-doublings cause an abrupt decrease of this measure. In the periodic regime, neighbours of a state are equal to the state itself, leading to the largest possible clustering coefficient $\mathscr{C} = 1$, and to the shortest possible path lengths between neighbours giving $\mathscr{L} = 1$. However, $\mathscr{L}$ shows a more interesting behaviour. In our interpretation of a recurrence matrix, $\mathscr{L}$ characterises not only the total phase space diameter, but also its fragmentation. With respect to the logistic map, each time two bands in phase space merge (e.g. at $a = 3.5736$ or $a = 3.5916$), this does not

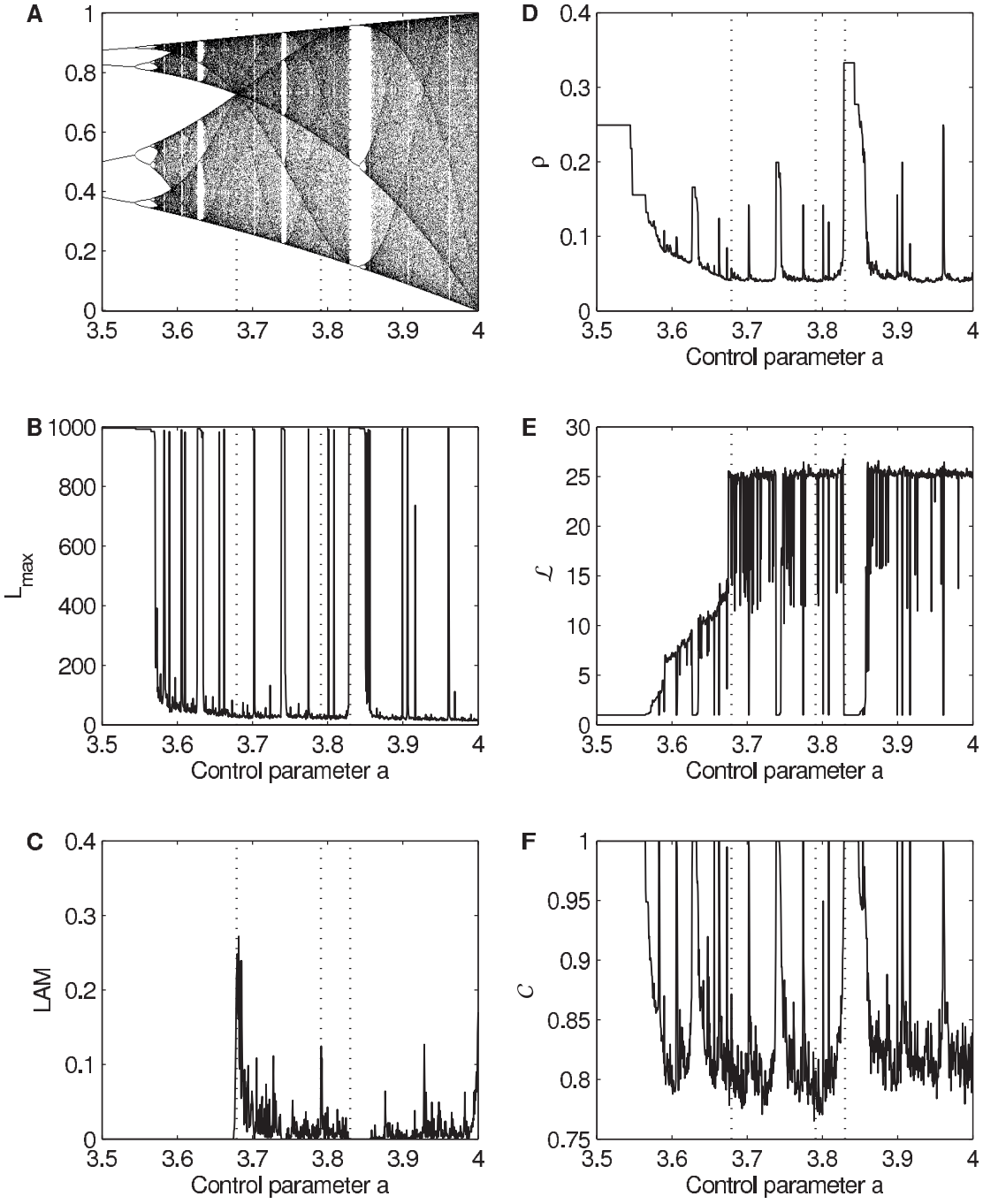

Figure 11.3: (A) Bifurcation diagram of the logistic map. Selected RQA measures (B) maximal diagonal line length $L_{\max}$ and (C) laminarity LAM, as well as complex network measures (D) link density ρ, (E) average path length $\mathscr{L}$, and (F) clustering coefficient $\mathscr{C}$. The dotted lines mark the discussed regimes at period-3 window ($a = 3.830$), band merging ($a = 3.679$), cross points of supertrack functions ($a = 3.791$), and outer crisis ($a = 4$). Parameters as in Fig. 11.2.

only lead to an increase of the occupied phase space, but also yields a merging of formerly disjoint network clusters. As the definition of the average path length does not consider pairs of points in disconnected clusters, the average distance of connected nodes suddenly increases shortly before the band merging point as soon as the distance between the different bands falls below ε, since the clusters then become connected. This is clearly expressed by jumps in $\mathscr{L}$ (Fig. 11.3E). The distribution of k_v is discrete in the periodic windows, which are therefore clearly identifiable (Fig. 11.4). Analogous to the link density ρ, the location of the maxima of the degree distribution in periodic windows is related to the number of periods, e.g., for period-4 we have $N/4-1=249$, for period-3 $N/3-1=332$ (for a time series length of $N=1,000$). The degree distribution $P(k)$ before the band merging point is broad and reveals higher degrees than after the band merging point, which again relates to the connection of the distinct network clusters. For increased control parameter a, $P(k)$ becomes more localised around small degrees, disclosing the decrease of recurrences due to the increasingly chaotic behaviour (increasing Lyapunov exponent).

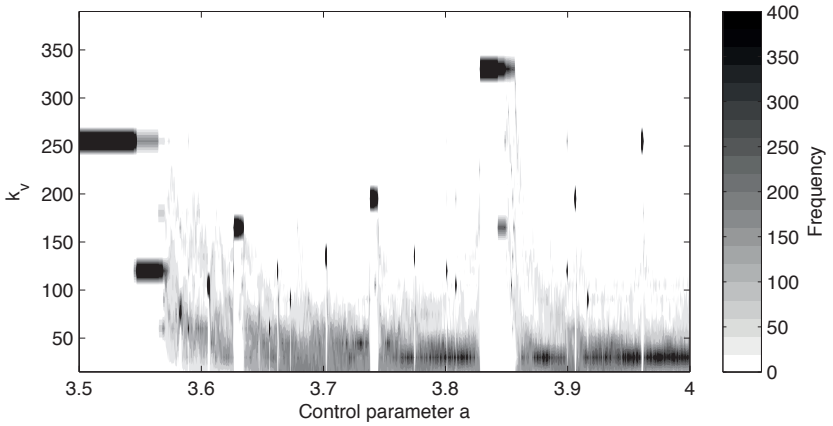

Figure 11.4: Distribution of the degree centrality k_v of the logistic map for a range of the control parameter a. Same parameters as in Figs. 11.2 and 11.3.

11.4 Application to marine dust record

Long-term variations in aeolian dust deposits are related to changes in terrestrial vegetation and are often used as a proxy for changing climate regimes in the past. For example, marine terrigenous dust records can be used to infer epochs of arid continental climate. In particular, a marine record from the Ocean Drilling Programme (ODP) derived from a drilling in the Atlantic, ODP site 659, was used to infer changes in African climate during the last 4.5 Ma (Fig. 11.5A) [388]. This time series has a length of $N=1,240$ with an average sampling time of 4.1 ka. Applying spectral analysis to these data, it was claimed that the African climate has shifted towards arid conditions at 2.8, 1.7 and 1.0 Ma before present (BP) [62]. These transitions correspond to epochs of different dominant Milankovich cycles (mid-Pleistocene transition with a "41 ka world" between 2.7 and 1.0 Ma BP and a "100 ka world" since about 1.0 Ma BP), the end of the Early Pliocene Warm Period at about 2.8 Ma BP, and the development of the Walker circulation around 1.9–1.7 Ma BP [309]. However, a recent thorough investigation of several marine dust records demonstrated more complex relationships between vegetational coverage, aeolian transport processes and the dust flux record [391]. The analysis revealed transitions between different regimes of variability, mostly driven by a variation of the solar irradiation due to different dominant Milankovich

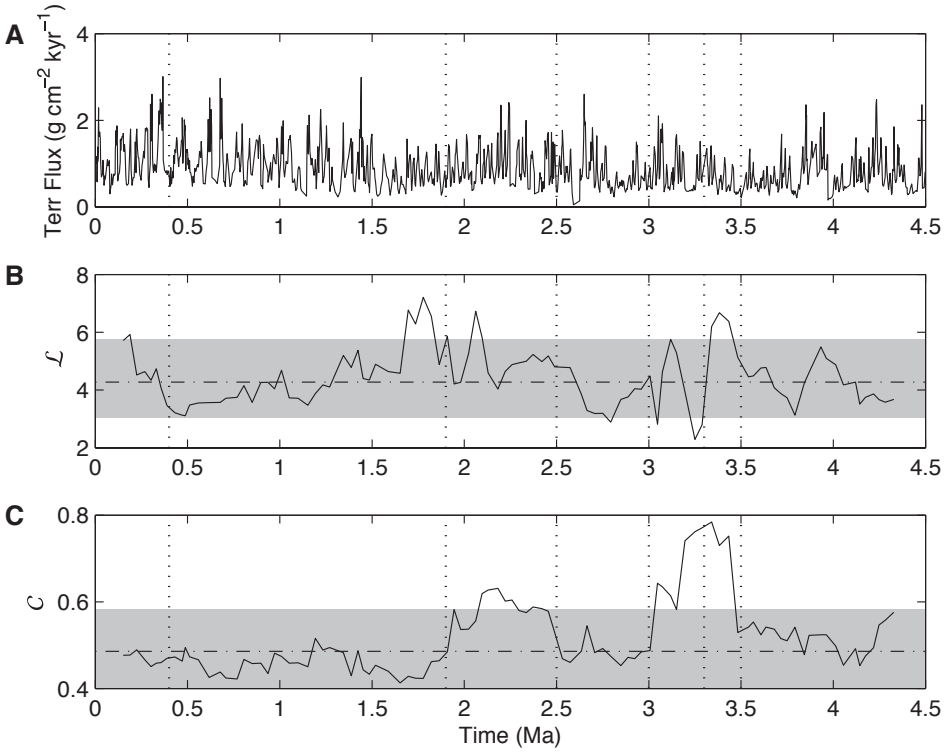

Figure 11.5: (A) Terrigenous dust flux record of ODP site 659, and corresponding network measures (B) $\mathscr{L}$ and (C) $\mathscr{C}$. The dotted lines mark pronounced transitions in the dynamical regime at 3.5, 3.3, 3, 2.5, 1.9, and 0.4 Ma BP, the dash-dotted line corresponds to the mean value of the null-model and the shaded area corresponds to the 90% confidence bounds. Same parameters as in Fig. 11.6, window size 420 ka.

cycles. For example, Trauth et al. found an interval of a dominant 100 ka frequency (related to orbital eccentricity) between 3.2 and 3.0 Ma BP, and of dominant 19–23 ka frequency band (precession) between 2.3 and 2.0 Ma BP [391]. The Early Pliocene Warm Period ended between 3.3 and 2.8 Ma BP with the Pliocene optimum (3.24–3.05 Ma BP) and the onset of the northern hemisphere glaciation (2.8–2.7 Ma BP) [265, 309], which was intensified during the mid-Pleistocene climate shift at 1.0–0.7 Ma BP [358]. It has been hypothesised that the latter transition was connected with a period of strong Walker circulation between 1.5–0.5 Ma BP [248].

We illustrate the capabilities of our recurrence analysis using complex network measures for the ODP 659 dust flux record in order to find transitions in the dynamics. For this purpose, we use a time delay embedding with dimension $m = 3$ and delay $\tau = 2$ (these parameters have been determined by applying the standard procedure using false nearest neighbours and mutual information [165]). The threshold is chosen to preserve a constant recurrence rate of 5% (which means that the link density ρ will be constant) [239, 338]. In order to study transitions in the dust record, we calculate the recurrence matrix in moving windows of size 100 time points (corresponding approximately to 410 ka) and with an overlap of 90%. For the time-scale of the windowed measurements, we use the mid-point of the window. Note that the time-scale is not equidistant (equidistant time-scale is not necessary for our network approach). On average, the sampling time is 4.1 ka with a standard deviation of $\sigma = 2.7$ ka. Compared to the long (geological) scale this deviation is still rather small. However, the application of linear methods often requires equidistant time-scales.

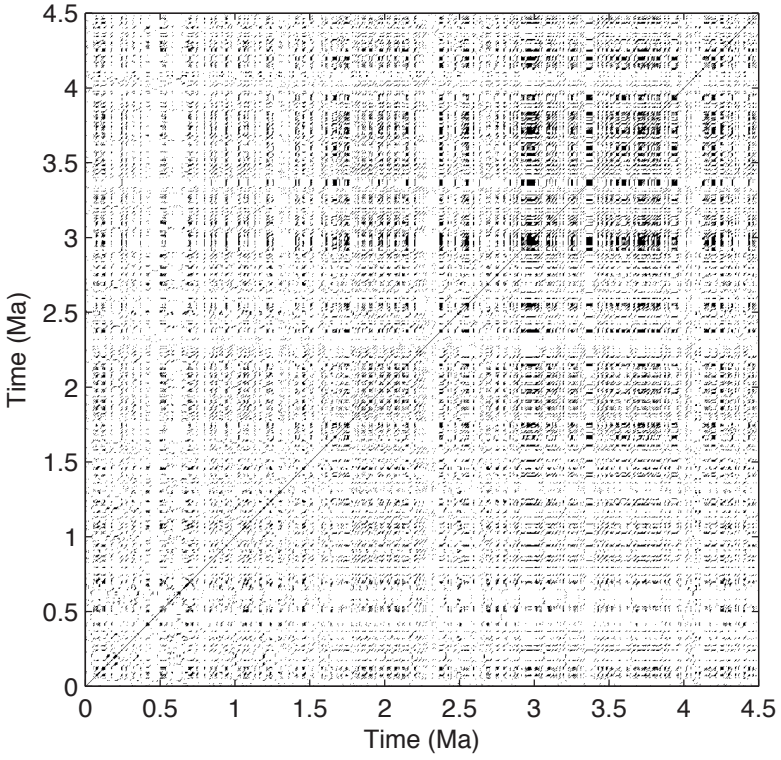

Figure 11.6: Recurrence plot of the terrigenous dust flux record of ODP site 659. Parameters are $m = 3$, $\tau = 2$, ε is chosen such that $\rho = 0.05$, phase space distances are measured using maximum norm.

We will apply a simple statistical test in order to test the null-hypothesis to see whether the network characteristics at a certain time differs from the general network characteristics. In order to create an appropriate null-model, we use the following approach. In contrast to the RQA measures, where the time-ordering is important requiring a more advanced approach for a statistical test [341], for the network measures we can simply randomise the time series: we randomly draw 100 values (corresponding to the window size of 100 points) from the time series and then calculate the RP and the network measures from this sample. By repeating this 10,000 times we get a test distribution for the measures $\mathscr{L}$ and $\mathscr{C}$ and estimate its 0.05 and 0.95 quantiles that may be interpreted as the 90% confidence bounds.

The RP of the dust data depicts a rather homogeneous recurrence structure, interrupted only by rather small bands of sparse recurrence point density (Fig. 11.6). Such sparse areas mark epochs of more frequently occurring extreme or rare events recorded by the marine dust data series. On the small-scale we find mostly very short diagonal lines, expressing the high variability and fast change of the states (with respect to the geological time-scale). Between 4.0 and 3.0 Ma and around 2.0 Ma BP, longer diagonal lines appear. Moreover, between 4.5 and 3.0 Ma BP, we find an increased number of vertical/ horizontal lines, indicating different dynamics than at other times.

The global network measures $\mathscr{L}$ and $\mathscr{C}$ also depict a distinct variability (Fig. 11.5B and C). $\mathscr{L}$ reveals epochs of significantly higher values between 3.5 and 3.3, ~ 2.1, 1.9–1.8, and after 0.4 Ma BP. Around 3.3, 2.0 and 1.9 Ma BP the RP exhibits sudden drops of $\mathscr{L}$ within a period of, in general, higher values. $\mathscr{C}$ discloses epochs of increased values between 3.5 and 3.0 Ma as well as between 2.5 and 2.0 Ma BP. Between 4.5 and 3.5 Ma, 3.0 and 2.5 Ma, and 1.0 and 0.4 Ma BP, the degree centrality possesses mostly small values, whereas between 2.5

and 1.0 Ma and after 0.4 Ma BP, it has larger values (Fig. 11.7).

With respect to the previously known results, we conclude that $\mathscr{C}$ identifies the epochs of more dominant Milankovich cycles (between 3.2 and 3.0 Ma and 2.3 and 2.0 Ma BP). k_v is increased in these periods, but also exhibits increased values for the period between 2.5 and 1.0 Ma BP. Note that the 3.5-3.0 Ma BP period is related to the intensification of the Northern hemisphere glaciation [23]. In contrast, $\mathscr{L}$ reveals transitions in climate dynamics on a different time-scale. Maxima of this measure tend to appear at the onset of changes in $\mathscr{C}$. Whereas $\mathscr{C}$ reveals the changed dynamics, $\mathscr{L}$ is sensitive to the transition periods, which is consistent with our results near the band-merging points of the logistic map. The increase of $\mathscr{L}$ at ~ 3.4, ~ 3.1, 1.9–1.8, and 0.4 Ma BP may also be related to the intensification of glaciation. However, the detected transitions are associated with different and more subtle dynamical changes, and not simply just an intensification of a certain Milankovich cycle.

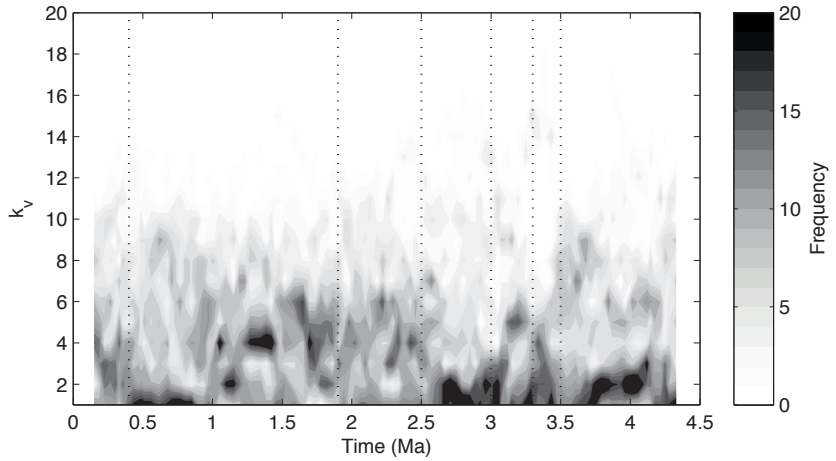

Figure 11.7: Degree centrality k_v of terrigenous dust flux record of ODP site 659. Same parameters as in Figs. 11.6 and 11.5.

11.5 Conclusions

We have linked the recurrence matrix with the adjacency matrix of a complex network, and have proposed the direct application of the corresponding network measures to the recurrence matrix. We have discussed the link density, degree centrality, average path length and clustering coefficient in some detail. In particular, the latter two complex network measures have no direct counterpart in recurrence quantification analysis and give additional insights into the recurrence structure of dynamical systems. In a further study, we have outlined the link between the complex network measures and the properties of the phase space trajectory of dynamical systems [77].

By applying our novel approach to the logistic map, we have illustrated the ability of the proposed measures to distinguish between the different dynamical regimes and to detect the corresponding transitions. Moreover, we have used our approach to investigate a marine climate proxy record representing the climate variability over Africa during the last 4.5 Ma. The different measures highlighted various transitions in the recurrence structure and, hence, in the dynamics of the studied climate system. By applying the recurrence approach and complex network measures, we were able to identify more subtle transitions than those that were previously reported from using linear approaches, like power spectral analysis [62], linear trend detection [265], Mann-Whitney or Ansari-Bradley tests [391]. In addition,

our proposed approach to detect transitions on the basis of time series does not require equidistant time-scales, as would be necessary for most other known techniques. From the network point of view, the recurrence plot approach can deliver a potential measure of information exchange in time series of complex systems [77, 423].

In the future, recurrence plots and their complex network interpretation will allow for further fruitful and natural transfer of ideas and techniques from complex network theory to time series analysis (and vice versa).

Acknowledgements

This work was partly supported by the German Research Foundation (DFG) project He 2789/8-2, SFB 555 project C1, and the Japanese Ministry for Science and Education.

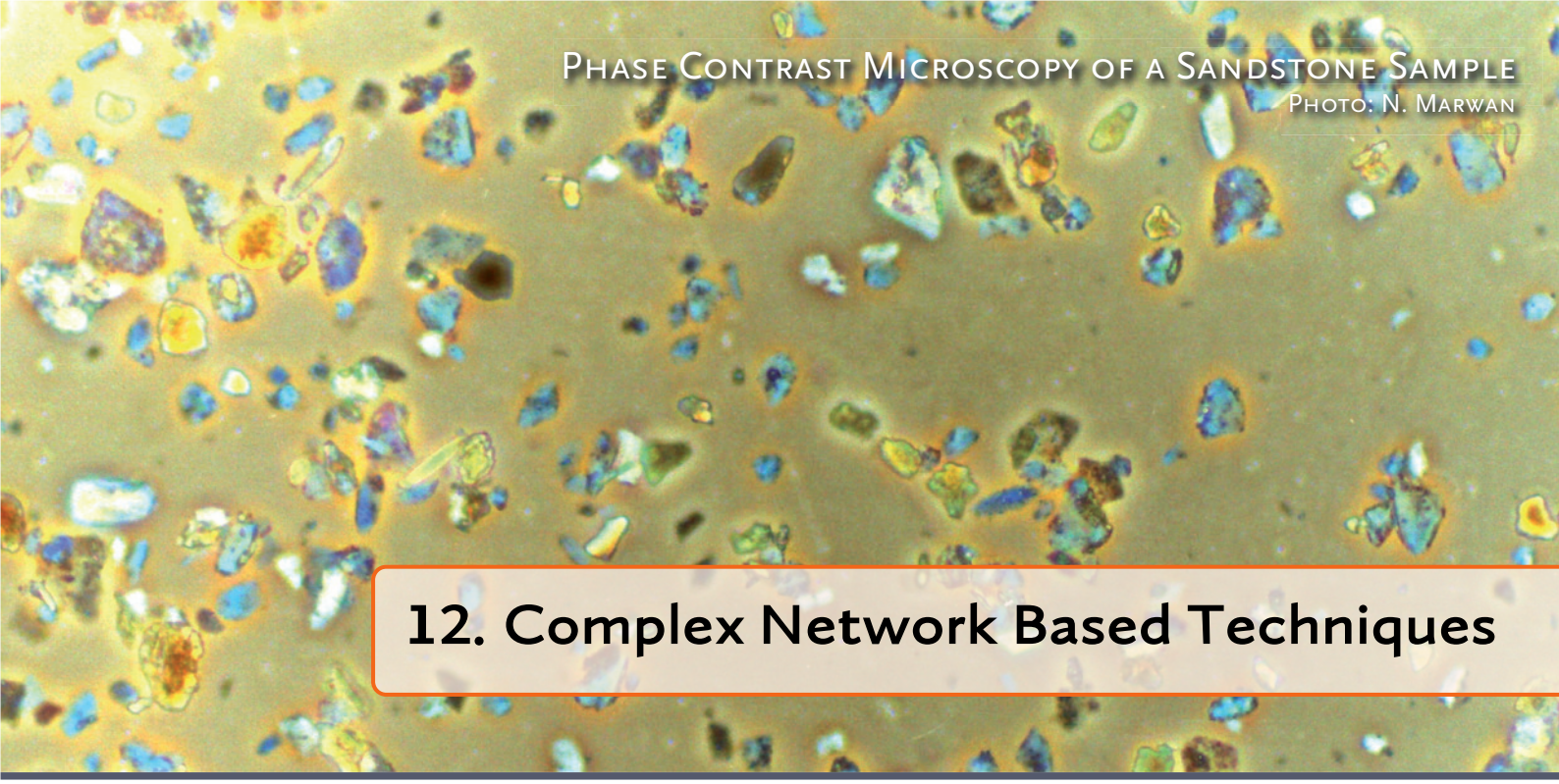

Phase Contrast Microscopy of a Sandstone Sample
Photo: N. Marwan

12. Complex Network Based Techniques

Paper 11 N. Marwan, J. Kurths: Complex network based techniques to identify extreme events and (sudden) transitions in spatio-temporal systems, Chaos, 25, 097609 (2015). DOI:10.1063/1.4916924

Abstract

We present here two promising techniques for the application of the complex network approach to continuous spatio-temporal systems that have been developed in the last decade and show large potential for future application and development of complex systems analysis. First, we discuss the transforming of a time series from such systems to a complex network. The natural approach is to calculate the recurrence matrix and interpret such as the adjacency matrix of an associated complex network, called recurrence network. Using complex network measures, such as transitivity coefficient, we demonstrate that this approach is very efficient for identifying qualitative transitions in observational data, e.g., when analyzing paleoclimate regime transitions. Second, we demonstrate the use of directed spatial networks constructed from spatio-temporal measurements of such systems that can be derived from the synchronized-in-time occurrence of extreme events in different spatial regions. Although there are many possibilities to investigate such spatial networks, we present here the new measure of network divergence and how it can be used to develop a prediction scheme of extreme rainfall events.

In the last decades various powerful techniques have been developed in nonlinear dynamics for the study of continuous spatio-temporal dynamic systems. Typically they are based on different discretization methods in space and time. Here, we discuss an unconventional approach based on complex networks for the investigation of such systems. In contrast to well-known examples of complex networks, such as social ensembles, neural networks, or power grids, where the nodes are clearly defined by humans, neurons or power generating stations, here the first step of the complex network approach can be interpreted as a very flexible way to discretize a continuous system, or to identify a backbone underlying the continuous system. This enables us to use in the next steps

the rich variety of methods from complex network theory even for the analysis of continuous systems. Based on this approach we treat two basic problems in high-dimensional nonlinear dynamics: (i) uncovering regime shifts and (ii) prediction of extreme events. We propose appropriate techniques for both by combining recurrence with networks resp. synchronization with extreme events. The potential of this approach is demonstrated here for the Earth system. In a first example we show that important main regime shifts of the East Asian Monsoon during the last 3 Million years can be identified from paleoclimate proxy records. In a second example we analyze recent satellite data from the tropical rainfall measurement mission (TRMM) and use the network divergence for developing an efficient prediction scheme for extreme precipitation events in the eastern Central Andes.

12.1 Introduction

Climate is as the brain a highly complex and high-dimensional system; both systems have a lot of joint properties, but there are also important distinctions. Understanding the mechanisms of climatic processes on all temporal and spatial scales is very difficult and even impossible in near future, but crucial for weather forecasts or assessment of long-term climate changes. A data-based investigation of the climate system is related with several challenges, in particular non-stationarity (e.g., abrupt vs. slow changes), high-dimensionality, non-Gaussian distributed data (e.g., extreme events), natural vs. anthropogenic influences, etc.

A basic first step in data-based studies of such a complex high-dimensional system is reducing the dimensionality. The most widely used method for this is a decomposition into a very finite number of Empirical Orthogonal Functions (EOFs). This approach also allows to identify main spatial patterns, such as large circulation patterns or teleconnections. However, the basis of the EOF approach is the covariance matrix, thus, only capturing the first two statistical moments and demanding for certain strict properties of the data, e.g., Gaussian distribution and stationarity [260]. Even more obvious are constraints due to event-like data, as typical for rainfall and extreme events, or limitations by nonlinear interrelations. Moreover, the found EOFs do not undoubtedly coincide with typical climate phenomena [68].

Modern measurement techniques has allowed in the last decades to extend our knowledge into the past, leading to paleoclimatology. However, these data generate further challenges: Dating uncertainties and irregularly sampled time series are problems that limit the direct application of standard methods.

An alternative and novel approach for the study of different aspects of the climate system is related to the progress in complex networks science in the past quarter century. At a first glance it might appear surprising that the complex network approach can be used to analyse a continuous system as the climate and in particular to identify spatio-temporal patterns in climate fields or regime shifts in the paleoclimate. However, the application of complex networks for climate analysis has become a lively and quickly progressive field in the last years. Although, this new approach is still in its infancy, first results are very promising and have already shown its impressive potential.

In the following we will present two techniques based on complex networks, recurrence networks (Sec. 12.3) and event synchronization (Sec. 12.5), and will show how they can be used to uncover regime transitions in the paleoclimate by analyzing proxy records (Sec. 12.4) and to analyze spatiotemporal patterns of extreme rainfall leading to new prediction schemes

(Sec. 12.5). Finally we summarize the potentials of this non-traditional approach, but discuss also open problems.

12.2 Complex networks

We give here only a few basics on complex networks which will be used later (see, e.g., [27, 271, 366] for more detailed reviews on complex network analysis). A network is a set of nodes and links. We define a network as complex when its topology is highly irregular. A network can be defined by the adjacency matrix **A**. For undirected and unweighted networks, **A** is a binary matrix, just indicating the existence of links between two nodes. In weighted networks, a link has a weight, i.e., **A** consists of real numbers; **A** is symmetric for undirected and asymmetric for directed networks. A network or its components (links, nodes) can be characterized by several measures. Here we mention only some selected measures.

The *node degree* in unweighted networks is simply the total number of links a node i has and is given by the column sum of the adjacency matrix **A**:

$$k_i = \sum_j^N A_{ji}. \tag{12.1}$$

The distribution of this measure can be used to investigate, e.g., whether a network is scale-free. On directed networks, we can distinguish between the column-wise and raw-wise sums in Eq. (12.1) that give us the in- and out-degree, respectively. For weighted networks the sum Eq. (12.1) becomes the so-called *node strength*, and for directed and weighted networks, we can consider the *in-* and *out-strength*

$$\mathscr{S}_i^{\text{in}} = \sum_{j=1}^N A_{ij} \quad \text{and} \quad \mathscr{S}_i^{\text{out}} = \sum_{j=1}^N A_{ji}. \tag{12.2}$$

Another important measure is the *transitivity coefficient*

$$\mathscr{T} = \frac{\sum_{i,j,k=1}^N A_{j,k}A_{i,j}A_{i,k}}{\sum_{i,j,k=1}^N A_{i,j}A_{i,k}}. \tag{12.3}$$

It measures the probability that the neighbors of a node are connected themselves.

12.3 Recurrence Networks – a time series analysis approach by means of complex networks

Analyzing time series by complex networks is a quite new idea that came up in the last decade. The generation of a complex network representation of a time series can be done using different approaches, e.g., by visibility graphs [187] or temporal succession of local rank orders [356]. A quite natural approach is to use the *recurrence matrix* [239] of a dynamical system

$$R_{i,j} = \Theta(\varepsilon - ||\vec{x}(i) - \vec{x}(j)||), \tag{12.4}$$

as the adjacency matrix of a complex network [78]:

$$\mathbf{A} = \mathbf{R} - \mathbb{I} \tag{12.5}$$

(with $\mathbb{I}$ the identity matrix, Θ the Heaviside function, $\vec{x}(i)$ a state at time $i = 1, \ldots, N$, and N the number of state vectors). The recurrence matrix itself has become a basic tool of

nonlinear time series analysis and was first introduced by Eckmann et al. as recurrence plots that "are rather easily obtained aids for the diagnosis of dynamical systems" [86]. Later this idea was extended by several quantification approaches [237, 442] leading to "an active field, with many ramifications we [Eckmann et al. –] had not anticipated" [240]. Fundamental works on such methodological developments have been published also in Chaos, e.g., on embedding issues and dynamical invariants [158, 384], time-delay systems and non-chaotic strange attractors [275, 347], heterogenous recurrence analysis [437], or twin surrogates [325].

Because of the striking similarity between the recurrence matrix and the adjacency matrix (i.e., a binary and square matrix), the idea to identify the recurrence matrix with the adjacency matrix was so obvious that it came up almost at the same time (around 2008) within different research groups [241, 368, 431]. Its main advantage is that the resulting recurrence network can be analyzed by the known network measures, i.e., further diagnostic tools become available for time series analysis. In particular the transitivity coefficient $\mathscr{T}$ is appropriate because it quantifies the geometry of the phase space trajectory and can be used to differentiate between different dynamics (e.g., regular and irregular) [241, 455]. It also allows to define a dimensionality measure [79], the *transitivity dimension*

$$D_{\mathscr{T}} = \frac{\log(\mathscr{T})}{\log(3/4)}. \tag{12.6}$$

The quantification of the recurrence matrices can also be performed by the recurrence quantification analysis (RQA) [239, 417]. In contrast to the network measures which describe the geometrical properties, the RQA measures characterize dynamical properties of the phase space trajectory. Therefore, the recurrence network based measures provide complementary information to the RQA and can, under certain circumstances, give more insights into the system's behavior.

As a paradigmatic example, let us consider the Rössler system [327]

$$\left(\frac{dx}{dt}, \frac{dy}{dt}, \frac{dz}{dt}\right) = \big(-y-z,\ x+ay,\ b+z(x-35)\big), \tag{12.7}$$

where we change the parameter $a = b$ in a range where the system shows chaotic and periodic dynamics: $a = 0.235, \ldots, 0.262$ (Figs. 12.1 and 12.2). Between $a = 0.24$ and 0.25, the system does not have a positive Lyapunov exponent and generates periodic behavior (Fig. 12.3(a)).

A frequently used RQA measure for differentiating periodic and chaotic dynamics is the ratio of recurrence points that form diagonal lines in the recurrence plot, called *determinism* [239, 397]:

$$DET = \frac{\sum_{l \geq l_{\min}} lP(l)}{\sum_{i,j} R_{i,j}}, \tag{12.8}$$

with $P(l)$ the histogram of line lengths in the recurrence plot. The idea of this measure is that the length of a diagonal line in the recurrence plot corresponds to the time the system evolves very similar as during another time. Such repeated similar state evolution that is also related to predictability is typical for deterministic systems. In contrast, systems with independent subsequent values, like white noise, have mostly single points in the recurrence plot. DET is sensitive to transitions between chaotic and periodic dynamics in maps [397], but for continuous systems, such as our Rössler example, this measure fails for this task [225, 455]. For the entire range of the considered a values, it has very high values, close to one

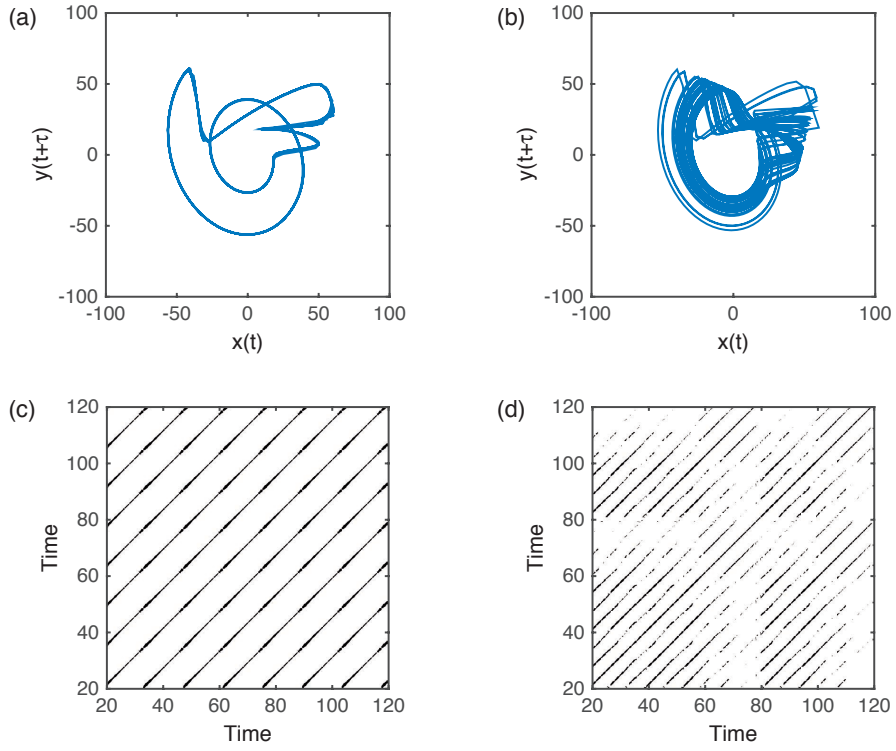

Figure 12.1: (a) Phase space reconstruction of the x-component of the Rössler system for $a = 0.245$ and (b) for $a = 0.29$. (c) Corresponding recurrence plot for $a = 0.245$, showing periodic structures, and (d) for $a = 0.29$, showing interrupted diagonal lines. The recurrence plots are calculated from the x-component using time-delay embedding with $m = 4$ and $\tau = 17$ (sampling time $\Delta t = 0.1$).

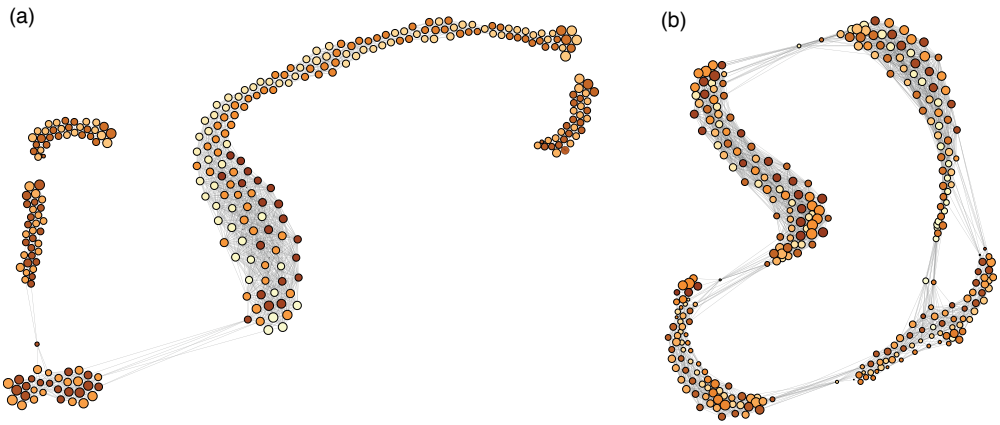

Figure 12.2: Network representation of the phase space reconstruction of the x-component of the Rössler system for (a) $a = 0.245$ and (b) $a = 0.29$. The network is constructed from the first 300 nodes of the recurrence matrix shown in Fig. 12.1 by a linear repulsion model. Node size and color can be used to represent selected node properties, here time (node color, the darker the larger t) and clustering coefficient (node size).

(Fig. 12.3(b), Tab. 12.1). However, $\mathcal{T}$ shows increased values within the periodic window, close to a value of 3/4. In general, the network based measures, such as $\mathcal{T}$, can add further important aspects in recurrence analysis, in particular for the uncovering of sudden changes of the dynamics.

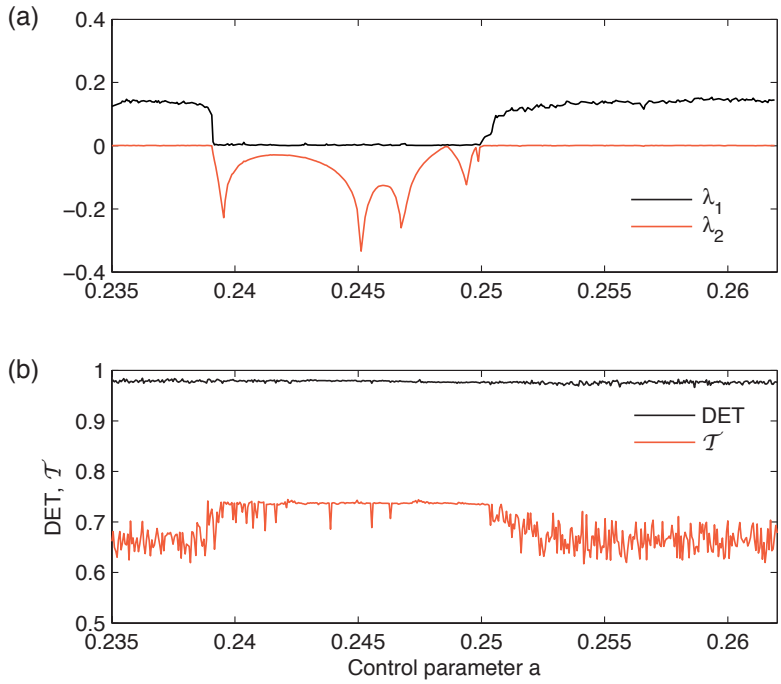

Figure 12.3: (a) The two largest Lyapunov exponents and (b) the recurrence measures DET and $\mathcal{T}$ for the x-component of the Rössler system for varying control parameter a. Within the interval $a = [0.24\ 0.25]$, the dynamics is periodic. Whereas $\mathcal{T}$ indicates the periodic behavior by increased values, it is difficult to detect the periodic window with DET [225].

Table 12.1: Typical values of DET and $\mathcal{T}$ for different dynamical regimes in the Rössler system.

a	DET	$\mathcal{T}$	dynamics
0.235	0.98	0.66	chaotic
0.245	0.98	0.74	periodic
0.260	0.97	0.63	chaotic

12.4 Identification of sudden transitions in paleoclimate

The recurrence network approach has great potential in different applications in many disciplines. Using as a classifier, it can help, e.g., to detect serious diseases, such as preeclampsia [304], to detect epileptic states [188], or to study multiphase fluid flows [113]. Another important application is to detect critical transitions in the dynamics [73, 93, 241]. Such transition detection is of crucial interest in studying variations of the past climate in order to better understand the climate system in general.

In the following we discuss a typical example from paleoclimate research. The investigation of relationships between sea surface temperature (SST) and specific climate responses, like the Asian monsoon system or the thermohaline circulation in the Atlantic, as well as their regime changes, represents an important scientific challenge for understanding the global climate system, its mechanisms, and its related variability. Its better understanding is of crucial importance as non-linear feedback mechanisms and tipping points cause high uncertainty and an unpredictable future for humankind[197, 319].

In paleoclimatology, different archives are used to reconstruct and study climate conditions of the past, as lake [238] and marine sediments [139] or speleothemes [171]. Alkenone remnants in the organic fraction of marine sediments, produced by phytoplankton, can be used to reconstruct SST of the past (alkenone paleothermometry), allowing to study the temperature variability of the oceans [138, 198]. Here we will use a SST reconstruction for the South China Sea and the past 3 Ma derived from alkenone paleothermometry of the Ocean Drilling Programme (ODP) site 1143[198] (Fig. 12.4 and 12.5(a)). The South China Sea is strongly linked to the East Asian Monsoon system (EAM) that consists of a winter part with strong winds and a precipitation related summer part. In general, the East Asian Monsoon is of crucial importance for China's socio-economic behavior, e.g., for agriculture or even for public health by its impact on prevalence of trace elements [26]. The understanding of the mechanism is, therefore, crucial for learning about the past and the future climate and its impacts.

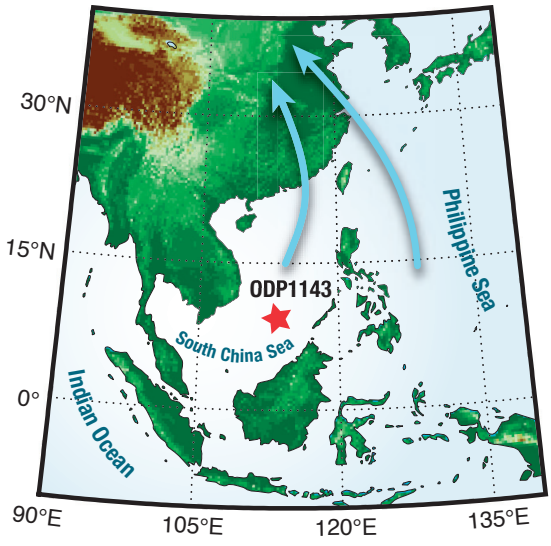

Figure 12.4: Location of the ODP 1143 site in the South China Sea (red star) and main directions of the East Asian Summer Monsoon (blue arrows).

First we are faced with a typical problem in paleoclimatology because the original time series of ODP 1143 is not equally sampled. The sampling time ranges from 0.2 to 28 ka, with a median of 2.1 ka. If applying standard techniques (linear methods or classical RQA) then we would first need to interpolate the time series to an equidistant time axis. However, when using the recurrence network approach, the correct timing of the nodes is not so important (and could even be exchanged without changing the network properties), because it is characterizing the geometrical structure [71, 73, 103].

We calculate the recurrence networks and the transitivity coefficient $\mathcal{T}$ for sliding windows of length 410 ka (thus, with varying number of data points within the windows) and a

moving step of 20 ka (Fig. 12.5). For the phase space reconstruction[286] we choose an embedding dimension of $m = 6$ (as suggested by the false nearest neighbors method[170]). The selection of the time delay is guided by the auto-correlation function and considered to be constant for all time windows to be approximately 20 ka (based on median sampling time within one time window). The threshold is chosen in such a way to preserve a constant recurrence rate of 7.5% [73, 239].

Moreover, we perform a bootstrapping approach using 1,000 resamplings of the windowed time series for preparing an empirical test distribution for $\mathscr{T}$. In this real world example, we use a confidence level of 90%. As we do not know which kinds of dynamical transition are there, we will consider both the upper and the lower confidence level.

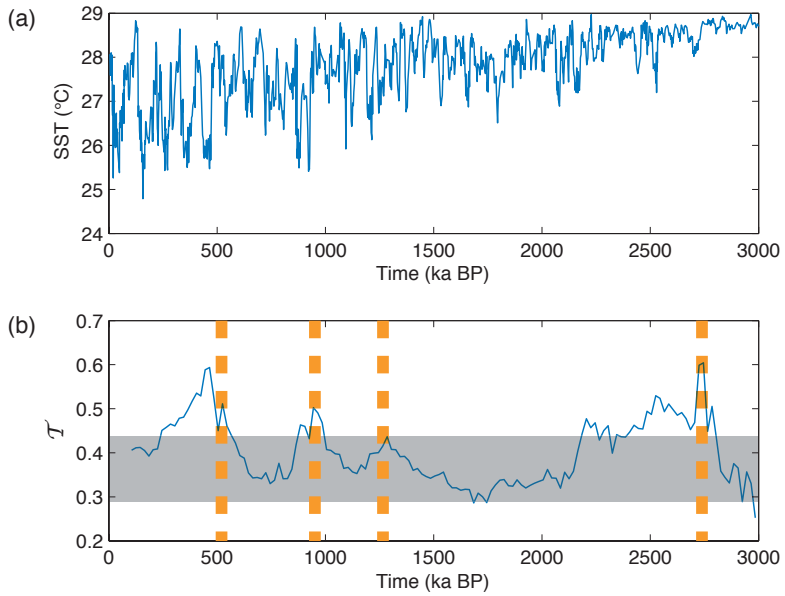

Figure 12.5: (a) Alkenone paleothermometry based SST estimates for the South China Sea and (b) corresponding transitivity coefficient $\mathscr{T}$. Dashed lines mark major climate shifts discussed in the text; the gray shading marks the confidence interval of 90%.

In the last 3 Ma several major and many smaller climate changes have appeared on regional but also global scale. Dramatic climate shifts are related with the Milankovich cycles [3, 135, 252] and major changes in ocean circulation patterns [167]. Due to a transition towards an obliquity-driven climate variability with a 41 ka period around 3.0 Ma ago, a period of warm climate has end and the northern hemisphere glaciation started after 2.8–2.7 Ma [3, 135, 139]. This transition is very well revealed by the significant increase of $\mathscr{T}$ between 2.8 and 2.2 Ma. Based on thorough investigations of loess sediments, it is known that 1.25 Ma ago the intensity of the winter monsoon of the EAM begun to be strongly coupled to global ice-volume change [3]. During this time, $\mathscr{T}$ increased (although not reaching significance). This time also marks the beginning of a transition phase towards glacial-interglacial cycles of 100 ka period (eccentricity dominated period of the Milankovich cycles). This 100 ka period dominance was well established after 0.6 ka and is clearly visible by the increased $\mathscr{T}$ between 0.6 and 0.2 ka [371]. From loess sediments it is also known that the summer monsoon has weakened between 2.0 and 1.5 ka and around 0.7 ka. During these periods, $\mathscr{T}$ shows lower values than during the previously discussed periods. The variation of $\mathscr{T}$ confirms the previous findings of a strong link between the EAM and the Milankovich cycles, in particular of increased and reduced regularity in the climate dynamics

(as presented by the SST and for the considered time scale) during dominant Milankovich cycles and periods of major climate transitions from one to another regime.

Similar conclusions based on $\mathscr{T}$ have been drawn from dust flux records around the African continent [73]. There, it was found that enhanced regular climate dynamics coincides well with lake level high stands in East Africa and, hence, indicating that climate regime transitions have triggered human evolution.

12.5 Complex networks for spatio-temporal analysis of continuous systems

Another important problem in complex systems analysis is the investigation of spatio-temporal dynamics. In the last decade, this field has also benefited from the complex network approach. In particular, its application to climate data in order to uncover climate mechanisms or characteristic spatial patterns and long-range interrelations has drawn attention to complex networks for spatio-temporal analysis of continuous systems. Complex networks are an alternative to EOFs and can shed light on different and complimentary aspects than EOFs. Beginning with the study of Tsonis et al. in 2004 [399], the climate network approach has received more and more interest for spatio-temporal data analysis[85, 256, 365]. The idea is to reconstruct a complex network from spatially embedded time series (in case of climate, e.g., from a surface air temperature field) by measuring the interrelationship $C_{i,j}$ between these time series. The location of the nodes can be arbitrary (e.g., weather stations when using instrumental data) or grid points (e.g., when using model or reanalysis data). In unweighted networks, links represent high correlations between the time series belonging to the nodes, simply considered by applying a threshold T on the interrelation matrix $\mathbf{C}$ (that could be, e.g., Pearson correlation)

$$A_{i,j} = \begin{cases} C_{i,j} & \text{if} \quad C_{i,j} > T, \\ 0 & \text{else.} \end{cases} \tag{12.9}$$

Such networks can be undirected or unweighted (as in Eq. (12.9)), but also directed or weighted.

Within the climate context, such network approach has been applied to study, e.g, climate communities [361, 399], the impact of the El Niño/ Southern Oscillation [433], major heat transport pathways and spatio-temporal scales [70, 85], external and internal atmospheric forcing[64], to create early warning indicators of critical regime shifts [256], or even for model intercomparison [105, 362]. When using Pearson correlation for describing the interrelationships $C_{i,j}$ between the nodes, then the node degree is obviously related to the first EOF [75]. Other network measures, such as betweenness centrality, provide further information that cannot be captured by the EOF analysis [70].

In general, interrelationships between spatially located time series cannot be considered to be only linear. In order to examine nonlinear interrelations, information based measures (e.g., mutual information) were suggested for network reconstruction [13, 65, 69, 147, 329]. In particular when investigating climatological or meteorological phenomena, we often face event-like data, such as daily (or hourly) rainfall series or extreme events time series. For such kind of data, Spearman rank correlation could be used [43]. However, an even more powerful approach for such data is the event synchronization approach [210, 301].

Event synchronization was developed to investigate the synchronous activity of the neurons in the brain [301]. It simply counts the number of temporally coinciding events in two event series x_1 and x_2 by allowing small deviations between the occurrence of the events, i.e., a dynamical delay between them. Let $e_1(m)$ and $e_2(n)$ be the time indices when events appear in x_1 and x_2 and $m, n = 1, \ldots, l$ the number of a specific event (l is the total number

of events in the event series). The waiting time between an event m in x_1 and event n in x_2 is $d_{1,2}(m,n) = e_1(m) - e_2(n)$. If this waiting time $d_{1,2}(m,n)$ is smaller than some dynamical delay $\tau(m,n)$, the two events $e_1(m)$ and $e_2(n)$ are considered to occur synchronously. The dynamical delay $\tau(m,n)$ is the half of the minimal waiting time of subsequent events in both time series around event $e_1(m)$ and $e_2(n)$ and not larger than a given maximal delay $\tau_{\max}$, i.e.,

$$\tau(m,n) = \min \frac{\{d_{11}(m,m-1), d_{11}(m,m+1), d_{22}(n,n-1), d_{22}(n,n+1), 2\tau_{\max}\}}{2}. \quad (12.10)$$

As soon as $|d_{1,2}(m,n)| \leq \tau(m,n)$ (or $0 < d_{1,2}(m,n) \leq \tau(m,n)$), we count it as undirected (or directed) synchronization of events $e_1(m)$ and $e_2(n)$

$$S(m,n) = \begin{cases} 1 & \text{if} \quad |d_{1,2}(m,n)| \leq \tau(m,n) \\ & (\text{or } 0 < d_{1,2}(m,n) \leq \tau(m,n) \text{ in the directed case}), \\ 0 & \text{else.} \end{cases} \quad (12.11)$$

Now we can define the *event synchronization* E between the two event series as the sum of $S(m,n)$

$$E = \sum_{m,n} S(m,n). \quad (12.12)$$

This measure has the advantage that it can quantify interrelations between event-like time series and that it allows for a flexible (dynamical) delay between the events. This is particularly different from the standard approach, where a considered lag (e.g., for cross-correlation) is constant and fixed at each time point.

Applying the event synchronization approach, Eq. (12.12), for comparing spatially embedded time series x_i and x_j at locations (nodes) i and j a network can be reconstructed in the same way as in Eq. (12.9). For selecting the threshold T several approaches are possible. One possibility is based on a significance test, where block bootstrapping can provide an empirical test distribution of the values of $\mathbf{E}$ and a preselected confidence level (e.g., 2% or 5%) provides the threshold T[29]. This procedure ensures that the network links represent only the strongest interrelations between the nodes.

Event synchronization based complex networks have been successfully used to investigate spatio-temporal patterns during the Indian Summer monsoon [210, 211, 365] or to study the origin and propagation of extreme rainfall in South America [28, 29]. Although there is an obvious dominance of climate applications, this approach is also promising for other fields, like plasma, turbulence, cardiological, or brain research.

12.6 Developing a prediction scheme for extreme events

To illustrate the potential of the complex network approach in the context of extreme climate events, we apply the approach on South American extreme rainfall data and use the network topology for developing a prediction scheme for extreme rainfall [29]. During the Australian summer season (December, January, February), the differential heating between land and ocean amplifies the trade winds that enhances transport of moisture from the tropical Atlantic into the tropical Amazonian Basin and, thus, causes extended rainfall[451]. Due to evapotranspiration, wind, and the Andean orographic barrier, this water is first further transported westwards and later, along the Andean mountain ridge, southwards towards the subtropics (Fig. 12.6). Here, a frontal system converging from the South and related with Rossby waves is responsible whether the moisture transport moves further eastward into

the southeastern (SE) Brazil or towards the SE South America (SESA, central Argentinian plains)[218]. This variability of the exit moisture regions is also called South American rainfall dipole [280].

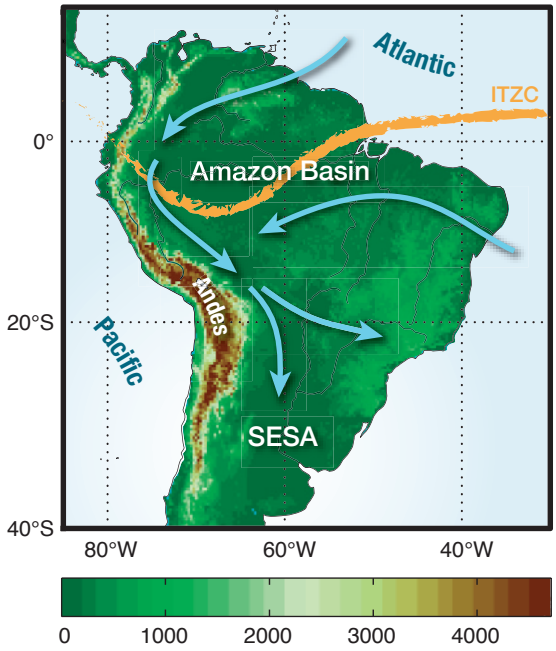

Figure 12.6: Key features of the South American monsoon system. The blue arrows indicate major moisture transport pathways.

The spatio-temporal rainfall data used in our example is collected from the satellite-based Tropical Rainfall Measurement Mission (TRMM 3B42 V7, [153]) with 3-hourly temporal and $0.25° \times 0.25°$ spatial resolution. In the following we will restrict the analysis to the Australian summer season and consider extreme rainfall events that are defined locally by rainfall exceeding the 99th percentile.

Using directed event synchronization, Eqs. (12.11–12.12), of the rainfall extremes we reconstruct weighted and directed networks and calculate the in-strength $\mathscr{S}_i^{\text{in}}$ and out-strength $\mathscr{S}_i^{\text{out}}$, Eq. (12.2). Now we define the *network divergence* as the difference between in- and out-strength:

$$\Delta\mathscr{S}_i = \mathscr{S}_i^{\text{in}} - \mathscr{S}_i^{\text{out}}. \tag{12.13}$$

Negative values of $\Delta\mathscr{S}$ indicate the source regions of extreme events whereas positive values indicate sinks. Surprisingly, we find negative $\Delta\mathscr{S}$ values within the SESA region (Fig. 12.7). This means that this region is a source region of extreme rainfall although it is one of the exit regions of the low-level moisture flow from the Amazon region. Now it would be interesting to see to which other places the extreme rainfall from the SESA region will propagate. For this purpose we consider the in-strength of all nodes conditioned by the source region SESA and call it impact $\mathscr{I}_i(R)$ of region R on node i:

$$\mathscr{I}_i(R) := \frac{1}{|R|}\sum_{j\in R} A_{ij}. \tag{12.14}$$

$|R|$ is the number of nodes within the region of interest R (here SESA). Casually speaking, $\mathscr{I}_i(R)$ measures the amount of extremes at site i that have their origin in region R.

For the SESA region we find high values of $\mathscr{I}_i$(SESA) not only in the direct vicinity of SESA but also at the eastern slopes of the Central Andes (Fig. 12.8). This result suggests that extreme rainfall at the Central (in particular Bolivian) Andes will precede after rainfall events in the SESA region.

The mechanism behind this is an interplay between the orographic barrier, frontal systems approaching from the South, and the southward moisture flow from the Amazon basin resulting in the establishment of a wind channel attracting warm and moist air from the western Amazon region into the SESA region[29]. Here it collides with the cold air of the frontal system from the South and produces extended rainfall. This rainfall propagates together with the northern migration of the frontal system and is bounded in the West by the Andean orography.

This fact can be used for defining a simple but very efficient prediction scheme as explained in detail by Boers et al.[29] The precondition is a low-pressure anomaly in the SESA (geopotential height anomaly < -10 m). As long as this condition is fulfilled, during two days extreme rainfall will appear at the eastern slopes of the Central Andes (in the range along the band that is marked by high values of $\mathscr{I}_i$(SESA)). This rule allows positive prediction rates of 60% and during El Niño conditions even of 90%.

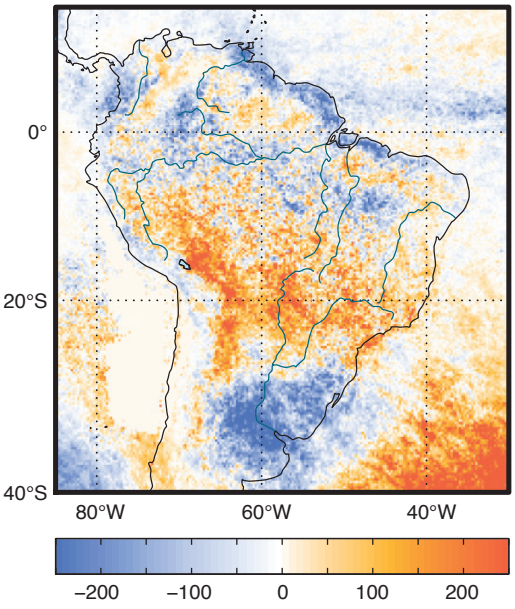

Figure 12.7: Network divergence $\Delta\mathscr{S}$ of extreme rainfall network during Austral winter season. Negative values indicate source and positive values sink regions of extreme rainfall.

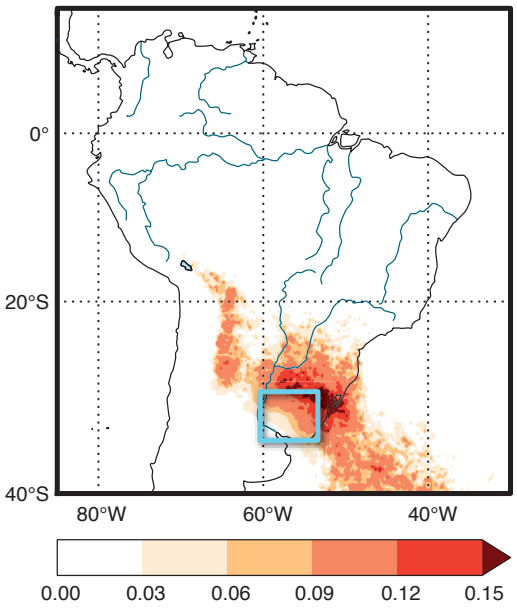

Figure 12.8: Impact $\mathscr{I}_i(R)$ of a region (here SESA, marked by the box) in form of contributing propagated extreme rainfall.

12.7 Conclusion and Outlook

In this paper we have presented an overview of a complex network based method for the analysis of continuous dynamical systems. These methods are mainly basing on two concepts: (i) recurrence networks and (ii) event synchronization. The first one combines recurrence, a basic principle in dynamical systems, with complex networks. This way a rich variety of complex networks characteristics become available for time series analysis. Its potential

have been demonstrated for the identification of sudden transitions from even short time series. The second one identifies events occurring almost synchronized in time in different spatial regions and uses then complex networks for the study of especially spreading and interactions of extreme events. We have uncovered with this technique a mechanism for the formation of extreme floods in the Andes which has led to a very efficient framework for predicting such extreme events. Additionally, this methodology can be used as a new tool for a critical comparison of different models of in particular natural systems. Such complex network approaches have a strong potential for various fields, ranging from turbulence, via neuroscience and medicine to socio-economy.

However, there are several open problems to study in future. One direction is to extend these concepts to multivariate (spatio-temporal) data, e.g., different climatological or physiological parameters. A further challenge is the study of interacting systems of possible very different nature, e.g., climate and renewable energy generation or climate and health, from the network perspective. Another problem is a comprehensive mathematical foundation of these techniques including an appropriate test statistics. Thus, we expect a pursuing and lively development and an increasing number of applications of these rather new concepts in the next future.

Acknowledgement

We would like to acknowledge support from the IRTG 1740/TRP 2011/50151-0, funded by the DFG/FAPESP, the DFG project “Investigation of past and present climate dynamics and its stability by means of a spatio-temporal analysis of climate data using complex networks” (MA 4759/4-1), and project “Gradual environmental change versus single catastrophe – Identifying drivers of mammalian evolution” (SAW-2013-IZW-2), funded by the Leibniz Association (WGL). Moreover, we thank Niklas Boers for calculations and helpful comments.

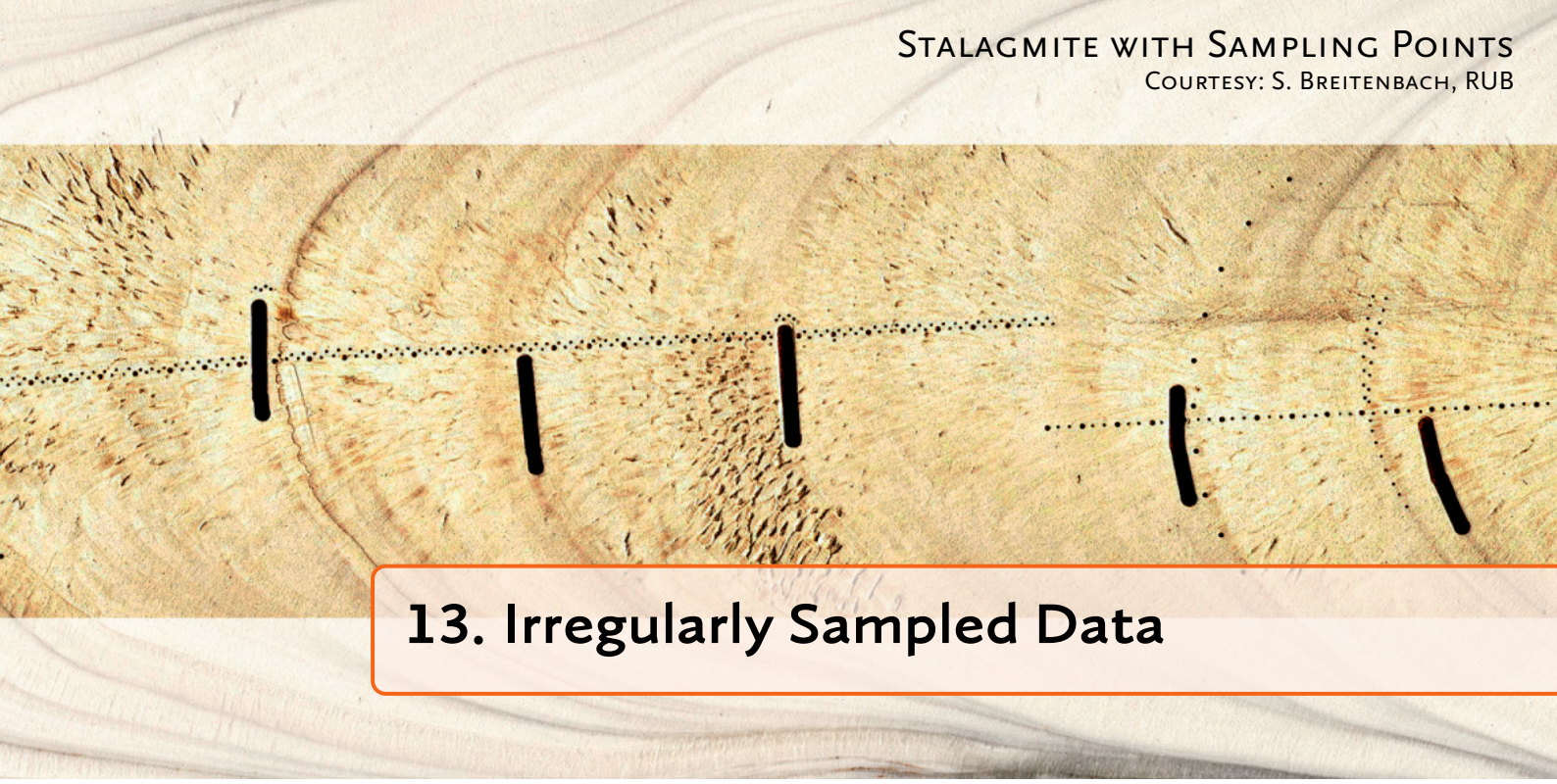

Stalagmite with Sampling Points
Courtesy: S. Breitenbach, RUB

13. Irregularly Sampled Data

Paper 12 D. Eroglu, F. H. McRobie, I. Ozken, T. Stemler, K.-H. Wyrwoll, S. F. M. Breitenbach, N. Marwan, J. Kurths: See-saw relationship of the Holocene East Asian-Australian summer monsoon, Nature Communications, 7, 12929 (2016). DOI:10.1038/ncomms12929

R The presented work in this chapter is a student's paper, where I developed the basic idea of adapting and applying the transformation cost method for irregular data analysis.

Abstract

The East Asian-Indonesian-Australian summer monsoon (EAIASM) links the Earth's hemispheres and provides a heat source that drives global circulation. At seasonal and interseasonal timescales, the summer monsoon of one hemisphere is linked via outflows from the winter monsoon of the opposing hemisphere. Long-term phase relationships between the East Asian summer monsoon (EASM) and the Indonesian-Australian summer monsoon (IASM) are poorly understood, raising questions of long-term adjustments to future greenhouse-triggered climate change and whether these changes could 'lock in' possible IASM and EASM phase relationships in a region dependent on monsoonal rainfall. Here we show that a newly-developed non-linear time series analysis technique allows confident identification of strong vs. weak monsoon phases at millennial to sub-centennial timescales. We find a see-saw relationship over the last 9000 years – with strong and weak monsoons opposingly phased and triggered by solar variations. Our results provide insights into centennial- to millennial-scale relationships within the wider EAIASM regime.

13.1 Introduction

High-resolution speleothem proxy records from cave KNI-51 (15.30°S, 128.61°E) in northwestern Australia and Dongge Cave (DA) (25.28°N, 108.08°E) from southern China (Fig.13.1) provide an outline of the summer monsoon states of the last 9000 years [428]. Details of the U/Th chronology and stable isotope records are given by Denniston et al. [63] and Wang et al. [414] respectively. Both caves are well placed to capture the summer monsoon regimes

located at the end points of the EAIASM system (Fig. 13.1 and Supplementary Figure 13.6 as well as Supplementary Discussion). Stalagmite δ^{18}O time series have prominently been used to identify and study past changes in summer monsoon strength [51]. The δ^{18}O signal recorded in Asian stalagmites depends on multiple factors, including moisture source composition and distance, Rayleigh fractionation during moisture transport, and amount of precipitation. These factors, and thus stalagmite δ^{18}O, are all directly related to summer monsoon strength [35, 63, 169, 313, 353, 376]. A more distal moisture source lengthens the transport pathway to the study site, and Rayleigh distillation during rainout, which in turn leads to more negative δ^{18}O in monsoonal rainfall and associated infiltrating and drip water, ultimately resulting in more negative stalagmite δ^{18}O. Thus, speleothem δ^{18}O is a complex integral of multiple factors, not exclusively reflecting local rainfall amount, but instead providing a valid proxy for monsoon strength in a more general sense [37, 51]. In some instances a pronounced amount effect is observed. For example, in the IASM realm, rainfall δ^{18}O is mainly linked to rainfall amount, as a comparison of rainfall amount and δ^{18}O at the Global Network of Isotopes in Precipitation (GNIP) station at Darwin (approximately 400 km SW of KNI-51) demonstrates ($R^2 = 0.8; p < 0.001$) [63]. Positive δ^{18}O excursions in stalagmites coincident with the timing of graffiti on cave walls telling of massive droughts, exemplify the sensitivity of δ^{18}O to drought in the EASM region [376]. A negative example was found in NE India, where the amount effect is clearly absent[35], but speleothem δ^{18}O still records changes in Indian summer monsoon strength linked to ENSO [268]. Thus, we emphasize again that the δ^{18}O variability acts as a proxy for monsoon strength and not rainfall amount alone. Moreover, advanced nonlinear time series analysis methods can be used to analyse the dynamical imprint of the monsoon activity in the δ^{18}O record and by analysing the time series it is possible to go beyond an interpretation of just the values of δ^{18}O.

The records of DA and KNI-51 are irregularly sampled, i.e., the time between two consecutive measurements is not constant and may vary largely along the length of the record. Most time series analysis methods, however, require regular sampling. Traditionally, some form of interpolation is used to deal with these irregularities, but this introduces additional information into the time series with much higher uncertainty than the real observations [311]. To avoid corrupting the quality of the proxy records, a newly developed method can be used (see [284, 373]) that is based on techniques used for neurological data [407]. This Transformation Cost Time Series (TACTS) method produces a detrended and regularly sampled time series, that can be further analysed with standard time series analysis methods to identify regime changes.

Here we show that the TACS method is well suited to analyse the records of DA and KNI-51 and can detect statistical significant dynamical details of the monsoon dynamics by distinguishing phases of strong/weak monsoon on centennial time scale. This allows us to substantiate and improve previous more qualitative interpretations of the DA and KNI-51 records [63, 152, 414]. Overall the phase relationship between major regime shifts in the two records is anti–correlated (see Fig. 13.2 and Fig. 13.3). Phases of strong (weak) monsoon activity in the northern hemisphere (DA proxy) coincide with phases of weak (strong) monsoon activity in the southern hemisphere (KNI-51 proxy). Solar activity provides a likely driver of this see-saw dynamics and our analysis confirms previous conclusions that solar activity can impact on the overall monsoon dynamics by shifting the position of the the Intertropical Convergence Zone (ITCZ) [414].

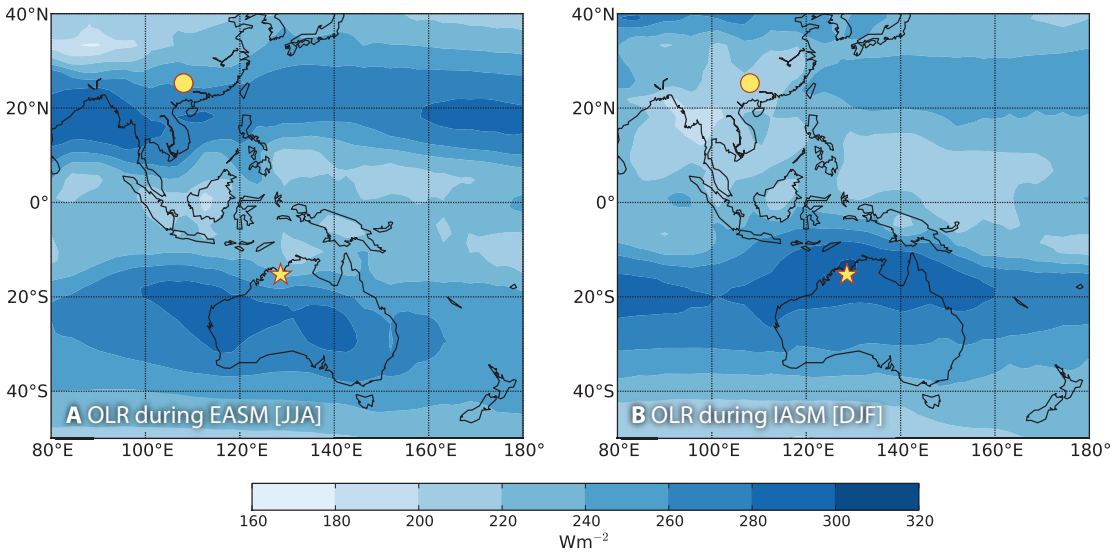

Figure 13.1: **Top of atmosphere outgoing long wave radiation during the monsoon months delimiting its extent** a) East Asian summer monsoon (EASM) during June, July and August (JJA); and b) Indonesian Australian summer monsoon (IASM) during December, January and February (DJF) [164]; Dongge Cave (dot) and KNI-51 cave (star).

13.2 Results

13.2.1 Transitions of the monsoon activity

Analysis of the DA and KNI-51 records reveals alternating periods of statistically significant centennial to millennial-scale strong/weak monsoon states (Fig. 13.2). Strong/weak states are defined as exceeding the confidence bands. Prolonged strong/weak states are identified, and the comparison given by the coloured bands in Fig. 13.2 highlights that our quantitative technique is able to reveal new details of the monsoon dynamics.

The strong/weak regimes identified improve upon previous, qualitative interpretations of the proxy records [63, 152, 414]. Here we provide a detailed discussion of where our method supports, corrects and improves earlier studies. We particularly focus on regimes which are newly identified or previously incorrectly interpreted.

Major strong(weak) phases occur in the northwest Australian summer monsoon domain between 8.5–6.4 ka BP (6.3–5.0 ka BP), 5.0–4.0 ka BP, possibly extending to 3.0 ka BP, (3.0–1.4 ka BP), 1.3–0.9 ka BP, with a transition at 0.9 ka BP to the present regime.

Embedded within these time intervals are additional events of centennial to sub-centennial duration. Unfortunately, the details of the Holocene summer monsoon of northwestern Australia are largely unknown, precluding any comparison of stratigraphic records. Nevertheless, a recent pollen-sediment record from Black Springs (northwestern Kimberley)[249] shows some correspondence to our phase record, but the pollen record is poorly resolved, supported by only four radiocarbon dates. Our analyses offers improved time resolution and greater details of the inherent variability within major monsoon phases.

13.2.2 Cross-hemispheric see-saw dynamics

The Dongge Cave record has been discussed by Wang et al. [414], further developed by Hu et al. [152] and more recently by Zhao et al. [450]. Wang et al. [414] recognised eight weak monsoon events lasting 100 to 500 years: at 0.5 ka BP, 1.6 ka BP, 2.7 ka BP, 4.4 ka BP, 5.5 ka BP, 6.3 ka BP, 7.2 ka BP and 8.3 ka BP. While adding some details, the Hu et al. [152] reconstructions essentially concur with those of Wang et al. [414]. Our results

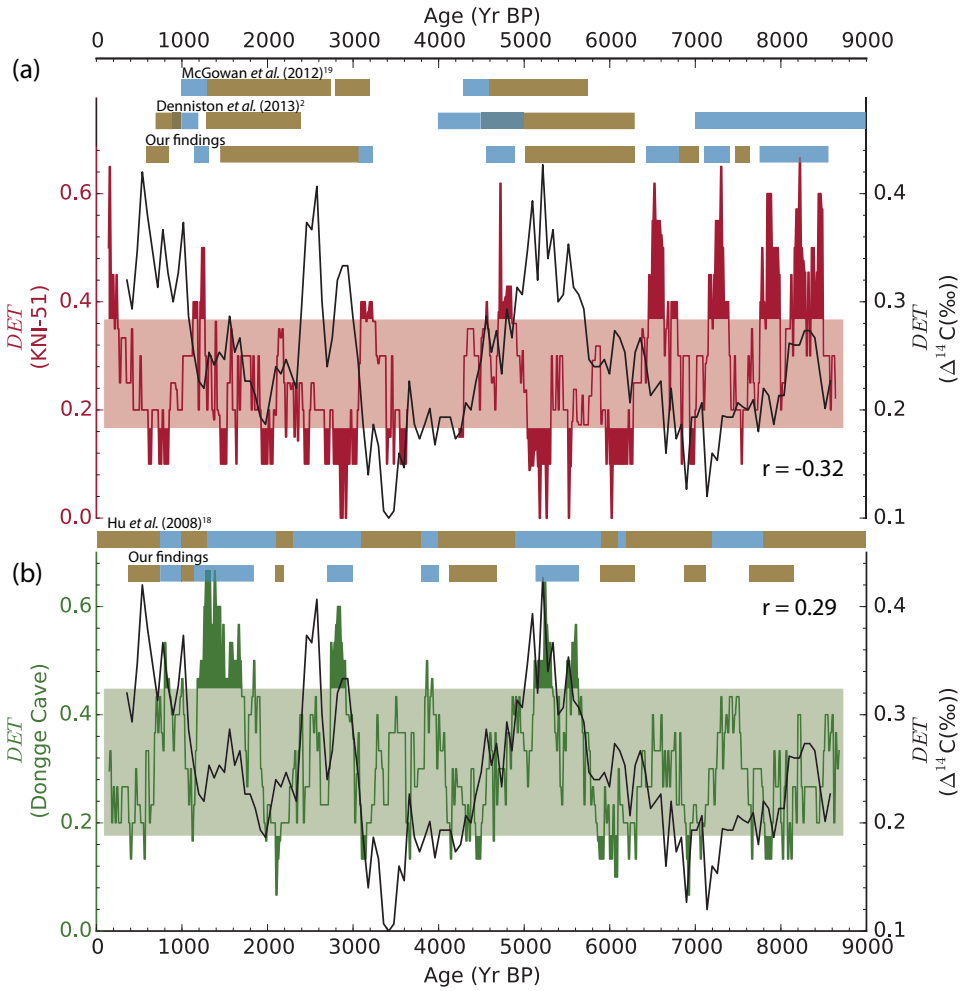

Figure 13.2: **Determinism of the KNI-51 Cave and Dongge Cave records with comparison to previous studies** (a) (red) KNI-51 cave and (b) (green) Dongge Cave (DA). The determinism is calculated from the corresponding transformation costs time series and statistical significance is indicated by the two horizontal bands (see Methods section for details). High (low) determinism values correspond to wet (dry) monsoon regimes. The coloured bands (blue indicating wet regimes; brown, dry) provide a comparison of our findings with those of previous, qualitative studies. In the text we provide a detailed discussion of previously unidentified or incorrectly identified wet and dry regimes uncovered by our method. (black) Determinism of the solar activity proxy Δ^{14} C time series. Cross-correlation between the determinism of the solar activity proxy Δ^{14} C time series and KNI-51 time series is $r = -0.32$, and DA time series is $r = 0.29$ (see Methods section for details).

indicate strong/weak regime intervals between (8.2–7.6 ka BP), 7.6–7.2 ka BP, (7.1–6.9 ka BP), (6.4–5.8 ka BP), 5.8–5.0 ka BP, (5.0–4.0 ka BP), 3.0–2.7 ka BP, (2.2–2.0 ka BP), 1.9–0.8 ka BP and (0.7–0.4 ka BP). A comparative study applying our method on the palaeo Summer Monsoon Index (SMI) derived from sediments of the Qinghai Lake [2] corroborates our findings (see Supplementary Discussion and Supplementary Figure 13.8 for details).

Our analysis has revealed details for KNI-51 and DA not previously recognised (Fig.13.2). In the KNI-51 record two events, absent from Denniston et al. [63], occur at 6.6–6.4 ka BP (weak monsoon/wet) and 7.0–6.8 ka BP (strong monsoon/dry). Furthermore, our results

improve upon the findings of Denniston et al. [63] and McGowan et al. [249] by reclassifying previously misinterpreted regimes. We identify a strong (wet) monsoon regime at 3.2–3.1 ka BP previously interpreted as dry [249] and similarly a weak (dry) regime at 7.6–7.5 ka BP incorrectly claimed to be wet by Denniston et al. [63].

Similarly, the results of our DA analysis contradict the conclusions of Hu et al. [152] for the time periods 6.2–6.1 ka BP (weak) and 7.8–7.6 ka BP (weak). In addition, there are three events identified by Hu et al. that are not statistically significant in our analysis (3.4–3.2 ka BP, 6.9–6.3 ka BP and 8.8–8.2 ka BP). We assert confidence in these revisions, as they are based on a rigorous, quantitative analysis, rather than rudimentary visual comparison of data sets. The detailed comparison of our findings and the literature summary is given in Supplementary Table 13.1 and 13.2.

Moreover, our results reveal a striking strong/weak, opposing relationship between the IASM [63] and EASM [414] (Fig. 13.2). The only time when this see-saw relationship is not observed is during 7.6–7.2 ka BP, when both monsoon records show a 'weak state'. Over the entire time scale, the cross-correlation of the DET time series is −0.27, and while this affirms an antiphased relationship, it does not capture the strong correspondence between the statistically significant strong/weak monsoon states. In fact the antiphased relationship is much stronger, if only the statistical significant parts of the time series are used and the internal variability on sub-centennial to decadal time scales is ignored. This may be calculated using a step function filter, yielding a cross-correlation of −0.33. This can be perceived by simultaneous plot of DET values for KNI-51 and DA in one figure (Fig. 13.3). Comparable results are found in the Qinghai Lake data (SMI) with a cross-correlation of −0.28 (Supplementary Figure 4). Therefore the variability at sub-centennial to decadal time scales in both the DA and KNI-51 records is emphasised; such short-term variability is evident in present day monsoon records from both regions [422].

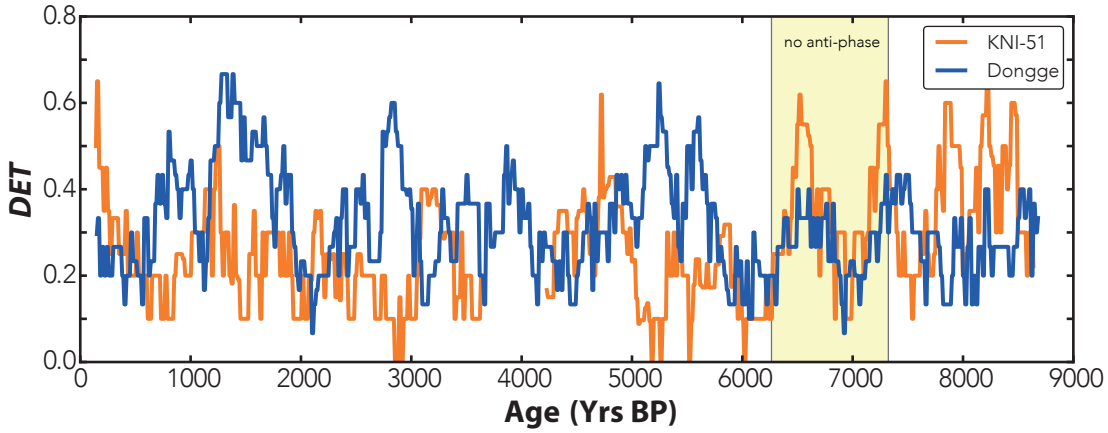

Figure 13.3: **Determinism of KNI-51 and Dongge Cave highlighting the antiphase relationship** There is a gap in the data of KNI-51 around ∼4000 Yr BP. Contrary to the general antiphase relation of the two determinism time series of KNI-51 and Dongge Cave proxies, the region around ∼7000 Yr BP shows a in–phased relationship, highlighted with yellow.

13.2.3 Impact of solar activity on monsoonal see-saw pattern

While the details of the controls and processes determining the function and latitudinal extent of the respective summer monsoons are more complex [48, 247] than simply relating them to the position of the ITCZ, still the ITCZ provides a convenient metric of monsoon extent [247, 342, 410]. For the broader EAIASM history, the displacement of the ITCZ is a driver that has

been advocated in a range of Quaternary paleoclimate studies [126, 127, 251, 330, 436]. The argument recognises that the ITCZ is displaced towards the warmer hemisphere in response to differential cooling [38, 52, 80]. This is an attractive and apparently straightforward explanation, with a caveat that the ITCZ over the region of the West Pacific Warm Pool (i.e. the Maritime Continent) is much less well defined than over the wider Pacific and Indian Oceans, with a more complex south-north (north-south) seasonal migration pattern [155, 410, 429].

In explaining the DA δ^{18}O record, Wang et al. [414] appeal to a likely displacement of the ITCZ driven by solar variability. They use the atmospheric Δ^{14}C record [20] as a proxy for solar activity with which they obtain a correlation of 0.3 with their speleothem δ^{18}O record. The inference is followed by Zhao et al. [450] who support the claim of a concordance of the DA δ^{18}O record with solar variability. We extend this claim further and ask whether the Holocene antiphase relationship that we have uncovered in the summer monsoons of the overall EAIASM is driven by solar variability.

To establish this, we compare the determinism-measure of solar activity with that derived from the EASM and IASM proxy records. The analysis identifies a statistically significant correlation between solar activity and both records from DA with correlation of 0.29 and KNI-51 with correlation of -0.32 (SMI: 0.35; see Supplementary Figure 13.8). Thus, when predictability of solar activity is high (low), the Dongge Cave record indicates a strong (weak) summer monsoon, while northern Australia experiences a weak (strong) summer monsoon. Increased predictability of solar activity corresponds to periods of a consistently high number of solar 'events', increasing the solar irradiance received by the Earth. Positive correlation with the Dongge Cave record therefore indicates a direct control, whereby periods of increased solar activity enhance the summer monsoon over East Asia. The asymmetric response in the Australian monsoon record suggests that periods of increased solar irradiance actually decrease monsoon strength. To explain this, we consider orbital-scale positioning of the ITCZ. Preferential heating of the Northern Hemisphere during periods of high tilt and Northern Hemisphere perihelion, as observed from 9-3 ka, provides a background driver for increased EASM strengthening. At a global scale, there is a northward shift in the ITCZ, weakening monsoon activity over north west Australia. Coupling this shift with solar activity, brief periods of increased irradiance would act to shift the ITCZ further north, and we would therefore expect a stronger EASM and corresponding weak IASM. This mechanism is supported by our analysis, and compounded by the observation that from c.2.5 ka onwards, as orbital controls begin to favour the Southern Hemisphere, correspondence between the determinism-measure of solar activity and EASM and IASM records diminishes. These findings lead us to conclude that solar activity provides a driver in the see-saw relationship observed between the EASM and IASM over the past 9000 years, modulated by orbital-scale ITCZ positioning.

13.3 Discussion

We note that in our interpretation we cannot rule out the likelihood of ENSO events playing a role. Mann et al. using the Zebiak-Cane model of the tropical Pacific ocean-atmosphere system demonstrated that changes in solar radiative forcing provokes an El Nino response [214]. However, the impact of ENSO events on both monsoon regimes is complex and difficult to disentangle. Summer rainfall records from the NW Australian monsoon region lack a significant ENSO signature (http://bom.gov.au/climate/enso/ninocomp.shtml). On the other hand, the Southern Oscillation Index, SOI, has been shown to influence this region [434], where a likely impact can be claimed only for very strong negative/positive SOI values. In contrast, the EASM is clearly influenced by ENSO [191, 268, 412, 427, 432], but with

regional (north-south) differences [427], complex phase-modulation relationships [106, 412] and with specific ENSO events having quite a different regional rainfall expression – for example the 1997/1998 and 1982/1983 events. The role of ENSO is an open question and the lack of well-expressed significant variation of the ENSO during the last 7000 years makes it difficult to answer it [56]. These facts, finally, do not allow to infer a clear ENSO driving of the antiphase relationship between the IASM and the EASM at the Holocene time-scale.

A significant body of work is now available that highlights the impact of solar variability on the tropical atmosphere [195, 203, 253, 349]. This work demonstrates that the Hadley and Walker circulation are affected by solar variability, and through this, trigger an increase in tropical precipitation during periods of high solar activity and an associated change in the position of the ITCZ. Thus, solar variability can force the north-south expansion and contraction of the ITCZ over the region of the East-Asian-Indonesian-Australian-Monsoon region [435]. We demonstrate that solar variability can impact summer monsoon strength, and more importantly provides the control of the antiphase relationship between the EASM and IASM over the last 9000 years. Our results reveal a strong coupling between the monsoons of the two hemispheres, expressed as a seesaw relationship, and driven by decadal to centennialscale variations in solar activity. A full understanding of how solar variability can drive the monsoon response requires focused model studies. From these will emerge the likelihood of disentangling the overall functioning of the EAIASM regime, forming a further step in understanding how this regime will respond to present-day Greenhouse forcing, which may help to secure the future of people living in the region.

13.4 Methods

13.4.1 TACTS method

In essence, the TACTS method determines the 'cost' of transforming one segment of a record into the following segment. For this transformation we allow three possible modifications: first changing the amplitude of a data point, second shifting a data point in time, and third creating or deleting a data point. The 'cost' for changing the amplitude and shifting a data point is linearly dependent on the size of the modification. However, creating and deleting data points should be 'expensive' enough to not favour this modification over the other two points.

Many time series, e.g., palaeoclimate proxy records, show cumulative trends which usually need to be removed in a preprocessing step before time series analysis. A common procedure for regularly sampled time series is to apply a difference detrending filter, $\Delta x = x(t) - x(t-1)$, simply taking the difference between consecutive points. The TACTS method is a similar approach for detrending but for irregularly sampled time series. Here the difference between subsequent sequences is expressed by an associated transformation cost as explained below (see Supplementary Discussion for details).

To calculate the transformation cost time series we determine the cost for transformation of one segment into another for two successive segments of a time series. Treating each observation as an 'event', we seek to transform the events in the first segment into those of the second. For a single transformation, this cost is a generalised distance between these two segments. Therefore, as a distance, the cost must be a positive number, symmetrical (i.e. transforming the first into the second is the same as transforming the second into the first), and must satisfy the triangle inequality.

The cost associated with each transformation is given by:

$$\begin{aligned} p(c) \quad = \quad & \sum_{(\alpha,\beta)\in C} \{\lambda_0 |t_a(\alpha) - t_b(\beta)| + \\ & \frac{1}{m}\sum_{k=1}^{m} \lambda_k |L_{a,k}(\alpha) - L_{b,k}(\beta)|\} + \\ & \lambda_S(|I| + |J| - 2|C|), \end{aligned} \tag{13.1}$$

where I and J are a set of indices of the events in starting set S_a and the final set S_b, respectively. These sets – S_a and S_b – correspond to the events in the two time series segments. The first summation quantifies the cost associated with shifting events in time. We sum over the pairs $(\alpha, \beta) \in C$, where the set C comprises the points that need to be shifted in time. α and β denote the αth event in S_a and βth event in S_b. The coefficient λ_0 is the cost factor for time shifts. The second summation calculates the cost due to changing the amplitude of events. This involves the difference $|L_{a,k}(\alpha) - L_{b,k}(\beta)|$, where $L_{a,k}(\alpha)$ is the amplitude of the αth event in S_a. The parameter λ_k has the unit of amplitude^{-1} and the sum is over the different components of the amplitude. That is, if we are dealing with one dimensional data $m = 1$, while for a three dimensional phase space m would be three. The last terms in the cost function deal with the events not in C which have to be added or deleted. Note that $|\cdot|$ denotes the size of the set and λ_S is the cost parameter for this operation. Suzuki *et al.* omitted this parameter, since they chose a cost of one for such an operation [373].

We determine the cost factors λ_0, λ_k based on the time series at hand:

$$\lambda_0 = \frac{M}{\text{total time}} \tag{13.2a}$$

$$\lambda_k = \frac{M-1}{\sum_i^{M-1} |x_i - x_{i+1}|}, \tag{13.2b}$$

where x_i is the amplitude of ith element and M is the total number of events in the time series. Note that λ_0 is the mean event frequency and λ_k is the inverse of the average amplitude difference.

The cost factor λ_S is an optimisation parameter. We constrain $\lambda_S \in [0, 4]$ and explore the costs of deleting or adding an event to our time series. If our time series consists of $n+1$ segments of equal length, we can calculate n costs for each individual transformation of the segments. Assuming that the costs are linearly independent, the central limit theorem indicates that the distribution of the costs should be a normal distribution. In particular, when dealing with non-stationary data we find that changing λ_S such that the distribution becomes normal greatly improves the skill of our time series analysis method.

In Fig. 13.4 we give an illustration of how to perform this transformation. Recall that the transformation is done by 3 elementary steps: (i) shifting an event in time; (ii) changing the amplitude of the event; and (iii) creating or deleting an event. The figure outlines the steps required to transform the top time series segment into the bottom one. This transformation consists of 7 elemental steps. Moves 1 and 2 move the first and second event to the right and, in addition, adjust their magnitude, i.e. a combination of the two elementary steps (i) and (ii). In move 3 the last event is deleted (that is, elementary step (iii)). As we can see it takes 4 additional elementary steps (combinations of (i) and (ii)) to transform the starting time series into the target time series.

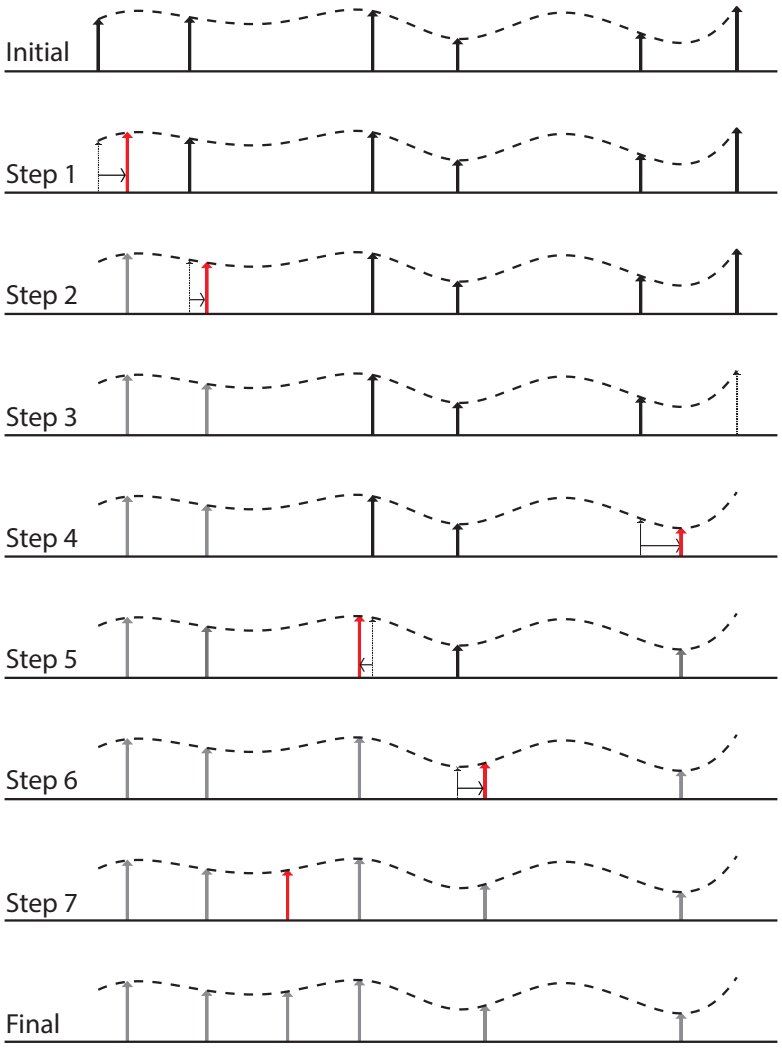

Figure 13.4: **Illustration of the transformation cost time series method** The true time series from which the two time series are sampled is indicated by the dashed line. The initial time series segment (top) is transformed into the final time series segment (bottom) in seven steps. Note that after seven steps the segment is identical to the final target time series. The steps 1, 2, 4, 5, 6 are combinations of the elementary operations (i) time shift and (ii) adjusting the amplitude (first two terms of eq. (13.2)) while in step 3 one event is deleted and therefore the (iii) elementary operation was applied (last term of eq. (13.2)).

13.4.2 Recurrence plot analysis

The resulting regularly sampled cost time series is analysed using recurrence plot analysis to derive the recurrence quantification measure determinism (DET) [239]. DET is a measure of predictability well suited to detect regime changes in time series. DET characterises a specific, recurrence-based dynamical property, independent of the state of the system (i.e., the amplitude of the δ^{18}O at a given time). Therefore, DET values are not directly related to a specific state value such as strong or weak monsoon regime). Nevertheless, it is possible that certain regime states (e.g., a strong monsoon regimes) are linked to a characteristic recurrence pattern, e.g., a more regular and periodic dynamics (enhanced monsoon regimes) or less periodic and less predictable dynamics (weak monsoon or monsoon failure). Such

relationships between states and recurrence properties seem typical in the climate system, where, e.g., cooling events have been linked to less predictable (less regular) climate dynamics [92, 284]. Depending on geographic location and regional climate mechanisms, such relationships can differ significantly and can even be opposite. Based on information from literature, we are able to link the characteristic dynamical property of determinism to a certain climate regime, such as dry or wet, for the considered proxy records.

For each proxy record, the transformation cost time series is divided into segment sizes of 20 years containing, on average, 4 to 5 points. The final results shown in Fig. 13.2 are relatively insensitive to the choice of segment size. The proportionality parameters for modifications (i) and (ii) are determined from the proxy records and are related to the average amplitude and sampling time. The creation and deletion cost factor λ is our optimisation parameter, chosen relative to the other parameters. Determining the costs of transformation provides a measure of how close one segment is to the following one and produces a regularly sampled transformation cost time series with a temporal resolution of 20 years. Using recurrence plot analysis, as described below, we are able to quantify the predictability of each segment by deriving the determinism [239]. Abrupt transitions into or out of a 'wet' or 'dry' state are hard to predict, while behaviour within a regime follows a somewhat similar pattern throughout. As a result, determinism is particularly effective at identifying regime changes.

Recurrence plots visualise a fundamental property of dynamical systems – namely, when a the system 'repeats' itself, returning to a previous state. Formally, for a set of observations $\vec{x}_i$ for $i = 1, \ldots, N$ this is defined as

$$R_{i,j}(\varepsilon) = \Theta(\varepsilon - \|\vec{x}_i - \vec{x}_j\|) \quad i, j = 1, \ldots, N \tag{13.3}$$

where ε is some threshold distance, $\|\cdot\|$ is some distance measure, and $\Theta(y) = 1$ if $y \geq 0$ and 0 otherwise [239]. This method is well suited to capture regime changes, as such an extreme event would result in a sudden reduction in the number of recurring events. Plotting this matrix allows visual analysis of the system, and from this quantitative measures can be derived. Diagonal structures within the plot, running parallel to the main diagonal (bottom left to top right), indicate sections of the trajectory with locally similar paths. Calculating the fraction of points in the recurrence plot that form diagonal lines with respect to all points gives us the measure determinism. This is a measure of the amount of predictability within the system, as stochastic or chaotic systems result in none or only short diagonals. For the selected threshold distance ε, a histogram of diagonal lengths, $P(\varepsilon, l)$, is derived and a minimal diagonal length, l_{min}, is set. Determinism is then given by

$$DET = \frac{\Sigma_{l=l_{min}}^{N} lP(\varepsilon, l)}{\Sigma_{l=1}^{N} lP(\varepsilon, l)} \tag{13.4}$$

In this analysis, the recurrence plot is derived using the Euclidean distance norm and ε-threshold distance is chosen adaptively to ensure a sensible density of 'ones' in the RP, fixed at 10%. In the determinism calculation, we take l_{min} to be 2. These parameters were selected to ensure a balance between stability and, particularly in the case of the threshold distance, the inclusion of enough data points for the recurrence structure of the underlying system to be captured. For details on the embedding required to transform time series data into a trajectory in phase space see [165].

The variation of a quantitative recurrence measure, such as DET, has to be tested whether its change is significant or not. We follow the approach by Marwan et al. and apply a bootstrapping technique [235]. The basic idea is that the dynamics of the system does not change over time. Such a change is usually measured by a sliding window approach,

where DET_i means the recurrence measure calculated in the ith window. Within these windows i, we also have the histograms of diagonal lengths, $P_i(\varepsilon, l)$. We now bootstrap the lengths l from the histograms of all windows and use these lengths to calculate DET of this bootstrapped histogram, allowing an average picture of the DET measure for the whole time. Repeating this procedure N times, we get an empirical test distribution for DET. The 5% and 95% quantiles are used to infer confidence (90%) about the variation of DET and allows us to judge whether the found variability of the measure DET is significantly different from an unchanged dynamics (i.e., whether a regime transition occurs) [235].

13.4.3 Cross correlation of two irregularly sampled time series

To compare the KNI-51 and Dongge Cave records with solar variability (see Supplementary Figure 13.5 (a,b)), we correlate these records with the atmospheric $\Delta^{14}C$ record compiled by Stuiver et al. [370] (see Supplementary Figure 13.5 (c)). This record, spanning 9,700 years, was compiled from radiocarbon tree ring ages and is a widely used proxy for solar irradiance with lower $\Delta^{14}C$ values inferring increased solar irradiance [414]. This record is already sampled at regular time intervals so we do not need to apply the transformation cost function. However, the time steps of this data set do not align with the determinism time series generated from the speleothem records. We cannot, therefore, calculate cross correlation without transforming the data sets again.

Interpolation is commonly used in such a scenario, but this creates artificial, and necessarily uncertain, data points in the time series. A Gaussian kernel based cross correlation (gXCF) has been demonstrated to reduce such biases relative to linear interpolation, as well as Lomb-Scargle, rectangular and quasi-sinusoidal kernel based cross correlation estimators [311]. We therefore use gXCF as our estimator of the similarity between the speleothem and solar activity data sets.

The benefit of kernel based techniques is that, rather than introducing new data to the time series, the two data sets are 'matched' using a weighting function. Pearson cross–correlation takes the sum of the product of paired data points in two time series X and Y. However, using the kernel, each data point in time series X is multiplied by every data point in Y, but with a weighting function dependent on the distance between the time that these observations occurred. Kernel based cross correlation is therefore given by

$$\hat{\rho}_{x,y} = \frac{\sum_i^{N_x} \sum_j^{N_y} x_i y_j b(t_j^y - t_i^x)}{\sum_i^{N_x} \sum_j^{N_y} b(t_j^y - t_i^x)} \tag{13.5}$$

where $b(t_j^y - t_i^x)$ is the kernel, determining how much weight to give to the product of two observations x_i and y_j, based on the time gap between them.

In the case of gXCF, the kernel is

$$b = \frac{1}{\sqrt{2\pi}\sigma} e^{-|d|^2/2\sigma^2} \tag{13.6}$$

where d is the distance between the observation times Δt_{ij}^{xy} and σ is the standard deviation of the kernel distribution, which scales the kernel. As there is no theory detailing the best choice of scaling parameter σ, we use $\sigma = \Delta t^{xy}/4$ as per Rehfeld et al. [311].

13.4.4 Data availability

The proxies from Dongge cave (δ^{18}O) and solar activity (δ^{14}C) are published/available data sets. δ^{18}O proxy from KNI-51 cave, Kimberley is available from the authors. Requests for the TACTS of proxies can be sent to D.E (eroglu@pik-potsdam.de).

Acknowledgement

D.E. and N.M. acknowledge support by the Leibniz Association (WGL) under Grant No. SAW-2013-IZW-2. F.H.M.'s research is funded through an Australian Postgraduate Award. I.O. is financially supported from TUBITAK under 2214/A program and by Ege University under the Research Project number 2015FEN028. This study received funding from the European Union's Horizon 2020 Research and Innovation programme under the Marie Skłodowska-Curie grant agreement No 691037. The publication of this article was funded by the Open Access Fund of the Leibniz Association. K.H.W. wishes to thank Rhawn F. Denniston for his wider involvement in the northwest Australian monsoon project and the Kimberley Foundation Australia for financial support for this project and Paul Wyrwoll for helpful comments. We are also grateful to Yanjun Cai for providing the Lake Qinghai record.

Author contributions

D.E., I.O., T.S. and N.M. developed the methods. D.E., F.H.M. and I.O. analyzed the data. K.H.W. and S.F.M.B. provided the data and interpreted the results with help of F.H.M. J.K. supervised the project. All authors contributed to the final manuscript.

Supplementary Material

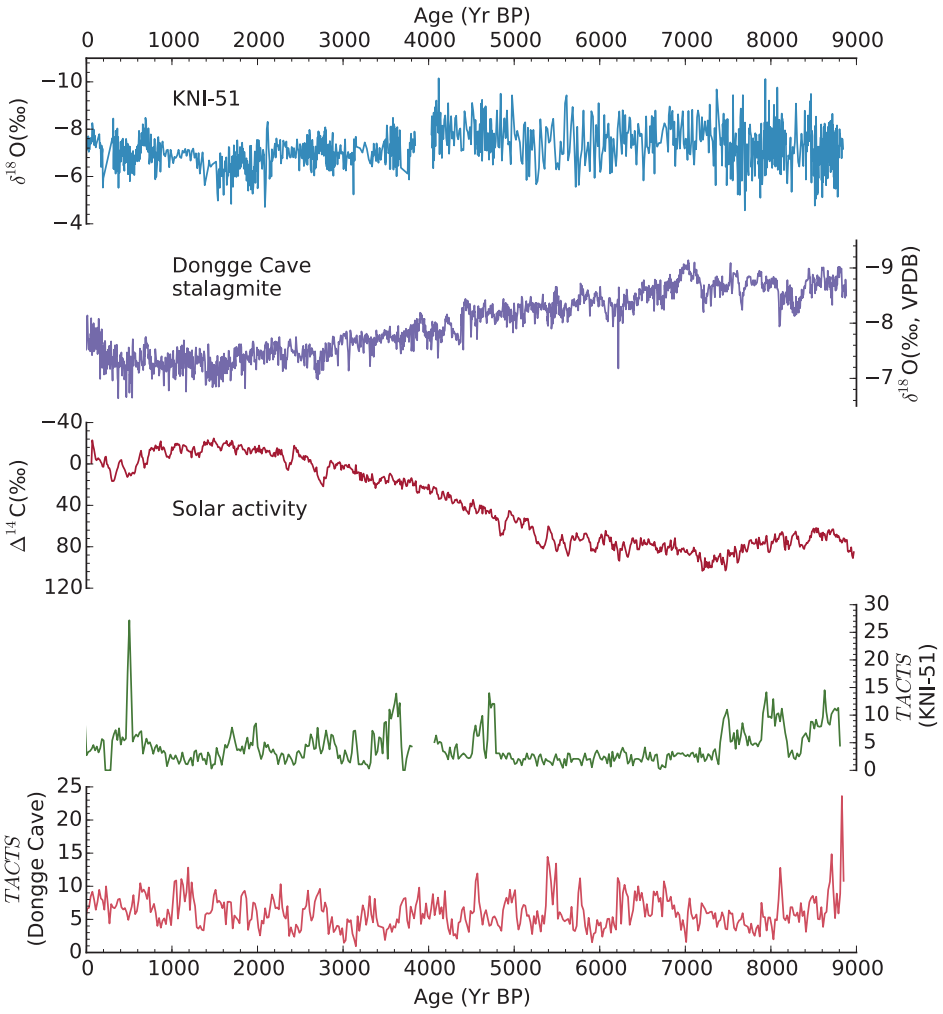

Supplementary Figure 13.5: **The proxies in the manuscript and their transformation cost time series.** δ^{18} O records of (a) KNI-51 and (b) Dongge Cave. (c) atmospheric $\Delta^{14}C$ record compiled by Stuiver et al. [370] and the transformation cost time series of (d) KNI-51 and (e) Dongge Cave determined by application of eq. (1) and (2) (equations in the main text).

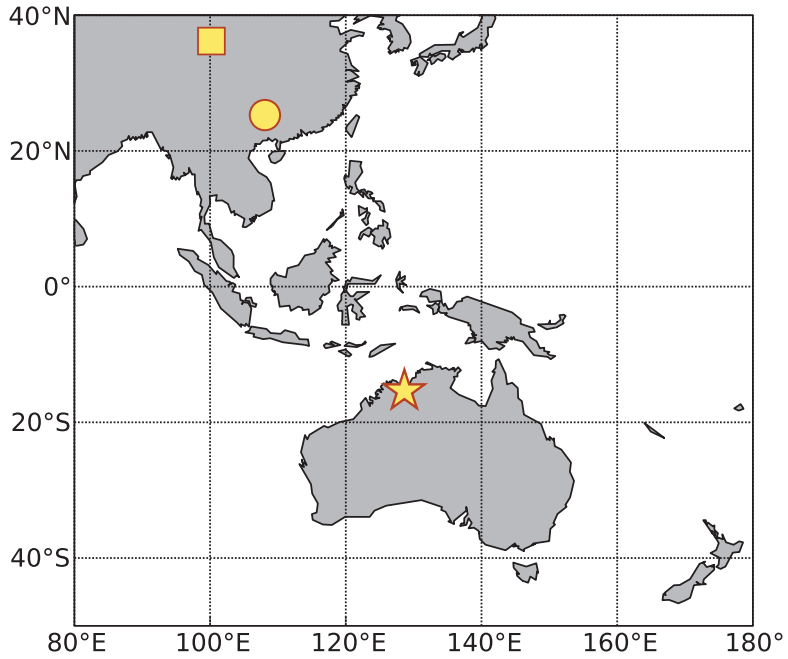

Supplementary Figure 13.6: **Location of the different proxies used in this study.** Dongge cave (circle), KNI-51 cave (star), and Qinghai Lake (square).

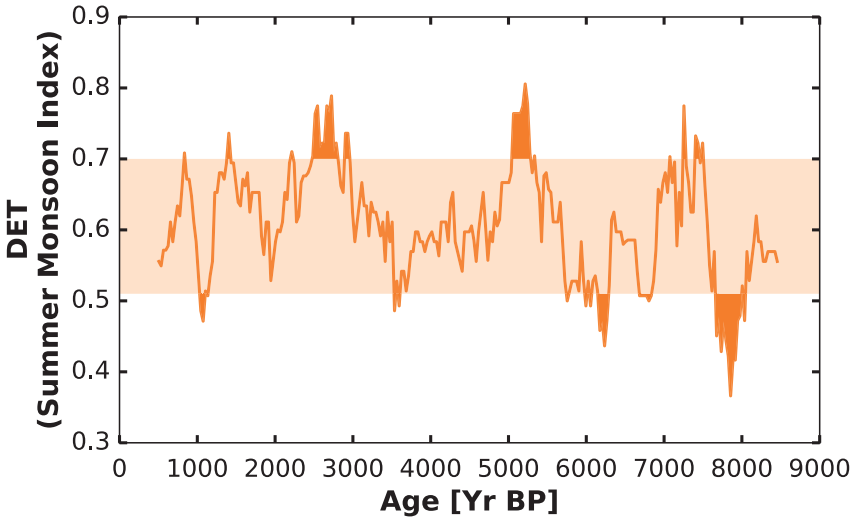

Supplementary Figure 13.7: **Determinism of the Summer Monsoon Index from Qinghai Lake.** Statistical significance is indicated by the horizontal band.

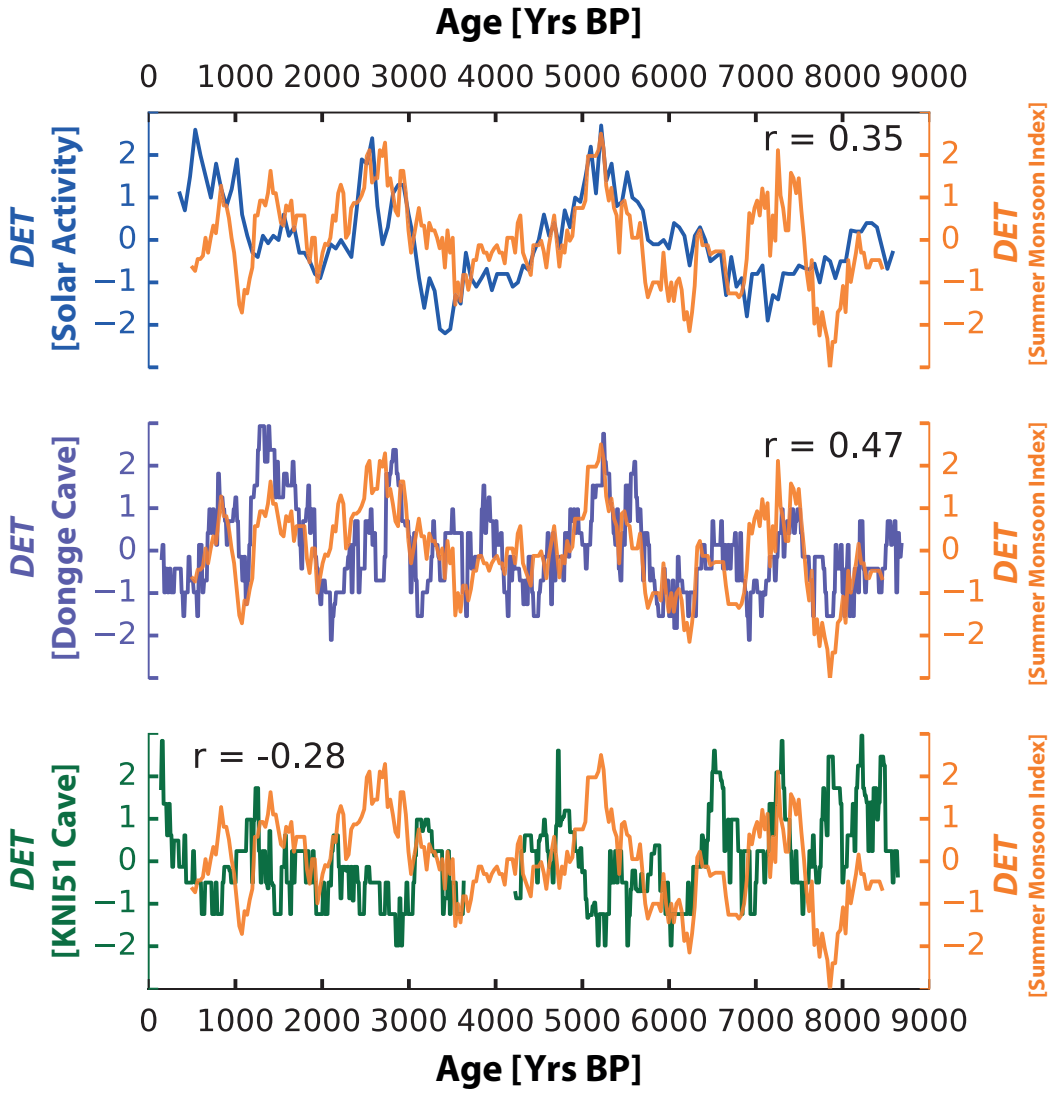

Supplementary Figure 13.8: **The analysis of SMI data from Qinghai Lake and its comparison with other proxies in the manuscript.** Solar activity, Dongge and KNI51 Caves.

North Australia			
Regimes	**Denniston et al. (2013)**	**McGowan et al. (2012)**	**Our Findings**
	KNI-51	**Pollen Data - Kimberley**	**KNI-51**
Strong Monsoon	9.0-7.0 ka BP 5.0-4.0 ka BP 1.2-0.9 ka BP	4.6-4.3 ka BP 1.3-1.0 ka BP	8.5-7.8 ka BP 7.4-7.1 ka BP 6.8-6.4 ka BP 4.9-4.6 ka BP 3.2-3.0 ka BP 1.3-1.1 ka BP
Weak Monsoon	6.3-4.5 ka BP 2.4-1.3 ka BP 1.0-0.7 ka BP	5.75-4.6 ka BP 3.20-2.8 ka BP 2.75-1.3 kaBP	7.6-7.5 ka BP 7.0-6.8 ka BP 6.2-5.0 ka BP 3.0-1.4 ka BP 0.8-0.6 ka BP

South China			
Regimes	**Hu et al. (2008)**	**Our Findings**	
	Heshang and Dongge Caves	**Dongge Cave**	**Qinghai Lake**
Strong Monsoon	7.8-7.2 ka BP 6.2-6.1 ka BP 5.9-4.9 ka BP 4.0-3.9 ka BP 3.1-2.3 ka BP 2.1-1.3 ka BP 1.0-0.7 ka BP	5.6-5.2 ka BP 4.0-3.8 ka BP 3.0-2.6 ka BP 2.8-1.2 ka BP 1.0-0.7 ka BP	7.5-7.2 ka BP 5.35-5.0 ka BP 2.9-2.2 ka BP 1.4-1.3 ka BP 0.84-0.83 ka BP
Weak Monsoon	9.0-7.8 ka BP 7.2-6.2 ka BP 6.1-5.9 ka BP 4.9-4.0 ka BP 3.8-3.1 ka BP 2.3-2.1 ka BP 1.3-1.0 ka BP 0.7-0.0 ka BP	8.2-7.6 ka BP 7.2-6.8 ka BP 6.3-5.9 ka BP 4.6-4.1 ka BP 2.2-2.1 ka BP 1.2-1.0 ka BP 0.7-0.4 ka BP	8.1-7.6 ka BP 6.8-6.6 ka BP 6.2-5.9 ka BP 3.6-3.5 ka BP 1.15-1.0 ka BP

Supplementary Table 13.1: **Comparison of our and previous results.** Results for Southern China

North Australia			
Regimes	**Denniston et al. (2013)**	**McGowan et al. (2012)**	**Our Findings**
	KNI-51	**Pollen Data - Kimberley**	**KNI-51**
Strong Monsoon	9.0-7.0 ka BP 5.0-4.0 ka BP 1.2-0.9 ka BP	4.6-4.3 ka BP 1.3-1.0 ka BP	8.5-7.8 ka BP 7.4-7.1 ka BP 6.8-6.4 ka BP 4.9-4.6 ka BP 3.2-3.0 ka BP 1.3-1.1 ka BP
Weak Monsoon	6.3-4.5 ka BP 2.4-1.3 ka BP 1.0-0.7 ka BP	5.75-4.6 ka BP 3.20-2.8 ka BP 2.75-1.3 kaBP	7.6-7.5 ka BP 7.0-6.8 ka BP 6.2-5.0 ka BP 3.0-1.4 ka BP 0.8-0.6 ka BP

South China			
Regimes	**Hu et al. (2008)**	**Our Findings**	
	Heshang and Dongge Caves	**Dongge Cave**	**Qinghai Lake**
Strong Monsoon	7.8-7.2 ka BP 6.2-6.1 ka BP 5.9-4.9 ka BP 4.0-3.9 ka BP 3.1-2.3 ka BP 2.1-1.3 ka BP 1.0-0.7 ka BP	5.6-5.2 ka BP 4.0-3.8 ka BP 3.0-2.6 ka BP 2.8-1.2 ka BP 1.0-0.7 ka BP	7.5-7.2 ka BP 5.35-5.0 ka BP 2.9-2.2 ka BP 1.4-1.3 ka BP 0.84-0.83 ka BP
Weak Monsoon	9.0-7.8 ka BP 7.2-6.2 ka BP 6.1-5.9 ka BP 4.9-4.0 ka BP 3.8-3.1 ka BP 2.3-2.1 ka BP 1.3-1.0 ka BP 0.7-0.0 ka BP	8.2-7.6 ka BP 7.2-6.8 ka BP 6.3-5.9 ka BP 4.6-4.1 ka BP 2.2-2.1 ka BP 1.2-1.0 ka BP 0.7-0.4 ka BP	8.1-7.6 ka BP 6.8-6.6 ka BP 6.2-5.9 ka BP 3.6-3.5 ka BP 1.15-1.0 ka BP

Supplementary Table 13.2: **Comparison of our and previous results.** Results for North Australia

Supplementary Discussion

Pre-processing paleoclimate proxy data

Paleoclimate proxy records commonly display long-term trends, such as in the Dongge Cave record [413]. Taking the difference between neighbouring data points in the sequence detrends the time series, and simultaneously transforms it such that it describes a different property of the underlying system. If we think of the original data set as corresponding to spatial 'positions' then this difference time series would give us the velocities. Such a method is common in time series analysis. In the paleoclimate context we are often faced with data sets with irregularly spaced time intervals between observations. We therefore employ the transformation cost function as our 'difference' metric. This not only detrends the data set, but produces a regularly spaced time series. We are now able to employ a number of well known techniques without having to account for unequal time steps.

Regional climate of Australian and Chinese proxy records

We use the high resolution speleothem paleoproxy records from cave KNI-51 (15.30°S, 128.61°E) in northwestern Australia and from Dongge Cave (DA) (25.28°N, 108.08°E) from southern China to outline the summer monsoon states of the last c. 9 ka. The details of the U/Th chronology and associated stable isotope records are provided by Denniston et al. [63] and Wang et al. [413] respectively. KNI-51 is located at the northern limits of Western Australia. Nearby Carlton Hill (15.49°S, 128.53°E) has a precipitation record extending back to 1897, with a mean annual rainfall over this period of 830mm (highest 1500mm/lowest 378mm) and an average 690 mm (83%) received during the monsoon season of December through to March [254]. Mean annual precipitation near Dongge Cave is 1753 mm with 80% of the rainfall falling during the monsoon season – May to October [84]. Both locations are well placed to capture the respective summer monsoon regimes located at the end points of the broader EAIASM system.

Summer Monsoon Index

In order to evaluate our findings we compare them with another proxy record from China, the summer monsoon index (SMI) (Supplementary Fig. 13.6). This index was derived from a ^{14}C-dated sediment record from Qinghai Lake (37°N, 100°E) [2]. The SMI time series is regularly sampled, therefore it is not necessary to apply TACTS, and the usual difference filter has been applied directly. As the two datasets in the manuscript, KNI-51 and DA, SMI is well placed to capture the respective summer monsoon regime. Quinghai lake is located at the northern end point of the broader EAIASM system and sensitive to EASM dynamics [2].

Our analysis of the lacustrine SMI strongly corroborates our results strongly and reveals alternating periods of statistically significant strong/weak monsoon activity states of centennial to millennial duration as in other proxies (see Supplementary Fig. 13.7 and Fig. 2 in main text). The shaded band in the figure depict the 90% confidence interval, with strong/weak monsoon states defined as exceeding these bands (see Recurrence plots, determinism and significance test section). Prolonged strong/weak states are clearly identified (Supplementary Tabs. 13.1 and 13.2). The direct comparison of SMI with DA, KNI-51, as well as with solar variation confirm our findings (Supplementary Fig.13.8).

14. Data with Uncertainties

Paper 13 B. Goswami, N. Boers, A. Rheinwalt, N. Marwan, J. Heitzig, S. F. M. Breitenbach, J. Kurths: Abrupt transitions in time series with uncertainties, Nature Communications, 9, 48 (2018). DOI:10.1038/s41467-017-02456-6

R The presented work in this chapter is postdoc research, where I suggested and developed the basic idea of using a real time axis and transform the age uncertainties into uncertainties of the proxy values.

14.1 Abstract

The identification of abrupt transitions is a key question in various disciplines such as (paleo)climate [220, 310], ecology [4], and finance [150]. Existing transition detection methods, however, do not rigorously account for time series uncertainties, often assuming them to be independently and identically distributed. Here, we introduce a new approach suited to handle uncertainties by representing the time series as a time-ordered sequence of probability densities. We show how abrupt transitions can be detected in such a probability density series using the community structure [272] of networks representing probabilities of recurrence. Using a synthetic example, we demonstrate that our approach allows more reliable detection of abrupt transitions. We then consider three real-world cases: financial stock indices, sea surface temperature (SST) anomalies from the Niño 3.4 region, and paleoclimatic proxies. The identified transitions in the stock indices relate to well-known periods of politico-economic volatility. In the SST example, the detected transitions coincide significantly to periods of 'phase-locking' between the Pacific Decadal Oscillation (PDO) and the El Niño Southern Oscillation (ENSO), uncovering a new aspect in the modulation of ENSO by PDO. For the paleoclimate proxies, we provide for the first time a clear, 'uncertainty-aware' framework that validates the hypothesis that ice rafting events in the North Atlantic [31], known as Bond Events (BEs), are synchronous with a weakening of the Asian summer monsoon [414] (ASM). Our approach also reveals previously unreported ASM transitions unrelated to BEs. We further establish unambiguously that time series uncertainties prevent the detection of the '4.2k event' in the Qunf cave speleothem record.

14.2 Introduction

Time series analysis is an indispensible framework that helps us to understand dynamical systems based on temporally ordered observations [165]; and uncertainties should, in principle, form a crucial part of our inferences made from time series. An important question addressed in time series analysis is the identification of *abrupt transitions*—time points when the observable suddenly shifts from one type of behaviour to another. However, current time series approaches tend to simplify the nature of uncertainties in the data in exchange for analytical tractability, thereby influencing whether or not a transition is detected in the dataset. In this letter, we contend that the lack of thorough uncertainty propagation stems from the way time series are represented. We thus put forth a new representation of time series that naturally includes its uncertainties and show how it can be used to detect abrupt transitions more reliably.

14.3 Results

A 'time series' is typically constructed as an ordered sequence of point-like measurements $\{x_t\}$, $t = 1, 2, \ldots, n$ of an observable X. Quantitative methods are thereafter employed to analyse $\{x_t\}$ and the propagation of uncertainties (if provided) is carried out as a separate excercise. This makes the error analysis highly non-trivial, and also allows investigators to ignore or postpone it, perceived often merely as an addition to the *core* analysis and results. Even if an error analysis is performed, the errors are often assumed to be independent and (qualitatively) identical, which is inaccurate for most real-world observables and may lead to substantial pitfalls (cf. supplementary information, SI). Here, we introduce a framework that merges the analysis of the measurements with that of their errors, and shifts the focus from *knowing the value* of an observable at a given time to *knowing how likely it is* that the observable had a chosen value at that time. We propose to consider the observable as a random variable X, non-independently and non-identically distributed at each time point unless known to be otherwise. Formally, in lieu of $\{x_t\}$, we use a time series of probability density functions $\{\varrho(x|t)\} := \{\varrho_t(x)\}$, $t = 1, 2, \ldots, n$ (Fig. 14.1a). This offers several advantages: It explicitly shows how observables might be non-identically, and often non-normally distributed (e.g., SST anomalies within the Niño 3.4 region during the 1997–98 El Niño, shown in Fig. 14.1b). It also brings to light implicit assumptions. For example, the classic Pearson's correlation coefficient between two observables is estimable only if we can estimate their joint distributions at each time point, or if they are independent when conditioned on a given $T = t$ (SI, Sec. *Correlation between two observables*).

To detect abrupt transitions, we use and extend the framework of *recurrence analysis* [239], a valuable tool to investigate features such as memory, disorder, and synchronization, from patterns encoded in the return characteristics of the observable. Traditionally, the first step is to estimate a binary *recurrence matrix* whose elements indicate (with a 1 or a 0) if a chosen time point recurred to an earlier state or not. Various estimates derived from the recurrence matrix quantify the processes underlying the observable [239]. Here, we use the $\{\varrho_t(x)\}$ series to estimate the probability of recurrence for all pairs of time points in a way such that *it does not require us to assume independence or to quantify the dependence* between the probability distributions at two different time instances (cf. Methods). We construct an estimator $\hat{\mathbf{A}}$ of the recurrence probabilities (Methods, Eq. 14.6), interpreted as the adjacency matrix of a network whose nodes are the observation time points and whose edge weights are the recurrence probabilities. Such a network obtained from a single time series is referred to as a *recurrence network* [241] (RN) and has been used to study many instances of complex systems [73, 112, 277, 303]. Next, we use the community structure of the RN as an indicator

of abrupt transitions: *Communities* [272] in a RN are time intervals with a higher similarity within themselves than to the rest of the time series, indicating a shift in the dynamics near the borders between different communities. We demonstrate this with a synthetic example where three different transitions are imposed on a noisy sinusoidal signal (Fig. 14.2). If we consider only the mean time series, we fail to detect the transition at $T = 675$ and can date the other two only much coarser, further highlighting why we should represent time series as $\{\varrho_t(x)\}$ rather than $\{x_t\}$.

We take three real-world examples with three different sources of uncertainty (noted in

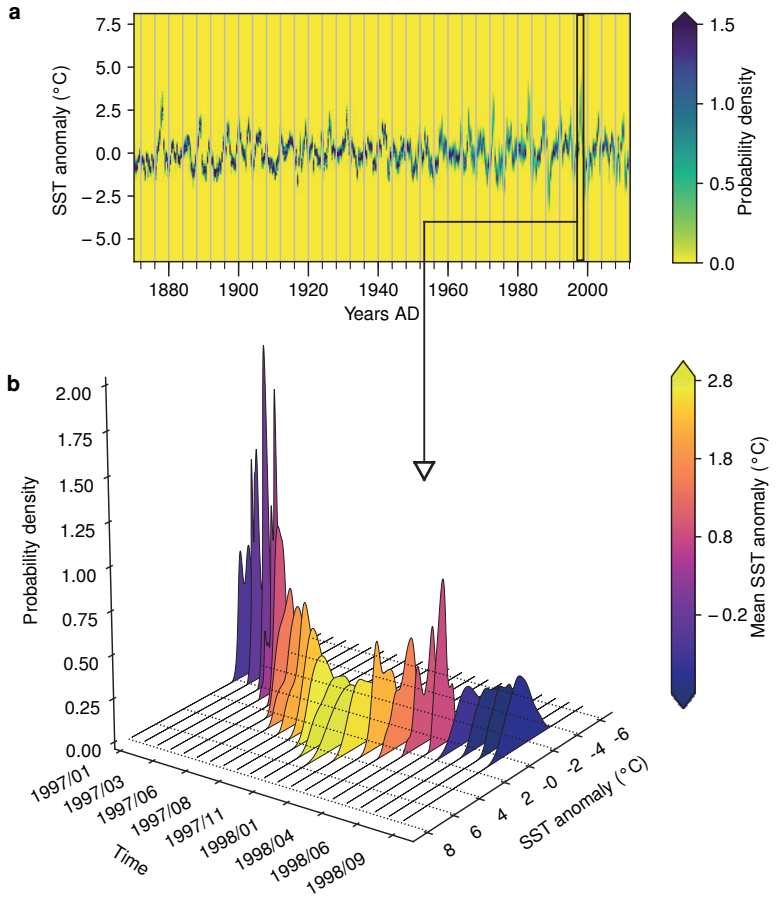

Figure 14.1: **Series of probability density functions.** The time series of probability densities $\varrho_t(x)$ is shown here for monthly SST anomalies from the Niño 3.4 region, from late 1870 to 2012. The densities are estimated using a kernel density estimation procedure (see Methods) which gives a probability density of SST anomalies for each month given the spatially distributed measurements. Each vertical column in **a** is a density $\varrho_t(x)$ color-coded according to its value. Darker (lighter) colors in each column thus represent higher (lower) chances of observing the corresponding SST anomalies for that month in the Ninño 3.4 region. We propose to consider such a series of $\varrho_t(x)$ instead of representing them as point esimates. Each monthly $\varrho_t(x)$ is shown in detail using a 3D representation in **b** for the SST anomalies during the '97-'98 El Niño (black box in **a**). The color of each density in **b** denotes the average SST anomaly for that month, clearly indicating the Niño-like conditions during the winter of '97-'98, but we also see the non-Gaussian nature of the probability densities throughout the period, calling into doubt the efficacy of representative point estimates such as the mean.

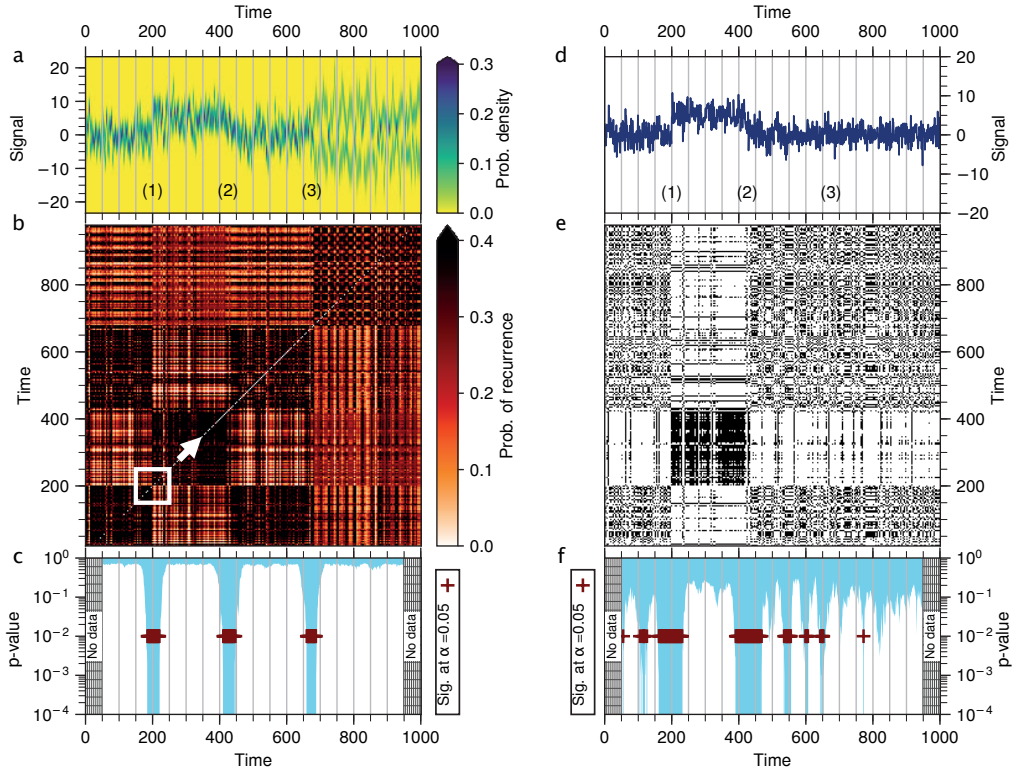

Figure 14.2: **Detecting abrupt transitions: Synthetic example.** The time series of probability densities $\varrho_t(x)$ for a synthetically generated noisy sinusoid (color map in **a**) and its mean (**d**). Three transitions are imposed: (1) a sudden jump at $T = 200$, (2) a linear decrease between $T = 400$ and $T = 450$, and (3) a change in the distribution at $T = 675$. The probability of recurrence matrix $\hat{\mathbf{A}}$ (in **b**) estimated from the densities in **a** shows the modular structure resulting from the imposed transitions. The recurrence matrix $\mathbf{R}$ estimated from the mean time series (**e**) only captures the first two transitions. We detect the timing of the transitions by moving a sliding window (white box in **b**) of 100 time points and estimating the p-value (**c**, **f**) for a 2-community structure under the null hypothesis of a random network. Statistically significant p-values ('+' markers in **c**) are determined at a level $\alpha = 0.05$, and after accounting for multiple comparisons using Holm's method with the Dunn-Šidák correction factor (cf. Methods). In **f**, the third transition is not detected and the first two are much more coarsely dated than in **c**.

parentheses): (i) daily financial stock index data from 2004 to 2016 (intra-day temporal variability), (ii) monthly SST anomalies from 1881 to 2012 for the Niño 3.4 region (spatial variability), and (iii) paleoclimatic proxy records from Asia covering important intervals of the Holocene (imprecision in determining proxy ages). A $\{\varrho_t(x)\}$ series is constructed from the data and used to detect abrupt transitions (see Methods, and SI Figs. 14.6–14.8). In each case, we repeat the analysis using only the mean time series, and find that using the probability density series gives more reliable and robust detection of abrupt transitions (cf. SI, Figs. 14.9–14.10).

First, as a proof-of-concept of the proposed approach, we consider three stock market indices: DAX (Frankfurt), NASDAQ-100 (New York), and BSE SENSEX (Mumbai). We identify three clusters of abrupt transitions (Fig. 14.3a–c) centered around the "mortgage crisis", the "Eurozone crisis", and the "Brexit"/"Grexit" crises, as indicated by corresponding

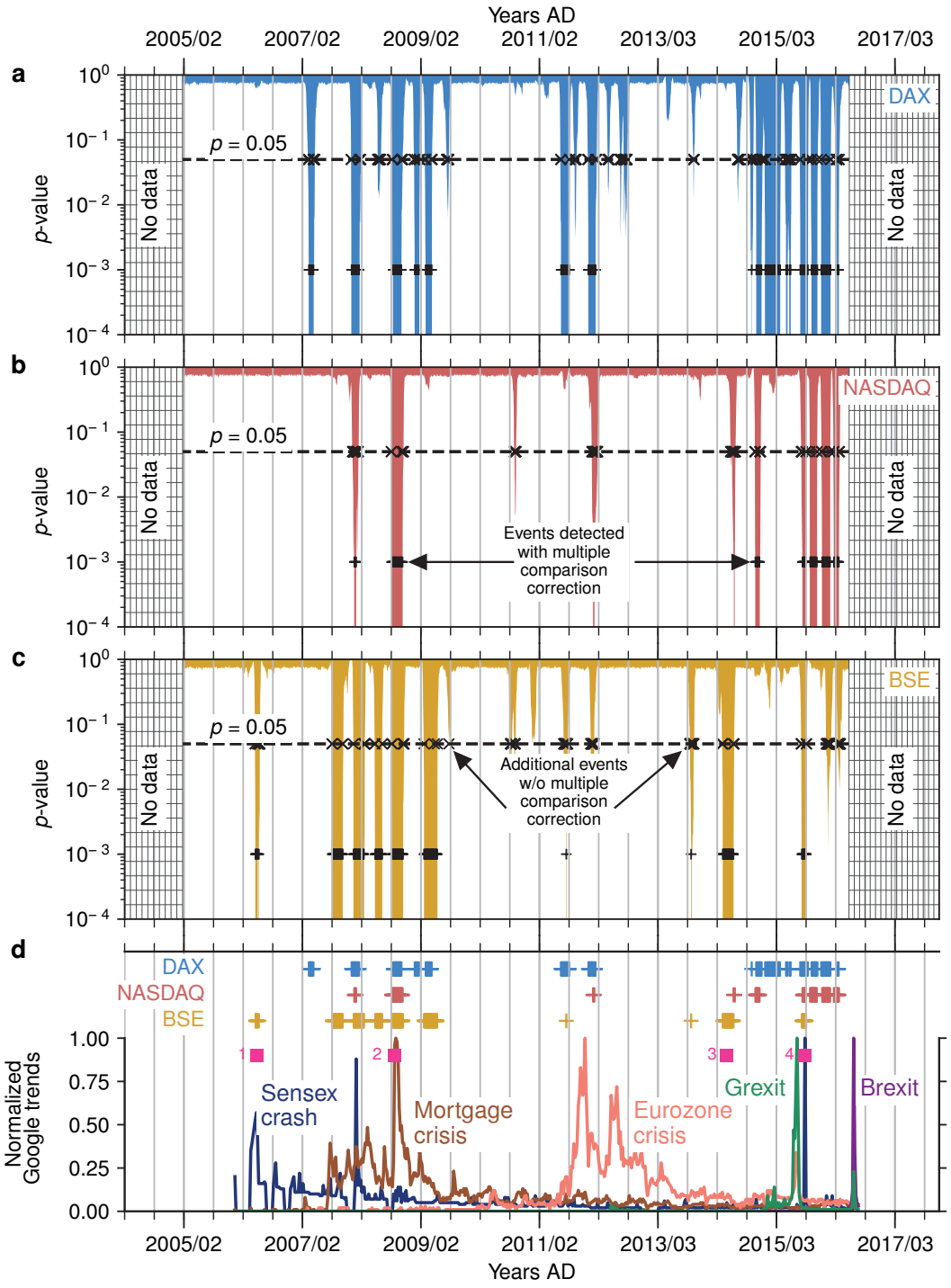

Figure 14.3: **Abrupt transitions in financial stock indices.** Applying our approach to three stock index datasets DAX (**a**), NASDAQ-100 (**b**), and S&P BSE SENSEX (**c**), we identify three major epochs centered around the "mortgage crisis", "Eurozone crisis", and the "Grexit"/"Brexit" crises, as seen from the normalized Google trends data in **d**. In each epoch we see a high number of statistically significant dynamical shifts at $\alpha = 0.05$ and these periods are interspersed with quiescent periods with far fewer of such shifts. Additional pink squares in **d** correspond to: (1) BSE SENSEX crash of 22 May 2006, (2) bankruptcy claim by Lehman Brothers on 15 September 2009, (3) Indian parliamentary elections from 7 April to 12 May 2014, and (4) SENSEX crash (1600 points) of 24 August 2015. The horizontal dashed lines in **a**–**c** indicates the confidence level $\alpha = 0.05$ of the statistical test. However, when multiple comparisons are taken into account (see Methods), only a subset of p-values below 0.05 are found to be significant (shown here with '+' markers).

peaks in the Google trends data (Fig. 14.3d). The end of 2009 marks a common period of abrupt transitions and instabilities for all three indices during the worst part of the US mortgage crisis, symbolised here by the bankruptcy claim of Lehmann Brothers. Of the two queries "Grexit" and "Brexit", we note that the transitions show a better correspondence with the former. Additional events in the BSE SENSEX in 2006 and 2015 coincide with large intra-day falls in the Mumbai-based stock index on 22 May 2006 and 24 August 2015. Abrupt shifts detected in the BSE in May 2014 roughly coincide with the national parliamentary elections held in India that year, and the shift from a decade-old rule by the centre-left United Progressive Alliance to the center-right National Democratic Alliance, suggesting a volatile period for the Mumbai-based stock exchange.

Our second real-world example involves recent climate data: The Niño 3.4 index is a standard index for estimating SST anomalies in the central-equatorial Pacific, calculated as the spatial averages of monthly gridded SST values in that region. Five consecutive 3-month (i.e. temporal) running averages of the index found above (below) a threshold of +0.5K (–0.5K) indicate El Niño (La Niña) conditions (Fig. 14.4b,d), two distinct phases of the ENSO which impact the climate worldwide. The transitions identified by our analysis (Fig. 14.4) show a relatively active period upto ca. 1906, after which the frequency of such shifts decreases, indicating a complex interdecadal variability *of the transitions themselves*, most likely modulated by the PDO [268]. Based on a statistical coincidence analysis between the detected transitions and 'phase-locked' periods of the PDO and the ENSO (cf. Methods, SI Fig. 14.13), we reveal that the detected transitions are coincident with periods of phase-locking (green markers in Figs. 14.4b, d) between the PDO and the ENSO. This implicates the *similarity of phases* of the PDO and the ENSO as a potential factor that modulates ENSO dynamics, in addition to the phase of the PDO itself, which has been reported earlier [406] to increase the propensity for El Niño (La Niña) events when the PDO is in its positive (negative) phase. The representation of observables as a series of probability density functions is particularly valuable in paleoclimate time series analysis because of the inherent chronological uncertainties that hamper the determination of the timings of short-lived events [377]. Here, we provide, for the first time, a transparent 'uncertainty-aware' framework to detect abrupt decadal-scale transitions in paleoclimate proxy records while taking into account dating uncertainties. We compare the transition detection results from speleothem datasets from the Dongge and Tianmen caves in China, and Qunf Cave in Oman with the timings of well-known climatic events [31, 308, 415]. We detect significant shifts scattered through the Holocene (Fig. 14.5a–c) which likely correspond to weak ASM events reported in an earlier study [414] (blue squares in Fig. 14.5d). The weak ASM events are postulated to be synchronous with North Atlantic BEs (green squares in Fig. 14.5d) [414]. Our analysis confirms this hypothesis, allowing for the fact that the timings of the Bond events themselves are still relatively poorly determined [415]. The BE at 1.4 kyr BP potentially has a corresponding event in the Dongge cave record. However, this is not statistically significant when accounting for multiple comparisons. Although all the BEs have a potential corresponding event in the ASM records, the opposite is not true. We detect events of weakened ASM events (ca. 6.4–6.8 kyr BP) which do not have a corresponding BE, suggesting additional influencing factors on ASM strength.

Our results further indicate a nontrivial spatial pattern in the hemispherical propagation of the events: the event at 8.2 kyr BP, for example, is experienced first at Qunf, followed by Dongge, and then at Tianmen. We note, from Fig. 14.5, that the weak ASM event at 4.2 kyr BP, well-known as the '4.2k event' [24], is not detected at Qunf, primarily because the Qunf cave $\{\varrho_t(x)\}$ time series has large uncertainties in the period between 3 and 5 kyr BP (SI, Fig. 14.8c) leading to large probabilities of recurrence for all pairs of time points (within

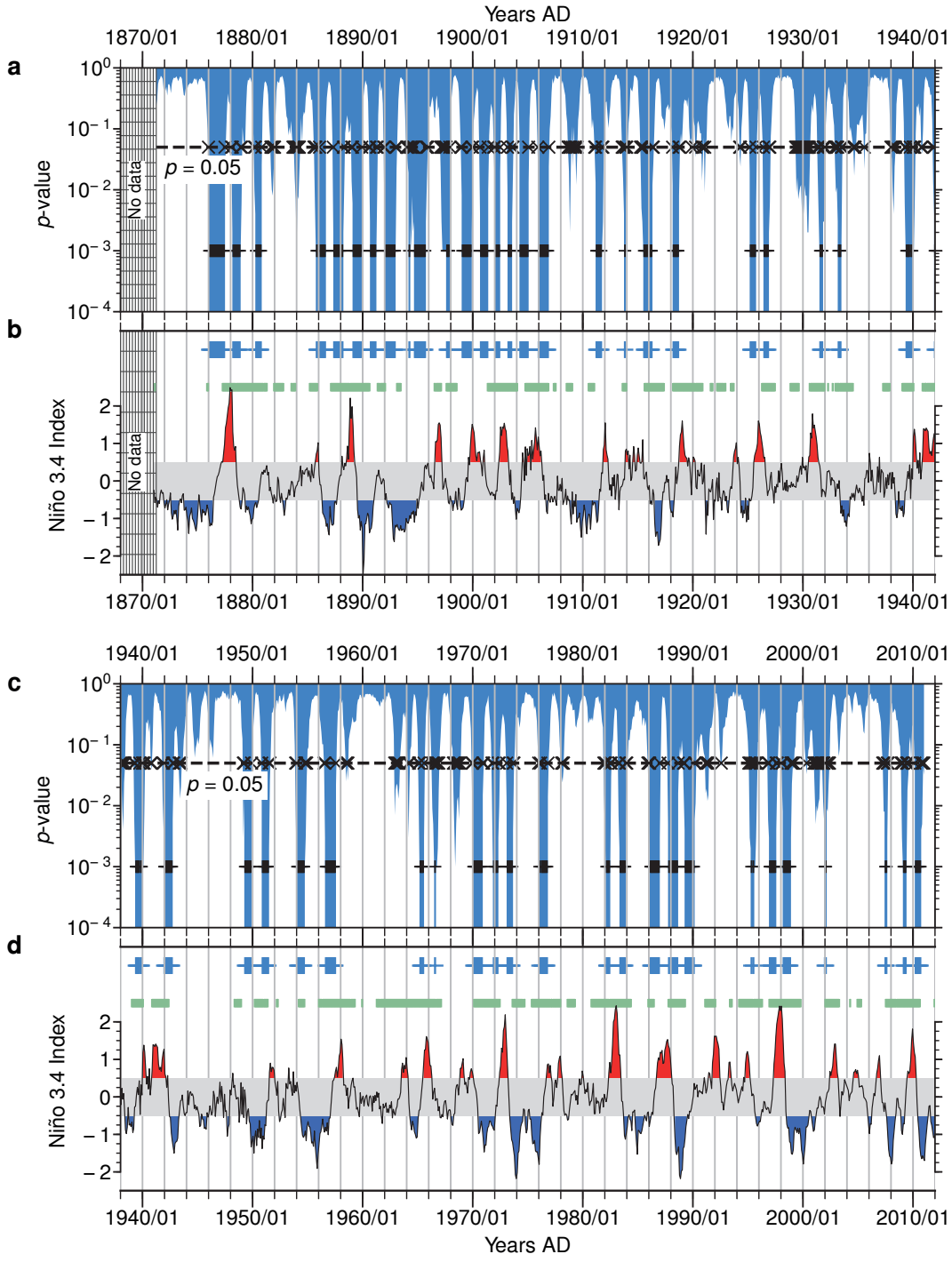

Figure 14.4: **Abrupt transitions in the equatorial central Pacific.** In **a** and **c**, '+' and '×' markers, and the horizontal dashed lines denote the same as in Fig. 14.3. We detect most of the transitions between El Niño (La Niña) phases, shown here as red (blue) shaded regions in **a**, **c**) during the past 150 years. Panels **a** and **b** cover the period from 1870 up to 1940, and panels **c** and **d** cover the period from around 1940 to 2012. From around 1906, the transitions show an intermittent burst-like behaviour, indicating a complex inter-decadal variability of the transitions themselves. A statistical coincidence analysis further reveals that the timing of the detected transitions are significantly coincident to the timings of phase-locked periods (shown here as green markers in **b** and **d**) between the PDO and the ENSO. This reveals a further potential aspect of the modulation of the ENSO by the PDO.

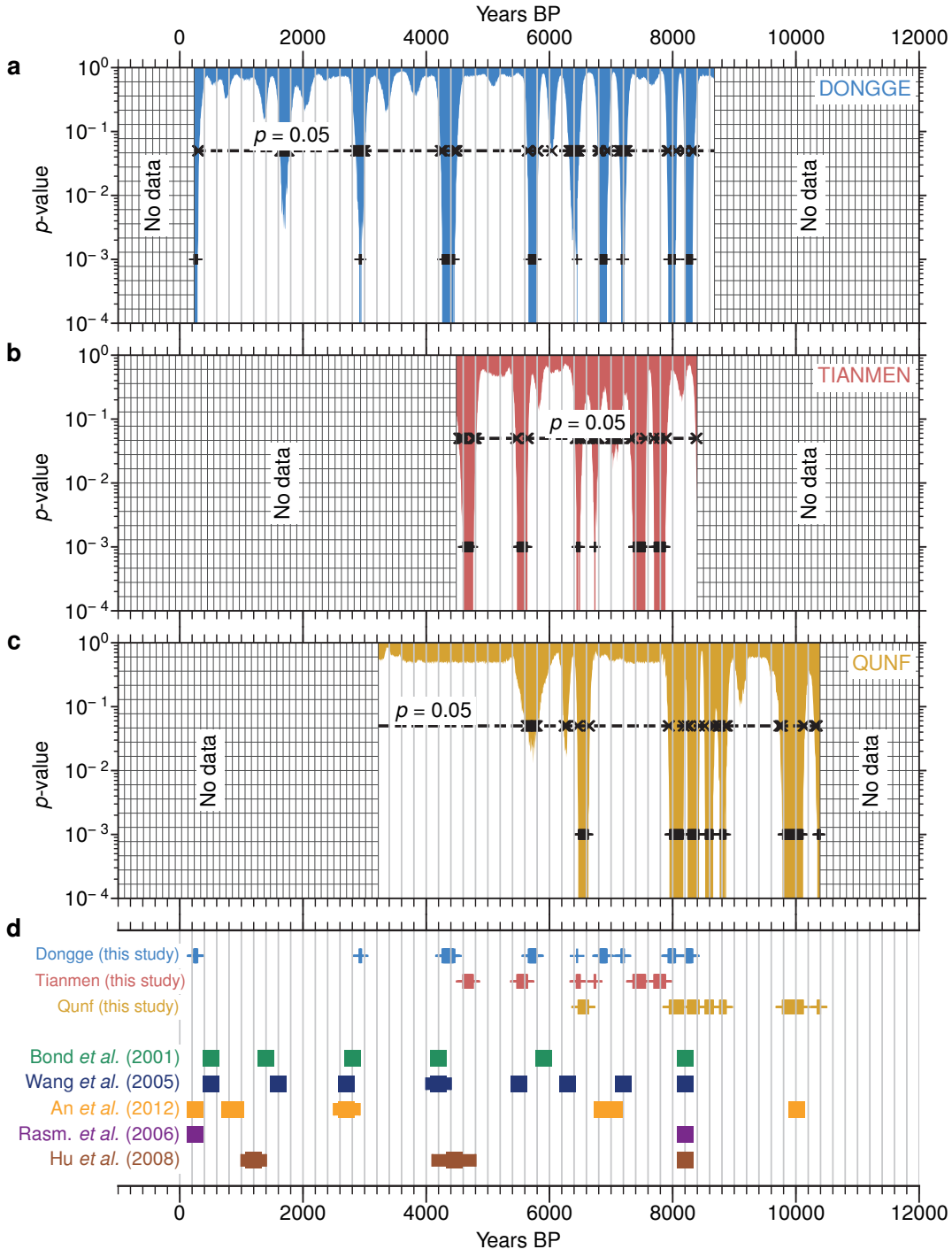

Figure 14.5: **Abrupt transitions in paleoclimatic datasets.** We apply our method to three paleoclimatic δ^{18}O proxy records from Dongge (**a**), Tianmen (**b**), and Qunf (**c**) caves in Asia. Statistically significant events ('+' markers) show a scatter of events throughout the Holocene, corresponding to periods of weakened ASM (blue squares in **d**). The weak ASM events are postulated to be synchronous with BEs in the North Atlantic (green squares in **d**), a hypothesis that we are able to confirm with the results from our transition detection analysis. Barring the BE at 1.4 kyBP, all other BEs have a corresponding weak ASM that has been detected. At 1.4 kyBP, the Dongge cave record shows a potential dip in the p-value, but which is not statistically significant after accounting for multiple comparisons. *Note:* In **a**–**c**, '+' and '×' markers, and the horizontal dashed lines denote the same as in Fig. 14.3.

this period), such that there are no well-defined community structures indicative of abrupt transitions (SI, Fig. 14.14). This is not to say that the Qunf cave did not experience the 4.2 kyr event, but rather to emphasise that, given the time series uncertainties, it is not possible to say with statistical confidence whether or not there was an ASM event at Qunf around 3–5 kyr BP. We can thus unambiguously link the detection of an abrupt ASM transition to the time series uncertainties of the speleothem proxy record. Time series uncertainties can therefore, by determining whether or not events 'show up' in a transition detection scheme, crucially influence subsequent inferences regarding the *spatio-temporal propagation patterns of the Holocene cold events*—an as yet unanswered question in Holocene paleoclimatology. Our analysis takes a first step towards solving this issue, by showing not only how to incorporate uncertainties in detecting abrupt ASM transitions, but by also helping us to clearly understand the importance of doing so.

14.4 Methods

14.4.1 Datasets

Synthetic example

The synthetic dataset is generated by imposing transitions on a noisy sinusoid,

$$x_0(t) = \sin(2\pi t/50) + 0.125\epsilon_t, \tag{14.1}$$

where $t = 1, 2, \ldots, 1000$ denotes time, and $\epsilon \in (0, 1)$ is uniformly distributed noise. In our proposed framework of probability density time series, x_0 serves as the mean of a Gaussian distribution whose standard deviation is equal to the error of estimation (see below, "Constructing $\varrho_t(x)$ from measurements"). We impose three transitions, of which the first two, at $T = 200$ and between $T = 400$ and $T = 450$, change the baseline value of this mean, and the third at $T = 675$ changes the distribution itself to create a bimodal distribution centered around two means. The mean(s) $x_s(t)$ are given by,

$$x_s(t) = \begin{cases} x_0(t), & 0 \leq t < 200 \\ x_0(t) + 5, & 200 \leq t < 400 \\ x_0(t) + 45 - 0.1t, & 400 \leq t < 450 \\ x_0(t), & 450 \leq t < 675 \\ 10x_0(t) \text{ or } -10x_0(t) \text{ with equal probability}, & 675 \leq t \leq 1000 \end{cases}. \tag{14.2}$$

Daily stock index values

The daily stock index data for the DAX (code: DAX, 30 companies from the Frankfurt Stock Exchange), NASDAQ-100 (code: NDX, 100 companies listed on the NASDAQ), and S&P BSE SENSEX (code: BSESN, 30 companies from the Bombay Stock Exchange) stock indices are obtained from `http://finance.yahoo.com/` with their appropriate codes under the section 'Historical Prices'. Google trends data (Fig. 14.3d) were obtained from `https://www.google.com/trends/` for the search queries: "mortgage crisis", "Eurozone crisis", "Brexit", and "Grexit" on 2 June 2016. The data were then normalized using a min-max transform such that they fall in the interval $[0, 1]$.

Niño 3.4 SST anomalies

The monthly SST anomalies were obtained from the gridded SST data product Merged Hadley-NOAA/OI Sea Surface Temperature & Sea-Ice Concentration released by National Centers for Environmental Prediction [156], and available for free download at: `http://www.esrl.noaa.gov/psd/data/gridded/data.noaa.oisst.v2.html`.

The Niño 3.4 region was extracted from the global data as those grid points falling within 5°N–5°S and 120°W–120°W. Anomalies were calculated with reference to the average climatology of the period: 1 January, 1950 to 31 December, 1979. The Niño 3.4 index data (Fig. 14.4b, d) was obtained from `http://www.cpc.ncep.noaa.gov/data/indices/`. The NCEI PDO index series (SI, Figs. 14.10, 14.12, 14.13) was obtained from `https://www.ncdc.noaa.gov/teleconnections/pdo/`.

Paleoclimate proxy records

The paleoclimate datasets for the Dongge [414], Tianmen [41], and Qunf [107] cave are obtained from the NOAA National Centers for Environmental Information (formerly the National Climatic Data Center) and they are available for free download at: `https://www.ncdc.noaa.gov/data-access/paleoclimatology-data`.

14.4.2 Constructing $\varrho_t(x)$ from measurements

Synthetic example

The synthetic signal $x(t)$ is sampled at every second time instant with a Gaussian sampling noise with a standard deviation $\sigma_s = 1.25$ (assumed here to be representative of instrumental errors) so that we have on our hands a sampled time series $x_s(t)$ for $t = 0, 2, 4, \ldots, 1000$ with the same error σ_s for all the 501 measurements. The probability distribution series is then constructed as a normal distribution $\mathcal{N}$ centered at the observed value $x_s(t)$ and with a standard deviation of σ_s. We can then estimate the cumulative distribution $P_t(x)$ using the corresponding relation for a normally distributed variable, i.e., $\varrho_t(x) \sim \mathcal{N}(x_s(t), \sigma_s)$.

Daily stock index values

Using the reported intra-day high $x_{hi}(t)$ and intra-day low $x_{lo}(t)$ values of the stock indices on a given day, we postulate that, without any further information about the intra-day variations of the stock indices, the stock index values fluctuate randomly according to a uniform random distribution $\mathcal{U}$ bounded from below and above by $x_{lo}(t)$ and $x_{hi}(t)$, respectively. This results in the probability distribution series $\varrho_t(x) \sim \mathcal{U}(x_{lo}(t), x_{hi}(t))$.

Niño 3.4 SST anomalies

For a given month in the SST data for the Niño 3.4 region, we take the spatially distributed SST anomaly values for that month and apply a kernel density estimation using an optimal bandwidth for Gaussian kernels with the Python toolkit Scikit-learn [290]. This results in an empirically estimated probability density $\varrho_t(x)$ constructed from the spatial distribution of SST values in a given month.

Paleoclimate proxy records

Using the obtained proxy-depth and age-depth data, we estimate the posterior probability of the paleoclimatic proxy at a chosen time instant of the past using a Bayesian approach reported in an earlier study [121].To summarize it briefly, consider the proxy, radiometric age, calendar age, and depth as the random variables X, R, T and Z respectively. In these terms, our quantity of interest is the probability $\varrho(x|t)$, which for a speleothem dated with U/Th radiometric dates, can be shown to be approximated by the Riemann sum

$$\varrho(x|t) \approx \frac{\sum_{j=1}^{M} b_j w_t(z_j^x)\, \varrho(x|z_j^x)}{\sum_{j=1}^{M} b_j w_t(z_j^x)} \tag{14.3}$$

where z_j^x, $j = 1, 2, \ldots, M$ denote the M depth values at which the proxy measurements are made, and where b_j is the width of the depth interval represented by z_j^x:

$$b_j = \frac{1}{2}\begin{cases} z_2^x - z_1^x & j = 1 \\ z_{j+1}^x - z_{j-1}^x & 1 < j < 1\,. \\ z_M^x - z_{M-1}^x & j = M \end{cases} \tag{14.4}$$

The probability that the proxy $X = x$ at a chosen time $T = t$ is thus expressed in terms of estimable or measured quantities. In applying this to the chosen datasets, we take a regular time grid at 5 year intervals starting (ending) at the minimum (maximum) age measurement.

14.4.3 Network of recurrence probabilities

We use the framework of recurrence analysis to analyse the chosen datasets. Typically, this is based on the construction of *recurrence matrix* $\mathbf{R}$ whose elements $\mathbf{R}_{ij}$ are either 1 if the observable recurred (within an ε vicinity) at times i and j, or 0 otherwise [239]. The recurrence matrix $\mathbf{R}$ can then be used to classify and investigate various classes of complex dynamics. More recently, $\mathbf{R}$ has been shown to be interpretable as the adjacency matrix $\mathbf{A} = \mathbf{R} - \mathbf{1}$ of a complex network where the nodes are the time points of the observations and edges are placed between those pairs of time points which recur within an ε neighbourhood. Here, $\mathbf{1}$ is the identity matrix of the same size as $\mathbf{R}$, which is subtracted from $\mathbf{R}$ to give us an adjacency matrix $\mathbf{A}$ without self-loops.

However, when we are given a time series with uncertainties represented as $\varrho_t(x)$ in our proposed framework, we are unable to estimate precisely whether time points i and j recurred. In this case, we aim to estimate instead the *probability that i and j recurred* in a chosen ε neighbourhood. In order to do so, the first step in estimating the recurrence probabilities is to estimate the cumulative distribution functions $P_t(x)$ corresponding to the probability densities $\varrho_t(x)$ estimated from the various datasets (see above). Using the results of an earlier study [424], we first estimate the upper and lower bounds m_{ij} and M_{ij} for the distribution $P_{Z_{ij}}$ of the difference $Z_{ij} = X_i - X_j$ as: $m_{ij}(z) = \max\{\sup_u f_{ij}(u, z_{ij}),\ 0\}$ and $M_{ij}(z) = \min\{\inf_u f_{ij}(u, z_{ij}),\ 0\} + 1$, where $f_{ij}(u, z_{ij}) = P_i(u) - P_j(u - z_{ij})$. These bounds ensure that $P_{Z_{ij}} \in [m_{ij}, M_{ij}] \subseteq [0, 1]$. Next, we determine upper and lower bounds $q_{ij}^l(\varepsilon)$ and $q_{ij}^u(\varepsilon)$ on the probability of recurrence $Q_{ij}(\varepsilon) := Prob\,(|Z_{ij}| < \varepsilon)$ given a recurrence threshold ε such that $Q_{ij}(\varepsilon) \in [q_{ij}^l(\varepsilon), q_{ij}^u(\varepsilon)] \subseteq [0, 1]$. These bounds are obtained as: $q_{ij}^l(\varepsilon) = \max\{m_{ij}(\varepsilon) - M_{ij}(-\varepsilon), 0\}$, and $q_{ij}^u(\varepsilon) = \min\{M_{ij}(\varepsilon) - m_{ij}(-\varepsilon), 1\}$. We drop ε in the following for notational clarity and with the understanding that ε is fixed.

We assume the probability Q_{ij} itself to be distributed in the obtained interval $[q_{ij}^l, q_{ij}^u]$, but in a way unknown to us. However, assuming $\mathbf{A}$ as the *true* adjacency matrix of the system's recurrence network, we can write down,

$$Prob\,(\mathbf{A}_{ij} = 1) = \int_{q_{ij}^l}^{q_{ij}^u} \varrho(\mathbf{A}_{ij} = 1 | q_{ij})\, \varrho_{Q_{ij}}(q_{ij})\, \mathrm{d}q_{ij} = \int_{q_{ij}^l}^{q_{ij}^u} q_{ij}\, \varrho_{Q_{ij}}(q_{ij})\, \mathrm{d}q_{ij} = \mathbf{E}_{\varrho_{Q_{ij}}}[Q_{ij}], \tag{14.5}$$

i.e., the total probability that A_{ij} equals 1 is simply the expectation of Q_{ij}. Here, $\varrho_{Q_{ij}}(q_{ij})$ is the (unknown) probability density function for the random variable Q_{ij}.

Assuming that $Q_{ij}(\varepsilon)$ is itself distributed symmetrically around the mean in the interval $[q_{ij}^l(\varepsilon), q_{ij}^u(\varepsilon)]$, the total probability that the observable at i and j recurred upto a threshold ε is $(q_{ij}^l(\varepsilon) + q_{ij}^u(\varepsilon))/2$. This allows us to define an estimator $\hat{\mathbf{A}}$ of the probabilities of recurrence of the observable X and interpret it as the adjacency matrix of a network whose nodes are

the time points of observation and whose edge weights are given by

$$\hat{\mathbf{A}}_{ij}(\varepsilon) := \begin{cases} \frac{1}{2}(q^l_{ij}(\varepsilon) + q^u_{ij}(\varepsilon)) & i \neq j, \\ 0 & i = j \end{cases} \tag{14.6}$$

where we put $\hat{\mathbf{A}}_{ii} = 0$ to avoid self-loops in the network. The elements of $\hat{\mathbf{A}}_{ij}$ encode the total probability that time points i and j have recurred within an ε vicinity, given the uncertainties in the dataset.

While applying the above to estimate the networks of recurrence probabilities for the applications, we use a bisection routine to arrive at a suitable ϵ threshold which results in a pre-specified link density of the RN. The link densities chosen are: (i) synthetic example, 30%, (ii) financial datasets, 24%, (iii) SST dataset, 25%, and (iv) paleoclimatic datasets, 30%.

14.4.4 Detecting abrupt transitions using recurrence network community structure

We define communities in the sense of Newman [272] as those parts of a network which have a higher link density within themselves than to the rest of the network. In the context of the networks based on probabilities of recurrence used in this study, such a subnetwork would correspond to a time period in which the states of the system are closer to each other than to the rest. The identified communities would correspond to stable regimes of dynamics and their borders would be the time points at which the system transited between regimes. Similar to Newman [272], we use the within-community link fraction S as an indicator of community structure. However, to determine the extent to which a value $S = s_{obs}$ obtained from the data is determined by a dynamical shift and not by randomness, we propose to use the p-value ($:= p^{s_{obs}}$) of a statistical test with the null hypothesis H_0: *S is determined by the degree-sequence of the given network*. If we define $\varrho_{s|H_0}(s)$ as the probability density of the within-community link fraction obtained from the null model,

$$p^{s_{obs}} = \int_{s_{obs}}^{1} \varrho_{s|H_0}(s)\,\mathrm{d}s, \tag{14.7}$$

which requires to specify the communities before we measure S. Note that this is in contrast to Newman's method, where the quantity of interest (modularity) is the difference between s_{obs} and the expectation value of S as obtained from the null model H_0. Next, in order to apply the above definition, we move a sliding window over the dataset (Fig. 14.2b), and after extracting the portion of $\hat{\mathbf{A}}$ which falls within that window, we partition it into two communities divided at the midpoint, and estimate $p^{s_{obs}}$. Those windows with a high value of S unexplained by a random network having the same degree sequence will have very low p-values (cf. Figs. 14.2–14.4). Finally, to determine the statistically significant windows at a given confidence level α, we apply the Holm's method for multiple testing [149] along with the Dunn-Šidák correction factor [350]. The distribution $\varrho_{s|H_0}(s)$ of S given H_0 is obtained from 1000 random realizations of the degree-configuration model.

The sizes of the sliding window were different for the different applications: (i) synthetic example, 90 time points, (ii) financial datasets, 60 time points (approx.2 months), (iii) SST data, 30 time points (2.5 years), and (iv) paleoclimatic datasets, 100 time points (500 years).

14.4.5 Coincidence analysis of detected transitions with phase-locking periods of the PDO and the ENSO

For this analysis, we define phases for the Niño 3.4 index and the PDO index (cf. Methods: *Datasets*) in the sense of Maraun & Kurths [215]. As a first step, the index time series were filtered using a low-pass forward-backward Butterworth filter that dampens all frequencies

higher than $1/12\,\text{months}^{-1}$. Then, we obtained the Hilbert transform of the time derivative of the filtered time series, an the ratio of the Hilbert transform to the input of the Hilbert transform (i.e., the time derivative of the index time series) is defined as the tangent of the instantaneous phase ϕ_t (SI, Fig. 14.12). This is used to define the phase difference between the PDO and the ENSO as $\Delta\phi_t = \phi_t^{PDO} - \phi_t^{ENSO}$, the time derivative of which is used to identify plateaus in $\Delta\phi_t$ i.e., when $\Delta\phi_t \approx 0$ (SI, Fig. 14.13a), defined here as those time points when $\Delta\phi_t$ falls between the 25-th and 75-th percentile of all obtained $\Delta\phi_t$ values (SI, Fig. 14.13b). These time points are identified as the time points of 'phase-locking' between the PDO and the ENSO and used to check for significant coincidences with the abrupt transitions detected using our current method on the probability density series from the SST anomalies in the Niño 3.4 region.

We define a coincident transition as a transition that occurs within an interval of 31 days to a time point of phase-locking as defined above. In total, 216 such coincidences are identified. To test whether such a high number of coincidences could be possible by pure random chance, we randomize the timings of the detected transitions 50000 times (so that the number of coincidences stays at 216) and compute the number of coincidences each time, resulting in a null distribution of coincidences occuring purely by random chance (SI, Fig. 14.13c). At a significance level of 5%, we find that the observed number of coincidences is significantly higher than that possible by pure random chance. This validates the hypothesis that the detected abrupt transitions in the Niño 3.4 region are significantly coincident to periods of phase-locking between the PDO and the ENSO. For more details, please refer to the SI.

Acknowledgements

This paper was developed within the scope of the IRTG 1740/TRP 2011/50151–0, funded by the DFG/FAPESP. N.B. acknowledges funding by the Alexander von Humboldt Foundation and the German Federal Ministry for Education and Research. J.K. acknowledges financial support from the Government of the Russian Federation (Agreement No. 14.Z50.31.0033). S.B., N.M., and B.G. have received funding from the European Union's Horizon 2020 Research and Innovation programme under the Marie Skłodowska-Curie grant agreement No 691037 (project QUEST). B.G. was partially supported by the MWFK Brandenburg.

Author contributions statement

B.G. wrote the main text and prepared the figures. B.G., N.M., and J.H. developed the estimation procedure of the probabilities of recurrence. B.G., A.R., and N.B. developed the RN community structure approach to detect abrupt transitions, and the associated significance tests. S.F.M. preprocessed the paleoclimate datasets, constrained the Holocene events reported in the scientific literature, and drew conclusions from the paleoclimatic results. All authors discussed the results, drew conclusions, and contributed to the manuscript text. All authors were involved in deciding the context and narrative within which the main results have been communicated.

Supplementary Material

Correlation between two observables

Consider the classic Pearson's cross-correlation coefficient $Cor(X,Y)$ between two normalized observables X and Y (i.e., with mean zero and standard deviation one). In the typical time series framework, this is the averaged pairwise product of the measurements x_t and y_t,

$$Cor(X,Y) = \frac{1}{n}\sum_{t=1}^{n} x_t y_t. \tag{14.8}$$

In our proposed framework based on the density series $\varrho_t(x)$ and $\varrho_t(y)$, we first note that the correlation of normalized variables is the expectation value,

$$Cor(X,Y) \quad = \mathbf{E}[X,Y] = \iint xy\,\varrho(x,y)\,\mathrm{d}x\,\mathrm{d}y, \tag{14.9}$$

where the joint density $\varrho(x,y)$ is expressed in terms of marginals $\varrho(x,y|t) := \varrho_t(x,y)$ as $\varrho(x,y) = (\sum_0^n \varrho_t(x,y)\,\mathrm{d}t)/n$. If we now assume X and Y to be independent when conditioned on t, i.e., $\int \varrho_t(x,y)\,\mathrm{d}t = \int \varrho_t(x)\varrho_t(y)\,\mathrm{d}t$, the correlation coefficient is given by

$$Cor(X,Y) = \frac{\sum_{t=1}^{n} \bar{x}_t \bar{y}_t}{n}, \tag{14.10}$$

where $\bar{\cdot}_t$ denotes the expected value of the observable at time $T = t$ as obtained from $\varrho_t(\cdot)$. Pearson's correlation is thus properly estimable only if we know the joint density $\varrho_t(x,y)$ or if X and Y are conditionally independent given T.

Probability density time series $\varrho_t(x)$

The probability density series for the three real-world examples dealt with in our study are shown in Figs. 14.6–14.8. In each case, the uncertainties arise from different sources. In the case of the financial stock indices(Fig. 14.6), the uncertainties arise due to intra-day variations which fall below the daily sampling frequency of the dataset, and are hence approximated using a uniform random distribution of the stock index values between the reported daily minimum and maximum values. Even though the uncertainties appear to be negligibly small when compared to the drift in the index values over the span of the entire dataset, we note that intra-day fluctuations can be sufficiently high at times of financial crashes and volatile periods. This is an important feature that is missed in typical point-like time series representations. For the Niño 3.4 SST anomalies (Fig. 14.7), the uncertainties arise due to the spatial heterogeneity of the SST values over the geographical grid demarcating the Niño 3.4 region in the equatorial Pacific. The distributions are thus estimated by pooling the monthly averaged SST values from all grid points for a given month into one sample and estimating their distribution using a kernel density estimate. In the case of the paleoclimate datasets, the uncertainties arise out of the imprecision in determining the age of the climate proxies. In most cases, it is important to note that the estimated distributions (Fig. 14.8) are rather non-Gaussian, often skewed, and exhibit non-negligible variance.

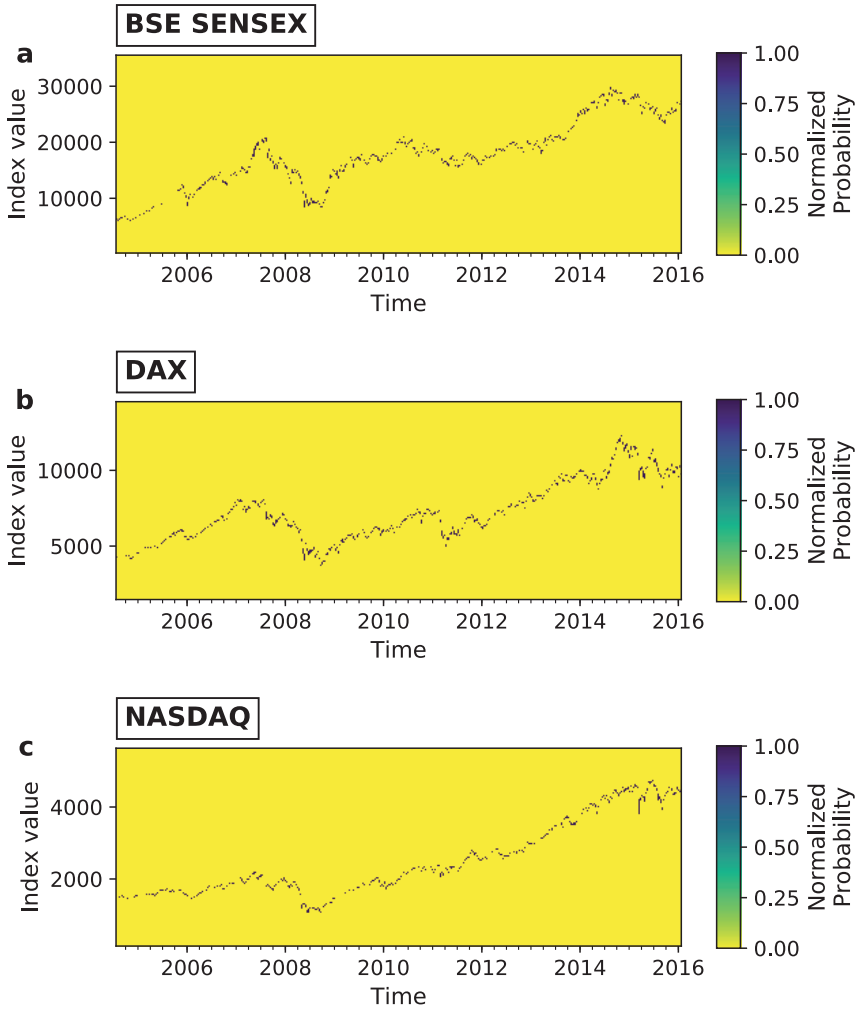

Figure 14.6: **Probability density time series: Stock indices.** The probability density time series for the three stock indices shown as a colormap: (a) BSE SENSEX (Mumbai, India), (b) DAX (Frankfurt, Germany), and (c) NASDAQ (New York, USA). The densities are obtained by assuming a uniform random distribution of the index values bounded by the reported daily maximum and minimum values.

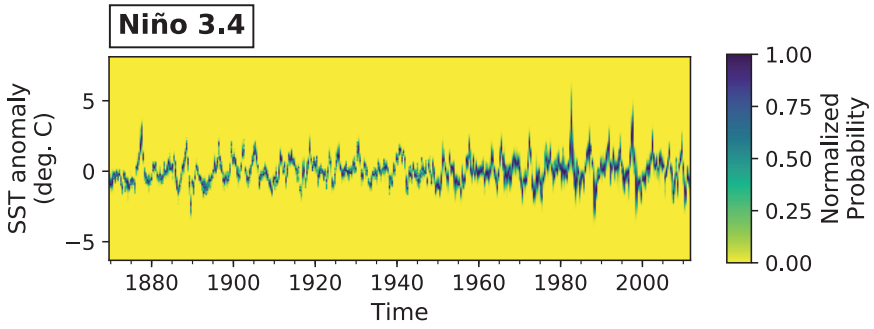

Figure 14.7: **Probability density time series: SST anomalies.** The probability density time series obtained by applying kernel density estimates on the monthly SST values for all grid points in the Niño 3.4 region at each time point of observation.

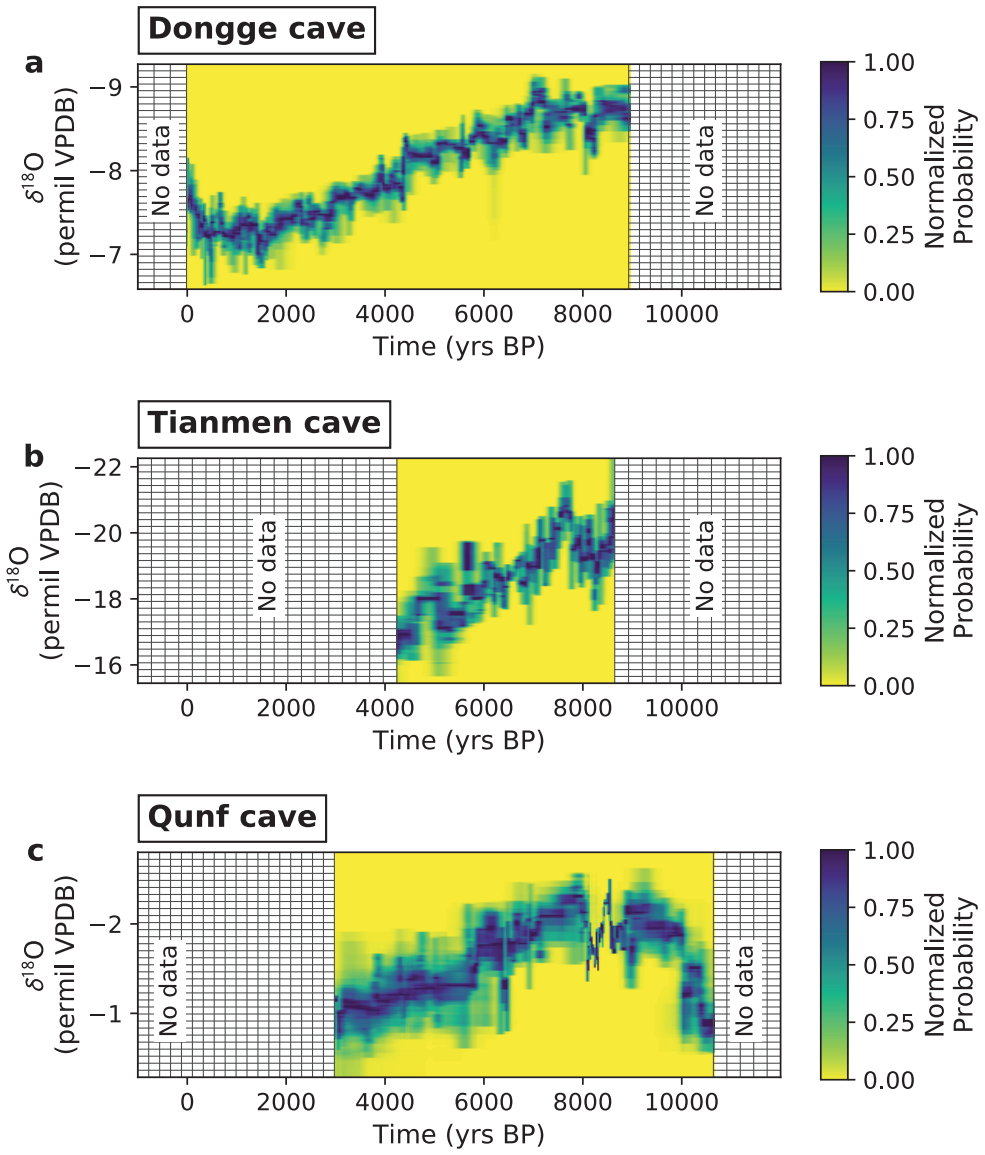

Figure 14.8: **Probability density time series: Paleoclimate proxies.** The probability density time series estimated from the age–depth and proxy–depth measurements for the δ^{18}O isotope datasets obtained from three caves in the Asian monsoon domain: (a) Dongge cave in south China, (b) Tianmen cave in south China, and (c) Qunf cave in Oman. The uncertainty in these datasetes arise primarily from the imprecision in assigning ages to the δ^{18}O values measured along the depth of the stalagmites.

Abrupt transitions detected by using the mean time series

The primary focus of our study is to emphasise the advantages of considering the probability density time series in lieu of a typical point-like time series. As done for the synthetic example (Fig. 2 of main text), we compare the results of the detection of abrupt transitions from our proposed approach on the density series to transitions detected when we use the mean value time series instead (Figs. 14.9–14.11). In the case of the financial datasets (Fig. 14.9), we see that the numbers of detected transitions are much higher when we use the mean time series, which we interpret as a lack of specificity, noting in particular that for the BSE SENSEX data, the entire period from mid-2007 to mid-2012 is filled with numerous 'transitions'. Even in the Niño 3.4 example (Fig. 14.10.), employing the mean time series to the transition detection method results in an almost contiguous series of 'transitions' throughout the entire timespan of the data. However, when we look at the results for the Dongge cave in the paleoclimate example (Fig. 14.11), we see that the results from the mean time series fail to detect the previously reported events at 4200 years BP and 8200 years BP (the famous '4.2k' and '8.2k' events). Thus, the impact of considering the mean time series on the final results of the abrupt transition detection may vary on the type, nature and magnitude of the uncertainties of the datasetes. While in some cases, (possibly random) fluctuations are detected as transitions, in others, large uncertainties (or a change in the underlying distribution) may wash out the transition signal in the expectation value. This further underscores the necessity for the proper representation and analysis of ucnertainties in time series. Otherwise, without proper care of the uncertainties, significant events might be missed out, but also non-significant events might be overemphasised.

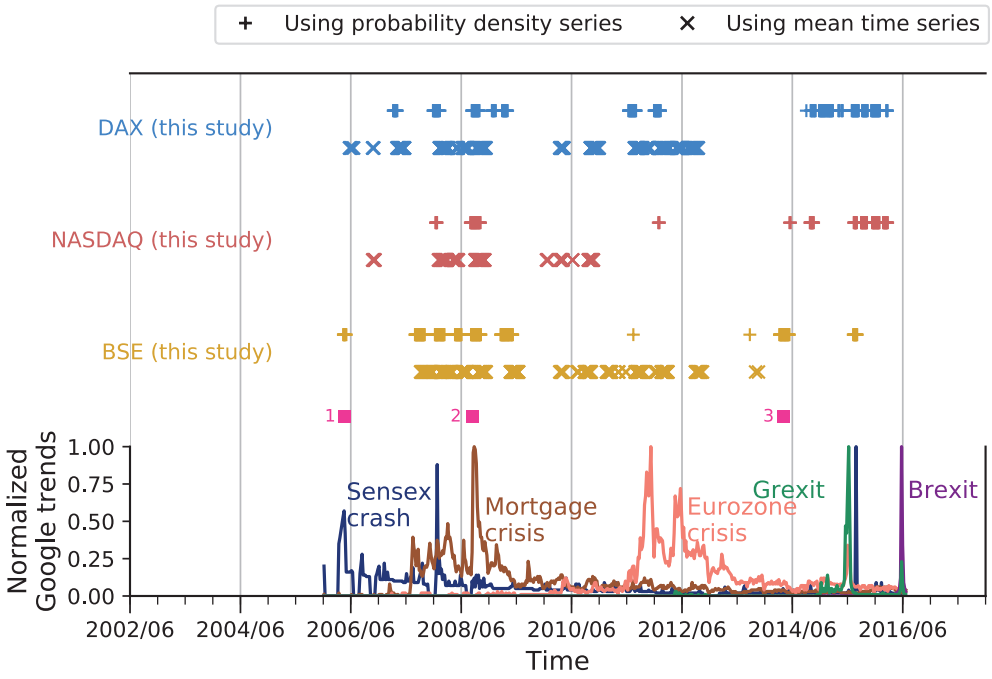

Figure 14.9: **Abrupt transitions in financial stock indices** detected using the probability density time series ('+' markers) and the mean time series ('x' markers). The bottom panel shows the normalized Google trends results for several relevant search terms. Additional pink squares correspond to: (1) BSE SENSEX crash of 22 May 2006, (2) bankruptcy claim by Lehman Brothers on 15 September 2009, and (3) Indian parliamentary elections from 7 April to 12 May 2014.

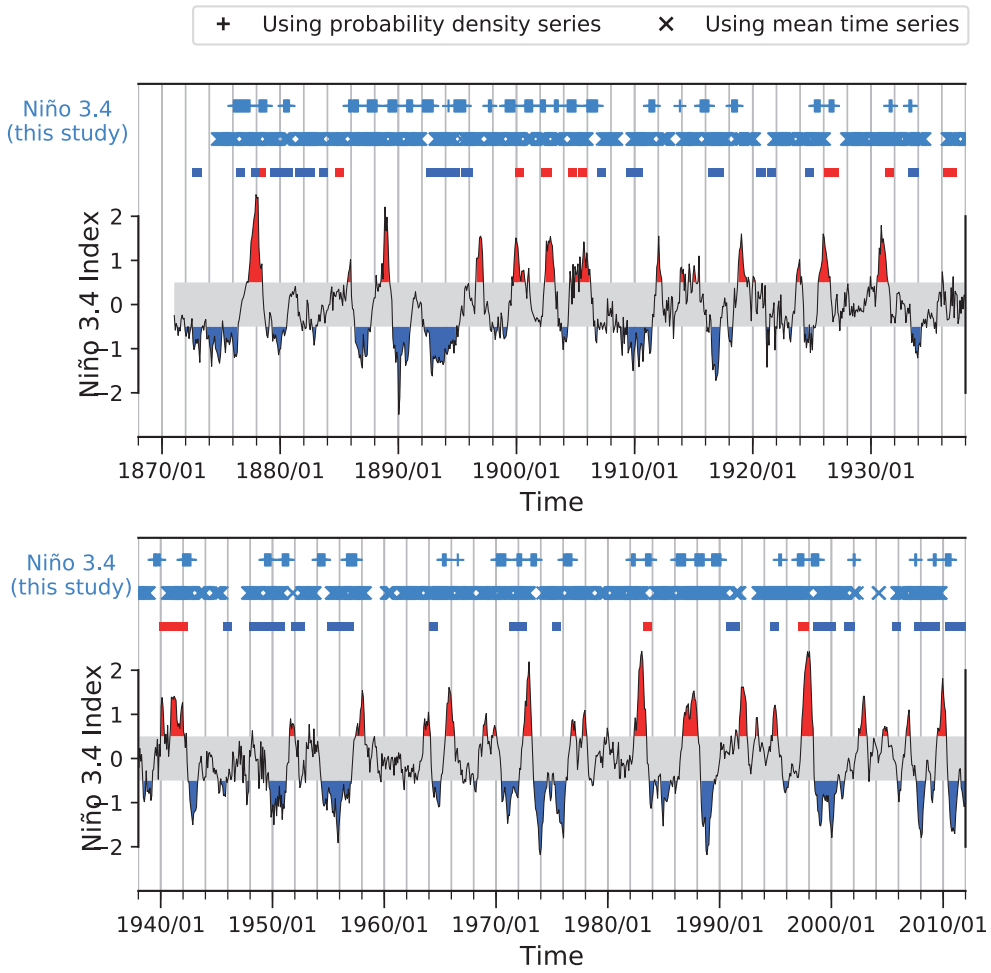

Figure 14.10: **Abrupt transitions in Niño 3.4 SST anomalies** detected using the probability density time series ('+' markers) and the mean time series ('x' markers). The top panel covers the period from 1870 up to 1940, while the bottom panel covers the period from around 1940 to 2012. Our results are compared to the Niño 3.4 index with red shaded regions denoting El Niño years and blue shaded regions denoting La Niña years. Extreme PDO states based on the NCEI PDO index are shown as little red (blue) squares corresponding to the positive (negative) phase of the PDO.

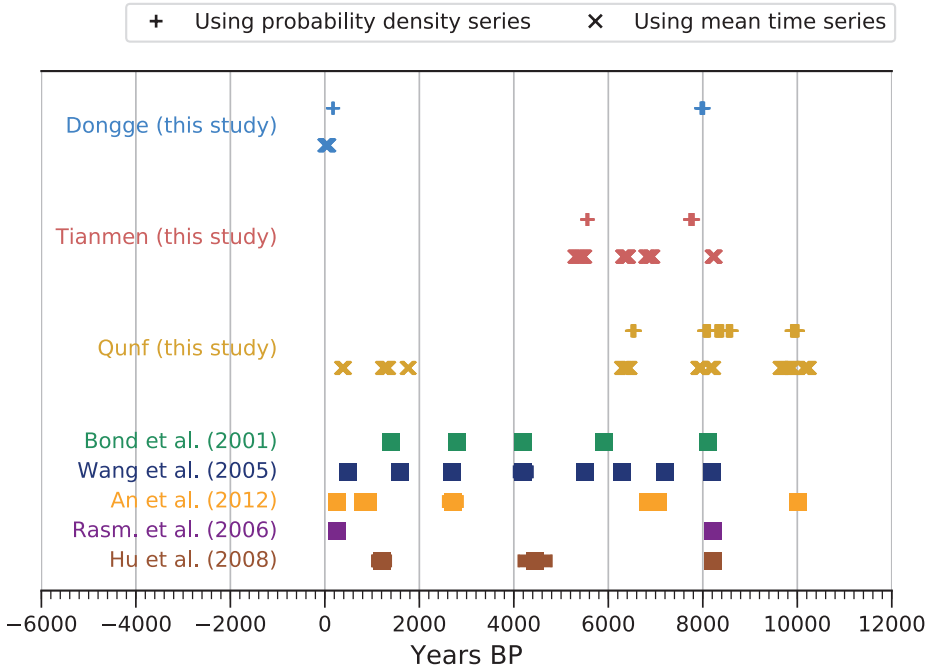

Figure 14.11: **Abrupt transitions in δ^{18}O isotopes** detected using the probability density time series ('+' markers) and the mean time series ('x' markers) for three caves in the Asian monsoon domain: (a) Dongge cave, (b) Tianmen cave, and (c) Qunf cave. The detected transitions are compared to previously reported events (squares) related to the weakening of the Asian monsoon during the Holocene.

Impact of uncertainties on abrupt transition detection

In the main text, we use the example of paleoclimate datasets to illustrate how uncertainties, when properly incorporated into the analysis, can impact the results of an abrupt transition detection scheme. We note how, in the case of the 4.2k event, we detect an abrupt transition around this time in the Dongge adn Tianmen speleothem records, but not in the Qunf cave record. The reason for not detecting this abrupt transition in the Qunf cave becomes clear from the estimated network of recurrence probabilities, whose adjacency matrix is visualised in Fig. 14.14a. In Fig. 14.14b and c, we magnify the probabitliies of recurrence around the 8.2k event and around the 4.2k event respectively. All pairs of time points around 4.2 kyrs BP have almost uniformly large probabilities of recurrence, such that there is not clear community (modular) strucure in the portion of the adjacency matrix represented in Fig. 14.14c. Contrast this to the situation around 8.2 kyrs BP, shown in Fig. 14.14b, where a clearer community structure is visibile which increases the statistical confidence with which we can infer abrupt transitions in this period. This is not possible in the time period around 4.2 kyrs BP. Furthermore, the primary reason for the uniformly large probabilities of recurrence around 4.2 kyrs BP is that the Qunf cave time series has large uncertainties in the period around 3–5 kyrs BP (Fig. 14.8c). During this period, when we choose a pair of time points and ask the question: "Did the observable recur at these time points?" we almost always come up with a non-negilible probability that they might have recurred. To put it in other words, it takes higher precision (i.e., less uncertainty) to say confidently that two time points *have not recurred*. As a result, we get almost equally high probabilities of recurrence for all pairs of time points in the priod ca. 3–5 kyrs BP for the Qunf cave time series.

This example illustrates how uncertainties can influence the transition detection results, and consequently influence all downstream analyses or inferences which are based on the list of transitions obtained. Proper representation of time series uncertainties and a thorough analysis which keeps the uncertainties in mind at each step along the way is thus an absolute necessity to avoid pitfalls in understanding abrupt transitions and their spatio-temporal characteristics.

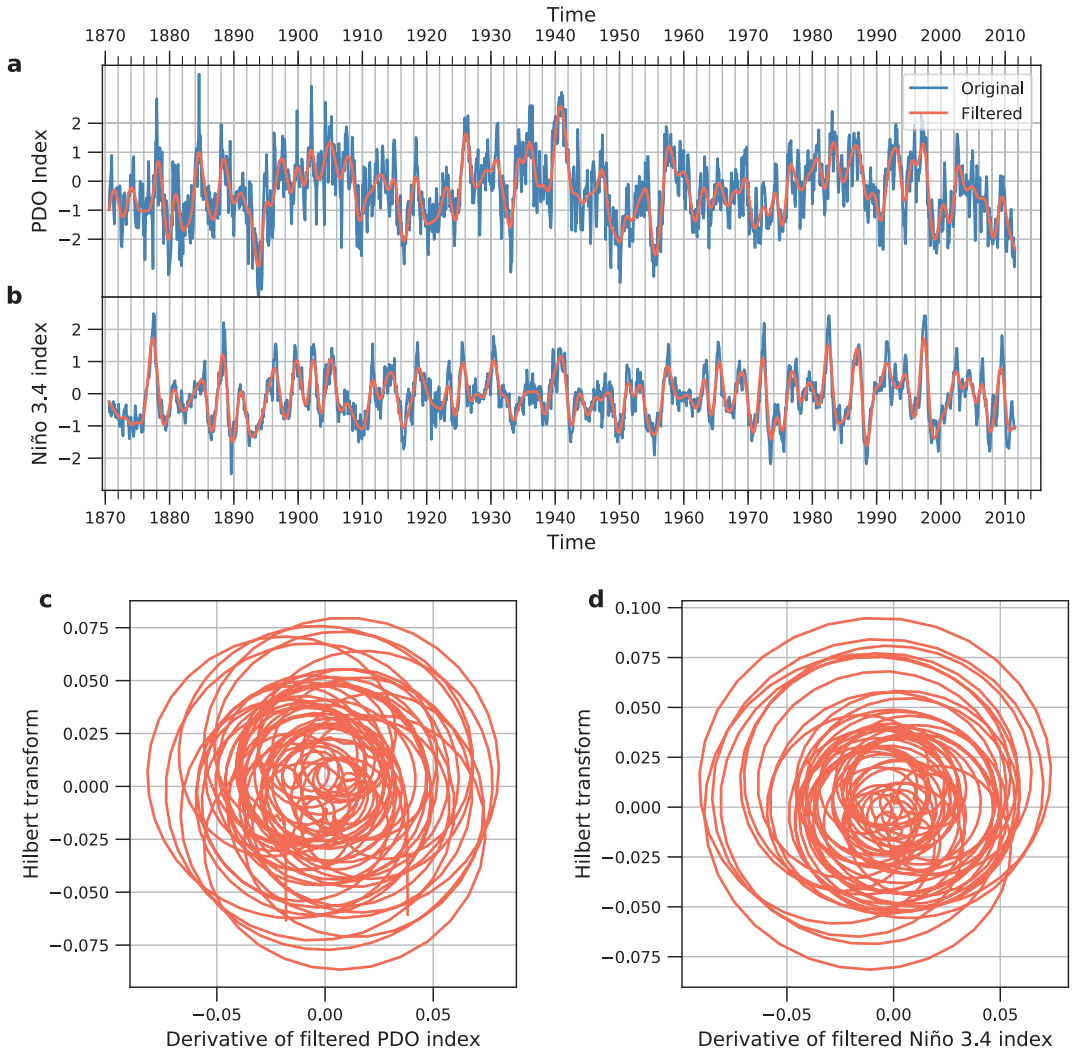

Figure 14.12: **Estimating the phase of PDO and Niño 3.4 indices** using the filtered time series for each of the two indices (shown in **a** and **b**). The filtered time series were obtained using a low-pass forward-backward Butterworth filter that dampens all frequencies higher than $1/12\,\text{month}^{-1}$. The filtered time series are then differentiated with respect to time to obtain the time derivative, which is used for the Hilbert transform (shown in **c** and **d**). The ratio of the Hilbert transform of the time derivative to the the time derivative is defined as the tangent of the *instantaneous phase*. The time derivative helps to ensure that the signal is phase coherent, i.e., it rotates (approximately) about a single center, as seen in **c** and **d**.

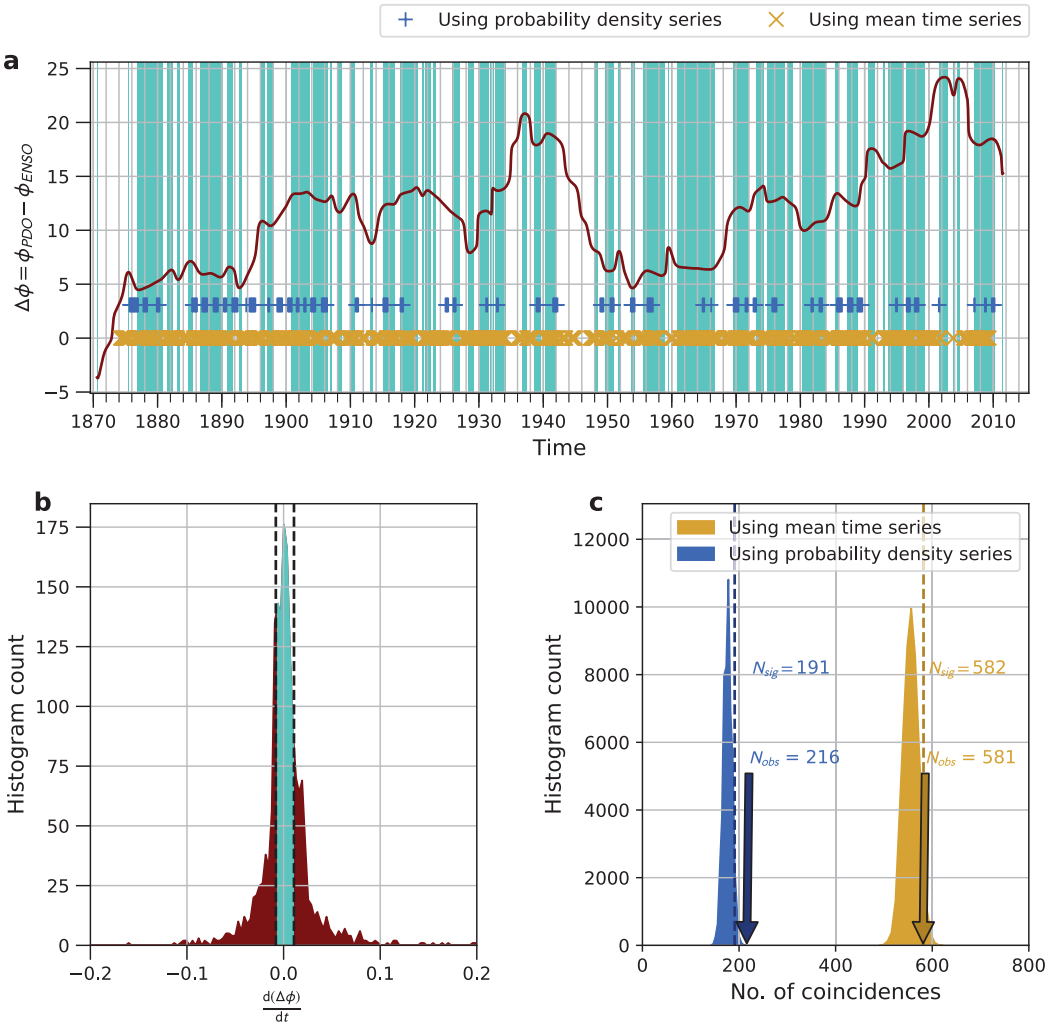

Figure 14.13: **Coincidence analysis** between the detected transitions and the periods of phase locking between the PDO and the ENSO (shown as turquoise shaded regions in **a**) using the probability density time series (blue +'s in **a**) and the mean time series (golden x's in **a**). The periods of phase-locking are identified by first defining the phase difference between the individual phases $\phi_t PDO$ and ϕ_t^{ENSO} as $\Delta\phi_t = \phi_t^{PDO} - \phi_t^{ENSO}$. The phase-locking periods are defined as plateaus in $\Delta\phi_t$ where $\Delta\phi_t \approx 0$. In practice this is determined by identifying those time points where the time derivative of the difference $\frac{d\Delta\phi_t}{dt}$ fall between the 25-th and 75-th percentile of all obtained $\frac{d\Delta\phi_t}{dt}$ values (shown as a histogram in **b**). The interval between the 25-th and 75-th percentile is shaded in turquoise in **b**, validating that this criterion satisfies the need that the values $\Delta\phi_t$ are close to zero. The number of random coincidences obtained by 50000 randomisations of the timings of the detected transitions using the probability density series and the mean time series are shown as histograms in **c**. At a statistical confidence of 5%, the threshold number of coincidences for significance is $N_{sig} = 191$ for the probability density series approach and $N_{sig} = 582$ for the mean time series approach. The corresponding observed number of coincidences N_{obs} equals 216 (581) for the probability density series (mean time series) approaches indicate that the probability density series approach offers a more robust and meaningful transition detection that allows us to validate the coincidence of hte transitions with phase-locking periods of the PDO and the ENSO.

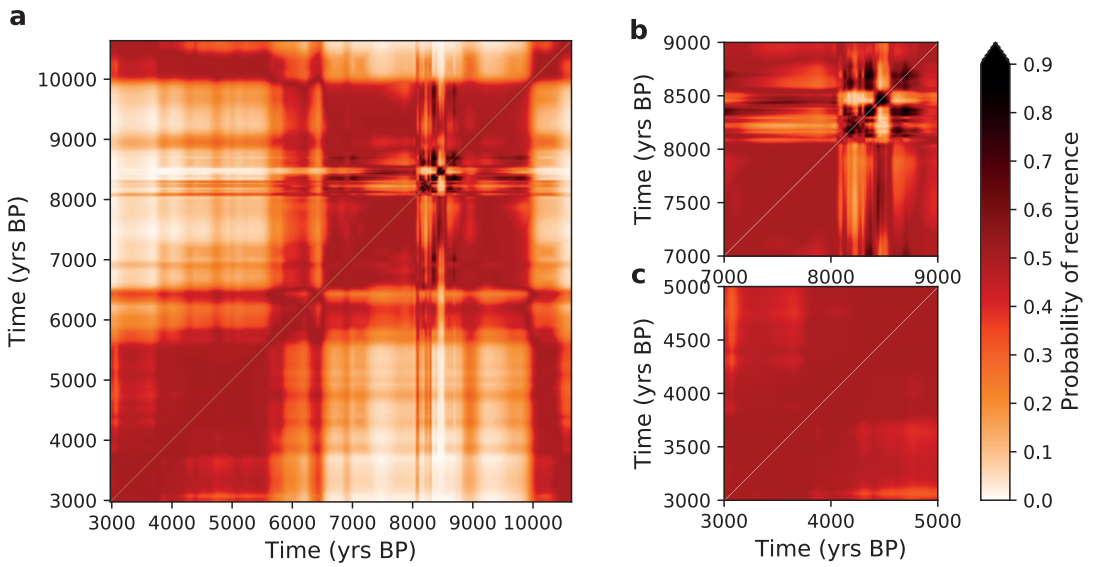

Figure 14.14: **Probabilty of recurrence matrix for Qunf cave**, for the entire time series in **a**, for the 8.2k event (for 7–9 kyrs BP) in **b**, and for the 4.2k event (for 3–5 kyrs BP) in **c**. In contrast to the modular structure of the recurrence matrix in **b**, the recurrence plot in **c** is almost structureless, as all pairs of time points in this period have high probabilities of recurrence. The ubiquity of the high probabilities of recurrence in **c** can be traced back to the large uncertainties in the proxy record in the corresponding period during 3–5 kyrs BP (see Fig. 14.8c).

Laminated Gypsum Deposits Capo Bianco (Sicily)
Courtesy: Kalima/Wikipedia

15. Gaining Confidence in Transitions

Paper 14 N. Marwan, S. Schinkel, J. Kurths: Recurrence plots 25 years later – Gaining confidence in dynamical transitions, Europhysics Letters, 101, 20007 (2013). DOI:10.1209/0295-5075/101/20007

15.1 Abstract

Recurrence plot based time series analysis is widely used to study changes and transitions in the dynamics of a system or temporal deviations from its overall dynamical regime. However, most studies do not discuss the significance of the detected variations in the recurrence quantification measures. In this letter we propose a novel method to add a confidence measure to the recurrence quantification analysis. We show how this approach can be used to study significant changes in dynamical systems due to a change in control parameters, chaos-order as well as chaos-chaos transitions. Finally we study and discuss climate transitions by analysing a marine proxy record for past sea surface temperature.

This paper is dedicated to the 25th anniversary of the introduction of recurrence plots.

15.2 Introduction

In the November issue of EPL in 1987, Eckmann et al. proposed the recurrence plot as a tool to get easily insights into even high-dimensional dynamical systems [86, 224]. Over the last 25 years, their paper has "led to an active field, with many ramifications [these authors] certainly had not anticipated" [240]. Starting from the visual concept of recurrence plots (RPs), different statistical and quantification approaches have been added, like recurrence quantification (RQA), dynamical invariants from RPs, and recurrence networks [77, 224, 239, 418]. 25 years after Eckmann's seminal paper, RPs and related methods are widely accepted tools for data analysis in various disciplines, as in physics [408] and chemistry [331], but also for real world systems as in life science [237, 447], engineering [262, 278], earth science [241], or finance and economy [17, 59, 120]. This interdisciplinary success is not only caused by the attractive appearance of RPs but also by the simplicity of the method [421]. Based on RPs, we can study the dynamics, transitions, or synchronisation of complex systems [86, 224, 239]. In particular, such transitions can be uncovered from a changing recurrence structure.

The different aspects of recurrences can be inferred by measures of complexity, also known as *recurrence quantification analysis* (RQA). Although these measures are often applied to real data and interpreted as indicators of a change of the system's dynamics, a statistical evaluation of the results was not yet satisfiably addressed. An early attempt has suggested to use a specific model class (e.g., auto-correlated noise) corresponding to the null-hypothesis and then testing the RQA results against such models [238]. For a general test of how significant the value of certain RQA measures (in particular determinism DET and laminarity LAM) is, a test distribution was derived using binomial distributions [145]. In order to compare time-dependent RQA measures of different observations, a bootstrap approach was introduced [341]. However, we still miss a method which can derive the important significance level of dynamical transitions within *one* dynamical system as indicated by RQA. Without providing some statement on the confidence of RQA results, any conclusions drawn from RQA might remain questionable [225].

In this letter we propose a method which calculates the confidence level for the most important, line-based RQA measures. We pick up the idea of bootstrapping [341] and develop a new algorithm allowing for gaining confidence in RQA based dynamical transition analysis. Using this approach we for the first time are able to provide a significance statement for detected transitions of not only qualitatively different systems dynamics based on RQA but using only a single observation. This will enable us to interpret the results of RQA in a more reliable way in the future research and, hence, will further increase the potentials and acceptance of RQA.

15.3 Recurrence Quantification Analysis

A RP tests for the pair-wise closeness of all possible pairs of states $(\vec{x}_i, \vec{x}_j)$ in an m-dimensional phase space, $R_{i,j} = \Theta\left(\varepsilon - d(\vec{x}_i, \vec{x}_j)\right)$, with Θ as the Heaviside function, ε as a threshold for closeness [239, 338], and $i, j = 1, \ldots, N$ where N is the number of observed states. The closeness $d(\vec{x}_i, \vec{x}_j)$ can be measured in different ways, using, e.g., spatial distance, string metric or local rank order [239]. Most often, the spatial distance using maximum or Euclidean norm $d(\vec{x}_i, \vec{x}_j) = \|\vec{x}_i - \vec{x}_j\|$ is used. Then, the binary recurrence matrix $\mathbf{R}$ contains the value one for all close pairs $\|\vec{x}_i - \vec{x}_j\| < \varepsilon$. A phase space trajectory can be reconstructed from a time series by time delay embedding [286].

Similar evolving epochs of the phase space trajectory cause diagonal structures parallel to the main diagonal in the RP [239]. The length of such diagonal line structures depends on the dynamics of the system (periodic, chaotic, stochastic) and can be directly related with dynamically invariant properties, like K_2 entropy [239]. Therefore, the distribution $P(l)$ of line lengths l is used by several RQA measures in order to characterise the system's dynamics [239]. Here we focus on the measure *determinism* (DET), which is the fraction of recurrence points forming diagonal structures, $DET = \sum_{l=l_{\min}}^{N} l\, P(l) / \sum_{l=1}^{N} l\, P(l)$. A minimal length $l_{\min}$ defines a diagonal line [239].

Slowly changing states, as occuring during laminar phases (intermittency), cause vertical structures in the RP. Therefore, the distribution $P(v)$ of line lengths v is used to quantify the laminar phases occuring in a system. Similar to DET, the measure *laminarity* (LAM) is defined as the fraction of the recurrence points forming vertical structures, $LAM = \sum_{v=v_{\min}}^{N} v\, P(v) / \sum_{v=1}^{N} v\, P(v)$ [237].

The later discussed approach will not only be applicable to these two measures DET and LAM, but to all line based RQA measures, including recurrence time based measures [276].

In order to study time dependent behaviour of a system or data series, we compute these RQA measures using a moving window, applied on the time series. The window has size

w and is moved with a step size s over the data in such a way that succeeding windows overlap with $w-s$. This technique was successfully applied to detect chaos-period transitions [397], but also more subtle ones such as chaos-chaos transitions [237], or different kinds of transitions between strange non-chaotic behaviour and period or chaos [274]. It is applicable to real world data, as demonstrated for the study of, e.g., cardiac variability [441], brain activity [340], changes in finance markets [367] or thermodynamic transitions in corrosion processes [262]. However, all these applications miss a clear significance statement.

With respect to our goal of a transition detection in the dynamical system, we formulate the following *null-hypothesis* $\mathcal{H}_0$: The dynamics of a system X does not change over time, thus, the recurrence structure does not change and the RQA measure M of such a system will therefore be distributed around an unknown, but non-zero mean $\mu(M)$ with unknown variance $\sigma(M)$.

For completely random systems the expected distribution of some RQA measures can be modeled [145]. However, for complex real systems it cannot be assumed that the underlying recurrence structure is completely random but rather features a certain recurrence structure at all times. A dynamical transition in the system changes the recurrence structure and, hence, the RQA measures. If the impact of the transition is large enough, it will push the RQA measure M out of its normal range. The deviation from this normal range can be considered as significant if the observed value of $M(t)$ at time point t is outside of a predefined interquantile range such as $[\alpha/2,\ 1-\alpha/2]$.

15.4 Variance estimation by bootstrapping

In order to test for significant deviations from the unknown mean of the data, we first have to estimate the variance of the RQA measures in question. To do so, we introduce a bootstrap approach in the calculation of the RQA measures [89]. Bootstrapping is a conceptually simple yet powerful statistical tool to estimate the variance of statistical parameters, such as the mean, even if the underlying distribution is unknown. Since we cannot assume that the distributions of line lengths $P(l)$ and $P(w)$ follow a known probability distribution, we use this advantage of the bootstrap approach to estimate the confidence bounds of the RQA measures M which rely on these distributions. We will use bootstrap resampling to create a test distribution of the RQA measures from which we can then estimate the overall mean and variance of those measures and, finally, to formulate the important significance statement.

The time dependent RQA analysis is based on moving windows, shifted over the time series, and calculating the RP within these windows. For each of the N_w time steps of the moving window t ($t = w/2, 3w/2, 5w/2, \ldots, N-w/2$), i.e., for different time points, we get the local RPs with $n(t)$ diagonal lines and then calculate the corresponding local histograms of diagonal lines $P_t(l)$. The time dependent RQA measures $M(t)$ (e.g., $M(t) = DET(t)$ are calculated from $P_t(l)$.

In order to estimate a general distribution of the RQA measures following our null-hypothesis $\mathcal{H}_0$, we suggest the following procedure. All local histograms $P_t(l)$ are merged together in order to get an overall histogram and thus a statistical average of the recurrence structure of the system, i.e., we bootstrap from the unification

$$\hat{P}(l) = \sum_t P_t(l) \tag{15.1}$$

of the local histograms. We draw $\bar{n}$ recurrence structures (i.e. diagonal lines) from $\hat{P}(l)$. The number $\bar{n}$ of drawings is the mean number of recurrence structures $n(t)$ contained in the

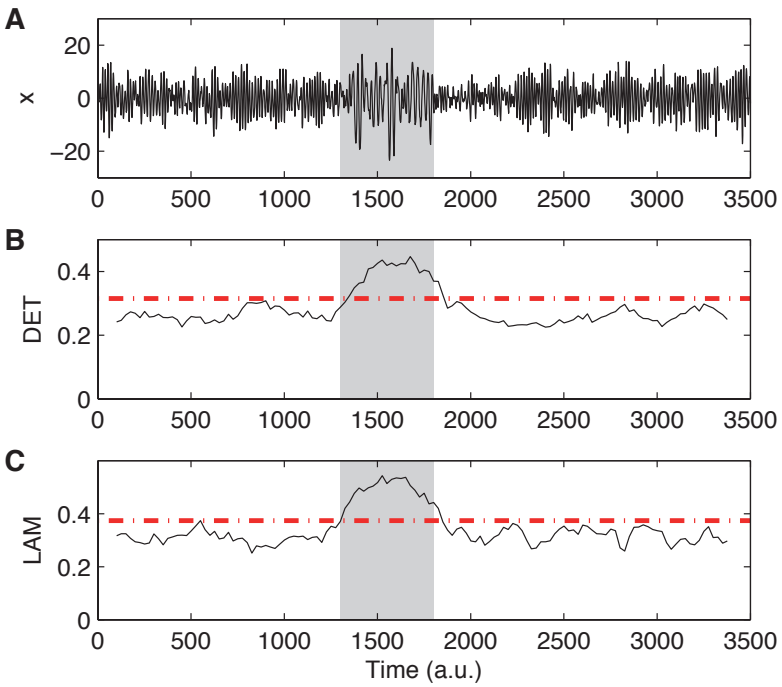

Figure 15.1: (Colour online) (A) Autocorrelated process with slight transitions of the parameters between time 1,300 and 1,800 (shaded region). Corresponding RQA measures (B) determinism DET and (C) laminarity LAM, indicating the epoch of changed dynamics in the autocorrelated process between 1,300 and 1,800 (shaded area) by an increasing of their values. This increase exceeds the 99% confidence interval (dashed line) as derived by the proposed bootstrapping approach.

local distributions $P_t(l)$,

$$\bar{n} = \frac{1}{N_w} \sum_{t=w/2}^{N-w/2} n(t) = \frac{1}{N_w} \sum_{t=w/2}^{N-w/2} \sum_{l=1}^{N} P_t(l). \tag{15.2}$$

From the resulting empirical distribution $P(l)^*$, we compute the corresponding RQA measure, say in our case DET. By repeating this procedure B times (e.g. $B = 1,000$), we get the test distribution for DET, say $F(DET)$. By calculation of the α-quantiles of the distribution $F(DET)$, we derive the confidence intervals of DET which can be used to statistically infer the significance of the changes of $DET(t)$, and thus the observed transitions.

15.5 Illustration of the method

We illustrate the proposed statistical test on two model systems: (1) a linear autocorrelated process and (2) a nonlinear process, both for changing parameters.

(1) Our first example is an autocorrelated stochastic signal with changing properties, i.e., an autoregressive process of order 2

$$x_i = a_1 x(i-1) + a_2 x(i-2) + b\xi(i) \tag{15.3}$$

with $a_1 = 1.80$, $a_2 = -0.972$ and $b = 0.64$. After time step 1,300, the AR coefficients slightly change to $a_1 = 1.85$, $a_2 = -0.917$ and $b = 0.76$ for 500 time steps. Afterwards these

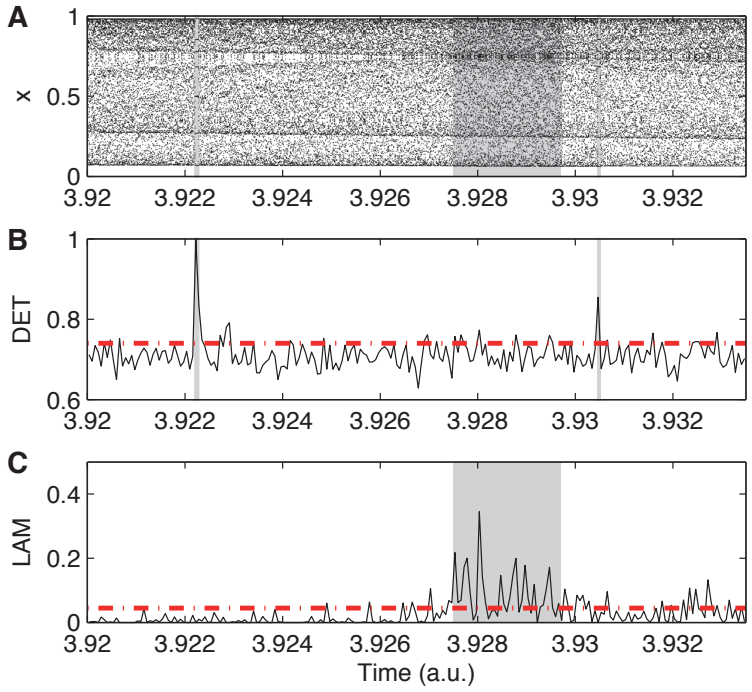

Figure 15.2: (A) Logistic map with chaos-period and chaos-chaos transitions for control parameter $a = [3.9200\ 3.9335]$ and corresponding RQA measures (B) DET and (C) LAM. For $a = [3.92221\ 3.92227]$ we have a period-7 window, for $a = [3.93047\ 3.93050]$ a period-8 window and at a broad range around $a = 3.928$ intermittency (marked with shaded area). (B) and (C) 99% significance levels are shown as dash-dotted lines.

coefficients are changed back to the initial values. With this procedure the signal contains a short epoch of slightly changed dynamics (Fig. 15.1A).

Next we compute the RQA measures DET and LAM from this data series (no embedding) using windows of size $w = 200$ and with a step size of $s = 25$. The threshold ε is chosen for each window separately to preserve a constant recurrence rate of 7.5% [338]. The bootstrap resampling is then applied using 1,000 resamplings. As we expect in the window of increased auto-correlation a larger number of diagonal and vertical lines, we will only consider the upper confidence level.

The DET measure reveals a high number of diagonal lines in the RP. Before time 1,300 and after time 1,800, DET values vary between 0.25 and 0.3. This coincides with the moderate auto-correlation of the process. Between the time 1,300 and 1,800, DET shows an increase and exceeds the confidence interval of 0.31, corresponding to a 99% confidence level. Similar, LAM varies before and after the inset of changed dynamics at a lower level ($LAM \approx 0.3$) and increases within the period between time 1,300 and 1,800 up to $LAM \approx 0.55$ due to its increased persistence. This increase of DET and LAM confirms the further increase of the auto-correlation of the considered process within this epoch.

(2) To test whether the proposed method is also capable of providing a quanatitative statement of more subtle changes in dynamics, like chaos-order and chaos-chaos transitions, we use a modified logistic map with mutual transitions [397]

$$x_{i+1} = a(i)x(i)(1-x(i)) \tag{15.4}$$

with the control parameter a in the range $[3.9200\ 3.9335]$ with increments of $\Delta a =$

2.5 10^{-7}. Using this intervall we find for $a = [3.92221\ 3.92227]$ a period-7 window, for $a = [3.93047\ 3.93050]$ a period-8 window and at a broad range around $a = 3.928\ldots$ intermittency (Fig. 15.2). Again, for these kind of dynamical transitions we can expect increased values of DET and LAM, hence, we only need to consider the upper confidence level.

Next we compute the RQA measures DET and LAM from this data series (no embedding) using windows of size $w = 250$ and with a step size of $s = 250$. The threshold ε is chosen for each window separately in order to preserve a constant recurrence rate of 5%. As a line structure we consider each line with a length of at least two points, i.e. $l_{\min} = v_{\min} = 2$.

The measure DET shows for the periodic windows at $a = [3.92221\ 3.92227]$ and $a = [3.93047\ 3.93050]$ maxima [237]. The periodic behaviour of the system causes only long diagonal lines, resulting in high values of DET. In contrast, LAM shows high values only for the region of intermittency around $a = 3.928\ldots$. In this region, the system has slowly changing, laminar states [237]. For the proposed bootstrapping approach, we use 1,000 resamplings in order to construct the test statistics. As the 99%-quantile we find for DET $q_{0.99} = 0.74$ and for LAM $q_{0.99} = 0.04$. These values provide the 99% confidence level for DET and LAM. Thus, the two maxima of DET in the periodic windows are significant on a 99% level ($p < 0.01$). For LAM we find several significant high values of 99% significance in the region of intermittency around $a = 3.928$. This is due to the longer range of intermittent behaviour in this region of the control parameter a.

15.6 Application to real world data

The climate system is a highly complex one which has undergone various transitions in the past. The investigation of relationships between sea surface temperature (SST) and specific climate responses, like the Asian monsoon system or the thermohaline circulation in the Atlantic, represents an important scientific challenge for understanding the global climate system, its mechanisms, and its related variability. In palaeoclimatology, different archives are used to reconstruct and study climate conditions of the past, as lake [238] and marine sediments [139] or speleothemes [171]. Alkenone remnants in the organic fraction of marine sediments, produced by phytoplankton, can be used to reconstruct SST of the past, allowing to study the temperature variability of the oceans [138]. Here we will use a marine record from the Ocean Drilling Programme (ODP) derived from a drilling in the Arabian see, ODP site 722. This record provides alkenone based reconstructed SST in the realm of the Asian monsoon system for the past 3.3 Ma (Fig. 15.3A) [139]. During this epoch, a dramatic climate change happened by two steps of global cooling [139]. The first step between 3.0 and 2.5 Ma coincides with the high-latitude Northern Hemisphere glaciation. The second step of cooling occurred between 2.0 and 1.5 Ma and is related with a continuous cooling of the subtropical oceans but a stationary high-latitude climate. Some mechanisms of these global-scale climate changes are known and coincide with a transition to an obliquity-driven climate variability with a 41 ka period after 2.8–2.7 Ma [139], a shift from that climate variability (with high-latitude glaciation) to glacial-interglacial cycles with a 100 ka period after a transition period between 1.25 and 0.7 Ma [266], and the development of the Walker circulation at 1.9–1.5 Ma [309]. The RQA and the proposed significance test are promising tools to analyze the alkenone SST record of the ODP site 722.

The original time series of ODP 722 is not equally sampled. Therefore, we interpolate it to a time series with sampling period of 2 ka. For performing the RQA we use a time delay embedding with dimension $m = 3$ and delay $\tau = 2$. The threshold is chosen to preserve a constant recurrence rate of 7.5%. The bootstrapping is performed using 1,000 resamplings. In this real world example, we use a reduced confidence level of 95%. As we do not know

which kinds of dynamical transition are there, we will consider both the upper and the lower confidence level.

The RQA measures DET and LAM reveal various significantly high and low values as summarised in Fig. 15.3 and Tab. 15.1.

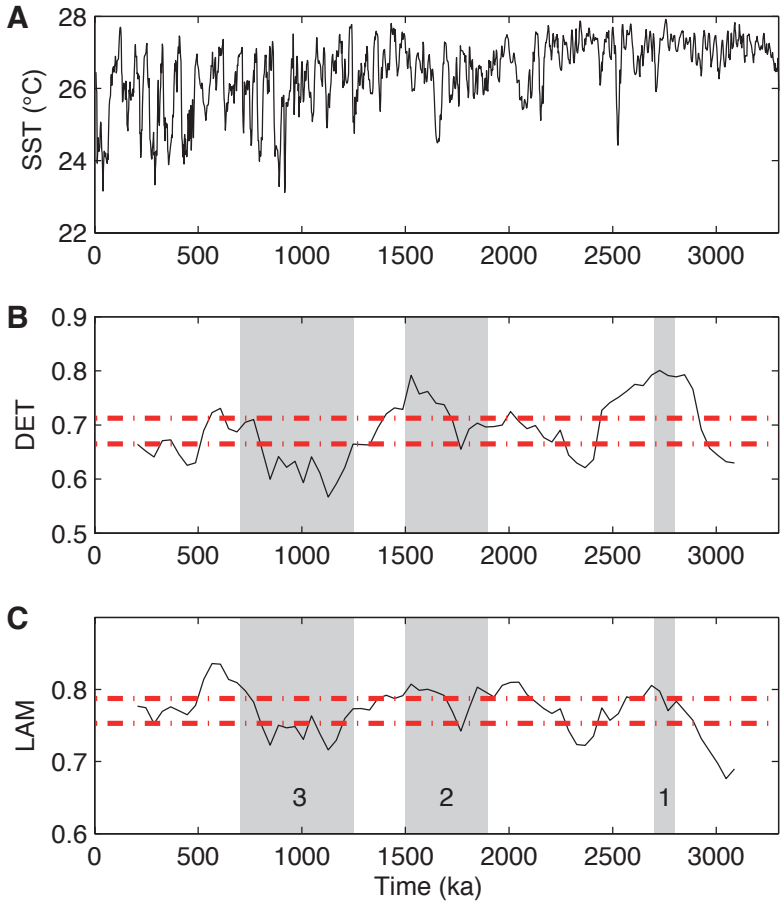

Figure 15.3: (A) Alkone SST record of ODP site 722, and corresponding (B) DET and (C) LAM measures (95% confidence bounds are shown with blue dash-dotted lines). The transition to (1) the Northern Hemisphere glaciation, the (2) intensification of the Walker circulation, and (3) the transition phase from glaciation to glacial-interglacial cycles are marked by shaded areas.

Around 3.0 Ma ago, a long-lasting period of warm climate with a permanent El Niño came to an end. This general change from a warm climate towards a more variable and cooler one is clearly indicated by a change from low to high DET and LAM values.

The first cooling phase between 3.0 and 2.5 Ma is well indicated by high values of the measure DET which can be considered to reflect an increase in regularity and auto-correlation of the system. The rapid onset of the Northern Hemisphere glaciation between 2.8 and 2.7 Ma is marked by an increase of LAM, corresponding to an intermittent behaviour. The fact that DET and, thus, the auto-correlation increased before the intermittent behaviour can be understood as a critical slowing down of the dynamics as it is typical for tipping points [60]. The increase of DET might, therefore, be an indication that the climate system reached a tipping point at 3.0–2.9 Ma, leading to the regime change of Northern Hemisphere glaciation.

Between 2.4 and 2.3 Ma, DET and LAM decreased, revealing a short period of more

irregular and stochastic variability. This might be an indication for a transition between two different regimes. This transition was not yet found in palaeoclimate literature, but is confirmed by another study also using a nonlinear measure for transition detection [212].

The period of the development of the Walker circulation between 1.9 and 1.5 Ma is marked by an increase in both, DET and LAM.

The transition period from the glaciation regime with dominant 41 ka cycle to the glacial-interglacial regime with 100 ka cycle is marked by a significant decrease of the measures DET and LAM. This corresponds to a phase of less regularity or more stochastic variability of the SST.

Further high values in DET and LAM occur at around 2.0 Ma and between 0.75 and 0.5 Ma. At 2.0 Ma, a reorganization of subtropical and tropical ocean circulation begun which was triggered by high-latitude cooling and its impact on deepwater formation. Between 0.75 and 0.5 Ma, the sensitivity of the high-latitude climate response to solar forcing reached its maximum [309]. This is consistent with recent findings of a coherence between solar forcing and climate variability in this region during this period [212].

The transitions found correspond to dynamical transitions caused by different changes in climate. The recurrence based analysis can not only detect these transitions but also provide additional information about the climate transitions, whose onsets are, at least partly, known [73, 212].

Table 15.1: Major regime changes in alkenone SST record from ODP site 722 as indicated by significant high values of determinism (DET+) and laminarity (LAM+) as well as significant low values (DET− and LAM−).

Period	DET+	DET−	LAM+	LAM−
Northern Hemisphere glaciation	2.9–2.5		2.75–2.65	
Interregime transition		2.4–2.3		2.4–2.3
(Sub-)Tropical reorganisation	2.0		2.05–1.95	
Development Walker circulation	1.7–1.4		1.7–1.5	
Transition 41 ka to 100 ka		1.25–0.8		1.2–0.8
Maximal climate sensitivity	0.65-0.55		0.75–0.5	

15.7 Conclusion

We have introduced a bootstrap based approach for providing confidence levels for line-based recurrence quantification measures, which are related to dynamical properties (like Lyapunov exponent or K_2 entropy). Using this technique, we are able to investigate changing dynamics by RQA and can, for the first time, provide confidence levels for the variation of the RQA measures and, thus, the changed dynamics. We have shown the potential of the approach by studying dynamical changes in an auto-correlated process and for chaos-order and chaos-chaos transitions. These examples have also demonstrated the importance of considering confidence intervals, as fluctuations in the RQA measures can be misinterpreted if the overall variance of these measures is not taken into consideration.

The application of our approach on sea surface temperature variability of the past has demonstrated that recurrence based analysis provides new insights in known palaeo-climate changes. Recurrence properties can be help for a better understanding of the mechanisms of the transitions between different climate regimes.

25 years after the introduction of recurrence plots by Eckmann et al. [86], the development of this technique still continues. With our paper we would like to honor the seminal work by these authors, but would also like to emphasize that the calculation of confidence levels for the RQA measures is an important requirement for the method to get widely accepted. It is highly desirable that future research using RQA comes along with corresponding confidence levels.

Acknowledgments

This work was supported by the Potsdam Research Cluster for Georisk Analysis, Environmental Change and Sustainability (PROGRESS, BMBF support code 03IS2191B), the DFG research groups FOR 1380 (HIMPAC) and FOR 868 ("Computational Modeling of Behavioral, Cognitive, and Neural Dynamics").

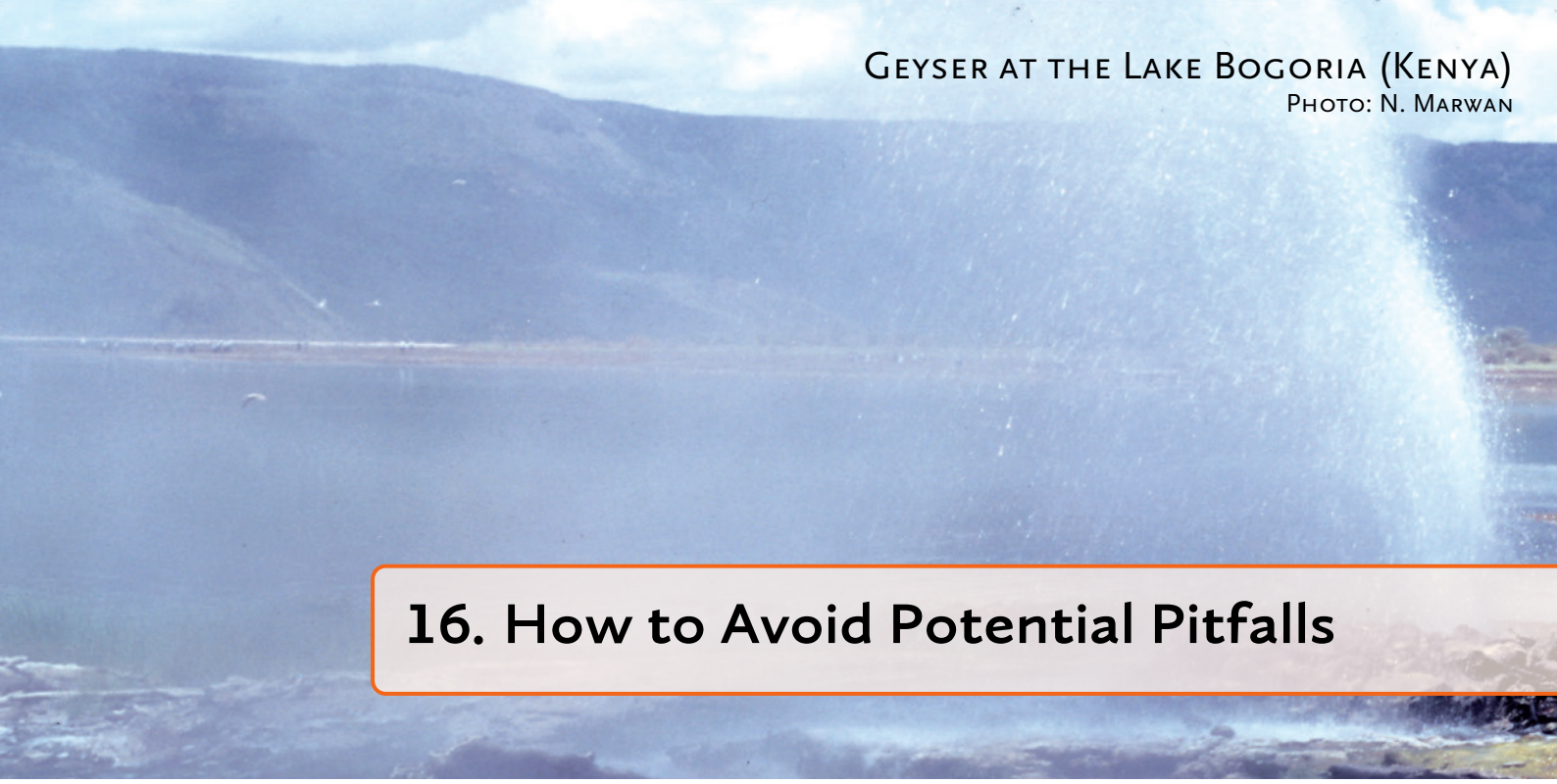

Geyser at the Lake Bogoria (Kenya)
Photo: N. Marwan

16. How to Avoid Potential Pitfalls

Paper 15 N. Marwan: How to avoid potential pitfalls in recurrence plot based data analysis, International Journal of Bifurcation and Chaos, 21(4), 1003–1017 (2011). DOI:10.1142/S0218127411029008

Abstract

Recurrence plots and recurrence quantification analysis have become popular in the last two decades. Recurrence based methods have on the one hand a deep foundation in the theory of dynamical systems and are on the other hand powerful tools for the investigation of a variety of problems. The increasing interest encompasses the growing risk of misuse and uncritical application of these methods. Therefore, we point out potential problems and pitfalls related to different aspects of the application of recurrence plots and recurrence quantification analysis.

16.1 Introduction

Since its introduction in 1987 by Eckmann, Oliffson Kamphorst, and Ruelle [86], and the development of different quantification approaches, recurrence plots (RPs) have been widely used for the investigation of complex systems in a variety of different disciplines, as physiology, ecology, finance or earth sciences [e.g., 16, 47, 100, 224, 289, 339, 392, 447]. RPs may attract attention because of their ability to produce beautiful or fancy pictures, as in the case of the colourful representations of fractal sets [213]. The recent remarkable increase of applications can be traced down in part to several free software packages available for calculating recurrence plots and the corresponding recurrence quantification analysis (RQA). Since these methods are also claimed to be very powerful even for short and non-stationary data, we should be careful not to consider them as a kind of a magic tool, which works on all kinds of data. Owing to the fact that these methods are indeed in some sense powerful and rather adaptable to various problems, it is really important that the user knows how these methods work and has understood the ideas behind the RP and the measures of complexity derived from it. Any uncritical application will lead to serious pitfalls and mis-interpretations. As the number of applicants increases, the risk of careless application of RPs and RQA grows.

In this article we try to highlight some of the pitfalls which can occur during the application of RPs and RQA and present future directions of research for a deep theoretical understanding of the method.

16.2 Recurrence plots and recurrence quantification

Although similar methods already existed before, the RP, $R_{i,j} = \Theta(\varepsilon - ||\vec{x}_i - \vec{x}_j||)$, for the analysis of the dynamics of a dynamical system by using its phase space trajectory was introduced by Eckmann, Oliffson Kamphorst, and Ruelle [86]. This method can be used in order to visualise the recurrence of a state, i.e., all the times when this state will recur. In the 1990's, a heuristic approach of quantification RPs by its line structures has led to the recurrence quantification analysis (RQA) [237, 418]. In this approach, the density of recurrence points as well as the histograms $P(l)$ of the lengths l of the diagonal and vertical lines in the RP are quantified. The density of recurrence points (recurrence rate) coincides with the definition of the correlation dimension [124]. Moreover, RPs contain much more information about the dynamics of the systems: dynamical invariants like Rényi entropy or correlation dimensions can be derived from the structures in RPs [101, 384], RPs can be used to study synchronisation [323, 346] or to construct surrogate time series [386] and long time series from ensemble measurements [173]. For a comprehensive introduction we point to [239].

16.3 Pitfalls

16.3.1 Parameter choice for recurrence analysis

RP and RQA depend on some parameters which should be properly chosen. For the actual recurrence analysis, a recurrence threshold is necessary. This measure is probably the most crucial one and is discussed in the next subsection.

As already mentioned, the quantification of recurrence structures depends on lines in the RP; by defining a minimal length of such lines, it is possible to adjust the sensitivity of line based recurrence measures. In Subsect. 16.3.3 and 16.3.4 we will come back to this parameter.

If we start our recurrence analysis from a time series, we have first to reconstruct a phase space by using a proper embedding, e.g., time-delay embedding [286]. This involves the proper setting of two additional parameters: the embedding dimension m and the time-delay τ. Although the estimation of dynamical invariants does not depend on the embedding [384], the RQA measures depend on the embedding. Standard approaches for finding optimal embedding parameters, like false nearest neighbours for embedding dimension and auto-correlation or mutual information for time-delay, can be widely found in the literature [e.g., 165]. However, it is recommended to visually cross-check the embedding parameters by looking at the resulting RP. Non-optimal embedding parameters can cause many interruptions of diagonal lines, small blocks, or even diagonal lines perpendicular to the LOI (this corresponds to parallel trajectory segments running in opposite time direction; Fig. 16.1). The experience has shown that the delay is sometimes overestimated by auto-correlation and mutual information. The embedding dimension has also to be considered with care, as it artificially increases diagonal lines (will be discussed in Subsect. 16.3.3) [239].

In general, it is recommended to study the sensitivity (or robustness) of the results of the recurrence analysis on the parameters (recurrence threshold, embedding parameters).

Although not really a parameter, it is worth to briefly discuss the different recurrence definitions. The most frequently used definition is the to consider neighbours in the phase

space which are smaller than a threshold value (the recurrence threshold). Distances can be calculated using different norms, like Maximum or Euclidean norm [239]. Maximum norm is sometimes preferred because of its better computational efficiency (only minor differences in the results when compared to Euclidean norm). Another definition of recurrence considers a fixed amount nearest neighbours. This recurrence criterion is used when the number of neighbours is important. Pitfalls related to these recurrence criteria are also discussed in Subsect. 16.3.7. More interesting are combinations of the above criteria with dynamical properties of the phase space trajectory, e.g., perpendicular RPs (Subsect. 16.3.3), or recurrence based on order patterns [128]. Order patterns are representations of the local rank order of a given number d of values of the time series (order pattern dimension). As the number of order patterns is equal to $d!$, the dimension should not be chosen too large, because many order patterns will appear rather seldom and the RP will be sparse. Even $d = 4$ is often already not appropriate, therefore, $d = 3$ is the best choice in most cases (depending on the problem of interest, $d = 2$ may also be appropriate).

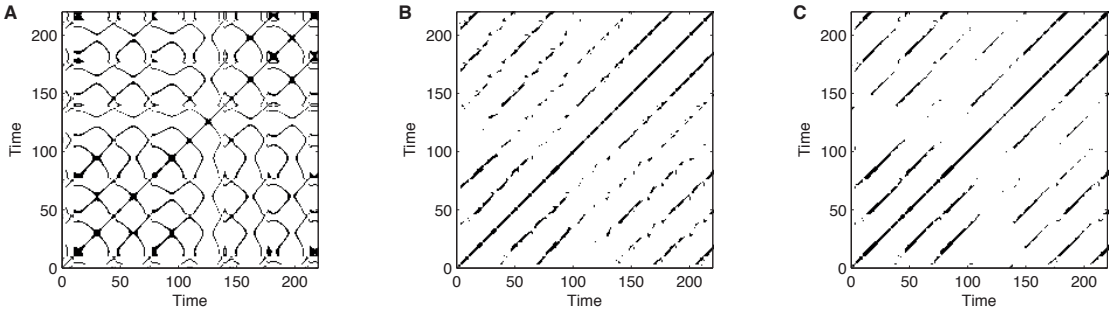

Figure 16.1: Recurrence plots of the Rössler oscillator with parameters $a = b = 0.25$ and $c = 40$ using different embedding: (A) $m = 1$, $\tau = 1$, (B) $m = 3$, $\tau = 12$, (C) $m = 3$, $\tau = 6$ (adaptive recurrence threshold to ensure (A) $RR = 0.1$, (B, C) $RR = 0.05$). Non-optimal embedding can cause line structures perpendicular to the main diagonal, wobbly or interrupted lines (A, B).

16.3.2 Recurrence threshold selection

The recurrence threshold ε is a crucial parameter in the RP analysis. Although several works have contributed to this discussion [e.g., 239, 245, 338, 383], a general and systematic study on the recurrence threshold selection remains an open task for future work. Nevertheless, recurrence threshold selection is a trade-off of to have a small threshold as possible but at the same time a sufficient number of recurrences and recurrence structures.

However, the diversity of applicability of RP based methods causes a number of different criteria for the selection of the threshold: studying dynamical properties (dynamical invariants, synchronisation) requires a very small threshold [76, 239]; twin surrogates or trajectory reconstruction methods may require larger thresholds [146]; noise corrupted observation data requires even larger thresholds [383]; for studying dynamical transitions, the threshold selection can be even without much importance, because the relative change of the RQA measures does not depend too much on it in a certain range; for the detection of certain signals a specific fraction of the phase space diameter (or standard deviation of the time series) can be required [338].

Several "rules of thumb" for the choice of ε have been advocated in the literature, e.g., a few per cent of the maximum phase space diameter [258], a value that should not exceed 10% of the mean or the maximum phase space diameter [172, 442], or that the recurrence

rate $RR = \sum_{i,j} R_{i,j}/N^2$ is approximately 1% [445]. A recently proposed criterion employing the relationship between recurrence rate and ε defines an optimal value by using the position of the maximum of the first derivative of the recurrence rate $\frac{dRR}{d\varepsilon}$ [111]. Such approach can produce ambiguous and highly unstable results, as slight variations in ε (as possible by minor errors in finding this value or by nonstationary time series) cause high variation in the recurrence structure. Next, the position of the maximum of $\frac{dRR}{d\varepsilon}$ depends strongly on the chosen norm and embedding, and may lead to an overestimation of an optimal ε. And, finally, there are systems which can have more than one maximum [76].

Another criterion for the choice of ε takes into account that a measurement of a process is a composition of the real signal and some observational noise with standard deviation σ [383]. In order to get similar results as for the noise-free situation, ε has to be chosen such that it is five times larger than the standard deviation of the observational noise, i.e., $\varepsilon > 5\,\sigma$. Although this criterion holds for a wide class of processes, it is difficult to estimate the amount of observational noise in the signal.

For (quasi-)periodic processes, it has been suggested to use the diagonal structures within the RP in order to find the optimal ε [245]. In this approach, the density distribution of recurrence points along the diagonals parallel to the LOI is investigated on dependence of ε in order to minimise the fragmentation and thickness of the diagonal lines with respect to the threshold. However, this choice of ε may not preserve the important distribution of the diagonal lines in the RP if observational noise is present (the estimated threshold can be underestimated).

The selection of an optimal recurrence threshold ε is not straightforward and depends on the particular problem and question.

16.3.3 Indicators of determinism

The length of a diagonal line in the RP corresponds to the time the system evolves very similar as during another time, i.e., a segment of the phase space trajectory runs parallel and within an ε-tube of another segment of the phase space trajectory. Deterministic systems are often characterised by repeated similar state evolution (corresponding to a local predictability), yielding in a large number of diagonal lines in the RP. In contrast, systems with independent subsequent values, like white noise, have RPs with mostly single points. Therefore, the fraction of recurrence points forming such diagonal lines (of length $l \geq l_{\min}$)

$$DET = \frac{\sum_{l \geq l_{\min}} lP(l)}{\sum_{i,j} R_{i,j}} \tag{16.1}$$

can be calculated and is, therefore, called *determinism* in the RQA. Somehow this measure can be interpreted as an indication of determinism in the data. But we should be careful in using the term determinism in a more general or mathematical sense. In a deterministic system we can calculate the same exact state by using given initial conditions, i.e., there is no stochastic process involved. Different methods can be used to test for determinism in time series, e.g., a combined modelling-surrogate approach [355] or an analysis of the directionality of the phase space trajectory [166].

High values of DET might be an indication of determinism in the studied system, but it is just a necessary condition, not a sufficient one. Even for non-deterministic processes we can find longer diagonal lines in the RP, resulting in increased DET values. For example, the following (non-deterministic) auto-regressive process $x_i = 0.8x_{i-1} + 0.3x_{i-2} - 0.25x_{i-3} + 0.9\xi$ (where ξ is white Gaussian noise) has a DET value of 0.6 (embedding dimension $m = 4$, delay $\tau = 4$, and fixed recurrence rate of 0.1). As it was shown in [380], stochastic processes can have RPs containing longer diagonal lines just by chance (although very rare). Moreover,

due to embedding we introduce correlations in the RP and, therefore, also uncorrelated data (e.g. from white noise process) have spurious diagonal lines [239, 382] (Fig. 16.2). Moreover, data pre-processing like low-passfiltering (smoothing) is frequently used. Such pre-processing can also introduce spurious line structures in the RP. Therefore, from just a high value of the RQA measure DET we have to be careful in infering that the studied system would be deterministic. For such conclusion we need at least one further criterion included in the RP: the directionality of the trajectory [166]. One possible solution is to use iso-directional RPs [151] or perpendicular RPs [53]; if then the measure reaches $DET \approx 1$ for a very small recurrence density (i.e. $RR < 0.05$), the underlying system will be a deterministic one (like a periodic or chaotic system).

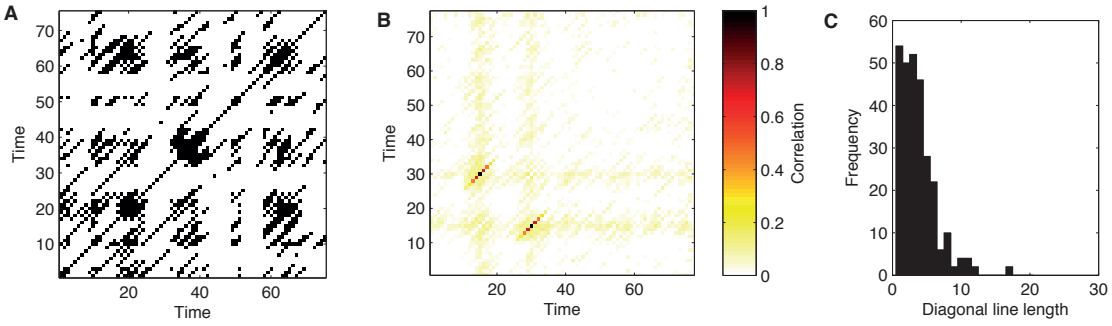

Figure 16.2: (A) Recurrence plot of one realisation of Gaussian white noise, calculated using embeddeding dimension $m = 6$, delay $\tau = 1$, and a recurrence threshold of $\varepsilon = 0.2$. The embedding causes a number of long lines. (B) Correlation between a single recurrence point at $(15, 30)$ and other recurrence points in the RP of white noise demonstrating the effect of embedding for a bogusly creation of long diagonal lines (estimated from 1,000 realisations). (C) The histogram of line lengths found in the RP shown in (A). The maximum length is $L_{\max} = 17$, a value, which would not be uncommon for a deterministic process.

16.3.4 Indicators of periodic systems

As explained in the previous section, deterministic systems cause a high value in the RQA measure DET. This measure has been successfully used to detect transitions in the dynamics of complex systems [397]. A frequently used example in order to present this ability is the study of the different dynamical regimes of the logistic map, where DET is able to detect the periodic windows (by values $DET = 1$). Therefore, it is often claimed that this measure is able to detect chaos-period transitions.

However, we can also find such high DET values for non-periodic, but chaotic systems. For example, the Rössler system [327],

$$\left(\frac{dx}{dt}, \frac{dy}{dt}, \frac{dz}{dt}\right) = \big(-y - z,\ x + 0.25y,\ 0.25 + z(x - c)\big), \tag{16.2}$$

exhibits in the parameter interval $c \in [35, 45]$ a transition from periodic to chaotic states (Fig. 16.3A). But due to the smooth phase space trajectory and high sampling frequency (sampling time $\Delta t = 0.1$), the RP for the chaotic trajectory consists almost exclusively on diagonal line structures (Fig. 16.4), resulting in a high value of DET, i.e., $DET \approx 1$ (Fig. 16.3B).

A very high value of DET is not a clear or even sufficient indication of a periodic system. High values can be caused by very smooth phase space trajectories. This should also be considered when looking for indications of unstable periodic orbits (UPOs), where DET

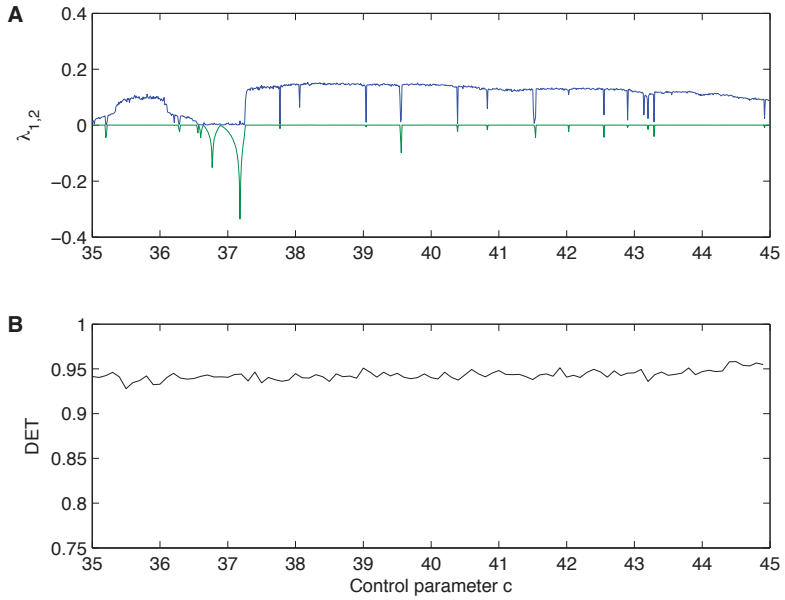

Figure 16.3: (A) 1st and 2nd positive Lyapunov exponents of the Rössler oscillator with parameters $a = b = 0.25$ and $c \in [35, 45]$. A periodic window occurs between $c = 36.56$ and $c = 37.25$. However, the DET measures reveals an almost constant very high value of approximately $DET = 0.94$. Used RP parameters: dimension $m = 3$, delay $\tau = 6$, adaptive recurrence threshold to ensure a $RR = 0.05$.

or mean and maximal line lengths L and $L_{\max}$ may not be sufficient. A solution could be to increase the minimal length $l_{\min}$ of a diagonal recurrence structure which is considered to be a line. However, a better solution is to look at the cumulative distribution of the diagonal line lengths and estimate the K_2 entropy (but this requires much longer time series, cf. Subsect. 16.3.9). Recent work has shown that measures coming from complex network theory, like clustering coefficient, applied to recurrence matrices are more powerful and reliable for the detection of periodic dynamics [78, 241, 455].

16.3.5 Indicators of chaos

The RP visualises the recurrence structure of the considered system (based on the phase space trajectory). The basic idea behind RPs comes, in general, from the study of chaos. Therefore it can be considered as a nonlinear tool for data analysis. But this cannot be a criterion to understand complex structures in the RP or high values of RQA measures as indicators of chaos or nonlinearity in the dynamical system.

As mentioned above, uncorrelated stochastic systems have mostly short or almost no diagonal line structures in their RPs, whereas deterministic and regular systems, like periodic processes, have mostly long and continuous diagonal line structures. Chaotic processes have also diagonal, but shorter lines, and can have single recurrence points. Nevertheless, only by looking at the appearance of an RP it is difficult (almost impossible) to infer about the type of dynamics; only periodic and white noise processes can be identified with some certainty.

The alternative is to look at the RQA measures quantifying the structures in an RP which are related to some dynamical characteristics of the system. As diagonal lines in the RP correspond to parallel running trajectory segments, it is clear that the length of these lines is somehow related to the divergence behaviour of the dynamical system. Divergence rate of phase space trajectories is measured by the Lyapunov exponent. In fact, the lengths of the

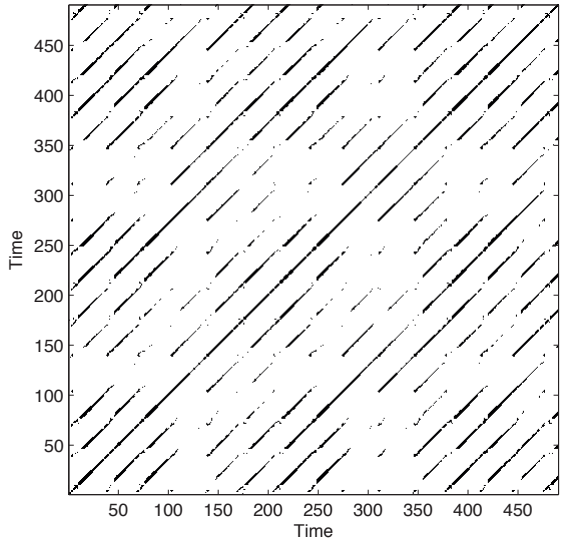

Figure 16.4: Recurrence plot of the Rössler oscillator with parameters $a = b = 0.25$ and $c = 40$. For this parameters, the Rössler system is in a chaotic regime ($\lambda_1 = 0.14$), but the RP consists almost only on diagonal lines. Used RP parameters: dimension $m = 3$, delay $\tau = 6$, adaptive recurrence threshold to ensure a $RR = 0.05$.

diagonal lines are directly related to dynamical invariants as K_2 entropy or D_2 correlation dimension [101, 384]. The K_2 entropy is the lower limit of the sum of the positive Lyapunov exponents.

For example, RQA measures based on the length of the diagonal lines, like determinism DET and mean line length L, also depend on the type of the dynamics of the systems (rather low values for uncorrelated stochastic (white noise) systems, higher values for more regular, correlated and also chaotic systems). It has been suggested to measure the length of the longest diagonal line $L_{\max}$ and interpret its inverse $DIV = 1/L_{\max}$ as an estimator of the maximal Lyapunov exponent [397]. However, this interpretation incorporates high potential of erroneous conclusions derived from RQA.

First, the main diagonal in the RP (i.e., the line of identity, LOI) is naturally the longest diagonal line, wherefore it is usually excluded from the analysis. However, due to the tangential motion of the phase space trajectory[1], subsequent phase space vectors are often also considered as recurrence points (known as sojourn points) [239]. These recurrence points lead to further continuous diagonal lines directly close to the LOI. Without excluding an appropriate corridor along the LOI (the Theiler window), $L_{\max}$ will be artificially large ($\approx N$) and DIV too small.

Second, as explained above, even white noise can have long diagonal lines [380], leading to a small DIV value just by chance (Fig. 16.2). Although the probability for the occurrence of such long lines is rather small, the probability that lines of length two occur in RPs of stochastic processes is, on the contrary, rather high. Only one line of length two is enough to get a finite value of DIV which might be mis-interpreted as a finite Lyapunov exponent and that the system would be chaotic instead stochastic.

Therefore, we have to be careful in interpreting the RQA measures themselves as indicators of chaos. Moreover, such conclusion cannot be drawn by applying a simple surrogate test where the data points are simply shuffled (such a test would only destroy the correlation structure within the data, and, thus, the frequency information).

[1]Tangential motion becomes even more crucial and influential for highly sampled or smooth systems.

RP or RQA alone cannot be used to infer nonlinearity from a time series. For this purpose, advanced surrogate techniques are more appropriate [307, 343].

16.3.6 Discrimination analysis and detection of deterministic signals

RQA is also a powerful tool in order to distinguish between different types of signals, different groups of dynamical regimes etc. [e.g., 100, 201, 237, 439]. However, the selection of applicable RQA measures is a crucial task. Not all measures will be useful for all questions. Their application needs justification in terms of the purpose of the intended analysis. For example, for processes which does not contain laminar regimes, or if we are not interested in the detection of such laminar regimes, it would not make sense to use RQA measures basing on vertical recurrence structures (like *laminarity* or *trapping time*) [231].

16.3.7 Indicators of nonstationarity and transition analysis

RQA is powerful for the analysis of slight changes and transitions in the dynamics of a complex system. For this purpose we need a time-dependend RQA (a RQA series) what can be realised in two ways (Fig. 16.5):

(1) The RP is covered with small overlapping windows of size w spreading along the LOI and in which the RQA will be calculated, $R_{i,j}|_{i,j=k}^{k+w-1}$.

(2) The time series (or phase space trajectory) is divided into overlapping segments $x_i|_{i=k}^{k+w-1}$ from which RPs and subsequent RQA will be calculated separately.

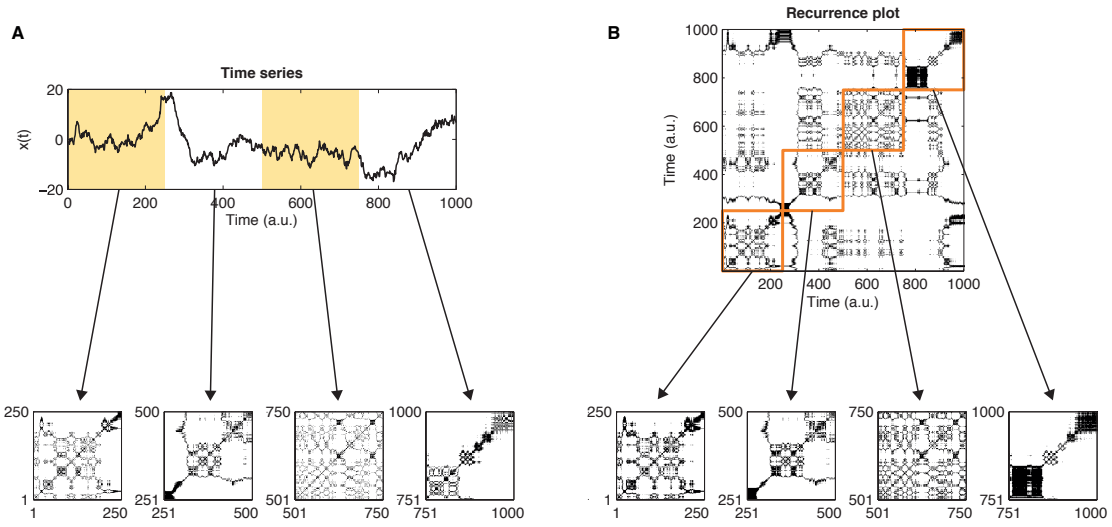

Figure 16.5: Two possibilities of windowed RQA: (A) Windowing of time series and (B) windowing of RP. The example is an auto-regressive process: $x_i = 0.95x_{i-1} + 0.05x_{i-2} + 0.9\xi$ (where ξ is white Gaussian noise), the RP is calculated using a constant number of neighbours (10% of all points) and without embedding. The sub-RPs at the bottom clearly demonstrate the differences between the two approaches.

Such time dependent approach can also be used to analyse the stationarity of the dynamical system.

Here we should note the following important points. The time scale of the RQA values depends on the choice which point in the window should be considered as the corresponding time point. Selecting the first point k of the window as the time point of the RQA measures allows to directly transfer the time scale of the time series to the RQA series. However, the window reaches into the future of the current time point and, thus, the RQA measures repre-

sent a state which lies in the future. Variations in the RQA measures can be misinterpreted as early signs of later state transitions (like a prediction). A better choice is therefore to select the centre of the window as the current time point of the RQA. Then the RQA considers states in the past and in the future. If strict causality is required (crucial when attempting to detect subtle changes in the dynamics just prior the onset of dramatic state changes), it might be even useful to select the end point of the window as the current time point of the RQA (using embedding we have to add $(m-1)\tau-1$). For most applications the centre point should be appropriate.

Another important issue can rise from the different windowing methods (1) or (2), which are only equivalent when we do not normalise the time series (or its pieces) from which the RP is calculated and when we chose a fixed threshold recurrence criterion. If we normalise the time series just before the RP calculation, we get differently normalised segments resulting in different sub-RPs (and thus different RQA results) than such derived directly by moving windows from the RP of the entire time series (Fig. 16.5 and Tab. 16.1). A similar problem arises when we use a fixed number of nearest neighbours for the definition of recurrence, because it is a big difference considering the entire time series in order to find the k nearest neighbours or just a small piece of it. Nevertheless, both approaches (1) and (2) can be useful and depend on the given question. If we know that the time series shows some nonstationarities or trends which are not of interest, then approach (2) can help to find transitions neglecting these nonstationarities. But, if we are interested in the detection of the overall changes (e.g., to test for nonstationarity), we should keep the numerical conditions for the entire available time constant and chose approach (1). Anyway, for each RQA we should explicitly state how the windowing procedure has been performed.

Table 16.1: Selected RQA measures derived from windowing of time series (top) and windowing of RP (bottom) of an auto-regressive process and windowing as shown in Fig. 16.5.

Window	1–250	251–500	501–750	751–1000
RR	0.10	0.10	0.10	0.10
DET	0.62	0.74	0.48	0.79
L	3.13	3.69	2.75	3.75

Window	1–250	251–500	501–750	751–1000
RR	0.18	0.12	0.20	0.19
DET	0.81	0.81	0.69	0.95
L	3.78	4.27	2.90	9.50

The choice of the window size itself needs the same attention. Because the RQA measures are statistical measures derived from histograms, the window should be large enough to cover a sufficient number of recurrence lines or orbits. A too small window can pretend strong fluctuations in the RQA measures just by weak statistical significance (the RQA measure $TREND$ is very sensitive to the window size and can reveal even contrary results, cp. Fig. 16.7B). Therefore, conclusions about nonstationarity of the system should be drawn with much care. Moreover, statements on stationarity of the system itself are questionable at all (if not enough knowledge about the system is available), because detected nonstationarity in an observed finite time series does not mean automatically nonstationarity in the underlying system. For example, an auto-regressive process is stationary by definition, but its RP and

RQA can reveal a nonstationary signal (Figs. 16.6 and 16.7).

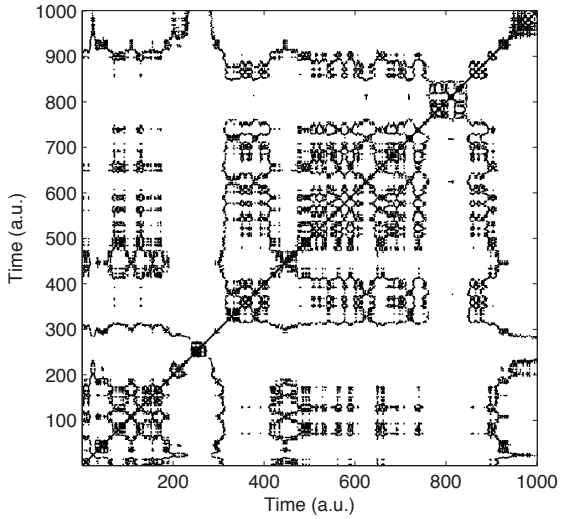

Figure 16.6: RP of the same auto-regressive process as presented in Fig. 16.5, which is by definition stationary. The RP is calculated using maximum norm, $\varepsilon = 2$ and without embedding.

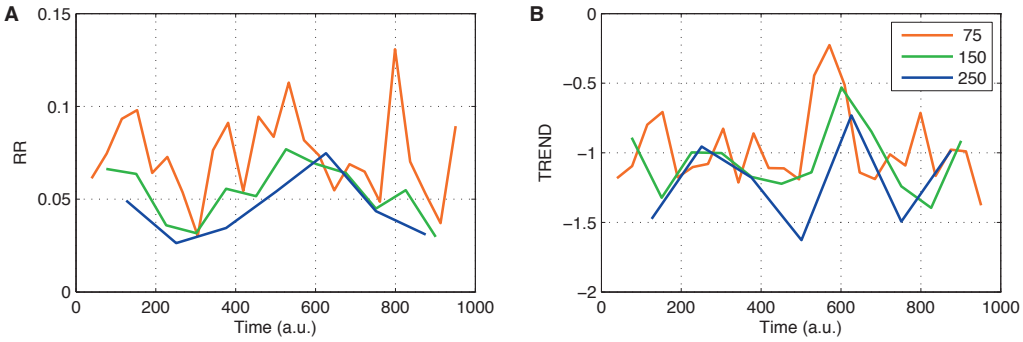

Figure 16.7: Two exemplary RQA measures, (A) recurrence rate *RR* and (B) paling trend (*TREND*), of the auto-regressive process as presented in Fig. 16.5 for three different window sizes w ($w = 75, 150, 250$). (A) The strong variation in *RR* pretends a nonstationarity in the signal. (B) *TREND* depends rather strongly on w, resulting in contrary outcomes, e.g., revealing high values for $w = 250$, but small values for $w = 75$ at the same time period $t = 700 \ldots 800$. The RQA is calculated using maximum norm, $\varepsilon = 0.3$ and without embedding (the windows are moved by $w/2$, i.e., 50% overlap; the RQA time point is set to the centre of the RQA window).

16.3.8 Significance of RQA measures

Related to the preceding issue on windowed RQA is the question on the significance of the RQA variation. A sub-optimal scaling of the variation of the RQA measures can mislead to conclusions that the studied system has changed its regime or that it would be nonstationary (Fig. 16.8A, B). Therefore, it is strongly recommended to cross-check the scaling of the presentation and to present confidence intervals (Fig. 16.8C, D). Confidence intervals can be calculated in various ways, but we should avoid to derive them by simply shuffling the

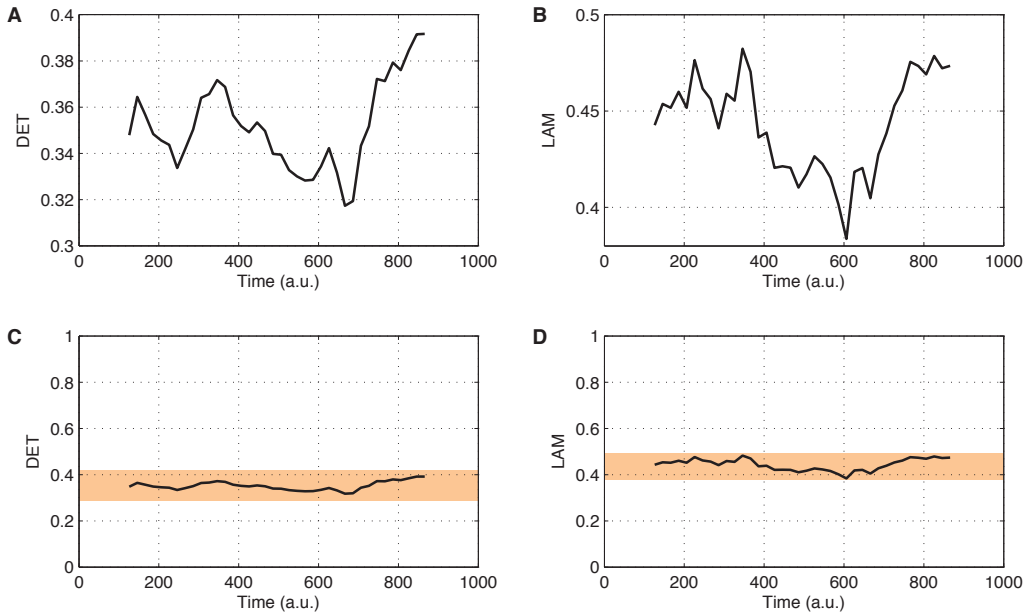

Figure 16.8: Two exemplary RQA measures, (A, C) determinism DET and (B, D) laminarity (LAM), of the auto-regressive process as presented in Fig. 16.5. (A, B) The scaling of the y-axis is affecting a strong variation in the RQA measures – a potential of wrong conclusions. (C, D) Considering a 5% confidence interval of the RQA measures (details can be found in [234]) and a better value range for the y-axis, we cannot infer that the values of the RQA measures as shown in (A) and (B) significantly vary. The RQA is calculated using a window size of $w = 250$ and a window step of $ws = 20$, using maximum norm, $\varepsilon = 0.3$ and without embedding (the RQA time point is set to the centre of the RQA window). LAM is the fraction of recurrence points forming vertical lines in an RP (analogously as DET for the diagonal lines).

original data. One approach could be a bootstrap resampling of the line structures in the RP [234, 341]. Another approach fits the probability of serial dependences (diagonal lines) to a binomial distribution [145]. Whatever approach we chose, the estimation of the confidence intervals is not a trivial task, but in the future the standard software for RQA should include such tests.

A common statement on recurrence analysis is that it is useful to analyse short data series. But we have to ask, how short is short? The required length for the estimation of dynamical invariants will be discussed in the following Subsect. Applying RQA analysis we should be aware that the RQA measures are statistical measures (like an average) and need some minimal length that a variation can be considered to be significant.

16.3.9 Dynamical invariants from short time series

An RP analysis is appropriate for analysing short and nonstationary time series, as it is often stated in many reports [95, 339, 439]. However, this statement holds actually only for the heuristic measures of complexity as introduced for the RQA or for the detection of differences or transitions in data series. If we are interested in the dynamical invariants derived from RPs, the length N of the time series becomes a more crucial part like it is for the standard methods of nonlinear data analysis.

The derivations of dimensions (D_1, D_2) and dynamical invariants (like K_2) from the RPs hold only in the limit $N \to \infty$ and small ε ($\varepsilon \to 0$). Nevertheless, an estimation of dynamical

invariants from shorter time series can be feasible. We have to regard the following factors if discussing the time series length: the number of orbits representing stretching, the number of recurrences filling out a sufficient part of the attractor, and the number of data points necessary for an acceptable phase space reconstruction [425]. Since these factors may require different minimal lengths, the largest of these lengths should be considered.

For example, numerical considerations for the estimation of the attractor (correlation) dimension D_2 using the Grassberger-Procaccia algorithm [124] lead to the requirement $\log N > \frac{D_2}{2} \log(\frac{1}{\varrho})$ (where $\varrho = \frac{S}{\varepsilon}$ is the fraction the recurrence neighbourhood of size ε covers on the entire phase space of diameter S) [88]. Considering a $\varrho = 0.1$ and a decimal logarithm, for finding a $D_2 = 10$ we need at least $N = 100,000$ data points. Furthermore, a $\varrho = 0.1$ is actually too large and we need much smaller ε, which consequently provokes that again a larger N is required.

For Lyapunov exponents (and analogously for K_2), a rough estimate based on the mentioned requirements suggests minimal time series lengths of 10^{D_2} to 30^{D_2} (with attractor dimension D_2) [425]. Accordingly, a system with $D_2 = 3$ requires 1000–30,000 data points (a more strict consideration even requires $\log N > D_2 \log(\frac{1}{\varrho})$ [88]).

Therefore, too guarantee useful results we need long time series. If we calculate dimensions or K_2 from short time series the results are probably worthless.

16.3.10 Synchronisation and line of synchronisation

Cross recurrence plots (CRPs) can be used for the investigation of the simultaneous evolution of two different phase space trajectories [157, 228, 236, 452]. The *line of identity (LOI)* in the RP becomes a *line of synchronisation (LOS)* in the CRP. Two more-or-less identical systems but with differences on the time-scale will reveal a bowed LOS [230, 236]. An off-set of the LOS away from the main diagonal is an indication of a phase shift or a delay between the two considered systems.

However, because this method tests if the two trajectories visit the same region in the phase space, it can be used only to study complete synchronisation (CS) or a kind of a generalised correlation (although with possible delays), or to get the relation between the transformations between their time-scales. Moreover, the data under consideration should be from the same (or a very comparable) process and, actually, should represent the same observable. Therefore, the reconstructed phase space should be the same.

For the study of the LOS the distance matrix may be more appropriate because it contains more information, especially if the data series show nonstationarities. Then, the LOS can be found by using efficient algorithms like dynamic time warping [332]. Nevertheless, it is always very important to check if the found LOS makes sense; for instance, it is possible to find several LOS (cp. Application in magneto-stratigraphy in [239]).

16.3.11 Macrostructures and sampling

For the visual interpretation of an RP and also for a reliable RQA we should remember that our data are discretised time or data series. The sampling of the signal has an importance which should not be underestimated. If the sampling frequency is just one magnitude higher than the system's main frequencies, and their ratio is not a multiple of an integer (i.e., we have an intrinsic phase error), an interference triggered by the sampling of the continuous signal can produce large empty regions in the recurrence matrix, although they should be there [96, 97]. Nonstationarities or modulations in frequency or phase cause non-trivial gaps or macrostructures in the recurrence matrix (Fig. 16.9). We should be aware that such gaps can occur in particular when we use a low sampling frequency. The recurrence structure of interest can appear rather different; diagonal lines can vanish or can be reduced to just

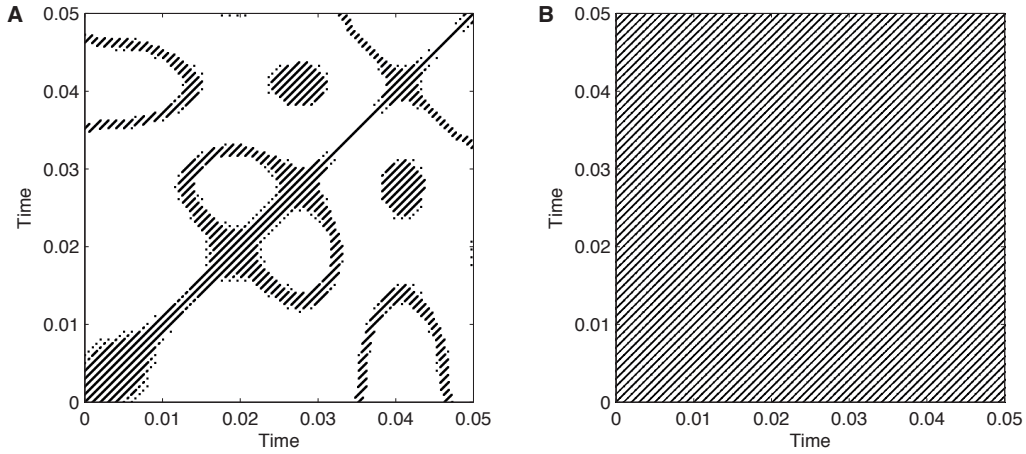

Figure 16.9: RP of a modulated harmonic oscillation $\sin(2\pi 1000(\pi + t) + 2\pi \sin(2\pi 44t)t)$. (A) Non-trivial macrostructures (gaps) in the RP due to the interference of the sampling frequency of 1 kHz and the frequency of the modulated harmonic signal. (B) Corresponding RP as shown in (A), but for a higher sampling frequency of 10 kHz. As expected, the entire RP now consists of the periodic line structures due to the oscillation. Used RP parameters: dimension $m = 3$, delay $\tau = 1$, recurrence threshold $\varepsilon = 0.05\sigma$, L_∞-norm.

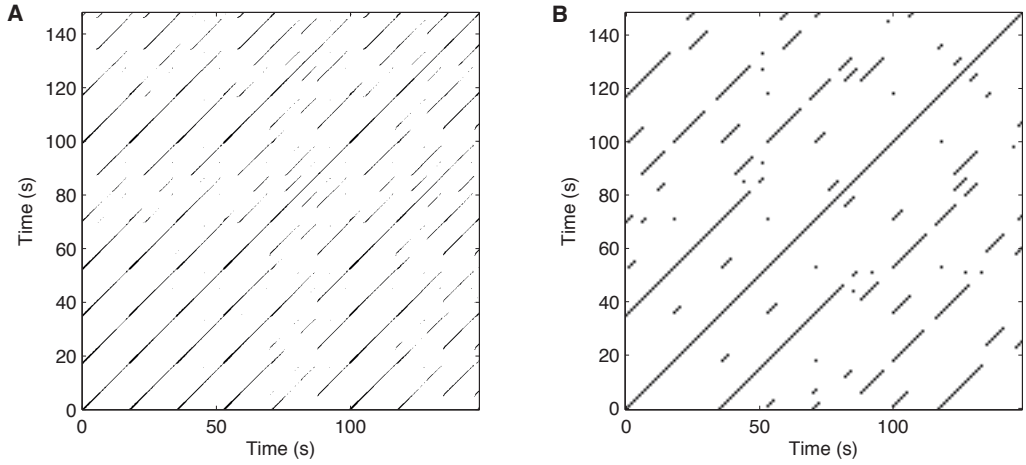

Figure 16.10: RP of the x-component of the Rössler oscillator, Eq. (16.2), with parameters $a = b = 0.2, c = 5.7$. The sampling time is (A) $\Delta t = 0.05$ and (B) $\Delta t = 1$. The embedding was chosen in both settings to be equivalent: dimension in (A) and (B) is $m = 3$, the delay in (A) $\tau = 20$, but in (B) $\tau = 1$; recurrence threshold $\varepsilon = 1.5$ (maximum norm). Due to the low sampling in (B), many diagonal lines vanish.

single points yielding in biased RQA measures (Fig. 16.10).

Nevertheless, tiny modulations in frequency or phase in oscillating signals can be detected by RPs, which are non-detectable by standard methods (spectral or wavelet analysis). This turns RPs to a powerful tool for the analysis of slight modulations in oscillatory signals like audio signals.

Please note that macrostructures are also an apparent problem when displaying large RPs on a computer screen (and up to a certain amount on print outs). The resolution of modern computer screens is around 72 ppi (points per inch, 72 ppi corresponds to around 28 points per centimetre). The presentation of RPs in a window of, e.g., 6 inch allows only the display

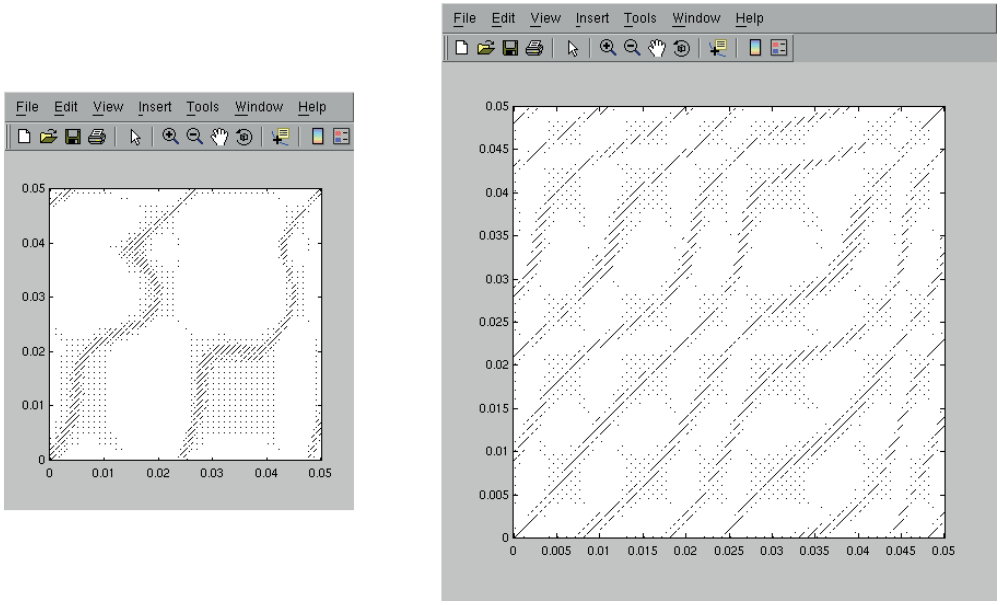

Figure 16.11: Screenshot of the RP as shown in Fig. 16.9B for two different window sizes of display on a computer screen (using MATLAB®). Although the RP consists only on continuous diagonal lines as represented in Fig. 16.9B, its size ($N = 5511$) exceeds the screen resolution and requires downsampling, leading to artifical macrostructures.

of around 430 points. Larger RPs will be rendered using downsampling or interpolation, resulting in similar interference effects and artificial secondary macrostructures as described above; such macrostructures will even change for different window sizes (Fig. 16.11). Therefore, we should take care in visual interpretation of patterns found in large RPs which are represented on computer screens.

16.4 Conclusions

We have illustrated several problems regarding the application of recurrence plots (RPs) and recurrence quantification analysis (RQA) which need our attention in order to avoid wrong results. The uncritical application of these methods can yield to serious pitfalls. Therefore, it is important to understand the basic principles and ideas behind the measures of complexity forming the RQA and the different techniques to study the numerous phenomena of complex systems, like transitions, synchronisation, etc. Nevertheless, the recurrence plot based techniques are still a rather young field in nonlinear time series analysis, and many open questions remain. For example, systematic research is necessary to define reliable criteria for the selection of the recurrence threshold, and the estimation of the confidence of the RQA measures will be a hot topic in the near future.

Acknowledgments

The work has been supported by the Potsdam Research Cluster for Georisk Analysis, Environmental Change and Sustainability (PROGRESS).

17. Avoiding Embedding Artifacts

Paper 16 D. Wendi, N. Marwan, B. Merz: In search of determinism-sensitive region to avoid artefacts in recurrence plots, International Journal of Bifurcation and Chaos, 28(1), 1850007 (2018). DOI:10.1142/S0218127418500074

R The presented work in this chapter is a student's paper, where the approach was mainly my idea.

Abstract

As an effort to reduce parameter uncertainties in constructing recurrence plots, and in particular to avoid potential artifacts, this paper presents a technique to derive artifact-safe region of parameter sets. This technique exploits both deterministic (incl. chaos) and stochastic signal characteristics of recurrence quantification (i.e. diagonal structures). It is useful when the evaluated signal is known to be deterministic. This study focuses on the recurrence plot generated from the reconstructed phase space in order to represent many real application scenarios when not all variables to describe a system are available (data scarcity). The technique involves random shuffling of the original signal to destroy its original deterministic characteristics. Its purpose is to evaluate whether the determinism values of the original and the shuffled signal remain closely together, and therefore suggesting that the recurrence plot might comprise artifacts. The use of such determinism-sensitive region shall be accompanied by standard embedding optimization approaches, e.g. using indices like false nearest neighbor and mutual information, to result in a more reliable recurrence plot parameterization.

17.1 Introduction

Recurrence is a fundamental property of many dynamical systems, which can be exploited to characterize the system's behavior in phase space, while a recurrence plot (RP) is the visualization tool for the analysis of this property. In this study, the phase space reconstruction method of time delay embedding [286, 375] is used (Eq. 17.1). Such a reconstruction is

particularly useful when not all variables required to describe the system are available (i.e. data scarcity or limited set of observation variables), and where the topology of the system dynamics $\vec{\hat{x}}_i$ can still be created using only a single variable or observation u_i.

$$\vec{\hat{x}}_i = \sum_{i=1}^{m} u_{i+(j-i)\tau} \vec{e}_j. \tag{17.1}$$

where m is the embedding dimension and τ is the time delay. The vectors $(\vec{e}_j)$ are unit vectors and span an orthogonal coordinate system $(\vec{e}_i \cdot \vec{e}_j) = \delta_{i,j}$. The calculation of recurrence as elements of the RP is based on Eq. 17.2:

$$R_{i,j}(\varepsilon) = \Theta(\varepsilon - \|\vec{x}_i - \vec{x}_j\|), i, j = 1, ..., N. \tag{17.2}$$

where N is the number of measured points $\vec{x}_i$, ε is a threshold distance, $\|\cdot\|$ is a norm and $\Theta(\cdot)$ the Heaviside function.

The RP is basically the visual representation of the square matrix, in which the matrix elements correspond to those times at which a state of a dynamical system recurs (columns and rows correspond then to a certain pair of times). RPs are especially useful for non-stationary pattern in time series [86, 239]. Besides using RPs for the visual analysis of time series, RPs can also quantify structures hidden within the series through recurrence quantification analysis (RQA)[239, 442]. In RQA, important elements are the diagonal and vertical/horizontal straight lines because they reveal typical dynamical features of the investigated system, such as range of predictability, chaos-order, and chaos-chaos transitions [397]. One of the prominent diagonal line measures is called determinism (DET, Eq. 17.3), from which the system predictability can be inferred.

$$DET = \frac{\sum_{l=lmin}^{N} lP(l)}{\sum_{i,j}^{N} R_{i,j}} \tag{17.3}$$

where $P(l) = \{l_i; i = 1, ..., N_l\}$ is the histogram of the lengths l of diagonal structures, and N_l is the absolute number of those diagonal lines.

For a deterministic signal (including chaos), many diagonal lines in the RP are typical, leading to high value of DET [225]. However, single, isolated recurrence points can occur if states are rare, if they do not persist, or if they fluctuate heavily. For instance, stochastic or random signals would comprise such single points and result in a very low DET.

Since the use of RPs relies on the reconstructed phase space, its parameters uncertainty includes those of the phase space reconstruction method, such as embedding dimension (m) and time delay (τ), in addition to the recurrence threshold (ε). Standard approaches for finding optimal embedding parameters are false nearest neighbours (FNN) for m, and auto-correlation or mutual information (MI) for τ [109, 165, 170]. Other methods include wavering-products, fill-factor or integral local deformation [40]. Moreover, Marwan [225] concludes that τ is sometimes overestimated by auto-correlation and mutual information, and that the choice of the embedding dimension has to be considered with care, as a wrong choice artificially increases diagonal lines, and hence DET, and leads to artifacts. For instance, an RP resulting from a random series should exhibit scattered or non-deterministic patterns (i.e. single points). However, when m increases to 2 and beyond with $\tau = 1$, the number and the length of diagonal lines start to increase and dominate the plot as artifacts. This may be misinterpreted as if the series was highly deterministic (Fig. 17.1).

In this study, we focus on the artifacts related to these embedding parameters. The impact of the recurrence threshold (ϵ) is not elaborated, since the selection of the optimal

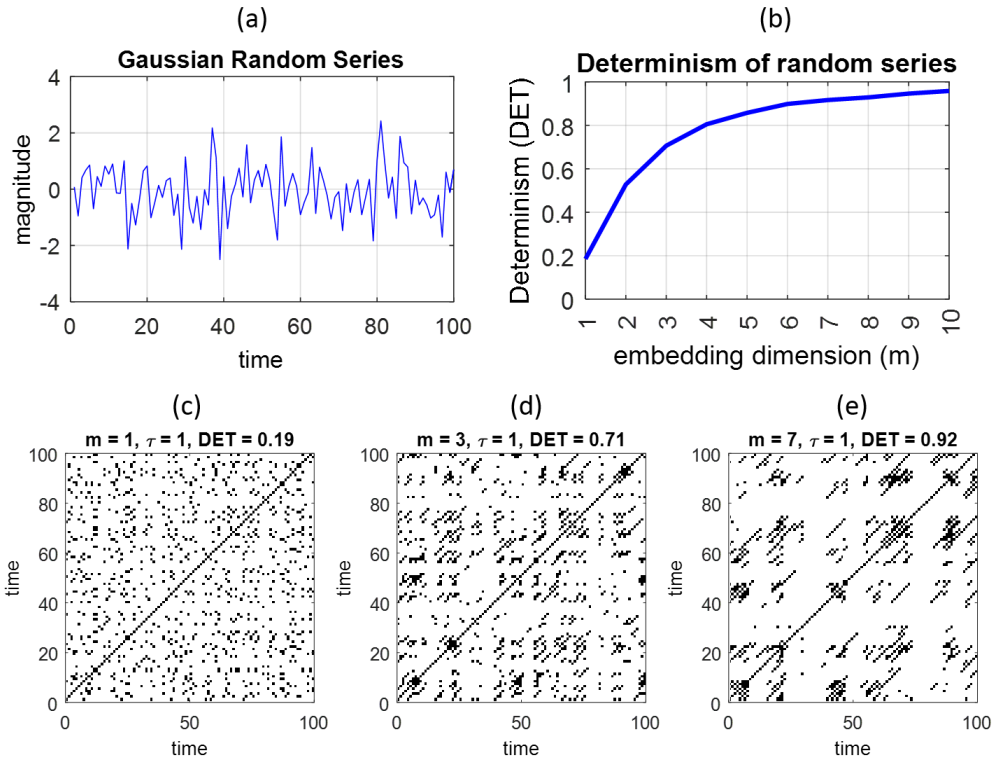

Figure 17.1: Misleading DET values of random series (a); sub-figure (b) shows the artificial increase of DET when embedding dimension (m) increases, while (c) to (e) show the corresponding RP with the increase of diagonal line structures at high embedding dimension ($m = 7$).

values of the recurrence threshold has been discussed earlier [111, 172, 258, 338, 383, 442, 445]. Hence, the recurrence threshold is fixed to a 10% recurrence rate (recurrence points density). Supplementary information on the impact of changing this threshold is enclosed in the appendix. The appendix also includes the evaluation of DET values of a correlated random series, using an AR1 series as example, to showcase that high DET values are indeed associated with deterministic systems instead of its auto-correlation structures, although there are also cases at certain parameter values where the number/ length of diagonal lines artificially increase. It is important to note that the proposed technique is not intended to be used as a new, independent method, but rather as an additional consideration during parameterization, when the dynamical system is known to be deterministic.

17.2 Methodology

Artificially biased line length distributions due to the embedding can overlay the true line length distributions and lead to wrong conclusions. Hence, it would be desirable to separate the contribution of the embedding induced line length distributions from the real underlying dynamics. However, separating both contributions is not possible without additional knowledge about the system (such as precise model or amount of observational noise). Therefore, we propose an approach that minimizes the contribution of the embedding. This approach is based on comparing the fraction of recurrence points that form diagonal lines in the RPs of the original time series (which includes both the real underlying dynamics as well as the

embedding effect) with that of a random time series (which consists of the embedding effect only). As random time series we use simply shuffled versions of the original time series, because this preserves its value distribution and, thus, allows to use the same recurrence threshold and allows to compare the resulting RPs. As mentioned above, RPs of random time series should consist mainly of single points, but embedding artifacts would increase the fraction of recurrence points that form diagonal lines in the RP. Thus, this fraction measure is well suited for our purpose. Moreover, this measure is equal to the DET measure. Other measures that use the line length distribution (e.g., average and longest line length, entropy of the length distribution) would be possible but are less intuitive and interpretable. The advantage of the DET measure is that it considers the influence of scattered points that appears within the RP as well in addition to just the diagonal lines. While the index of average and longest line length could easily suffer from large statistical uncertainty and are easily influenced by a few extreme values.

In order to compare the line length distributions of the original and the shuffled time series, we define DET_o for the original time series and DET_i for the shuffled version. For a number of shuffling iterations (i.e. n times), the resulting difference (called determinism distance, see Eq. 17.4) is calculated for each shuffle (Fig. 17.2).

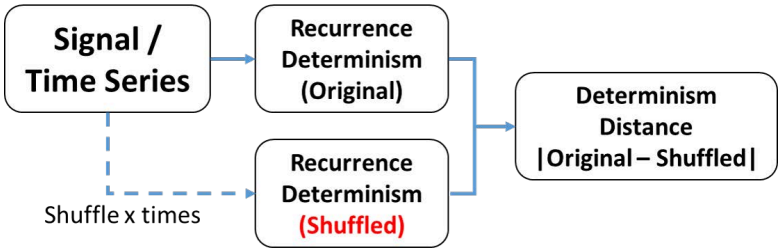

Figure 17.2: Scheme of the proposed artifact avoidance method.

For non-optimal embedding, we expect a rather high contribution of the embedding in the line length distributions in both, the original time series and in the shuffled version. Therefore, DET should have high values in both cases and should not differ so much from each other. For optimal embedding, and if there are deterministic structures in the RP of the original time series, the DET_i of the shuffled time series should be very low whereas DET_o of the original time series has still larger values. The distinctive high and low values of DET in deterministic and stochastic systems are exemplified in this paper using Lorenz and Gaussian random series. In this example, both the original and embedded Lorenz systems show DET values of around 0.8 to 0.9 with τ fixed at 3 following the first minimum of its auto-mutual information, with m varying from 1 to 10. In contrast, for the Gaussian random series, the DET values are shown to be between 0 to 0.2 (Fig. 17.3).

The resulting difference (determinism distance) between DET_i and DET_o would therefore be high. The undesired effect by the embedding should be minimal for the difference between DET_i and DET_o. Both median (M_d) and standard deviation (S_d) of these distances are used for identifying this determinism-sensitive region (Eqs. 17.4 and 17.5). The further (larger) the M_d of each parameter combination, the safer it is in terms of avoiding the mentioned

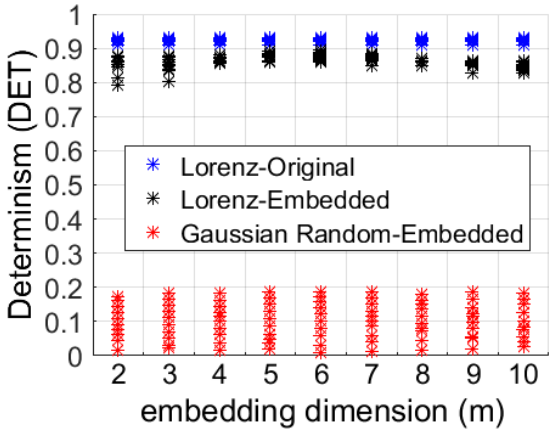

Figure 17.3: Examples for high and low DET values from deterministic (Lorenz) and stochastic (Gaussian random) signals.

artifacts, under the condition that S_d should be reasonably small (e.g. within 0.1).

$$M_d = \text{Median}_{i=1...n}(|DET_o - DET_i|). \tag{17.4}$$

$$S_d = \sqrt{\frac{1}{n-1}\sum_{i=1}^{n}\left[|DET_o - DET_i| - \frac{1}{n}\sum_{i=1}^{n}|DET_o - DET_i|\right]^2}. \tag{17.5}$$

where DET_o and DET_i are the recurrence determinism values of the original series and each shuffled iteration (i), and n is the total number of shuffling iteration.

17.3 Case study applications

This paper presents 2 application examples using Lorenz series derived from a mathematical model, and daily runoff observations from the station Burghausen at the Salzach River in south Germany. These signals are chosen for its non-linear characteristics with known presence of determinism [221, 354]. The resulting region of artifact-safe parameter set will be presented and discussed in section 4. Caution should be taken when $\tau = 1$ because artificially high DET values can lead to misinterpretations (Figs. 17.1b, d, and e), and hence should be excluded. In addition to the resulting artifact-safe region as the boundary of the parameter sets, the final choice of the parameter set is still necessary to be optimal, i.e. being able to reconstruct the topology of system dynamics and minimal in the sense not to over-reduce data points in the signal. There are many approaches to find optimal embedding parameters, such as the standard approaches mentioned in section 17.1.

17.3.1 Lorenz Series

The Lorenz system with known non-linear, non-periodic, 3-dimensional and deterministic chaos behaviour (i.e. with parameters $\alpha = 10$, $\rho = 28$, $\beta = 8/3$ and sampling time $\Delta t = 0.05$) is chosen as the first application example, following Eq. 17.6) [204, 357]. Its RP and characteristics have also been studied by Marwan et al. [239]

$$\frac{dx}{dt} = \alpha(y - x); \quad \frac{dy}{dt} = x(\rho - z) - y; \quad \frac{dz}{dt} = xy - \beta z. \tag{17.6}$$

This Lorenz system is described by 3 variables and integrated using the Euler scheme, and hence, we know the 3-dimensional phase space that describes the topology of the system dynamics. In this study, the x variable is used as our Lorenz series test set (Fig. 17.4a) with its phase space reconstructed using the time delay embedding method. Thereafter, its DET is calculated. The reliability of these DET values is checked by using median and standard deviation of their determinism distance values (M_d and S_d) to qualitatively evaluate how much the constructed RP of a certain parameter set is influenced by artifacts.

This Lorenz series is derived from a mathematical model with well-known phase space topology and recurrence characteristics, whereas real world observations are most likely contaminated by noise. Therefore, we also investigate the impact of noise on the method, i.e. in respect to the values of determinism and determinism distance. Gaussian white noise with a magnitude range corresponding to the standard deviation of the Lorenz signal is applied, i.e. added to the signal (Eq. 17.7),

$$\tilde{x}(t) = x(t) + k\beta(t). \tag{17.7}$$

where, $\tilde{x}(t)$ is the resulting new series with the addition of noise and $x(t)$ is the original series (Lorenz); k is the noise level, while $\beta(t)$ is the Gaussian white noise with magnitude range corresponding to the standard deviation of $x(t)$. The noise levels used are 5%, 10%, 30% and 50%. For each of the noise-added signal, its determinism and determinism distance are calculated.

17.3.2 River Runoff Series

The second test application uses daily river runoff observations extracted from station Burghausen in south Germany for the year 1961. This station measures the streamflow of the Salzach River with a catchment area of 6,600 km^2. The time series (Fig. 17.4b) is used as a test set representing real world data, i.e.it is potentially non-stationary and contaminated by noise and observation error.

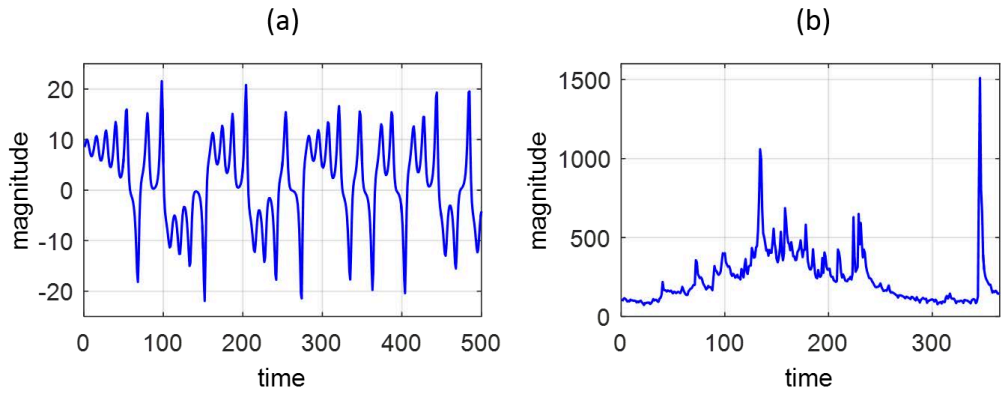

Figure 17.4: Test applications of (a) Lorenz – x variable and (b) Burghausen daily runoff series (1961).

17.4 Results and Discussion

This section presents the results of our proposed method for selecting an artifact-safe parameter region with the assumption of recurrence rate fixed at 10%. The range of embedding parameters bounds embedding dimension (m) from 1 to 10 and time delay (τ) from 1 to 20.

17.4.1 Lorenz Series

The Lorenz series is known for its deterministic feature, i.e.high determinism value, yet certain parameter combinations can give incorrect, low determinism values, e.g.when $m = 1$ or $m = 10, \tau = 6$ (Figs.17.5a, b, and c). Increasing the time delay at high embedding dimension is also seen to thicken the line structures of the RP (Fig. 17.5i). Low determinism values reflect non-optimal parameterization, and hence, misleading RP structures (Figs.17.5d and g) with diagonal lines structures as wobbly and perpendicular to the main diagonal [239]. In order to assess the reliability of the resulting RP corresponding to the m and τ parameter combinations, the proposed shuffling techniques is applied to find the determinism-sensitive region.

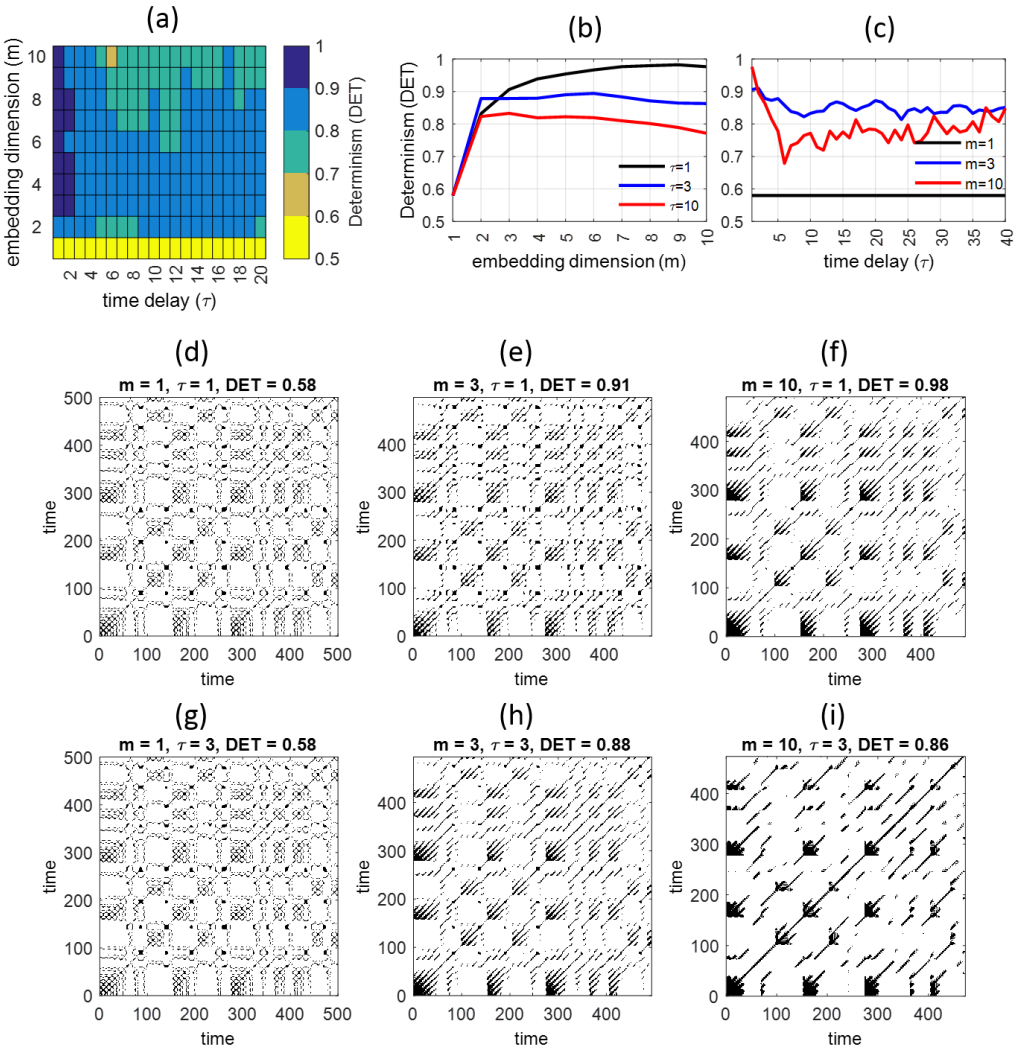

Figure 17.5: Recurrence characteristics of the chaotic, deterministic Lorenz signal: (a) determinism corresponding to m and τ; (b) change in determinism corresponding to an increase of the embedding dimension (m) from the RP, with $\tau = 1$, 3, and 10; (c) change in determinism corresponding to an increase of the time delay (τ), with $m = 1$, 3, and 10; (d) to (f) RP of different embedding dimension with fixed $\tau = 1$; and (g) to (i) RP of different embedding dimension with fixed τ=3. All RPs and recurrence measures are calculated based on fixed 10% recurrence rate.

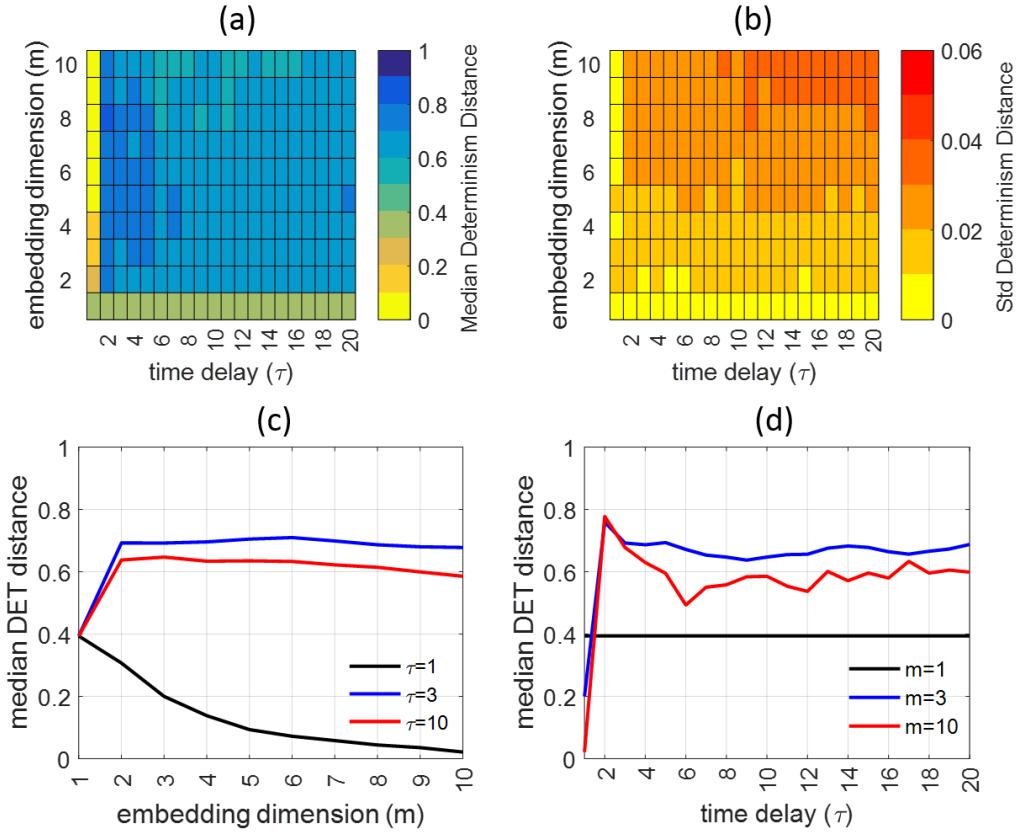

Figure 17.6: Determinism distance of the Lorenz series: (a) median (M_d) and (b) standard deviation (S_d) of determinism distance between the RP of shuffled and original Lorenz series. (c) and (d) show the median determinism distance corresponding to $\tau = 1$, 3, 10 and $m = 1$, 3, 10.

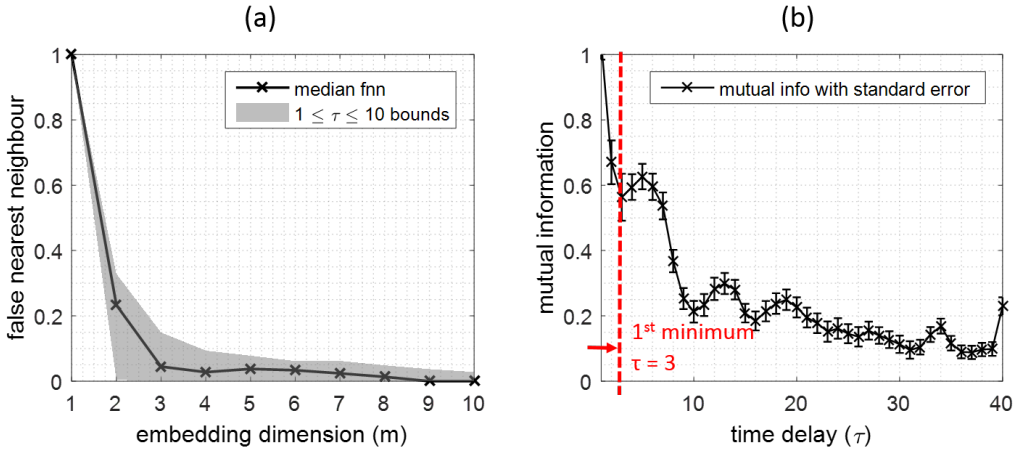

Figure 17.7: Embedding parameters for the Lorenz series resulting from standard approaches: (a) false nearest neighbor (FNN) with median and bounds derived from parameter set $1 \leq \tau \leq 10$, and (b) mutual information (MI).

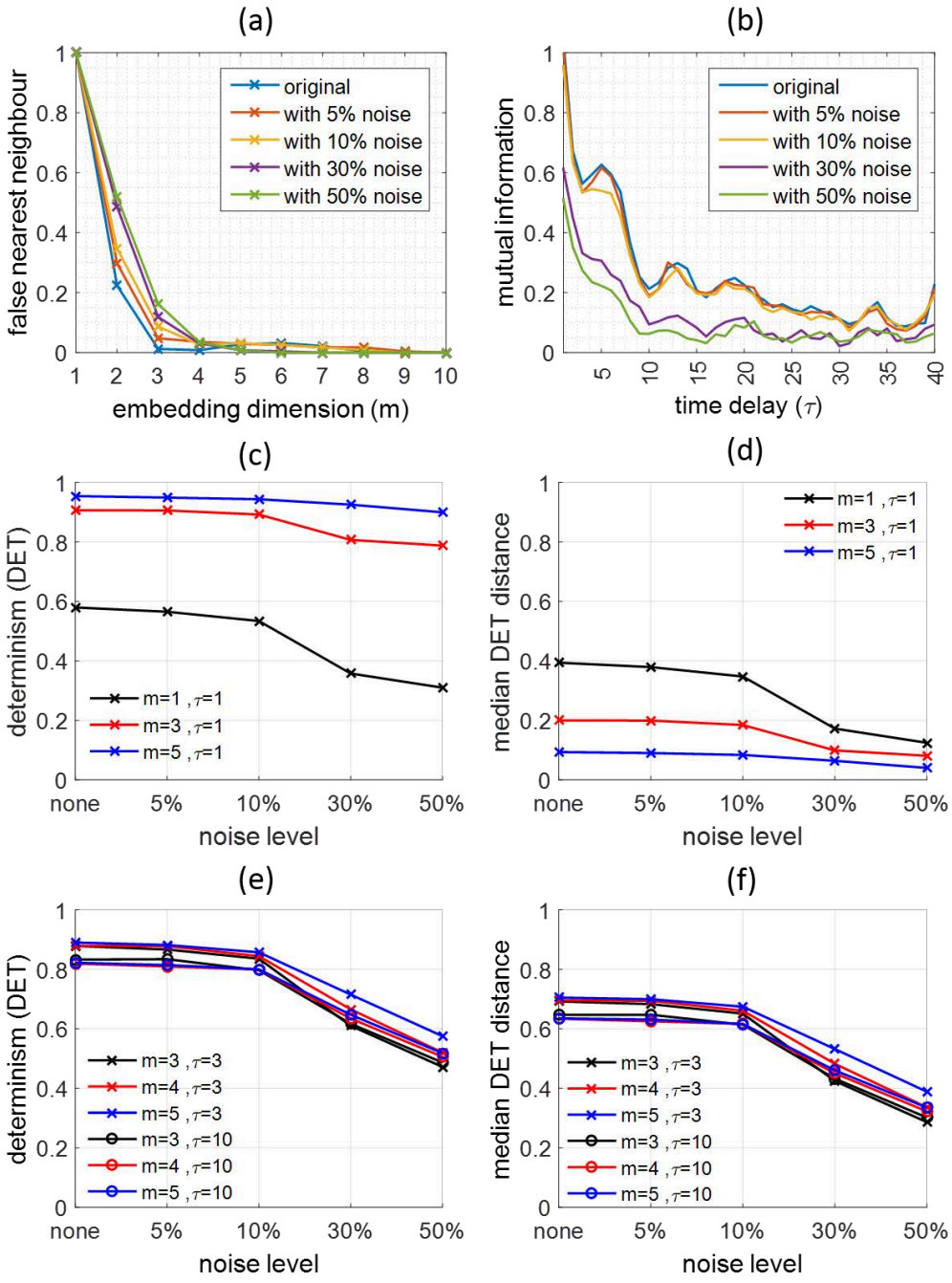

Figure 17.8: Impact of noise levels of the Lorenz series on (a) false nearest neighbor, (b) mutual information, (c) determinism, and (d) median determinism distance extracted at m=1, 3, 5 with τ=1. (e) and (f) present the extracted values with parameter bounds of $3 \leq m \leq 5$, τ=3 and 10, and 10% recurrence rate (ϵ). Noise added is Gaussian white noise with noise levels derived from the percentage of the signal standard deviation.

Using the proposed technique ($n = 100$ shuffles), M_d is low for the case without embedding ($m = 1$) as well as for $\tau = 1$, when $m > 1$ (Fig. 17.6). The latter suggests artifacts due to embedding. Those parameter values where M_d is high, e.g. for $\tau \geq 2$, when $m > 1$, can be considered to be less influenced by embedding artifacts. It can be noticed that when τ and m are higher, M_d starts to decrease and to fluctuate, as indicated by S_d. In this case, the use of the median is quite reliable due to the low S_d value (i.e. below 6%).

The identified determinism-sensitive region is suggested to be referenced with the standard approaches, such as FNN and MI, to find the optimal parameter set. This also serves to prevent the use of unnecessarily high parameter values that result in the reduction of data points (i.e. by $(m-1)\tau$). For instance, in the case of the Lorenz series, the optimal parameter set found by the standard approach is $m = 3$ and $\tau = 3$ (Fig. 17.7) which coincides well with the domain of high M_d values.

To investigate the impact of noise as in a real world scenario, Gaussian white noise with different noise levels is added to the signal as described in section 17.4.1. Figs. 17.8a and b show both false nearest neighbor and mutual information characteristics for the added-noise signal. The false nearest neighbor approach slightly increases at the optimal dimension of 3 causing a shift to the next dimension value, i.e. $m = 4$). When the noise level reaches 30 and 50%, the mutual information characteristics start to differ from the original, whereas the noise levels of 5 and 10% still preserve the original signal characteristics. Noise needs to be handled with care, as high level noise contamination potentially alters the determinism of the signal. It decreases in this case when Gaussian white noise is added, hence the determinism distance between the original and the shuffled series gets smaller.

17.4.2 River Runoff Series

A river runoff series is used to represent an example for field observations which are usually contaminated with noise. River runoff is typically a non-linear deterministic series and exhibits chaos properties [221, 293, 354], hence, its DET is expected to be high. However, its recurrence determinism is low when parameter $m = 1$ and when both m and τ reach high values, e.g. $m > 8$ and $\tau > 9$ (Fig. 17.9a). For instance, for $\tau = 10$ the DET value starts to decrease when $m > 7$ (Fig. 17.9b), while for $m = 10$ the increase of τ (i.e. above 4) also starts to reduce DET values (Fig. 17.9c).

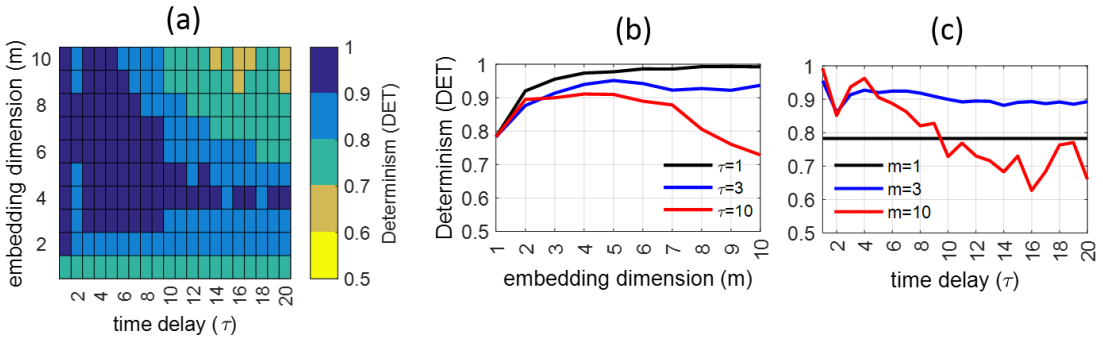

Figure 17.9: Recurrence characteristics of daily river runoff series: (a) determinism corresponding to m and τ, (b), change in determinism corresponding to increasing embedding dimension (m) from the RP, with τ=1, 3, 7; and (c) change in determinism corresponding to increasing time delay (τ), with m=1, 3, 7.

When evaluated through 100 shuffles, the parameter set of $\tau = 1, m > 1$ should not be used due to the clear artifact potential suggested by its low determinism distance (see

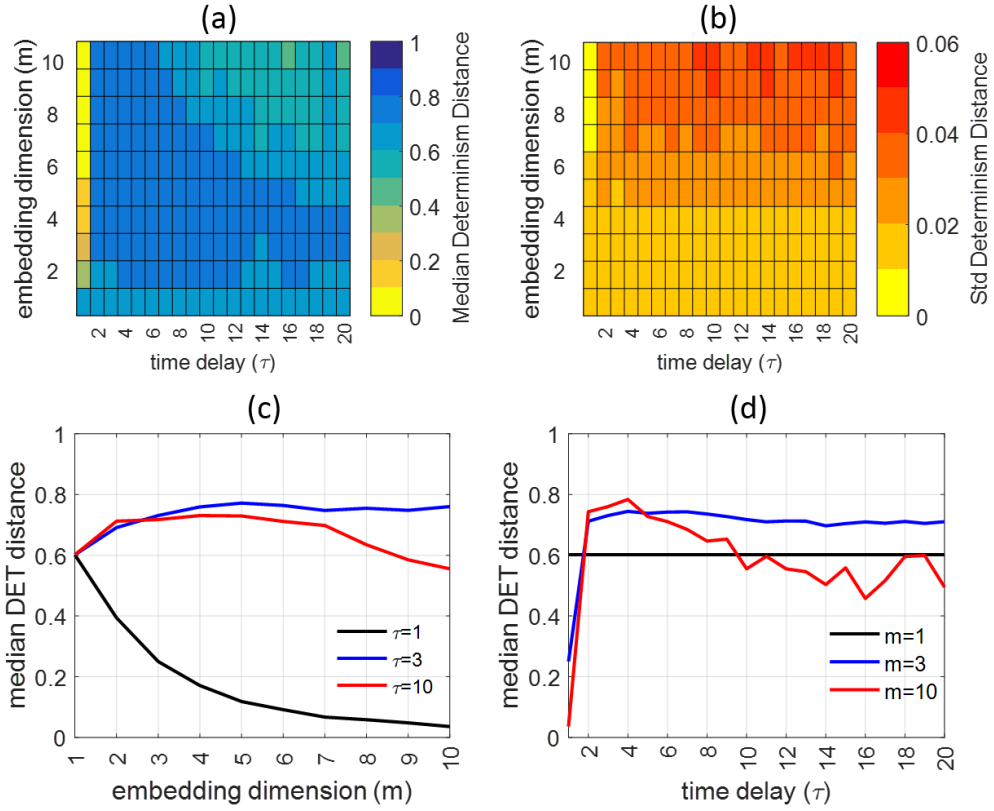

Figure 17.10: Determinism distance of runoff series: (a) median and (b) standard deviation of the determinism distance between the RP of shuffled and original runoff series. (c) and (d) show the median determinism distance corresponding to $\tau = 1$, 3, 10 and $m = 1$, 3, 10.

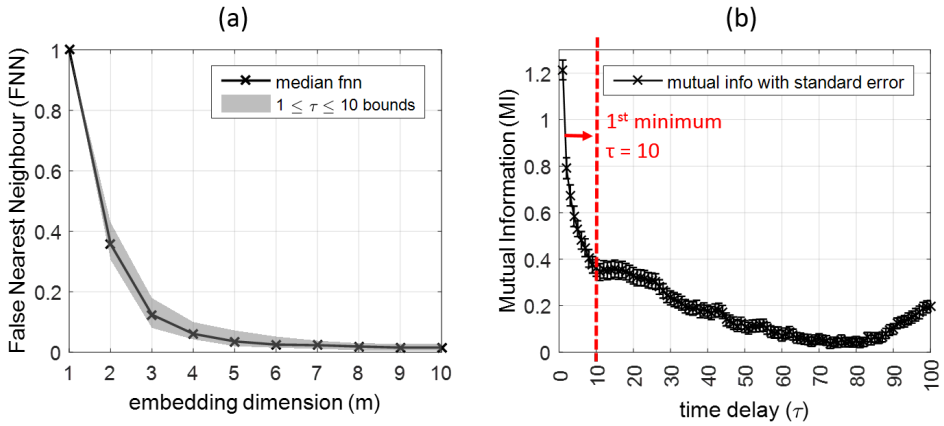

Figure 17.11: Embedding parameter selection for daily river runoff using the standard approach: (a) false nearest neighbor with median and bounds derived from parameter set $1 \leq \tau \leq 10$ and (b) mutual information with first minimum found at $\tau = 10$

.

Fig. 17.10a: first column and Fig. 17.10c: black line). The artifact-safe region could then be deduced from the high determinism distance domain corresponding to different combination parameter sets. For example when median determinism distance values above 0.8 imply high dissimilarity between the recurrence of the original signal and the shuffled ones (see Fig. 17.10a). The S_d values in this case are also low to safely use the median values (see Fig. 17.10b).

As cross-checked with the standard approach of parameter identification (Fig. 17.11a), the suggested optimal embedding parameters in this case would be $\tau = 10$ days and $m = 5$.

17.5 Summary

We propose a method to identify a determinism-sensitive parameter region with minimal impact of artifacts due to embedding when constructing a Recurrence Plot (RP). The method utilizes both deterministic (incl. chaos) and stochastic characteristics of recurrence quantification, i.e. diagonal structures, as indicated by their determinism values. It is useful when the evaluated signal is known to be deterministic. The method involves randomly shuffling the time series for an abundant number of times in order to destroy its original characteristics and its determinism. Thereafter, determinism values are calculated for each shuffle iteration and compared with the determinism of the original signal at a range of parameters, resulting in a measure called determinism distance.

The matrix of the median values of this measure is plotted to depict the determinism-sensitive parameter region. The larger the determinism distance, i.e. the closer to 1, the safer the parameter set is to avoid potential artifacts. The optimal parameter set can be selected from the consideration of this artifact-safe region together with the standard approach of using false nearest neighbors and mutual information and auto correlation.

Noise needs to be handled with care, since it affects the determinism structures of the signal or decreases the determinism values, therefore reducing the determinism distance between original and shuffled series. One could apply this method as an artifact-precautionary measure especially when intending to choose high values of embedding parameters.

Acknowledgement

This research was carried out within the Research Training Group “Natural Hazards and Risks in a Changing World” (NatRiskChange; GRK 2043/1) funded by the “Deutsche Forschungsgemeinschaft” (DFG).

Appendix A

The following figure describes the impact of recurrence threshold (i.e. recurrence rate) on the determinism distance between the original and all shuffled Lorenz time series. It can be seen that large recurrence threshold would lead the recurrence plot into artefact as implied by its low determinism distance (Fig. 17.12 b, c, e and f). Similarly when $\tau = 1$, $m > 1$, the increase of recurrence rate further decrease the determinism distance (Fig. 17.12 d). This confirms us to ignore the use of such parameter value regardless of the choice of recurrence threshold. However when $m = 1$, there is an increase of determinism distance i.e peaking at 20% recurrence rate and decreases thereafter (Fig. 17.12 d). Despite the increase, the determinism distance is still regarded low (i.e. below 0.5).

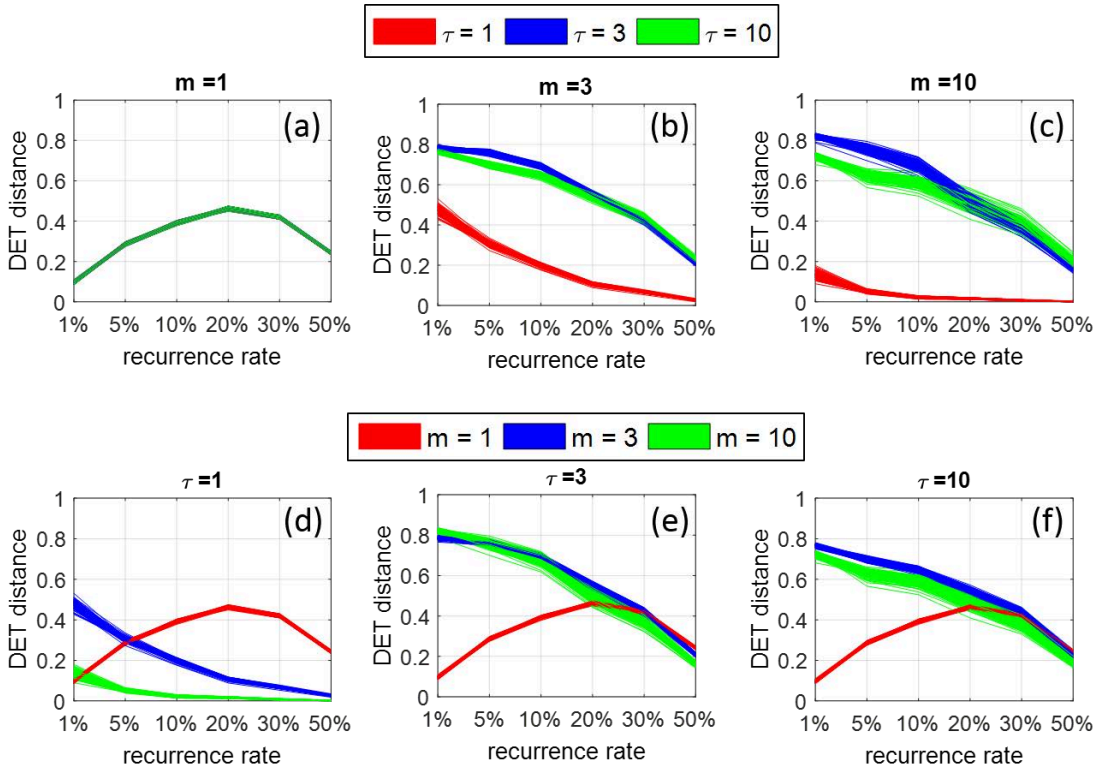

Figure 17.12: Impact of recurrence threshold (i.e. recurrence rate) on determinism distances (100x shuffles) corresponding to different embedding parameters. Note: on sub-figure a, red and blue band lines are overlapped by green bands, hence not visible

Both original and shuffled time series experience increase of their determinism values when recurrence rate is increased (Fig. 17.13 a, b, c). However, unlike when $m > 1$ the increase of determinism values is rather sharp, changing significantly from low to high. While the shuffled series recurrence plots at $m = 1$, with recurrence rate of 20% (i.e. at the peak of DET distance) still do not present any noteworthy deterministic features (Fig. 17.13 d, e, f). In this case, users should avoid using large threshold values and special attention should be made on using such shuffling technique (i.e. when choosing $m = 1$).

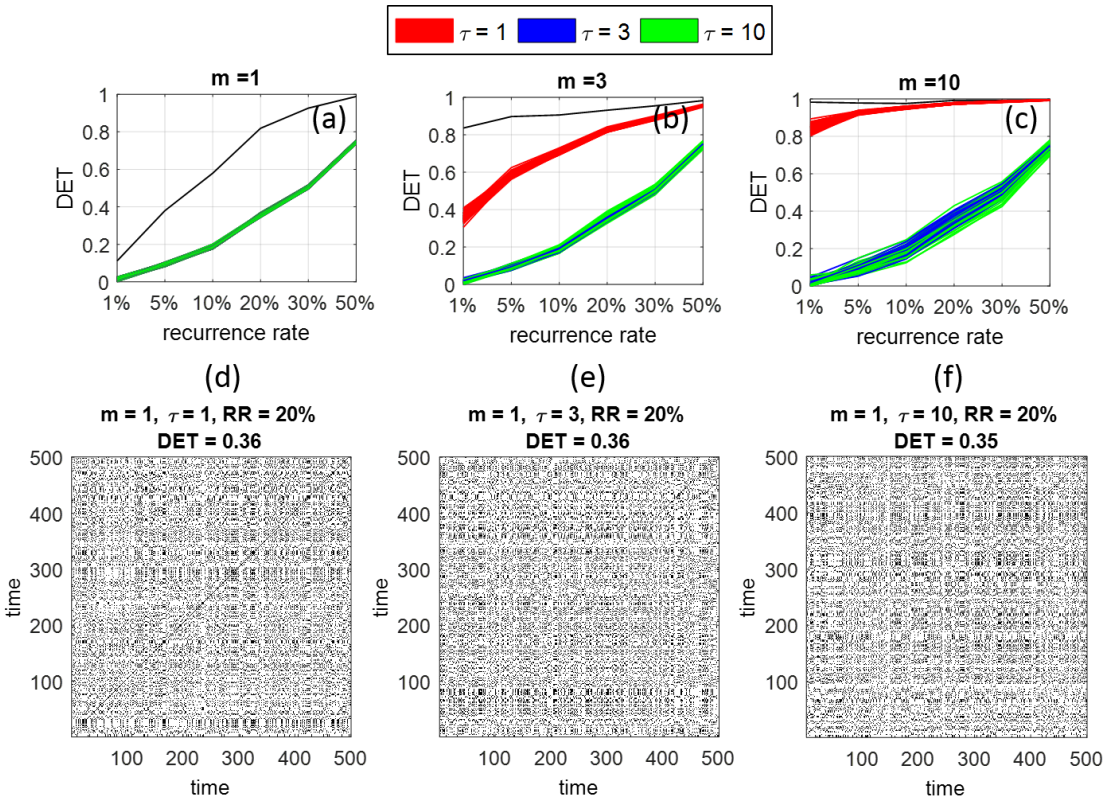

Figure 17.13: Impact of recurrence threshold (i.e. recurrence rate) on determinism (black line is resulted from original Lorenz time series, while the each coloured ones are resulted from 100 shuffled series, while the color corresponds to different selection of τ) with m =1, 3 and 10 respectively for sub-figures a, b and c .Sub-figures d to e present an extracted sample of the shuffled recurrence plot with fixed $m = 1$ and $\tau = 1$, 3, and 10 respectively. Note: on sub-figure a, red and blue band lines are overlapped by green bands, hence not visible

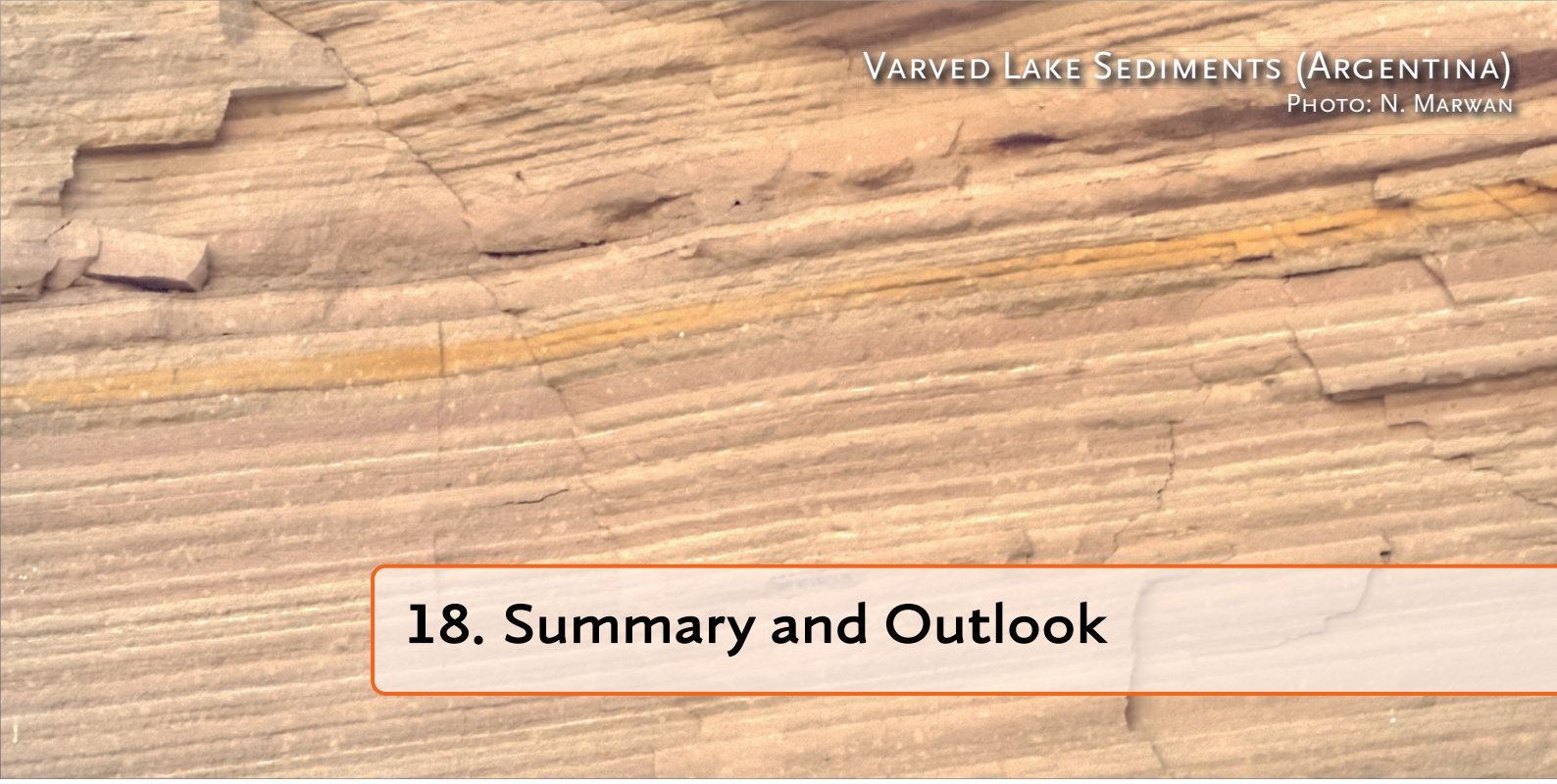

Varved Lake Sediments (Argentina)
Photo: N. Marwan

18. Summary and Outlook

Recurrence is a fundamental and general property of many systems studied in the geosciences. However, using recurrence features for numerical investigations is mostly limited to classical methods, such as power spectra or wavelet analysis. In my research I have developed and extended the numerical method of recurrence plots (RPs) in order to apply it to specific research questions in the geosciences. I have shown that RP based methods can be modified and adopted to study different aspects such as classification, characterization, transitions, couplings, external forcings, spatial patterns, etc. and that such analyses substantially enrich quantitative geoscience by revealing successfully further insights to important and challenging research questions.

18.1 Methodological developments

The main methodological contributions of this thesis are summarized in the following.

18.1.1 Selection of the recurrence threshold

For the selection of the recurrence threshold several rules of thumb have been suggested in the literature, but no systematic study has considered the power of the RP approach with respect to the threshold when detecting signals. In chapter 3, we have used the receiver-operator characteristic (ROC) as a meaningful test statistic for a systematic study of the performance of the RQA for detecting deterministic and stochastic signals and compared it to the available rules of thumb. For the purpose of signal detection, we found that 5 to 6% of the maximal phase space diameter would be the optimal value for the recurrence threshold. The selection of the threshold with respect to other statistical properties like mean phase space diameter or standard deviation (as often suggested in the literature) would not allow a consistent selection criterion. This finding was confirmed recently by one of my students, who finally suggested to use the quantiles of the distance distribution for the selection of the threshold [177]. However, this selection schema still comes with an arbitrary number (the 5 to 6%) and even with a range where the threshold could be considered to be optimal. It would be preferable, to have a selection scheme where the threshold is a fixed value and can be directly calculated from some desired features in the RP.

In chapter 4, we developed the idea to use the network property of connectedness as a

criterion for threshold selection. Such a threshold would be unique and directly computable. For a network, the second largest eigenvalue of the Laplace matrix represents whether the network has isolated nodes or whether everything is connected (for the latter the value is larger zero). Using this relationship, we suggested to transform the RP matrix into the Laplace matrix and check at which value for the recurrence threshold the second largest eigenvalue becomes larger zero. The resulting recurrence threshold is unique and ensures that all states are connected by recurrences (see also chapter 11 on recurrence networks).

18.1.2 Recurrence plot features

The visual appearance of an RP already allows for a first impression of the dynamics [239]. We can distinguish large-scale impressions (*typology*), such as *homogeneous*, *periodic*, *drift*, and *disrupted* ones, important, e.g., for the study of stationarity. Even more important and used for the recurrence quantification are the small-scale structures that can be found in the RP (*texture*; Fig. 1.3D). These structures can be typically classified in *single dots*, *diagonal lines* as well as *vertical* and *horizontal lines* [239]. In addition, even *bowed lines* may occur, i.e., lines with a non-constant slope. The shape of a bowed line depends on the local time relationship between the corresponding close trajectory segments and have been studied systematically in chapter 5. By knowing the meaning of the the local slope of the lines in the RP, the method can be used for specific tasks in geoscientific data analysis: the detection of changes in the temporal development of geological processes (e.g., changing sedimentation rates) or the alignment of the time axes of two proxy measurements (see also subsection 18.2.1).

The variation of the density of recurrence points along diagonals apart of the main diagonal corresponds to the probability of recurrence after a certain delay. This recurrence rate distribution contains information about the time scales of the variability, such as the period lengths of cycles and was considered in chapter 6. The application of the Wiener Khinchin theorem allows to derive a specific power spectrum based on the recurrences, providing information about the frequency components of the signal. In contrast to the standard power spectrum estimation, the recurrence based power spectrum revealed all periods a nonlinear signal was composed of (the standard approach found only two frequencies). Moreover, the novel approach would allow us to analyse high-dimensional systems.

18.1.3 Extending the recurrence plot approach for spatial data

Recurrences are not only a property of states that change with time. We can also find spatial recurrences, i.e., spatial structures that recur in the spatial domain. The investigation of spatial recurrences can be of interest for the evaluation of the complexity of spatial patterns. The extension of the RP concept to 2-dimensional or 3-dimensional spatial objects is not trivial because the additional spatial dimensions require additional pair-wise tests of similarity resulting in higher-dimensional RPs. In fact, an RP for a 2-dimensional spatial pattern will have four dimensions, for a 3-dimensional object, the RP will be of six dimensions. In chapter 8, I have introduced a generalization of RPs and corresponding quantification for the study of recurrences in higher dimensional objects and illustrated the potential by an analysis of complex 3-dimensional medical images. Simplified versions of this generalized RP approach have been used in other studies to analyse spatial complex patterns such as Turing structures derived from reaction-diffusion systems [81, 98, 99, 259, 294, 315, 402].

Another purpose of RP analysis of spatial data is the investigation of recurring spatial patterns over time. In chapter 9, we have used the mapogram as a metric to measure differences between spatial information, such as differences between satellite images. By thresholding the image differences of a series of images, we can produce an RP which

represents recurring patterns over time and which can be further analysed, e.g., using RQA or to derive the external forcing (as finally done in this chapter and summarized in subsection 18.1.5).

18.1.4 Recurrence plot approach for high-dimensional data

In general, RP based studies have so far been restricted to rather low-dimensional systems. However, when studying the complex behavior of real world systems, we often end up with extended complex systems, and the question arises whether RP based tools can be applied to high-dimensional systems, such as exhibiting high-dimensional chaos. Classic characterization of complex dynamics by using, e.g., entropy [87], correlation dimension [125], and Lyapunov exponents requires very long time-series [88] or the knowledge of the differential equations of the system which are in real world examples not known. The study of extended spatio-temporal dynamics is even more challenging because of the large degrees of freedom. In chapter 7, I have investigated the performance of the recurrence based measures of complexity for the detection of different dynamical regimes in the Lorenz96 model as an example of a high-dimensional and extended dynamical system [168, 205]. This model is a conceptual time-continuous linear lattice model and demonstrates fundamental aspects of weather predictability. The surprising finding is that the recurrence measures (the classical as well as the network based measures) can distinguish between the different dynamical regimes even for quite short time series of such a high-dimensional system. The applicability on extended dynamical systems suggests new application fields, such as analyzing satellite time series imagery, as illustrated in chapter 7 (and summarized in subsection 18.2.2).

18.1.5 Extracting driving forces from recurrence plots

The potential of RPs to extract an external driving force from a measured time series was demonstrated already in 1997 by Casdagli [45]. We have further improved this approach and extended it to spatio-temporal data. By combining the mapogram approach for measuring the pair-wise distance within a series of images with a kernel estimator the systemic changes that result from an external forcing become visible (and extractable) in the RP. The variation of the external forcing is visible in the RP along horizontal bands. However, this approach requires the existence of at least two parts of the state space where the trajectory stays longer than the period of the main cycle, such as present in the Lorenz system, but also in many real world examples. Testing this approach at an ecological phenomenon has demonstrated its potential (see subsection 18.2.4).

18.1.6 New measures for recurrence plot quantification

In chapters 11 and 12, I have introduced and discussed the concept of complex network analysis of RPs. The RP was identified as the adjacency matrix of a complex network, allowing the complex network measures to be used to quantify the recurrence properties of the phase space trajectory. In contrast to the classical recurrence measures basing on the line structures in RPs and, thus, characterizing the *dynamical properties* of the system, these network based measures capture the *geometric properties* associated to a trajectory in phase space. Such complementary information is useful when studying regime changes (subsection 18.2.3), characterizing different dynamics [112, 455], or even for the detection of coupling directions [103, 104]. In particular the transitivity coefficient $\mathscr{T}$ is appropriate because it quantifies specific aspects of the geometry of the phase space trajectory and can be used to differentiate between different dynamics (e.g., regular and irregular) [79, 241, 455].

18.1.7 Coping with irregularities

Irregularly sampled time series are a frequent complication in Earth sciences (and also in other disciplines, such as astrophysics). Regular spatial sampling of a palaeoclimate archive (e.g., lacustrine sediment, stalagmite) translates into irregularly spaced sampling intervals in the time domain due to varying deposition rates. For the representation of an RP, this irregular sampling is not a problem, because we can simply use the available time points for plotting the pair-wise recurrences. Quantifying the recurrence network structure by network measures is also not a problem (as long as phase space reconstruction using time delay embedding is not applied). However, for quantifying the line structures in an RP using RQA, an equidistant time axis is required. One possible solution, often commonly used, could be to interpolate the time series to an equidistant time axis.

As an alternative approach, in chapter 13 we have demonstrated the TACTS (Transformation costs time series) method that combines a difference filter with a specific resampling procedure in order to get a time series with regular sampling. A difference filter is a simple high-pass filter, where the resulting series is the difference of subsequent data points in the original time series. By this procedure, trends and slow variations can be removed from data. The novel TACTS approach compares two short subsequent sequences in an irregularly sampled time series by measuring the effort (the cost) that is needed to transform the first segment to the second one when we have only a limited set of operations for this transformation. The operations are assigned with a cost: The minimal cost necessary for such transformation can be used as the difference value, leading to the resulting, regularly sampled difference time series. Such time series can then be further analysed with RPs and RQA, e.g., in order to detect regime transitions or identify coupling regimes [244, 284] (subsection 18.2.3).

18.1.8 Recurrence analysis of data with uncertainties

Dating uncertainties are a challenging problem in palaeoclimate research, because time series analysis tools expect a fixed and true time information without uncertainties. In chapter 14, we have introduced a concept that provides such a fixed and true time axis, but, at the same time, incorporates the uncertainties. The uncertainties within the time domain are transferred to the state domain (i.e., the proxies), resulting in a sequence of probability distributions. Such a representation allows subsequent analyses to be carried out with respect to the uncertainties, e.g., to reconstruct ensembles of chronologies [36] or to perform an ensemble based correlation analysis [176]. Additionally, representing the evolution of the system's states using probability distributions requires also a redefinition of the recurrence property. Instead of the exact (binary) statement that a selected state recurs, the new approach provides the probability that this state might recur. The binary RP is, thus, replaced by a probability matrix. Another problem is that the standard RQA measures are not applicable to such a recurrence representation. Therefore, for a detection of regime transitions, in chapter 14 an alternative approach based on the idea of network community was proposed. This novel method can be used to indicate abrupt transitions in numerous applications where uncertainties are important to be considered (three different examples are described in this chapter).

18.1.9 Coupling analysis with recurrences

Based on the joint RP, a method for studying the interrelationship between dynamical systems had been suggested [324, 456]. The idea is using the fraction of joint recurrences in the joint RP (derived from two time series $\vec{x}_i$ and $\vec{y}_i$), the joint recurrence rate JRR. This is the joint probability of recurrences in both systems $\vec{x}_i$ and $\vec{y}_i$ and is then used to define a lagged

recurrence-based measure of dependence. By considering a lag in this measure, we can infer which system depends on the other one. In chapter 10, we introduce the procedure for the detection of couplings in a complex system and apply it to study the complex interrelations between the drivers of global temperature (see subsection 18.2.5).

18.1.10 Significance test for recurrence based transition detection

Transitions or regime changes in the dynamics of a dynamical system leave their marks in the recurrence properties that can be identified using RPs and RQA. Several measures of complexity have been introduced, representing different aspects of the dynamics. However, the fundamental issue when drawing conclusions about the variation of these RP based measures is whether the variation over time is *significant* or not (see also discussion in subsection 16.3.8). In order to get an impression about the significance of the results, I have developed and introduced a statistical approach that provides a confidence interval for these RP measures in chapter 15. The proposed test uses the distribution of line lengths within all sliding windows together and applies a bootstrap test on this merged line length distribution. The performance of this test was demonstrated by a study of marine palaeoclimate proxy data.

18.1.11 Potential problems and pitfalls in recurrence plot analysis

RPs and their quantification have a deep foundation in the theory of dynamical systems and are easy to use but powerful tools for the investigation of a variety of scientific problems. The striking visual characteristics of RPs as well as freely available software packages contribute to the spread of RP based methods to various scientific disciplines (see chapter 2). Nevertheless, users should be careful not to consider the approach as a magic black box that works on all kinds of data [225, 231]. Given that the methods are indeed in some sense powerful and adaptable to various problems, it is important that users know how these methods work and have understood the ideas behind the RP and the measures of complexity derived from it. An uncritical application can lead to serious pitfalls and mis-interpretations.

In chapter 16, I provide an overview on potential pitfalls related to the most common aspects of RP based analysis. For example, I discuss the interpretation of the RQA measures as indicators of non stationary, periodic, deterministic, or chaotic processes. The interference between signal frequency with sampling frequency or even screen resolution can also produce artificial macrostructures that disturb visual and quantitative analysis. The choice of the embedding parameters (embedding dimensions and delay) is important in order to unfold the dynamics. However, any higher embedding dimension causes spurious correlations and artificially long line structures in the RP, affecting any quantification based on RPs. In chapter 17, we suggest a procedure to evaluate exactly this effect by simply shuffling the data and applying different embedding parameters. This allows us to estimate a range of values for the embedding delay and dimension that would reduce this artifact.

18.2 Study of Recurrences in Earth processes

The developed methods for analysing the recurrence properties in geoscientific data have demonstrated their potential by confirming previous findings of and revealed new insights into specific Earth processes.

18.2.1 Integration of proxy records

The cross recurrence plot has been used to compare the temporal differences of two proxy records and to derive the corresponding temporal alignment function (chapter 5). Rock-

magnetic measurements (normalized remanent magnetization intensity and susceptibility) from two cores sampled in an Italian lake represent similar variability but cannot be directly integrated due to different sedimentation rates. The CRP provides a time transfer function that has been used to align one of the two records with the other one. As a result, both records finally share the same temporal sequence and can be integrated to create a stacked record or further analysed using time series analysis.

18.2.2 Spatial recurrence analysis of vegetation variability

In the application of analysing spatially extended satellite image time series of vegetation cover, I have investigated the contrasting dynamics which occur due to different landuse and climate (chapter 7). I considered regions in Brazil and Spain, where the recurrence analysis revealed mainly the seasonal variability, but with differences in the appearance of the periodic patterns: for Spain the recurring patterns are more line-like, whereas for Brazil they are more block-like, indicating substantial differences in the spatial dynamics. The RQA measures allow the interpretation of these differences regarding the dynamics, with a more erratic or chaotic variability in Brazil than in Spain. The vegetation (or land use) dynamics in Brazil is probably less regulated and less predictable than in Spain. The example shows the potential of recurrence based spatio-temporal analysis, for example, to study land use changes, vulnerability, and vegetation dynamics [458].

18.2.3 Identifying palaeoclimate transitions

The main focus of the recurrence analysis in my research was the identification of changes and transitions in palaeoclimate. For this task, I have used the regular RP approach, (chapter 15), the recurrence network approach (chapters 4 and 11), and the TACTS approach for irregularly sampled time series (chapter 13). Additionally I have strengthened this analysis with the significance test developed in chapter 15.

Different marine Plio-Pleistocene palaeoclimate proxies were considered, such as the terrigenuous dust flux record from the Atlantic (ODP site 659) and Alkenone palaeothermometry based SST estimates from the South China Sea (ODP site 1143) and from the Arabian sea (ODP site 722). Although these proxies differ in nature, location, and how they archive the climate signals, the recurrence analyses of these palaeoclimate time series have unveiled global climatic transitions due to the Milankovich cycles, such as the transition to the Northern Hemisphere glaciation, the intensification of the Walker circulation, and the transition phase from glaciation to glacial-interglacial cycles. Moreover, temporal changes of the recurrence measures can be used to understand the type of change. For example, during the epochs of northern hemisphere glaciation, 3 to 2.5 Ma BP, elevated values of RQA measure *determinism* and of network measure *clustering coefficient* (in Arabian and South China sea) suggest that the climate dynamics was more regular, more predictable than immediately before or after. This coincides with the known transition from the Early Pliocene Warm Period towards an epoch of glaciation at around 3 Ma ago, because of the beginning of a dominance of obliquity-driven climate variability (with a 41 ka period). A similar result has been found for the Atlantic with elevated climate regularity between 3.2 and 3.0 Ma and between 2.3 and 2.0 Ma BP. The dominating Milankovich regime with 41 ka cycles has changed between 1.3 Ma and 0.7 Ma BP to a regime with 100 ka cycles. This was related to a transition from glaciation to a regime with glacial-interglacial cycles. Referring to the alternating variation of the network measure *transitivity* for the South China Sea and the low determinism value for the Arabian sea, this transition phase was probably neither an abrupt nor a gradual one, but with alternating dominance of the mentioned Milankovich cycles. The SST estimates are from the Asian monsoon realm, the dust flux record from the

Atlantic; the mechanisms how the climate signal is archived into these proxies differ; and furthermore, the temporal resolution differs for these records (with average sampling time of 2000 and 2500 years for the SST estimates and of 120 years for the dust flux record) – all these issues cause smaller and larger deviations in the timing and the type of the identified transitions and would require a further, more comprehensive analysis including further proxy records from different places.

A similar study (chapter 4) considered an aragonite proxy for the younger Pleistocene measured in lake sediments from the Lake Lisan in the Near East. The RN analysis revealed abrupt transitions between alternating episodes of highly regular and relatively less regular dynamics. The periods of low regularity coincide with the known Bond and Heinrich events, whereas during the interstadials, we found high regular dynamics. This indicated a dominant role of the (more or less periodic) solar forcing via its influence on the temperature in the higher latitudes. During phases of a colder North Atlantic (Bond and Heinrich events), the solar forcing became less important for the local climate, but regional effects more important and dominating, causing a more complex, irregular local climate variability. Cold events (Bond events) have also been found in other Holocene palaeoclimate records based on stalagmites collected in the Dongge, Tianmen, and Qunf cave in China (chapter 14). Here the achievement was the detection of the abrupt transitions to weak Asian summer monsoon states during the Bond events with explicit consideration of the age uncertainties.

In a further example, terrestrial, Holocene palaeoclimate records (based on speleothems) from China and Australia have been analysed (chapter 13), where the irregular sampling of the original time series was challenging to identify and compare the transitions. The considered palaeoclimate proxy data represent the northern and the southern extent of the complex East Asian-Indonesian-Australian summer monsoon, where the East Asian summer monsoon and the Indonesian-Australian summer monsoon mutually influence each other. The combination of the TACTS approach with recurrence analysis has identified periods of alternating, see-saw like weaker and stronger regular dynamics for those palaeoclimate records. The variation in regularity in the dynamics can be understood in terms of strong and weak monsoons opposingly phased between Asia and Australia. A comparison with solar variability suggested that the change from weak to strong monsoon in the East Asian summer monsoon and, vice versa, in the Indonesian-Australian summer monsoon, was probably triggered by solar variations via shifting the position of the the Intertropical Convergence Zone (ITCZ) [414].

In general, recurrence analysis provides information about subtle changes and changes in the type of the dynamics – complementing the information obtainable with the more simpler statistics like time series mean and variance. This helps in better understanding the mechanisms behind the palaeoclimate transitions.

18.2.4 Identifying external forcing from spatio-temporal data

By using the novel idea of combining mapogram with RPs, we have studied spatio-temporal recurrences of phytoplankton growth in the Southern Californian Bight from 1998 to 2016 (chapter 9), where variation of chlorophyll concentration was derived from satellite and in situ measurements in this region. The RP method has been used to derive the potential external forcing that influences the phytoplankton growth. This analysis was repeated for the sea surface temperature (SST) in the Southern Californian Bight and the results were compared with the El Niño-Southern Oscillation index NINO3.4 in order to better understand the mechanism of phytoplankton growth. We found remarkable coincidence between the detected driving forces derived from the chlorophyll and SST data with the NINO3.4. This indicates the impact of the El Niño-Southern Oscillation on the phytoplankton growth via

SST. Moreover, we found significant regime shifts after 1998 and between 2014 to 2015 by means of an abrupt change between two levels of the reconstructed forcing.

18.2.5 Identifying interactions in drivers of global temperature

In a student's study we investigated the drivers of global temperature, such as the ENSO, volcanic activity (represented by aerosols), greenhouse gas concentration, and solar irradiance (chapter 10). We applied a recurrence based measure of conditional dependence to two different time series representing global mean temperature (which extends from 1950 till present).

We found interactions and feedbacks at different time scales. For example, greenhouse gases have the strongest impact on the global mean temperature on all time scales. ENSO influences the global temperature at short time scales (half a year) but also on longer, decadal time scales. Volcanic aerosols also affect the global temperature at different time scales, such as immediate response (within few months) but also, because aerosols would have some lifetime in the atmosphere, up to 5 and even 10 years. This reveals the important time scales of the volcanic activity on the atmospheric processes.

Even more interesting are the interactions between the different drivers of global temperature. We identified a feedback loop from the global temperature to the ENSO around the quasi-biennial period. Greenhouse gases are influenced by both solar and volcanic activity on time scales of 4 to 5 years, representing their influence on the Earth's carbon cycle. At a first glance, the detected influence of ENSO and solar activity on the volcanic activity might be surprising. But the volcanic activity is represented in this study by aerosols and their distribution in the atmosphere is strongly affected by solar activity and ENSO.

For a more visual representation of the findings, the complex interactions between and within the global temperature and their different forcings were finally represented in form of a network.

18.3 Outlook

The last decade has witnessed diverse methodological progress on recurrence plot based methods and brought forward this method with respect to the challenging problems in geoscientific data analysis. Nevertheless, many open questions remain and give potential for future research. Some of them are summarised below.

An important question is whether a detected regime transition or change is abrupt or gradual and how this can be separated by RPs. Questions, such as whether RPs and RQA could identify the type of a shift [83] and whether they allow to create RP based precursor indicators, are going in a similar direction. Such abilities are much desired, because they would be helpful in investigating and predicting climate and ecological tipping points with respect to the ongoing climate change.

From a palaeoclimate perspective, where uncertainties are a major confounding factor, it is important to develop a quantification for probabilistic RPs. The key would be to find a definition for line lengths in the probability matrices. Another important matter are changes in the sampling time within one proxy record. Small changes are manageable, e.g., using the TACTS approach [285]. But drastic sampling time differences, such as of factor 5 or even 10, are possible and can, if interpolation is used, mimic changes in the dynamics although changes are absent. The limits of the RP method with respect to such changes need to be systematically investigated in order to avoid misleading result or to find alternative recurrence definitions for this special case. A change in the sampling time can also require a change in the embedding parameters, making a windowed analysis more complicated. On

the other hand, a change in the embedding could also be a sign of a drastic change in the system's dynamics. In a first study we used such a change of the embedding parameters as an indicator of a transition [269], but the effect on the RP was not investigated up to now.

As a final example, event-like data should be mentioned. First ideas suggest to use the cost of transforming short sequences of events for the RP creation [373]. However, time series with only few events are still difficult to characterise with RPs and to quantify with RQA. The limits have not been worked out yet and alternative approaches, such as event synchronisation [301] for the definition of recurrences have not been considered yet, although they seem to be promising.

Apart from these methodological questions, some new lines of research are of further geoscientific interest. For example, using further climate proxy records from different places would allow to study the mechanisms of transitions in the Plio-Pleistocene climate. Further research on how solar variability has influenced the monsoon regimes would also be necessary. The question, whether certain climate regime transitions, such as the African humid period, started and terminated gradually or abruptly, or whether they could even be considered as tipping points, is also still open and requires interdisciplinary research.

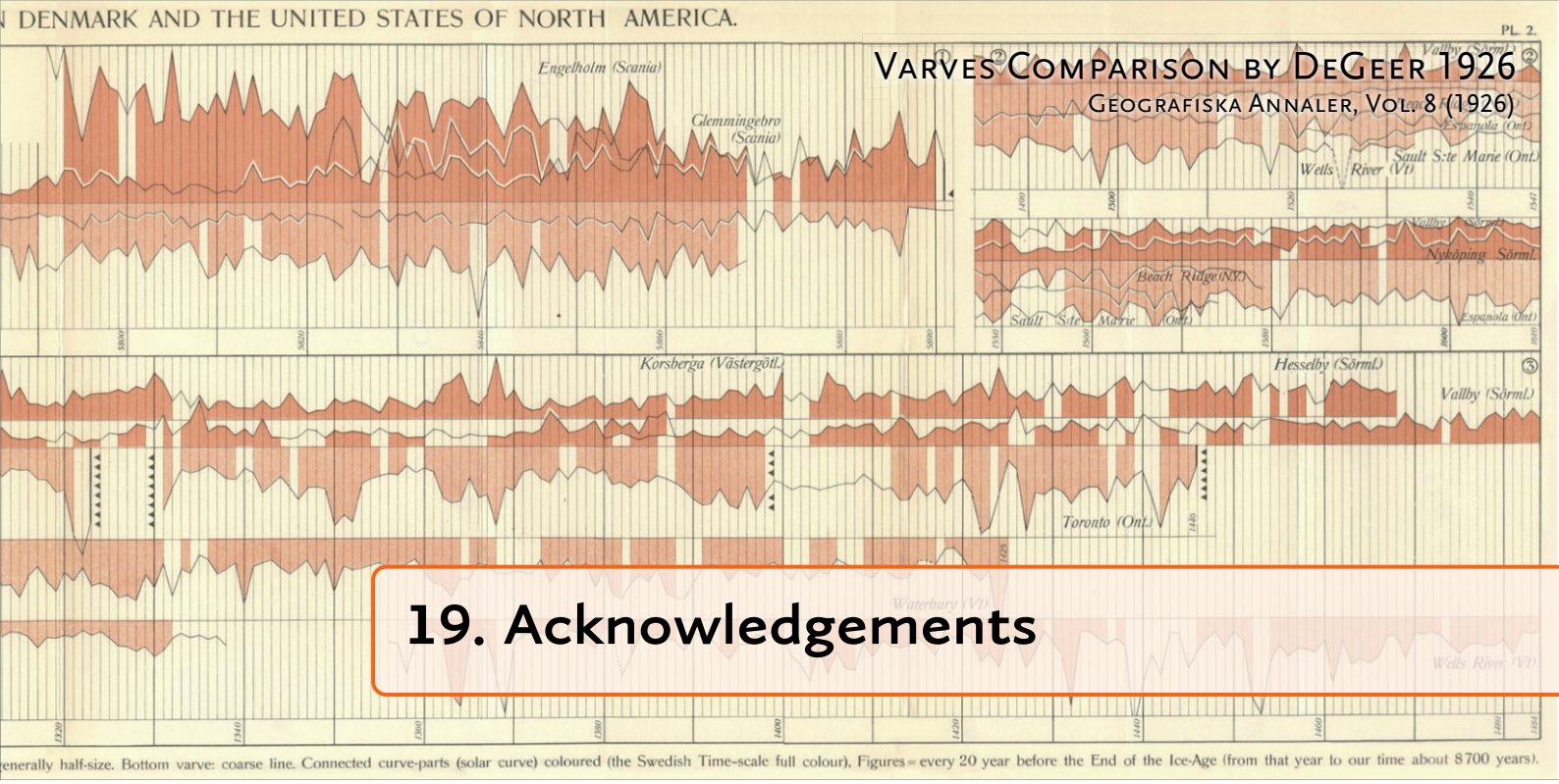

VARVES COMPARISON BY DEGEER 1926
GEOGRAFISKA ANNALER, VOL. 8 (1926)

generally half-size. Bottom varve: coarse line. Connected curve-parts (solar curve) coloured (the Swedish Time-scale full colour), Figures = every 20 year before the End of the Ice-Age (from that year to our time about 8700 years).

19. Acknowledgements

I am strongly thankful to my teacher, mentor, and friend Jürgen Kurths, who continually supported and encouraged me to finish this step of my carreer, and who was always open to my ideas which have finally been condensed in the presented thesis. Without his strong and continuous support I would not have been able to perform this research.

Many young and senior scientists have more and less intensively collaborated with me during the last years. Some of the methodological developments and results emerged from fruitful discussions and close collaborations with them. I am in particular grateful to Sebastian Breitenbach and Yoshito Hirata; to our former students Chandrasekaran Komalapriya, Kira Rehfeld, Niklas Boers, Jonathan Donges, Deniz Eroglu, Jan Feldhoff†, Bedartha Goswami, Nishant Malik, Ibrahim Ozken, Aljoscha Rheinwalt, Jakob Runge, Stefan Schinkel, and Dadiyorto Wendi, to which I had the great opportunity to (co-)supervise them; to our postdocs and senior scientists, including Reik Donner, Jobst Heitzig, Georg Feulner, Eulalie Ngamga, Maik Riedl, Thomas Stemler, Niels Wessel, Yong Zou; and to numerous external collaborators including all co-authors of my publications, in particular Bodo Bookhagen, Bruno Merz, Michael Small, Martin Trauth, Charles Webber Jr., and Joseph Zbilut†. I also thank all members of our group and external collaborators, which were not explicitly mentioned, for fruitful discussions and support.

Last but not least, I thank my family for their strong support and understanding.

Parts of this work were supported by DFG, ESA, Leibniz, and BMBF. The details of the funding are provided at the end of each chapter.

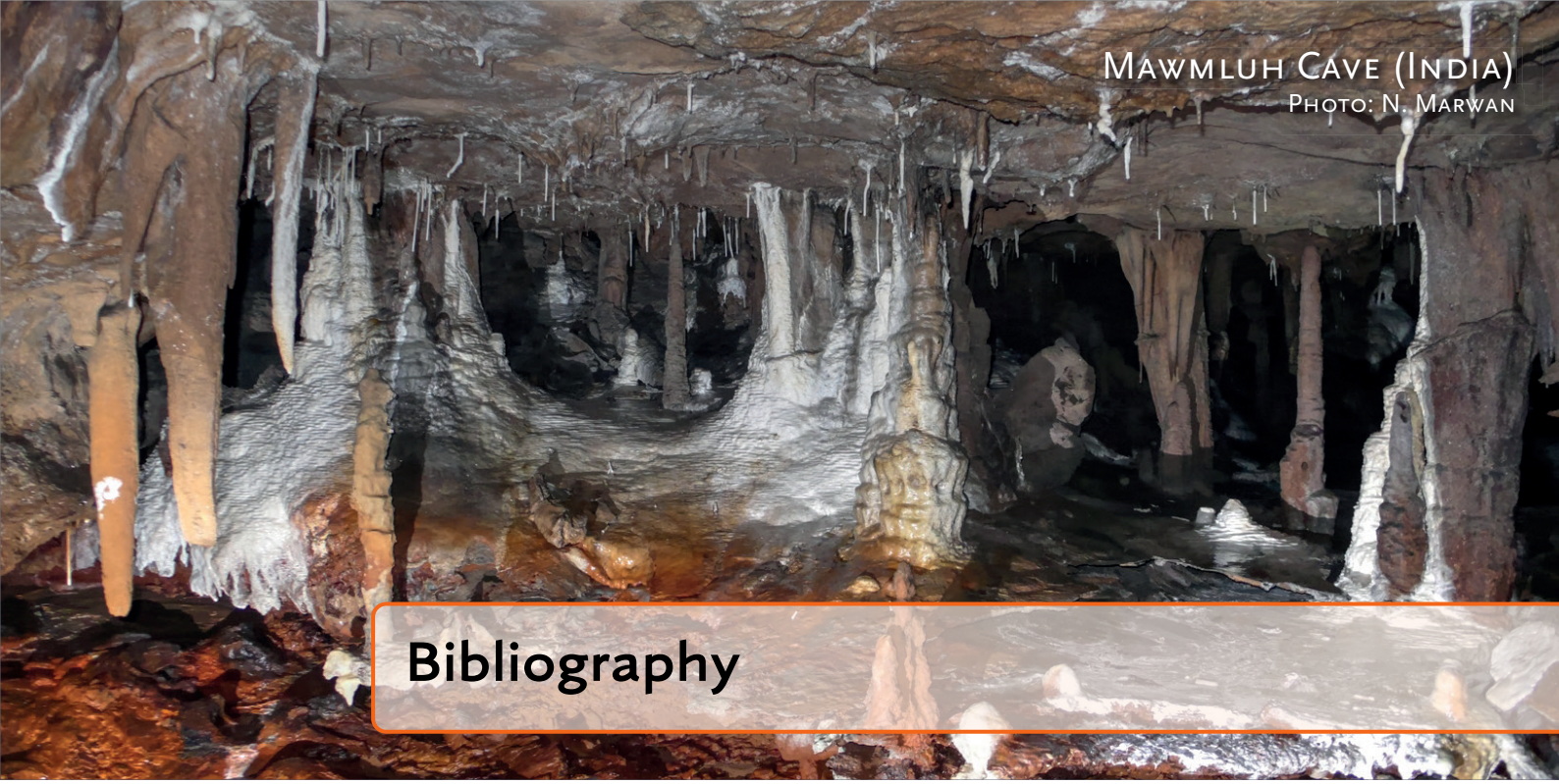

Mawmluh Cave (India)
Photo: N. Marwan

Bibliography

[1] R. Albert, I. Albert, and G. L. Nakarado. "Structural vulnerability of the North American power grid". In: *Physical Review E* 69 (2004), page 025103. DOI: 10.1103/PhysRevE.69.025103.

[2] Z. An et al. "Interplay between the Westerlies and Asian monsoon recorded in Lake Qinghai sediments since 32 ka". In: *Scientific Reports* 2 (2012), pages 1–7. DOI: 10.1038/srep00619.

[3] Z. An et al. "Chinese Loess and the East Asian Monsoon". In: *Late Cenozoic Climate Change in Asia*. Edited by Z. An. Volume 16. Developments in Paleoenvironmental Research. Dordrecht: Springer Netherlands, 2014. ISBN: 978-94-007-7816-0. DOI: 10.1007/978-94-007-7817-7_2.

[4] T. Andersen et al. "Ecological thresholds and regime shifts: Approaches to identification". In: *Trends in Ecology & Evolution* 24.1 (2009), pages 49–57. DOI: 10.1016/j.tree.2008.07.014.

[5] V. S. Anishchenko and S. V. Astakhov. "Poincaré recurrence theory and its applications to nonlinear physics". In: *Physics-Uspekhi* 56.10 (2013), pages 955–972. DOI: 10.3367/UFNe.0183.201310a.1009.

[6] T. Aparicio, E. F. Pozo, and D. Saura. "Detecting determinism using recurrence quantification analysis: Three test procedures". In: *Journal of Economic Behavior & Organization* 65.3–4 (2008), pages 768–787. DOI: 10.1016/j.jebo.2006.03.005.

[7] H. Apel et al. "Flood risk assessment and associated uncertainty". In: *Natural Hazards and Earth System Science* 4.2 (2004), pages 295–308. DOI: 10.5194/nhess-4-295-2004.

[8] A. Arenas et al. "Synchronization in complex networks". In: *Physics Reports* 469.3 (2008), pages 93–153. DOI: 10.1016/j.physrep.2008.09.002.

[9] N. Asghari et al. "Stability of terrestrial planets in the habitable zone of Gl 777 A, HD 72659, Gl 614, 47 Uma and HD 4208". In: *Astronomy & Astrophysics* 426 (2004), pages 353–365. DOI: 10.1051/0004-6361:20040390.

[10] V. Balakrishnan, G. Nicolis, and C. Nicolis. "Recurrence time statistics in deterministic and stochastic dynamical systems in continuous time: A comparison". In: *Physical Review E* 61.3 (2000), pages 2490–2499. DOI: 10.1103/PhysRevE.61.2490.

[11] C. Bandt et al. "Analysis of Bivariate Coupling by Means of Recurrence". In: *Mathematical Methods in Time Series Analysis and Digital Image Processing*. Edited by R. Dahlhaus et al. Understanding Complex Systems. Berlin, Heidelberg: Springer, 2008, pages 153–182. ISBN: 978-3-540-75631-6. DOI: 10.1007/978-3-540-75632-3_5.

[12] H. A. Barbosa, A. R. Huete, and W. E. Baethgen. “A 20-year study of NDVI variability over the Northeast Region of Brazil”. In: *Journal of Arid Environments* 67 (2006), pages 288–307. DOI: 10.1016/j.jaridenv.2006.02.022.

[13] M. Barreiro, A. C. Marti, and C. Masoller. “Inferring long memory processes in the climate network via ordinal pattern analysis.” In: *Chaos* 21.1 (2011), page 013101. DOI: 10.1063/1.3545273.

[14] Y. Bartov et al. “Catastrophic arid episodes in the Eastern Mediterranean climate linked with the North Atlantic Heinrich events”. In: *Geology* 31.5 (2003), pages 439–442.

[15] J. A. Bastos and J. Caiado. “Recurrence quantification analysis of global stock markets”. In: *Physica A* 390.7 (2011), pages 1315–1325. DOI: 10.1016/j.physa.2010.12.008.

[16] J. Belaire-Franch. “Testing for non-linearity in an artificial financial market: a recurrence quantification approach”. In: *Journal of Economic Behavior & Organization* 54.4 (2004), pages 483–494. DOI: 10.1016/j.jebo.2003.05.001.

[17] J. Belaire-Franch, D. Contreras, and L. Tordera-Lledó. “Assessing nonlinear structures in real exchange rates using recurrence plot strategies”. In: *Physica D* 171.4 (2002), pages 249–264. DOI: 10.1016/S0167-2789(02)00625-5.

[18] R. E. Benestad. “Reconciliation of global temperatures”. In: *Environmental Research Letters* 7.1 (2012), page 011002. DOI: 10.1088/1748-9326/7/1/011002.

[19] C. L. Benhamou et al. “Fractal Organization of Trabecular Bone Images on Calcaneus Radiographs”. In: *Journal of Bone and Mineral Research* 9.12 (1994), pages 1909–1918.

[20] A. Berger and M. Loutre. “Insolation values for the climate of the last 10 million years”. In: *Quaternary Science Reviews* 10.4 (1991), pages 297–317. DOI: 10.1016/0277-3791(91)90033-Q.

[21] A. Berger. “The Milankovitch astronomical theory of paleoclimates: A modern review”. In: *Vistas in Astronomy* 24 (1980), pages 103–122. DOI: 10.1016/0083-6656(80)90026-4.

[22] A. L. Berger. “Long-Term Variations of Caloric Insolation Resulting from the Earth’s Orbital Elements”. In: *Quaternary Research* 9.02 (1978), pages 139–167. DOI: 10.1016/0033-5894(78)90064-9.

[23] W. H. Berger and E. Jansen. “Mid-Pleistocene climate shift – the Nansen connection”. In: *The Polar Oceans and Their Role in Shaping the Global Environment*. Edited by O. M. Johannessen, R. D. Muench, and J. E. Overland. Volume 85. Geophysical Monograph. Washington: American Geophysical Union, 1994, pages 295–311.

[24] M. Berkelhammer et al. “An Abrupt Shift in the Indian Monsoon 4000 Years Ago”. In: *Geophysical Monograph Series*. Edited by L. Giosan et al. 2013, pages 75–88. ISBN: 978-1-118-70432-5. DOI: 10.1029/2012GM001207.

[25] N. Bigdeli and K. Afshar. “Characterization of Iran electricity market indices with pay-as-bid payment mechanism”. In: *Physica A* 388.8 (2009), pages 1577–1592. DOI: 10.1016/j.physa.2009.01.003.

[26] T. Blazina et al. “Terrestrial selenium distribution in China is potentially linked to monsoonal climate.” In: *Nature communications* 5 (2014), page 4717. DOI: 10.1038/ncomms5717.

[27] S. Boccaletti et al. “Complex networks: structure and dynamics”. In: *Physics Reports* 424.4–5 (2006), pages 175–308. DOI: 10.1016/j.physrep.2005.10.009.

[28] N. Boers et al. “Complex networks identify spatial patterns of extreme rainfall events of the South American Monsoon System”. In: *Geophysical Research Letters* 40.16 (2013), pages 4386–4392. DOI: 10.1002/grl.50681.

[29] N. Boers et al. “Prediction of extreme floods in the eastern Central Andes based on a complex networks approach”. In: *Nature Communications* 5 (2014), page 5199. DOI: 10.1038/ncomms6199.

[30] G. Bond et al. “A Pervasive Millennial-Scale Cycle in North Atlantic Holocene and Glacial Climates”. In: *Science* 278.5341 (1997), pages 1257–1266. DOI: 10.1126/science.278.5341.1257.

[31] G. Bond et al. “Persistent solar influence on North Atlantic climate during the Holocene.” In: *Science* 294.5549 (2001), pages 2130–2136. DOI: 10.1126/science.1065680.

[32] P. Bosák et al. “Magnetostratigraphy and unconformities in cave sediments: case study from the Classical Karst, SW Slovenia”. In: *Geologos* 5 (2000), pages 13–30.

[33] W. H. Bradley. “Mediterranean Sediments and Pleistocene Sea Levels”. In: *Science* 88.2286 (1938), pages 376–379. DOI: 10.1126/science.88.2286.376.

[34] U. Brandt et al. “Palaeomagnetism of Holocene and late Pleistocene sediments from Lago di Mezzano and Lago Grande di Monticchio (Italy): Initial Results”. In: *Quaternary Science Reviews* 18.7 (1999), pages 961–976. DOI: 10.1016/S0277-3791(99)00008-6.

[35] S. F. M. Breitenbach et al. “Strong Influence of Water Vapor Source Dynamics on Stable Isotopes in Precipitation Observed in Southern Meghalaya, NE India”. In: *Earth and Planetary Science Letters* 292.1–2 (2010), pages 212–220. DOI: 10.1016/j.epsl.2010.01.038.

[36] S. F. M. Breitenbach et al. “COnstructing Proxy-Record Age models (COPRA)”. In: *Climate of the Past* 8 (2012), pages 1765–1779. DOI: 10.5194/cp-8-1765-2012.

[37] S. F. M. Breitenbach et al. “Cave ventilation and rainfall signals in dripwater in a monsoonal setting – a monitoring study from NE India”. In: *Chemical Geology* 402 (2015), pages 111–124. DOI: 10.1016/j.chemgeo.2015.03.011.

[38] A. J. Broccoli, K. a. Dahl, and R. J. Stouffer. “Response of the ITCZ to Northern Hemisphere cooling”. In: *Geophysical Research Letters* 33 (2006), pages 1–4. DOI: 10.1029/2005GL024546.

[39] P. Brohan et al. “Uncertainty estimates in regional and global observed temperature changes: A new data set from 1850”. In: *Journal of Geophysical Research* 111.D12 (2006), page D12106. DOI: 10.1029/2005JD006548.

[40] T. Buzug and G. Pfister. “Comparison of algorithms calculating optimal embedding parameters for delay time coordinates”. In: *Physica D: Nonlinear Phenomena* 58.1-4 (1992), pages 127–137. DOI: 10.1016/0167-2789(92)90104-U.

[41] Y. Cai et al. “The Holocene Indian monsoon variability over the southern Tibetan Plateau and its teleconnections”. In: *Earth and Planetary Science Letters* 335-336 (2012), pages 135–144. DOI: 10.1016/j.epsl.2012.04.035.

[42] L. Cao. “Practical method for determining the minimum embedding dimension of a scalar time series”. In: *Physica D* 110.1–2 (1997), pages 43–50. DOI: 10.1016/S0167-2789(97)00118-8.

[43] L. Carpi et al. “Structural evolution of the Tropical Pacific climate network”. In: *The European Physical Journal B* 85.11 (2012), page 389. DOI: 10.1140/epjb/e2012-30413-7.

[44] S. Carrubba et al. “Increased determinism in brain electrical activity occurs in association with multiple sclerosis”. In: *Neurological Research* 34.3 (2012), pages 286–290. DOI: 10.1179/1743132812Y.0000000010.

[45] M. C. Casdagli. “Recurrence plots revisited”. In: *Physica D* 108.1–2 (1997), pages 12–44. DOI: 10.1016/S0167-2789(97)82003-9.

[46] H. Castellini and L. Romanelli. “Applications of recurrence quantified analysis to study the dynamics of chaotic chemical reaction”. In: *Physica A* 342.1–2 (2004), pages 301–307. DOI: 10.1016/j.physa.2004.06.028.

[47] V. Čermák. “Recurrence Quantification Analysis of Borehole Temperatures: Evidence of Fluid Convection”. In: *International Journal of Bifurcation and Chaos* 19.3 (2009), pages 889–902. DOI: 10.1142/S0218127409023366.

[48] C.-P. Chang et al. “Maritime continent monsoon; annual cycle and boreal winter variability”. In: *East Asian Monsoon*. Edited by C.-P. Chang. Volume 2. World Scientific Series on Asia-Pacific Weather and Climate. Singapore: World Scientific Publishing, 2004, pages 107–150.

[49] C. Chatfield. *The Analysis of Time Series,* 6th edition. Chapman & Hall/CRC, 2003.

[50] Y. Chen and H. Yang. “Multiscale recurrence analysis of long-term nonlinear and nonstationary time series”. In: *Chaos, Solitons & Fractals* 45.7 (2012), pages 978–987. DOI: 10.1016/j.chaos.2012.03.013.

[51] C. Cheng et al. “Ultra-precision Machining Process Dynamics and Surface Quality Monitoring”. In: *Procedia Manufacturing* 1 (2016), pages 607–618. DOI: 10.1016/j.promfg.2015.09.044.

[52] J. C. H. Chiang, M. Biasutti, and D. S. Battisti. “Sensitivity of the Atlantic Intertropical Convergence Zone to Last Glacial Maximum boundary conditions”. In: *Paleoceanography* 18.4 (2003), n/a–n/a. DOI: 10.1029/2003PA000916.

[53] J. M. Choi, B. H. Bae, and S. Y. Kim. “Divergence in perpendicular recurrence plot; quantification of dynamical divergence from short chaotic time series”. In: *Physics Letters A* 263.4–6 (1999), pages 299–306. DOI: 10.1016/S0375-9601(99)00751-3.

[54] F. Christiansen and H. H. Rugh. “Computing Lyapunov spectra with continuous Gram – Schmidt orthonormalization”. In: *Nonlinearity* 10.5 (1997), pages 1063–1072. DOI: 10.1088/0951-7715/10/5/004.

[55] K. W. Church and J. I. Helfman. “Dotplot: A Program for Exploring Self-Similarity in Millions of Lines of Text and Code”. In: *Journal of Computational and Graphical Statistics* 2.2 (1993), pages 153–174.

[56] K. M. Cobb et al. “Highly Variable El Niño–Southern Oscillation Throughout the Holocene”. In: *Science* 339 (2013), pages 67–70.

[57] P. Collet and J.-P. Eckmann. *Iterated maps on the interval as dynamical systems*. Basel Boston Stuttgart: Birkhäuser, 1980.

[58] A. Cramp and G. O’Sullivan. “Neogene sapropels in the Mediterranean: A review”. In: *Marine Geology* 153.1-4 (1999), pages 11–28. DOI: 10.1016/S0025-3227(98)00092-9.

[59] P. M. Crowley and A. Schultz. “Measuring the Intermittent Synchronicity of Macroeconomic Growth in Europe”. In: *International Journal of Bifurcation and Chaos* 21.4 (2011), pages 1215–1231. DOI: 10.1142/S0218127411028957.

[60] V. Dakos et al. “Slowing down as an early warning signal for abrupt climate change”. In: *Proceedings of the National Academy of Sciences of the United States of America* 105.38 (Sept. 2008), pages 14308–12. DOI: 10.1073/pnas.0802430105.

[61] W. Dansgaard et al. “Evidence for general instability of past climate from a 250-kyr ice-core record”. In: *Nature* 364.6434 (1993), pages 218–220. DOI: 10.1038/364218a0.

[62] P. B. deMenocal. “Plio-Pleistocene African Climate”. In: *Science* 270.5233 (1995), pages 53–59. DOI: 10.1126/science.270.5233.53.

[63] R. F. Denniston et al. “A Stalagmite record of Holocene Indonesian–Australian summer monsoon variability from the Australian tropics”. In: *Quaternary Science Reviews* 78.0 (2013), pages 155–168. DOI: 10.1016/j.quascirev.2013.08.004.

[64] J. I. Deza, C. Masoller, and M. Barreiro. “Distinguishing the effects of internal and forced atmospheric variability in climate networks”. In: *Nonlinear Processes in Geophysics* 21.3 (2014), pages 617–631. DOI: 10.5194/npg-21-617-2014.

[65] J. Deza, M. Barreiro, and C. Masoller. “Inferring interdependencies in climate networks constructed at inter-annual, intra-season and longer time scales”. In: *The European Physical Journal – Special Topics* 222.2 (2013), pages 511–523. DOI: 10.1140/epjst/e2013-01856-5.

[66] Y. Dixit et al. “Intensified summer monsoon and the urbanization of Indus Civilization in northwest India”. In: *Scientific Reports* 8.1 (2018), page 4225. DOI: 10.1038/s41598-018-22504-5.

[67] E. Domany. “Protein folding in contact map space”. In: *Physica A* 288.1–4 (2000), pages 1–9. DOI: 10.1016/S0378-4371(00)00410-6.

[68] D. Dommenget and M. Latif. “A cautionary note on the interpretation of EOFs”. In: *Journal of Climate* 15 (2002), pages 216–225. DOI: 10.1175/1520-0442(2003)016<1087:COACNO>2.0.CO;2.

[69] J. F. Donges et al. “Complex networks in climate dynamics – Comparing linear and nonlinear network construction methods”. In: *European Physical Journal – Special Topics* 174 (2009), pages 157–179. DOI: 10.1140/epjst/e2009-01098-2.

[70] J. F. Donges et al. “The backbone of the climate network”. In: *Europhysics Letters* 87 (2009), page 48007. DOI: 10.1209/0295-5075/87/48007.

[71] J. F. Donges et al. “Identification of dynamical transitions in marine palaeoclimate records by recurrence network analysis”. In: *Nonlinear Processes in Geophysics* 18 (2011), pages 545–562. DOI: 10.5194/npg-18-545-2011.

[72] J. F. Donges et al. “Investigating the topology of interacting networks”. In: *European Physical Journal B* 84 (2011), pages 635–651. DOI: 10.1140/epjb/e2011-10795-8.

[73] J. F. Donges et al. “Nonlinear detection of paleoclimate-variability transitions possibly related to human evolution”. In: *Proceedings of the National Academy of Sciences* 108.51 (2011), pages 20422–20427. DOI: 10.1073/pnas.1117052108.

[74] J. F. Donges et al. “Analytical framework for recurrence network analysis of time series”. In: *Physical Review E* 85 (2012), page 046105. DOI: 10.1103/PhysRevE.85.046105.

[75] J. F. Donges et al. “How complex climate networks complement eigen techniques for the statistical analysis of climatological data”. In: *Climate Dynamics* 45.9 (2015), pages 2407–2424. DOI: 10.1007/s00382-015-2479-3.

[76] R. V. Donner et al. “Ambiguities in recurrence-based complex network representations of time series”. In: *Physical Review E* 81 (2010), 015101(R). DOI: 10.1103/PhysRevE.81.015101.

[77] R. V. Donner et al. “Recurrence networks – A novel paradigm for nonlinear time series analysis”. In: *New Journal of Physics* 12.3 (2010), page 033025. DOI: 10.1088/1367-2630/12/3/033025.

[78] R. V. Donner et al. “Recurrence-based time series analysis by means of complex network methods”. In: *International Journal of Bifurcation and Chaos* 21.4 (2011), pages 1019–1046. DOI: 10.1142/S0218127411029021.

[79] R. V. Donner et al. “The Geometry of Chaotic Dynamics – A Complex Network Perspective”. In: *European Physical Journal B* 84 (2011), pages 653–672. DOI: 10.1140/epjb/e2011-10899-1.

[80] A. Donohoe et al. “The Relationship between ITCZ Location and Cross-Equatorial Atmospheric Heat Transport: From the Seasonal Cycle to the Last Glacial Maximum”. In: *Journal of Climate* 26.11 (2013), pages 3597–3618. DOI: 10.1175/JCLI-D-12-00467.1.

[81] F. A. dos S. Silva et al. “Characterization of spatial patterns produced by a Turing instability in coupled dynamical systems”. In: *Communications in Nonlinear Science and Numerical Simulation* 19.4 (2014), pages 1055–1071. DOI: 10.1016/j.cnsns.2013.08.030.

[82] G. Dougherty and G. M. Henebry. “Fractal signature and lacunarity in the measurement of the texture of trabecular bone in clinical CT images”. In: *Medical Engineering & Physics* 23.6 (2001), pages 369–380.

[83] S. Drijfhout et al. “Catalogue of abrupt shifts in Intergovernmental Panel on Climate Change climate models”. In: *Proceedings of the National Academy of Sciences* 112.43 (2015), E5777–E5786. DOI: 10.1073/pnas.1511451112.

[84] C. A. Dykoski et al. “A high-resolution, absolute-dated Holocene and deglacial Asian monsoon record from Dongge Cave, China”. In: *Earth and Planetary Science Letters* 233.1–2 (2005), pages 71–86.

[85] I. Ebert-Uphoff and Y. Deng. “A new type of climate network based on probabilistic graphical models: Results of boreal winter versus summer”. In: *Geophysical Research Letters* 39 (2012). DOI: 10.1029/2012GL053269.

[86] J.-P. Eckmann, S. Oliffson Kamphorst, and D. Ruelle. “Recurrence Plots of Dynamical Systems”. In: *Europhysics Letters* 4.9 (1987), pages 973–977. DOI: 10.1209/0295-5075/4/9/004.

[87] J.-P. Eckmann and D. Ruelle. “Ergodic theory of chaos and strange attractors”. In: *Review of Modern Physics* 57.3 (1985), pages 617–656. DOI: 10.1103/RevModPhys.57.617.

[88] J.-P. Eckmann and D. Ruelle. “Fundamental limitations for estimating dimensions and Lyapunov exponents in dynamical systems”. In: *Physica D* 56.2–3 (1992), pages 185–187. DOI: 10.1016/0167-2789(92)90023-G.

[89] B. Efron and R. J. Tibshirani. *An Introduction to the Bootstrap*. Boca Raton, London, New York, Washington DC: Chapman & Hall/CRC, 1998, page 436. ISBN: 0-412-04231-2.

[90] A. S. Elwakil and A. M. Soliman. “Mathematical Models of the Twin-T, Wien-bridge and Family of Minimum Component Electronic Chaos Generators with Demonstrative Recurrence Plots”. In: *Chaos, Solitons & Fractals* 10.8 (1999), pages 1399–1411. DOI: 10.1016/S0960-0779(98)00109-X.

[91] E. D. Eneyew and M. Ramulu. “Tool wear monitoring using microphone signals and recurrence quantification analysis when drilling composites”. In: *Advanced Materials Research* 711 (2013), pages 239–244. DOI: 10.4028/www.scientific.net/AMR.711.239.

[92] D. Eroglu et al. “Entropy of weighted recurrence plots”. In: *Physical Review E* 90 (2014), page 042919. DOI: 10.1103/PhysRevE.90.042919.

[93] D. Eroglu et al. “Finding recurrence networks’ threshold adaptively for a specific time series”. In: *Nonlinear Processes in Geophysics* 21 (2014), pages 1085–1092. DOI: 10.5194/npg-21-1085-2014.

[94] D. Eroglu et al. “See-saw relationship of the Holocene East Asian-Australian summer monsoon”. In: *Nature Communications* 7 (2016), page 12929. DOI: 10.1038/ncomms12929.

[95] A. Fabretti and M. Ausloos. “Recurrence plot and recurrence quantification analysis techniques for detecting a critical regime. Examples from financial market indices”. In: *International Journal of Modern Physics C* 16.5 (2005), pages 671–706. DOI: 10.1142/S0129183105007492.

[96] A. Facchini and H. Kantz. “Curved structures in recurrence plots: The role of the sampling time”. In: *Physical Review E* 75 (2007), page 036215. DOI: 10.1103/PhysRevE.75.036215.

[97] A. Facchini, H. Kantz, and E. B. P. Tiezzi. “Recurrence plot analysis of nonstationary data: The understanding of curved patterns”. In: *Physical Review E* 72 (2005), page 021915. DOI: 10.1103/PhysRevE.72.021915.

[98] A. Facchini and C. Mocenni. “Recurrence Methods for the Identification of Morphogenetic Patterns”. In: *PLoS ONE* 8.9 (2013), e73686. DOI: 10.1371/journal.pone.0073686.

[99] A. Facchini, F. Rossi, and C. Mocenni. “Spatial recurrence strategies reveal different routes to Turing pattern formation in chemical systems”. In: *Physics Letters A* 373.46 (2009), pages 4266–4272. DOI: 10.1016/j.physleta.2009.09.049.

[100] A. Facchini et al. “Nonlinear time series analysis of dissolved oxygen in the Orbetello Lagoon (Italy)”. In: *Ecological Modelling* 203.3–4 (2007), pages 339–348. DOI: 10.1016/j.ecolmodel.2006.12.001.

[101] P. Faure and H. Korn. “A new method to estimate the Kolmogorov entropy from recurrence plots: its application to neuronal signals”. In: *Physica D* 122.1–4 (1998), pages 265–279. DOI: 10.1016/S0167-2789(98)00177-8.

[102] T. Fawcett. “An introduction to ROC analysis”. In: *Pattern Recognition Letters* 27.8 (2006), pages 861–874. DOI: 10.1016/j.patrec.2005.10.010.

[103] J. H. Feldhoff et al. “Geometric detection of coupling directions by means of inter-system recurrence networks”. In: *Physics Letters A* 376.46 (2012), pages 3504–3513. DOI: 10.1016/j.physleta.2012.10.008.

[104] J. H. Feldhoff et al. “Geometric signature of complex synchronisation scenarios”. In: *Europhysics Letters* 102.3 (2013), page 30007. DOI: 10.1209/0295-5075/102/30007.

[105] J. H. Feldhoff et al. “Complex networks for climate model evaluation with application to statistical versus dynamical modeling of South American climate”. In: *Climate Dynamics* (2014). DOI: 10.1007/s00382-014-2182-9.

[106] J. Feng and W. Chen. “Interference of the East Asian winter monsoon in the impact of ENSO on the East Asian summer monsoon in decaying phases”. In: *Advances in Atmospheric Sciences* 31.2 (2014), pages 344–354. DOI: 10.1007/s00376-013-3118-8.

[107] D. Fleitmann et al. “Holocene ITCZ and Indian monsoon dynamics recorded in stalagmites from Oman and Yemen (Socotra)”. In: *Quaternary Science Reviews* 26.1–2 (2007), pages 170–188. DOI: 10.1016/j.quascirev.2006.04.012.

[108] G. Foster and S. Rahmstorf. “Global temperature evolution 1979–2010”. In: *Environmental Research Letters* 6.4 (2011), page 044022. DOI: 10.1088/1748-9326/6/4/044022.

[109] A. M. Fraser and H. L. Swinney. “Independent coordinates for strange attractors from mutual information”. In: *Physical Review A* 33.2 (1986), pages 1134–1140. DOI: 10.1103/PhysRevA.33.1134.

[110] J. B. Gao and H. Q. Cai. “On the structures and quantification of recurrence plots”. In: *Physics Letters A* 270.1–2 (2000), pages 75–87. DOI: 10.1016/S0375-9601(00)00304-2.

[111] Z. Gao and N. Jin. “Flow-pattern identification and nonlinear dynamics of gas-liquid two-phase flow in complex networks”. In: *Physical Review E* 79.6 (2009), page 066303. DOI: 10.1103/PhysRevE.79.066303.

[112] Z. Gao et al. “Multivariate recurrence network analysis for characterizing horizontal oil-water two-phase flow”. In: *Physical Review E* 88 (2013), page 032910. DOI: 10.1103/PhysRevE.88.032910.

[113] Z. Gao et al. “Recurrence networks from multivariate signals for uncovering dynamic transitions of horizontal oil-water stratified flows”. In: *Europhysics Letters* 103.5 (2013), page 50004. DOI: 10.1209/0295-5075/103/50004.

[114] G. de Geer. “On the Solar Curve: As Dating the Ice Age, the New York Moraine, and Niagara Falls through the Swedish Timescale”. In: *Geografiska Annaler* 8 (1926), pages 253–283. DOI: 10.2307/519727.

[115] G. de Geer. “Geochronology of the last 12,000 years”. In: *International Journal of Earth Sciences* 91.1 (2002). Translated reprint of the original work., s100–s110. DOI: 10.1007/s00531-002-0287-6.

[116] M. Ghil and R. Vautard. “Interdecadal oscillations and the warming trend in global temperature time series”. In: *Nature* 350.6316 (1991), pages 324–327. DOI: 10.1038/350324a0.

[117] C. G. Gilmore. “Detecting Linear and Nonlinear Dependence in Stock Returns: New Methods Derived from Chaos Theory”. In: *Journal of Business Finance & Accounting* 23.9–10 (1996), pages 1357–1377. DOI: 10.1111/1468-5957.00084.

[118] A. Giuliani et al. “Nonlinear Signal Analysis Methods in the Elucidation of Protein Sequence-Structure Relationships”. In: *Chemical Reviews* 102.5 (2002), pages 1471–1492. DOI: 10.1021/cr0101499.

[119] Google Inc. Australia. *Google gDay*. Accessed: 2019-03-05. URL: https://web.archive.org/web/20080404002855/http://www.google.com.au/intl/en/gday/press.html.

[120] B. Goswami et al. “On interrelations of recurrences and connectivity trends between stock indices”. In: *Physica A* 391 (2012), pages 4364–4376. DOI: 10.1016/j.physa.2012.04.018.

[121] B. Goswami et al. “Estimation of sedimentary proxy records together with associated uncertainty”. In: *Nonlinear Processes in Geophysics* 21 (2014), pages 1093–1111. DOI: 10.5194/npg-21-1093-2014.

[122] W. Gowin et al. “Measures of complexity for cancellous bone”. In: *Technology and Health Care* 6 (1998), pages 373–390.

[123] K. Grant et al. “The timing of Mediterranean sapropel deposition relative to insolation, sea-level and African monsoon changes”. In: *Quaternary Science Reviews* 140 (2016), pages 125–141. DOI: 10.1016/j.quascirev.2016.03.026.

[124] P. Grassberger and I. Procaccia. “Characterization of strange attractors”. In: *Physical Review Letters* 50.5 (1983), pages 346–349. DOI: 10.1103/PhysRevLett.50.346.

[125] P. Grassberger and I. Procaccia. “Measuring the strangeness of strange attractors”. In: *Physica D* 9.1–2 (1983), pages 189–208. DOI: 10.1016/0167-2789(83)90298-1.

[126] M. L. Griffiths et al. “Increasing Australian–Indonesian monsoon rainfall linked to early Holocene sea-level rise”. In: *Nature Geoscience* 2.9 (2009), pages 636–639. DOI: 10.1038/ngeo605.

[127] M. L. Griffiths et al. “Evidence for Holocene changes in Australian-Indonesian monsoon rainfall from stalagmite trace element and stable isotope ratios”. In: *Earth and Planetary Science Letters* 292.1-2 (2010), pages 27–38. DOI: 10.1016/j.epsl.2010.01.002.

[128] A. Groth. “Visualization of coupling in time series by order recurrence plots”. In: *Physical Review E* 72.4 (2005), page 046220. DOI: 10.1103/PhysRevE.72.046220.

[129] Z. O. Guimarães-Filho et al. “Recurrence quantification analysis of electrostatic fluctuations in fusion plasmas”. In: *Physics Letters A* 372.7 (2008), pages 1088–1095. DOI: 10.1016/j.physleta.2007.07.088.

[130] Z. O. Guimarães-Filho et al. “Recurrence quantification analysis of turbulent fluctuations in the plasma edge of Tokamak Chauffage Alfvén Brésilien tokamak”. In: *Physics of Plasmas Beta* 17 (2010), page 012303. DOI: 10.1063/1.3280010.

[131] T. J. Haire et al. “A comparison of porosity, fabric and fractal dimension as predictors of the Young’s modulus of equine cancellous bone”. In: *Medical Engineering & Physics* 20.8 (1998), pages 588–593.

[132] J. Hansen et al. “Climate simulations for 1880–2003 with GISS modelE”. In: *Climate Dynamics* 29.7-8 (2007), pages 661–696. DOI: 10.1007/s00382-007-0255-8.

[133] J. Hansen et al. “Global Surface Temperature Change”. In: *Reviews of Geophysics* 48.4 (2010), RG4004. DOI: 10.1029/2010RG000345.

[134] W. Härdle. *Applied Nonparametric Regression*. Volume 90. Cambridge University Press, 1990, page 352. ISBN: 9780521429504.

[135] G. H. Haug and R. Tiedemann. “Effect of the formation of the Isthmus of Panama on Atlantic Ocean thermohaline circulation”. In: *Nature* 393 (1998), pages 673–676. DOI: 10.1038/31447.

[136] G. C. Hegerl et al. “Understanding and Attributing Climate Change”. In: *Climate Change 2007 – The Physical Science Basis: Working Group I Contribution to the Fourth Assessment Report of the IPCC*. Edited by S. Solomon et al. Cambridge University Press, 2007. Chapter 9, pages 663–746.

[137] R. Hegger, H. Kantz, and L. Matassini. “Denoising Human Speech Signals Using Chaoslike Features”. In: *Physical Review Letters* 84.14 (2000), pages 3197–3200. DOI: 10.1103/PhysRevLett.84.3197.

[138] T. D. Herbert. “Review of alkenone calibrations (culture, water column, and sediments)”. en. In: *Geochemistry Geophysics Geosystems* 2.2 (Feb. 2001), page 1005. DOI: 10.1029/2000GC000055.

[139] T. D. Herbert et al. “Tropical ocean temperatures over the past 3.5 million years”. In: *Science* 328.5985 (2010), pages 1530–1534. DOI: 10.1126/science.1185435.

[140] U. Herzschuh. “Palaeo-moisture evolution in monsoonal Central Asia during the last 50,000 years”. In: *Quaternary Science Reviews* 25.1-2 (2006), pages 163–178. DOI: 10.1016/j.quascirev.2005.02.006.

[141] F. Hilgen. “Astronomical calibration of Gauss to Matuyama sapropels in the Mediterranean and implication for the Geomagnetic Polarity Time Scale”. In: *Earth and Planetary Science Letters* 104.2-4 (1991), pages 226–244. DOI: 10.1016/0012-821X(91)90206-W.

[142] J. Hill et al. “Mediterranean desertification and land degradation. Mapping related land use change syndromes based on satellite observations”. In: *Global and Planetary Change* 64 (2008), pages 146–157. DOI: 10.1016/j.gloplacha.2008.10.005.

[143] M. Hirata, B. Saussol, and S. Vaienti. “Statistics of Return Times: A General Framework and New Applications”. In: *Communications in Mathematical Physics* 206.1 (1999), pages 33–55. DOI: 10.1007/s002200050697.

[144] Y. Hirata and K. Aihara. “Identifying hidden common causes from bivariate time series: A method using recurrence plots”. In: *Physical Review E* 81.1 (2010), page 016203. DOI: 10.1103/PhysRevE.81.016203.

[145] Y. Hirata and K. Aihara. “Statistical tests for serial dependence and laminarity on recurrence plots”. In: *International Journal of Bifurcation and Chaos* 21.4 (2011), pages 1077–1084. DOI: 10.1142/S0218127411028908.

[146] Y. Hirata, S. Horai, and K. Aihara. “Reproduction of distance matrices from recurrence plots and its applications”. In: *European Physical Journal – Special Topics* 164.1 (2008), pages 13–22. DOI: 10.1140/epjst/e2008-00830-8.

[147] J. Hlinka et al. “Reliability of Inference of Directed Climate Networks Using Conditional Mutual Information”. In: *Entropy* 15.6 (2013), pages 2023–2045. DOI: 10.3390/e15062023.

[148] L. Holm and C. Sander. “Protein Structure Comparison by Alignment of Distance Matrices”. In: *Journal of Molecular Biology* 233.1 (1993), pages 123–138. DOI: 10.1006/jmbi.1993.1489.

[149] S. Holm. “A simple sequentially rejective multiple test procedure”. In: *Scandinavian Journal of Statistics* 6.2 (1979), pages 65–70.

[150] U. Homm and J. Breitung. “Testing for Speculative Bubbles in Stock Markets: A Comparison of Alternative Methods”. In: *Journal of Financial Econometrics* 10.1 (2012), pages 198–231. DOI: 10.1093/jjfinec/nbr009.

[151] S. Horai, T. Yamada, and K. Aihara. “Determinism Analysis with Iso-Directional Recurrence Plots”. In: *IEEE Transactions - Institute of Electrical Engineers of Japan C* 122.1 (2002), pages 141–147.

[152] C. Hu et al. “Quantification of Holocene Asian monsoon rainfall from spatially separated cave records”. In: *Earth and Planetary Science Letters* 266 (2008), pages 221–232. DOI: 10.1016/j.epsl.2007.10.015.

[153] G. J. Huffman et al. “The TRMM Multisatellite Precipitation Analysis (TMPA): Quasi-Global, Multiyear, Combined-Sensor Precipitation Estimates at Fine Scales”. In: *Journal of Hydrometeorology* 8.1 (2007), pages 38–55. DOI: 10.1175/JHM560.1.

[154] C. Huggel, J. J. Clague, and O. Korup. “Is climate change responsible for changing landslide activity in high mountains?” In: *Earth Surface Processes and Landforms* 37.1 (2012), pages 77–91. DOI: 10.1002/esp.2223.

[155] C.-W. Hung and M. Yanai. “Factors contributing to the onset of the Australian summer monsoon”. In: *Quarterly Journal of the Royal Meteorological Society* 130.597 (2004), pages 739–758. DOI: 10.1256/qj.02.191.

[156] J. W. Hurrell et al. “A New Sea Surface Temperature and Sea Ice Boundary Dataset for the Community Atmosphere Model”. In: *Journal of Climate* 21.19 (2008), pages 5145–5153. DOI: 10.1175/2008JCLI2292.1.

[157] M. Ihrke, H. Schrobsdorff, and J. M. Herrmann. “Recurrence-Based Synchronization of Single Trials for EEG-Data Analysis”. In: *Lecture Notes in Computer Science: Intelligent Data Engineering and Automated Learning – IDEAL 2009* 5788 (2009), pages 118–125. DOI: 10.1007/978-3-642-04394-9_15.

[158] J. S. Iwanski and E. Bradley. “Recurrence plots of experimental data: To embed or not to embed?” In: *Chaos* 8.4 (1998), pages 861–871. DOI: 10.1063/1.166372.

[159] N. Jiang, J. D. Neelin, and M. Ghil. “Quasi-quadrennial and quasi-biennial variability in the equatorial Pacific”. In: *Climate Dynamics* 12.2 (1995), pages 101–112. DOI: 10.1007/BF00223723.

[160] C. D. Jones and P. M. Cox. “Modeling the volcanic signal in the atmospheric CO 2 record”. In: *Global Biogeochemical Cycles* 15.2 (2001), pages 453–465. DOI: 10.1029/2000GB001281.

[161] M. Kac. “On the notion of recurrence in discrete stochastic processes”. In: *Bulletin of the American Mathematical Society* 53 (1947), pages 1002–1010.

[162] M. Kahru et al. “Trends in the surface chlorophyll of the California Current: Merging data from multiple ocean color satellites”. In: *Deep-Sea Research Part II: Topical Studies in Oceanography* 77-80 (2012), pages 89–98. DOI: 10.1016/j.dsr2.2012.04.007.

[163] M. Kahru et al. “Optimized Merger of Ocean Chlorophyll Algorithms of MODIS-Aqua and VIIRS”. In: *IEEE Geoscience and Remote Sensing Letters* 12.11 (2015), pages 2282–2285. DOI: 10.1109/LGRS.2015.2470250.

[164] M. Kanamitsu et al. “NCEP-DOE AMIP-II Reanalysis (R-2)”. In: *Bulletin of the American Meteorological Society* 83.11 (2002), pages 1631–1643. DOI: 10.1175/BAMS-83-11-1631(2002)083<1631:NAR>2.3.CO;2.

[165] H. Kantz and T. Schreiber. *Nonlinear Time Series Analysis*. Cambridge: University Press, 1997.

[166] D. T. Kaplan and L. Glass. “Direct test for determinism in a time series”. In: *Physical Review Letters* 68.4 (1992), pages 427–430.

[167] C. Karas et al. “Mid-Pliocene climate change amplified by a switch in Indonesian subsurface throughflow”. In: *Nature Geoscience* 2.6 (2009), pages 434–438. DOI: 10.1038/ngeo520.

[168] A. Karimi and M. R. Paul. “Extensive chaos in the Lorenz-96 model.” In: *Chaos* 20.4 (2010), page 043105. DOI: 10.1063/1.3496397.

[169] G. Kathayat et al. “Indian monsoon variability on millennial-orbital timescales”. In: *Scientific Reports* 6 (2016), page 24374. DOI: 10.1038/srep24374.

[170] M. B. Kennel, R. Brown, and H. D. I. Abarbanel. “Determining embedding dimension for phase-space reconstruction using a geometrical construction”. In: *Physical Review A* 45.6 (1992), pages 3403–3411. DOI: 10.1103/PhysRevA.45.3403.

[171] D. J. Kennett et al. “Development and Disintegration of Maya Political Systems in Response to Climate Change”. In: *Science* 338.6108 (2012), pages 788–791. DOI: 10.1126/science.1226299.

[172] M. Koebbe and G. Mayer-Kress. “Use of Recurrence Plots in the Analysis of Time-Series Data”. In: *Proceedings of SFI Studies in the Science of Complexity*. Edited by M. Casdagli and S. Eubank. Volume XXI. Redwood City: Addison-Wesley, 1992, pages 361–378.

[173] C. Komalapriya et al. “An automated algorithm for the generation of dynamically reconstructed trajectories”. In: *Chaos* 20.1 (2010), page 013107. DOI: 10.1063/1.3279680.

[174] I. Konvalinka et al. “Synchronized arousal between performers and related spectators in a fire-walking ritual”. In: *Proceedings of the National Academy of Sciences* 108.20 (2011), pages 8514–8519. DOI: 10.1073/pnas.1016955108.

[175] O. Kopáček et al. “Transition from regular to chaotic circulation in magnetized coronae near compact objects”. In: *The Astrophysical Journal* 722.2 (2010), page 1240. DOI: 10.1088/0004-637X/722/2/1240.

[176] P. Köthur et al. “Visual Analytics for Correlation-Based Comparison of Time Series Ensembles”. In: *Computer Graphics Forum* 34.3 (2015), pages 411–420. DOI: 10.1111/cgf.12653.

[177] K. H. Kraemer et al. “Recurrence threshold selection for obtaining robust recurrence characteristics in different embedding dimensions”. In: *Chaos* 28.8 (2018), page 085720. DOI: 10.1063/1.5024914.

[178] B. Krese, M. Perc, and E. Govekar. “Experimental observation of a chaos-to-chaos transition in laser droplet generation”. In: *International Journal of Bifurcation and Chaos* 21.6 (2011), pages 1689–1699. DOI: 10.1142/S0218127411029367.

[179] A. Krishnan et al. “Implications from a Network-Based Topological Analysis of Ubiquitin Unfolding Simulations”. In: *PLoS ONE* 3.4 (2008), e2149. DOI: 10.1371/journal.pone.0002149.

[180] A. Krishnan et al. “Proteins As Networks: Usefulness of Graph Theory in Protein Science”. In: *Current Protein and Peptide Science* 9.1 (2008), pages 28–38.

[181] G. Krishnan, R. K. Kaul, and P. Jagadeeswaran. “DNA sequence analysis: a procedure to find homologies among many sequences”. In: *Nucleic Acids Research* 14.1 (1986), pages 543–550.

[182] J. B. Kruskal. “Multidimensional scaling by optimizing goodness of fit to a nonmetric hypothesis”. In: *Psychometrika* 29.1 (1964), pages 1–27. DOI: 10.1007/BF02289565.

[183] J. B. Kruskal. “An overview of sequence comparison”. In: *Time Warps, String Edits, and Macromolecules: The Theory and Practice of Sequence Comparison*. Edited by D. Sankoff and J. B. Kruskal. Reading, Mass.: Addison-Wesley, 1983, pages 1–44. ISBN: 0-201-07809-0.

[184] J. Kurths and H. Herzel. “An attractor in a solar time series”. In: *Physica D* 25 (1987), pages 165–172. DOI: 10.1016/0167-2789(87)90099-6.

[185] J. Kurths et al. “Testing nonlinearity in radiocarbon data”. In: *Nonlinear Processes in Geophysics* 1.1 (1994), pages 72–75.

[186] C. Kyrtsou and C. E. Vorlow. “Complex Dynamics in Macroeconomics: A Novel Approach”. In: *New Trends in Macroeconomics*. Edited by C. Diebolt and C. Kyrtsou. 2005, pages 223–238. DOI: 10.1007/3-540-28556-3_11.

[187] L. Lacasa et al. “From time series to complex networks: The visibility graph”. In: *Proceedings of the National Academy of Sciences* 105.13 (2008), page 4972. DOI: 10.1073/pnas.0709247105.

[188] P. Lang et al. “Recurrence Network Analysis of the Synchronous EEG Time Series in Normal and Epileptic Brains”. In: *Cell Biochemistry and Biophysics* 66.2 (2013), pages 331–336. DOI: 10.1007/s12013-012-9452-0.

[189] T. Lasanta and S. M. Vicente-Serrano. “Complex land cover change processes in semiarid Mediterranean regions: An approach using Landsat images in northeast Spain”. In: *Remote Sensing of Environment* 124 (2012), pages 1–14. DOI: 10.1016/j.rse.2012.04.023.

[190] D. P. Lathrop and E. J. Kostelich. “Characterization of an experimental strange attractor by periodic orbits”. In: *Physical Review A* 40.7 (1989), pages 4028–4031. DOI: 10.1103/PhysRevA.40.4028.

[191] K. M. Lau and H. Weng. “Coherent modes of global SST and summer rainfall over China: An assessment of the regional impacts of the 1997-98 El Nino”. In: *Journal of Climate* 14.6 (2001), pages 1294–1308. DOI: 10.1175/1520-0442(2001)014<1294:CMOGSA>2.0.CO;2.

[192] J. L. Lean and D. H. Rind. “How natural and anthropogenic influences alter global and regional surface temperatures: 1889 to 2006”. In: *Geophysical Research Letters* 35.18 (2008), pages 1–6. DOI: 10.1029/2008GL034864.

[193] J. L. Lean and D. H. Rind. “How will Earth’s surface temperature change in future decades?” In: *Geophysical Research Letters* 36.15 (2009), page L15708. DOI: 10.1029/2009GL038932.

[194] F. A. Lechleitner et al. “Tropical rainfall over the last two millennia: evidence for a low-latitude hydrologic seesaw”. In: *Scientific Reports* 7 (2017), page 45809. DOI: 10.1038/srep45809.

[195] J. N. Lee, D. T. Shindell, and S. Hameed. “The Influence of Solar Forcing on Tropical Circulation”. In: *Journal of Climate* 22.22 (2009), pages 5870–5885. DOI: 10.1175/2009JCLI2670.1.

[196] A. W. Leising et al. “State of the California current 2014-15: Impacts of the warm-water “blob””. In: *California Cooperative Oceanic Fisheries Investigations Report* 56 (2015), pages 31–68.

[197] T. M. Lenton et al. “Tipping elements in the Earth’s climate system.” In: *Proceedings of the National Academy of Sciences of the United States of America* 105.6 (2008), pages 1786–93. DOI: 10.1073/pnas.0705414105.

[198] L. Li et al. “A 4-Ma record of thermal evolution in the tropical western Pacific and its implications on climate change”. In: *Earth and Planetary Science Letters* 309.1-2 (2011), pages 10–20. DOI: 10.1016/j.epsl.2011.04.016.

[199] S. Li et al. “Identifying spatial patterns of synchronization between NDVI and climatic determinants using joint recurrence plots”. In: *Environmental Earth Sciences* 64.3 (2011), pages 851–859. DOI: 10.1007/s12665-011-0909-z.

[200] J. C. Liddicoat, N. D. Opdyke, and G. I. Smith. “Palaeomagnetic polarity in a 930-m core from Searles Valley, California”. In: *Nature* 286.5768 (1980), pages 22–25. DOI: 10.1038/286022a0.

[201] G. Litak et al. “Transient chaotic behaviour versus periodic motion of a parametric pendulum by recurrence plots”. In: *ZAMM – Journal of Applied Mathematics and Mechanics/ Zeitschrift für Angewandte Mathematik und Mechanik* 90.1 (2010), pages 33–41. DOI: 10.1002/zamm.200900290.

[202] M. A. Little et al. “Exploiting Nonlinear Recurrence and Fractal Scaling Properties for Voice Disorder Detection”. In: *BioMedical Engineering OnLine* 6.23 (2007), pages 1–19. DOI: 10.1186/1475-925X-6-23.

[203] H. van Loon, G. A. Meehl, and J. M. Arblaster. “A decadal solar effect in the tropics in July-August”. In: *Journal of Atmospheric and Solar-Terrestrial Physics* (2004). DOI: 10.1016/j.jastp.2004.06.003.

[204] E. N. Lorenz. “Deterministic Nonperiodic Flow”. In: *Journal of the Atmospheric Sciences* 20 (1963), pages 120–141.

[205] E. N. Lorenz. “Predictability: A problem partly solved”. In: edited by T. Palmer. Volume 1. ECMWF, Reading, UK, 1996, pages 1–18.

[206] E. N. Lorenz and K. A. Emanuel. “Optimal Sites for Supplementary Weather Observations: Simulation with a Small Model”. In: *Journal of the Atmospheric Sciences* 55.3 (1998), pages 399–414. DOI: 10.1175/1520-0469(1998)055$<$0399:OSFSWO$>$2.0.CO;2.

[207] P. C. Mahalanobis. “On the generalized distance in statistics”. In: *Proceedings of the National Institute of Science of India* 2.1 (1936), pages 49–55.

[208] J. V. Maizel and R. P. Lenk. “Enhanced Graphic Matrix Analysis of Nucleic Acid and Protein Sequences”. In: *Proceedings of the National Academy of Sciences* 78.12 (1981), pages 7665–7669.

[209] S. Majumdar et al. “Fractal analysis of radiographs: assessment of trabecular bone structure and prediction of elastic modulus and strength”. In: *Med Phys* 26.7 (1999), pages 1330–1340.

[210] N. Malik, N. Marwan, and J. Kurths. “Spatial structures and directionalities in Monsoonal precipitation over South Asia”. In: *Nonlinear Processes in Geophysics* 17.5 (2010), pages 371–381. DOI: 10.5194/npg-17-371-2010.

[211] N. Malik et al. “Analysis of spatial and temporal extreme monsoonal rainfall over South Asia using complex networks”. In: *Climate Dynamics* 39.3–4 (2012), pages 971–987. DOI: 10.1007/s00382-011-1156-4.

[212] N. Malik et al. “Dynamical regimes and transitions in Plio-Pleistocene Asian monsoon”. In: *Europhysics Letters* 97.4 (2012), page 40009. DOI: 10.1209/0295-5075/97/40009.

[213] B. B. Mandelbrot. *The fractal geometry of nature*. San Francisco: Freeman, 1982.

[214] M. E. Mann et al. “Volcanic and solar forcing of the tropical Pacific over the past 1000 years”. In: *Journal of Climate* 18.3 (2005), pages 447–456. DOI: 10.1175/JCLI-3276.1.

[215] D. Maraun and J. Kurths. “Epochs of phase coherence between El Niño/Southern Oscillation and Indian monsoon”. In: *Geophysical Research Letters* 32.15 (2005), page L15709. DOI: 10.1029/2005GL023225.

[216] T. K. March, S. C. Chapman, and R. O. Dendy. “Recurrence plot statistics and the effect of embedding”. In: *Physica D* 200.1–2 (2005), pages 171–184. DOI: 10.1016/j.physd.2004.11.002.

[217] S. L. Marcus. “Detection and Modeling of Nontidal Oceanic Effects on Earth’s Rotation Rate”. In: *Science* 281.5383 (1998), pages 1656–1659. DOI: 10.1126/science.281.5383.1656.

[218] J. A. Marengo et al. “Climatology of the low-level jet east of the Andes as derived from the NCEP-NCAR reanalyses: Characteristics and temporal variability”. In: *Journal of Climate* 17 (2004), pages 2261–2280. DOI: 10.1175/1520-0442(2004)017<2261:COTLJE>2.0.CO;2.

[219] A. A. Marino, E. Nilsen, and C. Frilot. “Consistent magnetic-field induced dynamical changes in rabbit brain activity detected by recurrence quantification analysis”. In: *Brain Research* 964.2 (2003), pages 317–326. DOI: 10.1016/S0006-8993(02)04093-3.

[220] B. R. Markle et al. “Global atmospheric teleconnections during Dansgaard–Oeschger events”. In: *Nature Geoscience* 10.1 (2017), pages 36–40. DOI: 10.1038/ngeo2848.

[221] O. Y. Martins, M. A. Sadeeq, and I. E. Ahaneku. “Nonlinear Deterministic Chaos in Benue River Flow Daily Time Sequence”. In: *Journal of Water Resource and Protection* 3 (2011), pages 747–757. DOI: 10.4236/jwarp.2011.310085.

[222] N. Marwan. “Untersuchung der Klimavariabilität in NW Argentinien mit Hilfe der quantitativen Analyse von Recurrence Plots”. Master’s thesis. Dresden University of Technology, 1999.

[223] N. Marwan. “Encounters With Neighbours – Current Developments Of Concepts Based On Recurrence Plots And Their Applications”. PhD thesis. University of Potsdam, 2003. ISBN: 3-00-012347-4.

[224] N. Marwan. “A Historical Review of Recurrence Plots”. In: *European Physical Journal – Special Topics* 164.1 (2008), pages 3–12. DOI: 10.1140/epjst/e2008-00829-1.

[225] N. Marwan. “How to avoid potential pitfalls in recurrence plot based data analysis”. In: *International Journal of Bifurcation and Chaos* 21.4 (2011), pages 1003–1017. DOI: 10.1142/S0218127411029008.

[226] N. Marwan, S. Foerster, and J. Kurths. “Analysing spatially extended high-dimensional dynamics by recurrence plots”. In: *Physics Letters A* 379 (2015), pages 894–900. DOI: 10.1016/j.physleta.2015.01.013.

[227] N. Marwan, A. Groth, and J. Kurths. “Quantification of Order Patterns Recurrence Plots of Event Related Potentials”. In: *Chaos and Complexity Letters* 2.2/3 (2007), pages 301–314.

[228] N. Marwan and J. Kurths. “Nonlinear analysis of bivariate data with cross recurrence plots”. In: *Physics Letters A* 302.5–6 (2002), pages 299–307. DOI: 10.1016/S0375-9601(02)01170-2.

[229] N. Marwan and J. Kurths. “Cross Recurrence Plots and Their Applications”. In: *Mathematical Physics Research at the Cutting Edge*. Edited by C. V. Benton. Hauppauge: Nova Science Publishers, 2004, pages 101–139. ISBN: 1-59033-939-8.

[230] N. Marwan and J. Kurths. “Line structures in recurrence plots”. In: *Physics Letters A* 336.4–5 (2005), pages 349–357. DOI: 10.1016/j.physleta.2004.12.056.

[231] N. Marwan and J. Kurths. “Comment on “Stochastic analysis of recurrence plots with applications to the detection of deterministic signals” by Rohde et al. [Physica D 237 (2008) 619–629]”. In: *Physica D* 238.16 (2009), pages 1711–1715. DOI: 10.1016/j.physd.2009.04.018.

[232] N. Marwan, J. Kurths, and P. Saparin. “Generalised Recurrence Plot Analysis for Spatial Data”. In: *Physics Letters A* 360.4–5 (2007), pages 545–551. DOI: 10.1016/j.physleta.2006.08.058.

[233] N. Marwan and A. Meinke. “Extended recurrence plot analysis and its application to ERP data”. In: *International Journal of Bifurcation and Chaos* 14.2 (2004), pages 761–771. DOI: 10.1142/S0218127404009454.

[234] N. Marwan, S. Schinkel, and J. Kurths. “Significance for a recurrence based transition analysis”. In: Budapest, Hungary, 2008, pages 412–415.

[235] N. Marwan, S. Schinkel, and J. Kurths. “Recurrence plots 25 years later – Gaining confidence in dynamical transitions”. In: *Europhysics Letters* 101 (2013), page 20007. DOI: 10.1209/0295-5075/101/20007.

[236] N. Marwan, M. Thiel, and N. R. Nowaczyk. “Cross Recurrence Plot Based Synchronization of Time Series”. In: *Nonlinear Processes in Geophysics* 9.3/4 (2002), pages 325–331. DOI: 10.5194/npg-9-325-2002.

[237] N. Marwan et al. “Recurrence Plot Based Measures of Complexity and its Application to Heart Rate Variability Data”. In: *Physical Review E* 66.2 (2002), page 026702. DOI: 10.1103/PhysRevE.66.026702.

[238] N. Marwan et al. “Comparing modern and Pleistocene ENSO-like influences in NW Argentina using nonlinear time series analysis methods”. In: *Climate Dynamics* 21.3–4 (2003), pages 317–326. DOI: 10.1007/s00382-003-0335-3.

[239] N. Marwan et al. “Recurrence Plots for the Analysis of Complex Systems”. In: *Physics Reports* 438.5–6 (2007), pages 237–329. DOI: 10.1016/j.physrep.2006.11.001.

[240] N. Marwan et al. “20 Years of Recurrence Plots: Perspectives for a Multi-purpose Tool of Nonlinear Data Analysis”. In: *European Physical Journal – Special Topics* 164.1 (2008), pages 1–2. DOI: 10.1140/epjst/e2008-00828-2.

[241] N. Marwan et al. “Complex network approach for recurrence analysis of time series”. In: *Physics Letters A* 373.46 (2009), pages 4246–4254. DOI: 10.1016/j.physleta.2009.09.042.

[242] N. Marwan et al. “Estimating coupling directions in the cardio-respiratory system using recurrence properties”. In: *Philosophical Transactions of the Royal Society A* 371.1997 (2013), page 20110624. DOI: 10.1098/rsta.2011.0624.

[243] N. Marwan et al. *Translational Recurrences – From Mathematical Theory to Real-World Applications*. Volume 103. Cham: Springer, 2014, page 230. ISBN: 978-3-319-09530-1. DOI: 10.1007/978-3-319-09531-8.

[244] N. Marwan et al. “Regime Change Detection in Irregularly Sampled Time Series”. In: *Advances in Nonlinear Geosciences*. Edited by A. A. Tsonis. Cham, Switzerland: Springer International, 2018, pages 357–368. ISBN: 978-3-319-58895-7. DOI: 10.1007/978-3-319-58895-7_18.

[245] L. Matassini et al. “Optimizing of recurrence plots for noise reduction”. In: *Physical Review E* 65.2 (2002), page 021102. DOI: 10.1103/PhysRevE.65.021102.

[246] T. Matcharashvili, T. Chelidze, and J. Peinke. “Increase of order in seismic processes around large reservoir induced by water level periodic variation”. In: *Nonlinear Dynamics* 51.3 (2008), pages 399–407. DOI: 10.1007/s11071-007-9219-0.

[247] J. L. McBride. “Indonesia, Papua New Guinea, and Tropical Australia: the Southern Hemisphere Monsoon”. In: *Meteorology of the southern hemisphere*. Edited by D. Karoly and D. Vincent. Springer, 1998, pages 89–99.

[248] E. L. McClymont and A. Rosell-Melé. “Links between the onset of modern Walker circulation and the mid-Pleistocene climate transition”. In: *Geology* 33.5 (2005), pages 389–392. DOI: 10.1130/G21292.1.

[249] H. McGowan et al. “Evidence of ENSO mega-drought triggered collapse of prehistory Aboriginal society in northwest Australia”. In: *Geophysical Research Letters* 39.22 (2012), page L22702. DOI: 10.1029/2012GL053916.

[250] G. McGuire, N. B. Azar, and M. Shelhamer. “Recurrence matrices and the preservation of dynamical properties”. In: *Physics Letters A* 237.1–2 (1997), pages 43–47. DOI: 10.1016/S0375-9601(97)00697-X.

[251] A. N. Meckler et al. “Interglacial Hydroclimate in the Tropical West Pacific Through the Late Pleistocene”. In: *Science* 336.6086 (2012), pages 1301–1304. DOI: 10.1126/science.1218340.

[252] M. Medina-Elizalde and D. W. Lea. “The mid-Pleistocene transition in the tropical Pacific.” In: *Science* 310.5750 (2005), pages 1009–12. DOI: 10.1126/science.1115933.

[253] G. A. Meehl et al. “Amplifying the Pacific Climate System Response to a Small 11-Year Solar Cycle Forcing”. In: *Science* 325.5944 (2009), pages 1114–1118. DOI: 10.1126/science.1172872.

[254] B. of Meteorology. *Climate Data Online*. 2013. URL: http://www.bom.gov.au/climate/data/.

[255] S. D. Meyers, J. J. O’Brien, and E. Thelin. “Reconstruction of Monthly SST in the Tropical Pacific Ocean during 1868?-1993 Using Adaptive Climate Basis Functions”. In: *Monthly Weather Review* 127.7 (1999), pages 1599–1612. DOI: 10.1175/1520-0493(1999)127<1599:ROMSIT>2.0.CO;2.

[256] M. van der Mheen et al. “Interaction network based early warning indicators for the Atlantic MOC collapse”. In: *Geophysical Research Letters* 40.11 (2013), pages 2714–2719. DOI: 10.1002/grl.50515.

[257] O. S. Miettinen and J.-D. Wang. “An alternative to the proportionate mortality ratio”. In: *American Journal of Epidemiology* 114.1 (1981), pages 144–148. DOI: 10.1093/oxfordjournals.aje.a113161.

[258] G. M. Mindlin and R. Gilmore. “Topological analysis and synthesis of chaotic time series”. In: *Physica D* 58.1–4 (1992), pages 229–242. DOI: 10.1016/0167-2789(92)90111-Y.

[259] C. Mocenni, A. Facchini, and A. Vicino. “Identifying the dynamics of complex spatio-temporal systems by spatial recurrence properties”. In: *Proceedings of the National Academy of Sciences* 107.18 (2010), pages 8097–8102. DOI: 10.1073/pnas.0910414107.

[260] A. H. Monahan et al. “Empirical Orthogonal Functions: The Medium is the Message”. In: *Journal of Climate* 22.24 (2009), pages 6501–6514. DOI: 10.1175/2009JCLI3062.1.

[261] R. A. Monserud and R. Leemans. “Comparing global vegetation maps with the Kappa statistic”. In: *Ecological modelling* 62.4 (1992), pages 275–293.

[262] L. S. Montalbán, P. Henttu, and R. Piché. “Recurrence quantification analysis of electrochemical noise data during pit development”. In: *International Journal of Bifurcation and Chaos* 17.10 (2007), pages 3725–3728. DOI: 10.1142/S0218127407019640.

[263] V. Moron, R. Vautard, and M. Ghil. “Trends, interdecadal and interannual oscillations in global sea-surface temperatures”. In: *Climate Dynamics* 14.7-8 (1998), pages 545–569. DOI: 10.1007/s003820050241.

[264] C. M. Moy et al. “Variability of El Niño/Southern Oscillation activity at millennial timescales during the Holocene epoch.” In: *Nature* 420.6912 (2002), pages 162–5. DOI: 10.1038/nature01194.

[265] M. Mudelsee and M. E. Raymo. “Slow dynamics of the Northern Hemisphere glaciation”. In: *Paleoceanography* 20 (2005), PA4022. DOI: 10.1029/2005PA001153.

[266] M. Mudelsee and M. Schulz. “The Mid-Pleistocene climate transition: onset of 100 ka cycle lags ice volume build-up by 280 ka”. In: *Earth and Planetary Science Letters* 151.1 (1997), pages 117–123.

[267] R. A. Muller and G. J. MacDonald. *Ice Ages and Astronomical Causes*. London, Berlin, Heidelberg: Springer, 2000, page 318. ISBN: 978-3-540-43779-6.

[268] C. G. Myers et al. “Northeast Indian stalagmite records Pacific decadal climate change: Implications for moisture transport and drought in India”. In: *Geophysical Research Letters* 42.10 (2015), pages 4124–4132. DOI: 10.1002/2015GL063826.

[269] Y. Neuman, N. Marwan, and Y. Cohen. “Change in the Embedding Dimension as an Indicator of an Approaching Transition”. In: *PLoS ONE* 9.6 (2014), e101014. DOI: 10.1371/journal.pone.0101014.

[270] Y. Neuman, N. Marwan, and D. Livshitz. “The Complexity of Advice-Giving”. In: *Complexity* 15.2 (2009), pages 28–30. DOI: 10.1002/cplx.20270.

[271] M. E. J. Newman. “The Structure and Function of Complex Networks”. In: *SIAM Review* 45.2 (2003), pages 167–256.

[272] M. E. J. Newman. “Detecting community structure in networks”. In: *The European Physical Journal B* 38.2 (2004), pages 321–330. DOI: 10.1140/epjb/e2004-00124-y.

[273] M. Newman. “Assortative mixing in networks”. In: *Physical Review Letters* 89.20 (2002), page 208701. DOI: 10.1103/PhysRevLett.89.208701.

[274] E. J. Ngamga et al. “Recurrence analysis of strange nonchaotic dynamics”. In: *Physical Review E* 75.3 (2007), page 036222. DOI: 10.1103/PhysRevE.75.036222.

[275] E. J. Ngamga et al. “Recurrence analysis of strange nonchaotic dynamics in driven excitable systems”. In: *Chaos* 18.1 (2008), page 013128. DOI: 10.1063/1.2897312.

[276] E. J. Ngamga et al. “Distinguishing dynamics using recurrence-time statistics”. In: *Physical Review E* 85.2 (2012), page 026217. DOI: 10.1103/PhysRevE.85.026217.

[277] E. J. Ngamga et al. “Evaluation of selected recurrence measures in discriminating pre-ictal and inter-ictal periods from epileptic EEG data”. In: *Physics Letters A* 380.16 (2016), pages 1419–1425. DOI: 10.1016/j.physleta.2016.02.024.

[278] J. M. Nichols, S. T. Trickey, and M. Seaver. “Damage detection using multivariate recurrence quantification analysis”. In: *Mechanical Systems and Signal Processing* 20.2 (2006), pages 421–437. DOI: 10.1016/j.ymssp.2004.08.007.

[279] M. Nilsson et al. “On histograms and spatiograms-introduction of the mapogram”. In: *Image Processing, 2008. ICIP 2008. 15th IEEE International Conference on*. IEEE. 2008, pages 973–976.

[280] J. Nogués-Paegle and K. C. Mo. “Alternating Wet and Dry Conditions over South America during Summer”. In: *Monthly Weather Review* 125.2 (1997), pages 279–291. DOI: 10.1175/1520-0493(1997)125<0279:AWADCO>2.0.CO;2.

[281] E. M. Oblow. “Supertracks, supertrack functions and chaos in the quadratic map”. In: *Physics Letters A* 128.8 (1988), page 406. DOI: 10.1016/0375-9601(88)90119-3.

[282] *Original experimental data retrived at http://complex.umd.edu/interestingdata/ on 7/7/2008*. URL: http://complex.umd.edu/interestingdata/.

[283] J. Overland et al. “North Pacific regime shifts: Definitions, issues and recent transitions”. In: *Progress in Oceanography* 77.2-3 (2008), pages 92–102.

[284] I. Ozken et al. “Transformation-cost time-series method for analyzing irregularly sampled data”. In: *Physical Review E* 91 (2015), page 062911. DOI: 10.1103/PhysRevE.91.062911.

[285] I. Ozken et al. “Recurrence plot analysis of irregularly sampled data”. In: *Physical Review E* 98 (2018), page 052215. DOI: 10.1103/PhysRevE.98.052215.

[286] N. H. Packard et al. “Geometry from a Time Series”. In: *Physical Review Letters* 45.9 (1980), pages 712–716. DOI: 10.1103/PhysRevLett.45.712.

[287] T. S. Parker and L. Chua. *Practical numerical algorithms for chaotic systems*. New York: Springer, 1989, page 348. ISBN: 978-1-4612-8121-4.

[288] D. Pazó et al. “Structure of characteristic Lyapunov vectors in spatiotemporal chaos”. In: *Physical Review E* 78.1 (2008), page 016209. DOI: 10.1103/PhysRevE.78.016209.

[289] B. Pecar. “The use of Visual Recurrence Analysis and Hurst exponents as qualitative tools for analysing financial time series”. In: 2003.

[290] F. Pedregosa et al. “Scikit-learn: Machine learning in Python”. In: *Journal of Machine Learning Research* 12 (2011), pages 2825–2830.

[291] W. T. Peterson et al. “The state of the California Current, 2005–2006: Warm in the north, cool in the south”. In: *California Cooperative Oceanic Fisheries Investigations Report* 47 (2006), pages 30–75.

[292] H. Poincaré. “Sur la probleme des trois corps et les équations de la dynamique”. In: *Acta Mathematica* 13 (1890), pages 1–271. DOI: 10.1007/BF02392506.

[293] A. Porporato and L. Ridolfi. “Nonlinear analysis of river flow time sequences”. In: *Water Resources Research* 33.6 (1997), pages 1353–1367. DOI: 10.1029/96WR03535.

[294] T. L. Prado et al. “Spatial recurrence analysis: A sensitive and fast detection tool in digital mammography”. In: *Chaos* 24 (2014), page 013106. DOI: 10.1063/1.4861895.

[295] S. Prasad, J. Negendank, and M. Stein. “Varve counting reveals high resolution radiocarbon reservoir age variations in palaeolake Lisan”. In: *Journal of Quaternary Science* 24.7 (2009), pages 690–696.

[296] S. Prasad et al. “Evidence from Lake Lisan of solar influence on decadal- to centennial-scale climate variability during marine oxygen isotope stage 2”. In: *Geology* 32.7 (2004), page 581. DOI: 10.1130/G20553.1.

[297] I. Procaccia, S. Thomae, and C. Tresser. “First-return maps as a unified renormalization scheme for dynamical systems”. In: *Physical Review A* 35.4 (1987), pages 1884–1900. DOI: 10.1103/PhysRevA.35.1884.

[298] R. Proulx, P. Côté, and L. Parrott. “Multivariate recurrence plots for visualizing and quantifying the dynamics of spatially extended ecosystems”. In: *Ecological Complexity* 6.1 (2009), pages 37–47. DOI: 10.1016/j.ecocom.2008.10.003.

[299] S. Prouteau et al. “Fractal analysis of bone texture: a screening tool for stress fracture risk?” In: *European Journal of Clinical Investigation* 34.2 (2004), pages 137–142.

[300] A. Provenzale et al. “Distinguishing between low-dimensional dynamics and randomness in measured time series”. In: *Physica D* 58.1–4 (1992), pages 31–49. DOI: 10.1016/0167-2789(92)90100-2.

[301] R. Quian Quiroga, T. Kreuz, and P. Grassberger. “Event synchronization: A simple and fast method to measure synchronicity and time delay patterns”. In: *Physical Review E* 66 (2002), page 041904. DOI: 10.1103/PhysRevE.66.041904.

[302] K. Ramasubramanian and M. Sriram. “A comparative study of computation of Lyapunov spectra with different algorithms”. In: *Physica D: Nonlinear Phenomena* 139.1-2 (2000), pages 72–86. DOI: 10.1016/S0167-2789(99)00234-1.

[303] G. M. Ramírez Ávila et al. “Classification of cardiovascular time series based on different coupling structures using recurrence networks analysis”. In: *Philosophical Transactions of the Royal Society A* 371.1997 (2013), page 20110623. DOI: 10.1098/rsta.2011.0623.

[304] G. M. Ramírez Ávila et al. “Classifying healthy women and preeclamptic patients from cardiovascular data using recurrence and complex network methods”. In: *Autonomic Neuroscience* 178.1–2 (2013), pages 103–110. DOI: 10.1016/j.autneu.2013.05.003.

[305] A. M. T. Ramos et al. “Recurrence measure of conditional dependence and applications”. In: *Physical Review E* 95 (2017), page 052206. DOI: 10.1103/PhysRevE.95.052206.

[306] M. R. Rampino, S. Self, and R. W. Fairbridge. “Can Rapid Climatic Change Cause Volcanic Eruptions?” In: *Science* 206.4420 (1979), pages 826–829. DOI: 10.1126/science.206.4420.826.

[307] P. E. Rapp et al. “Effective normalization of complexity measurements for epoch length and sampling frequency”. In: *Physical Review E* 64 (2001), page 16209. DOI: 10.1103/PhysRevE.64.016209.

[308] S. O. Rasmussen et al. “A new Greenland ice core chronology for the last glacial termination”. In: *Journal of Geophysical Research Atmospheres* (2006), page D06102. DOI: 10.1029/2005JD006079.

[309] A. Ravelo et al. “Regional climate shifts caused by gradual global cooling in the Pliocene epoch”. In: *Nature* 429.6989 (2004), pages 263–267. DOI: 10.1038/nature02567.

[310] J. Reeves et al. “A Review and Comparison of Changepoint Detection Techniques for Climate Data”. In: *Journal of Applied Meteorology and Climatology* 46.6 (2007), pages 900–915. DOI: 10.1175/JAM2493.1.

[311] K. Rehfeld et al. “Comparison of correlation analysis techniques for irregularly sampled time series”. In: *Nonlinear Processes in Geophysics* 18.3 (2011), pages 389–404. DOI: 10.5194/npg-18-389-2011.

[312] D. C. Richardson and R. Dale. “Looking To Understand: The Coupling Between Speakers’ and Listeners’ Eye Movements and Its Relationship to Discourse Comprehension”. In: *Cognitive Science* 29.6 (2005), pages 1045–1060. DOI: 10.1207/s15516709cog0000_29.

[313] H. Ridley et al. “High-resolution monitoring of Yok Balum Cave, Belize: An investigation of seasonal ventilation regimes and the atmospheric and drip-flow response to a local earthquake”. In: *Journal of Cave and Karst Studies* 77.3 (2015), pages 183–199. DOI: 10.4311/2014ES0117.

[314] M. Riedl, N. Marwan, and J. Kurths. “Multiscale recurrence analysis of spatio-temporal data”. In: *Chaos* 25 (2015), page 123111. DOI: 10.1063/1.4937164.

[315] M. Riedl, N. Marwan, and J. Kurths. “Extended generalized recurrence plot quantification of complex circular patterns”. In: *European Physical Journal B* 90.58 (2017), pages 1–9. DOI: 10.1140/epjb/e2017-70560-7.

[316] M. A. Riley, R. Balasubramaniam, and M. T. Turvey. “Recurrence quantification analysis of postural fluctuations”. In: *Gait & Posture* 9.1 (1999), pages 65–78. DOI: 10.1016/S0966-6362(98)00044-7.

[317] G. Robinson and M. Thiel. “Recurrences determine the dynamics”. In: *Chaos* 19 (2009), page 023104. DOI: 10.1063/1.3117151.

[318] A. Robock. “Volcanic eruptions and climate”. In: *Reviews of Geophysics* 38.2 (2000), pages 191–219. DOI: 10.1029/1998RG000054.

[319] J. Rockstrom et al. “A safe operating space for humanity”. In: *Nature* 461.7263 (2009), pages 472–475. DOI: 10.1038/461472a.

[320] G. K. Rohde et al. “Stochastic analysis of recurrence plots with applications to the detection of deterministic signals”. In: *Physica D* 237.5 (2008), pages 619–629. DOI: 10.1016/j.physd.2007.10.008.

[321] M. C. Romano, M. Thiel, and J. Kurths. “Generalized Synchronization Indices based on Recurrence in Phase Space”. In: volume 742. 1. 2004, pages 330–336. DOI: 10.1063/1.1846494.

[322] M. C. Romano et al. “Multivariate Recurrence Plots”. In: *Physics Letters A* 330.3–4 (2004), pages 214–223. DOI: 10.1016/j.physleta.2004.07.066.

[323] M. C. Romano et al. “Detection of synchronization for non-phase-coherent and non-stationary data”. In: *Europhysics Letters* 71.3 (2005), pages 466–472. DOI: 10.1209/epl/i2005-10095-1.

[324] M. C. Romano et al. “Estimation of the direction of the coupling by conditional probabilities of recurrence”. In: *Physical Review E* 76 (2007), page 036211. DOI: 10.1103/PhysRevE.76.036211.

[325] M. C. Romano et al. “Hypothesis test for synchronization: Twin surrogates revisited”. In: *Chaos* 19.1 (2009), page 015108. DOI: 10.1063/1.3072784.

[326] M. Rossignol-Strick. “African monsoons, an immediate climate response to orbital insolation”. In: *Nature* 304.5921 (1983), pages 46–49. DOI: 10.1038/304046a0.

[327] O. E. Rössler. “An equation for continuous chaos”. In: *Physics Letters A* 57.5 (1976), pages 397–398. DOI: 10.1016/0375-9601(76)90101-8.

[328] J. Runge et al. “Escaping the Curse of Dimensionality in Estimating Multivariate Transfer Entropy”. In: *Physical Review Letters* 108.25 (2012), page 258701. DOI: 10.1103/PhysRevLett.108.258701.

[329] J. Runge et al. “Quantifying causal coupling strength: A lag-specific measure for multivariate time series related to transfer entropy”. In: *Physical Review E* 86 (6 2012), page 061121. DOI: 10.1103/PhysRevE.86.061121.

[330] J. M. Russell et al. “Glacial forcing of central Indonesian hydroclimate since 60,000 y B.P.” In: *Proceedings of the National Academy of Sciences* 111.14 (2014), pages 5100–5105. DOI: 10.1073/pnas.1402373111.

[331] M. Rustici et al. “Transition Scenarios during the Evolution of the Belousov-Zhabotinsky Reaction in an Unstirred Batch Reactor”. In: *Journal of Physical Chemistry A* 103.33 (1999), pages 6564–6570. DOI: 10.1021/jp9902708.

[332] H. Sakoe and S. Chiba. “Dynamic Programming Algorithm Optimization for Spoken Word Recognition”. In: *IEEE Transactions on Acoustics, Speech and Signal Processing* ASSP-26.1 (1978), pages 43–49.

[333] P. I. Saparin et al. “Quantification of cancellous bone structure using symbolic dynamics and measures of complexity”. In: *Physical Review E* 58.5 (1998), page 6449. DOI: 10.1103/PhysRevE.58.6449.

[334] P. I. Saparin et al. “Measures of complexity to quantify bone loss and estimate strength of human lumbar vertebrae: comparison of pqct image analysis with bone histomorphometry and biomechanical tests”. In: *Journal of Gravitational Physiology* 12.1 (2005), pages 121–122.

[335] P. Saparin, W. Gowin, and D. Felsenberg. “Comparison of bone loss with the changes of bone architecture at six different skeletal sites using measures of complexity”. In: *Journal of Gravitational Physiology* 9.1 (2002), pages 177–178.

[336] M. Sato et al. “Stratospheric aerosol optical depths, 1850–1990”. In: *Journal of Geophysical Research* 98.D12 (1993), page 22987. DOI: 10.1029/93JD02553.

[337] M. Sauramo. “Geochronologische Studien über die spätglaziale Zeit in Südfinnland”. In: *Bulletin de la Commission Géologique de Finlande* 50 (1918), pages 3–48.

[338] S. Schinkel, O. Dimigen, and N. Marwan. “Selection of recurrence threshold for signal detection”. In: *European Physical Journal – Special Topics* 164.1 (2008), pages 45–53. DOI: 10.1140/epjst/e2008-00833-5.

[339] S. Schinkel, N. Marwan, and J. Kurths. “Order patterns recurrence plots in the anaylsis of ERP data”. In: *Cognitive Neurodynamics* 1.4 (2007), pages 317–325. DOI: 10.1007/s11571-007-9023-z.

[340] S. Schinkel, N. Marwan, and J. Kurths. “Brain signal analysis based on recurrences”. In: *Journal of Physiology-Paris* 103.6 (2009), pages 315–323. DOI: 10.1016/j.jphysparis.2009.05.007.

[341] S. Schinkel et al. “Confidence bounds of recurrence-based complexity measures”. In: *Physics Letters A* 373.26 (2009), pages 2245–2250. DOI: 10.1016/j.physleta.2009.04.045.

[342] T. Schneider, T. Bischoff, and G. H. Haug. “Migrations and dynamics of the intertropical convergence zone”. In: *Nature* 513.7516 (2014), pages 45–53. DOI: 10.1038/nature13636.

[343] T. Schreiber and A. Schmitz. “Surrogate time series”. In: *Physica D* 142.3–4 (2000), pages 346–382. DOI: 10.1016/S0167-2789(00)00043-9.

[344] A. Schuster. “On the investigation of hidden periodicities with application to a supposed 26 day period of meteorological phenomena”. In: *Journal of Geophysical Research* 3.1 (1898), page 13. DOI: 10.1029/TM003i001p00013.

[345] A. K. Sen et al. “Analysis of cycle-to-cycle pressure oscillations in a diesel engine”. In: *Mechanical Systems and Signal Processing* 22.2 (2008), pages 362–373. DOI: 10.1016/j.ymssp.2007.07.015.

[346] D. V. Senthilkumar, M. Lakshmanan, and J. Kurths. “Phase synchronization in time-delay systems”. In: *Physical Review E* 74 (2006), page 035205. DOI: 10.1103/PhysRevE.74.035205.

[347] D. V. Senthilkumar, M. Lakshmanan, and J. Kurths. “Transition from phase to generalized synchronization in time-delay systems”. In: *Chaos* 18.2 (2008), page 023118. DOI: 10.1063/1.2911541.

[348] J. Serrà, X. Serra, and R. G. Andrzejak. “Cross recurrence quantification for cover song identification”. In: *New Journal of Physics* 11 (2009), page 093017. DOI: 10.1088/1367-2630/11/9/093017.

[349] D. T. Shindell et al. “Solar and anthropogenic forcing of tropical hydrology”. In: *Geophysical Research Letters* 33.24 (2006), page L24706. DOI: 10.1029/2006GL027468.

[350] Z. Šidák. “Rectangular Confidence Regions for the Means of Multivariate Normal Distributions”. In: *Journal of the American Statistical Association* 62.318 (1967), pages 626–633. DOI: 10.1080/01621459.1967.10482935.

[351] B. Silverman. *Density Estimation for Statistics and Data Analysis*. London: Chapman & Hall/CRC, 1986, pages 42–43. ISBN: 9781315140919.

[352] W. Singer. “Neuronal synchrony: a versatile code for the definition of relations?” In: *Neuron* 24.1 (1999), pages 49–65, 111–125.

[353] A. Sinha et al. “Trends and oscillations in the Indian summer monsoon rainfall over the last two millennia”. In: *Nature Communications* 6 (2015), page 6309. DOI: 10.1038/ncomms7309.

[354] B. Sivakumar. “Chaos theory in hydrology: important issues and interpretations”. In: *Journal of Hydrology* 227.1 (2000), pages 1–20. DOI: 10.1016/S0022-1694(99)00186-9.

[355] M. Small and C. K. Tse. “Detecting Determinism in Time Series: The Method of Surrogate Data”. In: *IEEE Transactions on Circuits and Systems: Fundamental Theory and Applications* 50.5 (2003), pages 663–672.

[356] M. Small. “Complex networks from time series: Capturing dynamics”. In: *IEEE International Symposium on Circuits and Systems (ISCAS2013)*. 2013, pages 2509–2512. ISBN: 978-1-4673-5762-3. DOI: 10.1109/ISCAS.2013.6572389.

[357] C. Sparrow. *The Lorenz Equations: Bifurcations, Chaos, and Strange Attractors*. Volume 41. Applied Mathematical Sciences. New York, NY: Springer New York, 1982. ISBN: 978-0-387-90775-8. DOI: 10.1007/978-1-4612-5767-7.

[358] K. E. K. St. John and L. A. Krissek. “The late Miocene to Pleistocene ice-rafting history of southeast Greenland”. In: *Boreas* 31.1 (2002), pages 28–35. DOI: 10.1111/j.1502-3885.2002.tb01053.x.

[359] D. J. Stanley. “Ionian Sea sapropel distribution and late Quaternary palaeoceanography in the eastern Mediterranean”. In: *Nature* 274 (1978), page 149.

[360] M. Stein et al. “Strontium isotopic, chemical, and sedimentological evidence for the evolution of Lake Lisan and the Dead Sea”. In: *Geochimica et Cosmochimica Acta* 61.18 (2003), pages 3975–3992.

[361] K. Steinhaeuser and N. V. Chawla. “Identifying and evaluating community structure in complex networks”. In: *Pattern Recognition Letters* 31.5 (2010), pages 413–421. DOI: 10.1016/j.patrec.2009.11.001.

[362] K. Steinhaeuser and A. A. Tsonis. “A climate model intercomparison at the dynamics level”. In: *Climate Dynamics* 42.5-6 (2013), pages 1665–1670. DOI: 10.1007/s00382-013-1761-5.

[363] S. L. Stevenson. “Significant changes to ENSO strength and impacts in the twenty-first century: Results from CMIP5”. In: *Geophysical Research Letters* 39.17 (2012), page L17703. DOI: 10.1029/2012GL052759.

[364] S. Stevenson et al. “Will There Be a Significant Change to El Niño in the Twenty-First Century?” In: *Journal of Climate* 25.6 (2012), pages 2129–2145. DOI: 10.1175/JCLI-D-11-00252.1.

[365] V. Stolbova et al. “Topology and seasonal evolution of the network of extreme precipitation over the Indian subcontinent and Sri Lanka”. In: *Nonlinear Processes in Geophysics* 21 (2014), pages 901–917. DOI: 10.5194/npg-21-901-2014.

[366] S. H. Strogatz. “Exploring complex networks”. In: *Nature* 410.6825 (2001), pages 268–276. DOI: 10.1038/35065725.

[367] F. Strozzi, J.-M. Zaldívar, and J. P. Zbilut. “Application of nonlinear time series analysis techniques to high-frequency currency exchange data”. In: *Physica A* 312.3–4 (2002), pages 520–538. DOI: 10.1016/S0378-4371(02)00846-4.

[368] F. Strozzi et al. *From complex networks to time series analysis and viceversa: Application to metabolic networks*. Technical report. EU Joint Research Centre, 2009, pages 1–52. DOI: 10.2788/25588.

[369] M. Stuiver and P. Grootes. “GISP2 oxygen isotope ratios”. In: *Quaternary Research* 53 (2000), pages 277–283.

[370] M. Stuiver, P. J. Reimer, and T. F. Braziunas. “High-Precision Radiocarbon Age Calibration for Terrestrial and Marine Samples”. In: *Radiocarbon* 40.03 (1998), pages 1127–1151. DOI: 10.1017/S0033822200019172.

[371] Y. Sun et al. “Seven million years of wind and precipitation variability on the Chinese Loess Plateau”. In: *Earth and Planetary Science Letters* 297.3-4 (2010), pages 525–535. DOI: 10.1016/j.epsl.2010.07.004.

[372] S. Sutton et al. “Evoked potential correlates of stimulus uncertainty”. In: *Science* 150 (1965), pages 1187–1188.

[373] S. Suzuki, Y. Hirata, and K. Aihara. “Definition of distance for marked point process data and its application to recurrence plot-based analysis of exchange tick data of foreign currencies”. In: *International Journal of Bifurcation and Chaos* 20.11 (2010), pages 3699–3708. DOI: 10.1142/S0218127410027970.

[374] M. Tahmasebpour et al. “Characterization of various structures in gas-solid fluidized beds by recurrence quantification analysis”. In: *Particuology* 11.6 (2013), pages 647–656. DOI: 10.1016/j.partic.2012.08.005.

[375] F. Takens. “Detecting Strange Attractors in Turbulence”. In: *Dynamical Systems and Turbulence*. Edited by D. Rand and L.-S. Young. Volume 898. Lecture Notes in Mathematics. Berlin: Springer, 1981, pages 366–381.

[376] L. Tan et al. “A Chinese cave links climate change, social impacts, and human adaptation over the last 500 years”. In: *Scientific Reports* 5 (2015), page 12284. DOI: 10.1038/srep12284.

[377] R. Telford, E. Heegaard, and H. Birks. “All age–depth models are wrong: but how badly?” In: *Quaternary Science Reviews* 23.1–2 (2004), pages 1–5. DOI: 10.1016/j.quascirev.2003.11.003.

[378] J. Theiler. “Spurious dimension from correlation algorithms applied to limited time-series data”. In: *Physical Review A* 34.3 (1986), pages 2427–2432. DOI: 10.1103/PhysRevA.34.2427.

[379] J. Theiler et al. “Testing for nonlinearity in time series: the method of surrogate data”. In: *Physica D* 58 (1992), pages 77–94. DOI: 10.1016/0167-2789(92)90102-S.

[380] M. Thiel, M. C. Romano, and J. Kurths. “Analytical Description of Recurrence Plots of white noise and chaotic processes”. In: *Izvestija vyssich ucebnych zavedenij/ Prikladnaja nelinejnaja dinamika – Applied Nonlinear Dynamics* 11.3 (2003), pages 20–30.

[381] M. Thiel, M. C. Romano, and J. Kurths. “How much information is contained in a recurrence plot?” In: *Physics Letters A* 330.5 (2004), pages 343–349. DOI: 10.1016/j.physleta.2004.07.050.

[382] M. Thiel, M. C. Romano, and J. Kurths. “Spurious Structures in Recurrence Plots Induced by Embedding”. In: *Nonlinear Dynamics* 44.1–4 (2006), pages 299–305. DOI: 10.1007/s11071-006-2010-9.

[383] M. Thiel et al. “Influence of observational noise on the recurrence quantification analysis”. In: *Physica D* 171.3 (2002), pages 138–152. DOI: 10.1016/S0167-2789(02)00586-9.

[384] M. Thiel et al. “Estimation of dynamical invariants without embedding by recurrence plots”. In: *Chaos* 14.2 (2004), pages 234–243. DOI: 10.1063/1.1667633.

[385] M. Thiel et al. “Twin Surrogates to Test for Complex Synchronisation”. In: *Europhysics Letters* 75.4 (2006), pages 535–541. DOI: 10.1209/epl/i2006-10147-0.

[386] M. Thiel et al. “Generating surrogates from recurrences”. In: *Philosophical Transactions of the Royal Society A* 366.1865 (2008), pages 545–557. DOI: 10.1098/rsta.2007.2109.

[387] L. L. Thurstone. “A law of comparative judgment”. In: *Psychological Review* 34.4 (1927), pages 273–286.

[388] R. Tiedemann, M. Sarnthein, and N. J. Shackleton. “Astronomic timescale for the Pliocene Atlantic δ^{18}O and dust flux records of Ocean Drilling Program site 659”. In: *Paleoceanography* 9.4 (1994), pages 619–638.

[389] C. E. de Toledo, J. C. de Araújo, and C. L. de Almeida. “The use of remote-sensing techniques to monitor dense reservoir networks in the Brazilian semiarid region”. In: *International Journal of Remote Sensing* 35.10 (2014), pages 3683–3699. DOI: 10.1080/01431161.2014.915593.

[390] A. Torfstein et al. “Impacts of abrupt climate changes in the Levant from Last Glacial Dead Sea levels”. In: *Quaternary Science Reviews* 69 (2013), pages 1–7.

[391] M. H. Trauth, J. C. Larrasoña, and M. Mudelsee. “Trends, rhythms and events in Plio-Pleistocene African Climate”. In: *Quaternary Science Reviews* 28 (2009), pages 399–411. DOI: 10.1016/j.quascirev.2008.11.003.

[392] M. H. Trauth et al. “Multiple landslide clusters record Quaternary climate changes in the northwestern Argentine Andes”. In: *Palaeogeography, Palaeoclimatology, Palaeoecology* 194.1–3 (2003), pages 109–121. DOI: 10.1016/S0031-0182(03)00273-6.

[393] M. H. Trauth and M. R. Strecker. “Formation of landslide-dammed lakes during a wet period between 40,000 and 25,000 yr B.P. in northwestern Argentina”. In: *Palaeogeography, Palaeoclimatology, Palaeoecology* 153.1-4 (1999), pages 277–287. DOI: 10.1016/S0031-0182(99)00078-4.

[394] M. H. Trauth et al. “Climate change and mass movements in the NW Argentine Andes”. In: *Earth and Planetary Science Letters* 179.2 (2000), pages 243–256. DOI: 10.1016/S0012-821X(00)00127-8.

[395] K. E. Trenberth et al. “Observations: Atmospheric Surface and Climate Change”. In: *Climate Change 2007 – The Physical Science Basis: Working Group I Contribution to the Fourth Assessment Report of the IPCC*. Edited by S. Solomon et al. Cambridge University Press, 2007. Chapter 3, pages 235–336.

[396] K. E. Trenberth. “The Definition of El Niño”. In: *Bulletin of the American Meteorological Society* 78.12 (1997), pages 2771–2777. DOI: 10.1175/1520-0477(1997)078<2771:TDOENO>2.0.CO;2.

[397] L. L. Trulla et al. “Recurrence quantification analysis of the logistic equation with transients”. In: *Physics Letters A* 223.4 (1996), pages 255–260. DOI: 10.1016/S0375-9601(96)00741-4.

[398] A. A. Tsonis. “Reconstructing Dynamics from Observables: The Issue of the Delay Parameter Revisited”. In: *International Journal of Bifurcation and Chaos* 17.12 (2007), pages 4229–4243.

[399] A. Tsonis and P. Roebber. “The architecture of the climate network”. In: *Physica A: Statistical and Theoretical Physics* 333 (2004), pages 497–504. DOI: 10.1016/j.physa.2003.10.045.

[400] A. Vaks et al. “Speleothems Reveal 500,000-Year History of Siberian Permafrost”. In: *Science* 340.6129 (2013), pages 183–186. DOI: 10.1126/science.1228729.

[401] M. Valsecchi et al. “Microsaccadic inhibition and P300 enhancement in a visual oddball task”. In: *Psychophysiology* 46 (2009), pages 635–644.

[402] D. B. Vasconcelos et al. “Spatial recurrence plots”. In: *Physical Review E* 73 (2006), page 056207. DOI: 10.1103/PhysRevE.73.056207.

[403] A. Venkatesan and M. Lakshmanan. “Interruption of torus doubling bifurcation and genesis of strange nonchaotic attractors in a quasiperiodically forced map: Mechanisms and their characterizations”. In: *Physical Review E* 63.2 (2001), page 026219. DOI: 10.1103/PhysRevE.63.026219.

[404] E. L. Venrick. “Phytoplankton in the California Current system off southern California: Changes in a changing environment”. In: *Progress in Oceanography* 104 (2012), pages 46–58. DOI: 10.1016/j.pocean.2012.05.005.

[405] E. Venrick et al. “The state of the California Current, 2002-2003: Tropical and subarctic influences vie for dominance”. In: *California Cooperative Oceanic Fisheries Investigations Report* 44 (2003), pages 28–60.

[406] D. C. Verdon and S. W. Franks. “Long-term behaviour of ENSO: Interactions with the PDO over the past 400 years inferred from paleoclimate records”. In: *Geophysical Research Letters* 33.6 (2006), page L06712. DOI: 10.1029/2005GL025052.

[407] J. D. Victor and K. P. Purpura. “Metric-space analysis of spike trains: theory, algorithms and application”. In: *Network: Computation in Neural Systems* 8.2 (1997), pages 127–164. DOI: 10.1088/0954-898X_8_2_003.

[408] D. Vretenar et al. “Nonlinear dynamics of giant resonances in atomic nuclei”. In: *Physical Review E* 60.1 (1999), pages 308–319. DOI: 10.1103/PhysRevE.60.308.

[409] R. Wackerbauer et al. “A Comparative Classification of Complexity Measures”. In: *Chaos, Solitons & Fractals* 4.1 (1994), pages 133–173. DOI: 10.1016/0960-0779(94)90023-X.

[410] D. E. Waliser and C. Gautier. “A Satellite-derived Climatology of the ITCZ”. In: *Journal of Climate* 6.11 (1993), pages 2162–2174. DOI: 10.1175/1520-0442(1993)006<2162:ASDCOT>2.0.CO;2.

[411] D. Wang et al. “Intensification and spatial homogenization of coastal upwelling under climate change”. In: *Nature* 518.7539 (2015), pages 390–394. DOI: 10.1038/nature14235.

[412] Y. Wang, B. Wang, and J.-H. Oh. “Impact of the Preceding El Nino on the East Asian Summer Atmosphere Circulation”. In: 79.1B (2001), pages 575–588. DOI: 10.2151/jmsj.79.575.

[413] Y.-M. Wang, J. L. Lean, and N. R. Sheeley, Jr. “Modeling the Sun’s Magnetic Field and Irradiance since 1713”. In: *The Astrophysical Journal* (2005). DOI: 10.1086/429689.

[414] Y. Wang et al. “The Holocene Asian monsoon: Links to solar changes and North Atlantic climate”. In: *Science* 308.5723 (2005), pages 854–7. DOI: 10.1126/science.1106296.

[415] H. Wanner et al. “Structure and origin of Holocene cold events”. In: *Quaternary Science Reviews* 30.21-22 (2011), pages 3109–3123. DOI: 10.1016/j.quascirev.2011.07.010.

[416] D. J. Watts and S. H. Strogatz. “Collective dynamics of ’small-world’ networks”. In: *Nature* 393 (1998), pages 440–442. DOI: 10.1038/30918.

[417] C. L. Webber, Jr. and N. Marwan. *Recurrence Quantification Analysis – Theory and Best Practices*. Cham: Springer, 2015, page 421. ISBN: 978-3-319-07154-1. DOI: 10.1007/978-3-319-07155-8.

[418] C. L. Webber, Jr. and J. P. Zbilut. “Dynamical assessment of physiological systems and states using recurrence plot strategies”. In: *Journal of Applied Physiology* 76.2 (1994), pages 965–973.

[419] C. L. Webber, Jr. and J. P. Zbilut. “Recurrence quantification analysis of nonlinear dynamical systems”. In: *Tutorials in Contemporary Nonlinear Methods for the Behavioral Sciences Web Book*. Edited by M. A. Riley and G. C. Van Orden. National Science Foundation (U.S.), 2005, pages 26–94. URL: http://www.nsf.gov/sbe/bcs/pac/nmbs/nmbs.jsp.

[420] C. L. Webber, Jr. et al. “Elucidating protein secondary structures using alpha-carbon recurrence quantifications”. In: *Proteins: Structure, Function, and Genetics* 44.3 (2001), pages 292–303. DOI: 10.1002/prot.1094.

[421] C. L. Webber, Jr. et al. “Simpler methods do it better: Success of Recurrence Quantification Analysis as a general purpose data analysis tool”. In: *Physics Letters A* 373 (2009), pages 3753–3756. DOI: 10.1016/j.physleta.2009.08.052.

[422] P. J. Webster. “The Asian Monsoon”. In: *The Asian Monsoon*. Edited by B. Wang. Springer Praxis Publishing, Chichester,UK, 2006, pages 3–66.

[423] B. J. West, E. L. Geneston, and P. Grigolini. “Maximizing information exchange between complex networks”. In: *Physics Reports* 468.1–3 (2008), pages 1–99. DOI: 10.1016/j.physrep.2008.06.003.

[424] R. C. Williamson and T. Downs. “Probabilistic arithmetic. I. Numerical methods for calculating convolutions and dependency bounds”. In: *International Journal of Approximate Reasoning* 4.2 (1990), pages 89–158. DOI: 10.1016/0888-613X(90)90022-T.

[425] A. Wolf et al. “Determining Lyapunov Exponents from a Time Series”. In: *Physica D* 16.3 (1985), pages 285–317. DOI: 10.1016/0167-2789(85)90011-9.

[426] K. Wolter and M. S. Timlin. “Measuring the strength of ENSO events: How does 1997/98 rank?” In: *Weather* 53.9 (1998), pages 315–324. DOI: 10.1002/j.1477-8696.1998.tb06408.x.

[427] R. Wu, Z. Z. Hu, and B. P. Kirtman. “Evolution of ENSO-related rainfall anomalies in East Asia”. In: *Journal of Climate* 16.22 (2003), pages 3742–3758. DOI: 10.1175/1520-0442(2003)016<3742:EOERAI>2.0.CO;2.

[428] K.-H. Wyrwoll et al. “Sensitivity of the Australian summer monsoon to tilt and precession forcing”. In: *Quaternary Science Reviews* 26.25-28 (2007), pages 3043–3057. DOI: 10.1016/j.quascirev.2007.06.026.

[429] P. Xian and R. L. Miller. “Abrupt Seasonal Migration of the ITCZ into the Summer Hemisphere”. In: *Journal of the Atmospheric Sciences* (2008). DOI: 10.1175/2007JAS2367.1.

[430] L. Xu et al. “Causes of landslide recurrence in a loess platform with respect to hydrological processes”. In: *Natural Hazards* 64.2 (2012), pages 1657–1670. DOI: 10.1007/s11069-012-0326-y.

[431] X. Xu, J. Zhang, and M. Small. “Superfamily phenomena and motifs of networks induced from time series”. In: *Proceedings of the National Academy of Sciences* 105.50 (2008), pages 19601–19605. DOI: 10.1073/pnas.0806082105.

[432] F. Xue and C. Liu. “The influence of moderate ENSO on summer rainfall in eastern China and its comparison with strong ENSO”. In: *Chinese Science Bulletin* 53.5 (2008), pages 791–800. DOI: 10.1007/s11434-008-0002-5.

[433] K. Yamasaki, A. Gozolchiani, and S. Havlin. “Climate Networks around the Globe are Significantly Affected by El Niño”. In: *Physical Review Letters* 100.22 (2008), page 228501. DOI: 10.1103/PhysRevLett.100.228501.

[434] H. Yan et al. “A record of the Southern Oscillation Index for the past 2,000 years from precipitation proxies”. In: *Nature Geoscience* 4.9 (2011), pages 611–614. DOI: 10.1038/ngeo1231.

[435] H. Yan et al. “Dynamics of the intertropical convergence zone over the western Pacific during the Little Ice Age”. In: *Nature Geoscience* 8.April (2015), pages 8–13. DOI: 10.1038/ngeo2375.

[436] G. Yancheva et al. “Influence of the intertropical convergence zone on the East Asian monsoon”. In: *Nature* 445.7123 (2007), pages 74–77. DOI: 10.1038/nature05431.

[437] H. Yang and Y. Chen. “Heterogeneous recurrence monitoring and control of nonlinear stochastic processes”. In: *Chaos* 24 (2014), page 013138. DOI: 10.1063/1.4869306.

[438] Y. Yang and H. Yang. “Complex network-based time series analysis”. In: *Physica A* 387 (2008), pages 1381–1386. DOI: 10.1016/j.physa.2007.10.055.

[439] J. P. Zbilut, A. Giuliani, and C. L. Webber, Jr. “Detecting deterministic signals in exceptionally noisy environments using cross-recurrence quantification”. In: *Physics Letters A* 246.1–2 (1998), pages 122–128. DOI: 10.1016/S0375-9601(98)00457-5.

[440] J. P. Zbilut, A. Giuliani, and C. L. Webber, Jr. “Recurrence quantification analysis as an empirical test to distinguish relatively short deterministic versus random number series”. In: *Physics Letters A* 267.2–3 (2000), pages 174–178. DOI: 10.1016/S0375-9601(00)00098-0.

[441] J. P. Zbilut, N. Thomasson, and C. L. Webber, Jr. “Recurrence quantification analysis as a tool for nonlinear exploration of nonstationary cardiac signals”. In: *Medical Engineering & Physics* 24.1 (2002), pages 53–60. DOI: 10.1016/S1350-4533(01)00112-6.

[442] J. P. Zbilut and C. L. Webber, Jr. “Embeddings and delays as derived from quantification of recurrence plots”. In: *Physics Letters A* 171.3–4 (1992), pages 199–203. DOI: 10.1016/0375-9601(92)90426-M.

[443] J. P. Zbilut and C. L. Webber, Jr. “Recurrence quantification analysis”. In: *Wiley Encyclopedia of Biomedical Engineering*. Edited by M. Akay. Hoboken, NJ, USA: John Wiley & Sons, 2006. DOI: 10.1002/9780471740360.ebs1355.

[444] J. P. Zbilut and C. L. Webber, Jr. “Recurrence quantification analysis: Introduction and historical context”. In: *International Journal of Bifurcation and Chaos* 17.10 (2007), pages 3477–3481. DOI: 10.1142/S0218127407019238.

[445] J. P. Zbilut, J.-M. Zaldívar, and F. Strozzi. “Recurrence quantification based Liapunov exponents for monitoring divergence in experimental data”. In: *Physics Letters A* 297.3–4 (2002), pages 173–181. DOI: 10.1016/S0375-9601(02)00436-X.

[446] J. P. Zbilut et al. “Use of Recurrence Plots in the Analysis of Heart Beat Intervals”. In: IEEE Computer Society Press, 1990, pages 263–266. DOI: 10.1109/CIC.1990.144211.

[447] J. P. Zbilut et al. “Charge and Hydrophobicity Patterning along the Sequence Predicts the Folding Mechanism and Aggregation of Proteins: A Computational Approach”. In: *Journal of Proteome Research* 3 (2004), pages 1243–1253. DOI: 10.1021/pr049883+.

[448] J. Zhang and M. Small. “Complex network from pseudoperiodic time series: Topology versus dynamics”. In: *Physical Review Letters* 96.23 (2006), page 238701. DOI: 10.1103/PhysRevLett.96.238701.

[449] J. Zhang et al. “Characterizing pseudoperiodic time series through the complex network approach”. In: *Physica D* 237.22 (2008), pages 2856–2865. DOI: 10.1016/j.physd.2008.05.008.

[450] K. Zhao et al. “A high-resolved record of the Asian Summer Monsoon from Dongge Cave, China for the past 1200 years”. In: *Quaternary Science Reviews* 122 (2015), pages 250–257. DOI: 10.1016/j.quascirev.2015.05.030.

[451] J. Zhou and K.-M. Lau. "Does a Monsoon Climate Exist over South America?" In: *Journal of Climate* 11.5 (1998), pages 1020–1040. DOI: 10.1175/1520-0442(1998)011<1020:DAMCEO>2.0.CO;2.

[452] N. V. Zolotova et al. "Long-term asymmetry in the wings of the butterfly diagram". In: *Astronomy & Astrophysics* 505 (2009), pages 197–201. DOI: 10.1051/0004-6361/200811430.

[453] Y. Zou et al. "Characterization of stickiness by means of recurrence". In: *Chaos* 17.4 (2007), page 043101. DOI: 10.1063/1.2785159.

[454] Y. Zou et al. "Distinguishing quasiperiodic dynamics from chaos in short-time series". In: *Physical Review E* 76.1 (2007), page 016210. DOI: 10.1103/PhysRevE.76.016210.

[455] Y. Zou et al. "Identifying complex periodic windows in continuous-time dynamical systems using recurrence-based methods". In: *Chaos* 20.4 (2010), page 043130. DOI: 10.1063/1.3523304.

[456] Y. Zou et al. "Inferring Indirect Coupling by Means of Recurrences". In: *International Journal of Bifurcation and Chaos* 21.4 (2011), pages 1099–1111. DOI: 10.1142/S0218127411029033.

[457] Y. Zou et al. "Power-laws in recurrence networks from dynamical systems". In: *Europhysics Letters* 98 (2012), page 48001. DOI: 10.1209/0295-5075/98/48001.

[458] G. Zurlini et al. "Investigating landscape phase transitions in Mediterranean rangelands by recurrence analysis". In: *Landscape Ecology* 33.9 (2018), pages 1617–1631. DOI: 10.1007/s10980-018-0693-1.

[459] M. H. Zweig and G. Campbell. "Receiver-operating characteristic (ROC) plots: a fundamental evaluation tool in clinical medicine". In: *Clinical Chemistry* 39.4 (1993), pages 561–577.

ISBN 978-3-00-064508-2